DR 1131

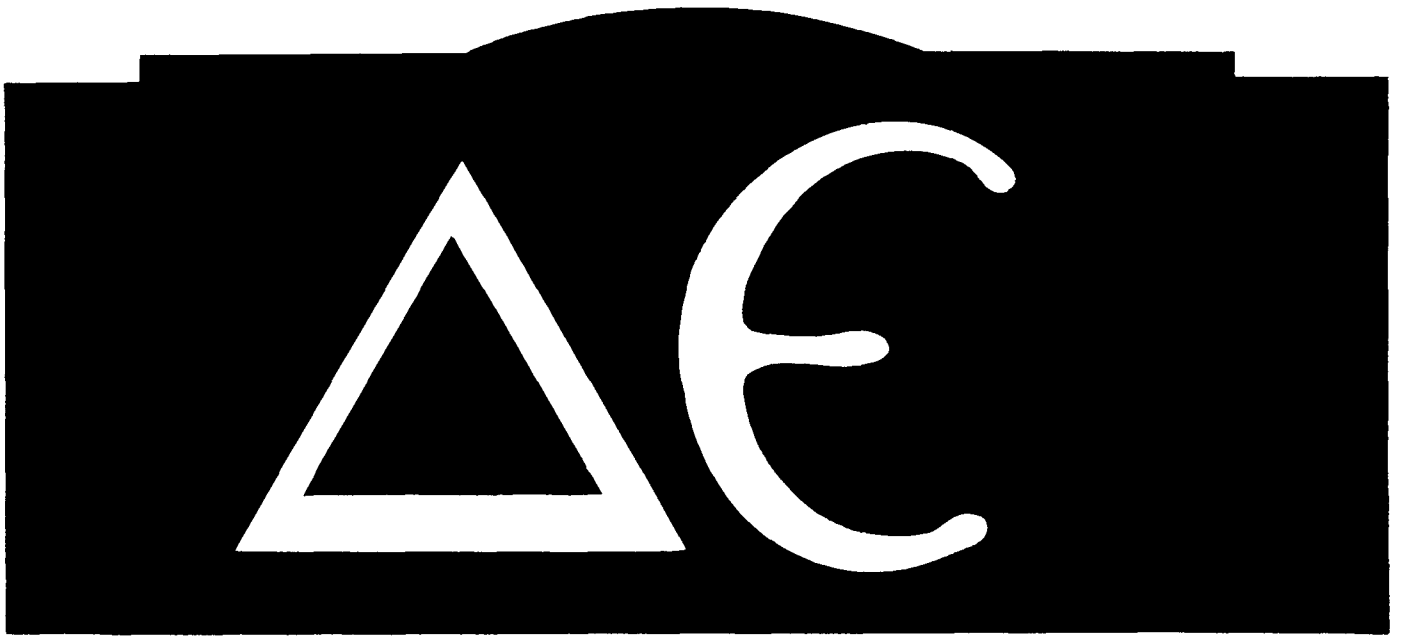

FATIGUE, TENSILE, AND RELAXATION BEHAVIOR OF STAINLESS STEELS

J. B. CONWAY, R. H. STENTZ, and J. T. BERLING

DISCLAIMER

TID-26135

FATIGUE, TENSILE, AND RELAXATION BEHAVIOR OF STAINLESS STEELS

by

J. B. CONWAY, R. H. STENTZ, and J. T. BERLING

Mar-Test Inc.
Cincinnati, Ohio

under a contract administered through the
University of Cincinnati
Cincinnati, Ohio

Prepared for
Division of Reactor Research and Development
U. S. Atomic Energy Commission

1975

Published by
Technical Information Center, Office of Information Services
UNITED STATES ATOMIC ENERGY COMMISSION

Available as TID 26135 for $7 60 from

National Technical Information Service
U S Department of Commerce
Springfield, Virginia 22161

International Standard Book Number 0 87079 013 1
Library of Congress Catalog Card Number 74 600115
AEC Distribution Category UC 25

Printed in the United States of America
USAEC Technical Information Center Oak Ridge Tennessee

January 1975

Foreword

This book is a detailed treatment of short-term tensile, relaxation, and low-cycle-fatigue behavior with special emphasis on stainless steels at elevated temperatures. Some new test procedures are highlighted and discussed rather thoroughly to focus on the types of information that can be obtained. Data generated using these procedures are summarized in a comprehensive manner, along with similar data reported in other studies. Methods of data analysis are also covered in considerable depth. Prediction techniques are reviewed along with cumulative-damage and creep–fatigue interaction considerations.

The U. S. Atomic Energy Commission, Division of Reactor Research and Development, in conjunction with the University of Cincinnati sponsored the preparation of this book.

Preface

The actual origin of this manuscript can properly be traced back to 1964 and the initiation of a high-temperature low-cycle-fatigue program by the U. S. Atomic Energy Commission, Fuels and Materials Branch, Division of Reactor Development and Technology (now known as the Division of Reactor Research and Development), Washington, D. C. This effort became a part of a high-temperature materials evaluation program which had been in effect since 1961 in the laboratories of the General Electric Company, Nuclear Materials and Propulsion Operation (name later changed to Nuclear Systems Program), located in Evendale, Ohio. This low-cycle-fatigue program at General Electric anticipated eventual AEC needs in pressure-vessel, piping, and fuel-cladding applications and was structured to focus on the best experimental approach to be employed, the acquisition of the necessary test facilities to assure an active implementation of this program, the identification of a comprehensive test matrix for evaluating a given material, the performance of all the tests required, and the development of a detailed approach to the analysis and correlation of the data obtained.

Following a detailed assessment of the available low-cycle-fatigue test procedures, we decided to use push–pull loading of inductively heated hourglass-shaped specimens and to use an elastic-hinge extensometer for diametral-strain measurements. This design provided a built-in mechanical advantage without moving parts, low contact pressure on the specimen, a geometry that is relatively insensitive to minor temperature fluctuations, and a large distance separating the heated specimen and the sensing element.

In anticipation of the strict requirements that would ultimately be placed on the accuracy of the test information, special emphasis was focused on the design and development of special closed-loop, servo-controlled, fatigue-testing machines that were uniquely suited to low-cycle-fatigue testing. These systems were built in-house and proved to possess the reliability desired. Induction-heating techniques were used exclusively since these were found to be both compatible with the extensometer design that was employed and particularly effective in generating the required specimen temperatures with the uniformity desired.

Another very important development associated with the low-cycle-fatigue program at General Electric Company, Nuclear Systems Program (GE–NSP), involved the conception, design, and fabrication of the analog strain computer. This device accepted instantaneous signals of the diametral strain and the axial load to provide an instantaneous computed value for the axial strain. Thus, for isotropic materials, a method was provided to allow low-cycle-fatigue tests to be performed in axial-strain control when a diametral-strain measurement was being made. This strain computer was described extensively in American Society for Testing and Materials,

Special Technical Publication 465, page 100, and it was this article that won for the authors (T. Slot, R. H. Stentz, and J. T. Berling) the 1971 ASTM Templin Award.

Materials selected for initial study at GE–NSP included AISI 304, 316, and 348 stainless steels obtained from the controlled heats of these materials, which were acquired by the General Electric Company's Hanford Laboratory for use in a program to study the effects of radiation on nuclear reactor materials. This material was obtained in the form of $\frac{5}{8}$-in.-diameter rod and was machined to yield the desired test-specimen configuration, after which all specimens received a stress-relief heat-treatment prior to test.

Test temperatures selected for use were 430, 650, and 816°C with strain ranges of about 0.5 to 4.0%. Strain-rate effects were studied over the range 4×10^{-5} to 4×10^{-3} sec^{-1} using a triangular wave form with zero mean strain. Subsequently strain rates to 4×10^{-6} sec^{-1} and to 1.6×10^{-2} sec^{-1} were evaluated to provide a fairly extensive study of the effects of this variable. And, once strain range, temperature, and strain-rate effects were outlined in some detail, particular attention was focused on hold-time effects. Hold periods at peak strain were introduced into only the tension portion of the cycle in some tests, only the compression portion of the cycle in other tests, and in both the tension and compression portions in other tests. Hold-period durations to 600 min were employed to provide a very extensive study of this parameter. Although the determination of hold-periods effects was the primary objective of this investigation, a significant amount of information was obtained relating to cyclic stress–strain behavior and relaxation phenomena.

Special mention should also be made of the technique development that led to the use of the servo-controlled fatigue machines in the measurement of short-term tensile properties at constant axial strain rate. Data obtained in such tests were used to correlate fatigue and tensile behavior over a wide range of temperatures.

The above remarks were made to emphasize the point that the AEC-sponsored low-cycle-fatigue program at GE–NSP led to the generation of a great deal of material-property data for the stainless steels involved. This information was considered to be extensive enough and important enough to warrant formal documentation in a summary publication. It was this consideration that stimulated the preparation of this publication.

As we traced the origin of this manuscript and briefly recounted some of the important events associated with this low-cycle-fatigue research effort, it was natural for us to reflect on the names of those men within the U. S. Atomic Energy Commission whose vision and long-range planning were responsible for the initiation and propagation of the work from which this publication has evolved. These men are J. M. Simmons, W. L. Rice, A. Van Echo, and K. Horton. The authors acknowledge their active participation and helpful cooperation.

June 1974

J. B. Conway
R. H. Stentz
J. T. Berling

Contents

Chapter 1

INTRODUCTION

In this introductory section the entire discussion is devoted to the basic principles of low-cycle fatigue with the suggestion that the reader refer to later sections for the fundamental concepts related to short-term tensile and relaxation behavior. This arrangement was adopted because the authors view this text as one dealing primarily with low-cycle fatigue and wish to emphasize the basic concepts of fatigue in this first chapter. Subsequent chapters gradually identify the very important relation between fatigue, tensile, and relaxation characteristics, and it was felt that a more logical arrangement would evolve by treating the fundamental concepts of tensile and relaxation properties in sections devoted exclusively to these specific areas.

DEFINITION AND CHARACTERIZATION OF FATIGUE

In general, the term "fatigue" relates to the special behavior pattern exhibited by materials in response to cyclic loading. Such loadings have been found to be particularly detrimental under certain conditions, resulting in fatigue damage in limited exposures and eventual fatigue failure (i.e., fracture) in continued exposures. The important aspect of such failures is that they occur in cyclic exposures when the peak stress is much lower than that which would be completely safe if imposed in a unidirectional (static) application.

Cyclic or repeated loading is particularly detrimental because this type of exposure gives rise to the formation of internal or surface microcracks that are propagated in continued exposures to reach, eventually, a critical size such that the remaining cross-sectional area is reduced to the point where it can no longer support the applied load. This general view of the fatigue process is essentially that proposed by Moore[1] and described recently by Gohn[2] in an excellent review of the mechanism of fatigue. In this view, "individual crystals of the metal are seen as yielding first at some point of localized weakness. This first yielding is considered to be a slipping action in which bonds between the atoms are broken and then frequently new and stronger bonds formed. Along with this slipping action, and perhaps caused by it, there seems to develop actual fractures, that is, the breaking of atomic bonds with no formation of new bonds. These fractures start minute cracks in the metal. At the ends of each minute crack the stress concentration is very high so that under successive loadings the cracks tend to spread like minute hacksaw cuts until insufficient sound metal is left to carry the load; at this point, sudden fracture occurs."

The development of a plausible explanation for the mechanism of fatigue has spanned more than a century. An excellent review of this development has been published by Gohn,[2] who, along with Peterson,[3] cited the work of Wohler[4] as the first source of fatigue experiments wherein special attention was given to the actual magnitude of the applied stress. Gohn reported that, although the experiments by Wohler were extremely important. these studies did not lead to any satisfactory explanation for the actual mechanism involved in fatigue failures. Many mechanisms and failure theories have appeared since, however, and, in the review by Gohn, special mention was made of the amorphous film theory, the dynamic theory, the attrition theory, the thermodynamic theory, and the strain-hardening theory. Gohn also gave special recognition to the excellent work of Gough and his associates[5-7] which has had an important bearing on the development of the mechanism proposed by Wood,[8] which is thought to provide the most plausible explanation for the fatigue mechanism.

From the comments made above, it is easy to appreciate the commonly accepted view that the three stages of fatigue involve crack initiation, crack propagation, and failure. An even finer subdivision of the fatigue process was described by Schijve[9] to indicate a progression from cyclic slip (which is the origin of the fatigue damage), to crack nucleation, to growth of microcracks, to growth of macrocracks, and to failure. These subdivisions, although admittedly qualitative, have assumed importance since they define the significant elements of the fatigue process that must be studied to obtain a detailed understanding of this phenomenon.

Fatigue life expresses the ability of a material to withstand a given cyclic exposure and is generally measured

in terms of the number of cycles to produce fracture. Exposure conditions are characterized by:

1. Stress or strain amplitude.
2. Mean stress or strain.
3. Cycling frequency.
4. Wave form of the stress or strain cycle.
5. Temperature.
6. Test environment.

Clearly, fatigue life at a given temperature and in a certain environment has significance only when associated with a specific description of the exposure cycle.

Another important facet of fatigue life is the differentiation that has evolved between high-cycle and low-cycle fatigue. The dividing line is important, although not well defined. Some definitions of the low-cycle-fatigue regime include cycles to failure below 100,000 cycles, whereas others set the limit at 10,000 cycles. A distinguishing feature of the low-cycle-fatigue regime is that the peak stresses are above the tensile yield strength, and hence the strains induced usually have a noticeable plastic component. In high-cycle fatigue the strains are confined, at least from a macroscopic point of view, to the elastic region. The differentiation between high- and low-cycle fatigue is most logical when based on elastic- and plastic-strain differences, even though it is really no great obstacle to have no clear and distinct dividing line between the two regimes.

Many different approaches to the measurement of fatigue behavior have evolved over the years, and these have served as the basis for various general classifications of fatigue behavior depending on the method of testing.[3,10] One broad classification has been defined which differentiates between uniaxial and biaxial investigations, and another classification has been described[10] which is related more specifically to actual test procedures and uses the categories of rotating bending, repeated bending, axial loading, torsional loading, and combined stressing. Still another classification[3] differentiates between load cycling and strain cycling and, of course, relates to the mode of control employed in the fatigue test. An extension of this latter classification has recently been recognized[11,12] depending on whether the strain control is based on diametral or axial strain.

Since all the above approaches imply isothermal testing, one other broad classification might distinguish between isothermal and nonisothermal determinations. Environmental variations could yield still another classification of fatigue evaluations. The wide variety of testing modes available introduces a long-recognized complexity into fatigue evaluations, and much remains to be done before an interrelation between the different types of fatigue measurements can be identified.

FATIGUE VARIABLES

Because of the cyclic nature of fatigue exposures, the number of independent variables involved is somewhat greater than that associated with static evaluations. In addition to specifying temperature and environment, it is also necessary to specify stress or strain range or amplitude, cycling frequency or strain rate, and stress or strain wave form. With these conditions of restraint specified, the fatigue test can yield a wide variety of material information. For example, in an axial-strain-controlled low-cycle-fatigue evaluation using hourglass-shaped specimens, the following data are typical:

1. Total, plastic, and elastic components of axial strain.
2. Total, plastic, and elastic components of diametral strain.
3. Stress range or amplitude as a function of imposed cycles; this determines whether cyclic hardening or softening is exhibited and can also be used with data from other tests to define the cyclic stress–strain curve for the material.
4. Cycles to failure.
5. Cycles to crack initiation.
6. Cycles to any specified reduction from the steady-state load.

When the strain is the controlled variable, the specimen is deformed within the same strain limits in each cycle. An example of a triangular strain wave is shown in Fig. 1.1 to define strain amplitude, strain range, and the time corresponding to one cycle. Related parameters are frequency (the reciprocal of the cycle time) and strain rate. In the triangular wave form, the strain varies linearly with time, and hence the strain rate is given by the slope of the linear segments in Fig. 1.1. For example, the slope of the linear segment OA is the strain rate and is

$$\text{Strain rate} = \dot{\epsilon}_t = \frac{\text{strain amplitude}}{\text{cycle time}/4} \tag{1.1}$$

Since the frequency (f) is inversely related to cycle time, Eq. 1.1 leads to

$$\dot{\epsilon}_t = 2f\,\Delta\epsilon_t \tag{1.2}$$

where $\Delta\epsilon_t$ is the total strain range (the subscript t on $\dot{\epsilon}$ and $\Delta\epsilon$ denote values based on total strain, including the elastic and plastic components).

Figure 1.1(a) shows a strain cycle in which the wave form is symmetrical about the abscissa. In such a cycle the peak tensile and compressive strains have the same absolute magnitude, and, of course, the mean strain is zero. This is a very common type of testing cycle and represents what is termed "completely reversed" strain cycling. A variation of this is shown in Fig. 1.1(b) for mean strain that is not zero.

Stress cycles corresponding to the strain cycles shown in Fig. 1.1 are presented in Fig. 1.2 to define stress amplitude and stress range. Some curvature is noted in the stress–time trace to indicate that the stress rate is not constant throughout the cycle.

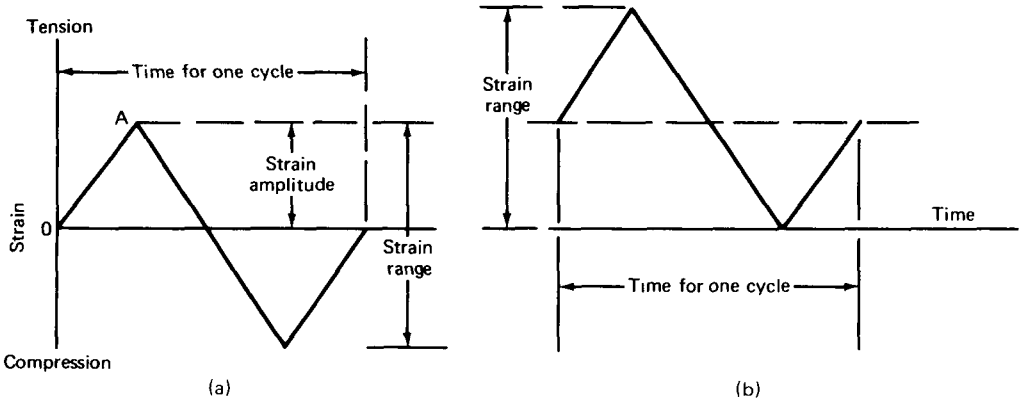

Fig. 1.1 Typical triangular strain waves.

Some important definitions[10] in terms of stress values are clearly illustrated through reference to Fig. 1.2. These are:

Maximum stress ($\sigma_{max.}$), the highest algebraic value of the stress in the cycle; tensile stress is considered positive, and compressive stress is considered to be negative.

Minimum stress ($\sigma_{min.}$), the lowest algebraic value of the stress in the cycle.

$$R = \frac{\text{minimum stress}}{\text{maximum stress}} = \frac{\sigma_{min.}}{\sigma_{max.}}$$

and

$$A = \frac{\text{alternating stress or stress amplitude}}{\text{mean stress}} = \frac{\sigma_a}{\sigma_m}$$

$$= \frac{(\sigma_{max.} - \sigma_{min.})/2}{(\sigma_{max.} + \sigma_{min.})/2} = \frac{\sigma_{max.} - \sigma_{min.}}{\sigma_{max.} + \sigma_{min.}}$$

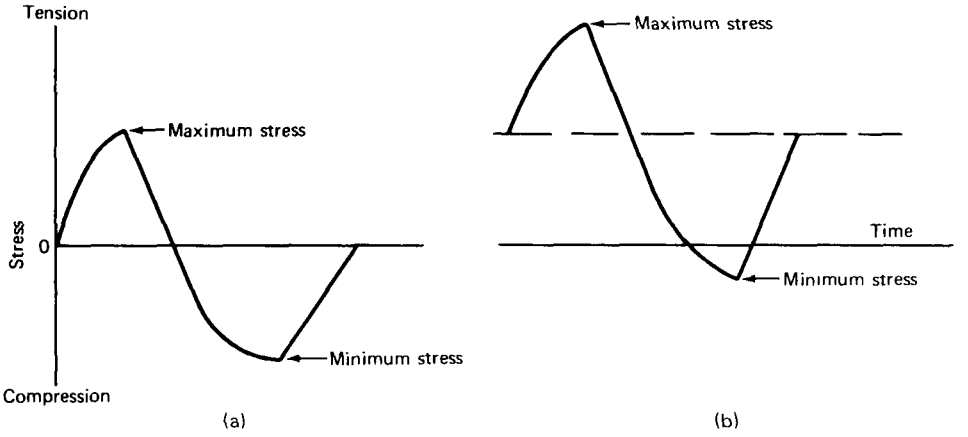

Fig. 1.2 Stress wave forms corresponding to the strain wave forms in Fig. 1.1.

Stress range ($\Delta\sigma$), the algebraic difference between the maximum and minimum stress in one cycle; i.e., $\sigma_{max.} - \sigma_{min.}$.

Stress amplitude (σ_a), one-half of the stress range; i.e., $\Delta\sigma/2$.

Mean stress (σ_m), the algebraic mean of the maximum and minimum stress values in one cycle; i.e., $(\sigma_{max.} + \sigma_{min.})/2$.

Two other definitions are in common usage to provide an exact description of the stress (or strain) cycle. Both are stress ratios and usually identified by the letters R and A; thus:

For the cycle in Fig. 1.2(a), it is obvious that R = −1 and A = infinity. It is also obvious that R and A are simply related through the equality:

$$A = \frac{R - 1}{R + 1} \tag{1.3}$$

Figure 1.3 graphically illustrates some typical stress cycles, along with the corresponding R and A values.

Other commonly used stress and strain wave forms are shown in Fig. 1.4. Hold periods have a direct effect on the cycle time and can have a pronounced effect on the fatigue life. When hold periods on strain are involved, the total

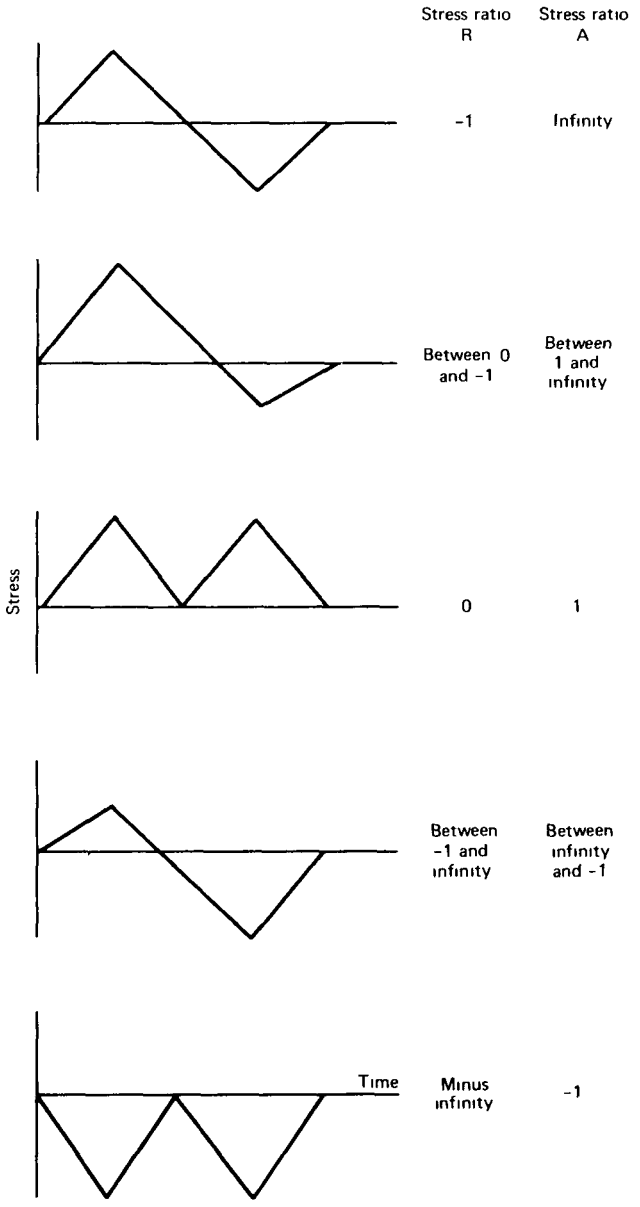

Fig. 1.3 Typical stress cycles.

strain is kept constant at the peak value, and stress relaxation takes place in each hold period. For constant-stress hold periods, the strain increases because of creep during the hold-time interval. Creep–fatigue interactions arise when any of the wave forms in Fig. 1.4 are used.

FATIGUE DATA

Hysteresis Loops

As previously noted, a fatigue test yields a great deal more than just a measurement of the fatigue life. One extremely valuable piece of information is the hysteresis loop that provides, in graphical form, a detailed description of the stress–strain behavior in a given cycle. Figure 1.5 is a schematic illustration of the development of a series of hysteresis loops. In this instance the loading begins at point A when a compressive force is applied. Elastic straining occurs initially, followed by yielding until a specified strain amplitude is reached at point B. At this point the load is reversed, and the material unloads elastically, followed by a tensile loading (and yielding) to attain point C. The strain amplitude at point C is equal and opposite to that observed at point B to define, of course, a completed reversed strain cycle.

At point C the desired total strain (i.e., elastic plus plastic) is reached, and the load is reversed again to trace another strain cycle through point D and back to E. It is important to note in Fig. 1.5 that the cycling always occurs between the same strain range, $\Delta\epsilon_t$. Also note in this graph that the stress necessary to attain a given strain amplitude increases with each cycle to define "cyclic strain hardening." A reverse effect is also possible to define "cyclic strain softening."

Eventually (usually within 10 or 20% of the fatigue life), the hysteresis loops become coincident to define a stabilized or saturated stress–strain behavior pattern. This stabilization or saturation indicates that the stress necessary to attain the given strain amplitude has assumed a constant value that will be reproduced in all subsequent cycles until noticeable specimen cracking develops. At this point the stress range required to achieve a given strain range decreases to reflect the onset of specimen failure.

A stable hysteresis loop is shown schematically in Fig. 1.6 to illustrate the important features of such a graph. Of course, the vertical tip-to-tip distance defines the stress range, and the values for $\sigma_{max.}$ and $\sigma_{min.}$ are read as the distances above and below the zero-stress abscissa. The horizontal tip-to-tip distance, as already stated, represents the total strain range ($\Delta\epsilon_t$) and consists of elastic and plastic components. Since the elastic strain range ($\Delta\epsilon_e$) is given by $\Delta\sigma/E$, it follows that this quantity is given by the sum of the two ϵ_e values in Fig. 1.6. Consequently the plastic strain range ($\Delta\epsilon_p$) is given by the width of the hysteresis loop measured along the zero-stress abscissa in this case. Another feature of the hysteresis loop is that the slope of the A segments (load-reversal regime) is equal to the modulus of elasticity of the material.

Figure 1.7 shows some typical hysteresis loops for tests under diametral-strain control. As the total diametral strain range is increased, more and more plastic strain is involved, and the width of the loops increases. The height of the loops increases to reflect the larger stresses required to obtain the larger strain. Loops for two different temperatures reflect the increase in stress range, associated with the attainment of the same strain range, as the temperature is lowered.

Hysteresis loops reflecting the behavior observed in strong, tough, and ductile materials,[14] tested at the same total strain range, are shown schematically in Fig. 1.8. Note

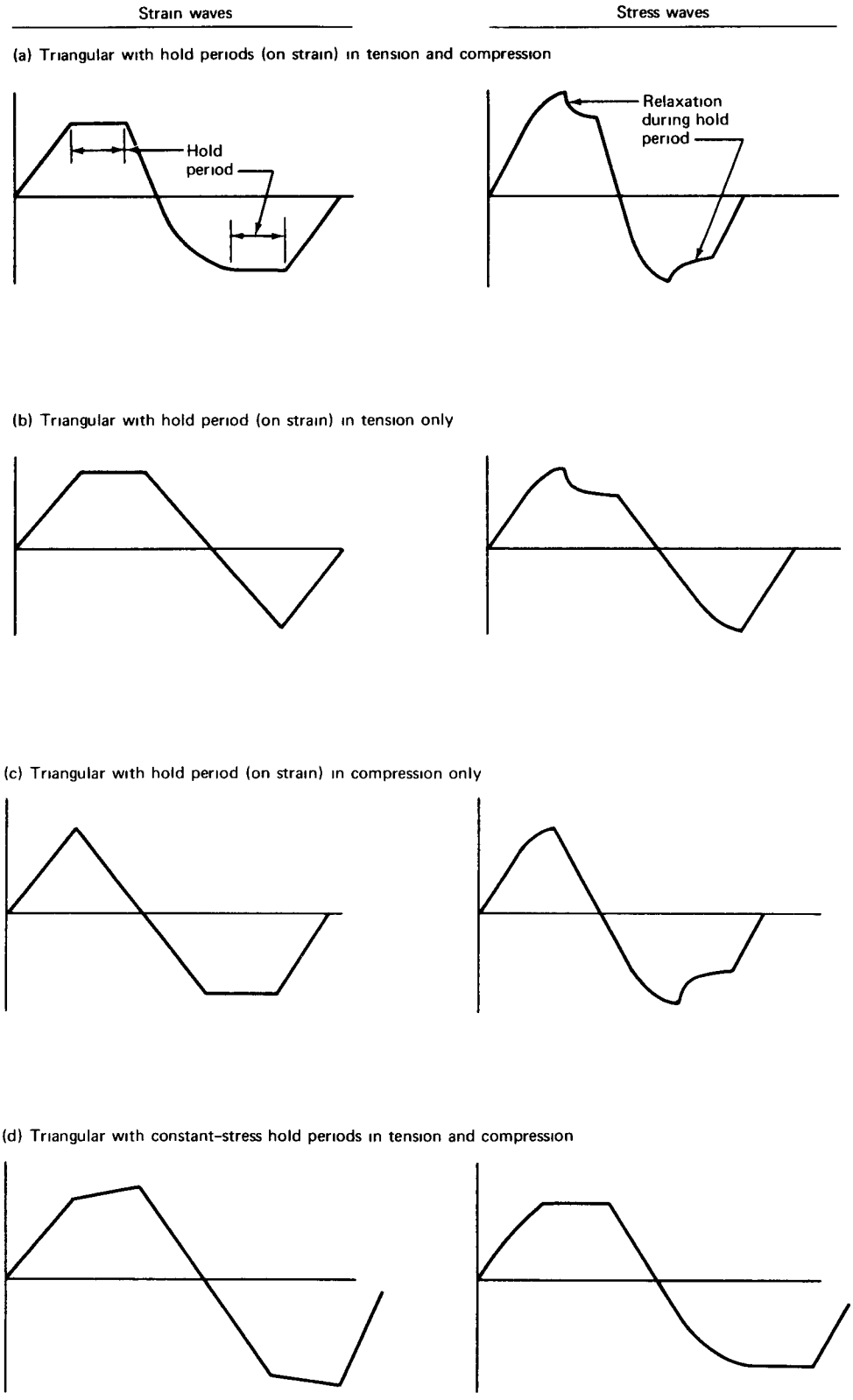

Fig. 1.4 Typical stress and strain waves.

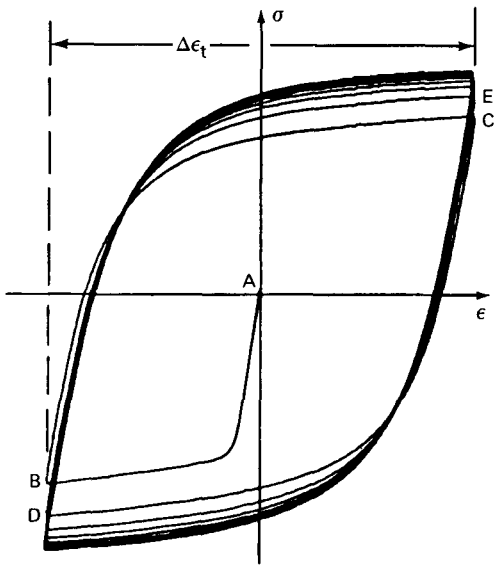

Fig. 1.5 Schematic illustration of the development[13] of hysteresis loops. Frequency = 3 cycles/min. $\Delta\epsilon_t = 1.6\%$. (From Ref. 13.)

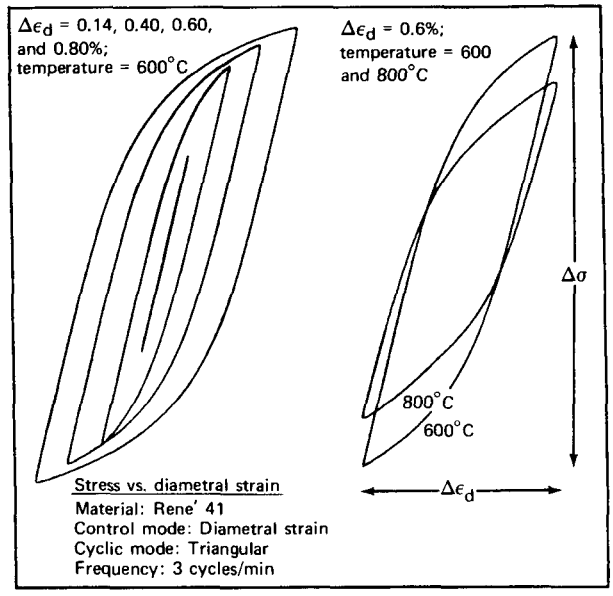

Fig. 1.7 Typical hysteresis loops obtained in diametral-strain control. (From Ref. 13.)

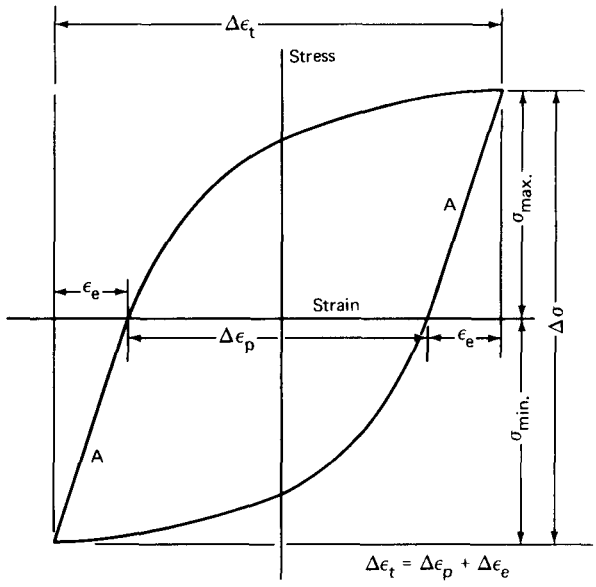

Fig. 1.6 Schematic version of a hysteresis loop.

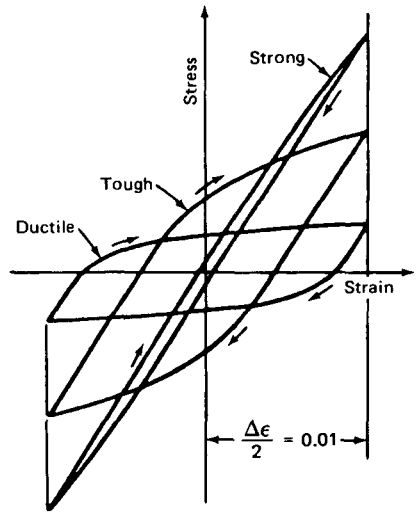

Fig. 1.8 Hysteresis loops showing idealized stress–strain behavior for different types of material. (From Ref. 14.)

the different stress ranges and the different plastic strain ranges corresponding to the different types of materials.

Fatigue Life

Load Cycling. Load-cycling results provide a definition of fatigue life in terms of the applied stress. Such information has led to the familiar S–N curve (stress amplitude, S, vs. N, the number of cycles to failure) of the form shown schematically in Fig. 1.9 to indicate an increase in fatigue life as the stress amplitude is decreased and an eventual trend toward a stress asymptote. This leveling off of the S–N curve defines, of course, the fatigue limit as the stress amplitude below which fatigue failure will not occur. For those materials which fail to exhibit a definite horizontal segment in the S–N curve, the fatigue limit is chosen as the stress amplitude corresponding to 10^7 or 10^8 cycles.

Previously, many S–N curves were represented by two linear segments on semilogarithmic coordinates (Fig. 1.10), but the current trend is to represent such data in the form of a flattened S-shaped curve on logarithmic coordinates (Fig. 1.11). Figure 1.11 shows the regions of the endurance

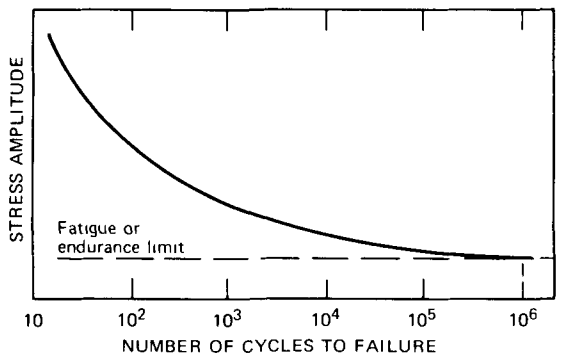

Fig. 1.9 Schematic representation of S–N curve.

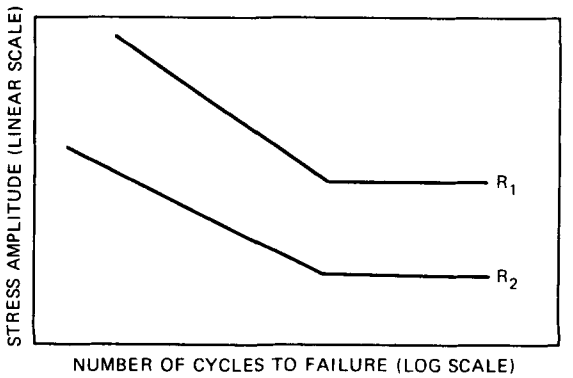

Fig. 1.10 Representation of S–N curve using two linear segments.

limit, the characteristic shape of such representations, and the location of the ultimate tensile and yield strengths. A family of S–N curves for various R ratios is shown in Fig. 1.12 (ordinate is maximum stress) to indicate a decided effect of mean stress on the fatigue life. The dashed vertical line in Fig. 1.12 identifies maximum stress values for a constant fatigue life of 10^7 cycles.

Figure 1.13 is a fairly detailed S–N chart that illustrates the behavior of notched and unnotched specimens; the endurance limit is indicated as S_f.

Strain Cycling. When strain rather than stress is the controlled parameter, the test specimen is subjected to a certain total strain range at a preselected frequency (or strain rate) and strain ratio (R or A written in terms of strain values). As the strain range decreases, the cyclic fatigue life increases to define a behavior pattern that is quite similar to that given by the S–N curve derived from load-controlled evaluations. In the usual graphical presentation on logarithmic coordinates, the characteristic shape shown in Fig. 1.14 is obtained to reveal a behavior pattern very similar to that given in Fig. 1.9. Note the tendency toward a fatigue limit in the lower strain-range regime and a continually increasing curvature as the strain range is increased. This reflects the well-established observation that a given incremental reduction in the total strain range leads

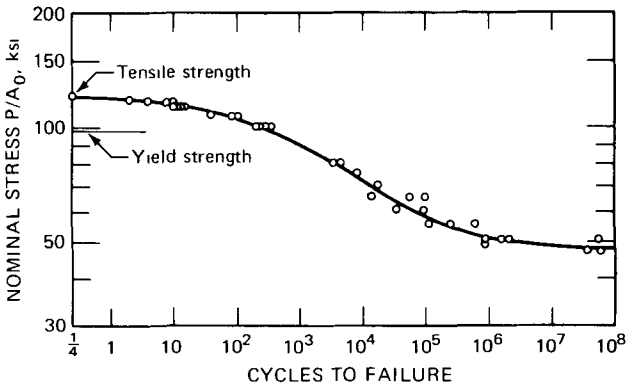

Fig. 1.11 S–N curve[3] for SAE 4130 normalized-steel-sheet specimens (unnotched); mean stress equal to zero. (From Ref. 3.)

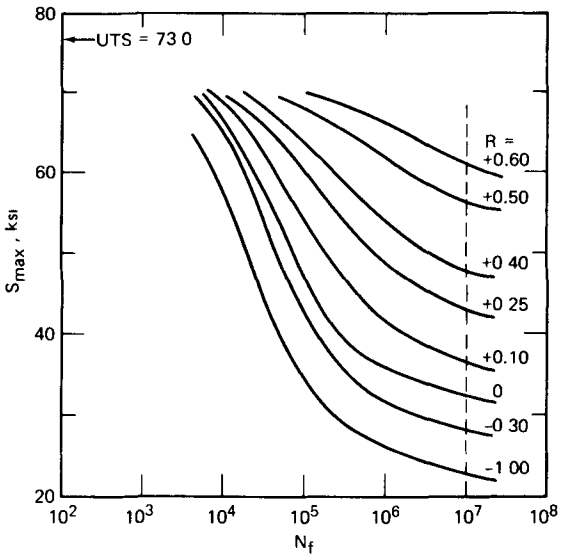

Fig. 1.12 A family of S–N curves[1,5] showing the effect of the R ratio on fatigue life for axial loading of 2024-T3 aluminum alloy.

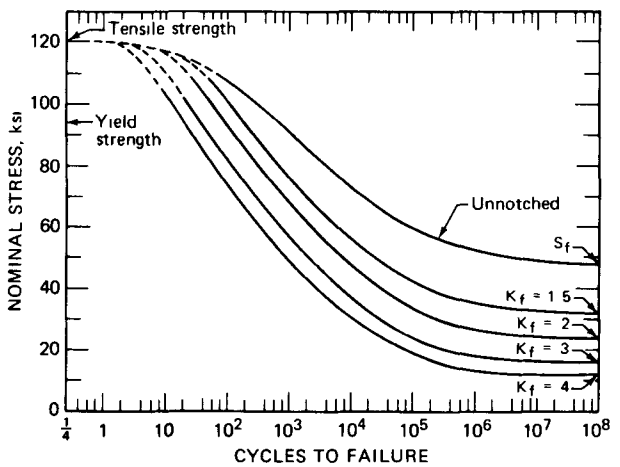

Fig. 1.13 S–N chart[3] for notched and unnotched specimens of SAE 4130 normalized steel; axial loading with R ratio of −1.0. (S_f gives the unnotched fatigue limit.) (From Ref. 3.)

to a comparatively small increase in fatigue life when it occurs in the high-strain-range region and a comparatively large increase in fatigue life when it occurs in the low-strain-range region.

In the low-strain-range region of Fig. 1.14, the strain is primarily elastic, and the stress range is close to that given by the product of the modulus of elasticity and the strain

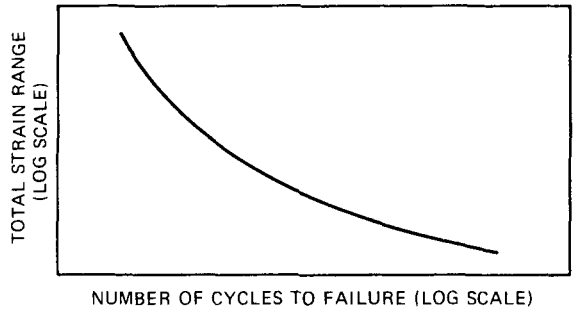

Fig. 1.14 Typical form of a low-cycle-fatigue curve relating total strain range and cycles to failure.

range. Furthermore, a given stress range in this regime should correspond to a cyclic fatigue life that is identical with, or at least comparable to, that which would be obtained in a load-cycling evaluation. Of course this would mean that the endurance limit measured in a strain-cycling evaluation should be essentially the same as that measured in a load-cycling study. No confirmation has been made of this point as yet, but it appears reasonable to predict that such an observation would evolve from an experimental evaluation of this point.

Some mention should also be made of the very high strain-range regime in Fig. 1.14 and how this compares with that shown in Fig. 1.9. Experimental studies in the regime above a strain range of 5 to 10% usually encounter the problem of specimen buckling in completely reversed testing (i.e., A ratio of infinity), and hence there are no data points to define the shape of the curve in this region. However, if the first straining is in a tensile direction, the fracture ductility would define a single data point to be located at a cyclic life of ¼ cycle. The use of such a data point would cause the curve shape in Fig. 1.14 to assume that shown in Fig. 1.9; two examples of this are given in Fig. 1.15. Fatigue data for 304 stainless steel and Incoloy 800 (see Chap. 3) were used along with the fracture ductility for these materials at the test conditions involved. A curve drawn to accommodate the tensile ductility could have the flattened S-shape characteristic of the usual S–N curve.

For strain-controlled fatigue evaluations, special attention has been devoted to the elastic and plastic components of the total strain range. Both the elastic strain range and the plastic strain range (the sum of these is, of course, the total strain range) have usually been considered to be simply related to N_f through the following expressions:

$$\Delta\epsilon_e = AN_f^{-a} \tag{1.4}$$

$$\Delta\epsilon_p = BN_f^{-b} \tag{1.5}$$

where A, B, a, and b are material constants. These formulations identify linear relations on logarithmic coordinates to define the behavior pattern shown in Fig. 1.16a. Note that the plastic line is steeper than the elastic line and that the addition of the two lines yields the curved relation described in Fig. 1.14.

Special recognition[16,17] has been given to Eq. 1.5 because it is viewed as one of the important equalities in fatigue evaluations. According to Coffin,[17] the relation between the plastic strain range and the fatigue life is given by

$$\Delta\epsilon_p = \frac{\epsilon_f}{2} N_f^{-1/2} \tag{1.6}$$

where ϵ_f is the tensile ductility. This relation, although extremely valuable, is only approximate and must be used with caution since many cases are known where the exponent on N_f differs from $-1/2$ and the constant is different from $\epsilon_f/2$. A similar equation was proposed by Manson[16,18] in the form of Eq. 1.5, where the value of b was taken to be 0.6 to yield:

$$\Delta\epsilon_p = \epsilon_f^{0.6} N_f^{-0.6} \tag{1.7}$$

Both the Coffin and Manson equations are discussed in more detail in Chap. 4.

Assessment of the general features of Fig. 1.16a shows that the plastic-strain component dominates in the high-strain-range region, whereas the elastic-strain component is of primary importance in the low-strain-range region. This observation also leads to the generalization that high ductility is important in a material if good resistance to large strain ranges is to be obtained, and a high tensile strength is desirable when exposures in the low-strain-range region are to be encountered. Figure 1.16b provides an

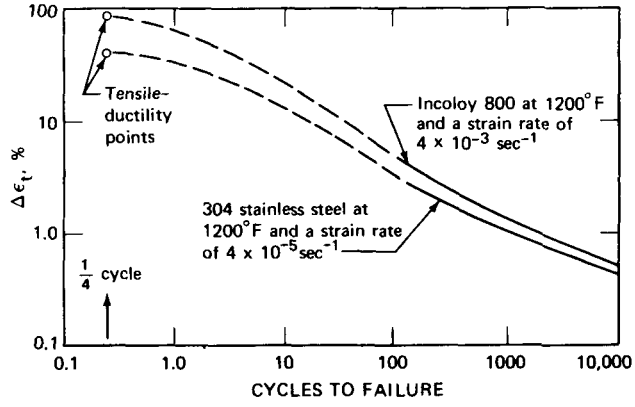

Fig. 1.15 Graph of $\Delta\epsilon_t$ vs. N_f to show relation with tensile-ductility values.

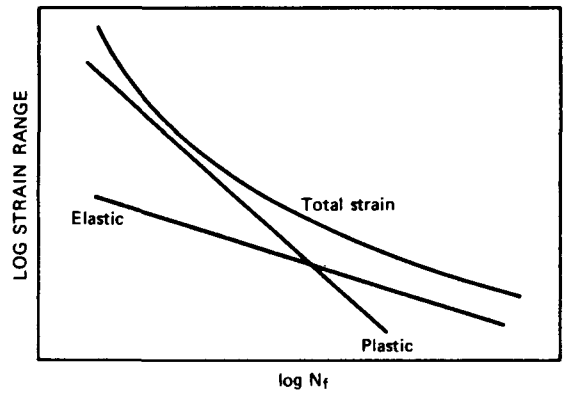

Fig. 1.16a Schematic of a logarithmic graph of strain range vs. cycles to failure.

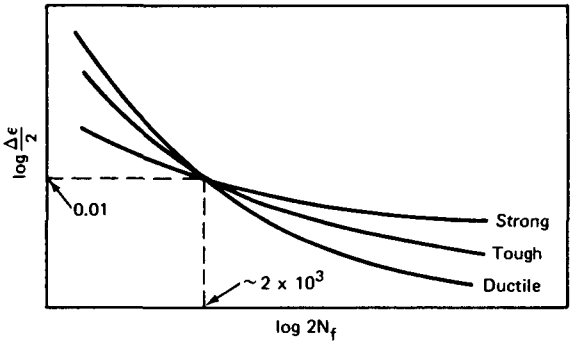

Fig. 1.16b Schematic representation[14] of different types of material behavior when plotted in terms of strain amplitude and number of reversals (i.e., 2 x N_f) to failure. (From Ref. 14.)

interesting comparison of these considerations to indicate the fatigue life for strong, tough, and ductile materials. In the low-strain-range region, the strong material exhibits a better fatigue resistance; but, since strong materials usually have low ductility, these types of materials have a lower fatigue resistance at the higher strain ranges. The reverse is true for the ductile material, whereas the tough material exhibits intermediate behavior.

All the curves in Fig. 1.16b are shown to cross at the same point. This has been found to be fairly typical and has led to the general rule of thumb that materials exhibit a fatigue life of 1000 cycles when subjected to a total strain range of 2%. This generalization[3] has been referred to as "Peterson's rule" and seems to offer a fairly good approximation of fatigue behavior.

Cyclic Strain Hardening and Strain Softening

For most materials the stress–strain behavior is affected by reversed loading and cyclic straining. As a result the first tensile-loading trace only applies to the initial portion of the first fatigue cycle. Even the corresponding trace obtained when the sample is cycled into compression will be slightly different from the trace obtained in the first loading. This phenomenon is shown in Fig. 1.17 for a test in which a specimen is subjected to completely reversed strain cycling within a fixed total strain range. Unloading begins at point A and follows along the path AO′; compressive loading begins at O′ and continues until the strain is reversed at A′. Cycling back into tension follows the path A′A″, and the stress at A″ is slightly higher than that at A. This strengthening is termed "cyclic strain hardening" and continues for a definite period. Eventually a stable or equilibrium condition exists, and a stable hysteresis loop is obtained which will describe the cycling stress vs. strain behavior until the specimen begins to show signs of internal damage.

During the strain-hardening sequence noted in Fig. 1.17, the stress range gradually increases, and the width of the hysteresis loop decreases. This of course is consistent with the equation in Fig. 1.6 which suggests that, for a

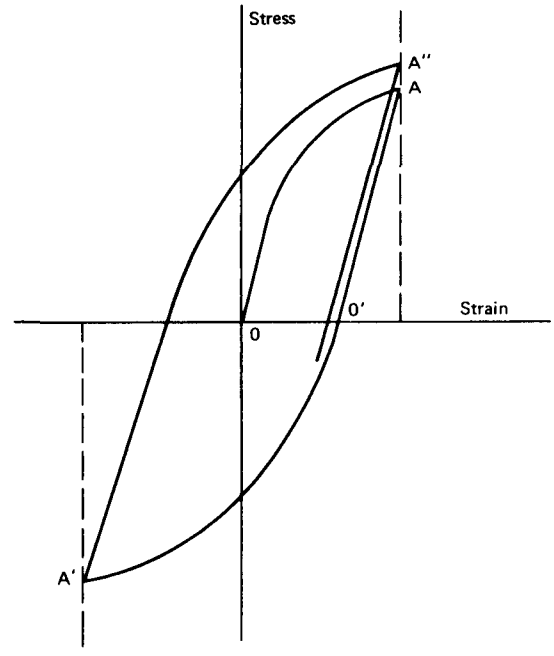

Fig. 1.17 Schematic stress–strain behavior for a material that exhibits cyclic strain hardening.

constant value of $\Delta\epsilon_t$, the value of the plastic strain range (width of hysteresis loop) decreases as the elastic strain range increases due to the increase in $\Delta\sigma$ brought about by the cyclic hardening.

Cyclic softening causes the stress range to decrease with the number of strain cycles until an equilibrium condition is reached. Once a stable hysteresis loop is obtained, this will persist until internal damage is noted. Mixed behavior (e.g., cyclic hardening followed by cyclic softening) is also a possibility and provides a fairly interesting material phenomenon.

In general,[19,20] materials that are initially soft will exhibit cyclic hardening, and materials that are initially

hard will probably exhibit cyclic softening. All metals with a ratio of ultimate strength to yield strength (σ_u/σ_{ys}) greater than 1.4 will cyclically harden; cyclic softening will be observed in those metals where the σ_u/σ_{ys} ratio is less than 1.2; both cyclic softening and cyclic hardening will be observed in the intermediate range (σ_{ys} is the 0.2% offset yield strength).

A study[21] of the cyclic hardening and softening characteristics of copper and steel yielded the results shown in Figs. 1.18 and 1.19. Annealed specimens tested at various strain ranges showed a definite cyclic hardening, whereas hard material showed a cyclic softening. Similar behavior was noted[22] in tests of annealed and cold-worked 1100 aluminum, as shown in Fig. 1.20. Cyclic hardening was observed in annealed materials, and cyclic softening was found in material that was prestrained 21% prior to use. After a certain number of strain cycles, the same stress range was attained independent of the condition of the starting materials. This interesting observation was not considered to be applicable to all materials, since a study of Figs. 1.18 and 1.19 fails to confirm the same behavior.

Figure 1.21 is a typical stress vs. time trace obtained[23] in a strain-controlled low-cycle-fatigue evaluation of annealed AISI 304 stainless steel, tested in air at 1500°F, a strain range of 3.26%, and a frequency of 3.33 cycles/min. The increase in the stress range within the first few strain cycles is clearly in evidence, as is the stable or equilibrium

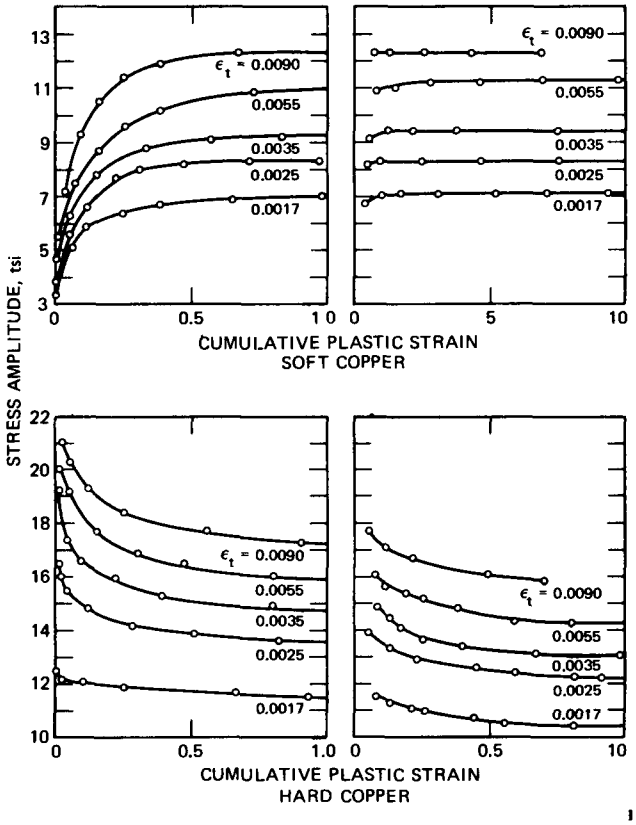

Fig. 1.18 Cyclic hardening and softening curves for copper.[21] [From D. S. Dugdale, *J. Mech. Phys. Solids*, 7: 138 (1959).]

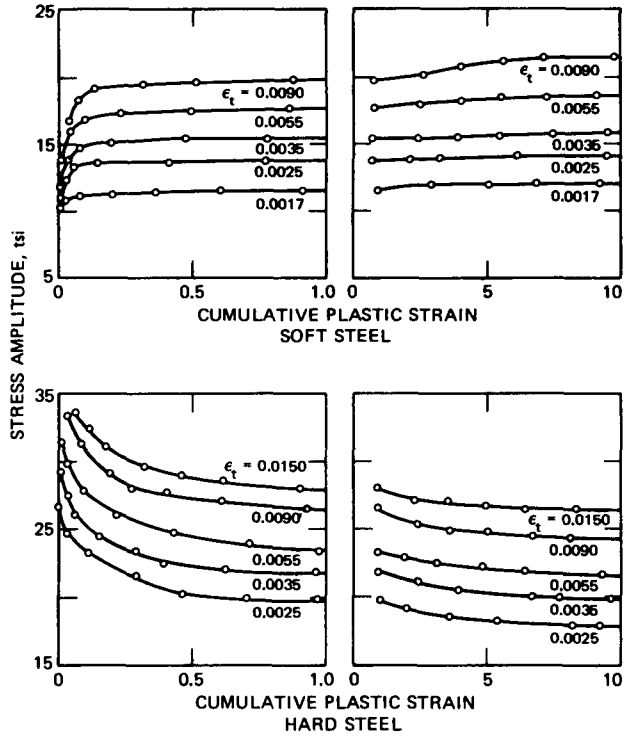

Fig. 1.19 Cyclic hardening and softening curves for steel.[21] [From D. S. Dugdale, *J. Mech. Phys. Solids*, 7: 139 (1959).]

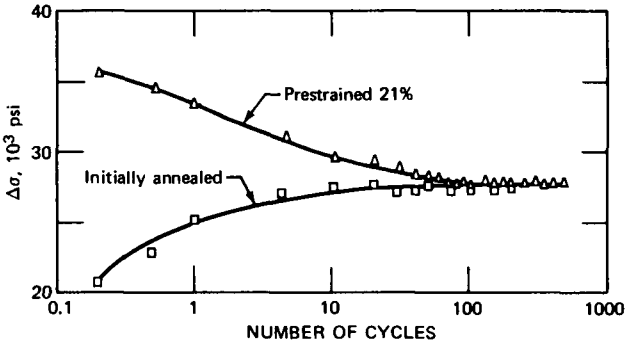

Fig. 1.20 Cyclic hardening and softening of 1100 aluminum tested[22] at room temperature using a strain range of 6%. (From Ref. 22.)

value that is achieved after some 60 cycles. This stress range remains relatively constant for the next 100 cycles or so, and then the stress range decreases as the specimen begins to undergo some deterioration.

Some data[24] defining cyclic hardening and softening behavior are reported in Fig. 1.22. These results were obtained in a study of annealed AISI 316 stainless steel tested in air at various strain ranges at 430°C and a strain rate of 4×10^{-3} sec^{-1}. In the low strain ranges, cyclic hardening is clearly defined, as is the equilibrium or saturation value of the stress range. After remaining essentially constant for many strain cycles, the stress range gradually falls off near specimen fracture. At strain ranges

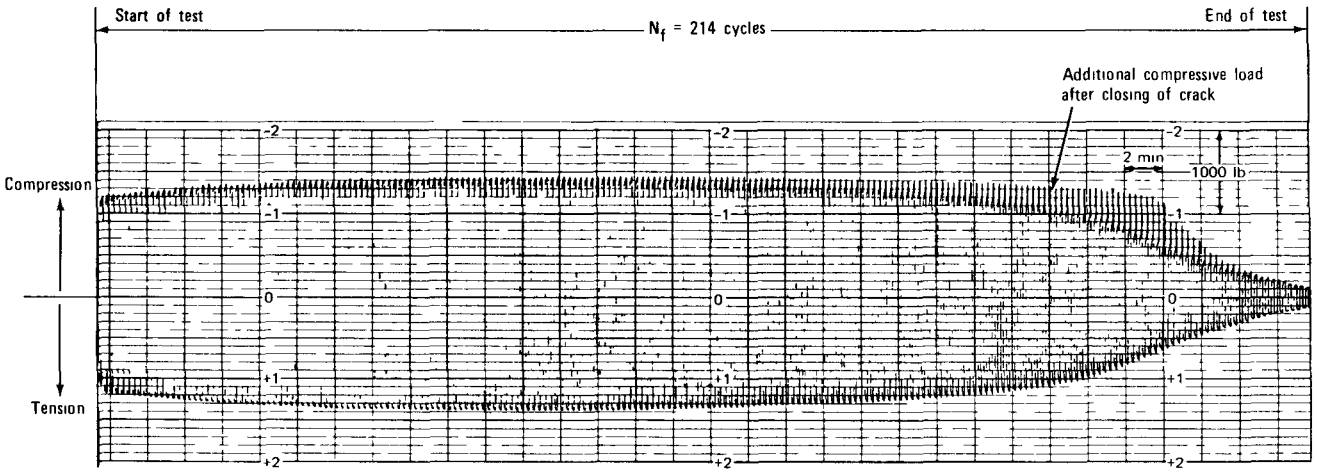

Fig. 1.21 Graph of stress vs. time for annealed AISI 304 stainless steel tested[23] in air at 816°C, a strain range of 3.26%, and a frequency of 3.33 cycles/min.

above 0.71%, the specimen cyclically hardens and then cyclically softens prior to fracture.

Cyclic Stress–Strain Behavior

An interesting discussion of cyclic hardening and cyclic softening and their effects on stress–strain behavior was provided by Manson.[18] For cyclic hardening, shown in Fig. 1.23, the static (monotonic) stress–strain curve shows a stress of σ_A, corresponding to a strain of 0.018. This same stress would be required to yield the same strain in the first strain cycle of a fatigue test. Because of cyclic strain hardening, however, the stress required to yield this same strain in subsequent cycles would be higher. This stress increase would follow a path similar to that given by $A'P_A$ in Fig. 1.23(b). After a certain number of cycles (about 600 in this illustration), the stress range reaches an equilibrium or saturation value and stays at this level for the remainder of the test. Manson referred to this as "saturation hardening." If the equilibrium or saturation value of the stress range at P_A is plotted against strain (or strain range), the point A″ is located. A similar reasoning for strain cycling to a total strain range of 0.036 yields point B″. In this way a new stress–strain relation is defined by A″B″ to identify a cyclic stress–strain diagram. In Fig. 1.23 the cyclic stress–strain curve is located above the static or monotonic stress–strain curve because of the strain-hardening effect.

A graph similar to Fig. 1.23 was applied[18] to cyclic strain softening and is shown in Fig. 1.24. In Fig. 1.24(a) the stress required to yield a strain of 0.015 is shown as point A in the static or monotonic test. For subsequent

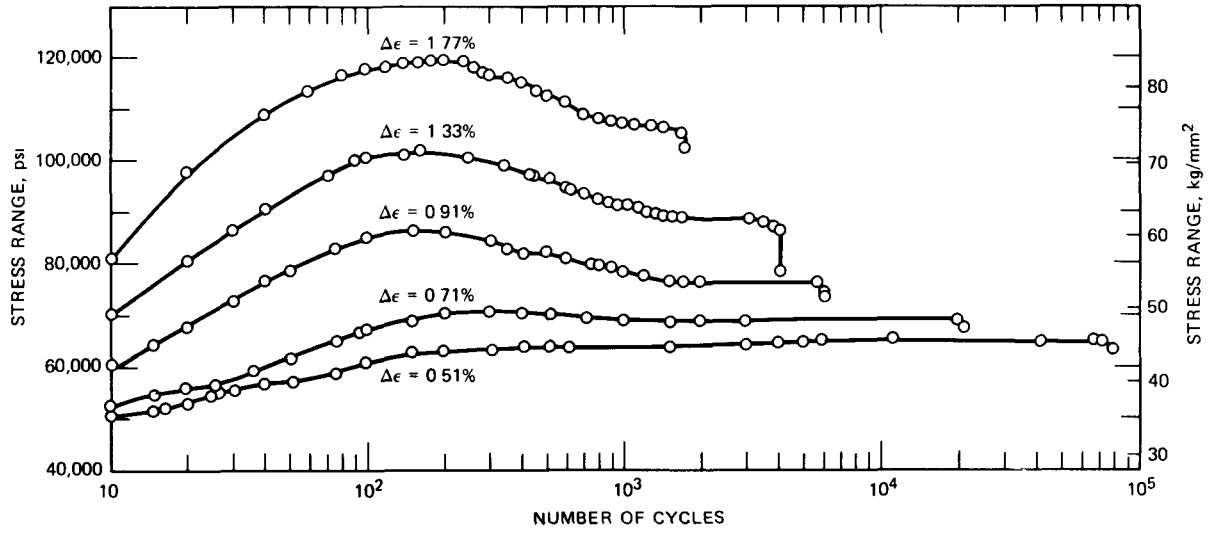

Fig. 1.22 Graph of stress range vs. cycles for AISI 316 stainless steel tested in air at 430°C and a strain rate of 4×10^{-3} sec^{-1}.

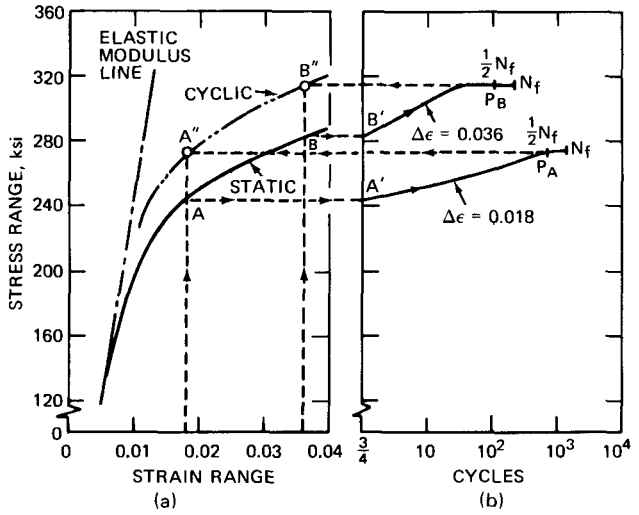

Fig. 1.23 Stress–strain behavior when cyclic strain hardening is present.[18] (a) Static and cyclic stress–strain characteristics. (b) Stress range as function of applied cycles; logarithmic scale. (From Ref. 18.)

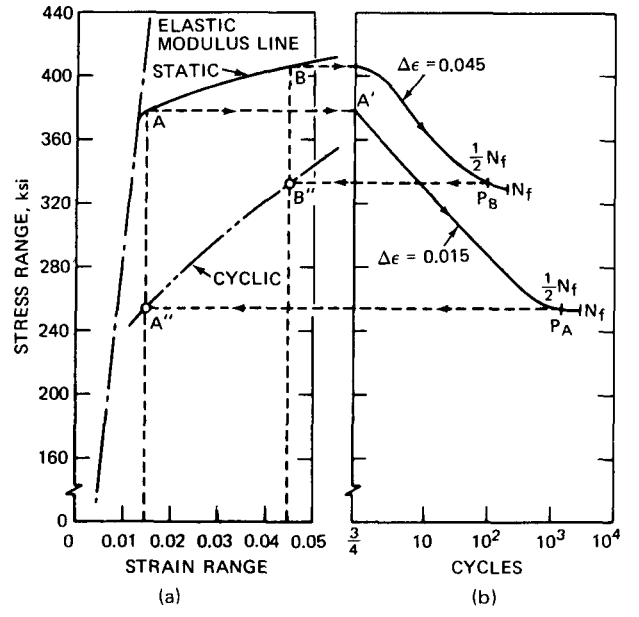

Fig. 1.24 Stress–strain behavior when cyclic strain softening is present.[18] (a) Static and cyclic stress–strain characteristics. (b) Stress range as function of applied cycles; logarithmic scale. (From Ref. 18.)

strain applications, the stress required to yield the same strain decreases along the curve $A'P_A$. An equilibrium stress range is eventually reached to define "saturation softening." Data for a strain range of 0.045 were used as in Fig. 1.23 to yield the cyclic stress–strain curve defined by A″B″. For cyclic strain softening, the curve is located below the monotonic stress–strain relation.

A material cycled at a given strain range, $\Delta\epsilon_A$, until a stable hysteresis loop is obtained will yield the corresponding value for the saturation stress range given by $\Delta\sigma_A$ in Fig. 1.25. If the strain range is now changed to $\Delta\epsilon_B$ and the cycling continued until another stable hysteresis loop is

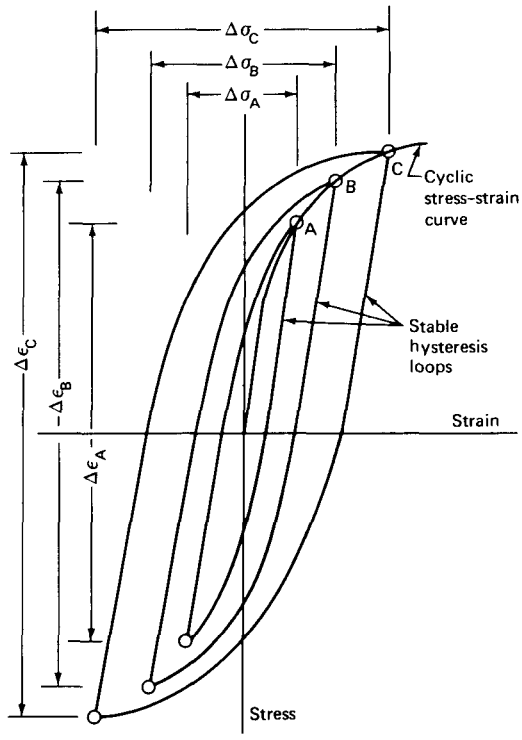

Fig. 1.25 Schematic cyclic stress–strain curve established with stable hysteresis loops; circles represent the tips of the stable loops.

obtained, the value of $\Delta\sigma_B$ will be identified. Another strain-range change and a new stable hysteresis loop will identify $\Delta\sigma_C$, etc. A curve connecting the tips of these stable hysteresis loops is shown in Fig. 1.25 to identify cyclic stress–strain behavior. In this way a single specimen can be used to establish the cyclic stress–strain behavior for a given material at a specific test temperature.

Logarithmic graphs of the stress amplitude vs. the plastic strain amplitude using data obtained at the tips (points A, B, C, etc., in Fig. 1.25) of the stable hysteresis loops have been found to yield linear relations. The slope of such a line is the cyclic strain-hardening exponent and usually has a value close to 0.15. This method of plotting will be recognized as identical to that used in the identification of the strain-hardening exponent in a monotonic stress–strain evaluation. Morrow and Tuler reported values of 0.15 to 0.18 for the cyclic strain-hardening exponents for several nickel-base alloys.[25]

REFERENCES

1. H. F. Moore, Manual of the Endurance of Metals Under Repeated Stress, Publication No. 13, Engineering Foundation, New York, N. Y., 1927.
2. G. R. Gohn, The Mechanism of Fatigue, *Mater. Res. Stand.*, 3: 106 (1963).
3. R. E. Peterson, Engineering and Design Aspects, *Mater. Res. Stand.*, 3: 122 (1963).

4. A. Wohler Versuche uber die Festigkeit der Eisenbahnwagen—Ashsen, *Z. Bauwesen* (1860).
5. H. J. Gough, Crystalline Structure in Relation to Failure of Metals—Especially by Fatigue, in *Amer. Soc. Test. Mater. Proc.*, 33(Pt. II) 3-114 (1963).
6. H. J. Gough, *The Fatigue of Metals*, Scott, Greenwood & Son, London, 1924.
7. H. J. Gough and D. Hansen, The Behavior of Metals Subjected to Repeated Stresses, *Proc. Roy. Soc. (London), Ser. A*, 104: 538-565 (1923).
8. W. A. Wood, Failure of Metals Under Cyclic Strain, in *Proceedings of the International Conference on Fatigue of Metals*, pp 531-534, The Institution of Mechanical Engineers, London, 1956.
9. J. Schijve, Analysis of the Fatigue Phenomenon in Aluminum Alloys, Report NLR-TR-M2122, Material Aero- and Astronautical Research Institute, Amsterdam, 1964.
10. *Manual of Fatigue Testing*, American Society for Testing and Materials, Special Technical Publication No. 91, 1949.
11. *Fatigue at High Temperature*, American Society for Testing and Materials, Special Technical Publication No. 459, 1969.
12. *Manual on Low-Cycle Fatigue Testing*, American Society for Testing and Materials, Special Technical Publication No 465, 1969.
13. T. Slot and R. H. Stentz, Experimental Procedures for Low-Cycle Fatigue Research at High Temperatures, *Exp. Mech.*, 8(3) 107 (March 1968)
14. R. W. Landgraf, The Resistance of Metals to Cyclic Deformation, in *Achievement of High Fatigue Resistance in Metals and Alloys*, pp 3-36, American Society for Testing and Materials, Special Technical Publication No 467, Philadelphia, 1970
15. Fatigue of Aircraft Structures, NAVAIR Report 01-1A-13.
16. S. S. Manson, Behavior of Materials Under Conditions of Thermal Stress, National Advisory Committee for Aeronautics, Technical Note 2933, 1953.
17. L. F. Coffin, Jr., A Study of the Effects of Cyclic Thermal Stresses on a Ductile Material, *Trans. ASME (Amer. Soc. Mech. Eng.)*, 76: 931-950 (1954).
18. S. S. Manson, Fatigue A Complex Subject—Some Simple Approximations, *Exp. Mech.*, 5(7) 193 (July 1965)
19. S. S. Manson and M. Hirschberg, *Fatigue—An Interdisciplinary Approach*, p. 133, Syracuse University Press, Syracuse, N. Y 1964.
20. R. Smith, M. Hirschberg, and S. S Manson, Fatigue Behavior of Materials Under Strain Cycling in Low and Intermediate Life Range, Report NASA-TN-D-1574, National Aeronautics and Space Administration, April 1963.
21. L. F. Coffin, Jr., Strain Softening Effects in Metals, *ASM (Amer. Soc. Metals) Trans. Quart.*, 60(2) 160-175 (1967)
22. M. H. Raymond and L. F. Coffin, Jr., Geometrical Effects in Strain Cycled Aluminum, *Trans. ASME (Amer. Soc. Mech. Eng.), Ser. D, J. Basic Eng.*, 85: 550 (1963).
23. T. Slot, Experimental Developments in Low-Cycle Fatigue Research on Pressure Vessel Steels at Elevated Temperatures, GE-TM66-6-11, General Electric Company, June 1966.
24. J. T. Berling and T. Slot, Effect of Temperature and Strain Rate on Low-Cycle Fatigue Resistance of AISI 304, 316, and 348 Stainless Steels, in *Fatigue at High Temperature*, pp 3-30, American Society for Testing and Materials, Special Technical Publication No 459, 1969, also, USAEC Report GEMP-642, General Electric Company, 1968.
25. Jo Dean Morrow and F. R. Tuler, Low-Cycle Fatigue Evaluation of Inconel-713C and Waspaloy, *Trans. ASME (Amer. Soc. Mech. Eng.), Ser. D, J. Basic Eng.*, 87: 2, 275 (1965).

Chapter 2

LOW-CYCLE-FATIGUE TEST SYSTEMS AND PROCEDURES

It is not the purpose of this chapter to present a detailed discussion of fatigue testing in general, since this has been done extensively and creditably in other publications.[1,2] Instead, this chapter is meant to supplement these previous discussions by presenting a complete description of electrohydraulic systems and components and their relation to low-cycle-fatigue testing. Emphasis is focused exclusively on uniaxial-fatigue testing involving push–pull loading. And the discussion is oriented to emphasize the recent experience of the authors with closed-loop, hydraulically actuated, servo-controlled systems devoted to evaluating low-cycle-fatigue characteristics to 2000°F. Special attention is given to the analog strain computer,[3a] which is particularly effective in allowing axial-strain-controlled fatigue tests to be performed using diametral-strain measurements. Appropriate discussion is also devoted to some new developments in diametral extensometry since new sensitivity and reliability appear to be realizable with the new designs that have evolved in this area.

ISOTHERMAL LOW-CYCLE-FATIGUE TESTING

Although, in general terms, a fatigue test consists in subjecting a specimen or component to a cyclic force or forces until "failure" occurs or a predetermined cyclic life is surpassed, a more rigorous definition will be applied in this chapter. Of primary interest are those tests which cause failure in a relatively low number of cycles (100 to 100,000 cycles). Also, an attempt is made to control the strain rather than the stress or force during the test. This is not to say that the stress or force is not measured or is unimportant but rather that it is not the controlled variable. Stress-controlled tests can be performed with equal ease, in which case the strain is left as the uncontrolled variable.

Also to be described is the testing of specimens rather than components. Specimen testing enables a gage section to be defined precisely so that the test variables of temperature, stress, and strain can be measured and recorded throughout the test, providing a maximum of data for design- and materials-development purposes.

Pertinent to the initiation of this discussion is the highlighting of points that should be considered in specifying a strain-controlled low-cycle-fatigue test. Although the following important points are merely mentioned here, most of them will be considered in greater detail later in the chapter.

1. Specimen size and shape.
2. Test temperature.
3. Controlled parameter: axial strain, diametral strain, plastic strain, etc.
4. Strain range and strain bias.
5. Strain rate or cyclic frequency.
6. Strain wave form, i.e., triangular, sine wave, hold period.
7. Testing environment.

Test Equipment

It might be well to examine the practical significance of some of the actual test requirements in order to understand the reasons for the rigorous specifications on fatigue equipment. Assuming a well-designed test specimen (see later sections), it is first necessary to measure a strain that results from the application of a force on the specimen. To cause failure within the low-cycle regime, this axial strain range will probably be on the order of 0.2 to 4%, with a very common axial strain range being about 1%. For 1% strain, a displacement is measured which corresponds to about 0.010 in. over a gage length of 1.000 in., with a proportionately smaller displacement if a smaller gage length is used. If 1% accuracy is requested in this strain measurement of 1%, this displacement measurement over the 1-in. length must be within 0.0001 in. One even more extreme requirement is that this displacement be cyclically controlled for long periods of time (sometimes weeks or more) with no appreciable drift in mean strain or amplitude. Such performance requirements demand much from testing machines in the sense of sensitivity, resolution, stability, and reliability. The normal requirement to perform this measurement at elevated (or cryogenic) temperatures, and perhaps in a special atmosphere, will further intensify the problem. It may be necessary to cycle the

specimen between the required strain limits several times a second or perhaps only a few times a day. Furthermore, the forces needed to obtain the required strain may vary from a few hundred pounds to several thousand pounds. And, if the temperature is to be other than ambient, the heating or cooling must be done without interfering with strain or force measurement or specimen loading. The same can be said for any special environmental testing. Also of special importance in the strain-controlled testing is the requirement for differentiating between the effects of thermal expansion and mechanical displacement (see page 31).

Because of an ever-increasing need for precision in low-cycle-fatigue testing, the use of automatic servo-controlled equipment is considered to be a necessity. This is equipment containing high-gain low-drift components connected together in a negative-feedback closed-loop configuration.

The basic principles of operation behind negative-feedback control systems are discussed in terms of the block diagrams given in Fig. 2.1. Figure 2.1(b) is a simplified version of Fig. 2.1(a), but both versions represent the components that might be found in a system containing no

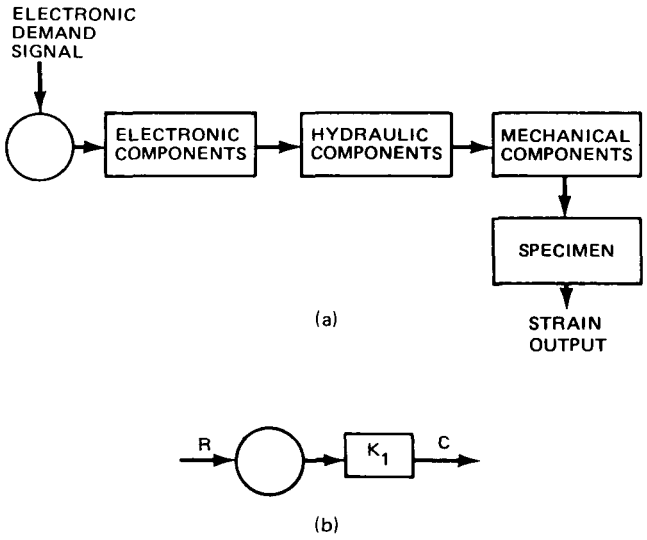

Fig. 2.1 Block diagrams for open-loop systems.

feedback, i.e., an open-loop system. The equation governing the system is, simply,

$$C = K_1 R \tag{2.1}$$

Any changes in characteristics of the components comprising K_1 will cause the output "C" to change proportionately. Clearly such a system would not be satisfactory, since these changes will surely occur, and the largest variable will probably be the specimen itself.

In addition, the other components are apt to change characteristics with time and temperature. In other words the electronic components may drift slightly, the behavior of hydraulic components may change with temperature, contamination, and wear, and the mechanical components may vary because of thermal expansion or varying stresses.

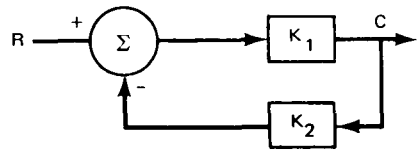

Fig. 2.2 Block diagram of a closed-loop system.

Figure 2.2 shows the same system with only the addition of negative feedback to form a closed-loop system. The equation of this system is

$$C = \left(\frac{K_1}{1 + K_1 K_2}\right) R \tag{2.2}$$

which can be rewritten as

$$C = \left(\frac{1/K_2}{(1/K_1 K_2) + 1}\right) R \tag{2.3}$$

Now, if $K_1 K_2$ is made large with respect to 1, the denominator will approach unity, and C will be approximately equal to $(1/K_2)R$.

This is a mathematical way of stating that the behavior of a closed-loop system of sufficient gain is primarily dependent on the characteristics of only the feedback components. Thus a tremendous improvement has been obtained by isolating the desired output from the changes that will occur in the components comprising K_1. The necessary high gain is easily obtained, usually through electronic amplification at various places in the loop. It should be emphasized also that the desired output will now be proportional to any changes that occur in the feedback components (K_2), and care should be taken to assure very stable (reliable) components for this application. Fortunately the characteristics of the transducer and electronic components generally comprising K_2 usually permit this requirement to be satisfied.

The components comprising a typical electrohydraulic low-cycle-fatigue system can now be described (Fig. 2.3). Most of the components can take various forms, and several commercially manufactured units are available for each; and, of course, some can be readily made in the laboratory. No attempt will be made in these discussions to endorse any particular product; rather, specifications that are considered important in a low-cycle-fatigue system will be emphasized. Complete systems can be obtained commercially, but in the following discussion each major component will be analyzed separately.

Programmer. The programmer, also variously called signal generator, function generator, or oscillator, is the device that supplies the command signal or signals to the system. The programmer generally produces a time-varying

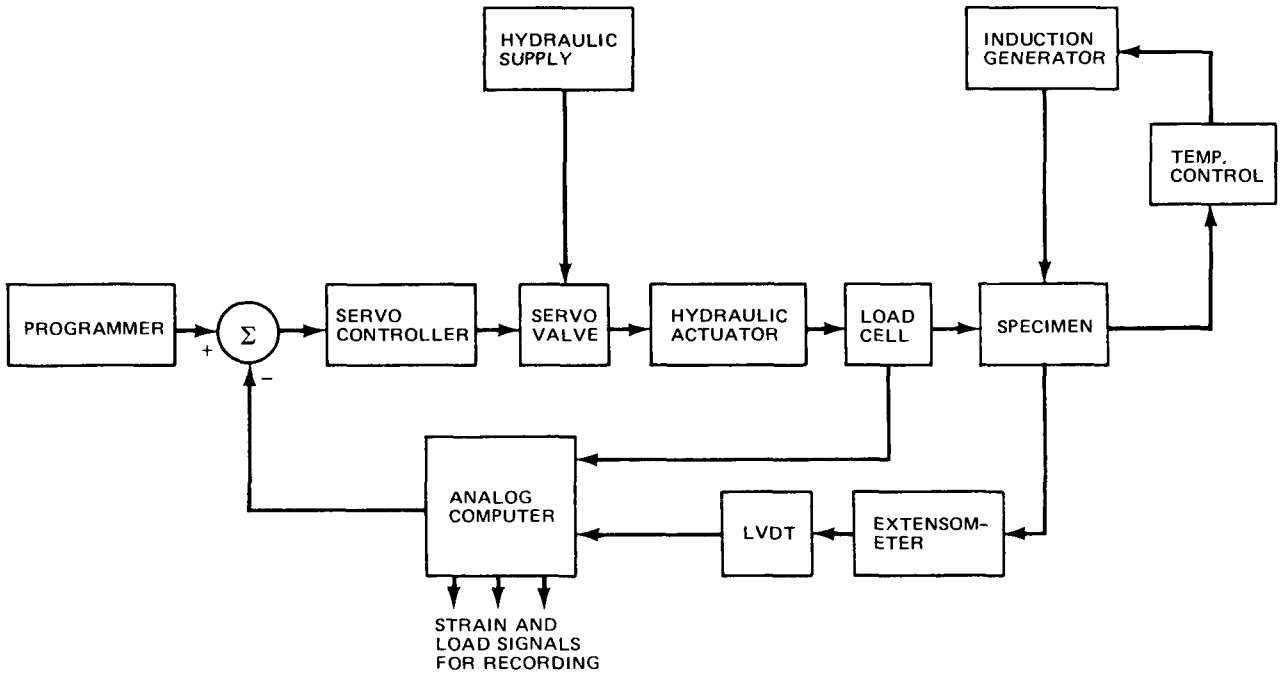

Fig. 2.3 Schematic of components in fatigue-testing machine.

electrical voltage that represents the required test parameter to be controlled in the experiment.

There are many commercially available units of this type. The selection of one or more will depend on several factors. Included are the compatibility with the servo controller, the wave form or wave forms required, the frequency range to be covered in the testing, or whether or not any unusual or special features are desired. Programmers for low-cycle-fatigue use are generally capable of supplying a ±10-V signal with a current capability of a few milliamperes or so. Of course, if the programmer is to be operated with a particular servo controller, the voltage and current requirements will be determined by the input characteristics of the servo controller being considered.

Before the desired wave-form capability of the programmer can be specified, it is first necessary to determine the requirements of the time-dependent cyclic variation of the controlled parameter to be employed in the specimen tests. Of course, standard wave shapes, such as sine wave (for constant-amplitude constant-frequency testing) and triangular wave (constant-amplitude, -frequency, and -strain-rate testing), are very common and readily available. A desirable feature not always available, however, is the ability to shift the mean voltage of the generator output so that mean stress and strain levels of the specimen can be conveniently programmed and controlled. The mean level and amplitude and frequency stability of the generator should also be evaluated seriously. Any changes in generator output during a test will result in a corresponding change in the controlled variable. It is difficult enough to obtain the desired control over the specimen parameter of interest without having to continuously adjust a generator whose output varies with time.

Although the highest frequency required for low-cycle-fatigue testing is seldom more than a few cycles per second and does not impose a severe requirement on any electronic programmer (some electromechanical function generators produce inferior wave forms above 1 Hz), the very low frequencies sometimes encountered are more difficult to obtain. When frequencies of less than 1×10^{-3} cycle/sec are required, the drift characteristics of the generator can become significant and affect the output wave form. Some hybrid devices (containing digital and analog circuits) can offer lower frequency operations but usually at a higher cost than conventional generators.

Curve-follower programmers are generally devices that, through a servo system, electronically follow a specially prepared curve in a cyclic manner. The following head is mechanically linked to the shaft of a potentiometer, the wiper of which provides an electrical analog of the drawn curve. These programmers offer a great deal of flexibility in their ability to produce almost any desired shape of wave form. Such programmers are relatively expensive, however, and are subject to some following errors generally associated with their limited frequency response. Also, many wave forms that are composed of straight-line segments can be produced more easily, more reliably, and at lower cost by using motor-driven, continuously wound, tapped potentiometers.

Wave forms needed for hold-period tests require somewhat unique behavior from a programmer. It must be possible to program the wave-form amplitude, time slope of the ramp, position of hold period (tension, compression, or both), and the length of the hold period. Some generators provide for the means to connect an auxiliary timer to vary the length of the hold period. It is also possible to use the

continuously wound motor-driven potentiometer mentioned earlier and to stop the driving motor with auxiliary circuits. All-electronic hold-time generators can also be designed and built by any good electronic job shop. An important criterion, however, is a constant-output signal during the hold period. This is especially necessary in a strain-controlled hold-period test. Any reduction in the output voltage of the generator will cause an elastic unloading of the specimen. A very small decrease in the generator output will therefore cause a large decrease in the force on the specimen. This could very well have a significant effect on specimen life and certainly would present a false stress-relaxation indication.

Generally the programmer in a closed-loop testing system is located outside the "loop"; that is, the controlled variable can have no effect on the programmer output. There is a trend, however, in materials testing to use a technique that modifies the programmer output as a result of changes in the controlled variable. For example, it may be desirable to perform a creep test under constant true stress conditions. In this case it is possible to use a closed-loop system, operating in "force control," whereby the force "demand signal" is automatically reduced in direct proportion to the reduction of the minimum diameter of the specimen. This is just one example of how the programmer output can be modified during a test. The system usually requires the addition of an analog or digital computer to accomplish this end. Thus the types of testing are limited primarily by the imagination of the operator and, of course, the self-imposed limitations in loss of resolution and/or sensitivity of measurement and control that the "hybriding" might cause.

Servo Controller. The primary purpose of the servo controller is to provide the proper signal to the control device (in an electrohydraulic system the control device is usually a flow-control servo valve) so that the desired parameter (stress, strain, etc., of the specimen) follows as closely as possible a prescribed behavior. In general, the functions of a servo controller can be listed as follows:

1. Acceptance and comparison of command and feedback signals.
2. Generation of a control signal.
3. Auxiliary functions and readouts.

The first of these functions can best be understood by reference to Fig. 2.4, but this figure does not mean to imply any limitation on the number of demands and feedback signals that may be involved. The "K" blocks signify variable gain or attenuation networks that permit adjustments on the amplitudes of the signals to be compared at the summing junction, signified by the Σ symbol. In effect, the summing junction subtracts a selected feedback signal representing the desired parameter from a single or composite demand signal to produce the difference between them. This "error signal" thus produced (a very small signal in any good servo-controlled system) is

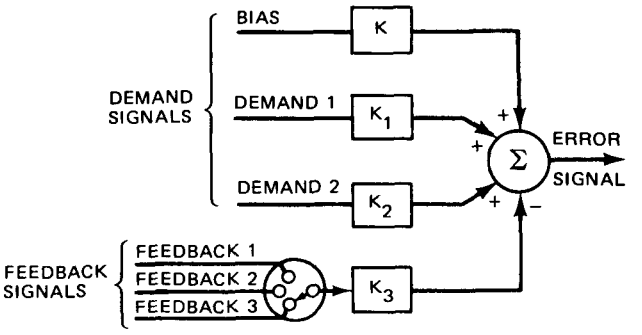

Fig. 2.4 Block diagram to illustrate functions of servo controller.

what initiates the corrective action of the system. In effect, the servo controller senses the error signal and initiates system action through the control device to reduce the error to a minimum level.

Servo controllers for materials-testing machines contain a multitude of adjustable controls, the functions of which can be somewhat confusing to operating personnel. The specimen, being a component in the servo system, forces this degree of complexity, and most of the controls can be thought of as compensating devices for different specimen characteristics. If specimens of the same material having the same geometry were always tested under identical conditions of temperature, force range, and frequency, the servo controller could be made much less complicated. Such a controller, however, would be next to useless to the materials-testing laboratory.

The most common, and perhaps one of the most easily understood, of the adjustable controls is the "gain control," sometimes referred to as the "proportional band" control. Generally, all other operating conditions being the same, the higher the gain setting (the lower the setting if called proportional band), the smaller the error signal and therefore the closer the controlled variable to the demand signal. Any servo system can become unstable, however, if the gain is increased above some level. Therefore the objective in making a gain adjustment is to obtain good control over the variable of interest while retaining a stable operating condition; this unfortunately is not always easy to do. Even when the gain is increased gradually to "reduce the error signal" or "improve the wave form" of the controlled variable, the realization that the gain is already too high sometimes comes too late for that specimen. Consequently it is extremely good practice to keep a log of representative servo-controller settings under different operating conditions with different specimens. Thus, with experience, it is possible to make good "educated guesses" as to satisfactory settings.

In the previous paragraph the authors do not mean to imply that the whole procedure of control adjustment needs to be a completely unscientific manipulation for the testing personnel. The point is that it is well for all concerned to be aware of possible difficulties in testing new materials and perhaps to provide for an extra specimen or

two in the testing program. Seldom is nothing known about the specimen to be tested, and a little understanding of the effect of the specimen and its test conditions on the testing-machine performance will significantly reduce the amount of "experimentation" required.

As an example, consider the low-cycle-fatigue testing at elevated temperature with a hydraulically actuated, servo-controlled system. Because the specimen and associated load-train components are really part of the control-system loop, any nonlinear or time-dependent changes that occur in these components can result in dramatic changes in system response. Before the specimen exceeds the proportional limit, the ratio of gage-section deformation to hydraulic-actuator displacement is a constant and is always less than unity. After the proportional limit is exceeded, however, this ratio will increase, often significantly, approaching unity as a limit. This causes an increase in the gain of the system which is sometimes enough to force the system into an unstable operating condition. It is certainly helpful to know if a large gain increase can be expected when making an initial gain setting on the servo controller. Two conditions that will cause a large gain change are:

1. The specimen design is such that the elastic deflection of the gage section is small compared to the total elastic deflection outside the gage section.
2. The material and test conditions are such that the stress–strain slope changes significantly when the proportional limit is exceeded.

In addition to the increase in system gain just discussed, a constant-load plastic deformation can occur at elevated temperatures, introducing a time effect and changing the dynamic response of the system. Also, some materials display metallurgical strain- or temperature-induced changes in the specimen which can produce another nonlinear effect referred to as "ratchetting," a sudden strain change for a small force change.

These disturbing effects can be compensated for to some extent by using two special circuits provided on some servo controllers. One circuit, sometimes referred to as the "stability" or "nonlinear gain" circuit, can compensate somewhat for the gain change of the specimen. The circuit generally uses the nonlinear conduction characteristics of semiconductors to provide the greatest attenuation of the error signal when the system gain would be the highest, and vice versa. By proper adjustment of the control associated with the circuit, the effect of the specimen gain change can be minimized.

Another circuit, sometimes referred to as a "rate" or "derivative feedback," can be used to stabilize the system when the specimen introduces detrimental time problems. Essentially the circuit provides another feedback signal that is proportional to the rate of change of the controlled variable. Use of the circuit will not only alleviate time effects but will also reduce the effect of nonlinear behavior of the specimen and other system components on system performance. The way in which the circuit works, however, is beyond the scope of this chapter, and the interested reader should refer to a book on servo-systems theory and specifically "lead network compensation" and "inner loop stabilization."

Some servo controllers provide "reset" circuits that attempt to reduce any steady-state error signal with an integration network. The characteristic of this type of network is that it produces a higher system gain at lower frequencies, theoretically becoming infinite under steady-state conditions. For low-cycle-fatigue testing, the feature is not generally necessary. For one thing the servo valve associated with these systems is an integrating device and accomplishes much of what a reset circuit would do. There are conditions, however, when a reset circuit can produce some improved performance. Since the servo valve is not a perfect integrator, some error signal will still be required under steady-state conditions to obtain the desired value of the controlled variable. Therefore, when very precise, low-frequency control is desired (such as in hold-period testing, where relaxation studies are being made), a reset circuit can be advantageous.

Dither circuits are generally available in servo controllers that drive hydraulic servo valves. This circuit produces a high-frequency signal (a few hundred cycles per second) that is applied to the servo valve along with the normal control signal. The frequency of the dither signal is always above the frequency response of the valve, but it has the effect of reducing static friction or "stiction" of the valve and actuator. The result is an increase in the resolution of the system. This is very important in low-cycle-fatigue testing, where very small and slow movements are often required of the hydraulic components. The control associated with this circuit varies the amplitude of the dither signal being applied to the valve. Generally the "vibration" produced in the hydraulic components can be felt by placing a hand on the servo valve. Since such vibration does represent a motion and can cause component wear, it is good practice to keep the amplitude of the dither signal as small as possible consistent with good resolution.

Valve-balance circuits are usually found on those servo controllers used in electrohydraulic systems. Owing to slight bias conditions in the electronic components of the servo controller and electromechanical unbalances of the valve itself, a small error signal is often required to produce a "no-flow" condition of the servo valve. This is objectionable not only because it is misleading in relation to total system null but also because it will retard the proper performance of the nonlinear gain circuit. Also, an unbalanced condition will cause an output shift if the gain is adjusted. The valve-balance circuit provides a means to introduce another small signal to the valve to overcome this unbalanced condition. It is generally sufficient to place the system in closed-loop control under steady-state zero-force conditions and then adjust the valve-balance control to obtain the zero-load zero-error-signal condition.

Limiter circuits are used to place an upper limit on the output of the servo controller regardless of the amplitude of the error signal. This feature in an electrohydraulic system provides a means to adjust the maximum velocity of the hydraulic actuator; however, the authors have found little use for such a circuit in materials-testing applications.

Another feature often found in servo controllers is the ability to initiate a system "shutdown." The primary objective in this shutdown is, of course, the deactivation of the force-producing device. In the electrohydraulic system, this deactivation is generally accomplished by stopping the flow of hydraulic fluid to the ram. This function should be capable of manual operation at the operator's discretion and automatic in the event of system malfunction or in the fatigue test, when the specimen fails or reaches some other desired terminal condition. Although the manner in which the deactivation occurs will be discussed later, the sensing mechanism will now be covered. One very good reason why this mechanism is often located in the servo controller is because the error signal contains a great deal of the information that should initiate a shutdown. The error signal will reflect most system malfunctions and, in many types of fatigue tests, will also sense specimen fracture. Thus it is generally only necessary to electronically monitor the error-signal amplitude and impose limits above which the shutdown will be automatically initiated. All-electronic error detectors are standard features of some controllers. Front-panel potentiometers provide for the adjustment of the plus-and-minus error limits before the test is started. Exceeding one of these limits in either direction generally deactivates a relay in the shutdown circuit. Once this occurs, it is usually necessary for the operator to manually reset the circuit. Such systems are capable of high-speed operation and are very sensitive and reliable. There are, however, two disadvantages to such a system. One disadvantage is the possibility of a shutdown being initiated by a high-frequency "noise signal" caused by some external electrical transient. Such a signal could possibly be tolerated by the lower response hydraulic system when no other cause for shutdown was present. In other words, there can be a large mismatch between the frequency responses of error circuit and the total system. Another disadvantage is the lack of a visual indication of the limit settings. Limits are therefore somewhat difficult to establish before the test and "tricky" at best to set after the test is started.

Another error-detection technique and one the authors prefer for low-cycle-fatigue testing is the use of a meter relay. These devices give a continuous visual indication of the system error. In addition, meter relays contain easily adjustable vanes that depict the plus-and-minus settings of the error limits. Although the meter relay does not have the high response of an all-electronic circuit, it is usually more closely matched to the system as a whole, will not respond to a "noise spike," and is generally adequate in response for low-cycle-fatigue applications. The device also permits final adjustments of the error limits after the test has started and the "normal" error cycle has been established.

Sometimes shutdown cannot be initiated by the error signal simply because the proper information is not contained therein. For example, if axial strain is controlled with an axial-strain measurement being used, it is possible, and even likely, that no appreciable system error will occur when the specimen completely separates. In this case and in other situations where it is desired to terminate the test prior to failure, some other means must be used to cause the shutdown. It may be desired, for example, to terminate a test when the peak, cyclic tensile force on the specimen drops below some preset limit. A logic circuit can then be used to sense this condition and to cause the proper action. These circuits will probably be located elsewhere than in the servo controller.

The readout and/or monitoring functions of the servo controller are very important for test setup and assurance of proper operation during the test. Only one of these functions will be discussed. Probably the most useful is a meter that indicates the system error signal. This is sometimes referred to as the "null meter" (frequently the same meter through a switching network is used for monitoring other parameters, such as the feedback signal or the valve current). It is necessary to know, prior to placing the test machine in automatic operation or before "closing the loop," whether or not an initial error exists between the demand signal and the parameter to be controlled. The meter (usually a center-zero galvanometer type) will indicate any error. Initial error is removed by bias adjustments in either the feedback or demand circuits to avoid any inadvertent initial forces being placed on the specimen. The meter also indicates relative dynamic system error while the test is in progress. The authors have found it practical to combine the functions of error indication and meter-relay shutdown in their testing machines.

Servo Valve. The function of the servo valve is to supply the hydraulic ram with fluid having the proper flow and pressure conditions to satisfy system requirements. Characteristics of the device are approximately such that the output flow from the valve, under constant-output-pressure conditions, is proportional to the input electric current. Also, the input current is approximately proportional to the square root of output pressure when the flow is constant. The first of the two characteristics is generally the more important since it is the one which, in conjunction with the hydraulic ram, imparts the integration feature to the servo system. Most of the servo-valve specifications are quite competitive, and the reader can choose for himself from the many models offered for sale from several manufacturers. Among the features to consider are frequency response, linearity, symmetry, resolution, gain, dependability, and compatibility with the servo controller and the hydraulic ram. It is this last consideration, that of compatibility, and the applicability for low-cycle-fatigue testing which are considered within the scope of this discussion.

Actually the compatibility between servo valve and servo controller is not difficult to obtain, since most manufacturers recognize the need for such. Some servo controllers even provide the means to adapt to valves having a range of input-current requirements. In addition, servo valves usually contain two input coils that can be wired in series or parallel to provide more flexibility in achieving the desired match. The compatibility between servo valve and hydraulic ram is basically determined by system requirements. Once the hydraulic ram has been selected to supply the required force (more about this selection will be discussed later), the servo valve must be able to supply sufficient flow to produce the ram speed required. The following equation may be helpful in this selection:

$$\text{Flow required} = \frac{\text{ram speed} \times \text{effective ram piston area}}{231} \qquad (2.4)$$

where flow is in gallons per minute (if flow is required in cubic inches per second, the denominator is 60), ram speed is in inches per minute, and ram area is in square inches. Reference should then be made to the load–flow–pressure characteristic curves for specific valves which take into consideration the total system pressure and the pressure drops across the valve and hydraulic ram. Frequency considerations of the valve and associated hydraulic components are not discussed here, since they are not generally sources of problems in low-cycle-fatigue testing. Although obtaining a valve with sufficient flow capacity can be considered an obvious requirement, not necessarily so obvious is the fact that the flow capacity of the valve can be too large. Precision control in materials-test machines is sometimes made difficult because of linearity, symmetry, hysteresis, and resolution problems that are partially determined by maximum flow capacity. A specific valve size may be needed for high-rate testing, but it will generally not perform as well as a smaller size for those tests which involve very slow rates.

Perhaps a word is in order here with regard to the necessity of maintaining clean hydraulic fluid for the proper and reliable operation of the system hydraulic components. Servo valves in particular are very susceptible to improper operation and possible damage by the presence of very small particles in the fluid. Proper filtration of the fluid is therefore essential. The use of more than one filter in series is also recommended. In addition, it is well to provide bypass valves and lines (with filters) so that filter elements can be periodically changed or cleaned without the need to stop operation. A new system should also be flushed through filters for several hours before servo valves are installed. Most servo-valve manufacturers can provide flushing blocks specifically made for this purpose.

Hydraulic Rams. Hydraulic rams, or actuators, suitable for materials-testing applications are available from many sources and vary in price from several thousand dollars to a few hundred dollars. Considerations pertinent to low-cycle-fatigue testing will be discussed to assist those who want to select a ram from the many available as separate components or perhaps to evaluate those which may be part of an integrated system.

A primary consideration, of course, is to choose a ram having sufficient force capability. The following equation can be of some help in this determination:

$$F = (P_s - P_v)A_p \qquad (2.5)$$

where F = available force, lb
P_s = hydraulic supply pressure, psi
P_v = pressure drop across servo valve, psi
A_p = effective ram piston area, $in.^2$

Under steady-state conditions (very little flow), the valve drop will approach zero, and the maximum force will approach the supply pressure times the net piston area. A very common pressure rating for hydraulic components is 3000 psi, and the capability exists therefore to generate 15,000 lb with a 5-$in.^2$ piston area. It is the authors' opinion, however, that it is better to utilize a much lower pressure than this for the bulk of low-cycle-fatigue testing. The lower operating pressure will be safer and less apt to cause leaks, and the hydraulic components will generally last much longer at a derated pressure. This is especially so for actuator seals. Hydraulic systems for low-cycle-fatigue testing generally work very well at pressures in the 1000- to 2000-psi range. Of course, this means that a larger piston area is required of the hydraulic ram. In the frequency range used for most low-cycle-fatigue testing, this does not prove to be any major limitation.

For a particular servo valve-hydraulic ram combination, the force available during dynamic conditions will depend also on the flow required and hence the servo-valve pressure drop. Here again, reference should be made to the load–flow–pressure characteristic curves for the valve.

The stroke required during operation in low-cycle-fatigue testing is usually very small (<0.5 in.), including specimen, fixture, load cell, and frame deflections. Consideration should be given, however, to specimen setup procedures, and a much longer stroke than this is generally needed (even on test frames having movable crossheads or other adjustment) to accommodate different-sized specimens, the attachment of specimen fixturing, and transducers. The upper limit on the ram stroke is sometimes determined by dynamic considerations in high-frequency testing, but, in low-cycle-fatigue testing, it is determined by rigidity and physical-space considerations. Since double-ended rams are considered necessary for this kind of testing and since they are usually mounted below the lower platen on the test stand, there must be space for full retraction of the ram under the platen. Although a pit can be provided under the stand to accept the ram shaft, and this is advocated with some machines, it requires a more expensive and less versatile installation. The use of the double-ended

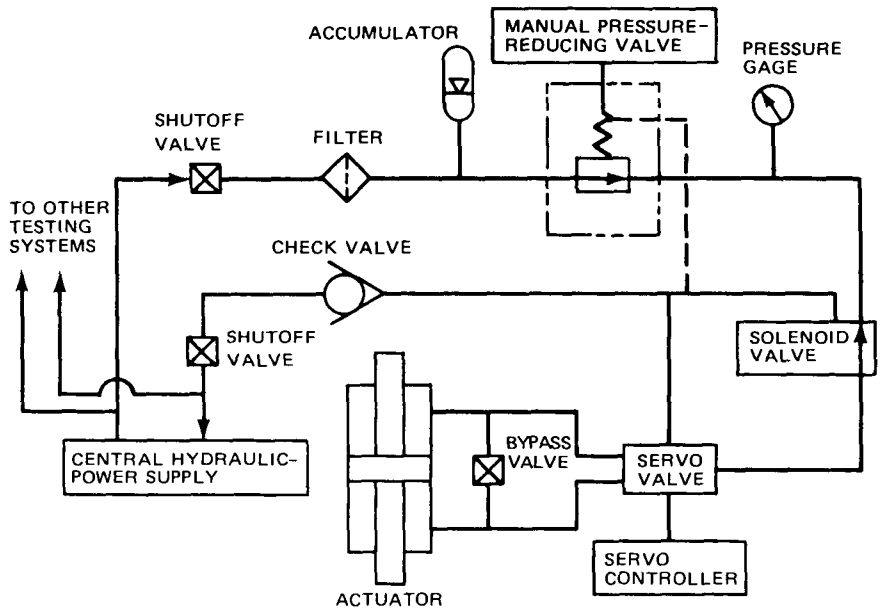

Fig. 2.5 Block diagram of hydraulic system.

rams is just about universal since they provide more balanced flow and force characteristics desirable for push–pull testing. Extra rigidity is provided by the additional rod-end seals as well. Low-leakage, smooth operating, and dependable piston and rod-end seals should also be evaluated, as well as availability of hydraulic cushions, ease of maintenance, and cost.

Other Hydraulic Components. Although the servo valve and hydraulic ram have been covered in some detail, a less extensive coverage will be given the other hydraulic components in the system.

The hydraulic-power supply can be a small unit capable of driving only one testing machine or it can be a large general-purpose unit for use with many machines or even with more than one laboratory. The power supply can be part of a system furnished by the manufacturer of the testing machines or it can be obtained separately from one of many hydraulic-component suppliers. These organizations are usually qualified to design and furnish satisfactory systems when given the proper operating specifications. Listed below are some of the more important considerations in selecting or specifying the hydraulic-power supply.

1. Dependability and use factor.
2. Pressure rating and flow capacity sufficient for immediate and future needs.
3. Low noise, especially if located in a laboratory area.
4. Variable-volume pump if possible (for economy of operation).
5. Reservoir and cooler necessary to keep fluid temperature down.
6. Filtration and safety features.
7. Pressure and flow regulation and adjustment.
8. Accumulator requirements.

Figure 2.5 shows how the hydraulic-power supply may be connected to other hydraulic components in the system. In this case, one central supply operates several testing machines, connected as shown. The interconnection between components is that which is used in the authors' laboratory. Although it is certainly not the only satisfactory interconnection possible, it does provide the following important features:

1. The separate valves, filters, accumulators, and pressure-reducing valves isolate the testing stations from one another. They permit different pressures to be used if desired and reduce the possibility of transmitting hydraulic transients.

2. The three-way solenoid valve connects the input of the servo valve to either the high pressure or return side of the hydraulic supply. The solenoid is actuated by the system shutdown circuit and provides a very good method of immediately removing the force from the hydraulic ram.

3. The bypass valve across the input to the hydraulic ram is, in the authors' opinion, an extremely important item for inclusion in a system of this type. The bypass valve consists of a hand-operated valve that, when open, prohibits the hydraulic ram from generating a force regardless of the positions of any other valves in the system. A means is therefore provided for starting a test without introducing any unwanted conditions into the system. The hand valve can be gradually closed and in effect permits "creeping" into closed-loop control of the specimen. With this technique, system malfunctions and improper null or control adjustments can be identified before harmful forces are applied to the specimen. In addition, initial hydraulic surges are completely avoided.

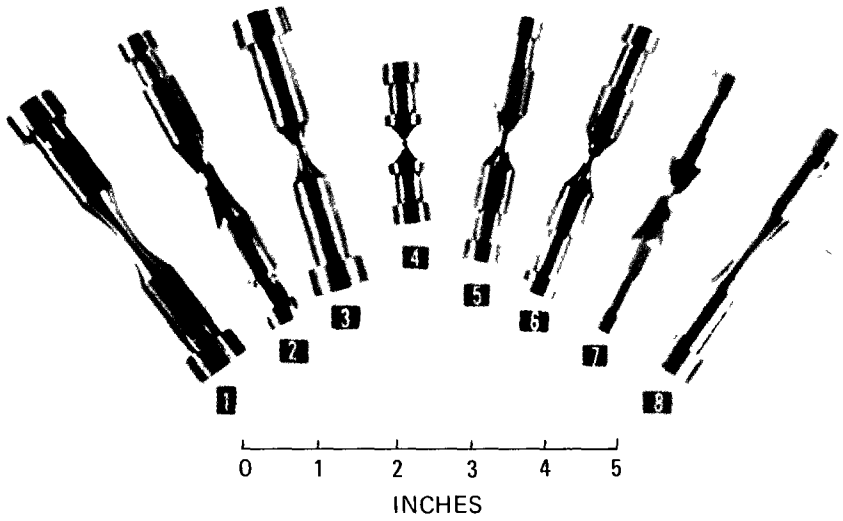

Fig. 2.6 Various test-specimen configurations for low-cycle-fatigue testing.[3b] (Published by permission of the American Society for Testing and Materials.)

Specimens

Because of the interactions between specimen design, loading and heating techniques, and stress, strain, and temperature measurement and control, there has not been the evolution of a standard low-cycle-fatigue specimen. There are, however, certain general features that every specimen should possess. These will be itemized, as well as some of the more important characteristics evident in currently used specimen designs. The comments will be primarily applicable to specimens tested in uniaxial push–pull machines.

General Specimen Characteristics. 1. It must be possible to precisely align and rigidly attach the specimen to the loading fixtures and to maintain this alignment and rigidity throughout the test. The specimen must be compatible with the loading fixtures and loading technique to the extent that the gage section of the specimen will not be subjected to harmful forces during the attachment process.

2. A gage section should be established wherein the parameters of primary interest (stress, strain, and temperature) will be at a maximum, will be uniform, and can be measured and controlled accurately.

3. The previous requirement implies a compatibility with one or more transducers for making these measurements. Attachment of any transducers to the gage section should not significantly affect the normal reaction of the specimen to the imposed test conditions.

4. Specimen size, shape, surface characteristics or material orientation can be primarily determined by a necessary relation to the raw material or an in-service component.

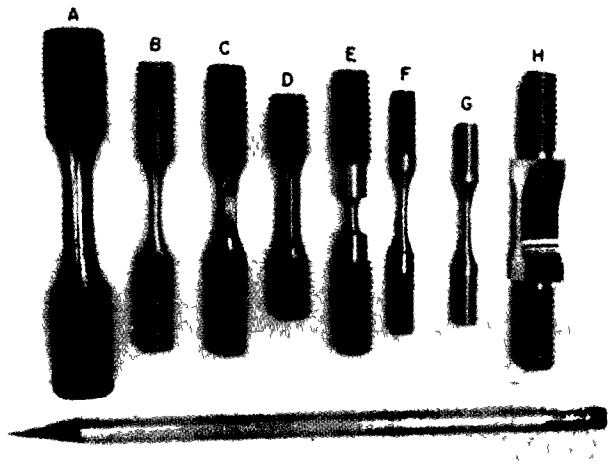

A, normal specimen for controlled strain tests on lower strength materials.
B, normal specimen for controlled strain tests on higher strength materials.
C, flat-sided specimen for surface topography studies.
D, used for high-amplitude tests with low L/D to minimize buckling.
E, low-temperature test specimen.
F, G, special specimens the sizes of which are limited by casting limitations and material availability
H, plain-notched specimen.

Fig. 2.7 Various specimen configurations used in fatigue testing.[3c] (Published by permission of the American Society for Testing and Materials.)

Specific Specimen Characteristics. Figures 2.6 to 2.8 show actual low-cycle-fatigue specimens that are used in various testing laboratories at the present time. They can be classified according to the types of ends, the configurations

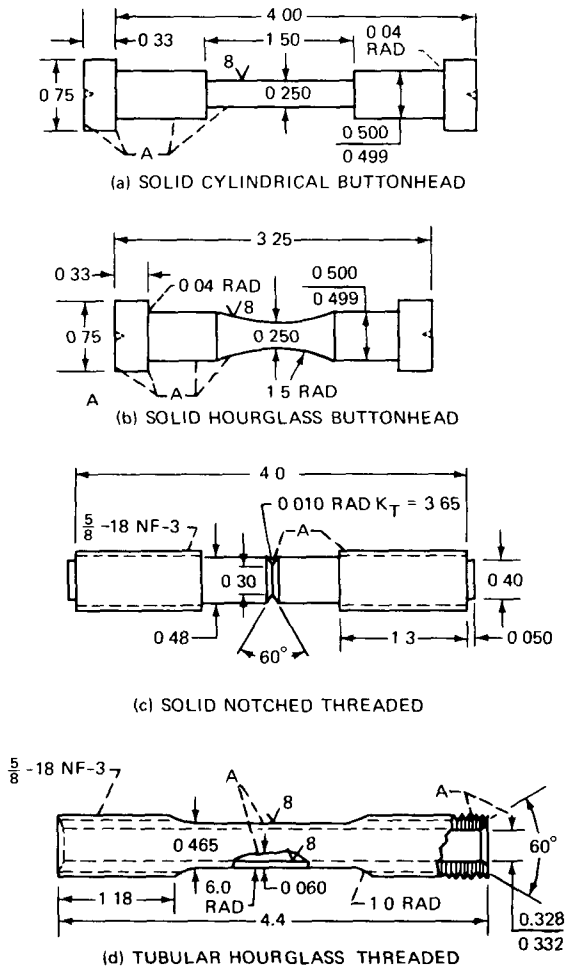

Fig. 2.8 Various specimen configurations used in fatigue evaluations.[3 d] (Published by permission of the American Society for Testing and Materials.)

of the gage sections, and whether they are solid or hollow. All specimens shown are of either the threaded or buttonhead type, indicating the most common means of attachment.

The following points can be made about these two types:

1. Failure in the attachment region is usually easier to avoid with buttonhead specimens. This is often an important consideration with low-ductility or notch-sensitive materials.

2. Threaded specimens generally require less material to fabricate.

3. Buttonhead specimens can usually be more precisely aligned and securely clamped. When a threaded specimen design is selected, however, it is desirable to specify close tolerance, flat ends (perpendicular to the axis) that will match up with similar flat surfaces in the loading fixtures. This is much more satisfactory than relying on the threads for alignment.

4. Disconnecting threaded specimens from loading fixtures can be more difficult, especially after the specimens have been exposed to elevated temperatures. Specific problems can be minimized by using high-temperature coatings or oxide treatments.

Common forms of the specimen gage section are cylindrical, hourglass-shaped, and various shapes containing stress concentrations. However, in keeping with the general theme of this chapter relating to strain-controlled, low-cycle-fatigue testing, only smooth unnotched specimens will be discussed. It will be assumed that the stress concentration due to the hourglass shape is negligible. The following comparisons can therefore be made between the hourglass-shaped and cylindrical gage sections.

The maximum strain is produced in a shorter section in the hourglass-shaped specimen than in the cylindrical specimen. This results in a greater resistance to buckling under the influence of large compressive strains. In addition, proper specimen heating is more readily accomplished with the hourglass shape since a long, flat temperature profile is not needed. It is generally sufficient to produce the maximum temperature at the minimum diameter. Also, use of the hourglass shape more closely approximates point-strain testing rather than the average-strain testing obtained with cylindrical specimens. This may or may not be desirable.

The shape of the gage section has a large effect on the extensometry and overall strain-control technique. Cylindrical specimens are generally used with axial extensometers that directly produce an axial-strain signal. This is a significant advantage since the axial strain is frequently the desired control parameter. One major problem area, however, is the attachment of the extensometer to the cylindrical gage section. This procedure must not damage the specimen to the extent of causing premature failure. Also, at least a portion of the extensometer must withstand the test temperature. Thus most commercially available extensometers are not suitable for fatigue testing above 500°F.

The hourglass shape does not permit a direct axial-strain measurement to be made. With these specimens a diametral extensometer is positioned at the minimum diameter. Attachment of the extensometer presents little difficulty since it can be suspended or balanced external to the specimen, with the only necessary contacts resulting in light diametrically opposed clamping forces at the minimum diameter. The small contact area between extensometer and specimen also minimizes the heat transfer to the extensometer. When a heat-resistant material (such as quartz) is used as contact members, the specimen temperature effect on the extensometer can be virtually eliminated.

Because of the heating and extensometry advantages, the hourglass-shaped specimen is widely used today. The major disadvantage, that of measuring diametral rather than axial strain, can usually be minimized with two basic techniques. One technique involves controlling diametral strain throughout the test and, later, mathematically determining the axial-strain values present at selected intervals

during the test. With this procedure the axial-strain amplitude can vary slightly as a function of strain hardening or softening, and specific mean strain (axial) values are difficult to set up and maintain. In general, however, satisfactory results can usually be obtained.

A better technique consists in instantaneously and continuously producing an electronic analog of the axial strain during the test and then automatically controlling this value rather than the diametral strain. Hardening or softening in this case will not affect the axial strain amplitude or mean value. This technique will be discussed in greater detail in the section covering the analog strain computer.

The conversion to axial strain used in both techniques assumes isotropic materials. The conversion of diametral to axial strain becomes much more difficult with anisotropic materials. Although the conversion may possibly be performed by using multiple diametral extensometers, it is recommended that cylindrical specimens and axial-strain measurements be used with these materials.

Most low-cycle-fatigue specimens are solid, but a significant number of hollow (both cylindrical and hourglass-shaped) specimens are being used. With such specimens, heating is accomplished at the inside surface by means of a small resistance element. This design permits faster heating and cooling rates when cyclic temperature tests are conducted. It is also possible that fatigue behavior of thin material is better approximated by testing tubular specimens having wall thicknesses of similar dimensions. One of the major disadvantages involves fabrication difficulties and cost since desired tolerances in wall thickness and inside surface finish can sometimes present special problems.

Force- and Deflection-Measuring Devices

Two variables of special interest in low-cycle-fatigue testing are the stress and strain in the specimen. The quantities measured, however, are the axial force on the end of the specimen and the deflection of the gage section. In general, however, the stress and strain are usually assumed to be directly related to the measured quantities, with the "constants" of proportionality being the gage-section cross-sectional area and length, respectively.

Force Measurement. The most widely used force-measuring device for fatigue testing is the strain-gaged load cell. Here an external force produces an elastic deformation in the cell, resulting in a resistance change in the attached strain-gage bridge. When an input voltage is applied to the bridge, it will produce an output voltage representing the applied force.

There are a large number of features to be evaluated in selecting a load cell for a particular application. The most common are the deflection constant, natural resonant frequency, sensitivity, linearity, hysteresis, zero balance, temperature stability, capacity, overload rating, extraneous load ratings, fatigue rating, compatibility with load-frame testing machine and fixtures, delivery, and price. Most commercially available cells are very competitive in most of these features, with a selection usually being made on the basis of compatibility, delivery, and price. A few points should be made, however, on the relation between some of these specifications and low-cycle-fatigue testing.

The maximum capacity rating of the load cell should be selected with some care. Although the cell capacity must be large enough to accommodate the maximum load expected in the testing program, it can also be too large. Because the force limitation of a load cell is based on a maximum allowable elastic strain, the maximum voltage output from the strain-gage bridge will be approximately the same regardless of the capacity of the cell. Thus the sensitivity or voltage output per unit force will decrease as the cell capacity increases. Also, the load-cell error components due to nonlinearity, hysteresis, and thermal effects are usually proportional to maximum cell capacity and may become significant for critical measurements. Examples are evaluations involving small amounts of plastic strain or changes in stress amplitude or bias due to strain hardening or softening, creep, or relaxation.

The fatigue rating of the cell is, of course, an important consideration. A large number of cycles can be accumulated on a load cell, and cell failure because of high-cycle fatigue is a common occurrence. Some manufacturers produce specially made cells for fatigue testing which are capable of many millions of cyclic force measurements to the rated capacity. A "standard" load cell can be used for fatigue applications if it is derated. A fairly common practice is to limit such a cell to 60% of its nominal force capacity.

Another feature that makes some load cells more applicable for low-cycle-fatigue testing is their resistance to extraneous loading. Side loading or torsional loading can occur during specimen installation or removal from the load train. Bending of the cell must be resisted when the specimen cracks or fractures completely.

Space limitations and the desirability to keep the load-train length to a minimum to prevent bending of the specimen often require the load cell to be as short as possible. A relatively new type of cell, referred to as a flat or low-profile load cell, is produced by several manufacturers and satisfies these requirements. This type of cell also generally satisfies the other special fatigue requirements discussed above.

Strain-Measuring Devices. The measurement of strain in the gage section of a low-cycle-fatigue specimen presents some very unique and challenging problems. In fact, as mentioned previously, the strain-measuring technique is often the dominant consideration in specimen design. The use of strain gages directly is generally not satisfactory because of their inability to survive the large cyclic strain amplitudes and temperature environment usually encountered. Some type of transducer is therefore needed to sense the deflection in the gage section of the specimen and to

convert it to an electrical signal that can be used for measurement and control purposes. Noncontacting methods, such as those using optical, eddy-current, and capacitive measurement techniques, have been used with varying degrees of success. Although these approaches may eventually prove to be the most satisfactory means of strain sensing, at this writing the contacting type of sensor, which will be referred to as an extensometer, is the most popular.

The general requirements of an extensometer are that it accurately produce an electrical analog of gage-section strain throughout the test while not in itself having a significant effect on the measured strain or on the fatigue life of the specimen. This often means that deflections as small as 0.001 in. or less be measured within a few microinches. To do this, the extensometer must not slip on the specimen, yet it must not grip so tightly that it causes damage to the specimen. The extensometer must take these small measurements across the gage section while the total gage section is moving, and at least a portion of the extensometer has to be capable of withstanding the gage-section environment without damage. Also, the complete assembly should be very insensitive to all external inputs except the gage-section deflection. This means that the electrical output should not change, for example, if the room temperature changes a few degrees.

These requirements obviously imply devices that have a very high degree of resolution, stability, and linearity and a low hysteresis. It must also be possible to easily and accurately position the extensometer on the specimen. Of course, accurate calibration of the extensometer is of prime importance. The calibration technique should be such that the response of the extensometer to the calibration deflection should be identical to the gage-section deflection.

Figures 2.9 to 2.16 show some of the strain extensometers in present use. Two major types are evident, those capable of diametral measurements on hourglass-shaped specimens and those for use with cylindrical specimens. When these extensometers are used, two types of electrical transducers can be specified. One type of transducer converts the deflection in the gage section to an elastic strain in the extensometer, which is then measured with strain gages. Another transducer converts this deflection to a relative motion between the coil assembly and core of a linear-variable-differential transformer (LVDT). Rather than attempt to describe in detail each of the extensometers shown, this discussion will be devoted to one of the extensometers used extensively in the authors' laboratory, and emphasis will be placed on materials used, important design features, and performance characteristics.

Figure 2.9 shows the diametral extensometer currently in use in the authors' laboratory. The choice of materials was primarily influenced by temperature exposure and stability requirements. Quartz was used for the contacting tips, as well as for the lever arms and LVDT core rod. Since this material is not heated directly by the induction coil and because it has a low thermal conductivity (about 0.8 Btu hr^{-1} ft^{-2} $°F^{-1}$ ft), it is very insensitive to the specimen temperature. In addition, the low coefficient of thermal expansion of quartz (about 0.28×10^{-6} in. $in.^{-1}$ $°F^{-1}$) minimizes the effect on extensometer output of those temperature changes which do occur.

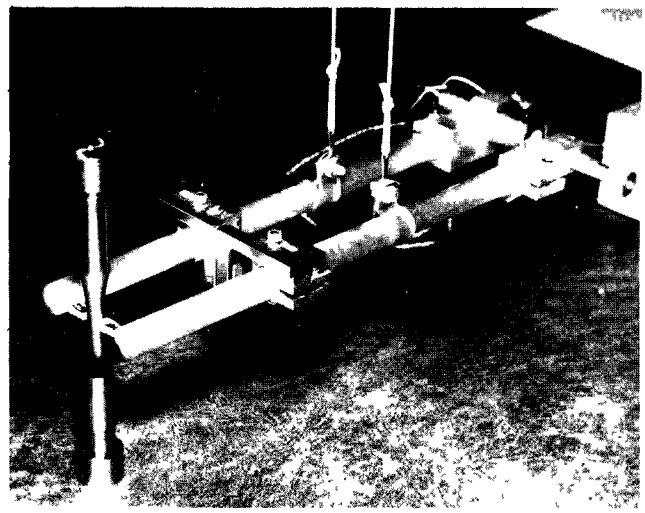

Fig. 2.9 Diametral extensometer used in the Mar-Test laboratory.

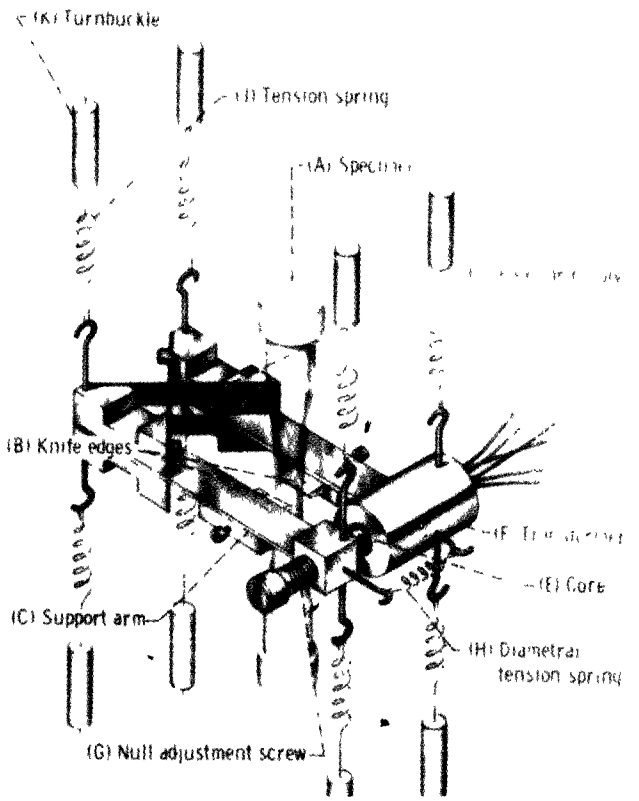

Fig. 2.10 Diametral strain gage and supports.[3d] (Published by permission of the American Society for Testing and Materials.)

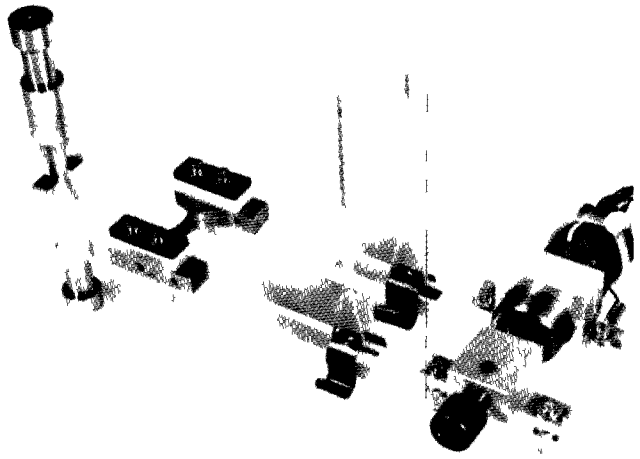

Fig. 2.11 Diametral extensometer.[3a] (Published by permission of the American Society for Testing and Materials.)

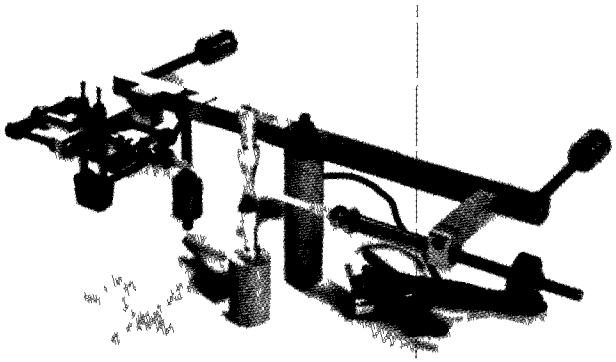

Fig. 2.12 Diametral extensometer.[3b] (Published by permission of the American Society for Testing and Materials.)

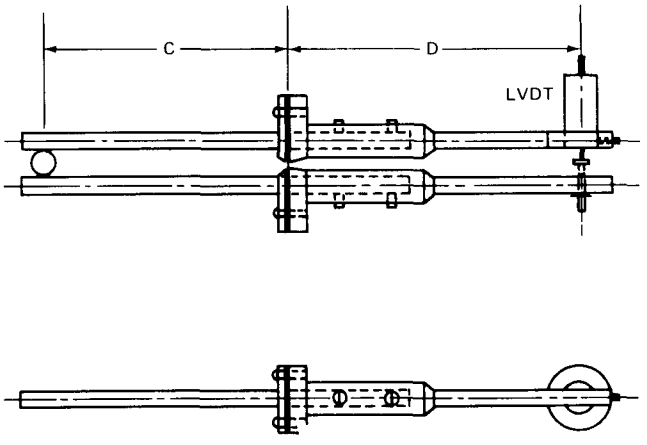

Fig. 2.13 Diametral extensometer.[3e] (Published by permission of the American Society for Testing and Materials.)

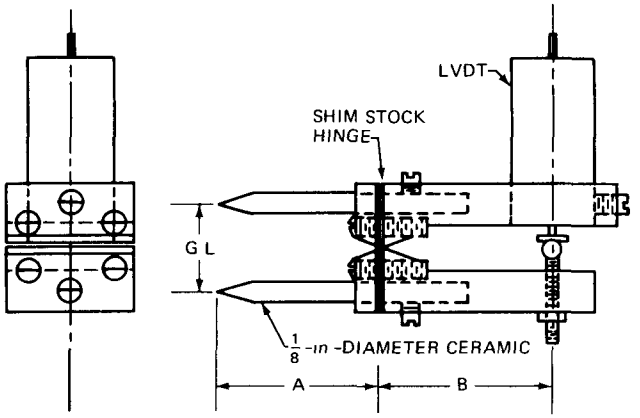

Fig. 2.14 Longitudinal extensometer.[3e] (Published by permission of the American Society for Testing and Materials.)

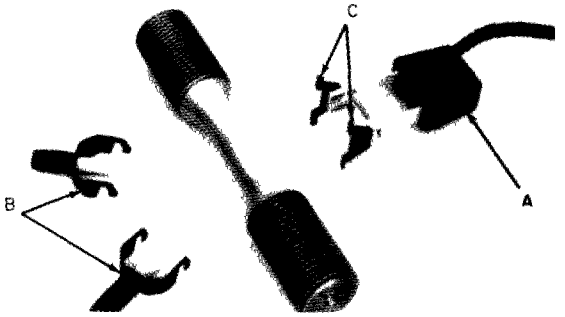

Fig. 2.15 Clip gage extensometer for axial-strain measurements.[3c] The extensometer A uses strain gages as sensing elements and is attached to the specimen via the slips B, which are spring loaded. The gage length of this extensometer is the distance between the knife edges $\mathcal{L}$ and is normally $\frac{1}{2}$ in. (Published bypermission of the American Society for Testing and Materials.)

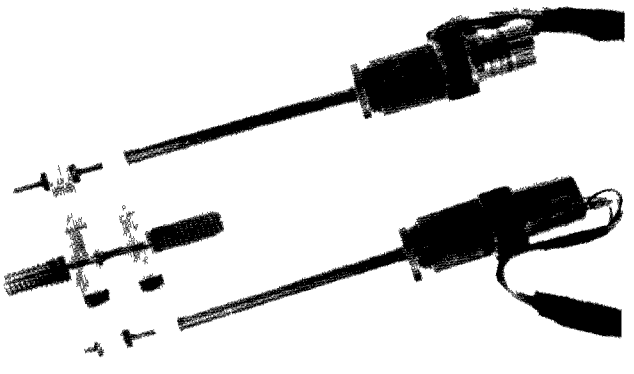

Fig. 2.16 Longitudinal extensometer.[3c] (Published by permission of the American Society for Testing and Material.)

The elastic-hinge assembly of the extensometer was fabricated from Invar because of its low thermal-expansion properties ($\alpha = 0.70 \times 10^{-6}$ in. in.$^{-1}$ °F^{-1} at room temperature). The LVDT mounting bracket and core-adjustment bracket were made of aluminum because of its low weight and nonmagnetic qualities.

The overall design of the extensometer was influenced by the following general requirements:

1. Efforts were made to keep the width to a minimum. Any change in thermal expansion of the extensometer in the width direction will result in an error signal since it is interpreted as a change in specimen diameter.

2. It was desirable to obtain some mechanical amplification from the displacement at the tips to the displacement of the core of the LVDT. At the same time, it was important to locate the hinge assembly sufficiently far from the specimen and induction coil to avoid unnecessary heating. These two requirements, along with suspension and balance considerations, resulted in an extensometer 10 in. long. The hinge is located 2.5 in. from the tips, producing a 3–1 advantage.

3. One requirement is that of being able to use the same extensometer with different-sized specimens. A hinge assembly was designed that permits lateral adjustments to be made to vary tip separation while maintaining the desired clamping force on the specimen. Specimens of approximately $\frac{1}{8}$ to $\frac{1}{2}$ in. in diameter can be accommodated. The hinge assembly also permits the easy replacement of the elastic hinge and contains adjustable clamps for attachment to the extensometer arms.

4. It was desirable to use standard quartz rod stock to eliminate the necessity for machining operations on this material. The only operations required are the fusing of the tips to the extensometer arms and the subsequent hand shaping of the contact portion of the tips.

5. Additional considerations are the weight of the overall assembly and the elastic constant (force/unit deflection) of the hinge. For maximum frequency response the weight should be kept to a minimum, and the elastic constant should be as large as possible. However, the hinge must not exert a damaging force on the specimen as it moves to follow the diametral expansion and contraction of the specimen, and the extensometer arms must be strong and rigid enough to bend only a negligible amount when the hinge is flexed. The weight and elastic constant are therefore, of necessity, compromise specifications. The extensometer in Fig. 2.9 weighs about 14 oz and has a resonant frequency of about 15 Hz. The contact force on the specimen is a fraction of an ounce.

6. The extensometer is suspended from strings attached to the test frame to accommodate the vertical motion of the specimen without introducing any adverse restraints on its normal deflection. Such suspension imparts a slight pivoting action to the contact tips relative to the specimen, but it does not seem to be detrimental from either a measurement or a damage standpoint.

The extensometer shown in Fig. 2.9 is calibrated in the special calibration fixture shown in Fig. 2.17. The suspension technique is exactly the same as that used in operation. The tips of the extensometer grip an axially split 0.250-in.-diameter pin, one side of which can be moved relative to the other by means of a precision micrometer. Thus the apparent diameter of the pin can be varied a known amount to an accuracy of about 10 μin. The sensitivity or gain of the system can be established by inserting a representative "strain" into the extensometer while monitoring the resultant change in output voltage from the strain sensing circuit.

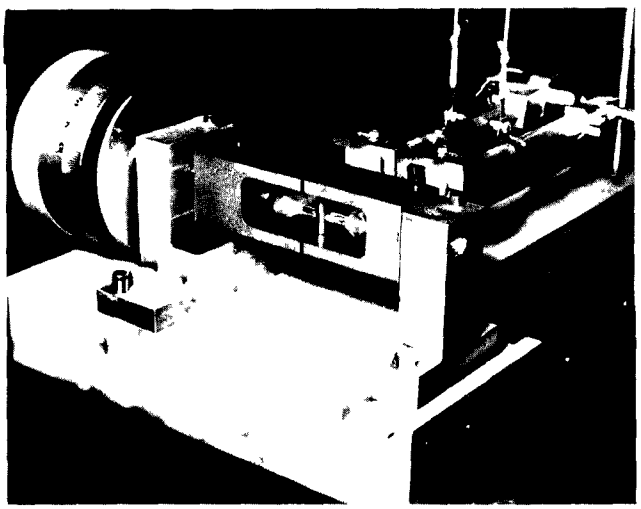

Fig. 2.17 Extensometer calibration device for use with the extensometer shown in Fig. 2.9.

Although the need for a reliable method of calibration of strain sensors is readily apparent, an often overlooked point is the establishment of the stability characteristics of these devices. Since strain is generally the controlled parameter in low-cycle-fatigue testing, it is possible to be misled when trying to evaluate the strain circuits under "closed-loop" conditions. The servo system will force the strain signal to correspond to the demand signal. Thus the strain signal under these conditions will only reflect the stability of the demand signal and the ability of the servo system to follow this demand. An open-loop evaluation of the extensometer and associated circuits is the better approach. A high-gain strip-chart recorder should be used to monitor the output of the strain circuit for a sufficient time to establish its drift characteristics. (At least a 24-hr period is recommended.) The gain of the system should be such that the equivalent of just a few microinches' change in output can be detected. During this time the extensometer can be connected to a section of quartz rod or tubing so that the effects due to changes in the mechanical input to the extensometer are minimized. The equivalent displacement drift recorded with this technique should then be divided by the specimen gage length to approximate the

mean strain error that may be expected in a strain-controlled fatigue test of similar duration.

Load Frames and Fixtures

In a fatigue-testing machine, the rod of the hydraulic ram provides a force to one end of the specimen to produce the desired stress–strain behavior. The resultant reaction forces, to the other end of the specimen and to the body of the ram, are provided by the load frame. Many different designs are commercially available; however, load frames made specially for low-cycle-fatigue testing are not common. Consequently many investigators build their own frames or perform certain modifications on general-purpose load frames. Therefore it seems in order to describe some of the desirable features of a low-cycle-fatigue load frame.

The load frame should be strong enough to survive an infinite number of fully reversed loads of a magnitude expected in fatigue work. Therefore, for evaluation of commercial frames, a proper understanding of the manufacturers' rating specification should be obtained. Usually the "dynamic" rating of the frame is the proper value to evaluate. In addition, three- or four-column frames are preferred over two-column designs because of the increased lateral rigidity. A common technique is the use of flex plates or sliding platens in the load train, near the specimen, to provide the maximum lateral stability while minimizing the axial constraint. The additional column or columns greatly facilitate this technique. This is especially important when large compressive strains are to be encountered while avoiding buckling of the specimen.

Proper frame adjustments are also desirable to accommodate many different-sized specimens. This can be accomplished by using load-frame-column or actuator-rod extensions. Some frames have adjustable platens or crossheads. Whatever the method, however, realignment of the frame should not be necessary when a height adjustment is made.

Vibration- or shock-isolation pads of some sort are often necessary on load frames. One common problem area is the severe shock that can be generated when a specimen fractures under the influence of several thousand pounds. Without some isolation device, the disturbance can be transmitted to neighboring equipment. For example, delicate extensometry can easily be disturbed. The authors have found the use of hard rubber mounting pads under the feet of the machines to be very effective; however, it may be wise to plan for the placement of very-high-capacity, or even very sensitive, machines at some distance from other equipment whenever possible.

The fixtures required for low-cycle-fatigue testing can assume a multitude of configurations in providing the mechanical interface connections for a large variety of specimens, load cells, and load frames. Consequently many fixtures are custom-designed for compatibility with the components and techniques of the particular investigator. However, whether fixtures are bought "off the shelf" or are custom-made, they have several desirable common features.

The necessary strength and rigidity of the fixtures will be assumed. Also, water cooling must usually be provided to avoid thermal distortion in the fixtures or a detrimental effect on the load cell when heating the specimen. One of the most important considerations must be the ability to connect the specimen to the load train in a manner that avoids stressing the gage section of the specimen in the process. Not only are proper manufacturing tolerances for specimen and fixtures required but also some means of self-alignment may be necessary in the load train to compensate for less-than-perfect conditions. In any case it is a good practice to provide a means whereby the alignment of the specimen and attached fixtures can be checked prior to making the final connection in the load train. One very satisfactory method is to provide flat, parallel, bolted flanges for this final connection. During the assembly operation the flanges can be brought very close together without actually touching each other. The degree of alignment can then be estimated by sighting along the surfaces and checking the uniformity of the gap between them. Only when this observation is satisfactory should the surfaces be brought in contact and bolted together.

Whenever large threaded members are used in the load train, whether part of the specimen, load cell, ram, or adapters, their purpose should simply be to supply the clamping forces needed in the train, and in so doing bring other alignment surfaces together. Never attempt to use the threads alone for alignment. Care should also be taken that the connections thus made possess sufficient frictional forces, or are locked in some way, to prevent loosening during operation.

Although perfect alignment should always be the objective, it will not always be achieved. Thus it is necessary to at least indicate the relative seriousness of the kinds of misalignment sometimes encountered. When the axes of the various members of the load train are not parallel to each other, bending of the specimen and the load cell will result, perhaps in assembly and certainly during testing. Less serious, however, is a slight amount of axial float. This is the condition where the axes are not exactly aligned but are at least parallel to each other. A testing machine having a sufficient amount of lateral stability can sometimes tolerate the latter situation.

Specimen Heating

Various heating methods are used in elevated-temperature low-cycle-fatigue testing. The particular method may be influenced by other preferences, such as type of loading or extensometry or perhaps just the availability of heating and temperature-control equipment. The most common techniques being used are (1) radiant heating, using a resistance furnace or resistance-heating element in close proximity to the specimen; (2) direct resistance heating of the specimen by forcing a large electric current through it;

and (3) induction heating, where an induction coil surrounding the specimen induces eddy currents into it, again heating it resistively.

In the authors' laboratory, induction heating has been selected because of the following advantages:

1. The location and intensity of the eddy currents in the specimen can generally be controlled by the spacing and number of turns in the induction coil. This approach gives a great deal of flexibility in shaping the temperature profile in the gage section and eliminates any dependency on geometry alone.

2. Test setup is very fast. Since the specimen alone is heated, thermal equilibrium is established in a minimum time.

3. The induction coil does not greatly interfere with extensometry, being more easily penetrated (between the turns) than a furnace wall.

4. The generation of heat in the gage section minimizes heating of other load-train components, such as grips and load cell. Cooling of the grips is easily accomplished. In addition, electrical insulation in the grips is not required, since they are not in the conduction path of the heating currents.

5. Good temperature control is possible with fast-response electronic circuits, facilitating cyclic temperature testing as well as stable isothermal testing.

There also are certain disadvantages associated with induction heating, however. The equipment needed is expensive when compared, for example, with direct resistance heating. Also, with some coil designs, an undesirable increase in temperature may occur at a fatigue crack. This problem is not as extreme as with direct resistance heating, however, since the electric currents are generally parallel to the crack with induction heating rather than perpendicular to the crack, as is the case with the axial currents in directly heated specimens.

Some materials, such as copper or copper alloys, are difficult to heat with any resistance technique, including induction heating. The low resistance hinders the transfer of adequate power to the specimen. In addition, for copper, the high-thermal conductivity allows a large heat loss through the ends of the specimen. One solution is to eliminate the heat loss by also heating special adapters attached to the ends of the specimen. These serve as high-resistance couplings to the rest of the load train.

Another technique is to heat troublesome materials and unfavorably shaped specimens with a susceptor. This is an easily heated metal cylinder that is located between the coil and the specimen. Thus, in effect, a small furnace is made, and the specimen derives its heat by radiation from the walls of the susceptor. It is apparent, however, that extensometry problems can result from the use of this method.

The most common methods of temperature measurement and control involve the use of thermocouples because of their dependability, high resolution, and accuracy. Thermocouples are often attached directly to the specimen, usually by resistance welding, as close to the gage section as possible. Sometimes, however, this method results in a specimen failure being initiated at a weld junction. This is especially likely when testing low-ductility materials and those specimen designs in which the cross-sectional area of the specimen at the location of the thermocouple is little, if any, larger than that in the gage section. In these cases it is sometimes possible to weld the thermocouples at a location much farther from the gage section. Before the test is started, the correct gage-section temperature can be established by a wrap-on or probe-type couple, at the same time noting the temperature at the welded junctions. The wrap-on couple can then be removed and the welded thermocouples used for control. Satisfactory results can be obtained with this technique. However, large differences between the gage-section temperature and that at the location of the welded thermocouple should be avoided since it is possible for the gage-section temperature to change if there are changes in the heat-transfer characteristics of the specimen. For example, the gage-section temperature can change as the specimen becomes more oxidized during the test even though the temperature at the control couple remains constant. Obviously the more delicately the thermocouples can be applied, the closer they can be positioned to the gage section, and the better will be the temperature control. The thermocouples must stay attached for the duration of the test, however, and it is often desirable to parallel two sets of thermocouples located close together on the specimen.

Auxiliary Equipment

Additional equipment needed for low-cycle-fatigue testing not previously covered in this chapter include recorders and calibration devices. There must be some means to record the length of the test or the number of loading cycles imposed on the specimen. Elapsed-time indicators and even counters are used for these purposes. In addition, varying amounts of continuous stress and strain information are often recorded as functions of time on strip-chart recorders. The instantaneous relation between stress and strain at selected intervals during the test is usually displayed on an x–y recorder. Of course, dependability and durability are primary requisites for these components. Most specifications are very competitive, however, and frequently the selections are made on such things as type of chart paper or chart-paper capacity and the inking or writing system of the strip-chart recorders. In x–y recorders a fast slewing speed necessary to produce good hysteresis loops is often a deciding factor.

Some sort of calibration equipment is needed to assure that temperature, force, and strain measurements are correct. The strain-calibration device is the one likely to be specifically tailored for low-cycle-fatigue testing. As was indicated previously, the type of extensometer and the way in which it is mounted on the specimen will determine the

configuration of the calibration device. Calibrators are often commercially available for the direct calibration of axial extensometers and can sometimes be modified for use with diametral extensometers as well. Since these extensometers are generally custom-made, however, the calibrator is often designed and built specifically for them. The requirement in all cases is that the response of the extensometer to a displacement in the calibrator be the same as its response to an identical deformation in the specimen gage section. This requires that the extensometer be mounted the same way during calibration as during operation. With deflections requiring measurements within microinches, even the force of gravity on the extensometer can be significant and should be duplicated in calibration and operation as closely as possible. The actual measurement of the displacement in the calibrator can be made with a precision micrometer or dial gage. Of course, any hysteresis or dead band in the calibrator should be removed prior to introducing the known deflection.

Special Test Circuits

A great deal of potential versatility exists in the average closed-loop servo-controlled testing machine; it simply requires the individual investigator to get the most from the equipment by specifying the correct control parameters and test-setup techniques. In some cases it may even be necessary to perform slight machine modifications or to use specialized auxiliary equipment. Although some special tests are really only gimmicks, there are several that produce unique and very valuable information for little if any additional setup time or test costs. The following paragraphs will describe in detail some of the things that can be done.

Strain Computer. The hourglass-shaped specimen has received wide usage because of its many advantages for low-cycle-fatigue testing (see page 23). Unfortunately, however, the measured variable from such a specimen is the diametral strain, whereas the axial strain is generally of primary interest. Various techniques have been adopted to circumvent this difficulty.

A very common practice consists in measuring and controlling the diametral strain throughout the test and afterward computing the axial strain. This is a fairly simple procedure since, for isotropic materials, the following relation can be established:

$$\epsilon = \frac{-\epsilon_d}{\nu_p} + \frac{F}{AE}\left(1 - \frac{\nu_e}{\nu_p}\right) \qquad (2.6)$$

where ϵ = axial strain
ϵ_d = measured diametral strain
F = applied force
A = cross-sectional area of the specimen
E = modulus of elasticity
ν_e = Poisson's ratio elastic
ν_p = Poisson's ratio plastic

Although the above equation permits an after-the-fact computation of the axial strain, it also indicates this strain can change during the test. In those tests in which the force range or force bias changes as a function of hardening, softening, relaxation, etc., the axial strain range or strain bias will also change, somewhat complicating later data analysis. The largest changes will occur in those tests in which the elastic and plastic components of strain are of approximately the same magnitude. Little if any axial-strain change will occur when the controlled diametral strain is almost all plastic or almost all elastic. In these cases the following approximate relations exist:

$$\epsilon \approx \frac{-\epsilon_d}{\nu_p} \qquad \text{when } \epsilon_d \text{ is almost all plastic}$$

and

$$\epsilon \approx \frac{-\epsilon_d}{\nu_e} \qquad \text{when } \epsilon_d \text{ is almost all elastic}$$

The preceding difficulties can be eliminated with the assistance of a small special-purpose computer connected to the testing machine. This device uses the diametral-strain and axial-force signals, along with the specimen material constants, to instantaneously produce an electrical signal representing the axial strain. This then becomes the feedback signal for the servo controller, replacing the diametral-strain signal. Thus continuous control of the axial strain is possible.

The computer can be digital or analog. The authors prefer the latter, however, since the normal transducer output signals, as well as the servo-controller signals, are analog, and no interface equipment is needed. Figure 2.18 is a block diagram of the kind of computer module connected to each of the authors' testing machines. The device operates separately on the elastic and plastic components of strain in much the same manner in which a

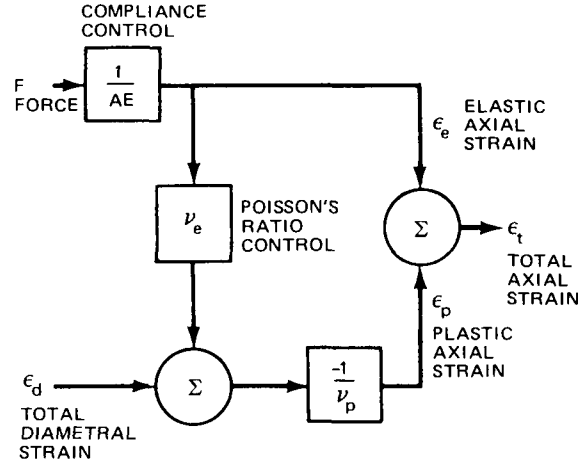

Fig. 2.18 Block diagram of strain computer.

hysteresis loop would be analyzed. The effect is the solution of Eq. 2.6 while generating analogs of all important strain components in the process. These analogs can then be monitored or used for control purposes at the operator's discretion.

Calibration of the computer consists in inserting the correct values of E and A for each test specimen at its operating temperature prior to the start of the test. The value of ν_p is assumed to be 0.5 for all materials at all test temperatures, in accordance with the constant-volume plastic deformation of isotropic materials. This value is a nonadjustable constant in the computer. A value of ν_e is determined for each specimen at the test temperature by cycling the specimen within the elastic region while adjusting the ν_e control to produce a zero plastic-strain signal. This procedure automatically inserts the correct value of ν_e into the computer and shows the value on a calibrated front-panel dial.

Other Special Control Modes. Sometimes it is desirable to control a test using other combinations of specimen parameters. As long as obvious inconsistencies are avoided, many combinations are possible. One useful technique consists in controlling the tension and compression force amplitudes on a specimen in combination with a limit on the maximum creep-strain amplitude. For example, a tensile force of a certain magnitude can be imposed on a specimen while monitoring the axial-strain amplitude. When the axial strain creeps to a predetermined limit, the control system can reverse the specimen loading into compression, causing creep toward some compressive limit. In this manner cyclic creep can continue between tensile and compressive limits for the duration of the test. Many different circuit variations are possible to accomplish the above. Basically it is necessary to be able to control the system programmer with an external command signal, furnished by a limit-sensing circuit. This circuit can be as simple as adjustable switches mounted on the strain recorder, which are capable of being actuated by the writing mechanism. Very inexpensive, solid-state limiter-relay modules can also be obtained to accomplish the same thing.

Another similar test would be to control the rate of one variable and the amplitude of another. For plastic-strain-amplitude correlations, for example, it may be desirable to cycle the specimen between tensile and compressive levels of plastic strain even though the instantaneous diametral strain rate is controlled. Controlling the plastic strain rate as well is a more difficult possibility. Even though the strain computer provides a plastic-strain signal that can be used as a feedback signal, the specimen under these conditions introduces a dead band into the system. During the elastic unloading of the specimen, the plastic strain will not change, and hence dynamic control is lost. The difficulty is greatest when the controlled-strain rate approaches the creep rate of the material. Generally satisfactory results can be obtained under complete plastic-strain control at the higher strain rates. The dynamic-control problem at these strain rates is only noticeable as a slight degradation of the plastic-strain wave form as the specimen unloads elastically.

THERMAL–MECHANICAL TESTING*

It is also desirable to modify the extensometer signal when conducting combined thermal–mechanical tests. Whenever the temperature of the specimen changes during the test (intentionally or accidentally), a thermal-strain component will be inserted into the extensometer signal along with the mechanical-strain component (that caused by a force on the specimen). This behavior causes control difficulties when an attempt is made to use the normal extensometer signal in the feedback circuit of the control system. For example, when an axial-strain extensometer is used, a temperature increase will cause an apparent increase in tensile strain which the control system will automatically correct by shifting the force in a compressive direction. In effect, the increased thermal strain will result in a decreased mechanical strain of the same magnitude. If a diametral extensometer is used for control purposes, however, the temperature increase will cause the force to shift in a tensile direction. The direction of the force shift will also be into tension if a diametral extensometer is used in conjunction with a strain computer for control purposes. However, the magnitude of the force shift will not be as large as with simple diametral-strain control.

In any case, it is apparent that the thermal-strain component has to be reckoned with to control the mechanical strain. The simplest way is to generate a system command signal, synchronized with a programmed temperature change, that contains a component representing the expected thermal strain in the specimen. The mechanical strain will then be represented by the remaining component in the composite command signal. This approach is facilitated by obtaining a representative thermal-strain signal, produced by the normal temperature cycle, prior to the test. This can be done by monitoring the extensometer output while the temperature of the specimen is cycled and the force is controlled at zero.

Another approach, and one which generally produces more satisfactory results, consists in electronically removing the thermal-strain component from the extensometer output before it is used in the feedback circuit. One way of accomplishing this is to create a separate thermal-strain signal as a function of temperature which is equal in amplitude and phase to that produced by the extensometer. A simple electronic subtraction will then produce an

*All previous discussions on test equipment, specimen design, force and strain measurements, load frames and fixtures, and specimen heating apply equally well to this special type of nonisothermal testing.

isolated mechanical strain signal to be used for control. Often it is possible to produce a satisfactory separate thermal component by driving a variable gain variable phase amplifier circuit with a specimen thermocouple signal. However more complex circuitry may be required when linearity and phasing problems occur as a consequence of large and fast temperature changes. Again the adjustment and evaluation of the particular circuit can be made by cycling the specimen temperature under zero force conditions. The objective of course is to produce a zero mechanical strain signal during the complete temperature cycle. It should be apparent that any output component caused by the temperature sensitivity of the extensometer itself will cause additional difficulties in proper compensation whatever the technique.

REFERENCES

1 *Manual on Fatigue Testing*, American Society for Testing and Materials Special Technical Publication No. 91, 1949.

2 *Metal Fatigue*, G. Sines and J. L. Waisman (Eds.), p. 89, McGraw Hill Book Company, Inc., New York, 1959.

3 *Manual on Low Cycle Fatigue Testing*, American Society for Testing and Materials Special Technical Publication No. 465, 1969.

(a) T. Slot, R. H. Stentz, and J. I. Berling, Controlled Strain Testing Procedures, p. 100.

(b) D. C. Lord and L. F. Coffin, Jr., High Temperature Materials Behavior, p. 129.

(c) C. F. Feltner and M. R. Mitchell, Basic Research on the Cyclic Deformation and Fracture Behavior of Materials, p. 27.

(d) M. H. Hirschberg, A Low Cycle Fatigue Testing Facility, p. 67.

(e) A. L. Carden, Thermal Fatigue Evaluation, p. 163.

Chapter 3

LOW-CYCLE-FATIGUE DATA

STAINLESS STEELS 304, 316, AND 348

Strain-Range and Strain-Rate Effects

A very extensive study[1] of the low-cycle-fatigue behavior of AISI 304, 316, and 348 stainless steels was performed in air at temperatures of 430 to 816°C (800 to 1500°F); strain ranges varied from 0.25 to 4.0%, and the strain rates varied from 4×10^{-5} to 4×10^{-3} sec^{-1}, with a few studies at both higher and lower strain rates. In addition, this program led to a fairly detailed evaluation of hold-time effects using hold periods from 0.1 to 600 min. The effect of various strain wave shapes was also studied[2-5] to provide a comparison of the effect of hold periods in tension only, in compression only, and in both tension and compression.

The chemical analyses for the materials studied in this program are presented in Table 3.1. A detailed material and specimen history is provided in Table 3.2. All test specimens had the hourglass shape shown in Fig. 3.1 with a minimum diameter of 6.35 mm (0.25 in.).

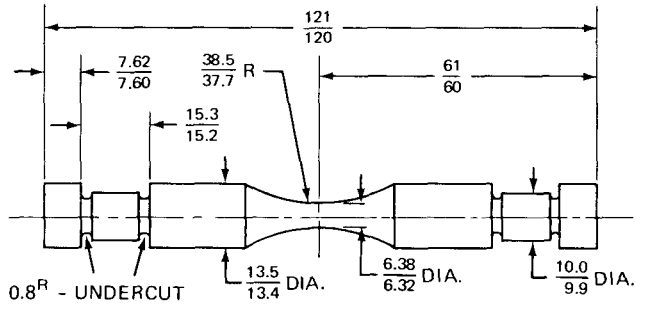

Fig. 3.1 Low-cycle-fatigue specimen. All dimensions are in millimeters.

Mechanical-property data for the three stainless steels studied are summarized in Table 7.21 of Chap. 7. These measurements were made in conjunction with the low-cycle-fatigue evaluations and served to more completely characterize the materials being studied.

In the early portions of this low-cycle-fatigue program, the measurements were made in diametral-strain control to yield the results presented in Table 3.3. Included in this summarization are:

1. The total, plastic, and elastic components of axial strain (calculated for $N_f/2$).
2. The total, plastic, and elastic components of diametral strain (the plastic and elastic components correspond to $N_f/2$).
3. The total diametral and axial strain rates.
4. The frequency of loading.
5. The stress range at $N_f/2$.
6. Various expressions for the fatigue life; in addition to N_f, the number of cycles to failure, values are also listed for N_0, the number of cycles to the first noticeable trend toward a decrease in the load below the steady-state or saturation value, and N_5, the number of cycles corresponding to a 5% decrease in the load. The times corresponding to each of these N values are also listed.

The fatigue-test results plotted in Fig. 3.2 show the correlation between total strain range ($\Delta\epsilon_t$) and fatigue life (N_5) at three temperatures for a strain rate of 0.004 sec^{-1}, the highest strain rate employed. A significant decrease in fatigue life with increase in temperature is apparent. It appears from Fig. 3.2 that at 650°C the 348 stainless steel has better fatigue resistance than the other two steels.

Some other comparisons based on the N_5 data presented in Table 3.3 are shown in Figs. 3.3 to 3.6. Additional comparisons based on the plastic strain range ($\Delta\epsilon_p$) are shown in Figs. 3.7 to 3.13 (the lines and curves in these figures were positioned manually to reflect what was felt to be average behavior).

A rather detailed comparison was made of these test results with fatigue data estimated for these test conditions using the Universal Slopes equation:[6,7]

$$\Delta\epsilon_t = 3.5 \frac{\sigma_u}{E} N_f^{-0.12} + \epsilon_f^{0.6} N_f^{-0.6} \qquad (3.1)$$

along with a subsequent extension[8,9] of this expression (see Chap. 4), where $\Delta\epsilon_t$ is the total axial strain range corresponding to N_f, σ_u is the ultimate tensile strength, E is the modulus of elasticity, and ϵ_f is the tensile ductility. Material-property data for use in Eq. 3.1 were taken from Table 7.21 in Chap. 7 to derive the comparisons presented in Figs. 3.14 to 3.28. In these graphs the solid curves represent average behavior as well as the upper and lower

TABLE 3.1

CHEMICAL ANALYSIS* FOR AISI 304, 348, AND 316 STAINLESS STEELS

Mat'l	Heat	C	Mn	Si	Cr	Ni	Mo	Co	Sn	Cu	S	P	Cb	N_2
304	55697	0.051	0.83	0.47	18.30	9.50	0 18		0 004	0 21	0.012	0 020		0.034
348	55700	0.04	1.67	0.51	17.52	9 67	0.06	0 018	0.009	0.06	0.009	0.014	0 58	0.037
316	65808	0.086	1 73	0.52	18.16	13.60	2.47	0 074	0.040	0.078	0.006	0.010		0 050

*In weight percent.

TABLE 3.2

MATERIAL AND SPECIMEN PROCESSING HISTORY

Material	Vendor processing	GE–NSP* processing	Grain structure	Average ASTM grain size	Average VHN hardness
AISI 304 stainless steel	Billets 49 cm^2 in cross-sectional area, rolled at 1180°C to rods 16 mm in diameter rods coiled, annealed 60 min at 1066°C, and water quenched sections cut from coil, straightened, and cut to 1 5-m lengths, stress relieved 30 min at 1010°C and water quenched	Specimens ground to hourglass configuration†, surface of gage section longitudinally polished annealed for 30 min at 1092°C in argon, cooling rate approximately 100°C/min	Equiaxed	3–5	139
AISI 316 stainless steel	Billets 7 cm^2 in cross-sectional area, rolled at 1180°C to rods 16 mm in diameter, rods coiled, annealed 60 min at 1066°C, and water quenched, sections cut from coil, straightened, and cut to 1.5-m lengths	Sample blanks annealed 30 min at 1070°C in air and water quenched, specimens ground to hourglass configuration†, surface of gage section longitudinally polished, stress relieved 60 min at 760°C in argon, cooling rate approximately 100°C/min	Equiaxed	3–5	171
AISI 348 stainless steel	Processing same as that used for AISI 304 stainless steel	Processing same as that used for AISI 304 stainless-steel specimens	Duplex, fine-grained core surrounded by a coarse-grained outer layer	Fine, 9–10, coarse, 3–5	155

*General Electric Company, Nuclear Systems Programs, Cincinnati, Ohio.
†Contour radius, 38 mm, minimum diameter, 6 35 mm.

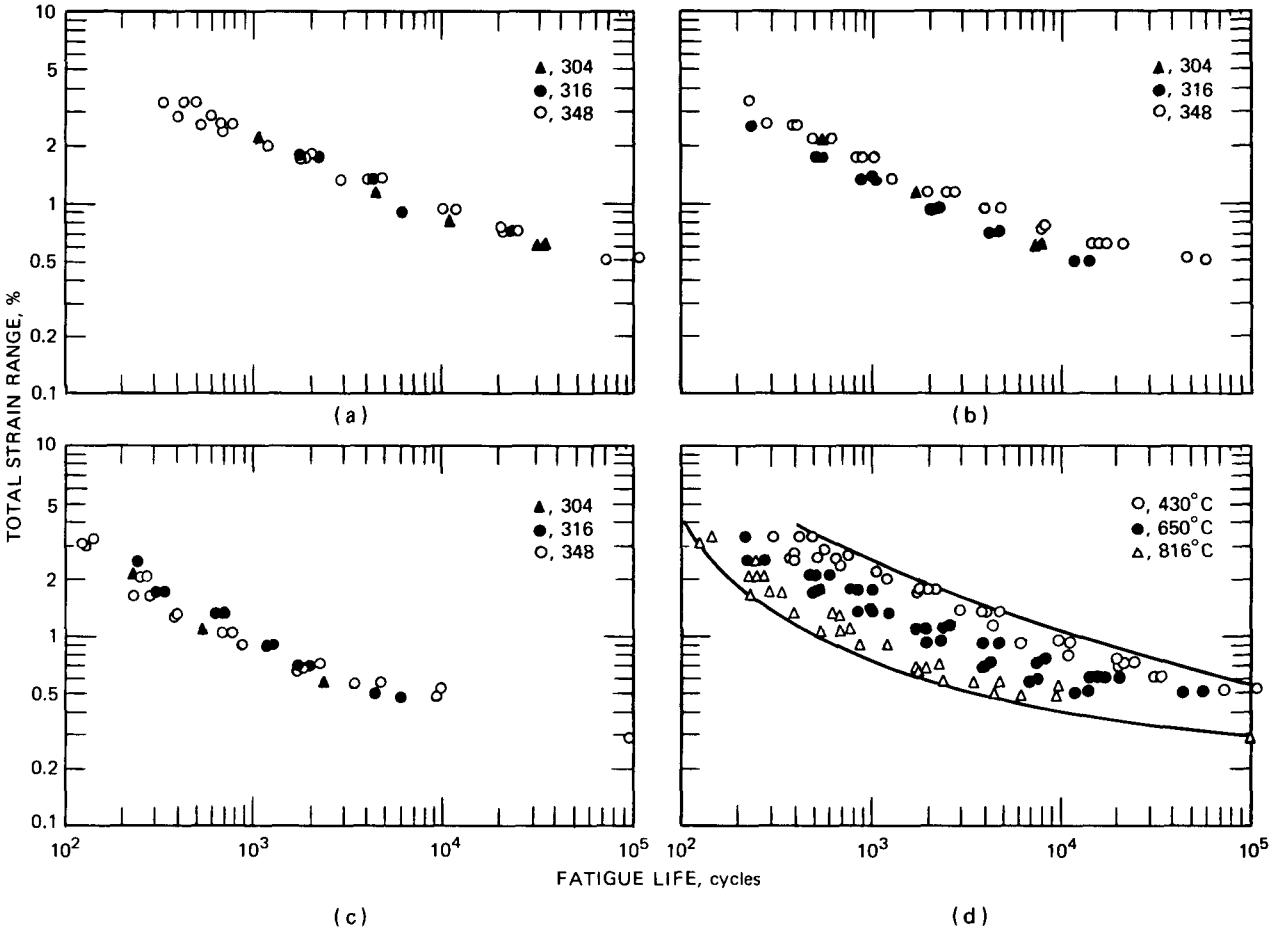

Fig. 3.2 Fatigue-test results for AISI 304, 316, and 348 stainless steels at a strain rate of 0.004 sec^{-1}. (a) At 430°C. (b) At 650°C. (c) At 816°C. (d) Data for all temperatures combined.

bounds on fatigue life; these curves have been positioned to show the extent of agreement with experimental results. The predictions are in good agreement with experimental results in the range to 10,000 cycles. Conservative predictions are seen to result in the lower strain-range region.

Graphs of plastic strain range vs. N_5 and N_f for the data presented in Table 3.3 exhibit definite linearity in accordance with:

$$\Delta\epsilon_p = cN_f^{-m} \tag{3.2}$$

or

$$\Delta\epsilon_p = cN_5^{-m} \tag{3.3}$$

A least-squares approach was used to identify the values of c and m for use in these expressions. The results are presented in Table 3.4 (p. 51) with calculated values of $\Delta\epsilon_p$ at the ¼-cycle point. In general, the values for m are essentially the same whether N_f or N_5 results are employed. Fairly large differences, however, are noted in the intercept (c) values, depending on whether N_f or N_5 data are considered. Some mention should also be made of the relation between these intercept values and the tensile ductility (ϵ_f) obtained in a short-term tensile test. On the basis of observations by Coffin,[10] the strain range at the ¼-cycle point should be equal to the tensile ductility, in which case, $2c = \epsilon_f$. A brief study of the results presented in Table 3.4 indicates fair agreement with this observation but only when the value of m is close to 0.5. For other values of m, the ¼-cycle intercept seems quite different from the tensile ductility. Additional studies of this point are needed for $m \neq 0.5$ before the proper significance of this intercept value can be established.

Cyclic Stress–Strain Behavior

Most of the fatigue tests reported in Table 3.3 exhibited cyclic-strain hardening during the early part of the tests. Typically, the stress range reached a saturation value in relatively few cycles, after which it remained stationary until cracks developed. An exception to this behavior was noted for 304 and 316 stainless steels at 430°C. At this temperature cyclic hardening was followed by cyclic softening before the stress range reached a steady-state condition. Some typical results for 316 stainless steel are presented in Fig. 3.29. *(Text continues on page 41.)*

TABLE 3.3

LOW CYCLE-FATIGUE DATA* FOR ANNEALED AISI 348, 304, AND 316 STAINLESS STEELS TESTED IN AIR AT 430, 650, AND 816°C

Temp., °C	Axial strain, %			Diametral strain, %			Strain rate, sec^{-1}		Frequency of loading, cycles/sec	Stress range at $N_f/2$		Fatigue life					
	$\Delta\epsilon_t$	$\Delta\epsilon_p$	$\Delta\epsilon_e$	$\Delta\epsilon_d$	$\Delta\epsilon_{dp}$	$\Delta\epsilon_{de}$	ϵ_d	ϵ_t		Psi	Kg/mm^2	N_0, cycles	N_0, hr	N_5, cycles	N_5, hr	N_f, cycles	N_f, hr
									348 Stainless Steel								
430	0 52	0 25	0 27	0 20	0 13	0 07	$1\,8 \times 10^{-3}$	$4\,6 \times 10^{-3}$	0 444	63,200	44 5			104,000	65 1	104,250	65 2
	0 73	0 46	0 27	0 31	0 23	0 07	$1\,8 \times 10^{-3}$	$4\,4 \times 10^{-3}$	0 3	64,200	45.2			20,129	18 6	20,329	18 8
	0 72	0 46	0 25	0 30	0 23	0 07	$1\,8 \times 10^{-3}$	$4\,2 \times 10^{-3}$	0 296	60,200	42 3			21,000	19 7	21,157	19 9
	0 72	0 46	0 27	0 30	0 23	0 07	$1\,8 \times 10^{-3}$	$4\,3 \times 10^{-3}$	0 296	63,200	44 5			24,000	22 5	24,126	22 6
	0 71	0 42	0 29	0 30	0 21	0 09	$1\,7 \times 10^{-3}$	$3\,5 \times 10^{-3}$	0 296					20,563	19 3	20,663	19 4
	0 93	0 64	0 29	0 40	0 32	0 08	$1\,8 \times 10^{-3}$	$4\,2 \times 10^{-3}$	0 228	68 300	48 0			9,724	11 8	9,824	12 0
	0 92	0 64	0 28	0 40	0 32	0 08	$1\,8 \times 10^{-3}$	$4\,1 \times 10^{-3}$	0 222	67,300	47 3			11,340	14 2	11,440	14 3
	1 37	1 01	0 35	0 60	0 51	0 10	$1\,8 \times 10^{-3}$	$4\,1 \times 10^{-3}$	0 15	84,300	59 3	2,607	4 83	2,855	5 29	2,945	5 45
	1 34	1 01	0 34	0 60	0 50	0 09	$1\,8 \times 10^{-3}$	$4\,0 \times 10^{-3}$	0 148	80,300	56 5	3,850	7 23	3,971	7 45	4,007	7.52
	1 36	0 99	0 37	0 60	0 49	0 10	$1\,8 \times 10^{-3}$	$4\,0 \times 10^{-3}$	0 148	87,300	61 4	4,484	8 42	4,653	8 73	4,776	8 96
	1 76	1 36	0 41	0 79	0 68	0 11	$1\,8 \times 10^{-3}$	$3\,9 \times 10^{-3}$	0 111	97,400	68 5	1,620	4 05	1,712	4 28	1,724	4 31
	1 78	1 36	0 42	0 79	0 68	0 12	$1\,8 \times 10^{-3}$	$3\,9 \times 10^{-3}$	0 111	100,400	70 6	1,823	4 56	1,833	4 59	1,875	4 69
	1 81	1 41	0 40	0 81	0 70	0 11	$1\,6 \times 10^{-3}$	$3\,6 \times 10^{-3}$	0 1	95,400	67 0	1,799	5 00	1,961	5 45	2,000	5 56
	1 99	1 55	0 44	0 90	0 78	0 12	$1\,8 \times 10^{-3}$	$3\,9 \times 10^{-3}$	0 099	104,400	73 4	1,081	3 03	1,170	3 28	1,182	3 32
	2 37	1 92	0 46	1 08	0 96	0 13	$2\,1 \times 10^{-3}$	$4\,7 \times 10^{-3}$	0 099	109 400	76 9	589	1 65	678	1 90	690	1 94
	2 58	2 10	0 49	1 18	1 05	0 13	$1\,8 \times 10^{-3}$	$3\,8 \times 10^{-3}$	0 074	115,400	81 2	466	1 75	512	1 92	538	2 02
	2 60	2 12	0 48	1 19	1 06	0 13	$1\,8 \times 10^{-3}$	$3\,8 \times 10^{-3}$	0 074	113,400	79 7	642	2 41	652	2 45	680	2 55
	2 64	2 16	0 48	1 21	1 08	0 13	$1\,8 \times 10^{-3}$	$3\,9 \times 10^{-3}$	0 074	114,400	80 5	736	2 76	751	2 82	762	2 86
	2 84	2 35	0 49	1 31	1 18	0 13	$1\,9 \times 10^{-3}$	$4\,2 \times 10^{-3}$	0 074	116,400	81 9	377	1 42	387	1 45	417	1 57
	2 88	2.41	0 48	1 33	1 20	0 13	$2\,0 \times 10^{-3}$	$4\,3 \times 10^{-3}$	0 074	113,400	79 7	582	2 18	589	2 21	607	2 28
	3 38	2 90	0 48	1 58	1 45	0 13	$1\,7 \times 10^{-3}$	$3\,7 \times 10^{-3}$	0 055	113,400	79 7	303	1 53	325	1 64	348	1 76
	3 41	2 93	0 48	1 60	1 46	0 13	$1\,8 \times 10^{-3}$	$3\,7 \times 10^{-3}$	0 055	114,400	80 5	403	2 04	420	2 12	430	2 17
	3 39	2 91	0 48	1 59	1 46	0 13	$1\,7 \times 10^{-3}$	$3\,7 \times 10^{-3}$	0 055	114,400	80 5	453	2 29	483	2 44	490	2 47
650	0 61	0 33	0 28	0 25	0 17	0 08	$2\,0 \times 10^{-5}$	$4\,9 \times 10^{-5}$	0 004	60,200	42 3			5,464	379 4	7,811	542 4
	0 62	0 32	0 30	0 25	0 16	0 09	$2\,0 \times 10^{-5}$	$4\,9 \times 10^{-5}$	0 004	66 100	46 5	2,323	161 3	3,236	224 7	3,661	254.2
	0 61	0 32	0 29	0 24	0 16	0 09	$2\,0 \times 10^{-4}$	$4\,9 \times 10^{-4}$	0 04	63,700	44 8	10,204	70 9	10,948	76 0	11,596	80 5
	0 61	0 32	0 29	0 25	0 16	0 09	$2\,0 \times 10^{-4}$	$4\,9 \times 10^{-4}$	0 04	63 700	44 8	6,819	47 4	7,269	50 5	7,807	54 2
	0 61	0 33	0 28	0 25	0 16	0 08	$2\,0 \times 10^{-3}$	$4\,9 \times 10^{-3}$	0 4	61,500	43 2	19,552	13 6	20,652	14 3	21,432	14 9
	0 61	0 33	0 28	0 25	0 16	0 08	$2\,0 \times 10^{-3}$	$4\,9 \times 10^{-3}$	0 4	60,700	42 7	14,663	10 2	15,010	10 4	15,192	10 6
	0 61	0 33	0 18	0 25	0 17	0 08	$2\,0 \times 10^{-3}$	$4\,9 \times 10^{-3}$	0 4	60,200	42 3	14,616	11 5	16,676	11 6	17,016	11 8
	0 61	0 33	0 28	0 25	0 17	0 08	$2\,0 \times 10^{-3}$	$4\,9 \times 10^{-3}$	0 4	60,500	42 5	13,272	9 22	14,012	9 73	14,172	9 84
	0 51	0 23	0 28	0 20	0 11	0 08	$1\,8 \times 10^{-3}$	$4\,5 \times 10^{-3}$	0 444	61,900	43 5			55,750	34 9	57,650	36 1
	0 52	0 25	0 27	0 21	0 12	0 08	$1\,8 \times 10^{-3}$	$4\,6 \times 10^{-3}$	0 444	59,700	42 0			44,320	27 7	46,140	28 9

	1 12	0 79	0 33	0 49	0 40	0 10	$2\ 0 \times 10^{5}$	$4\ 5 \times 10^{5}$	0 002	71,600	50 3	606	84 2	680	94 4	950	131 9
	1 11	0 81	0 30	0 49	0 41	0 09	$2\ 0 \times 10^{5}$	$4\ 4 \times 10^{5}$	0 002	65,100	45 8	731	101 5	762	105 8	870	120 8
	1 13	0 81	0 32	0 50	0 40	0 09	$2\ 0 \times 10^{5}$	$4\ 5 \times 10^{5}$	0 002	69,000	48 5	617	85 7	692	96 1	847	117 6
	1 11	0 82	0 29	0 49	0 41	0 08	$2\ 0 \times 10^{4}$	$4\ 4 \times 10^{4}$	0 02	62,700	44 1	806	11 2	989	13 7	1 259	17 5
	1 13	0 79	0 34	0 49	0 39	0 10	$2\ 0 \times 10^{4}$	$4\ 5 \times 10^{4}$	0 02	74,600	52 4	1,012	14 1	1,133	15 7	1,360	18 9
	1 12	0 79	0 33	0 49	0 40	0 10	$2\ 0 \times 10^{3}$	$4\ 5 \times 10^{3}$	0 2	72,000	50 6	2,190	3 04	2,607	3 62	2,685	3 73
	1 12	0 79	0 33	0 49	0 40	0 10	$2\ 0 \times 10^{3}$	$4\ 5 \times 10^{3}$	0 2	71,600	50 3	2 213	3 07	2,359	3 28	2,635	3 66
	0 76	0 44	0 32	0 32	0 22	0 09	$1\ 9 \times 10^{3}$	$4\ 5 \times 10^{3}$	0 296	69,600	48 9	7,362	6 91	7,866	7 38	8,010	7 52
	0 73	0 40	0 33	0 30	0 20	0 10	$1\ 8 \times 10^{3}$	$4\ 3 \times 10^{3}$	0 296	71,600	50 3	7,411	6 95	7,490	7 03	8,254	7 75
	0 93	0 59	0 34	0 40	0 30	0 10	$1\ 8 \times 10^{3}$	$4\ 1 \times 10^{3}$	0 222	73,800	51 9	3,608	4 51	3,770	4 72	4,040	5 06
	0 93	0 60	0 33	0 40	0 30	0 10	$1\ 8 \times 10^{3}$	$4\ 1 \times 10^{3}$	0 222	72,600	51 0	4,336	5 43	4,630	5 79	4,830	6 04
	2 14	1 79	0 35	1 00	0 89	0 10	$2\ 0 \times 10^{5}$	$4\ 3 \times 10^{5}$	0 001	76,600	53 8	167	46 4	177	49 2	208	57 8
	2 14	1 77	0 37	0 99	0 88	0 11	$2\ 0 \times 10^{5}$	$4\ 3 \times 10^{5}$	0 001	80,600	56 6	168	46 7	193	53 6	217	60 3
	2 15	1 76	0 39	0 99	0 88	0 12	$2\ 0 \times 10^{4}$	$4\ 3 \times 10^{4}$	0 01	85,100	59 9	301	8 36	335	9 31	370	10 3
	2 15	1 77	0 38	1 00	0 88	0 11	$2\ 0 \times 10^{4}$	$4\ 3 \times 10^{4}$	0 01	83 500	58 7	279	7 75	320	8 89	329	9 14
	3 41	2 95	0 46	1 61	1 48	0 13	$1\ 8 \times 10^{3}$	$3\ 7 \times 10^{3}$	0 055	99 700	70 1	175	0 88	216	1 09	226	1 14
	2 54	2 13	0 41	1 19	1 06	0 12	$1\ 8 \times 10^{3}$	$3\ 8 \times 10^{3}$	0 074	89,500	62 9	312	1 17	381	1 43	412	1 55
	2 54	2 13	0 40	1 19	1 07	0 12	$1\ 8 \times 10^{3}$	$3\ 8 \times 10^{3}$	0 074	87 700	61 7	340	1 28	377	1 42	398	1 49
	2 57	2 13	0 44	1 20	1 07	0 13	$1\ 8 \times 10^{3}$	$3\ 8 \times 10^{3}$	0 074	95 500	67 1	214	0 80	268	1 01	286	1 07
	2 14	1 74	0 39	0 99	0 87	0 12	$2\ 0 \times 10^{3}$	$4\ 3 \times 10^{3}$	0 1	85,500	60 1	443	1 23	471	1 31	550	1 53
	2 16	1 76	0 40	1 00	0 88	0 12	$2\ 0 \times 10^{3}$	$4\ 3 \times 10^{3}$	0 1	87,100	61 3	517	1 44	585	1 63	596	1 66
	1 74	1 35	0 40	0 79	0 67	0 12	$1\ 8 \times 10^{3}$	$3\ 9 \times 10^{3}$	0 111	86,500	60 8	907	2 27	980	2 45	1,024	2 56
	1 73	1 36	0 37	0 79	0 68	0 11	$1\ 8 \times 10^{3}$	$3\ 8 \times 10^{3}$	0 111	80,800	56 8	707	1 77	841	2 10	895	2 24
	1 72	1 35	0 37	0 78	0 67	0 11	$1\ 7 \times 10^{3}$	$3\ 8 \times 10^{3}$	0 111	79,800	56 1	726	1 82	815	2 04	834	2 09
	1 36	0 99	0 37	0 60	0 49	0 11	$1\ 8 \times 10^{3}$	$4\ 0 \times 10^{3}$	0 148	79,800	56 1	1 100	2 06	1,229	2 31	1,244	2 33
	1 12	0 79	0 33	0 49	0 40	0 10	$1\ 8 \times 10^{3}$	$4\ 0 \times 10^{3}$	0 178	72,600	51 0			1 850	2 89	1,926	3 01
816	0 55	0 38	0 17	0 25	0 19	0 06	$2\ 0 \times 10^{5}$	$4\ 4 \times 10^{5}$	0 004	32,100	22 6	1,474	102 4	1,554	107 9	1,862	129 3
	0 54	0 40	0 14	0 25	0 20	0 05	$2\ 0 \times 10^{5}$	$4\ 3 \times 10^{5}$	0 004	27 200	19 1	1,531	106 3	1,613	112 0	1,892	131 4
	0 55	0 38	0 17	0 25	0 19	0 06	$2\ 0 \times 10^{4}$	$4\ 4 \times 10^{4}$	0 04	32,600	22 9	1,616	11 2	1,874	13 0	2 461	17 1
	0 54	0 37	0 17	0 24	0 19	0 06	$2\ 0 \times 10^{4}$	$4\ 3 \times 10^{4}$	0 04	32,100	22 6	2,657	18 5	2 714	18 8	3,161	22 0
	0 56	0 34	0 22	0 25	0 17	0 07	$2\ 0 \times 10^{3}$	$4\ 5 \times 10^{3}$	0 4	41,500	29 2	3 054	2 12	3,379	2 35	4,281	2 97
	0 57	0 33	0 23	0 25	0 17	0 08	$2\ 0 \times 10^{3}$	$4\ 5 \times 10^{3}$	0 4	44,300	31 1	4,430	3 08	4,656	3 23	4,896	3 40
	0 29	0 12	0 17	0 12	0 06	0 06	$1\ 0 \times 10^{3}$	$2\ 6 \times 10^{3}$	0 444	32,600	22 9			98,130	61 4	98,130	61 4
	0 48	0 26	0 21	0 20	0 13	0 07	$1\ 8 \times 10^{3}$	$4\ 2 \times 10^{3}$	0 444	40,900	28 8	8,500	5 32	9,282	5 81	9,772	6 11
	0 53	0 30	0 22	0 23	0 15	0 08	$2\ 0 \times 10^{3}$	$4\ 7 \times 10^{3}$	0 444	42,700	30 0			9,610	6 01	9,874	6 18
	1 03	0 89	0 13	0 49	0 45	0 05	$2\ 0 \times 10^{5}$	$4\ 1 \times 10^{5}$	0 002	25,700	18 1	318	44 2	439	61 0	582	80 8
	1 04	0 89	0 15	0 50	0 45	0 05	$2\ 0 \times 10^{5}$	$4\ 2 \times 10^{5}$	0 002	28,300	19 9	350	48 6	385	53 5	586	81 4
	1 05	0 84	0 21	0 49	0 42	0 07	$2\ 0 \times 10^{4}$	$4\ 2 \times 10^{4}$	0 02	39,500	27 8	529	7 35	595	8 26	681	9 46
	1 05	0 84	0 21	0 49	0 42	0 07	$2\ 0 \times 10^{4}$	$4\ 2 \times 10^{4}$	0 02	40,100	28 2	386	5 36	462	6 42	729	10 1
	1 06	0 82	0 24	0 49	0 41	0 08	$2\ 0 \times 10^{3}$	$4\ 3 \times 10^{3}$	0 2	46,500	32 7	643	0 89	746	1 04	1 170	1 63
	1 06	0 82	0 25	0 49	0 41	0 08	$2\ 0 \times 10^{3}$	$4\ 3 \times 10^{3}$	0 2	47,400	33 4	596	0 83	682	0 95	949	1 32
	0 66	0 42	0 25	0 29	0 21	0 08	$1\ 7 \times 10^{3}$	$3\ 9 \times 10^{3}$	0 296	46,900	32 9	1,512	1 42	1,700	1 60	1,956	1 84
	0 69	0 48	0 21	0 31	0 24	0 07	$1\ 8 \times 10^{3}$	$4\ 1 \times 10^{3}$	0 296	39,900	28 1	1,722	1 62	1,820	1 71	1,974	1 85
	0 71	0 47	0 23	0 32	0 24	0 08	$1\ 9 \times 10^{3}$	$4\ 2 \times 10^{3}$	0 296	44,700	31 4	1,540	1 45	2,210	2 07	2,690	2 52

*Control mode, diametral strain, strain wave form, triangular with zero mean strain

(Table continues on next page)

TABLE 3.3 (Continued)

Temp., °C	Axial strain, %			Diametral strain, %			Strain rate, sec^{-1}		Frequency of loading, cycles/sec	Stress range at $N_f/2$		Fatigue life					
	$\Delta\epsilon_t$	$\Delta\epsilon_p$	$\Delta\epsilon_e$	$\Delta\epsilon_d$	$\Delta\epsilon_{dp}$	$\Delta\epsilon_{de}$	ϵ_d	ϵ_t		Psi	Kg/mm^2	N_0, cycles	N_0, hr	N_5, cycles	N_5, hr	N_f, cycles	N_f, hr
	0 90	0.66	0 24	0 41	0 33	0 08	$1\,8 \times 10^{-3}$	$4\,0 \times 10^{-3}$	0 222	45,100	31 7	711	0 89	860	1 08	1,335	1 67
	2 02	1.87	0 15	0 99	0 93	0 05	$2\,0 \times 10^{-5}$	$4\,0 \times 10^{-5}$	0 001	28,700	20 2	102	28 3	122	33 9	239	66 4
	2 02	1 86	0 17	0 99	0 93	0 06	$2\,0 \times 10^{-5}$	$4\,0 \times 10^{-5}$	0 001	31,600	22 2	94	26 1	118	32 8	183	50 8
	2 04	1 82	0 22	0 99	0 91	0 07	$2\,0 \times 10^{-4}$	$4\,1 \times 10^{-4}$	0 01	41,500	29 2	114	3 17	158	4 39	220	6 11
	2 04	1 82	0 22	0 99	0 91	0 08	$2\,0 \times 10^{-4}$	$4\,1 \times 10^{-4}$	0 01	42,100	29 6	132	3 67	176	4 89	315	8 75
	2 06	1 79	0 27	0 99	0 89	0 09	$2\,0 \times 10^{-3}$	$4\,1 \times 10^{-3}$	0 1	51,800	36 4	182	0 51	266	0 74	317	0 88
	2 05	1 80	0 26	0 99	0 90	0 09	$2\,0 \times 10^{-3}$	$4\,1 \times 10^{-3}$	0 1	48,900	34 4	181	0 50	245	0 68	326	0 91
	1 30	1 03	0 27	0 61	0 51	0 09	$1\,8 \times 10^{-3}$	$3\,9 \times 10^{-3}$	0 148	52,200	36 7	306	0 57	390	0 73	662	1 24
	1 29	1 01	0 28	0 60	0 50	0 09	$1\,8 \times 10^{-3}$	$3\,8 \times 10^{-3}$	0 148	52,800	37 1	279	0 52	380	0 71	477	0 90
	1 68	1 41	0 27	0 80	0 70	0 09	$1\,8 \times 10^{-3}$	$3\,7 \times 10^{-3}$	0 111	51,000	35 9	215	0 54	283	0 71	358	0 90
	1 67	1 38	0.30	0 79	0 69	0 10	$1\,6 \times 10^{-3}$	$3\,3 \times 10^{-3}$	0 099	56,300	39 6	120	0 34	230	0 65	304	0 85
	1 67	1 38	0 28	0 79	0 69	0 10	$1\,6 \times 10^{-3}$	$3\,3 \times 10^{-3}$	0 099	53,800	37 8	155	0 43	230	0 65	290	0 81
	3 11	2 83	0 28	1 51	1 41	0 10	$1\,7 \times 10^{-3}$	$3\,4 \times 10^{-3}$	0 055	53,800	37 8	90	0 45	122	0 62	150	0 76
	3 01	2 71	0 30	1 46	1 36	0 10	$1\,6 \times 10^{-3}$	$3\,3 \times 10^{-3}$	0 055	56,500	39 7	64	0 32	125	0 63	158	0 80
	3 34	3 05	0 30	1 62	1 52	0 10	$1\,8 \times 10^{-3}$	$3\,7 \times 10^{-3}$	0 055	56,300	39 6			140	0 71	214	1 08
								304 Stainless Steel									
430	0 60	0 36	0 24	0 25	0 18	0 07	$2\,1 \times 10^{-3}$	$5\,0 \times 10^{-3}$	0 414	56,600	39 8	33,400	22 4	33,900	22 7	34,160	22 9
	0 60	0 36	0 24	0 25	0 18	0 07	$2\,0 \times 10^{-3}$	$4\,8 \times 10^{-3}$	0 400	56,200	39 5	30 658	21 3	31,210	21 7	31,450	21 8
	0 79	0 53	0 26	0 34	0 26	0 07	$2\,0 \times 10^{-3}$	$4\,6 \times 10^{-3}$	0 293	61,200	43 0	9 297	8 81	10,887	10 3	10,917	10 3
	1 13	0 81	0 32	0 50	0 41	0 09	$2\,0 \times 10^{-3}$	$4\,5 \times 10^{-3}$	0 201	74,500	52 4	4,131	5 71	4,370	6 04	4,432	6 12
	2 19	1 72	0 47	0 99	0 86	0 13	$2\,0 \times 10^{-3}$	$4\,4 \times 10^{-3}$	0 100	109,400	76 9	974	2 71	1,060	2 94	1,070	2 97
650	0 57	0 36	0 22	0 25	0 18	0 07	$2\,0 \times 10^{-5}$	$4\,6 \times 10^{-5}$	0 004	46 900	33 0	1 618	112 4	1,966	136 5	3,124	216 9
	0 57	0 35	0 21	0 24	0 18	0 07	$1\,9 \times 10^{-3}$	$4\,5 \times 10^{-5}$	0 004	45,600	32 1	1,329	92 3	1,533	106 5	2,134	148 2
	0 58	0 34	0 24	0 25	0 17	0 08	$2\,0 \times 10^{-4}$	$4\,7 \times 10^{-4}$	0 04	51,500	36 2	2,517	17 5	3 009	20 9	3,549	24 6
	0 59	0 33	0 26	0 25	0 16	0 08	$2\,0 \times 10^{-3}$	$4\,7 \times 10^{-3}$	0 4	57,000	40 1	6,264	4 35	7 176	4 98	7,944	5 52
	0 59	0 33	0 26	0 25	0 17	0 08	$2\,0 \times 10^{-3}$	$4\,7 \times 10^{-3}$	0 4	56,100	39 5			7,000	4 93	7,320	5 08
	1 09	0 82	0 27	0 49	0 41	0 08	$2\,0 \times 10^{-5}$	$4\,3 \times 10^{-5}$	0 002	57,700	40 6	479	66 5	527	73 2	660	91 7
	1 10	0 80	0 30	0 49	0 40	0 09	$2\,0 \times 10^{-4}$	$4\,4 \times 10^{-4}$	0 02	65,100	45 8	604	8 39	748	10 4	805	11 2
	1 11	0 79	0 32	0 49	0 39	0 10	$2\,0 \times 10^{-3}$	$4\,4 \times 10^{-3}$	0 2	69,700	49 0	1 530	2 13	1,656	2 30	1,740	2 42
	2 08	1 80	0 28	0 99	0 90	0 09	$2\,0 \times 10^{-5}$	$4\,2 \times 10^{-5}$	0 001	60,700	42 7	153	42 5	194	53 9	261	72 5
	2 10	1 76	0 34	0 99	0 88	0 11	$2\,0 \times 10^{-4}$	$4\,2 \times 10^{-4}$	0 01	73,600	51 8	252	7 00	287	7 97	310	8 61
	2 10	1 71	0 39	0 98	0 86	0 12	$2\,0 \times 10^{-3}$	$4\,2 \times 10^{-3}$	0 1	84,000	59 0	418	1 16	524	1 46	566	1 57
816	0 56	0 38	0 18	0 25	0 19	0 06	$2\,0 \times 10^{-5}$	$4\,4 \times 10^{-5}$	0 004	33,600	23 6	487	33 8	591	41 0	788	54 7
	0 56	0 36	0 19	0 24	0 18	0 06	$2\,0 \times 10^{-4}$	$4\,5 \times 10^{-4}$	0 04	36,000	25 7	927	6 44	1,055	7 33	1,334	9 26
	0 56	0 36	0 20	0 25	0 18	0 06	$2\,0 \times 10^{-4}$	$4\,5 \times 10^{-4}$	0 04	37,600	26 4	1,139	7 91	1,202	8 35	1,351	9 38
	0 57	0 36	0 21	0 25	0 18	0 07	$2\,0 \times 10^{-3}$	$4\,5 \times 10^{-3}$	0 4	39,300	27 7	1,610	1 12	2,346	1 63	2,477	1 72
	1 05	0 87	0 18	0 49	0 43	0 06	$2\,0 \times 10^{-5}$	$4\,2 \times 10^{-5}$	0 002	33,800	23 8	166	23 1	204	28 3	307	42 6

	1 06	0 86	0 20	0 49	0 43	0 06	$2\,0 \times 10^{4}$	$4\,2 \times 10^{4}$	0 02	37,200	26 1	333	4 63	379	5 26	429	5 96
	1 07	0 83	0 24	0 49	0 42	0 08	$2\,0 \times 10^{3}$	$4\,3 \times 10^{3}$	0 2	44 500	31 3	469	0 65	529	0 73	784	1 09
	2 05	1 86	0 19	0 99	0 93	0 06	$2\,0 \times 10^{5}$	$4\,1 \times 10^{5}$	0 001	35,000	24 6	71	19 7	80	22 2	130	36 1
	2 05	1 83	0 22	0 99	0 92	0 07	$2\,0 \times 10^{4}$	$4\,1 \times 10^{4}$	0 01	40,500	28 5	88	2 44	117	3 25	145	4 03
	2 06	1 81	0 25	0 99	0 90	0 08	$2\,0 \times 10^{3}$	$4\,1 \times 10^{3}$	0 1	46 900	33 0	173	0 48	226	0 63	260	0 72
								316 Stainless Steel									
430	0 51	0 22	0 29	0 20	0 11	0 09	$1\,8 \times 10^{3}$	$4\,5 \times 10^{3}$	0 444	69,900	49 1			72,100	45 1	80,231	50 2
	0 71	0 41	0 29	0 30	0 21	0 09	$1\,8 \times 10^{3}$	$4\,2 \times 10^{3}$	0 296	70 300	49 4	20 347	19 1	21,329	20 0	21,898	20 5
	0 91	0 59	0 32	0 40	0 30	0 10	$1\,8 \times 10^{3}$	$4\,1 \times 10^{3}$	0 222	76,800	54 0			6,094	7 63	6,325	7 91
	1 33	0 96	0 37	0 60	0 48	0 12	$1\,8 \times 10^{3}$	$3\,9 \times 10^{3}$	0 148	88,600	62 3	4 047	7 60	4,101	7 70	4,118	7 73
	1 77	1 33	0 44	0 80	0 66	0 14	$1\,8 \times 10^{3}$	$3\,9 \times 10^{3}$	0 111	106,400	74 8	2 150	5 38	2,162	5 41	2,202	5 51
	1 75	1 31	0 45	0 79	0 65	0 14	$1\,8 \times 10^{3}$	$3\,9 \times 10^{3}$	0 111	107,600	75 7			1,738	4 35	1,764	4 41
650	0 59	0 32	0 26	0 25	0 16	0 09	$2\,0 \times 10^{5}$	$4\,7 \times 10^{5}$	0 004	57,900	40 7	4,469	310 3	4,663	323 8	4,886	339 3
	0 60	0 30	0 30	0 25	0 15	0 10	$2\,0 \times 10^{5}$	$4\,8 \times 10^{5}$	0 004	66 300	46 6	2,587	179 7	2,792	193 9	2,934	203 8
	0 61	0 28	0 33	0 25	0 14	0 11	$2\,0 \times 10^{4}$	$4\,9 \times 10^{4}$	0 04	73,100	51 4	2,248	15 6	2,926	20 3	3,110	21 6
	0 61	0 28	0 33	0 25	0 14	0 11	$2\,0 \times 10^{4}$	$4\,9 \times 10^{4}$	0 04	72,100	50 7	2,840	19 7	3,444	23 9	3,906	27 1
	0 61	0 28	0 33	0 25	0 14	0 11	$2\,0 \times 10^{4}$	$4\,9 \times 10^{4}$	0 04	72,600	51 1	2,579	17 9	3,180	22 1	3,965	27 5
	0 60	0 30	0 30	0 25	0 15	0 10	$2\,0 \times 10^{4}$	$4\,8 \times 10^{4}$	0 04	65,700	46 2	10,947	76 0	11,677	81 1	11,883	82 5
	0 60	0 29	0 32	0 25	0 14	0 10	$2\,0 \times 10^{4}$	$4\,8 \times 10^{4}$	0 04	69,700	49 0	3,794	26 3	4,208	29 2	4,490	31 2
	0 50	0 20	0 30	0 20	0 10	0 10	$1\,8 \times 10^{3}$	$4\,5 \times 10^{3}$	0 444	66,900	47 0	12,878	8 06	13,394	8 38	13,527	8 46
	0 50	0 20	0 30	0 20	0 10	0 10	$1\,8 \times 10^{3}$	$4\,5 \times 10^{3}$	0 444	66,100	46 5			11,631	7 28	11,761	7 36
	1 10	0 77	0 33	0 49	0 39	0 11	$2\,0 \times 10^{5}$	$4\,4 \times 10^{5}$	0 002	73 200	51 5	538	74 7	562	78 1	611	84 9
	1 10	0 78	0 33	0 49	0 39	0 11	$2\,0 \times 10^{5}$	$4\,4 \times 10^{5}$	0 002	71,600	50 4	460	63 9	570	79 2	829	115 1
	1 12	0 74	0 38	0 49	0 37	0 12	$2\,0 \times 10^{4}$	$4\,5 \times 10^{4}$	0 02	83,600	58 8	616	8 56	764	10 6	808	11 2
	1 16	0 70	0 45	0 50	0 35	0 15	$2\,0 \times 10^{4}$	$4\,6 \times 10^{4}$	0 02	99 500	70 0	523	7 26	649	9 01	763	10 6
	0 71	0 38	0 34	0 30	0 19	0 11	$1\,8 \times 10^{3}$	$4\,2 \times 10^{3}$	0 296	73,600	51 8	4,086	3 83	4,183	3 93	4,432	4 16
	0 71	0 37	0 34	0 30	0 19	0 11	$1\,8 \times 10^{3}$	$4\,2 \times 10^{3}$	0 296	75,000	52 8	3,864	3 63	3,961	3 72	4,304	4 04
	0 93	0 52	0.41	0 40	0 26	0 13	$1\,8 \times 10^{3}$	$4\,1 \times 10^{3}$	0 222	89,600	63 0	1,698	2 12	1,931	2 42	2,089	2 61
	0 94	0 54	0 40	0 40	0 27	0 13	$1\,8 \times 10^{3}$	$4\,2 \times 10^{3}$	0 222	86,900	61 1	2,110	2 64	2,227	2 79	2,333	2 92
	2 11	1 72	0 39	0 99	0 86	0 13	$2\,0 \times 10^{5}$	$4\,2 \times 10^{5}$	0 001	86,400	60 7	56	15 6	93	25 8	102	28 3
	2 10	1 74	0 36	0 99	0 87	0 12	$2\,0 \times 10^{5}$	$4\,2 \times 10^{5}$	0 001	80,100	56 3	83	23 1	115	31 9	150	41 7
	2 11	1 72	0 39	0 99	0 86	0 13	$2\,0 \times 10^{5}$	$4\,2 \times 10^{5}$	0 001	86,000	60 4	71	19 7	95	26 4	98	27 2
	2 11	1 73	0 38	0 99	0 87	0 12	$2\,0 \times 10^{5}$	$4\,2 \times 10^{5}$	0 001	82,600	58 1	71	19 7	139	38 6	153	42 5
	2 15	1 70	0 45	1 00	0 85	0 15	$2\,0 \times 10^{4}$	$4\,3 \times 10^{4}$	0 01	99,500	70 0	148	4 11	193	5 36	223	6 19
	2 12	1 68	0 44	0 98	0 84	0 14	$2\,0 \times 10^{4}$	$4\,2 \times 10^{4}$	0 01	95,500	67 2	166	4 61	213	5 92	241	6 69
	2 56	2 03	0 53	1 19	1 01	0 17	$1\,8 \times 10^{3}$	$3\,8 \times 10^{3}$	0 074	115,800	81 4	137	0 51	219	0 82	228	0.86
	1 33	0 90	0 43	0 59	0 45	0 14	$1\,7 \times 10^{3}$	$3\,9 \times 10^{3}$	0 148	94,500	66 5	707	1 33	847	1 59	945	1 77
	1 34	0 90	0 45	0 59	0 45	0 15	$1\,8 \times 10^{3}$	$4\,0 \times 10^{3}$	0 148	97,900	68 8	943	1 77	1,006	1 89	1,032	1 94
	1 37	0 93	0 44	0 61	0 46	0 14	$1\,8 \times 10^{3}$	$4\,1 \times 10^{3}$	0 148	96,700	68 0	912	1 71	980	1 84	1,002	1 88
	1 75	1 26	0 49	0 79	0 63	0 16	$1\,8 \times 10^{3}$	$3\,9 \times 10^{3}$	0 111	106,700	75 0	419	1 05	496	1 24	522	1 31
	1 74	1 28	0 47	0 79	0 64	0 15	$1\,8 \times 10^{3}$	$3\,9 \times 10^{3}$	0 111	102,500	72 1	423	1 06	514	1 29	553	1 38
816	0 55	0 36	0 19	0 24	0 18	0 06	$1\,9 \times 10^{5}$	$4\,4 \times 10^{5}$	0 004	35,600	25 0	1,467	101 9	1,530	106 3	1,832	127 2
	0 56	0 37	0 19	0 25	0 18	0 06	$2\,0 \times 10^{5}$	$4\,5 \times 10^{5}$	0 004	35,600	25 0			1,600	111 1	2 006	139 3

(Table continues on next page)

TABLE 3.3 (Continued)

Temp., °C	Axial strain, %			Diametral strain, %			Strain rate, sec^{-1}		Frequency of loading, cycles/sec	Stress range at $N_f/2$		Fatigue life					
	$\Delta\epsilon_t$	$\Delta\epsilon_p$	$\Delta\epsilon_e$	$\Delta\epsilon_d$	$\Delta\epsilon_{dp}$	$\Delta\epsilon_{de}$	ϵ_d	ϵ_t		Psi	Kg/mm^2	N_0, cycles	N_0, hr	N_s, cycles	N_s, hr	N_f, cycles	N_f, hr
	0.59	0.32	0.27	0.25	0.16	0.09	2.0×10^{-4}	4.7×10^{-4}	0.04	49,400	34.8	1,938	13.5	2,046	14.2	2,208	15.3
	0.58	0.34	0.23	0.25	0.17	0.07	2.0×10^{-4}	4.6×10^{-4}	0.04	42,500	29.9	2,008	13.9	2,236	15.5	2,596	18.0
	0.58	0.33	0.25	0.25	0.17	0.08	2.0×10^{-4}	4.7×10^{-4}	0.04	45,900	32.3	1,497	10.4	1,718	11.9	2,121	14.7
	0.48	0.24	0.24	0.20	0.12	0.08	1.7×10^{-3}	4.3×10^{-3}	0.444	43,500	30.6	5,338	3.34	5,984	3.74	6,443	4.03
	0.50	0.25	0.25	0.21	0.13	0.08	1.8×10^{-3}	4.4×10^{-3}	0.444	45,500	32.0	3,813	2.39	4,375	2.74	4,961	3.10
	1.06	0.85	0.21	0.49	0.42	0.07	2.0×10^{-5}	4.2×10^{-5}	0.002	39,500	27.8	468	65.0	524	72.8	637	88.5
	1.08	0.81	0.28	0.49	0.40	0.09	2.0×10^{-4}	4.3×10^{-4}	0.02	50,600	35.6	463	6.43	547	7.60	712	9.89
	1.08	0.82	0.26	0.49	0.41	0.08	2.0×10^{-4}	4.3×10^{-4}	0.02	47,000	33.0	506	7.03	590	8.19	811	11.3
	0.70	0.40	0.29	0.30	0.20	0.09	1.7×10^{-3}	4.1×10^{-3}	0.296	53,400	37.5	1,579	1.48	1,742	1.63	1,938	1.82
	0.68	0.41	0.27	0.29	0.20	0.09	1.7×10^{-3}	4.0×10^{-3}	0.296	49,800	35.0	1,792	1.68	1,933	1.81	2,406	2.26
	0.89	0.61	0.28	0.40	0.31	0.09	1.8×10^{-3}	4.0×10^{-3}	0.222	51,800	36.4	1,046	1.31	1,181	1.48	1,381	1.73
	0.89	0.60	0.29	0.39	0.30	0.09	1.7×10^{-3}	4.0×10^{-3}	0.222	53,400	37.5	1,093	1.37	1,199	1.50	1,485	1.86
	2.06	1.86	0.20	1.00	0.93	0.06	2.0×10^{-5}	4.1×10^{-5}	0.001	36,400	25.6	84	23.3	107	29.7	169	46.9
	2.05	1.83	0.22	0.99	0.91	0.07	2.0×10^{-5}	4.1×10^{-5}	0.001	40,700	28.6	122	33.9	131	36.4	165	45.8
	2.06	1.81	0.26	0.99	0.90	0.08	2.0×10^{-4}	4.1×10^{-4}	0.01	47,000	33.0	156	4.33	210	5.83	278	7.72
	2.07	1.79	0.28	0.99	0.90	0.09	2.0×10^{-4}	4.1×10^{-4}	0.01	51,400	36.1	171	4.75	215	5.97	270	7.50
	2.50	2.18	0.32	1.19	1.09	0.10	1.8×10^{-3}	3.8×10^{-3}	0.075	59,500	41.8	177	0.66	241	0.89	253	0.94
	1.30	1.00	0.29	0.60	0.50	0.09	1.8×10^{-3}	3.8×10^{-3}	0.148	53,900	37.9	575	1.08	628	1.18	684	1.28
	1.29	0.98	0.31	0.59	0.49	0.10	1.7×10^{-3}	3.8×10^{-3}	0.148	56,600	39.8	570	1.07	658	1.23	802	1.51
	1.69	1.37	0.32	0.79	0.69	0.10	1.7×10^{-3}	3.8×10^{-3}	0.111	58,900	41.4	303	0.76	335	0.84	398	1.00
	1.70	1.36	0.34	0.79	0.68	0.11	1.7×10^{-3}	3.8×10^{-3}	0.111	61,700	43.4	219	0.55	291	0.73	358	0.90

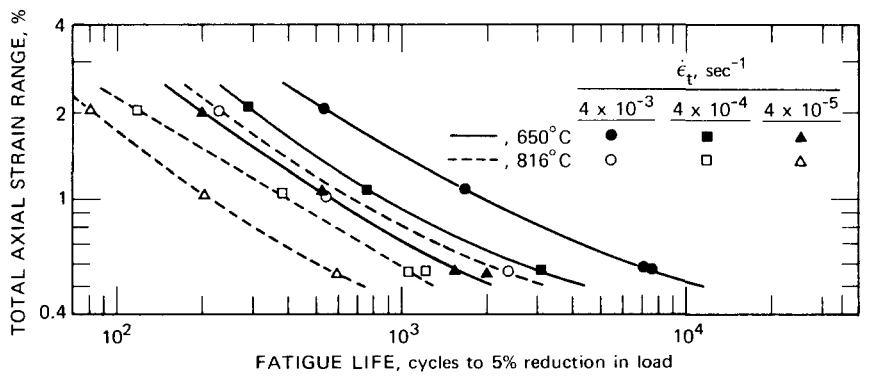

Fig. 3.3 Low-cycle-fatigue data for AISI 304 stainless steel at 650 and 816°C for various strain rates.

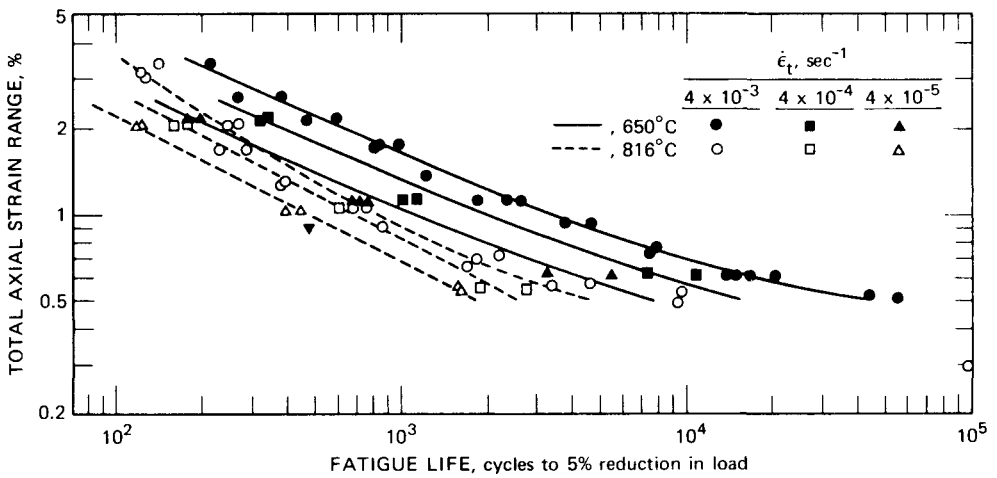

Fig. 3.4 Low-cycle-fatigue data for AISI 348 stainless steel at 650 and 816°C for various strain rates.

In Figs. 3.30 to 3.36, the relation between monotonic and cyclic stress–strain behavior is considered. The open circles correspond to the values of $\Delta\sigma$ and $\Delta\epsilon_t$ in Table 3.3 and therefore represent individual fatigue tests. The closed circles represent test results obtained with a single specimen. With the same strain rate used in the fatigue tests (4×10^{-3} sec^{-1}), the specimen was cyclically loaded for a relatively short number of cycles at each of several successively higher strain levels. Each data point shown gives the stress amplitude reached in 50 to 100 cycles at the particular strain level. The cyclic stress–strain diagram obtained by joining these data points is generally slightly lower than the results of the completed fatigue tests; however, the data generated for a single specimen are a good approximation of the curve representing many specimens.

The least agreement is apparent in the 430°C data obtained for 316 and 304 stainless steels. Here the closed circles essentially represent maximum values reached by the stress amplitude because of cyclic hardening. However, as mentioned previously, cyclic hardening at this temperature is followed by strain softening, and the open circles reflect the subsequent steady-state condition.

For comparison with the cyclic data, the monotonic true-stress–true-strain data obtained in tension tests at the same strain rate are also shown in the graphs. The differences between the monotonic and cyclic stress- strain diagrams are quite pronounced for all three materials.

Metallographic Evaluations

The photomicrographs in Figs. 3.37 to 3.39 show the pretest microstructure of the AISI 304, 348, and 316 stainless steels, respectively. The 348 stainless steel exhibits (Fig. 3.38) a duplex grain structure. The duplex structure at the controlled-strain region of the test specimen was such that the fine grains were located in the center and were surrounded by a coarse-grained outer layer. The depth of penetration of the coarse-grained layer toward the center was about 1.2 mm; however, in some cases, this length was closer to 2.5 mm.

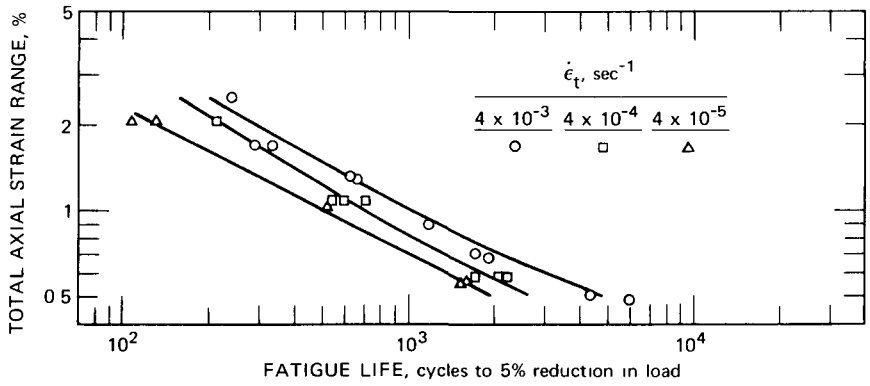

Fig. 3.5 Low-cycle-fatigue data for AISI 316 stainless steel at 816°C for various strain rates.

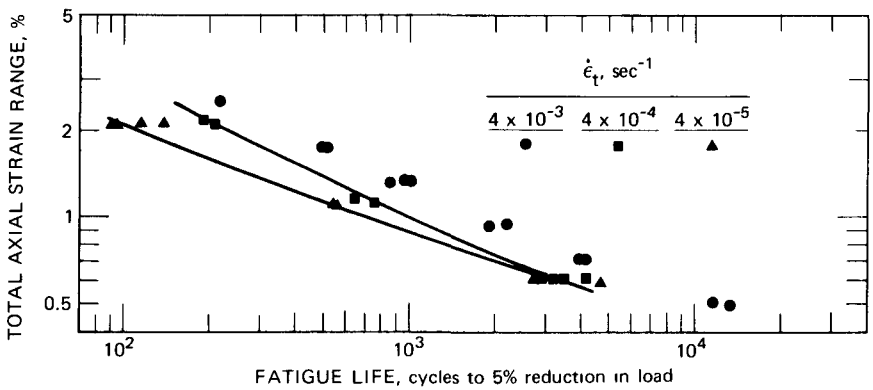

Fig. 3.6 Low-cycle-fatigue data for AISI 316 stainless steel at 650°C for various strain rates.

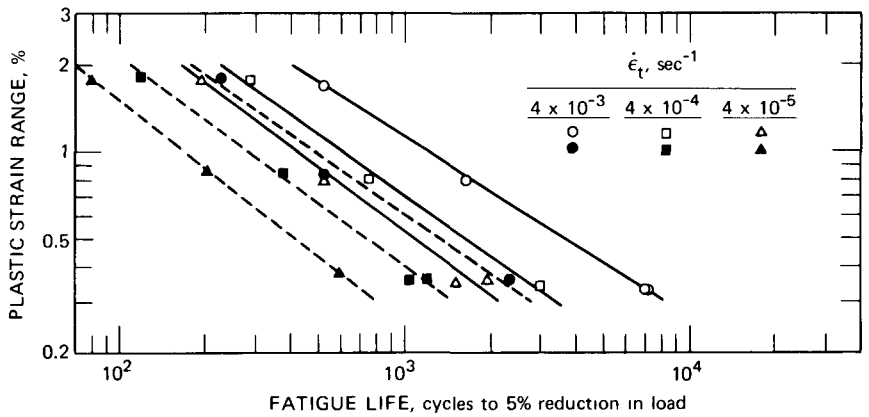

Fig. 3.7 Correlation of plastic-strain range and fatigue life for AISI 304 stainless steel at 650 and 816°C and axial strain rates of 4 x 10^{-3}, 4 x 10^{-4}, and 4 x 10^{-5} sec^{-1}.

Metallographic analyses were made of the longitudinal cross sections obtained at the fracture point from several 304 and 348 stainless-steel fatigue specimens. Identification of fracture mode and specific observations characteristic of the various test conditions are summarized in Table 3.5 (p. 55). Though specimens tested at 430°C were not evaluated, it is expected that, at strain rates of 4 x 10^{-3} sec^{-1}, the mode of initiation and propagation would be transgranular and that a gradual trend toward an intergranular mode would be observed as the strain rate is decreased.

Hold-Time Effects

A detailed study of hold-time effects was also a part of the General Electric Company, Nuclear Systems Programs

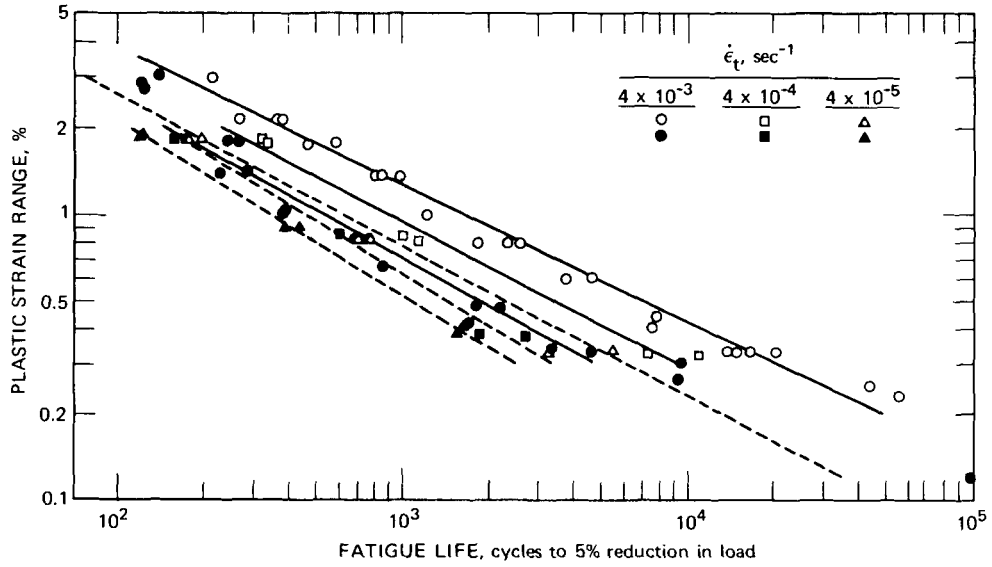

Fig. 3.8 Correlation of plastic-strain range and fatigue life for AISI 348 stainless steel at 650 and 816°C and axial strain rates of 4×10^{-3}, 4×10^{-4}, and 4×10^{-5} sec^{-1}.

(GE–NSP) low-cycle-fatigue program. Just before this evaluation began, a new technique development based on the analog strain computer was introduced (see Chap. 2). This device functioned to accept instantaneous values of the diametral strain and the axial load and converted these to instantaneous values of axial strain. These values were then used to provide axial-strain-controlled fatigue tests. Both axial strain range and axial strain rate were then the controlled variables.

The strain wave forms studied in this evaluation of hold-time effects are shown in Fig. 3.40. Strain wave form 1 represents the familiar triangular pattern; data obtained in these tests were compared with data obtained in hold-time tests to evaluate the effect of hold time on fatigue resistance. Wave form 2 represents hold periods in both the tension and compression portions of the cycle, and data have been obtained for hold periods that are equal (symmetrical holding) and unequal (unsymmetrical holding). The dashed curves are drawn to indicate schematically what the stress wave form would be like as a result of the relaxation that occurs during the hold period. Wave forms 3 and 4 represent hold periods in compression only and in tension only, respectively. Values for the strain rates employed correspond to the slope of the linear segments connecting the maximum and minimum points of the wave form and do not include the hold period itself.

(Text continues on page 49.)

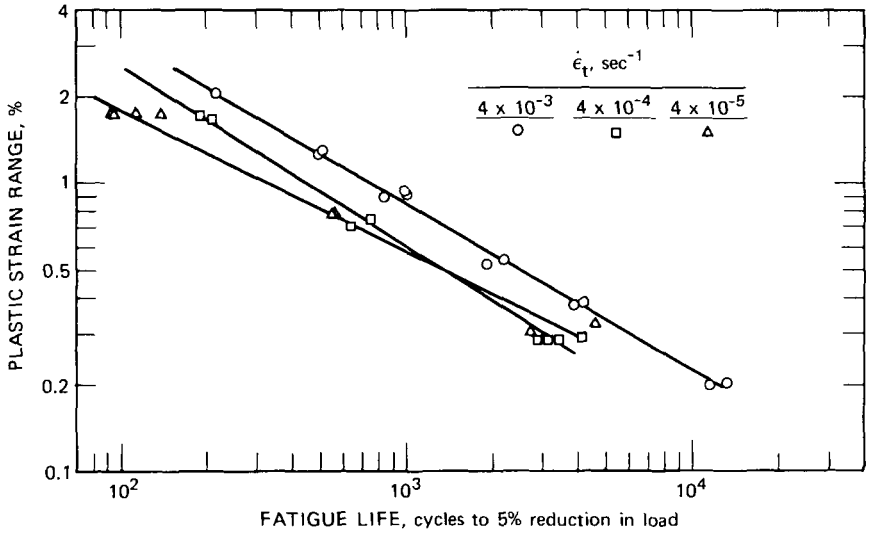

Fig. 3.9 Correlation of plastic-strain range and fatigue life for AISI 316 stainless steel at 650°C and axial strain rates of 4×10^{-3}, 4×10^{-4}, and 4×10^{-5} sec^{-1}

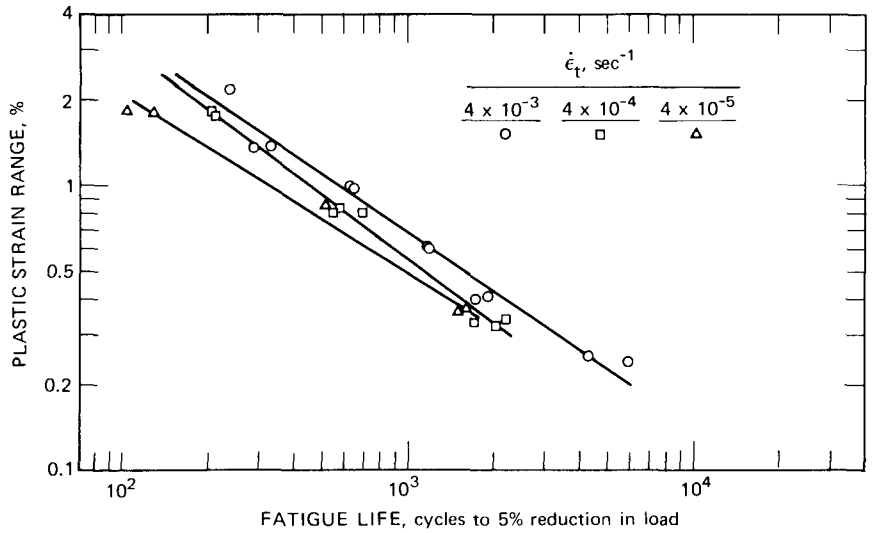

Fig. 3.10 Correlation of plastic strain range and fatigue life for AISI 316 stainless steel at 816°C and axial strain rates of 4×10^{-3}, 4×10^{-4}, and 4×10^{-5} sec^{-1}.

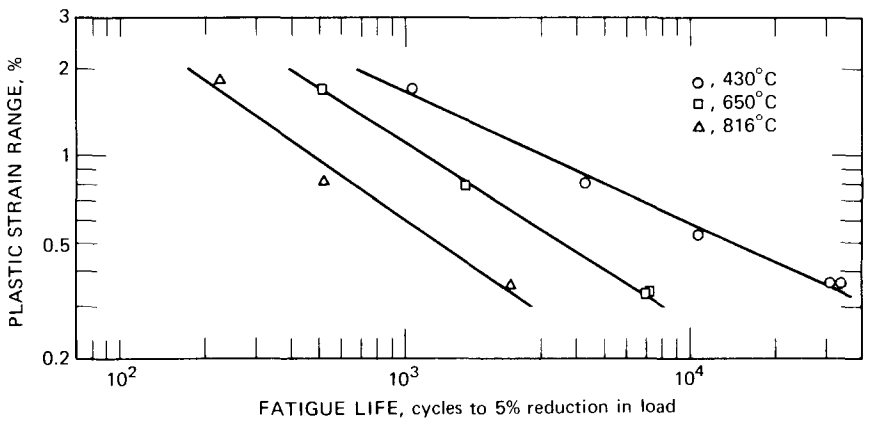

Fig. 3.11 Correlation of plastic strain range and fatigue life for AISI 304 stainless steel at 430, 650, and 816°C and an axial strain rate of 4×10^{-3} sec^{-1}.

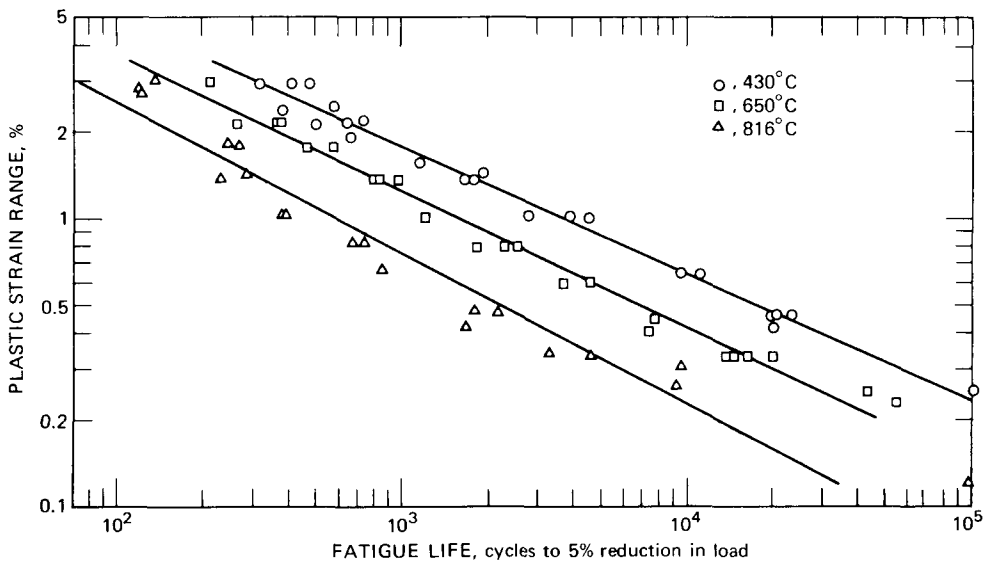

Fig. 3.12 Correlation of plastic strain range and fatigue life for AISI 348 stainless steel at 430, 650, and 816°C and an axial strain rate of 4×10^{-3} sec^{-1}.

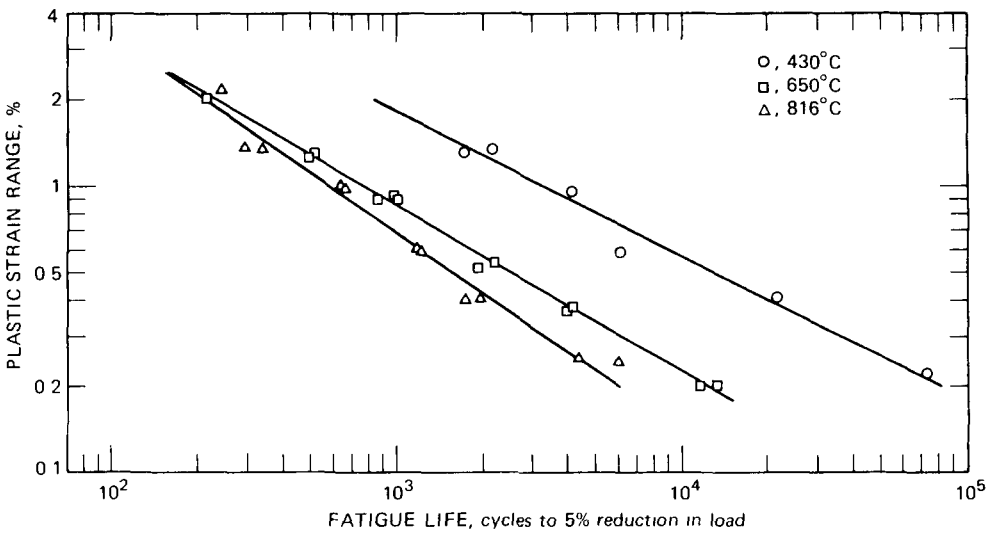

Fig. 3.13 Correlation of plastic strain range and fatigue life for AISI 316 stainless steel at 430, 650, and 816°C and an axial strain rate of 4×10^{-3} sec^{-1}.

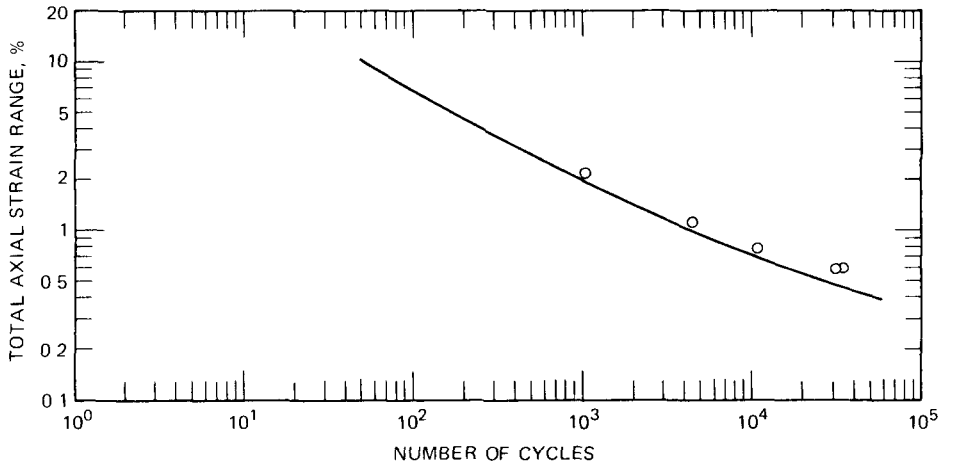

Fig. 3.14 Low-cycle-fatigue data for AISI 304 stainless steel at 430°C and an axial strain rate of 4×10^{-3} sec^{-1}.

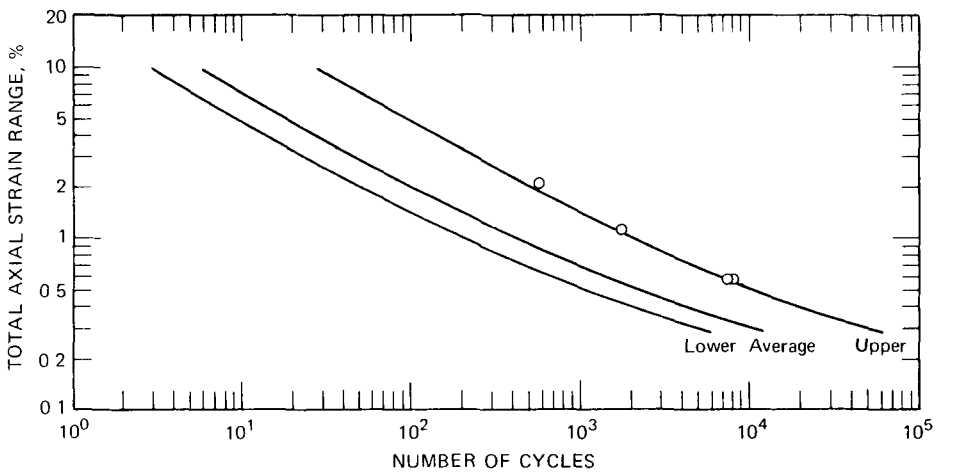

Fig. 3.15 Low-cycle-fatigue data for AISI 304 stainless steel at 650°C and an axial strain rate of 4×10^{-3} sec^{-1}.

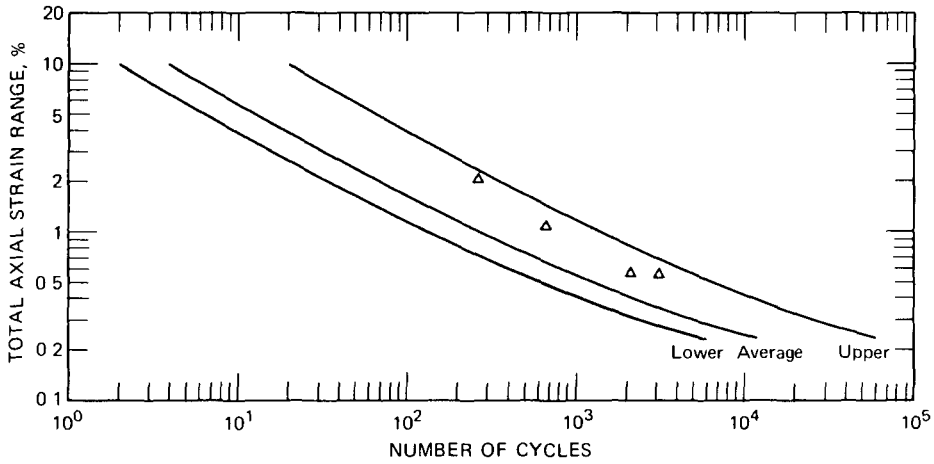

Fig. 3.16 Low-cycle-fatigue data for AISI 304 stainless steel at 650°C and an axial strain rate of 4×10^{-5} sec^{-1}.

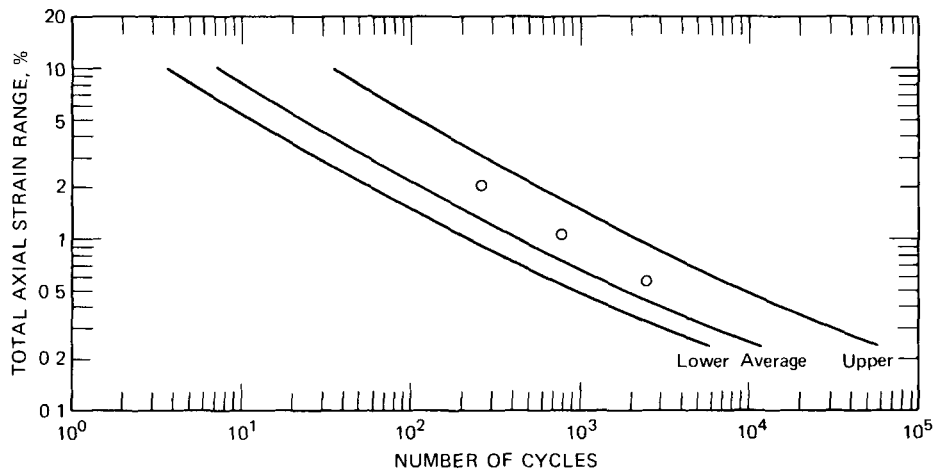

Fig. 3.17 Low-cycle-fatigue data for AISI 304 stainless steel at 816°C and an axial strain rate of 4×10^{-3} sec^{-1}.

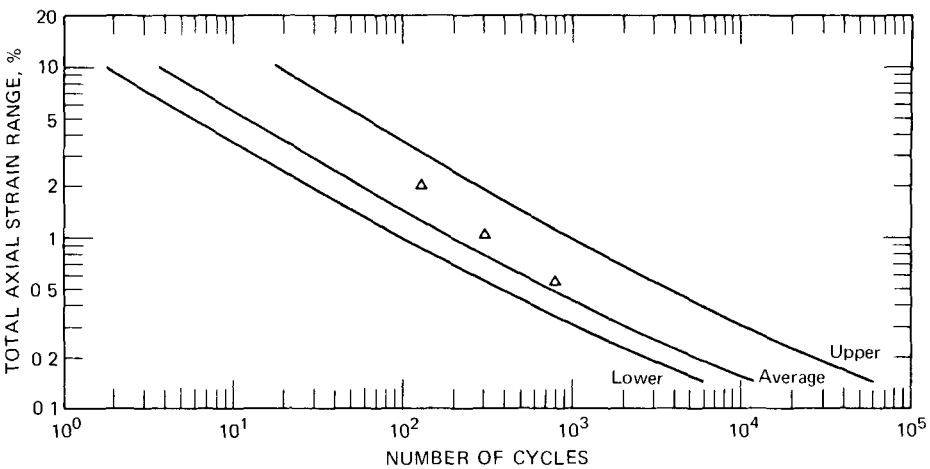

Fig. 3.18 Low-cycle-fatigue data for AISI 304 stainless steel at 816°C and an axial strain rate of 4×10^{-5} sec^{-1}.

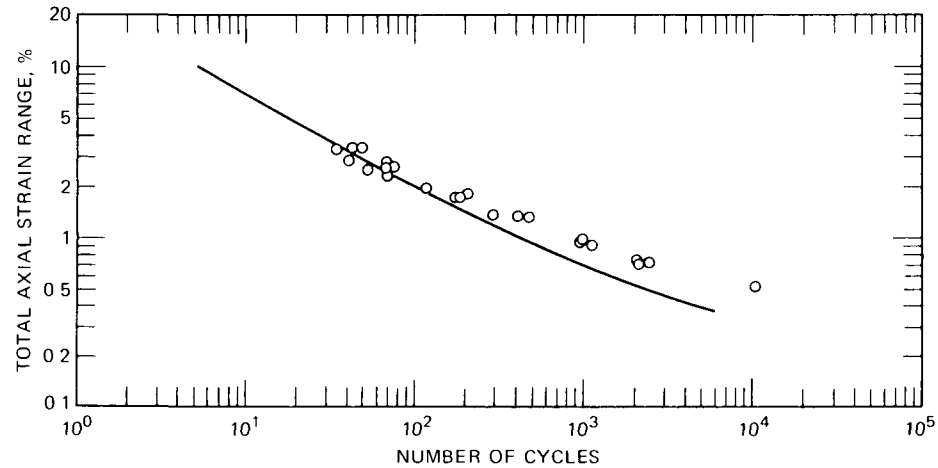

Fig. 3.19 Low-cycle-fatigue data for AISI 348 stainless steel at 430°C and an axial strain rate of 4×10^{-3} sec^{-1}.

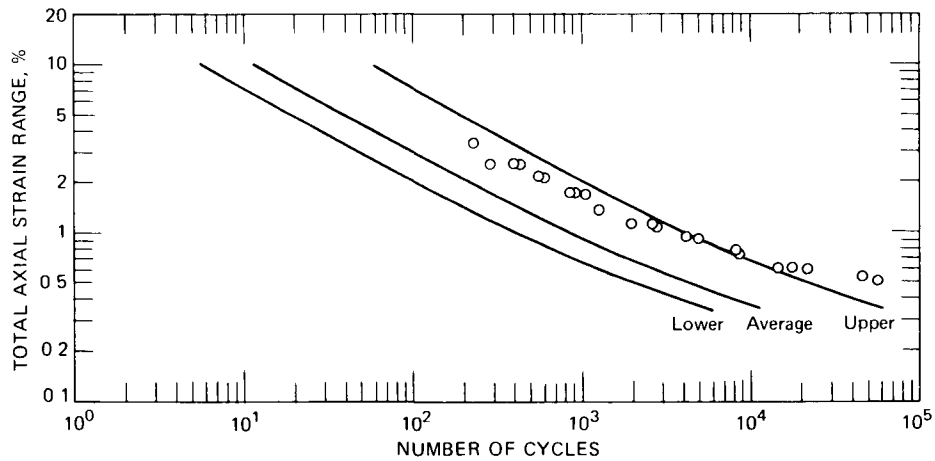

Fig. 3.20 Low-cycle-fatigue data for AISI 348 stainless steel at 650°C and an axial strain rate of 4×10^{-3} sec^{-1}.

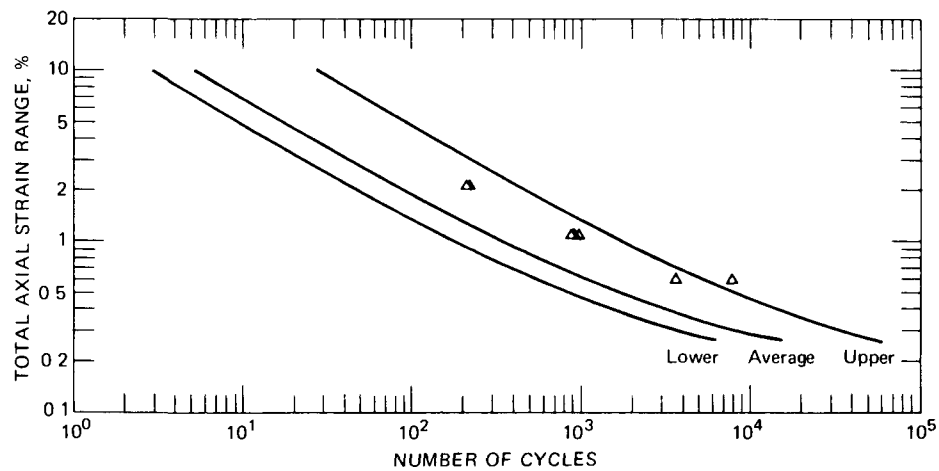

Fig. 3.21 Low-cycle-fatigue data for AISI 348 stainless steel at 650°C and an axial strain rate of 4×10^{-5} sec^{-1}.

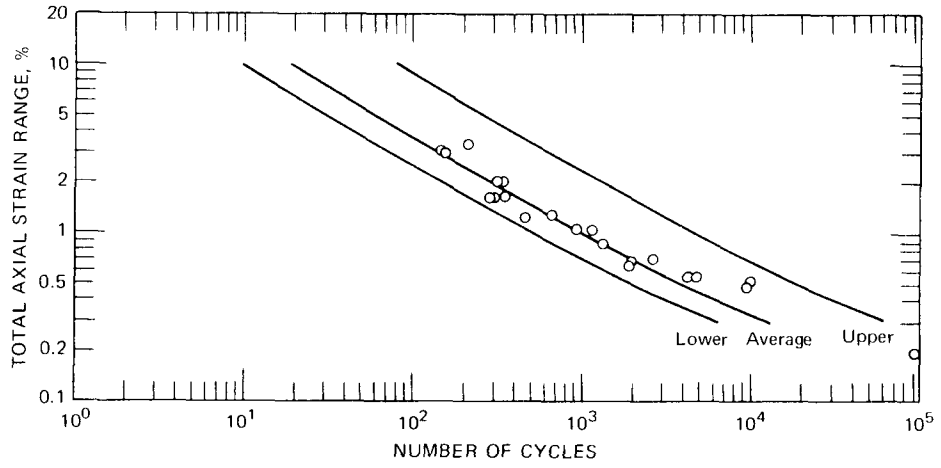

Fig. 3.22 Low-cycle-fatigue data for AISI 348 stainless steel at 816°C and an axial strain rate of 4×10^{-3} sec^{-1}.

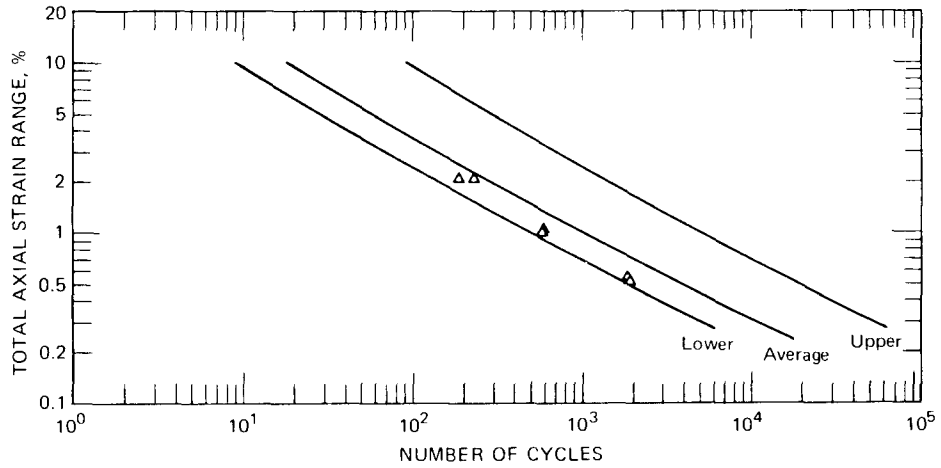

Fig. 3.23 Low-cycle-fatigue data for AISI 348 stainless steel at 816°C and an axial strain rate of 4×10^{-5} sec^{-1}.

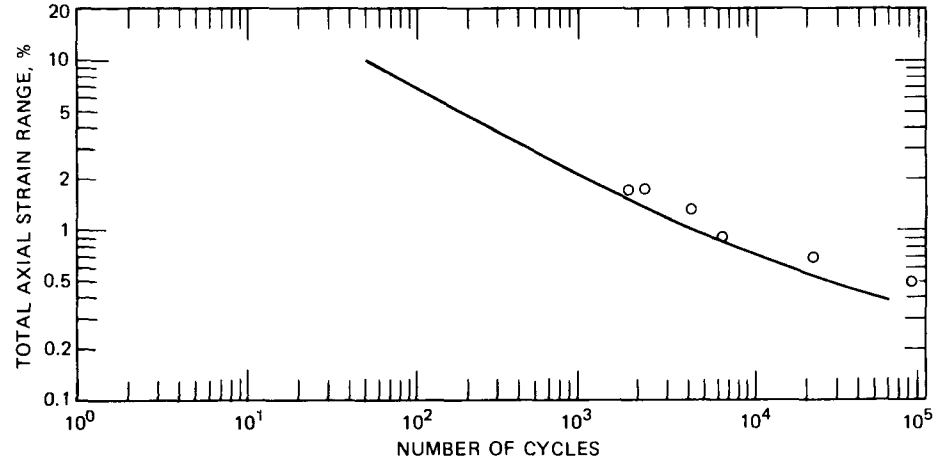

Fig. 3.24 Low-cycle-fatigue data for AISI 316 stainless steel at 430°C and an axial strain rate of 4×10^{-3} sec^{-1}.

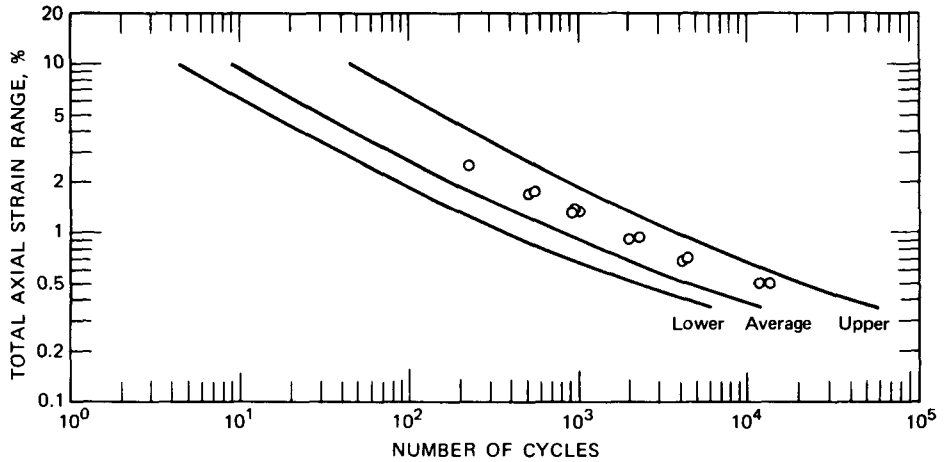

Fig. 3.25 Low-cycle-fatigue data for AISI 316 stainless steel at 650°C and an axial strain rate of 4×10^{-3} sec^{-1}.

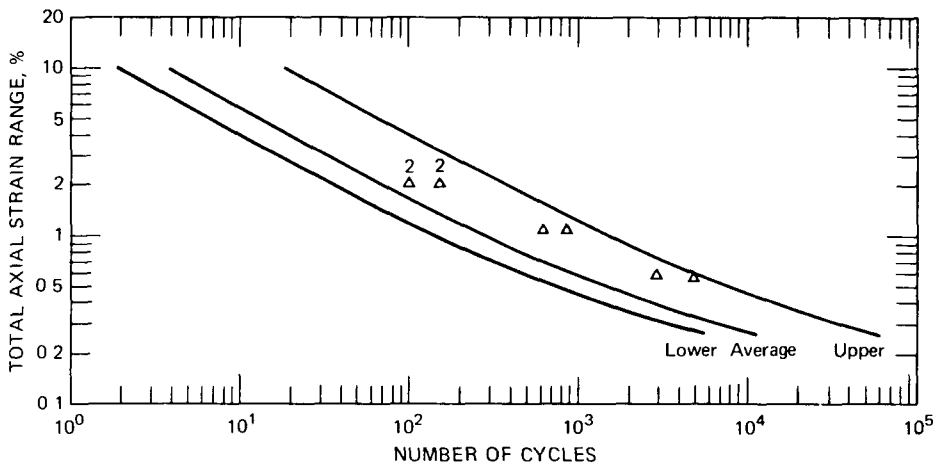

Fig. 3.26 Low-cycle-fatigue data for AISI 316 stainless steel at 650°C and an axial strain rate of 4×10^{-5} sec^{-1}.

Hold times at peak strain have an effect on fatigue resistance which is dependent not only on the length of the hold period but also on the strain wave shape being used. For example, in tests of 304 stainless steel at 650°C, hold times in the tension portion of the cycle only (wave form 4 in Fig. 3.40) are particularly detrimental and result in reductions in fatigue life which are much greater than those noted with wave forms 2 and 3. Figure 3.41 illustrates this behavior for a strain rate of 4×10^{-3} sec^{-1}. On the basis of this total strain-range graph, a 30-min hold period in only the compression portion of the cycle leads to a slight reduction in fatigue resistance. A slightly greater reduction is observed when 30-min hold periods are employed in both the tension and compression portions of the cycle. Finally, a significant reduction is observed for a 30-min hold period in only the tension portion of the cycle.

The data obtained in symmetrical-hold and compression-hold-only tests indicated an interesting correlation with plastic strain range. These results are presented in Fig. 3.42 and indicate that, on the basis of plastic strain range,* the data obtained using wave forms 2 and 3 are essentially identical with those obtained in no-hold tests (wave form 1). These results suggest that the decreases in the low-cycle-fatigue resistance noted in Fig. 3.41 (except for the tension-hold-only tests) are due to increases in plastic strain. In other words, even though Fig. 3.41 is based on data obtained at certain constant values of total strain range, the plastic strain ranges associated with all the data points at a given total strain range are not the same. Obviously the relaxation effects are somewhat different for each wave form, and this leads to variations in the plastic-strain-range component at a given value of the total strain range. When the data (again except for tension-hold-only data) are compared at the same value of the plastic strain range, a decided consistency is noted.

*In these hold-time tests, the plastic strain range was based on the relaxed stress range, $\Delta\sigma_r$, at $N_f/2$.

Data obtained in the tension-hold-only tests are not consistent with the plastic-strain-range correlation. As shown in Fig. 3.42, these results describe a fatigue life that is much lower than would be predicted by the plastic-strain-range correlation. Apparently holding only in the tension portion of the cycle leads to extensive material damage and drastically reduced fatigue life. As a matter of fact, some success has been attained in comparing the tension-hold-only data with stress-rupture behavior. This comparison is shown in Fig. 3.43, where the fatigue data were plotted as $\sigma_{t\ av.}$ vs. the total time in the fatigue test during which the specimen is exposed to a tensile stress. Here $\sigma_{t\ av.}$ was taken as the arithmetic mean of $\sigma_{t\ max.}$ and $\sigma_{t\ min.}$, where $\sigma_{t\ max.}$ is the maximum tensile stress imposed to attain the desired tensile-strain amplitude and $\sigma_{t\ min.}$ is the tensile stress after relaxation during the hold period at a constant value of total strain. Fairly good agreement with the published[11] stress-rupture data is indicated. While this correlation is interesting, it should be viewed with some reservation because it has been tested in only this one instance. This correlation can also be criticized because the average tensile stress used in it makes conversion to the corresponding stress components difficult without some knowledge of the relaxation behavior of the material.

Tension-hold-only tests have indicated that serious damage is encountered even when the hold period is on the order of 1 min. The data obtained in the evaluation of this effect at 2% strain range are summarized in Table 3.6 (p. 58). A saturation effect appears to be observed when the hold period is close to 30 min. These data are also presented in Fig. 3.44, where, for reference purposes, the data obtained in the no-hold tests have been arbitrarily plotted at a hold period of 1×10^{-2} min.

For no-hold, compression-hold-only, and symmetrical-hold testing, a consistent behavior is indicated, as shown in Fig. 3.44. Data for the tension-hold-only testing indicate deviations from this graph, and the direction of the deviation is toward reduced fatigue life. It is interesting that

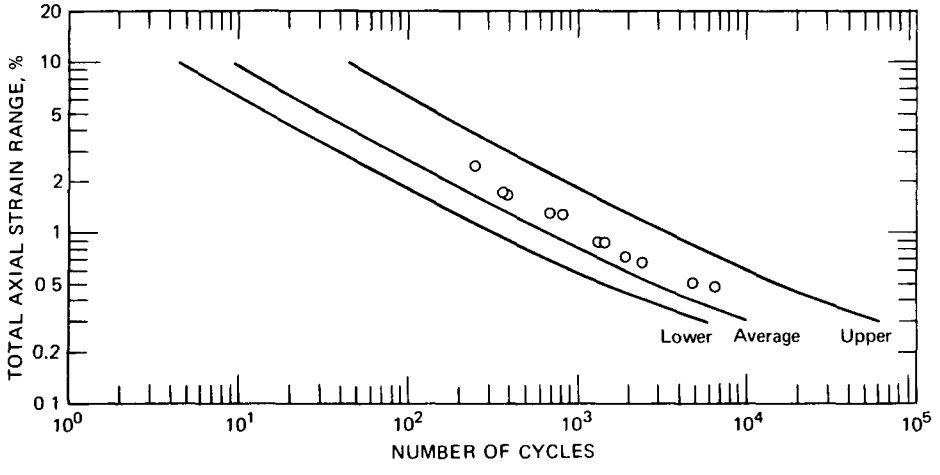

Fig. 3.27 Low-cycle-fatigue data for AISI 316 stainless steel at 816°C and an axial strain rate of 4×10^{-3} sec^{-1}.

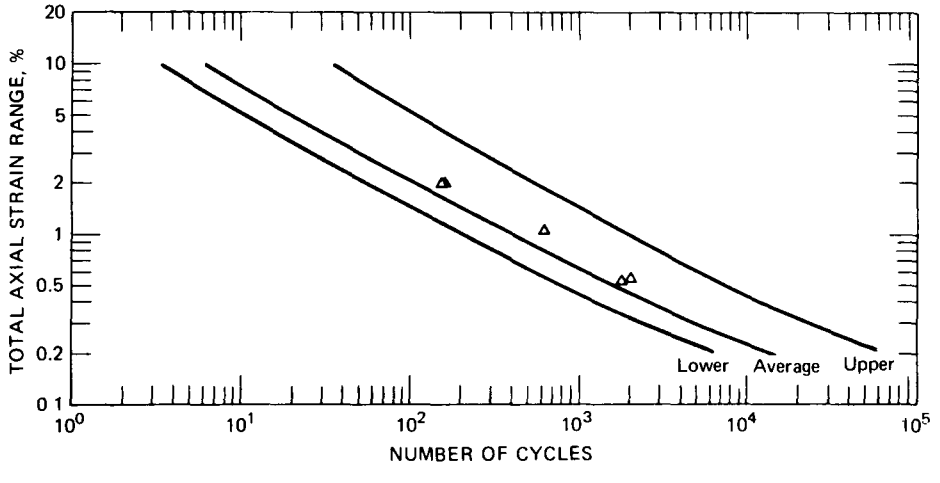

Fig. 3.28 Low-cycle-fatigue data for AISI 316 stainless steel at 816°C and an axial strain rate of 4×10^{-5} sec^{-1}.

TABLE 3.4

VALUES OF c AND m FOR USE IN THE COFFIN–MANSON EQUATION FOR PLASTIC STRAIN RANGE

Material	Temp., °C	Strain rate, sec^{-1}	Material constants based on fatigue life (N_f)		Material constants based on fatigue life (N_5)		Tensile ductility,* %	Calculated $\Delta\epsilon_p$ at 1/4 cycle based on N_f, %	Calculated $\Delta\epsilon_p$ at 1/4 cycle based on N_5, %
			c	m	c	m			
304	430	4×10^{-3}	39.2	0.455	38.9	0.455	102.2	73.6	73.0
	650	4×10^{-3}	89.2	0.628	84.7	0.626	54.8	213.0	201.7
	650	4×10^{-4}	79.4	0.673	87.9	0.698		201.8	231.5
	650	4×10^{-5}	84.1	0.699	86.5	0.738	40.6	221.7	240.5
	816	4×10^{-3}	97.7	0.717	70.7	0.688	71.3	263.8	183.5
	816	4×10^{-4}	71.7	0.734	60.3	0.727		198.5	165.2
	816	4×10^{-5}	121.0	0.864	54.4	0.778	38.7	400.7	159.9
348	430	4×10^{-3}	39.5	0.446	38.1	0.443	109.1	73.3	70.4
	650	4×10^{-3}	34.8	0.478	33.1	0.475	115.8	67.4	63.9
	650	4×10^{-4}	34.7	0.515	32.4	0.514		70.8	66.1
	650	4×10^{-5}	29.6	0.528	29.7	0.544	51.8	61.4	63.1
	816	4×10^{-3}	38.6	0.551	28.3	0.524	175.0	82.8	58.5
	816	4×10^{-4}	73.3	0.668	40.4	0.606		185.1	93.5
	816	4×10^{-5}	84.3	0.714	34.2	0.607	183.3	226.9	79.5
316	430	4×10^{-3}	54.1	0.493	58.6	0.503	96.9	107.1	117.9
	650	4×10^{-3}	50.4	0.586	47.5	0.582	89.4	113.5	106.3
	650	4×10^{-4}	51.7	0.633	47.1	0.631		124.3	113.0
	650	4×10^{-5}	19.5	0.500	17.4	0.492	38.7	39.0	34.5
	816	4×10^{-3}	90.4	0.691	81.8	0.690	95.5	235.9	211.2
	816	4×10^{-4}	169.1	0.804	106.3	0.760		515.7	305.0
	816	4×10^{-5}	56.9	0.665	38.4	0.629	69.3	143.0	91.7

*$\epsilon_f = \ln \frac{100}{100-RA}$, where RA is the percentage of reduction in area.

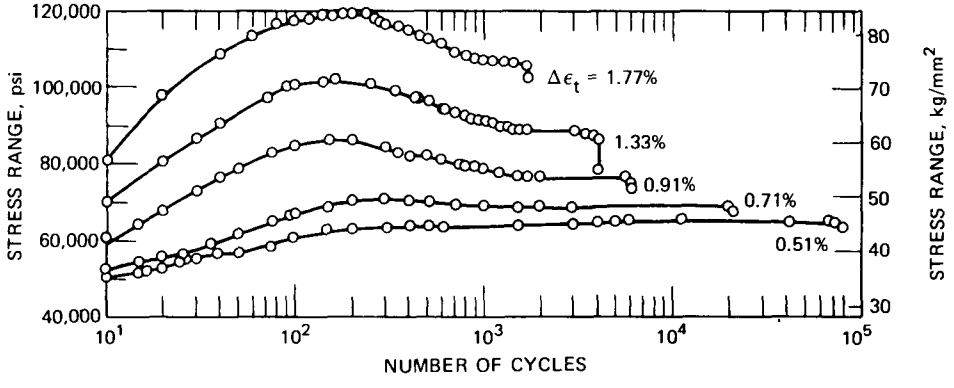

Fig. 3.29 Stress range vs. cycles obtained for AISI 316 stainless steel at 430°C with an axial strain rate of 4×10^{-3} sec^{-1}.

the hold period corresponding to the point of this deviation is about 1×10^{-1} min for both the 0.5 and 2.0% total strain range. Note also that some saturation is indicated at the 0.5% strain range to yield a behavior similar to that observed at the higher strain range. Only a few tests have been made at a strain rate of 4×10^{-5} sec^{-1}. In tests at the 2% strain range, the tension-hold-only data at the slow strain rate are identical with the data in the saturation region of the higher strain rate. Owing to the limited data available at the lower strain rate, no definite conclusions can be made as yet regarding these observations.

Tests involving a 30-min hold period in tension plus a shorter hold period in compression (unsymmetrical holding) have shown that the very detrimental effect of a hold

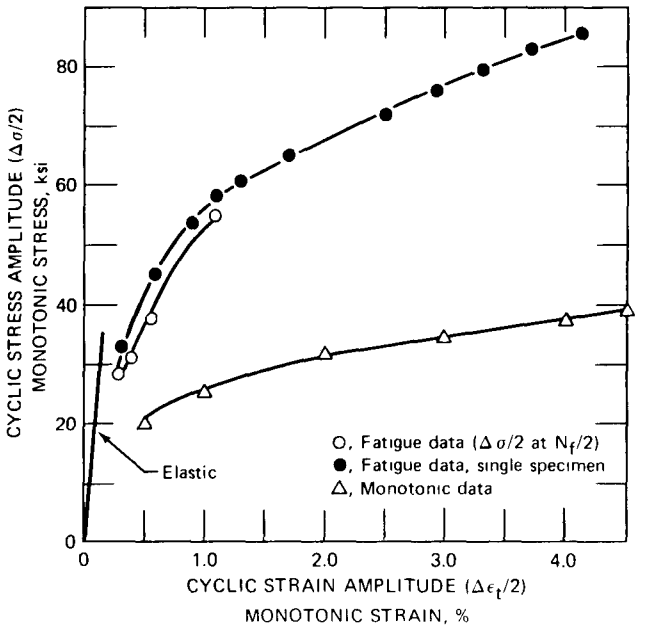

Fig. 3.30 Cyclic and monotonic stress–strain data for AISI 304 stainless steel at 430°C and an axial strain rate of 4×10^{-3} sec^{-1}.

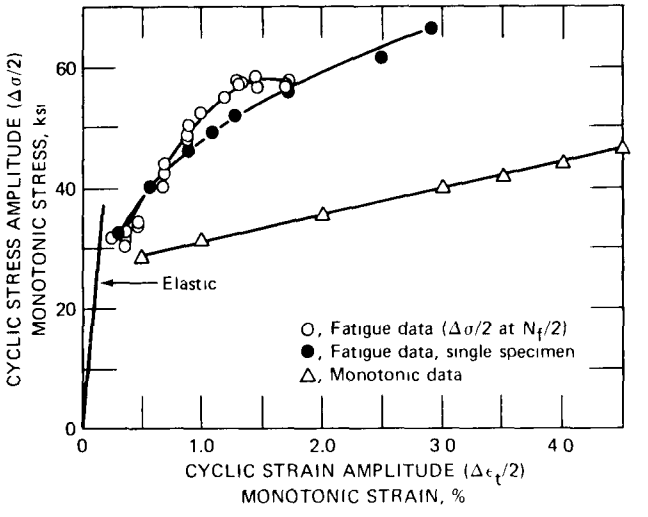

Fig. 3.31 Cyclic and monotonic stress–strain data for AISI 348 stainless steel at 430°C and an axial strain rate of 4×10^{-3} sec^{-1}.

period in tension only can be significantly reduced by just a short period in the compression portion of the cycle. This effect is shown in Table 3.7 (p. 59). When the tension hold period is 30 min and a 3-min compression hold period is introduced, the fatigue life is within 80% of the fatigue life observed in the 30-min symmetrical-holding tests, whereas, without this small hold period in compression, the fatigue life is reduced to about 40% of the 30-min symmetrical-holding fatigue life. Obviously, in this type of testing, the hold period in compression exerts a "healing" effect or provides a mechanism that reduces the tendency for internal void formation. These data involving unsymmetrical holding appear to be the first information of this type reported in the literature.

Table 3.8 (p. 60) summarizes in detail all the fatigue data generated in this study of hold-time effects. In addition to the fracture data in terms of cycles, values are also included for the time to fracture. Data are also given for the fatigue life in terms of N_5, the cycles corresponding to a 5% reduction in load, and, in terms of N_0, the cycles at which the load just begins to decrease.

Studies of the hold-time test data obtained to date have produced several significant findings:

1. All tests exhibited cyclic-hardening characteristics, although the steady-state stress region was usually achieved within 10 cycles, compared to the no-hold tests that usually required 40 to 200 cycles.

2. For a given hold period, the value of $\sigma_{t\ max.} - \sigma_{t\ min.}$ was independent of cycles, although the absolute values of both stresses changed during cycling.

3. The value of $\sigma_{t\ max.}$ depended on the hold period for a given strain range and decreased as the hold period increased.

4. The relaxation curve in tension was identical to the relaxation curve obtained in compression.

5. For all practical purposes, $\sigma_{t\ max.}$ equaled the maximum compressive-stress amplitude ($\sigma_{c\ max.}$) for all strain wave forms evaluated.

6. For a constant strain range, the configuration of the relaxation curve is independent of hold time.

7. The shape of the relaxation curve is strongly dependent on strain range.

8. Knowledge of the monotonic relaxation characteristics will yield one piece of information, i.e., $\sigma_{t\ max.} - \sigma_{t\ min.}$, which is identical to that obtained under cyclic conditions.

Table 3.9 (p. 62) summarizes some of the relaxation results obtained in this study. All the quantities used in this tabulation are defined in Fig. 3.45. One of the

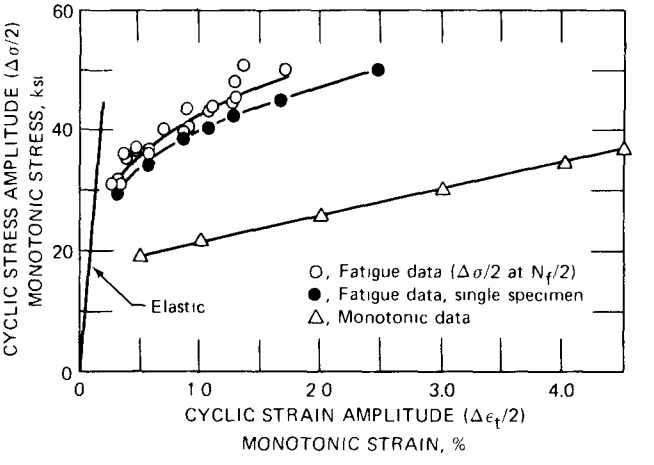

Fig. 3.32 Cyclic and monotonic stress–strain data for AISI 348 stainless steel at 650°C and an axial strain rate of 4×10^{-3} sec^{-1}.

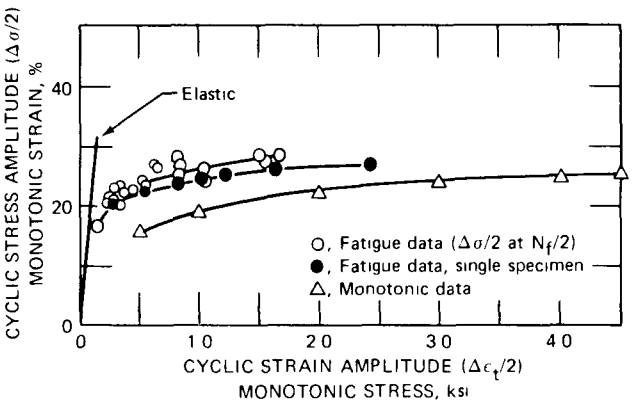

Fig. 3.33 Cyclic and monotonic stress–strain data for AISI 348 stainless steel at 816°C and an axial strain rate of 4×10^{-3} sec^{-1}.

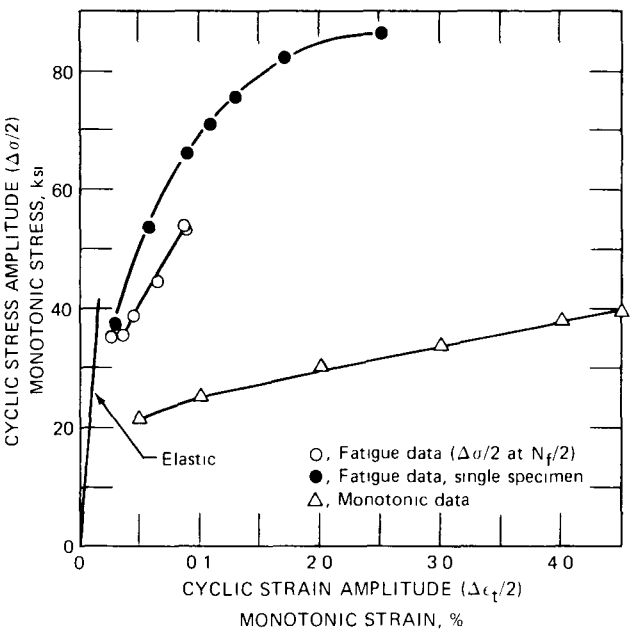

Fig. 3.34 Cyclic and monotonic stress–strain data for AISI 316 stainless steel at 430°C and an axial strain rate of 4×10^{-3} sec^{-1}.

effects just mentioned (see item 3 above) is illustrated in Fig. 3.46. One other important observation involving relaxation behavior is shown in Fig. 3.47. Good agreement exists between $\sigma_{t\,max.} - \sigma_{t\,min.}$ values from cycling (tension-hold-only) tests and those from monotonic stress-relaxation tests.

Some additional hold-time data for AISI 304 stainless steel tested at 538°C are presented in Tables 3.10 and 3.11 (p. 63). A limited amount of hold-time data for AISI 316 stainless steel was also made available in this program; these data are shown in Tables 3.12 and 3.13 (p. 64).

Logarithmic graphs[2] of stress range or stress amplitude vs. time to fracture are of interest because of their similarity to stress-rupture graphs. The presentations in Fig. 3.48 reveal this similarity and also point to the fact that the data for 316 stainless steel are definitely higher than those for 304 stainless steel. For the stress amplitudes involved, it appears that linear relations are indicated, although this linearity is known to exist only over a limited range of stress. As the stress amplitude is reduced further, the data define a definite curvature that is concave upward.

The time-to-fracture data in Fig. 3.48 show that decreasing the strain rate increases the time to fracture. This effect is opposite to that noted for the analyses[1] in terms of cycles to fracture; in these cases the cycles to fracture decreased as the strain rate was decreased.

A special correlation has evolved from an application of the above analysis to the hold-time data[4] for 304 stainless steel given in Table 3.8. All the tension-hold-only data were considered in terms of time to fracture, and the correlation shown in Fig. 3.49 was obtained. The no-hold-time results, corresponding to a strain rate of 4×10^{-3} sec^{-1} as given in Fig. 3.48, have been plotted along with a few additional no-hold-time data points presented in Table 3.8. Particu-

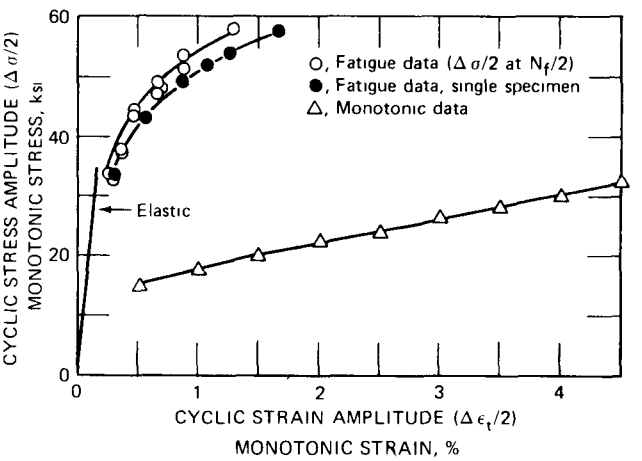

Fig. 3.35 Cyclic and monotonic stress–strain data for AISI 316 stainless steel at 650°C and an axial strain rate of 4×10^{-3} sec^{-1}.

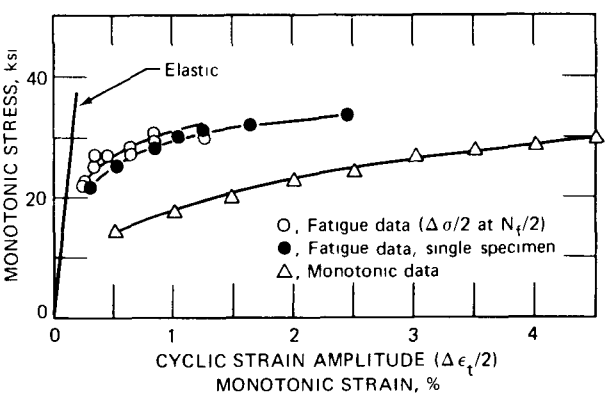

Fig. 3.36 Cyclic and monotonic stress–strain data for AISI 316 stainless steel at 816°C and an axial strain rate of 4×10^{-3} sec^{-1}.

larly significant in this analysis is the fact that the tension-hold-only data obtained in both the 2 and 0.5% strain range (strain rate of 4×10^{-3} sec^{-1}) yield a linear relation on this logarithmic graph. It is also noteworthy that the lines described for the two strain ranges are essentially parallel (slope of about −0.05) and seem to intersect the no-hold-time line at the associated strain-range value. These are extremely important observations, for, if this type of behavior is typical, a method of predicting the effect of tension-hold periods would be made available. For example, if the stress-amplitude vs. time-to-fracture graph were available from tests involving no hold periods, then hold-time effects could be estimated for a given strain range by locating this point on the no-hold-time line and drawing a line having a slope of −0.05 through this point. Estimates at other strain ranges could be made using similar constructions. It is to be emphasized, however, that these constructions lead to nothing more than qualitative predictions of hold-time effects. Any point on one of these construction lines (slope of −0.05) will define an operating life in a hold-time test which is larger than that corresponding to a no-hold-time test at the same strain range, but it is not possible to assign a specific value of the hold period to this particular point. Other analyses must supply this information.

Another correlation involving the tension-hold-only data for annealed AISI 304 stainless steel tested in air at 650°C and a strain rate of 4×10^{-3} sec^{-1} is presented in Fig. 3.50. A logarithmic graph of time to fracture vs. the tension-hold period in minutes yields a curve that is concave upward. However, if the value for the time to fracture with no hold periods is subtracted from each time-to-fracture value, a definite linearity is obtained. This leads to

$$t_f - t_{f_o} = AH_T^{0.81} \tag{3.4}$$

Fig. 3.38 Photomicrograph showing the pretest structure of the 348 stainless steel (longitudinal cross section) used in low-cycle-fatigue testing ($50HNO_3$, $50H_2O$, electrolytic etch; magnification, 100 ×1.

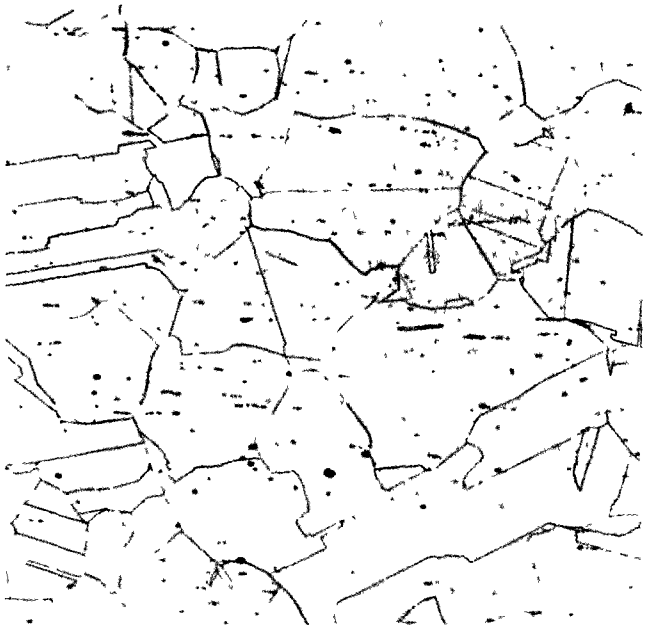

Fig. 3.37 Photomicrograph showing the pretest structure of the 304 stainless steel (longitudinal cross section) used in low-cycle-fatigue testing [$22H_2SO_4$, $12H_2O_2$ (30%), $66H_2O$, electrolytic etch; magnification, 100 ×].

Fig. 3.39 Photomicrograph showing the pretest structure of the 316 stainless steel (longitudinal cross section) used in low-cycle-fatigue testing [$22H_2SO_4$, $12H_2O_2$ (30%), $66H_2O$, electrolytic etch; magnification, 100 ×].

TABLE 3 5

FRACTURE MODE CHARACTERIZATION OF AISI 304 AND 348 STAINLESS STEEL LOW CYCLE FATIGUE SPECIMENS

Test temp °C	Axial strain range %	Axial strain rate, sec^{-1}	Cycles to 5% reduction in load (N_5)	Mode crack initiation	Intergranular crack length from point of initiation, mm	Mode of crack propagation to shear point	Specific observations
				304 Stainless Steel			
650	2 08	4 16 x 10^{-5}	194	Intergranular	0 3	Intergranular + transgranular	Continuous unidentified phase observed in grain boundaries etch pits observed in highly strained regions
650	2 10	4 20 x 10^{-4}	287	Intergranular	0 1	Predominantly transgranular	
650	2 10	4 20 x 10^{-3}	524	Transgranular		Predominantly transgranular	
650	0 57	4 52 x 10^{-5}	1 533	Intergranular	0 6	Intergranular + transgranular	Continuous unidentified phase observed in grain boundaries etch pits observed in highly strained regions
650	0 58	4 65 x 10^{-4}	3 009	Intergranular	0 2	Predominantly transgranular	
650	0 59	4 73 x 10^{-3}	7 176	Transgranular		Predominantly transgranular	
816	2 06	4 12 x 10^{-5}	80	Intergranular	4.0	Predominantly intergranular	Intermittent unidentified phase observed in grain boundaries subgrains observed in highly strained regions
816	2 05	4 09 x 10^{-4}	117	Intergranular	1 2	Predominantly intergranular	Continuous unidentified phase observed in grain boundaries a few etch pits and subgrains observed in highly strained regions
816	2 06	4 11 x 10^{-3}	226	Intergranular	1 0	Predominantly intergranular	Continuous unidentified phase observed in grain boundaries few etch pits observed in highly strained regions
816	0 56	4 44 x 10^{-5}	591	Intergranular	0 7	Predominantly intergranular	Intermittent unidentified phase observed in grain boundaries no etch pits observed in highly strained regions
816	0 56	4 05 x 10^{-4}	1 055	Intergranular	0 8	Predominantly intergranular	Continuous unidentified phase observed in grain boundaries etch pits observed in highly strained regions
816	0 57	4 53 x 10^{-3}	2 346	Intergranular	0 8	Predominantly intergranular	Continuous unidentified phase observed in grain boundaries subgrains observed in highly strained regions
				348 Stainless Steel			
650	2 14	4 27 x 10^{-5}	193	Intergranular	0 2	Transgranular	Large amounts of secondary cracking grain boundaries relatively clean as compared to 304 stainless steel
650	2 15	4 30 x 10^{-4}	320	Intergranular	0 1	Transgranular	
650	2 16	4 31 x 10^{-3}	585	Intergranular	0 1	Transgranular	
650	0 61	4 85 x 10^{-5}	5 464	Intergranular	0 4	Transgranular	Limited secondary cracking crack propagation very regular flat and perpendicular to specimen axis
650	0 61	4 87 x 10^{-4}	10 948	Intergranular	0 2	Transgranular	
650	0 61	4 86 x 10^{-3}	15 010	Intergranular	0 1	Transgranular	
816	2 02	4 03 x 10^{-5}	122	Intergranular	<0 1	Transgranular	Large number of secondary cracks
816	2 04	4 07 x 10^{-4}	158	Intergranular	<0 1	Transgranular	
816	2 06	4 11 x 10^{-3}	266	Intergranular	<0 1	Transgranular	
816	0 54	4 34 x 10^{-5}	1 613	Intergranular	<0 1	Transgranular	Crack propagation very regular flat and almost perpendicular to specimen axis cracks developed at ~60° angle to the primary fracture surface in the direction of propagation
816	0 54	4 34 x 10^{-4}	2 714	Intergranular	<0 1	Transgranular	
816	0 57	4 53 x 10^{-3}	4 656	Intergranular	<0 1	Transgranular	Crack propagation very regular flat and perpendicular to specimen axis

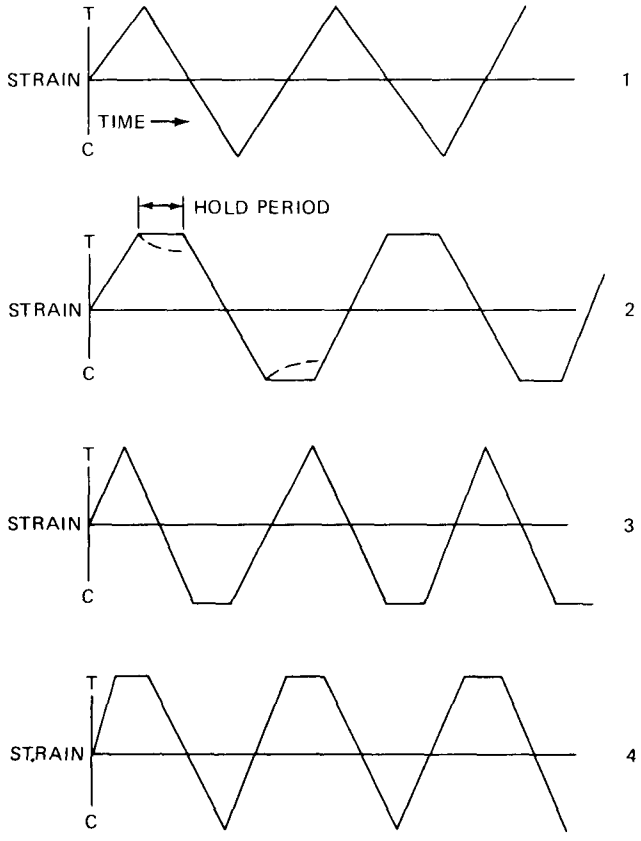

Fig. 3.40 Strain wave forms used in evaluating effects of hold time on low-cycle-fatigue resistance.

where t_f = time to fracture (hr)
t_{f_0} = time to fracture using no hold periods
A = a constant
H_T = hold period in tension (min)

A similar relation was found to apply to the 0.5% strain-range data. These relations can be used to calculate (for 304 stainless steel and the condition involved) the time to fracture for any tension-hold-only period, which can then be used in conjunction with Fig. 3.49 to yield the stress amplitude for any hold period. A value for the cycles to fracture, N_f, will also follow from

$$\text{Time to fracture} = \frac{N_f}{f} + N_f H_T \tag{3.5}$$

where H_T is the hold time in tension and f is the cycling frequency. For the triangular wave form,

$$f = \frac{\dot{\epsilon}_t}{2\Delta\epsilon_t} \tag{3.6}$$

and hence

$$\text{Time to fracture} = \frac{2N_f\,\Delta\epsilon_t}{\dot{\epsilon}_t} + N_f H_T \tag{3.7}$$

Thus it is a simple matter to convert the data plotted in Fig. 3.49 to data involving cycles to fracture. This conversion will, of course, lead to the same results shown in Figs. 3.42 and 3.44 to indicate that the fatigue life measured in cycles to fracture is decreased as the length of

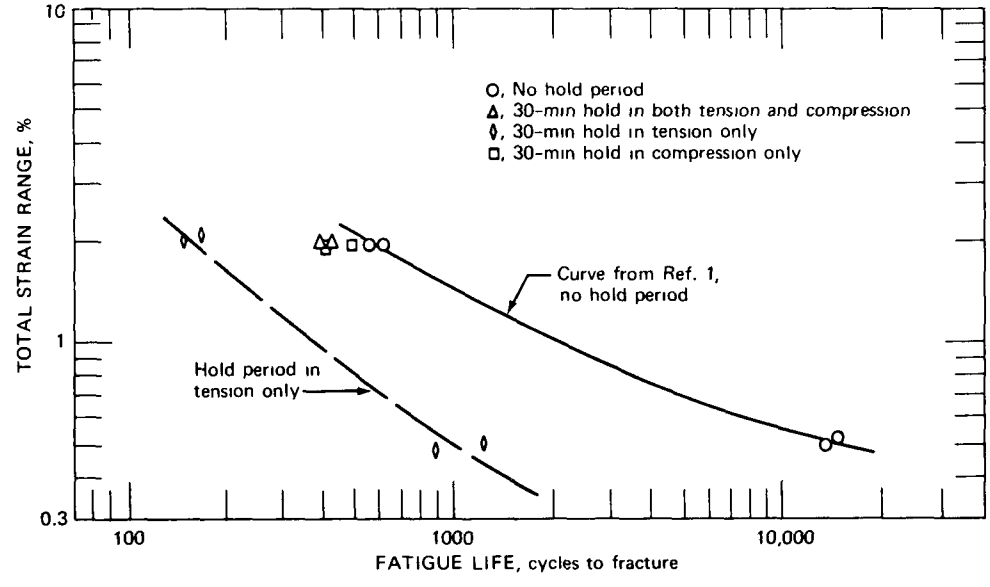

Fig. 3.41 Effect of hold period and strain wave form on the low-cycle-fatigue resistance of AISI 304 stainless steel tested in air at 650°C and a strain rate of 4×10^{-3} sec^{-1}.

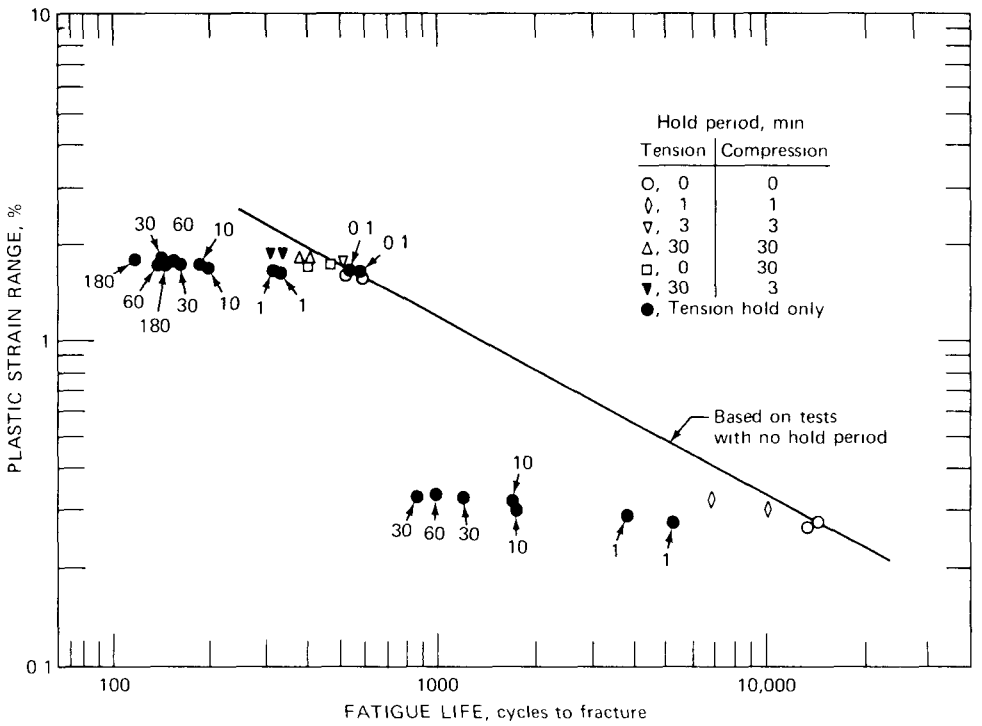

Fig. 3.42 Effect of hold period and strain wave form on the plastic-strain fatigue resistance of AISI 304 stainless steel tested in air at 650°C and a strain rate of 4×10^{-3} sec^{-1}.

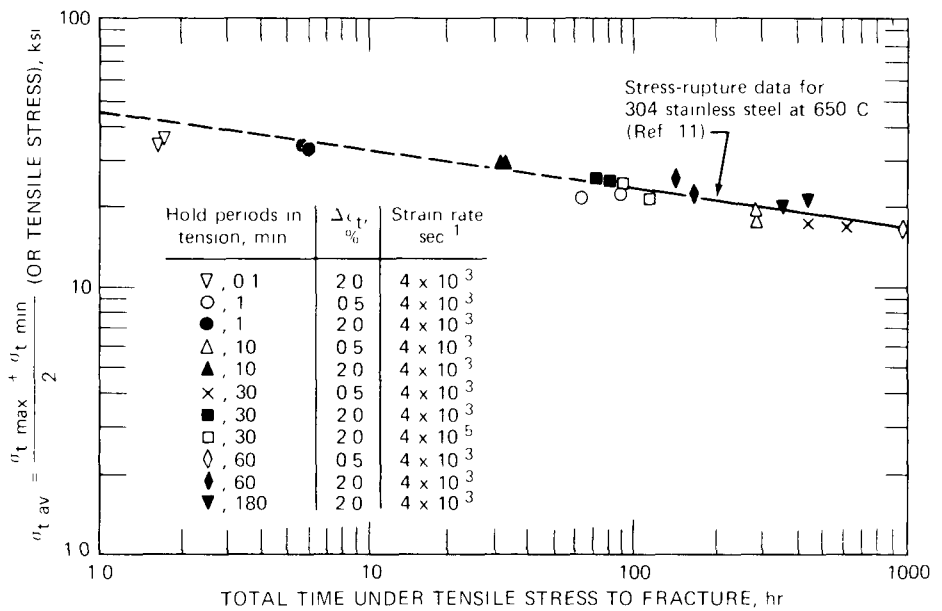

Fig. 3.43 Correlation of fatigue data involving hold periods in tension only with typical stress-rupture data for AISI 304 stainless steel tested in air at 650°C.

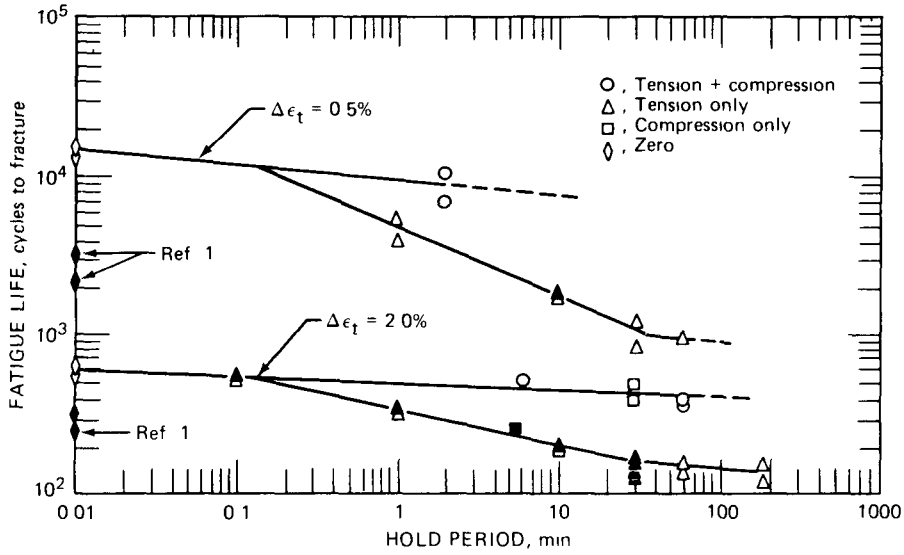

Fig. 3.44 Fatigue life vs. hold-period time for AISI 304 stainless steel tested in air at 650°C and strain rates of 4×10^{-3} sec^{-1} (open symbols) and 4×10^{-5} sec^{-1} (solid symbols) using various strain wave forms.

TABLE 3.6

EFFECT OF HOLD-PERIOD LENGTH IN TENSION-HOLD-ONLY TESTING ON THE FATIGUE RESISTANCE OF AISI 304 STAINLESS STEEL*

Hold period, min	Cycles to failure (N_f)	
	Test 1	Test 2
0	592	546
0.1	570	545
1.0	329	331
10.0	193	201
30.0	146	165
60.0	144	158
180.0	150	120

*Tested in air at 650°C and a strain rate of 4×10^{-3} sec^{-1} at a strain range of about 2.0%.

the hold period is increased. This effect might appear to be in contradiction to Fig. 3.49, which indicates an increase in the time to fracture as the length of the hold period increases. Actually no contradiction exists since both effects are correct and mutually consistent. Introducing a hold period into the strain cycle does indeed lead to a decrease in N_f. However, this hold period increases the cycle time by a factor that is greater than that corresponding to the reduction in N_f. As a result, even though N_f is decreased by the introduction of the hold period, the time of the test or time to fracture is increased. In other words the operating life of the specimen has been increased owing to the effect of the hold period.

An extremely valuable observation follows from the relation identified in Fig. 3.49. Consider, for example, that the stress-amplitude vs. time-to-fracture graph is available from no-hold-time strain-controlled tests at a given strain rate and temperature. If it is also considered that these data are employed for design purposes to achieve a given operating life at a given strain rate and strain amplitude, then it can be concluded that the introduction of hold periods into the tension portion of the cycle will yield an operating life that is in excess of the design life. For example, in Fig. 3.49 the time to fracture at the 2% strain range is about 1.5 hr in a no-hold test and about 150 hr in a test involving a 60-min hold period in the tension portion of the cycle. Since hold periods in tension only have been

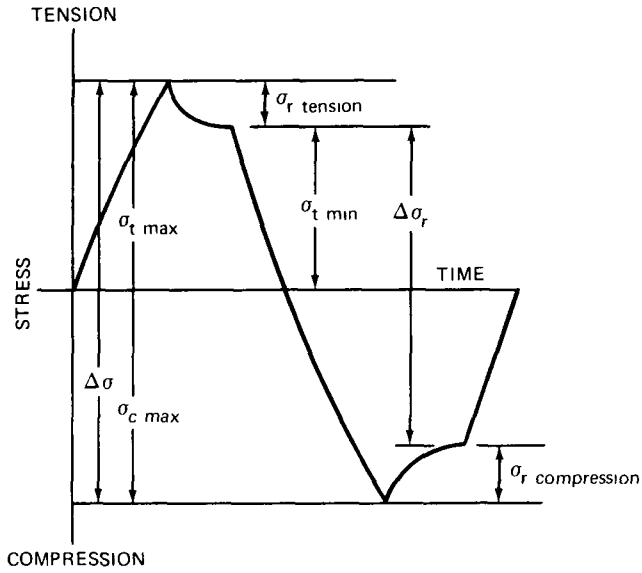

Fig. 3.45 Definition of various stress values observed in hold-time tests.

TABLE 3.7

SUMMARY OF TEST RESULTS OF AISI 304 STAINLESS STEEL OBTAINED USING A 30-MIN HOLD PERIOD IN TENSION PLUS A SHORT HOLD PERIOD IN COMPRESSION*

Hold period, min		Total strain range, %	Cycles to failure (N_f)	
Tension	Compression		Test 1	Test 2
0	0	1 98	592	546
30	30	1 98	380	416
30	0	2 08	146	
30	0	2 02		165
30	3	1 98	308	
30	3	2 00		336

*Tested in air at 650°C and a strain rate of 4×10^{-3} sec^{-1}

shown (see Fig 3 42) to be the most detrimental in terms of reducing the cyclic life, it follows that, for a given hold period, even longer operating times will be associated with wave forms involving hold periods in both tension and compression or in compression only In other words, tests involving a 60-min hold period in compression or a 30 min hold period in both tension and compression will yield operating times in excess of 150 hr On the basis of this important observation, a design life based on no-hold time test results can be concluded to be completely satisfactory for any application at the same strain amplitude when any type of hold period is introduced This is true even though a smaller value of N_f is associated with the hold-time data A brief study of Fig 3 49 will confirm the conclusion that, for a given strain range, longer operating times are associated with the smaller N_f values observed in the hold-time tests And hence, if a design life is based on the no-hold-time data, a specimen or component tested with

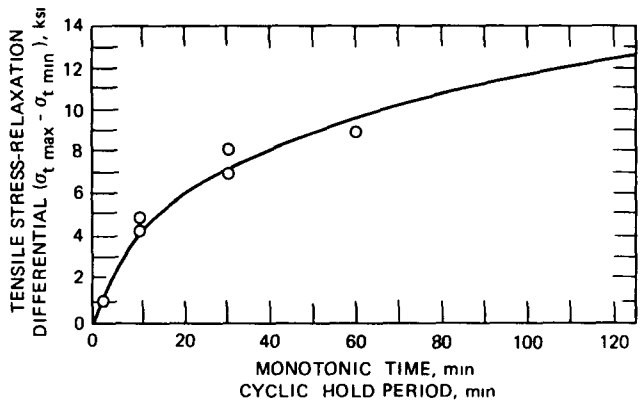

Fig 3.47 Comparison of monotonic stress relaxation data with cyclic (tension-hold-only) data obtained for AISI 304 stainless steel tested in air at 650°C and a strain rate of 4×10^{-3} sec^{-1} —, monotonic data at 0.25% tensile strain. ○, cyclic data for ($\Delta\epsilon_t$/2) = 0 25% in tension hold only.

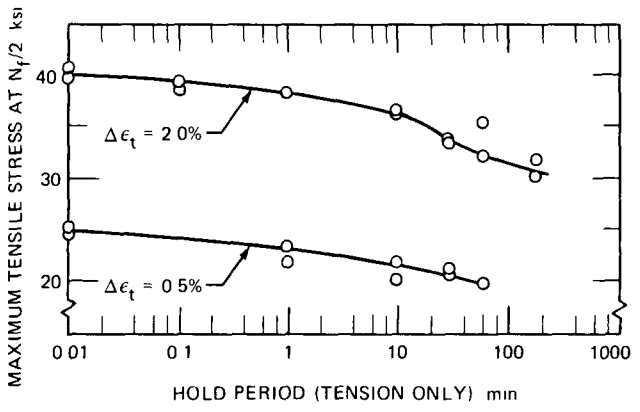

Fig. 3.46 Maximum tensile stress ($\sigma_{t\ max.}$) vs hold period in tension-hold-only tests of AISI 304 stainless steel tested in air at 650°C and a strain rate of 4×10^{-3} sec^{-1} (Data obtained in no-hold-time tests have been arbitrarily plotted at a hold period of 0.01 min.)

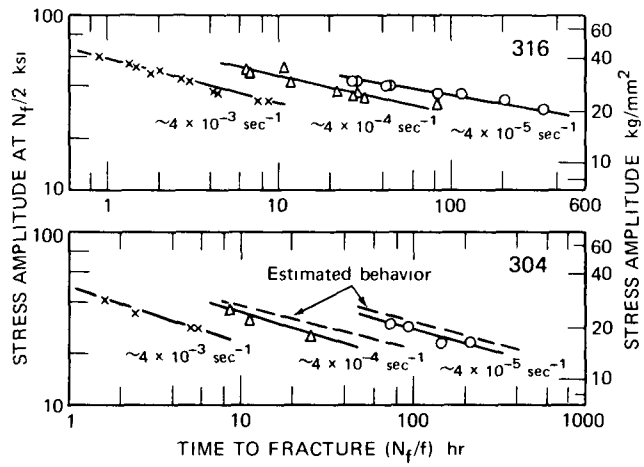

Fig. 3.48 Stress-amplitude vs. time-to-fracture data obtained in low-cycle-fatigue tests of annealed AISI 304 and 316 stainless steels in air at 650°C

TABLE 3 8

FATIGUE DATA OBTAINED IN HOLD-TIME TESTS OF AISI 304 STAINLESS STEEL*

Spec No	Hold period, min		Axial strain range, %			Fatigue life							
	Tension	Compression	$\Delta\epsilon_t$	$\Delta\epsilon_p$†	$\Delta\epsilon_e$†	N_0, cycles	N_0, hr	N_0/N_f	N_s, cycles	N_s, hr	N_s/N_f	N_f, cycles	N_f, hr
66 6	0	0	0 25	0 11	0 14							1,000,000†	333 3‡
63 3	10 0	0	0 25	0 10	0 15				7,800	1,300 0	0 90	8,640	1,440 1
54 12	0	0	0 50	0 27	0 24	13,086	9 08	0 98	13,325	9 25	0 99	13 400	9 30
54 11	0	0	0 52	0 28	0 24	12,201	8 47	0 83	12,513	8 68	0 86	14,620	10 10
57-8	1 0	1 0	0 49	0 32	0 17				6,400	217 7	0 92	6,916	235 3
65-3	1 0	1 0	0 49	0 31	0 18				9,688	329 6	0 94	10,266	349 3
63 1	10 0	3 0	0 49	0 34	0 15				4,061	880 0	0 92	4,430	960 0
65-10	10 0	10 0	0 49	0 37	0 12				6,376	2,125 0	0 91	7,001	2,333 0
57 11	1 0	0	0 49	0 29	0 20				3,419	57 2	0 88	3,869	64 7
57-9	1 0	0	0 49	0 28	0 22				4,823	80 7	0 90	5 351	89 6
57 12	10 0	0	0 49	0 32	0 17				1,510	252 7	0 89	1,703	285 0
65 1	10 0	0	0 49	0 31	0 18				1,587	265 6	0 93	1 713	286 6
56-2	30 0	0	0 48	0 34	0 16	630	315 0	0 73	791	395 5	0 92	862	431 0
56 3	30 0	0	0 49	0 33	0 17	705	352 0	0 58	1,061	508 0	0 84	1,216	603 0
65-4	60 0	0	0 49	0 34	0 15	476	476 4	0 48	740	740 7	0 74	995	996
66 10	10 0	0	0 99	0 78	0 21	260	43 69	0 48	472	79 33	0 86	547	91 26
53-11	0	0	1 98	1 58	0 40	464	1 28	0 78	546	1 52	0 92	592	1 64
54 5	0	0	1 98	1 58	0 40	411	1 14	0 75	476	1 32	0 87	546	1 52
63 2§	0	0	1 98	1 68	0 29	200	55 5	0 63	257	71 4	0 82	315	87 5
53 8	3 0	3 0	1 98	1 71	0 27	350	36 0	0 67	440	45 2	0 84	526	54 0
65 11	30 0	3 0	1 98	1 77	0 21	210	116 0	0 68	293	162 0	0 95	308	170 2
65 9	30 0	3 0	2 0	1 79	0 21	240	132 6	0 71	302	167 0	0 90	336	185 7
53 9	30 0	30 0	1 98	1 80	0 18	285	285 6	0 75	321	321 8	0 84	380	381 0
54 9	30 0	30 0	1 98	1 84	0 14	301	302 0	0 72	376	377 0	0 90	416	417 0
57-2	0 1	0	1 98	1 64	0 33	440	1 95	0 77	510	2 26	0 89	570	2 53
56 12	0 1	0	1 98	1 64	0 33	395	1 76	0 72	501	2 22	0 91	545	2 42
57-1	1 0	0	1 98	1 66	0 32	230	4 47	0 70	295	5 74	0 90	329	6 39
56-11	1 0	0	1 98	1 66	0 32	223	4 33	0 67	290	5 63	0 88	331	6 43
65 12§	0	5 5	1 98	1 71	0 26	160	62 2	0 62	205	79 7	0 79	258	100 5
56 5	10 0	0	2 00	1 71	0 27	107	17 8	0 55	164	27 3	0 85	193	32 7
56 1	10 0	0	2 00	1 71	0 27	113	18 8	0 56	169	28 2	0 84	201	33 0
53-10	30 0	0	2 08	1 79	0 29	63	31 6	0 43	95	47 8	0 65	146	73 4
53 12	30 0	0	2 02	1 76	0 25	60	30 2	0 36	105	52 8	0 64	165	82 9
57-10§	30 0	0	1 98	1 74	0 23	90	70 0	0 63	125	97 2	0 88	142	110 4
57 4§	30 0	0	1 96	1 75	0 21	120	93 3	0 66	162	126 0	0 89	182	141 5
54-2	60 0	0	1 98	1 77	0 21	45	45 1	0 31	100	100 2	0 69	144	144 3
54-1	60 0	0	1 98	1 78	0 20	52	52 1	0 33	124	124 3	0 78	158	158 4
57-6	180 0	0	1 98	1 78	0 20	70	210 0	0 47	140	420 0	0 93	150	450 0
57-7	180 0	0	2 00	1 80	0 20	80	240 0	0 67	109	327 0	0 91	120	360 0
66 1	600 0	0	1 98	1 80	0 18	80	800 0		115	1,150 0		149	1,493 0
54-3	0	30 0	1 98	1 70	0 28	357	179 5	0 74	412	207 1	0 86	480	241 3
52-11	0	30 0	1 97	1 70	0 27	348	174 8	0 85	384	193 0	0 94	409	205 6
66-8	0	0	3 95	3 49	0 46	130	0 72	0 71	170	0 94	0 92	184	1 01
66 9	10 0	0	3 95	3 64	0 32	38	6 2	0 64	53	8 9	0 90	59	10 1

*Tested in air at 650°C and a strain rate of 4×10^{-3} sec^{-1}, control mode, axial strain

†Values are based on data at $N_f/2$, in hold-time tests the relaxed stress range is used.

‡Test terminated, no fracture

§Strain rate, 4×10^{-5} sec^{-1}

hold periods at peak strain could not, within this design life, be subjected to the number of cycles necessary to cause it to fracture.

Another important point evolving from the analysis presented in Fig. 3.49 concerns the effect of hold times (tension only) on the time to fracture at the two different strain ranges. It is interesting that the ratio of t_f/t_{f0} for a given hold time is essentially independent of strain range. This consistency is only approximate at the very low hold times but is quite exact for hold periods above 10 min. The ratio t_f/t_{f0} is about 50 for a 30-min hold period at strain-range values of 2 and 0.5%, it is 100 for a 60-min hold period. This relation may prove to be valuable in estimating the failure times at certain ranges when hold-time results are available at other strain ranges. Mention should also be made of the fact that (see Table 3.8) the t_f/t_{f0} ratio is a function of strain rate. This is shown emphatically in the data for a 30-min tension-hold period at a strain range of 2% and a strain rate of 4×10^{-5} sec^{-1}. At this slow strain rate, the time to fracture with no hold

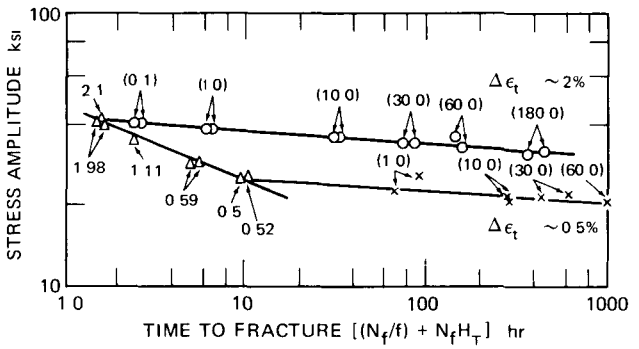

Fig. 3.49 Stress-amplitude vs. time-to-fracture correlation of hold-time data involving hold periods in tension only for AISI 304 stainless steel tested in air at 650°C and a strain rate of 4×10^{-3} sec^{-1} ○ and ×, hold-time data, numbers in parentheses are tension-hold periods in minutes. △, no-hold-time data, numbers represent total strain range in percent.

period is about 87 hr, whereas the time to fracture is between 110 and 142 hr with a 30 min hold period At the slow strain rate, therefore, the t_f/t_{f0} ratio is something close to 1 5, as compared to a value of 50 at a strain rate of 4×10^{-3} sec^{-1} Few data are available at the slow strain rate so it is not possible to make more than this one limited observation of this effect It is impressive though that these hold time data at the slow rate are extremely consistent with the cycle time concept, which will be discussed later (see Fig 3 54)

Only a few hold-time tests were completed in the evaluation of 316 stainless steel, but these data seem to exhibit the same behavior noted in Fig 3 49 A summary of these results is presented in Tables 3 12 and 3 13 These data were used in conjunction with no-hold-time results[1] to provide the graph shown in Fig 3 51 It is interesting that, as in Fig 3 49, a line drawn through the 2% strain range data point on the no-hold time line and having a slope of

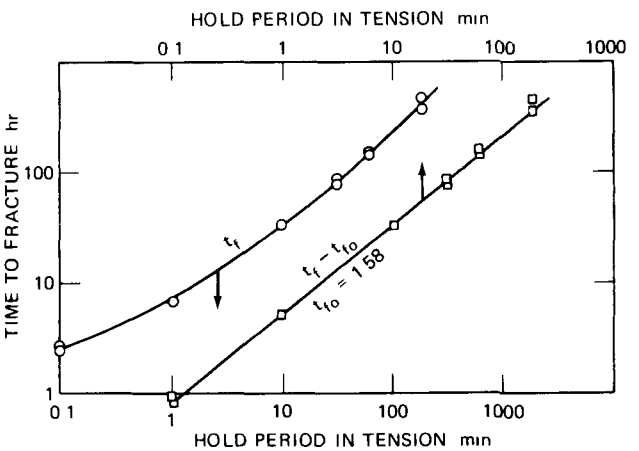

Fig. 3.50 Low-cycle-fatigue data for annealed AISI 304 stainless steel obtained in tension-hold-only tests in air at 650°C, a total strain range of 2%, and a strain rate of 4×10^{-3} sec^{-1}.

−0 05 is in good agreement with the hold time results Also in accord with Fig 3 49 is the fact that the introduction of hold periods leads to fracture times that are larger than those associated with a no hold-time test at the same strain range As the hold time increases, the time to fracture also increases

Confirmation of the trends noted in Figs 3 49 and 3 50 was provided by data reported by Dawson et al[12] and Walker[13] In the study by Walker, hold times were introduced in only the tension portion of the cycle (push–pull loading) in tests of the following cast steels 1% Mo, 1% Cr–1% Mo, 12% Cr–0 5% Mo, and an austenitic 316 containing niobium All tests were performed in air at 510°C (950°F), and hold periods ranged from 15 sec to 12 hr These data were plotted in the graph shown in Fig 3 52 As in Fig 3 50, a logarithmic graph of time to fracture vs the length of the hold period (tension hold only) yields a curve that is concave upward However, when

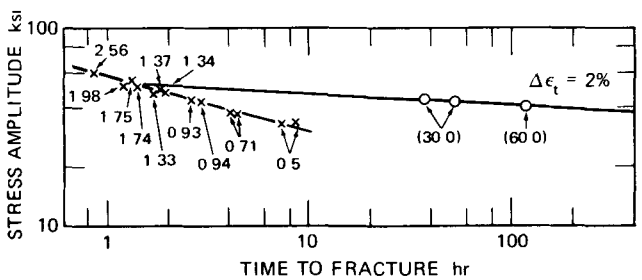

Fig. 3.51 Stress-amplitude vs. time-to-fracture graph for annealed AISI 316 stainless steel tested in air at 650°C and a strain rate of 4×10^{-3} sec^{-1}. x, no-hold-time data, numbers represent total strain range in percent. ○, hold-time data, numbers in parentheses represent tension-hold period in minutes

the graph is modified to represent $t_f - t_{f0}$, a fairly definite linearity is observed (time to fracture with no hold time was not given by Walker, but it appears to be close to 0 8 hr for these data) Particularly interesting is the fact that the slope of this line is essentially identical to that of the line in Fig 3 50

Some additional low cycle fatigue data involving hold periods in only the tension portion of the strain cycle were reported by Coles et al[14] and by Coles and Skinner[15] In these studies of Cr–Mo–V steel at 565°C, reversed bending was employed at 10 cycles/min Hold times in tension ranged from 6 to 1440 min, and these hold periods led to serious reductions in the cyclic fatigue life These data for Cr–Mo–V steel also exhibit the type of behavior shown in Fig 3.50. A graph of this type is shown in Fig 3.53, where a fairly definite linearity is observed This graph is particularly interesting inasmuch as the linearity extends to a hold period of 1440 min (24 hr), which represents the longest hold period reported to date

Coles and Skinner,[15] used the frequency–time relation proposed by Eckel[16] Values for the frequency were

TABLE 3.9

STRESS-RELAXATION DATA OBTAINED IN LOW-CYCLE-FATIGUE TESTS OF AISI 304 STAINLESS STEEL*

Spec. No.	$\Delta\sigma$ at $N_f/2$		$\Delta\sigma_r$ at $N_f/2$		σ_t max. at $N_f/2$		σ_t min. at $N_f/2$		σ_c max. at $N_f/2$		σ_r tension		$\frac{\sigma_t \text{ max.} + \sigma_t \text{ min.}}{2}$		Total time under tensile stress for fracture, hr
	Psi	Kg/mm²	Psi	Kg/mm²	Psi	Kg/mm²	Psi	Kg/mm²	Psi	Kg/mm²	Psi	Kg/mm²	Psi	Kg/mm²	
66-6	30,600	21.5			15,300	10.8	15,300	10.8	15,300	10.8			15,300	10.8	166.6
63-3	32,820	23.1	31,330	22.0	16,410	11.5	14,920	10.5	16,410	11.5	1,490	1.1	15,670	11.0	1,440.0
54-12	50,200	35.3			25,100	17.6	25,100	17.6	25,100	17.6			25,100	17.6	4.65
54-11	49,500	34.8			24,750	17.4	24,750	17.4	24,750	17.4			24,750	17.4	5.05
57-8	39,800	28.0	37,800	26.6	19,900	14.0	18,900	13.3	19,900	14.0	990	0.7	19,400	13.6	117.6
65-3	41,780	29.4	39,790	28.0	20,890	14.7	19,900	14.0	20,890	14.7	990	0.7	20,390	14.3	174.6
63-1	40,980	28.8	33,120	23.3	20,490	14.4	15,020	10.6	20,490	14.4	5,470	3.8	17,750	12.5	739.0
65-10	37,800	26.6	25,860	18.2	18,900	13.3	12,930	9.1	18,900	13.3	5,970	4.2	15,910	11.2	1,166.0
57-11	44,760	31.5	43,760	30.8	21,890	15.4	20,890	14.7	22,880	16.1	990	0.7	21,390	15.0	63.9
57-9	47,740	33.6	46,750	32.9	23,480	16.5	22,480	15.8	24,270	17.1	990	0.7	22,980	16.2	89.4
57-12	41,980	29.5	37,800	26.6	20,090	14.1	15,910	11.2	21,880	15.4	4,180	2.9	18,000	12.7	284.4
65-1	43,760	30.8	39,190	27.6	21,880	15.4	17,310	12.2	21,880	15.4	4,580	3.2	19,590	13.8	285.4
56-2	41,770	29.4	34,810	24.5	20,900	14.7	13,900	9.8	20,900	14.7	6,960	4.9	17,400	12.2	430.0
56-3	42,800	30.1	34,800	24.5	21,400	15.0	13,400	9.4	21,400	15.0	8,000	5.6	17,400	12.2	602.0
65-4	39,790	28.0	32,820	23.1	19,890	14.0	12,930	9.1	19,890	14.0	6,960	4.9	16,410	11.5	995.0
66-10	53,710	37.8	45,560	32.0	27,350	19.2	18,200	12.8	27,350	19.2	9,150	6.4	22,780	16.0	90.85
53-11	79,600	56.0			39,800	28.0	39,800	28.0	39,800	28.0			39,800	28.0	0.82
54-5	81,600	57.4			40,800	28.7	40,800	28.7	40,800	28.7			40,800	28.7	0.76
63-2†	63,460	44.6			31,730	22.3	31,730	22.3	31,730	22.3			31,730	22.3	43.75
53-8	67,600	47.5	46,700	32.8	33,800	23.8	23,350	16.4	33,800	23.8	10,440	7.3	28,500	20.1	27.0
65-11	66,640	46.9	44,560	31.3	33,320	23.4	18,800	13.2	33,320	23.4	14,520	10.2	26,060	18.3	154.4
65-9	67,440	47.4	44,160	31.0	33,620	23.6	17,900	12.6	33,820	23.8	15,720	11.1	25,760	18.1	168.0
53-9	62,000	43.6	33,800	23.8	31,000	21.8	16,900	11.9	31,000	21.8	14,120	9.9	23,950	16.8	190.5
54-9	63,700	44.8	33,800	23.8	31,850	22.4	16,900	11.9	31,850	22.4	14,920	10.5	24,380	17.1	208.0
57-2	79,070	55.6	72,110	50.7	38,790	27.3	31,830	22.4	40,280	28.3	6,960	4.9	35,310	24.8	1.74
56-12	80,560	56.6	71,120	50.0	39,390	27.7	29,940	21.0	41,180	29.0	9,450	6.6	34,660	24.4	1.66
57-1	79,070	55.6	68,630	48.3	38,290	26.9	27,850	19.6	40,780	28.7	10,440	7.3	33,070	23.3	5.94
56-11	79,070	55.6	68,630	48.3	38,290	26.9	27,850	19.6	40,780	28.7	10,440	7.3	33,070	23.3	6.0
65-12†	65,650	46.2	56,890	40.0	32,820	23.1	32,820	23.1	32,820	23.1			32,820	23.1	39.8
56-5	73,600	51.7	59,680	42.0	36,800	25.9	22,880	16.1	36,800	25.9	13,920	9.8	29,840	21.0	32.7
56-1	73,600	51.7	59,680	42.0	36,800	25.9	22,880	16.1	36,800	25.9	13,920	9.8	29,850	21.0	32.5
53-10	67,240	47.3	51,720	36.4	33,600	23.6	18,100	12.7	33,600	23.6	15,520	10.9	25,850	18 2	73.0
53-12	67,440	47.4	51,520	36.2	33,700	23.7	17,800	12.5	33,700	23.7	15,910	11.2	25,750	18.1	82.4
54-2	71,100	50.0	51,700	36.3	35,500	25.0	16,150	11.4	35,550	25.0	19,390	13.6	25,850	18.2	144.0
54-1	64,700	45.5	45,800	32.2	32,350	22.7	13,450	9.5	32,350	22.7	18,900	13.3	22,900	16.1	158.0
57-6	63,660	44.8	42,770	30.1	31,830	22.4	10,940	7.7	31,830	22.4	20,890	14.7	21,380	15.0	451.6
57-7	62,160	43.7	42,270	29.7	30,340	21.3	10,440	7.3	31,830	22.4	19,890	14.0	20,390	14.3	360.0
66-1	58,100	40.8	38,000	26.7	28,050	19.7	7,960	5.6	30,040	21.1	20,090	14.1	18,000	12.7	1,492.5

57 10†	65,250	45 9	50,530	35 5	31,630	22 2	16,910	11 9	33,620	23 6	14,720	10 3	24,270	17 1	90 7
57 4†	58,090	40 8	45,160	31 8	27,850	19 6	14,920	10 5	30,240	21 3	12,930	9 1	21,390	15 0	116 3
54 3	76,600	53 9	61,700	43 4	38,300	26 9	38,300	26 9	38,300	26 9			38,300	26 9	0 62
52-11	67,800	47 7	52,900	37 2	33,900	23 8	33,900	23 8	33,900	23 8			33,900	23 8	0 56
66-8	99,100	69 7			49,550	34 8	49,550	34 8	49,550	34 8			49,550	34 8	0 50
66 9	89,520	62 9	68,430	48 1	44,760	31 5	23,670	16 6	44,760	31 5	21,090	14 8	34,220	24 1	9 99

*Tested in air at 650°C and a strain rate of 4×10^{-3} sec^{-1}
†Strain rate, 4×10^{-5} sec^{-1}

TABLE 3 10

FATIGUE DATA OBTAINED IN HOLD-TIME TESTS OF AISI 304 STAINLESS STEEL*

Spec. No	Hold period, min		Axial strain range, %			Fatigue life								
	Tension	Com pression	$\Delta\epsilon_t$	$\Delta\epsilon_p$†	$\Delta\epsilon_e$†	N_0, cycles	N_0, hr	N_0/N_f	N_5, cycles	N_5, hr	N_5/N_f	N_f, cycles	N_f, hr
67 3‡	0	0	0 50	0 27	0 22							43,377	15 06
67 4	1 0	0	0 50	0 24	0 25	14,000	233 3	0 78	16 750	279 1	0 93	17,920	299 6
66-12	0	0	3 96	3 42	0 54	174	0 97	0 71	233	1 29	0 95	244	1 36
66 11	10 0	0	3 96	3 46	0 50	86	14 3	0 61	130	21 6	0 92	141	23 55

*Tested in air at 538°C and a strain rate of 4×10^{-3} sec^{-1}, control mode axial strain.
†Values are based on data at $N_f/2$, in hold time tests the relaxed stress range is used
‡Strain rate, 8×10^{-3} sec^{-1}

TABLE 3 11

STRESS RELAXATION DATA OBTAINED IN LOW CYCLE FATIGUE TESTS OF AISI 304 STAINLESS STEEL*

Spec No	$\Delta\sigma$ at $N_f/2$		$\Delta\sigma_r$ at $N_f/2$		σ_t max at $N_f/2$		σ_t min. at $N_f/2$		σ_c max at $N_f/2$		σ_r tension		$\frac{\sigma_t \text{ max} + \sigma_t \text{ min}}{2}$		Total time under tensile stress for fracture, hr
	Psi	Kg/mm^2	Psi	Kg/mm^2	Psi	Kg/mm^2	Psi	Kg/mm^2	Psi	Kg/mm^2	Psi	Kg/mm^2	Psi	Kg/mm^2	
67 3†	50,000	35 2			25,000	17 6	25,000	17 6	25,000	17 6			25,000	17 6	7 53
67 4	58,000	40 8	57,000	40 1	29,000	20 4	28,000	19 7	29,000	20 4	1,000	0 7	28,500	20 0	292 8
66 12	122,000	85 8			61,000	42 9	61,000	42 9	61,000	42 9			61,000	42 9	0 68
66 11	124,000	87 2	112,000	78 7	62,000	43 6	50 000	35 2	62,000	43 6	12,000	8 4	56,000	39 4	23 1

*Tested in air at 538°C and a strain rate of 4×10^{-3} sec^{-1}
†Strain rate, 8×10^{-3} sec^{-1}

TABLE 3.12

LOW-CYCLE-FATIGUE DATA FOR ANNEALED AISI 316 STAINLESS STEEL*

Specimen No.	Hold period, min		Axial strain range, %			Fatigue life			
	Tension	Compression	$\Delta\epsilon_t$	$\Delta\epsilon_p$†	$\Delta\epsilon_e$ †	N_0, cycles	N_5, cycles	N_f, cycles	N_f, hr
10-7	0	0	0.49	0.21	0.28	12,031	12,439	13,087	9.09
10-10	0	0	1.98	1.51	0.47	370	430	440	1.22
10-3	0	0	1.98	1.51	0.47	340	430	460	1.28
10-5	0	0	1.98	1.53	0.45	399	469	489	1.35
10-6	30	0	1.98	1.69	0.29	63	77	103	51.95
10-9	30	0	1.98	1.67	0.31	41	58	76	38.2
10-11	60	0	1.98	1.71	0.27	70	90	117	117.3

*Tested in air at 650° C and a ramp strain rate (slope of line connecting the peak strain values and is equal to strain rate in a test with no hold period) of 4×10^{-3} sec^{-1}; control mode; axial strain.

†Values are based on data at $N_f/2$; in hold-time tests the relaxed stress range is used.

TABLE 3.13

SUMMARY OF STRESS-RELAXATION DATA OBTAINED FROM LOW-CYCLE-FATIGUE TESTS OF ANNEALED AISI 316 STAINLESS STEEL*

Spec. No.	$\Delta\sigma$ at $N_f/2$		$\Delta\sigma_r$ at $N_f/2$		σ_t max. at $N_f/2$		σ_t min. at $N_f/2$		σ_c max. at $N_f/2$		σ_r tension		$\frac{\sigma_t \text{ max.} + \sigma_t \text{ min.}}{2}$		$\frac{\sigma_t \text{ min.}}{\sigma_t \text{ max.}}$	Total time under tensile stress for fracture, hr
	Psi	Kg/mm²	Psi	Kg/mm²	Psi	Kg/mm²	Psi	Kg/mm²	Psi	Kg/mm²	Psi	Kg/mm²	Psi	Kg/mm²		
10-7	61,860	43.5	61,860	43.5	30,930	21.7	30,930	21.7	30,930	21.7			30,930	21.7	1.0	4.54
10-10	103,440	72.7	103,440	72.7	51,720	36.4	51,720	36.4	51,720	36.4			51,720	36.4	1.0	0.61
10-3	103,440	72.7	103,440	72.7	51,720	36.4	51,720	36.4	51,720	36.4			51,720	36.4	1.0	0.64
10-5	98,960	69.6	98,960	69.6	49,480	34.8	49,480	34.8	49,480	34.8			49,480	34.8	1.0	0.67
10-6	83,750	58.9	63,660	44.8	41,870	29.4	21,980	15.5	41,870	29.4	19,890	14.0	31,925	22.4	0.524	51.60
10-9	87,930	61.8	67,830	47.7	43,960	30.9	23,870	16.8	43,960	30.9	20,090	14.1	33,916	23.8	0.543	38.1
10-11	79,970	56.2	58,090	40.8	39,980	28.1	18,102	12.7	39,980	28.1	21,881	15.4	29,043	20.4	0.453	117.2

*Tested in air at 650° C and a ramp strain rate of 4×10^{-3} sec^{-1}.

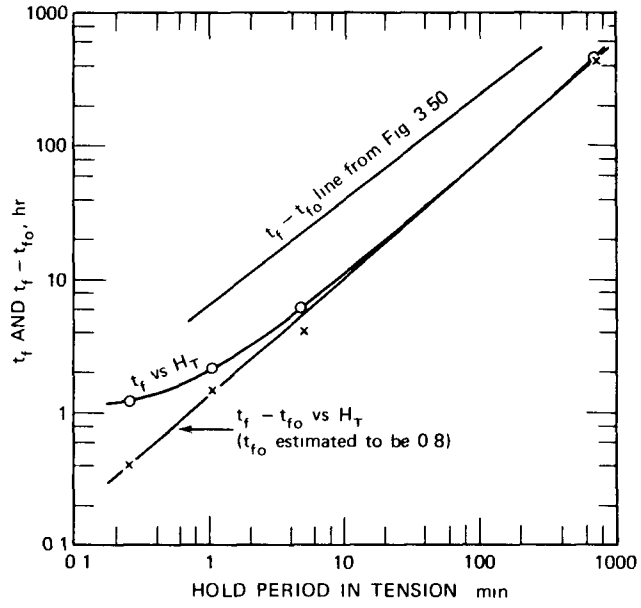

Fig. 3.52 Time to fracture vs. length of hold period in tension for cast 1% molybdenum steel tested[12] at 510°C at a total strain range of 2.0%.

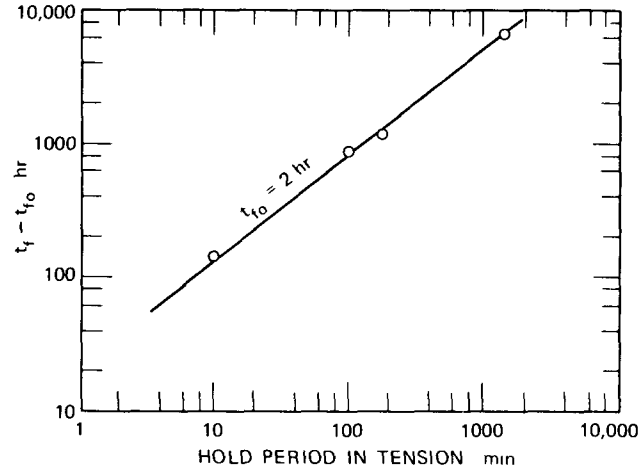

Fig. 3.53 Graph of $t_f - t_{f_0}$ vs. hold time in tension only for Cr–Mo–V steel data[14,15] obtained at 565°C and 10 cycles/min for a total strain range of 1%.

calculated by Coles and Skinner to reflect the hold period involved in each test A logarithmic graph of frequency vs. time to fracture was shown to be linear up to about 200 hr At this point a break in the lines for the three different strain ranges used was associated with a change in the fracture mode from transgranular to intergranular A slight modification of this approach led to the logarithmic graph presented in Fig 3 54, which shows that, when the hold-time data are in terms of cycle time, a linear relation (logarithmic coordinates) with time to fracture is identified Also important in Fig 3 54 is the fact that the data points corresponding to tests with no hold periods at other strain rates are in complete accord with the cycle-time concept The conclusion from this correlation is that, once the time-to-fracture data are generated at one strain rate in hold-time tests, a relation is identified to characterize the fatigue behavior Times to fracture at other strain rates with or without hold periods can be obtained simply by using the appropriate cycle time in conjunction with Fig. 3 54. Testing at other strain rates will therefore be minimized if not completely eliminated Much importance, therefore, is to be attached to Fig. 3 54, for it shows a way to effect certain testing economies in low-cycle-fatigue programs Figure 3 54 also reveals that a given cycle time, whether it is associated with a given strain rate or a faster strain rate plus a given hold period in tension, will yield the same fracture time Although this correlation appears to have some merit, it is far from completely evaluated and hence should be used with some caution The effect of strain wave form has not been investigated at all in this correlation, and the behavior at other strain ranges has received only limited attention There are some definite indications, for example, that the strain-rate and hold-time data begin to become divergent as the strain rate decreases. Some divergence seems to be evident at the cycle time in Fig. 3.54 corresponding to the continuous-cycling data for 4×10^{-5} sec^{-1} Although not completely confirmed as yet, this divergence seems to occur at smaller cycle times as the strain range decreases The conclusion here is that the correlation at the 2% strain range should not be generally applied, since the cycle time at which hold-time effects are more damaging than strain-rate effects decreases as the strain range decreases This point is therefore in need of additional study before a quantitative evaluation can be made of this behavior pattern.

An illustration of how the Fig. 3.54 type of graph can be used to estimate fatigue behavior at other strain rates is provided by the following example Consider that the two lines in Fig 3.54 (for strain-range values of 0 5 and 2.0%)

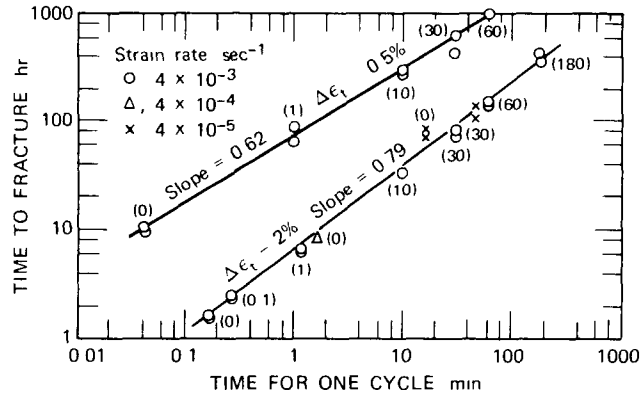

Fig. 3.54 Correlation of low-cycle-fatigue data for AISI 304 stainless steel tested in air at 650°C using no hold times and hold times at peak strain in only the tension portion of the cycle. Numbers in parentheses indicate hold time in minutes in tension-hold-only tests.

are based on measurements at a strain rate of 4×10^{-3} sec^{-1}. If it is desired to estimate the fatigue behavior at a strain rate of 4×10^{-4} sec^{1}, the times for 1 cycle are calculated to be 100 and 25 sec, respectively, for the 2 and 0.5% strain ranges. Figure 3.54 yields t_f values of 9.3 and 41.5 hr, respectively, for these two strain ranges. Since

$$t_f = \frac{N_f}{f} \tag{3.8}$$

and, for a triangular strain wave form,

$$\dot{\epsilon}_t = 2f\,\Delta\epsilon_t \tag{3.9}$$

where $\dot{\epsilon}_t$ is the total strain rate, f is the cyclic frequency, and $\Delta\epsilon_t$ is the total strain range, it follows that

$$N_f = \frac{t_f \dot{\epsilon}_t}{2\,\Delta\epsilon_t} \tag{3.10}$$

This expression allows conversion of the t_f values to N_f. Applying Eq. 3.10 to the above t_f data, N_f is estimated to be 335 and 5980, respectively, at the 2.0 and 0.5% strain ranges. These estimated values of N_f are plotted in Fig. 3.55 and show fairly good agreement with the experimental data.[1] If data were available for several other strain ranges in the Fig. 3.54 type of graph, enough estimated points would be made available to almost completely define the fatigue behavior at the new strain rate. Also shown for comparison in Fig. 3.55 is the fatigue curve based on experimental results[1] at a strain rate of 4×10^{-3} sec^{-1}. Estimating fatigue data at one strain rate from experimental results at another strain rate is an interesting and valuable application of the Fig. 3.54 correlation.

Expressed mathematically, the behavior in Fig. 3.54 yields

$$t_f = A(C_t)^n \tag{3.11}$$

where C_t is the cycle time. Rearrangement will be seen to give

$$N_f C_t = A(C_t)^n \tag{3.12}$$

and

$$N_f = AC_t^{n-1} \tag{3.13}$$

Since n is positive but less than unity, it follows that the exponent on C_t in Eq. 3.13 will be negative. This defines the type of behavior which should be observed in logarithmic plots of N_f vs. cycle time.

Some mention should also be made of another correlation involving strain-rate effects. As already noted in Fig. 3.48, a decrease in the strain rate leads to an increase in the fracture time. This effect will be seen to parallel that corresponding to the introduction of hold periods since it is clear that decreasing the strain rate increases the cycle time. For a strain range of 2%, the cycle times corresponding to strain rates of 4×10^{-3}, 4×10^{-4}, and 4×10^{-5} sec^{-1} are 10, 100, and 1000 sec, respectively. Some difference in fatigue behavior is to be expected therefore as the strain rate is decreased, and, in accordance with Fig. 3.49, it is consistent that decreased strain rates lead to increased times to fracture. One possible association of strain rate and hold-time effects (see Fig. 3.54) is to compare data at equal cycle times. For example, cycling times of 100 and 1000 sec are brought about in the 2% strain-range tests at 4×10^{-3} sec^{-1} by considering the addition of tension-hold-only periods of 90 and 990 sec. Reference to Fig. 3.50 will yield the corresponding times to fracture as 8.6 and 57.6 hr, respectively. Reference now to Fig. 3.49 will yield

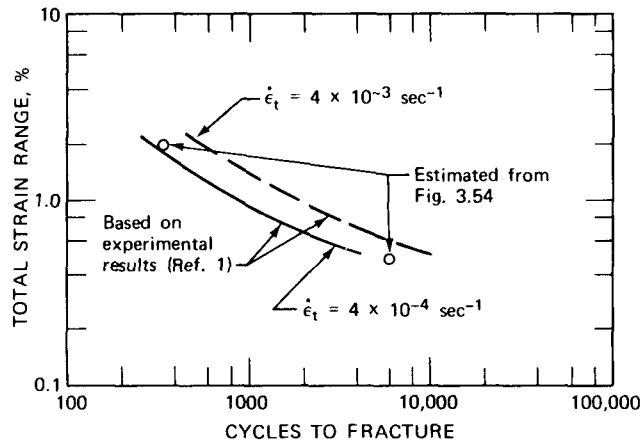

Fig. 3.55 Comparison of experimental and estimated fatigue behavior of AISI 304 stainless steel at 650°C.

values for the stress amplitudes associated with each of these fracture times. These points can then be considered as estimates of the stress-amplitude vs. time-to-fracture data at strain rates of 4×10^{-4} and 4×10^{-5} sec^{-1}. At the 0.5% strain range, similar calculations yield estimated data at these two strain rates. These results, shown as dashed lines in Fig. 3.48, are in very good agreement with experimental values.

Special Strain-Rate Effects

In all the low-cycle-fatigue tests described thus far, the strain rates were 4×10^{-3}, 4×10^{-4}, and 4×10^{-5} sec^{-1}. In general, it was noted that the cyclic fatigue life decreased as the strain rate decreased. These data at different strain rates were the basis for the correlation described in Fig. 3.54. More recently the effect of strain rate was studied in more detail, and data were obtained at strain rates as low as 4×10^{-6} sec^{-1} and as high as 3.2×10^{-2} sec^{-1}. The data obtained in these tests are summarized in Table 3.14.

TABLE 3.14

LOW-CYCLE-FATIGUE DATA FOR AISI 304 STAINLESS STEEL TESTED IN AIR

Spec. No.	Test temp., °C	Cyclic frequency, cycles/sec	Axial strain rate, sec^{-1}	Axial strain range obtained at $N_f/2$, %			Stress range obtained at $N_f/2$		N_0, cycles	Fatigue life		N_f, hr
				$\Delta\epsilon_t$	$\Delta\epsilon_p$	$\Delta\epsilon_e$	Psi	Kg/mm^2		N_5, cycles	N_f, cycles	
67-3	538	0 80	8×10^{-3}	0 50	0 27	0 22	50,000	35 2			43,377	15 06
66-12	538	0 05	4×10^{-3}	3 96	3 42	0 54	122,000	85 8	174	233	244	1 36
67-1	538	0 40	$3\ 2 \times 10^{-2}$	3 96	3 42	0 55	122,200	85 9	247	330	347	0.24
67-2	538	0 80	$6\ 4 \times 10^{-2}$	3 96	3 41	0 55	124,000	101 4	271	321	345	0 12
66-3	650	0.8	$8\ 0 \times 10^{-3}$	0 49	0 28	0 22	46,700	32 8	9,696	10,170	11,136	3.87
66-2	650	0 8	$1\ 6 \times 10^{-2}$	0 99	0 70	0 29	63,100	44 4	2,000	2,280	2,904	1 00
63-8	650	0 0001	4×10^{-6}	1 98	1 76	0 22	47,300	33 3	200	267	307	855.0
63-11	650	0 20	8×10^{-3}	1 98	1 61	0 36	78,200	55 0	536	644	734	1 02
63-7	650	0 40	$1\ 6 \times 10^{-2}$	1 98	1 61	0 37	79,600	56 0	465	621	705	0 49
63 12	650	0 80	$3\ 2 \times 10^{-2}$	1 98	1 62	0 36	77,800	54 7	481	641	765	0 265
66-8	650	0 05	4×10^{-3}	3 95	3 49	0 46	99,100	69 7	130	170	184	1 01
66-5	650	0 20	1.6×10^{-2}	3 95	3 47	0 48	103,200	72 6	152	208	223	0.31
66-4	650	0 20	$1\ 6 \times 10^{-2}$	3 95	3 49	0 46	99,500	70 0	172	277	292	0 40
66-7	650	0 40	3.2×10^{-2}	3 95	3 49	0 47	100,600	70 7	138	280	303	0 21

Originally this study was to be an evaluation of the effect of strain rate on fatigue behavior at various strain ranges. Since all the tests originally planned were not completed, the objectives of the study were not fully realized. Thus it is not possible to consider this effect as being fully identified. Some trends were noted, however, and these are worthy of special mention.

Data obtained at the 2% strain range are plotted in Fig. 3.56 to show the time to fracture (given by N_f/f, where f is the cycling frequency) corresponding to various cycling times (given by 1/f). Also included are the previously reported[1] data obtained at strain rates of 4×10^{-3}, 4×10^{-4}, and 4×10^{-5} sec^{-1} (see Table 3.3). At very fast strain rates (small cycling times), the data appear to define a linear relation with a slope of unity. This behavior (i.e., slope of unity) corresponds to a constant value for N_f, which is in exact agreement with the experimental results. In other words, in the range of high strain rates, the cyclic fatigue life (measured as N_f) is independent of strain rate.

As the strain rate decreases to 4×10^{-3} sec^{-1}, some slight deviation from the unity slope is indicated, and this deviation increases as the strain rate is decreased further. This behavior is interpreted to indicate that a creep effect becomes important near 4×10^{-3} sec^{-1} in the 2% strain-range tests. This creep effect leads to additional damage and to reductions in the time-to-fracture values. These reductions are noticed by the failure points located below the extension of the line of unit slope. In other words, at a cycle time of 16.6 min (strain rate of 4×10^{-5} sec^{-1}), the time to fracture is measured to be close to 80 hr, whereas, if the fatigue life were independent of strain rate, this value would be close to 220 hr. This reduction in fatigue life is viewed as the effect of creep damage, which becomes pronounced at the lower strain rates.

Another interesting observation in connection with Fig. 3.56 is related to the data at the lower strain rates. These points also seem to define a linear behavior with a slope of unity. And reference to Table 3.14 identifies that N_f is essentially constant, again independent of strain rate. Unfortunately these data at the 2% strain range are the only results of this type available, and it is probably premature

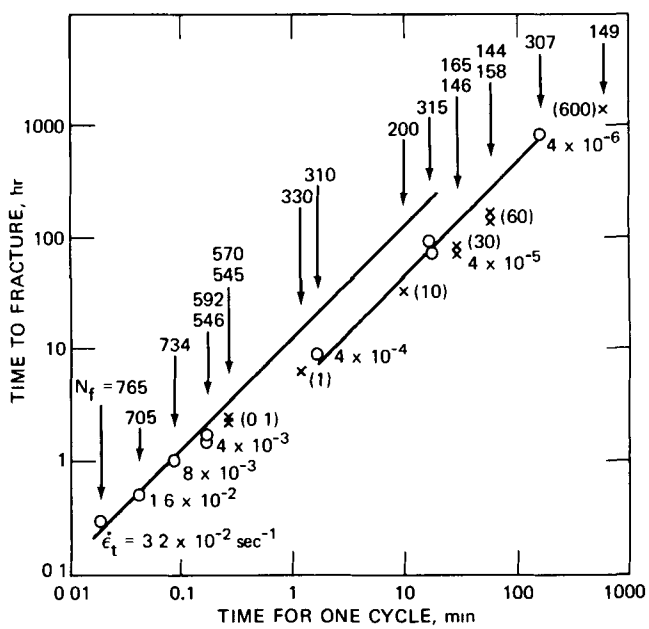

Fig. 3.56 Time to fracture vs. cycle time for AISI 304 stainless steel tested in air at 650°C and a strain range of 2%. Various strain rates and hold periods were used. ○, cycling tests with no hold period. ×, tests with hold times in tension only using a ramp strain rate of 4×10^{-3} sec^{-1}; numbers in parentheses are the hold periods in minutes.

to accept them as sufficient evidence of a general trend to be observed at all strain ranges Frequency effects are certainly an important aspect of fatigue behavior, and they warrant further study. It will be interesting to apply this analysis to data obtained in other studies[17-19] of frequency effects

Hold periods at peak strain also provide an opportunity for creep damage to occur, and data obtained in such tests have been related to strain-rate data in Fig. 3.54. Data obtained in tension-hold-only tests (see Table 3 8) have been included in Fig 3 56 for comparison.

Fatigue data obtained at strain ranges other than 2% are not extensive but can be compared to the behavior noted in Fig 3.56. Data obtained at strain ranges of 0 25, 0 5, 1, and 4% are presented in Fig 3.57, they indicate a definite similarity to the data obtained at the 2% strain range Hold-time data are also included in these graphs, and they describe about the same behavior pattern noted in Fig 3 56. Although no very low strain-rate tests were performed at strain ranges other than 2%, the behavior in Fig 3.56 would suggest that such data would be positioned very close to the hold-time data points obtained at the other strain ranges Further study is also suggested in this area

INCOLOY 800

A fairly extensive study[20] of the low cycle-fatigue behavior of Incoloy 800* was also included in the GE–NSP program. The test matrix proposed for this evaluation of the low-cycle-fatigue behavior of Incoloy 800 in air is presented in Table 3.15 In addition to these fatigue evaluations, the short-term tensile properties of Incoloy 800 at the test conditions given in Table 3.15 were determined, these are summarized in Table 3.16. Data for the elastic properties were also obtained and are given in Table 3 17.

Low-cycle-fatigue tests of Incoloy 800 were performed in air using inductively heated hourglass shaped specimens These tests employed axial-strain control in accordance with previously described test techniques The low cycle-fatigue data obtained in this study of mill-annealed and solution-annealed plate and bar stock are summarized in Tables 3.18 to 3 20 In general, these results provide fatigue behavior in accord with the test matrix outlined in Table 3.15.

Graphs relating $\Delta\epsilon_t$ and N_f are presented in Figs 3.58 to 3.65 Some typical data showing how the stress range varied with the number of cycles are presented in Figs 3.66 and 3.67

*Incoloy 800 is a high nickel austenitic steel and has the nominal composition Fe–20% Cr–32% Ni–0.75% Mn–0.35% Si–0 3% Cu–0 3% Al–0.3% Ti. Material was available in the form of mill-annealed (grade 1) bar stock and solution-annealed (grade 2) bar and plate stock Mill annealing involved heating to 980°C (1800°F) for 15 min, whereas solution annealing employed a heat treatment at 1145°C (2100°F) for 1 hr.

A study of the low-cycle-fatigue behavior of Incoloy 800 suggests a definite similarity to the fatigue behavior of annealed AISI 304 stainless steel This statement follows from the data compared in Fig 3.68

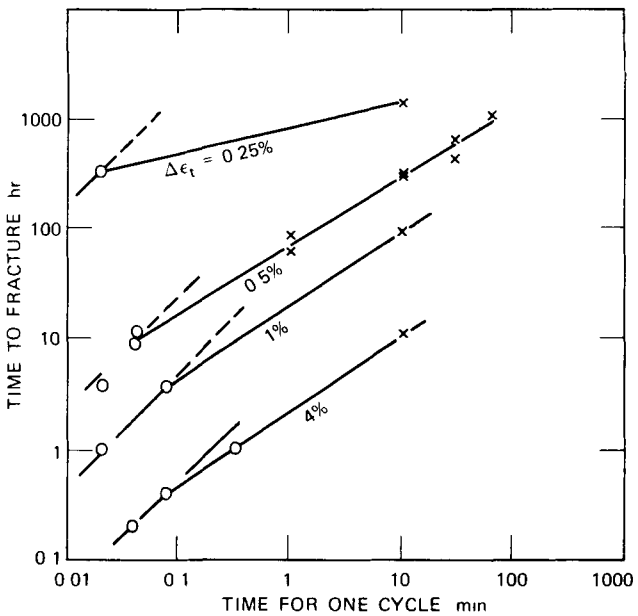

Fig. 3.57 Time to fracture vs. cycle time for AISI 304 stainless steel tested in air at 650°C and various strain rates and hold times for strain ranges of 0.25, 0.5, 1, and 4%. ○, cycling tests with no hold period. ×, tests with hold times in tension only using a ramp strain rate of 4×10^{-3} sec^{-1}

TABLE 3 15

TFST MATRIX PROPOSED FOR USF IN LOW CYCLE FATIGUE TEST PROGRAM FOR INCOLOY 800

Test temp, °C	Test temp, °F	Strain ranges,* %	True strain rate, sec^{-1}	Replication	Total tests
		Grade 1, Mill Annealed			
593	1100	1, 2, 3 4, 5	4×10^{-3}	2	10
593	1100	1, 3, 5	4×10^{-4}	1	3
538	1000	1, 2, 3, 4, 5	4×10^{-3}	2	10
538	1000	1 3, 5	4×10^{-4}	1	3
427	800	1, 2, 3, 4, 5	4×10^{-3}	2	10
427	800	1 3, 5	4×10^{-4}	1	3
					39
		Grade 2, Solution Annealed			
760	1400	1, 2 3 4 5	4×10^{-3}	2	10
760	1400	1 3 5	4×10^{-4}	1	3
704	1300	1 2, 3 4, 5	4×10^{-3}	2	10
704	1300	1 3, 5	4×10^{-4}	1	3
649	1200	1, 2, 3, 4, 5	4×10^{-3}	2	10
649	1200	1, 3, 5	4×10^{-4}	1	3
538	1000	1, 2, 3, 4, 5	4×10^{-3}	2	10
538	1000	1, 3, 5	4×10^{-4}	1	3
					52

*Determined such that failure occurs between 100 and 100,000 cycles (These strain ranges represent original objectives, the strain ranges actually used in the test program were slightly different)

TABLE 3.16

SUMMARY OF SHORT-TERM TENSILE DATA FOR INCOLOY 800 OBTAINED WITH HOURGLASS-SHAPED SPECIMENS TESTED IN AIR AT CONSTANT TRUE AXIAL STRAIN RATES

Spec. No.	Temp., °F	$\dot{\epsilon}_t$, sec^{-1}	σ_u, ksi	YS, ksi	RA, %	ϵ_f, %	t, hr
Grade 1, Mill-Annealed Bar Stock							
1-1	800	4×10^{-4}	78 7	33 2	57	84	0 579
1-3	800	4×10^{-3}	70 6	28 2	58	87	0 060
1-15	1000	4×10^{-4}	74 0	33 4	59	89	0 620
1 11	1000	4×10^{-3}	73 0	31 6	57	84	0 058
1 7	1100	4×10^{-5}	54 5	30.2	52	73	5 06
1-9	1100	4×10^{-4}	64 2	30 0	59	90	0 623
1-8	1100	4×10^{-3}	67 4	29 0	60	92	0 066
Grade 2, Solution-Annealed Plate Stock							
1 P	1200	4×10^{-5}	41 8	14 9	38	48	3 36
4-P	1200	4×10^{-4}	47 2	17 1	46	62	0 432
2-P	1200	4×10^{-3}	48 7	13 3	58	87	0 060
Grade 2, Solution-Annealed Bar Stock							
2 K-11	1000	4×10^{-4}	63 2	14 2	46	62	0 43
2 L-36	1000	4×10^{-3}	63 0	17 0	56	83	0 057
2-J-34	1200	4×10^{-4}	51 9	15 9	59	89	0 62
2-R 18	1200	4×10^{-3}	53 9	13 5	58	88	0 061
2-O-15	1300	4×10^{-4}	40 7	16 2	52	72	0 50
2-S-19	1300	4×10^{-3}	46 0	11 9	52	73	0 050
2 B-2	1400	4×10^{-4}	31 2	13 0	64	102	0 71
2 D-4	1400	4×10^{-3}	39 4	13 2	64	102	0 071

*Definitions of symbols

ϵ_t = true axial strain rate
σ_u = ultimate tensile stress
YS = 0 2% yield stress
RA reduction in area
ϵ_f fracture ductility.
t = time to fracture

In one analysis of the Incoloy 800 fatigue data, experimental results were compared with fatigue behavior estimated using the method of characteristic slopes[3] (see Chap. 4). For the data at 538°C, the agreement between estimated and experimental behavior is excellent (Fig. 3.69). At 649°C (Fig. 3.70), the agreement is not as good, but the estimated curve seems to parallel the experimental results. On the basis of previous experience with AISI 304 and 316 stainless steels, it was expected that the agreement at 649°C would be much better. Some further study of the method of characteristic slopes is suggested to determine under what conditions an overestimation of fatigue behavior is to be expected. Perhaps some feature of the short-term tensile behavior would suggest when overestimated fatigue life will be obtained from the method of characteristic slopes.

A few tests were performed to define the effect of a hold period at peak strain on the fatigue behavior of Incoloy 800. These tests involved hold periods in only the tension portion of the cycle (specimen was cycled into compression but not held there) and used the procedures reported previously.[1,3] A summary of the results obtained in these tests is presented in Tables 3.21 and 3.22. As was noted in the tests of AISI 304 and 316 stainless steels, a decided reduction in cyclic fatigue life was observed when hold times were introduced (see Figs. 3.62 and 3.64). For example, at a strain range of 2% and a strain rate of 4×10^{-3} sec^{-1} at 649°C, the cyclic fatigue life with no hold periods is about 510, as reported in Table 3.19. Under these

(Text continues on page 74.)

TABLE 3.17

ELASTIC CONSTANTS FOR INCOLOY 800*

Stock and (spec. No.)	Temp., °C	INCO tech. data† E, 10^6 psi	INCO tech. data† ν_e	GE–NSP meas. data for E/ν_e, 10^6 psi	GE–NSP calc. data for ν_e
Grade 1 bar (1-11)	R.T.	28.5	0.339	100.9	0.282
	427	24.6	0.363	78.0	0.315
	538	23.5	0.367	75.1	0.313
	593	22.9	0.372	71.6	0.320
Grade 2 plate (3-P)	R.T.	28.5	0.339	107.2	0.266
	427	24.6	0.363	85.1	0.289
	538	23.5	0.367	76.9	0.306
	649	22.4	0.377	73.0	0.307
	704	21.7	0.381	67.1	0.323
	760	21.1	0.389	64.2	0.329
Grade 2 bar (2A1)	R.T.	28.5	0.339	99.83	0.285
	538	23.5	0.367	74.91	0.313
	649	22.4	0.377	68.47	0.327
	704	21.7	0.381	64.58	0.336
	760	21.1	0.389	62.60	0.337
Grade 2 plate (13-P)					
Axis A	649	22.4	0.377	70.79	0.316
Axis B	649	22.4	0.377	65.07	0.343

*E = modulus of elasticity, ν_e = Poisson's ratio.
†From International Nickel Company, Technical Bulletin T-40.

TABLE 3.18

SUMMARY OF COMPLETED FATIGUE TESTS ON INCOLOY 800, GRADE 1, MILL-ANNEALED, BAR STOCK

Spec. No.	Test temp., °C	Strain rate, sec^{-1}	Axial strain range, %			Stress range, psi	Fatigue life			
			$\Delta\epsilon_t$	$\Delta\epsilon_p$*	$\Delta\epsilon_e$*		N_0, cycles	N_5, cycles	N_f, cycles	N_f, hr
1-38	427	4×10^{-3}	3.97	3.33	0.64	158,630	312	364	384	2.13
50	427	4×10^{-3}	3.97	3.34	0.63	154,620	274	287	294	1.64
1-6	427	4×10^{-3}	1.99	1.51	0.48	118,450	1,480	1,503	1,543	4.28
1-16	427	4×10^{-3}	0.99	0.56	0.44	107,640	10,695	11,510	11,751	16.32
1-23	427	4×10^{-3}	0.74	0.31	0.43	105,920	25,400	26,570	27,290	25.27
1-43	427	4×10^{-3}	0.74	0.32	0.43	105,420	19,308	19,664	20,208	21.1
1-18	427	4×10^{-3}	0.50	0.09	0.41	100,603			46,536	32.3†
1-14	427	4×10^{-3}	0.50	0.09	0.41	101,210			48,384	33.6‡
1-19	427	4×10^{-4}	1.99	1.48	0.51	124,900	1,161	1,365	1,461	40.6
1-41	427	4×10^{-4}	1.99							§
1-44	427	4×10^{-4}	0.74	0.30	0.44	109,040			20,043	208.7
48	538	4×10^{-3}	3.96	3.33	0.63	149,000	235	277	295	1.64
1-36	538	4×10^{-3}	3.96	3.35	0.61	144,100	216	244	264	1.47
49	538	4×10^{-3}	1.98	1.49	0.50	116,400	906	966	1,038	2.88
1-17	538	4×10^{-3}	1.98	1.50	0.48	113,600	731	899	947	2.63
1-12	538	4×10^{-3}	0.99	0.62	0.37	86,000	6,162	6,462	6,750	9.37
1-37	538	4×10^{-3}	0.99	0.62	0.37	86,600	6,027	6,130	6,228	8.65
1-32	538	4×10^{-3}	0.74	0.39	0.35	82,000			30,000	31.0¶
47	538	4×10^{-3}	0.74	0.38	0.36	84,800			39,326	36.4
1-35	538	4×10^{-3}	0.74	0.39	0.36	84,000			207,920	216.5**
1-28	538	4×10^{-3}	0.64	0.31	0.34	79,500			51,541	46.4¶
1-13	538	4×10^{-3}	0.50	0.16	0.34	79,400			121,375	84.2‡
1-42	538	4×10^{-4}	1.98	1.49	0.49	115,200	501	589	600	16.65
1-45	538	4×10^{-4}	0.74	0.40	0.35	81,600			100,000	1042.0**
1-24	538	4×10^{-4}	0.50	0.15	0.35	82,000			100,000	695.0**
46	593	4×10^{-3}	3.96	3.34	0.61	140,270	162	186	204	1.13
1-29	593	4×10^{-3}	3.96	3.34	0.62	141,260	128	190	206	1.15
1-10	593	4×10^{-3}	1.98	1.49	0.49	111,080	522	600	636	1.75
1-27	593	4×10^{-3}	1.98	1.49	0.49	111,970	451	560	595	1.66
1-25	593	4×10^{-3}	0.99	0.61	0.38	86,470	3,238	3,402	3,882	5.39
1-4	593	4×10^{-3}	0.99	0.61	0.37	85,870	2,950	3,250	3,274	4.54
1-34	593	4×10^{-3}	0.74	0.40	0.34	78,100	9,320	9,570	9,601	10.0
1-22	593	4×10^{-3}	0.74	0.41	0.34	77,100	8,028	8,766	9,126	8.45
1-30	593	4×10^{-3}	0.74	0.39	0.35	79,700				§
1-31	593	4×10^{-3}	0.64	0.31	0.34	76,900			101,750	91.7**
1-26	593	4×10^{-3}	0.59	0.25	0.34	78,900			142,120	118.4**
1-5	593	4×10^{-3}	0.51	0.20	0.32	72,720			243,624	169.0**
1-40	593	4×10^{-4}	1.98	1.49	0.49	112,370	353	402	466	12.95
1-20	593	4×10^{-4}	0.99	0.59	0.40	92,650	1,630	1,703	1,841	25.6
1-21	593	4×10^{-4}	0.74	0.39	0.35	79,700	5,180	5,540	5,765	53.4
1-28	593	4×10^{-4}	0.49	0.17	0.33	75,310			100,000	695.0**
1-39	649	4×10^{-3}	1.98	1.51	0.47	104,430	342	438	486	1.35

*At $N_f/2$.

†Specimen failed at thermocouple.

‡Specimen failed at buttonhead.

§System-control problem.

¶Test was terminated prematurely owing to power failure.

**Test was stopped intentionally when the cyclic life far exceeded expected behavior.

TABLE 3.19

SUMMARY OF COMPLETED FATIGUE TESTS ON INCOLOY 800, GRADE 2, SOLUTION-ANNEALED BAR STOCK

Spec. No.	Test temp., °C	Strain rate, sec^{-3}	Axial strain range, %			Stress range, psi	Fatigue life			
			$\Delta\epsilon_t$	$\Delta\epsilon_p$*	$\Delta\epsilon_e$*		N_0, cycles	N_s, cycles	N_f, cycles	N_f, hr
2U69	538	4×10^{-3}	3.96	3.35	0.61	144,000				†
2M61	538	4×10^{-3}	3.96	3.33	0.63	149,000				‡
2C51	538	4×10^{-3}	2.97	2.37	0.60	142,000	309	372	408	1.51
2R42	538	4×10^{-3}	2.97	2.35	0.62	146,800	220	311	374	1.38
2S43	538	4×10^{-3}	1.98	1.44	0.54	128,000	830	943	997	2.77
2X72	538	4×10^{-3}	1.98	1.43	0.55	130,400	516	768	786	2.18
2D52	538	4×10^{-3}	0.99	0.60	0.39	92,000	3,562	3,962	4,550	6.32
2M37	538	4×10^{-3}	0.99	0.59	0.40	93,500	3,652	4,348	4,684	6.51
2P64	538	4×10^{-3}	0.50	0.18	0.32	74,500			17,280	12.0
2T44	538	4×10^{-3}	0.50	0.17	0.33	76,000	15,614	16,046	16,526	11.47
2L60	538	4×10^{-3}	0.40	0.09	0.31	72,000			176,616	98.12
2Q41	538	4×10^{-3}	0.25	0.01	0.24	57,000			260,930	90.6§
2G7	538	4×10^{-4}	1.98	1.39	0.60	140,200	275	405	444	12.33
2H8	538	4×10^{-4}	0.99	0.55	0.44	104,000	2,180	2.702	2,834	39.36
2L12	538	4×10^{-4}	0.74	0.34	0.41	95,800		3,540	3,590	33.24
2I9	538	4×10^{-4}	0.50	0.12	0.38	88,800	21,818	22,946	23,510	163.3
2E77	649	4×10^{-3}	3.95	3.36	0.59	132,680	83	127	163	0.91
2E53	649	4×10^{-3}	3.95	3.36	0.60	133,280	69	116	123	0.68
2A73	649	4×10^{-3}	1.98	1.47	0.51	113,390	290	375	507	1.41
2F78	649	4×10^{-3}	1.98	1.48	0.50	111,800	340	441	513	1.43
2Q40	649	4×10^{-3}	0.99	0.56	0.43	95,880	1,420	1,570	1,600	2.22
2O63	649	4×10^{-3}	0.99	0.56	0.43	95,090	1,604	1,712	1,820	2.52
2G55	649	4×10^{-3}	0.49	0.19	0.31	68,430	10,300	10,784	11,000	7.63
2N38	649	4×10^{-3}	0.49	0.18	0.31	69,430			13,478	9.36
2Q65	649	4×10^{-3}	0.40	0.12	0.28	61,660			23,220	12.9
2R66	649	4×10^{-3}	0.40	0.11	0.29	63,860		13,950	16,200	9.0
2F54	649	4×10^{-3}	0.25	0.02	0.23	50,730			132,710	46.1§
2J10	649	4×10^{-4}	1.98	1.51	0.46	103,840	192	291	360	10.0
2N14	649	4×10^{-4}	0.99	0.58	0.41	90,310	988	1,162	1,414	19.63
2M13	649	4×10^{-4}	0.49	0.16	0.33	74,800	5,626	6,030	6,426	44.63
2N62	649	4×10^{-4}	0.25	0.02	0.23	50,730			101,784	353.0§
2V70	704	4×10^{-3}	3.95	3.43	0.52	113,210	77	88	93	0.52
2D76	704	4×10^{-3}	3.95	3.44	0.51	109,830	63	111	123	0.69
2U21	704	4×10^{-3}	1.97	1.53	0.45	97,320	287	335	407	1.13
2X24	704	4×10^{-3}	1.97	1.53	0.45	97,320	279	400	459	1.27
2J58	704	4×10^{-3}	0.99	0.62	0.37	79,440	1,392	1,512	1,656	2.30
2T20	704	4×10^{-3}	0.99	0.60	0.39	83,810	840	1,024	1,252	1.76
2H56	704	4×10^{-3}	0.99							¶
2I57	704	4×10^{-3}	0.49	0.20	0.29	63,950	5,010	5,655	6,055	4.21
2C3	704	4×10^{-3}	0.49	0.20	0.29	63,950	5,410	5,890	6,715	4.66
2U22	704	4×10^{-3}	0.30	0.04	0.26	55,610			74,720	31.1
2T68	704	4×10^{-3}	0.29	0.06	0.23	50,450		213,720	218,120	90.8
2Q17	704	4×10^{-4}	1.97	1.57	0.40	87,190	190	262	331	9.18
2P16	704	4×10^{-4}	0.99	0.65	0.34	73,880	491	629	830	11.52
2B74	704	4×10^{-4}	0.25	0.04	0.21	44,490			103,250	358.5
2A25	760	4×10^{-3}	3.94	3.51	0.43	90,100	102	126	138	0.76
2C75	760	4×10^{-3}	3.94	3.53	0.41	86,340	86	130	134	0.74
2A1	760	4×10^{-3}	1.92	1.58	0.35	73,070	228	312	432	1.2
2B26	760	4×10^{-3}	1.97	1.61	0.37	77,030	287	342	420	1.17
2C27	760	4×10^{-3}	0.99	0.68	0.30	63,960	859	1,075	1,351	1.88

(Table continues on next page.)

TABLE 3.19 (Continued)

Spec. No.	Test temp., °C	Strain rate, sec^{-1}	Axial strain range, %			Stress range, psi	Fatigue life			
			$\Delta\epsilon_t$	$\Delta\epsilon_p$*	$\Delta\epsilon_e$*		N_0, cycles	N_s, cycles	N_f, cycles	N_f, hr
2F6	760	4×10^{-3}	0.99	0.66	0.32	67,920	493	745	991	1.38
2W23	760	4×10^{-3}	0.49	0.24	0.25	52,970	3,254	3,614	4,046	2.81
2E5	760	4×10^{-3}	0.49	0.23	0.26	55,640	3,123	3,456	4,478	3.11
2D28	760	4×10^{-3}	0.30	0.08	0.22	46,530	12,360	13,160	14,480	6.03
2S67	760	4×10^{-3}	0.30	0.09	0.20	42,770			115,270	48.0
2K59	760	4×10^{-3}	0.25	0.06	0.19	40,000			218,448	75.8
2G79	760	4×10^{-3}	0.25	0.07	0.18	37,620			201,000	70.0§
2K35	760	4×10^{-4}	1.97	1.66	0.31	64,950	140	188	251	6.97
2G31	760	4×10^{-4}	1.97	1.67	0.30	63,170	144	183	252	7.0
2H32	760	4×10^{-4}	0.99	0.72	0.27	56,930	548	668	854	11.86
2I33	760	4×10^{-4}	0.49	0.28	0.21	44,560	2,005	2,401	2,545	17.68
2H80	760	4×10^{-4}	0.25	0.08	0.17	35,640	55,565	56,309	57,197	198.6

*At $N_f/2$.
†Specimen buckled after about 40 cycles.
‡Specimen buckled after about 60 cycles.
§Test was stopped intentionally when the cyclic life far exceeded expected behavior.
¶System-control problem.

TABLE 3.20

SUMMARY OF COMPLETED FATIGUE TESTS ON INCOLOY 800, GRADE 2, SOLUTION-ANNEALED PLATE STOCK

Spec. No.	Test temp., °C	Strain rate, sec^{-1}	Axial strain range, %			Stress range, psi	Fatigue life			
			$\Delta\epsilon_t$	$\Delta\epsilon_p$*	$\Delta\epsilon_e$*		N_0, cycles	N_s, cycles	N_f, cycles	N_f, hr
3-P	649	4×10^{-3}	1.98	1.49	0.48	108,410	421	450	482	1.34
13-P	649	4×10^{-3}	1.98	1.48	0.49	110,600	220	310	388	1.08
14-P	649	4×10^{-3}	1.98	1.52	0.45	101,650	265	382	481	1.34
5-P	649	4×10^{-3}	0.99	0.59	0.40	89,520	928	1,136	1,448	2.01
12-P	649	4×10^{-3}	0.49	0.21	0.28	63,660			7,626	5.29
11-P	649	4×10^{-4}	1.98	1.56	0.41	92,500	133	187	262	7.27
10-P	649	4×10^{-4}	0.99	0.66	0.33	74,400	1,059	1,197	1,257	17.46
9-P	649	4×10^{-4}	0.49	0.21	0.29	64,050	4,984	5,039	5,364	37.25

*At $N_f/2$.

TABLE 3.21

EFFECT OF HOLD PERIODS AT PEAK STRAIN ON THE LOW-CYCLE-FATIGUE BEHAVIOR OF INCOLOY 800, GRADE 2, SOLUTION-ANNEALED BAR STOCK*

Temp., °C	Spec. No.	Hold period, min		Ramp strain rate,† sec^{-1}	Axial strain range, %			Fatigue life			
		Tension	Compression		$\Delta\epsilon_t$	$\Delta\epsilon_p$‡	$\Delta\epsilon_e$‡	N_0, cycles	N_s, cycles	N_f, cycles	N_f, hr
649	2A49	10	0	4×10^{-3}	1.98	1.62	0.36	100	181	203	33.9
649	2B50	60	0	4×10^{-3}	1.98	1.63	0.34	76	111	134	134.7
760	2W71	10	0	4×10^{-3}	1.97	1.74	0.24	90	126	156	26.2

*Tested in air at 649 and 760°C; control mode; axial strain.
†Slope of line connecting the peak strain values and is equal to strain rate in a test with no hold period.
‡Values are based on the relaxed stress range obtained at $N_f/2$.

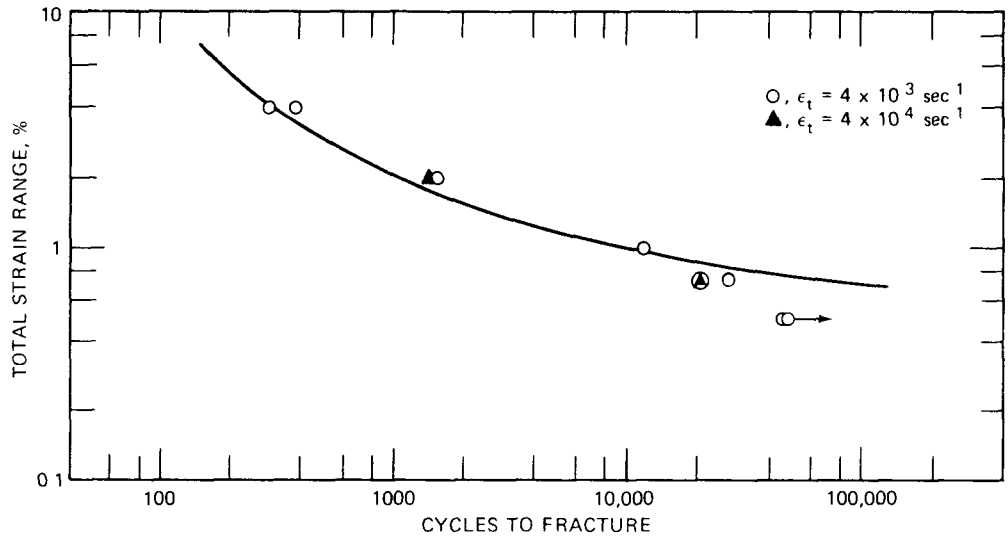

Fig. 3.58 Low-cycle-fatigue data for Incoloy 800, grade 1, mill-annealed bar stock tested in air at 427°C.

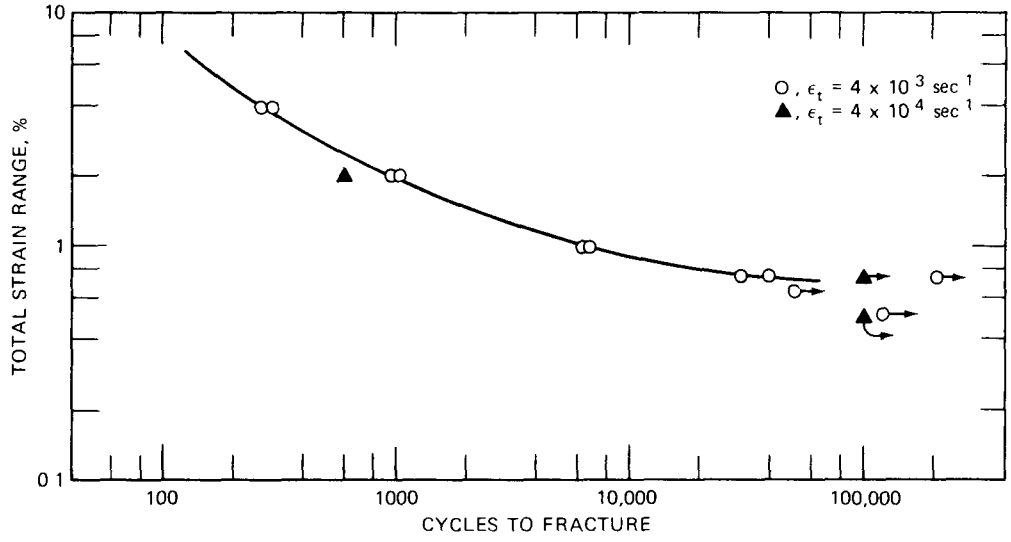

Fig. 3.59 Low-cycle-fatigue data for Incoloy 800, grade 1, mill-annealed bar stock tested in air at 538°C.

TABLE 3.22

STRESS-RELAXATION DATA OBTAINED IN HOLD-TIME TESTS OF INCOLOY 800, GRADE 2, SOLUTION-ANNEALED BAR STOCK IN AIR AT 649 AND 760°C[x]

Temp., °C	Spec. No.	$\Delta\sigma$ at $N_f/2$, psi	$\Delta\sigma_r$ at $N_f/2$, psi	σ_t max. at $N_f/2$, psi	σ_t min. at $N_f/2$, psi	σ_c max. at $N_f/2$, psi	σ_r tension, psi	$\left(\frac{\sigma_{t\ max.} + \sigma_{t\ min.}}{2}\right)$, psi	$\frac{\sigma_{t\ min.}}{\sigma_{t\ max.}}$	Total time under tensile stress for fracture, hr
649	2A49	105,430	80,570	52,720	27,850	57,720	24,870	40,280	0 53	33.3
649	2B50	107,420	76,590	53,710	22,880	53,710	30,830	38,300	0 42	134 2
760	2W71	77,230	49,500	38,610	10,890	38,610	27,720	24,750	0 28	26 0

*Definitions of symbols $\Delta\sigma$ = stress range $\Delta\sigma_r$ = stress range after relaxation. $\sigma_{t\ max.}$ = maximum tensile stress. $\sigma_{t\ min}$ = minimum tensile stress. $\sigma_{c\ max}$ = maximum compressive stress. σ_r = stress decrease during relaxation.

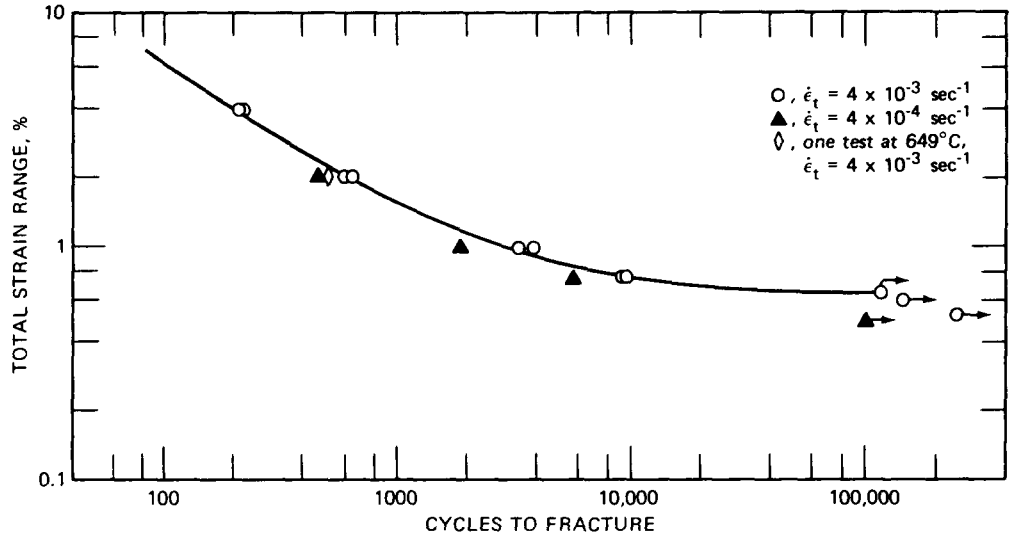

Fig. 3.60 Low-cycle-fatigue data for Incoloy 800, grade 1, mill-annealed bar stock tested in air at 593°C.

same conditions a 10- and 60-min hold period in tension only leads to a cyclic fatigue life of 203 and 134 cycles, respectively.

Special mention should be made of the correlation[2,3] between strain rate and hold-time effects (Fig. 3.54). A logarithmic graph of the fatigue life measured in hours vs. the time for 1 cycle was linear and allowed hold-time effects to be estimated from a knowledge of the fatigue behavior at several strain rates. Using the data in Table 3.19 at 4×10^{-3} and 4×10^{-4} sec^{-1} and a strain range of 2% at 649°C, a logarithmic graph was made of fatigue life in hours vs. the cycle time (given as 1/f in tests involving no hold periods). The curve was assumed to be linear, as it was found to be[2,3] for the case of AISI 304 stainless-steel data. Extrapolating this graph to cycle times corresponding to 10- and 60-min tension-hold-only periods led to cyclic fatigue-life values of 228 and 155 cycles, respectively. These values are in excellent agreement with the experimental fatigue-life values of 203 and 134 cycles (refer to the qualifications discussed in terms of Fig. 3.54).

A graph of various stress relations vs. the fatigue cycles (Fig. 3.71) clearly defines the cyclic strain-hardening characteristics of Incoloy 800.

DATA SUMMARIES AND COMPARISONS

In one of the first and probably the only extensive review of the available low-cycle-fatigue data for the austenitic stainless steels, Swindeman[21] reported results for

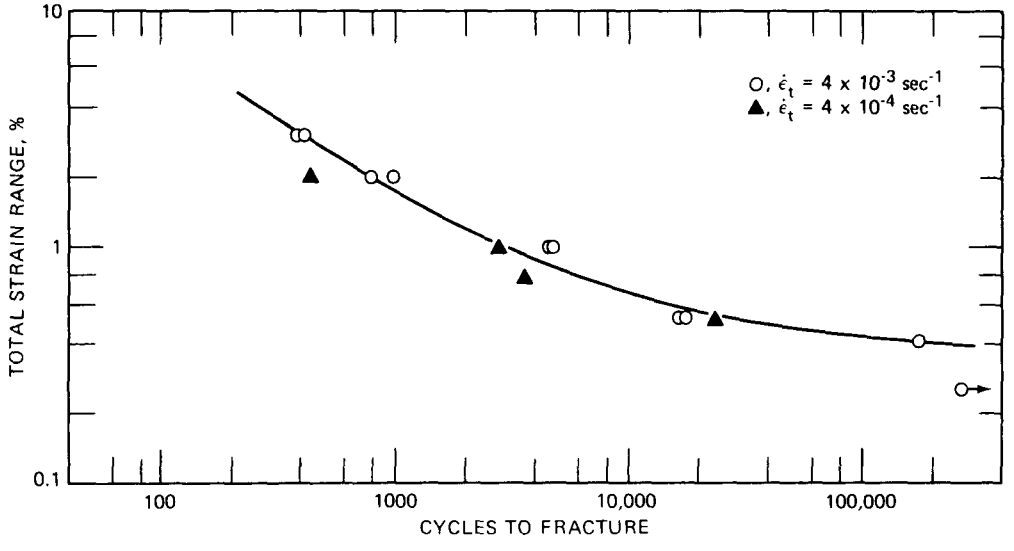

Fig. 3.61 Low-cycle-fatigue data for Incoloy 800, grade 2, solution-annealed bar stock tested in air at 538°C.

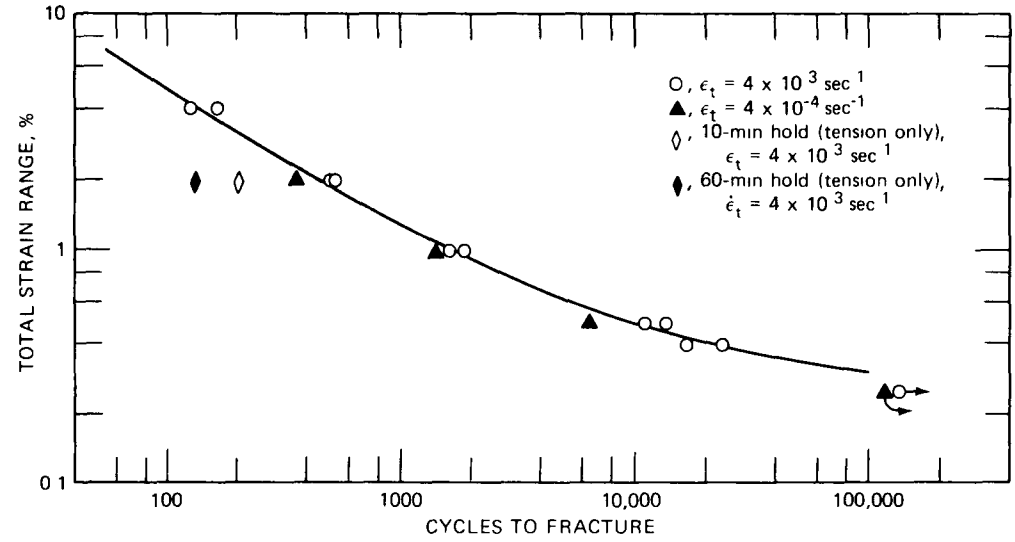

Fig. 3.62 Low-cycle-fatigue data for Incoloy 800, grade 2, solution-annealed bar stock tested in air at 649°C.

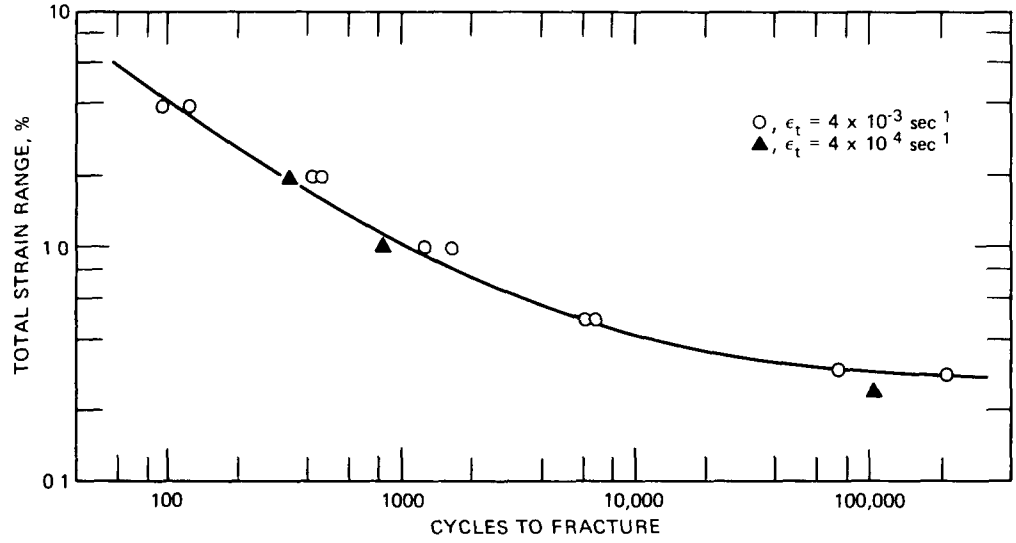

Fig. 3.63 Low-cycle-fatigue data for Incoloy 800, grade 2, solution-annealed bar stock tested in air at 704°C.

304, 316, and 347 stainless steels at temperatures ranging from room temperature to 871°C. One of the noteworthy features of this comprehensive summary is the very large differences that were recorded in the cycles to failure at some strain ranges. A variation of one order of magnitude was observed at several strain ranges at room temperature, 300, 500, 540, 600, and 650°C, whereas a scatter involving two orders of magnitude was noted at 704 and 815°C. Of course, much of this can be attributed to frequency differences, test-environment differences, and to the fact that the summary graphs included data obtained using sheet and rod specimens and several different test techniques.

When the data reported in Tables 3.3 and 3.8 for 304 stainless steel are included in the Swindeman graphs, the fatigue resistance at 500°C coincides with that defined by the upper boundary of all the data included in the Swindeman summary. A similar comment can be made regarding the data at 600°C; at 650°C the data in Table 3.8 define a fatigue resistance that is much higher than that reflected by any of the data reported by Swindeman. At 815°C the data in Table 3.3 are higher than all data reported by Swindeman except for some torsional-fatigue data obtained for 316 stainless-steel tubular material tested in argon.

A fairly extensive summary of fatigue data was reported recently by Conway, Berling, and Stentz[3] to show agreement with the $t_f - t_{f0}$ concept of Eq. 3.4. The comparison graph derived from this study (Fig. 3.72) reveals a striking

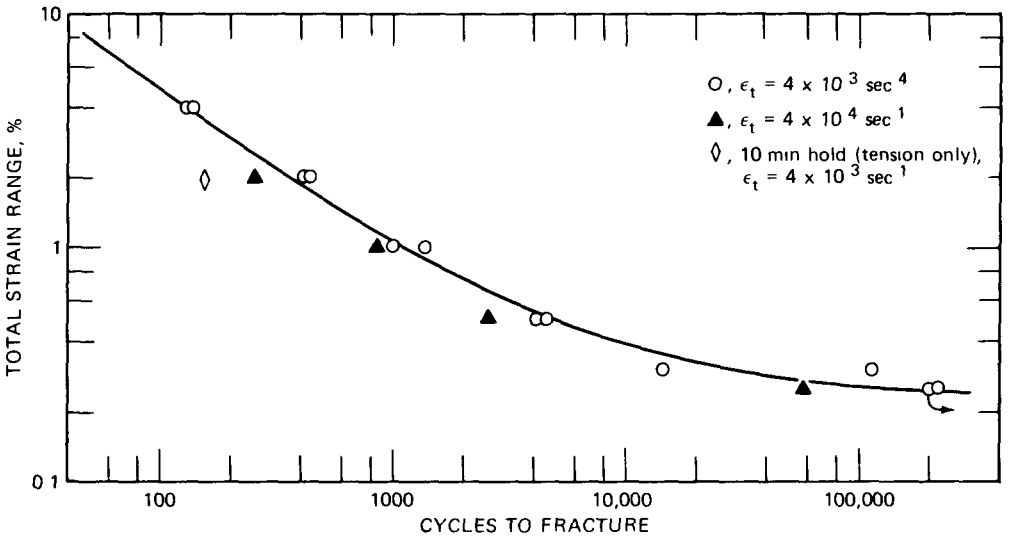

Fig. 3.64 Low-cycle-fatigue data for Incoloy 800, grade 2, solution-annealed bar stock tested in air at 760°C.

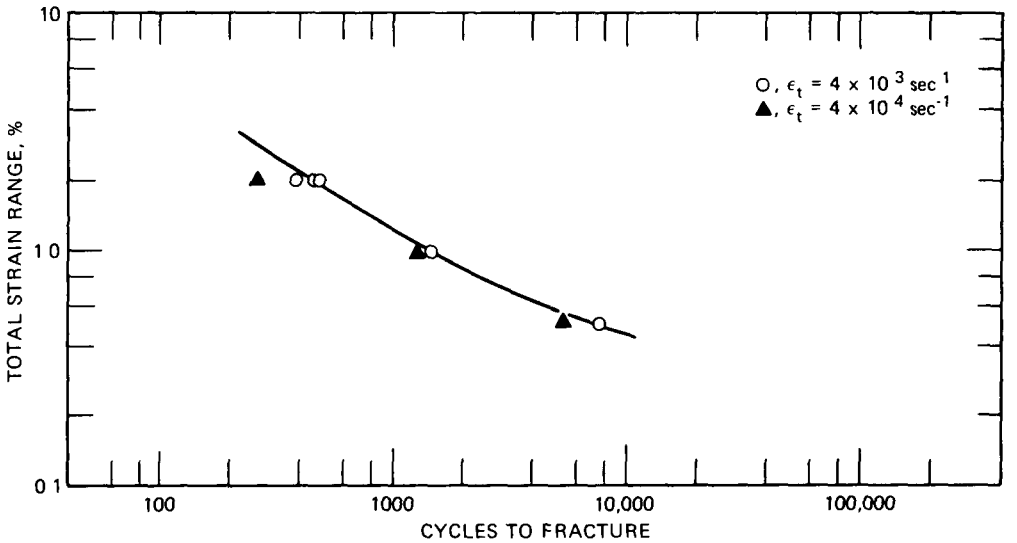

Fig. 3.65 Low-cycle-fatigue data for Incoloy 800, grade 2, solution-annealed plate stock tested in air at 649°C.

similarity. Note that the positions of the lines for a given material are affected by strain range. Lower strain-range data are positioned above the data corresponding to the higher strain-range results. For a given holding time, it follows that the $t_f - t_{f0}$ value is greater for the lower strain range. In other words, for a given holding time, the actual increase in the t_f value above the corresponding t_{f0} value is larger at the lower strain range. It is hard to attach much physical meaning to this observation because it seems related to the N_f behavior. At the 0.5% strain range, the value of N_{f0} is much greater (about 14,000 compared to about 550 at the 4×10^{-3} sec^{-1} strain rate) than the N_{f0} value at the 2% strain range. When a 10-min hold period is introduced, the ratio of N_f/N_{f0} is about 0.12 at the 0.5% strain range and about 0.36 at the 2% strain range. This indicates a greater reduction in the cyclic life at the lower strain range, but the higher value of N_f at this lower strain range leads to a higher value for the time to fracture.

The interesting comparison of hold-time data in Fig. 3.73 reveals the effect of the hold-period length on the cyclic fatigue life. Of special importance in this semi-logarithmic graph is the very rapid decrease in N_f in the region of short hold periods and the gradual approach to what appears to be an asymptotic value of N_f. This behavior pattern is very important because it identifies a saturation effect for hold times and suggests that durations beyond a certain value do little to further decrease N_f. Data from the two sources shown in Fig. 3.73 confirm the same

trend; hence there is ample justification for accepting this behavior pattern as an important material characteristic. Some reservation should be mentioned, however, since the data required to confirm this behavior pattern at other strain ranges and temperatures have not been made available as yet.

With the previously reported low-cycle-fatigue data for AISI 304 stainless steel, the cyclic fatigue life was found[2,3] to vary with temperature in the manner shown in Fig. 3.74. For a given strain range (the data used correspond to a strain rate of 4×10^{-3} sec^{-1}; data for other strain rates are limited but would be expected to exhibit a similar behavior pattern), the graph of log N_f vs. temperature is linear over a fairly wide temperature range. This is a useful relation insofar as interpolation for intermediate temperature behavior is concerned. Extrapolation into the

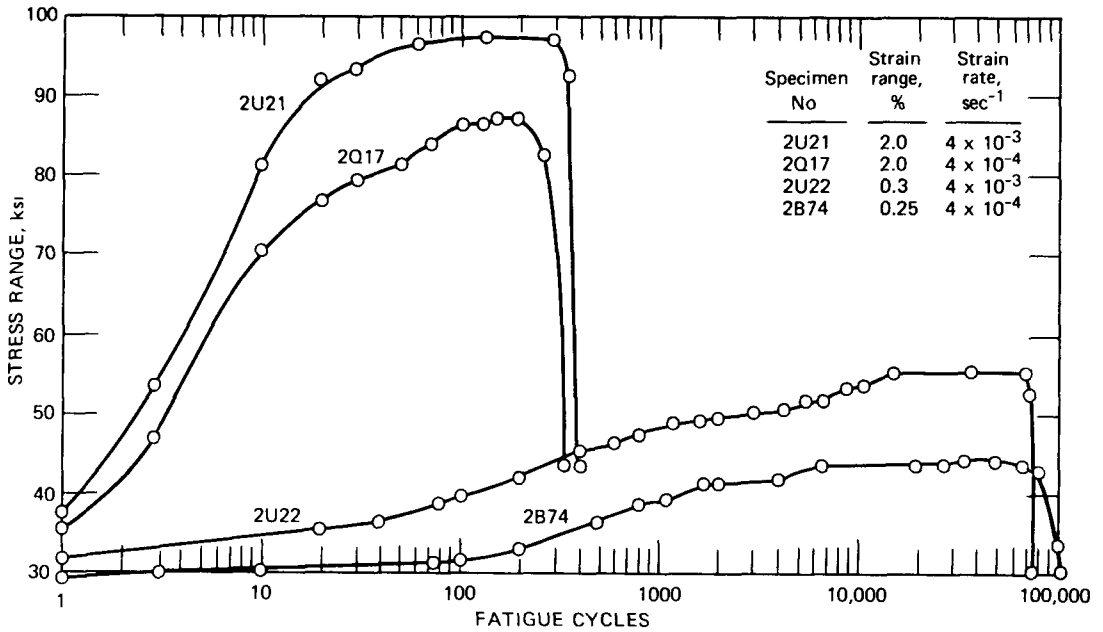

Fig. 3.66 Typical stress range vs. number of cycles for Incoloy 800, grade 2, solution-annealed bar stock tested in air at 704°C.

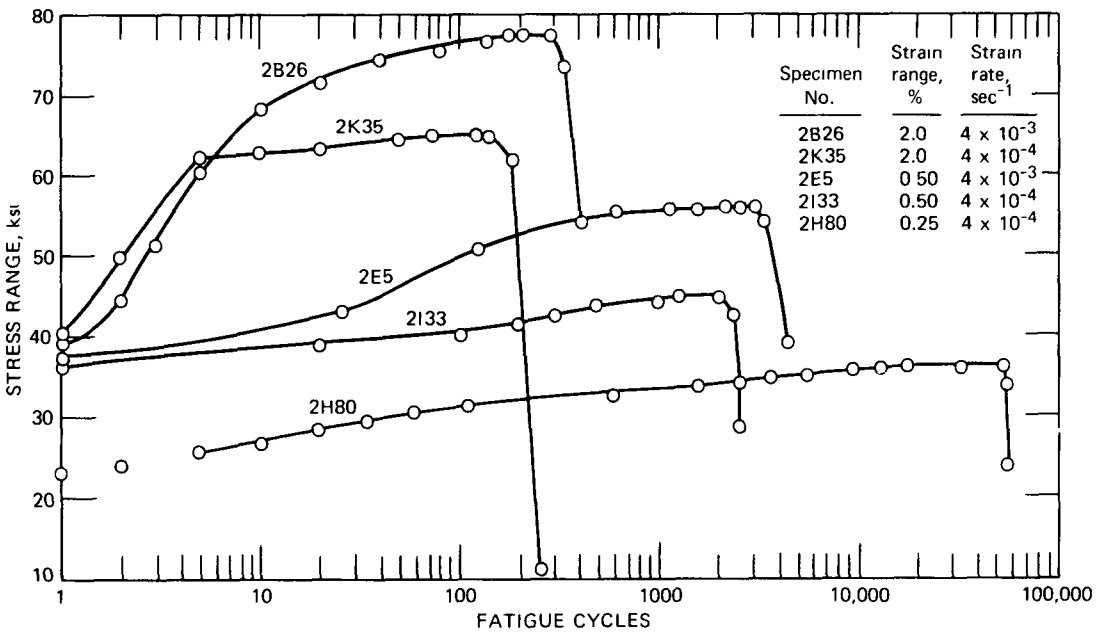

Fig. 3.67 Typical stress range vs. number of cycles for Incoloy 800, grade 2, solution-annealed bar stock tested in air at 760°C.

lower temperature regime is not recommended, because in this range the fatigue life becomes relatively, and in certain cases completely, independent of temperature. Just how much extrapolation into the higher temperature regime is permissible remains to be determined.

hold-period lengths of 1.0 and 10 min, another linearity is suggested. For the same strain range, the line describing hold-time data has a slope that is definitely steeper than that describing the no-hold-time data. Although the data available are too limited to completely confirm the linear

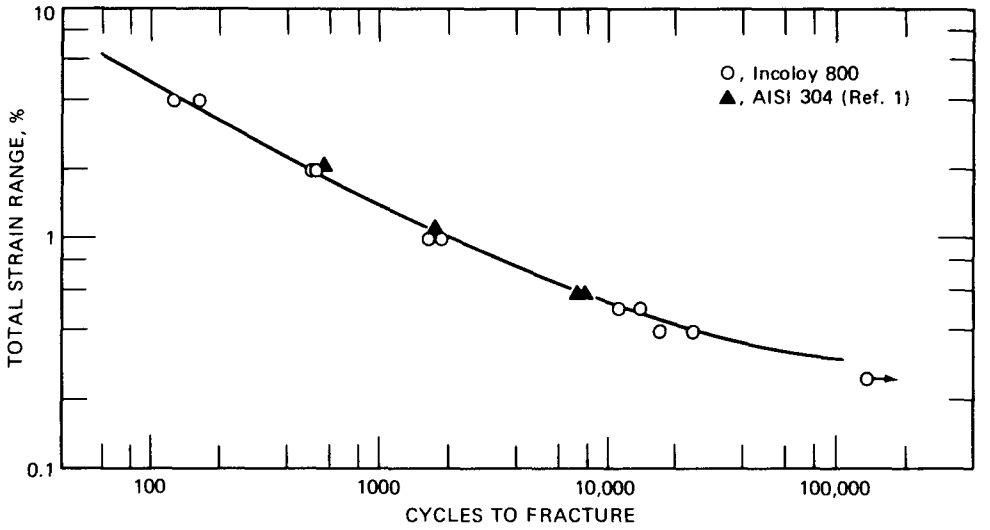

Fig. 3.68 Comparison of experimental low-cycle-fatigue results for Incoloy 800, grade 2, bar stock, and AISI 304 stainless steel tested in air at 649°C and a strain rate of 4×10^{-3} sec^{-1}.

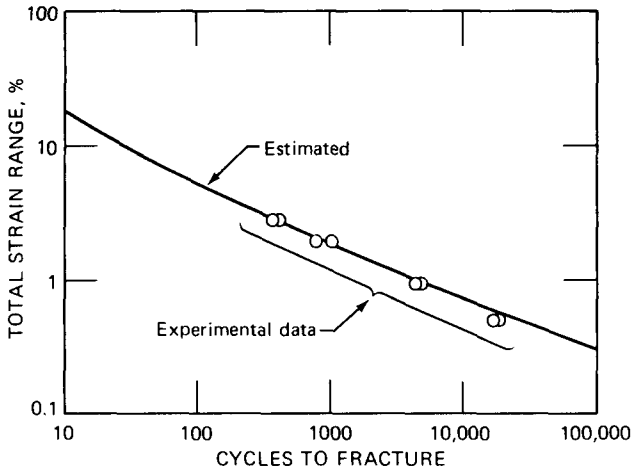

Fig. 3.69 Experimental low-cycle-fatigue data for Incoloy 800, grade 2, solution-annealed bar stock tested in air at 538°C and a strain rate of 4×10^{-3} sec^{-1} compared to estimated data obtained using the method of characteristic slopes (Ref. 3).

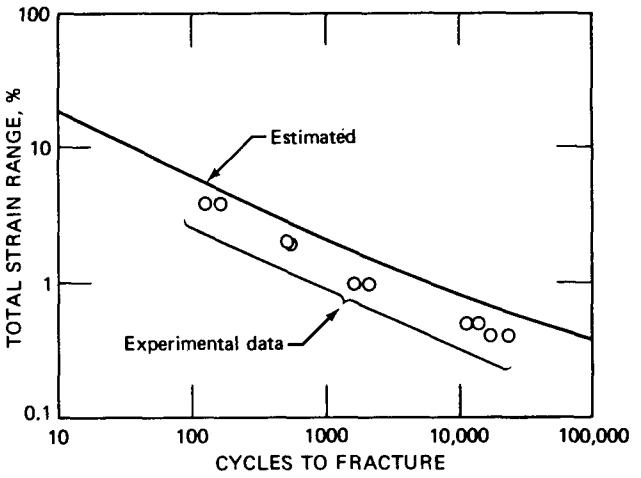

Fig. 3.70 Experimental low-cycle-fatigue data for Incoloy 800, grade 2, solution-annealed bar stock tested in air at 649°C and a strain rate of 4×10^{-3} sec^{-1} compared to estimated data obtained using the method of characteristic slopes (Ref. 3).

In Fig. 3.74 the lines corresponding to strain ranges of 4.0, 2.0, and 1.0% are essentially parallel. However, at a strain range of 0.5% the data define a line having a much different slope. It is expected that lines defining behavior at strain ranges below 0.5% will be even steeper.

Another interesting observation from Fig. 3.74 relates to the effect of temperature on hold-time behavior. For

behavior pattern for the hold-time results, it is felt that subsequent testing will substantiate this trend. In any case the trend in Fig. 3.74 is worthy of further study. Such a study could lead to an identification of the temperature below which hold periods would not affect the fatigue life.

The fatigue data for Incoloy 800 are found to be extremely consistent with the temperature correlation for

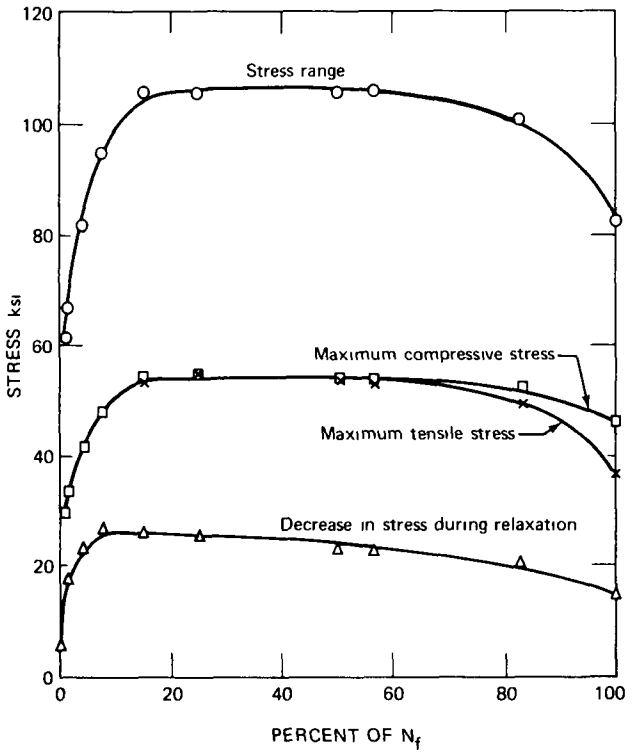

Fig. 3.71 Various stress components plotted as functions of the number of fatigue cycles for Incoloy 800, grade 2, solution-annealed bar stock tested in air at 649°C, a strain range of 1.98%, a ramp strain rate of 4×10^{-3} sec^{-1}, with a 60-min hold period in tension only. ($N_f = 134$.)

304 stainless steel presented in Fig 3.74. This consistency is shown in Fig 3.75 where the linearity in Fig 3 74 for strain ranges of 0 5 and 2.0% is reproduced to provide a comparison with the Incoloy 800 data This is an interesting correlation and defines a fatigue resistance for Incoloy 800 which is just slightly lower than that for 304 stainless steel

REFERENCES

1 J T Berling and T Slot, Effect of Temperature and Strain Rate on Low-Cycle Fatigue Resistance of AISI 304, 316, and 348 Stainless Steels, in *Fatigue at High Temperature*, pp 3 30, American Society for Testing and Materials, Special Technical Publication No 459, 1969, also, USAEC Report GEMP-642, General Electric Company, 1968

2 J B Conway, J T Berling, and R H Stentz, Correlating the Effects of Hold Time and Strain Rate on Low-Cycle Fatigue Behavior, in *Proceedings of the International Conference on Thermal Stresses and Thermal Fatigue*, held in Berkeley, England, 1969, D J Littler (Ed), Butterworth & Co (Publishers) Ltd , London, 1971.

3 J B Conway, J T Berling, and R H Stentz, New Correlations Involving the Low-Cycle Fatigue and Short Term Tensile Behavior of Irradiated and Unirradiated 304 and 316 Stainless Steel, *Nucl. Appl. Technol.*, 9 31 (1970)

4 J T Berling and J B Conway, Effect of Hold Time on the Low-Cycle Fatigue Resistance of 304 Stainless Steel at 1200°F, in *First International Conference on Pressure Vessel Technology*, held at Delft, Holland, 1969, Part 2, *Materials and Fabrication*, p 1233, American Society of Mechanical Engineers, New York

5 J B Conway and J T Berling, A New Correlation of Low Cycle Fatigue Data Involving Hold Periods, *Met Trans.*, 1(1) 324 (1970)

6 S S Manson, *Thermal Stress and Low Cycle Fatigue*, McGraw Hill Book Company, Inc , New York, 1966

7 S S Manson, Fatigue A Complex Subject—Some Simple Approximations, *Exp Mech.*, 5 193 (July 1965)

8 S S Manson and G Halford, A Method of Estimating High Temperature Low Cycle Fatigue Behavior of Materials, in *Proceedings of the International Conference on Thermal and High Strain Fatigue*, held in London, June 6–7, 1967, Monograph and Report Series No 32, The Metals and Metallurgy Trust, London, 1967

9 G R Halford and S S Manson, Application of a Method of Estimating High Temperature Low Cycle Fatigue Behavior of Materials, *ASM (Amer. Soc Metals), Trans. Quart.*, 61 94 (March 1968)

10 L F Coffin, Jr , Cyclic Strain and Fatigue Study of a 0 1% C, 2% Mo Steel, *Trans. Met Soc. AIME*, 230(7) 1690 1699 (1964)

11 W F Simmons and H C Cross, *Report on the Elevated Temperature Properties of Stainless Steels*, American Society for Testing and Materials, Special Technical Publication No 124, 1952

12 R A T Dawson, W J Elder, G J Hill, and A T Price, High Strain Fatigue of Austenitic Steels, in *Proceedings of the International Conference on Thermal and High Strain Fatigue*, held in London, June 6–7, 1967, Monograph and Report Series No 32, The Metals and Metallurgy Trust, London, 1967

13 C D Walker, Strain-Fatigue Properties of Some Steels at 950°F (510°C) with a Hold in the Tension Part of the Cycle, in *Joint Conference on Creep*, Session 3, Paper 24, p 49, The Institution of Mechanical Engineers, London, 1963

14 A Coles, G J Hill, R A T Dawson, and S J Watson, The High Strain Fatigue Properties of Low-Alloy Creep Resisting Steels, in *Proceedings of the International Conference on Thermal and High Strain Fatigue*, held in London, June 6–7, 1967, Monograph and Report Series No 32, The Metals and Metallurgy Trust, London, 1967

15 A Coles and D Skinner, Assessment of Thermal Fatigue Resistance of High Temperature Alloys, *J Roy Aeronaut. Soc.*, 69 53 (1965)

16 J F Eckel, The Influence of Frequency on the Repeated Bending Life of Acid Lead, *Amer. Soc. Test. Mater , Proc.*, 51 745 (1951)

17 L E Raraty and R W Suhr, Correlation of the Fatigue Properties of Magnox AL80 in Terms of the Plastic Strain Range, *J. Inst. Metals*, 94(8) 292-300 (1966)

18 G P Tilly, Influence of Static and Cyclic Loads on the Deformation Behavior of an Alloy Steel at 600°C, in *Proceedings of the International Conference on Thermal and High Strain Fatigue*, held in London, June 6–7, 1967, Monograph and Report Series No 32, The Metals and Metallurgy Trust, London, 1967

19 G R Gohn and W C Ellis, The Fatigue Test as Applied to Lead Cable Sheath, *Amer. Soc. Test. Mater., Proc.*, 51. 721 744 (1951)

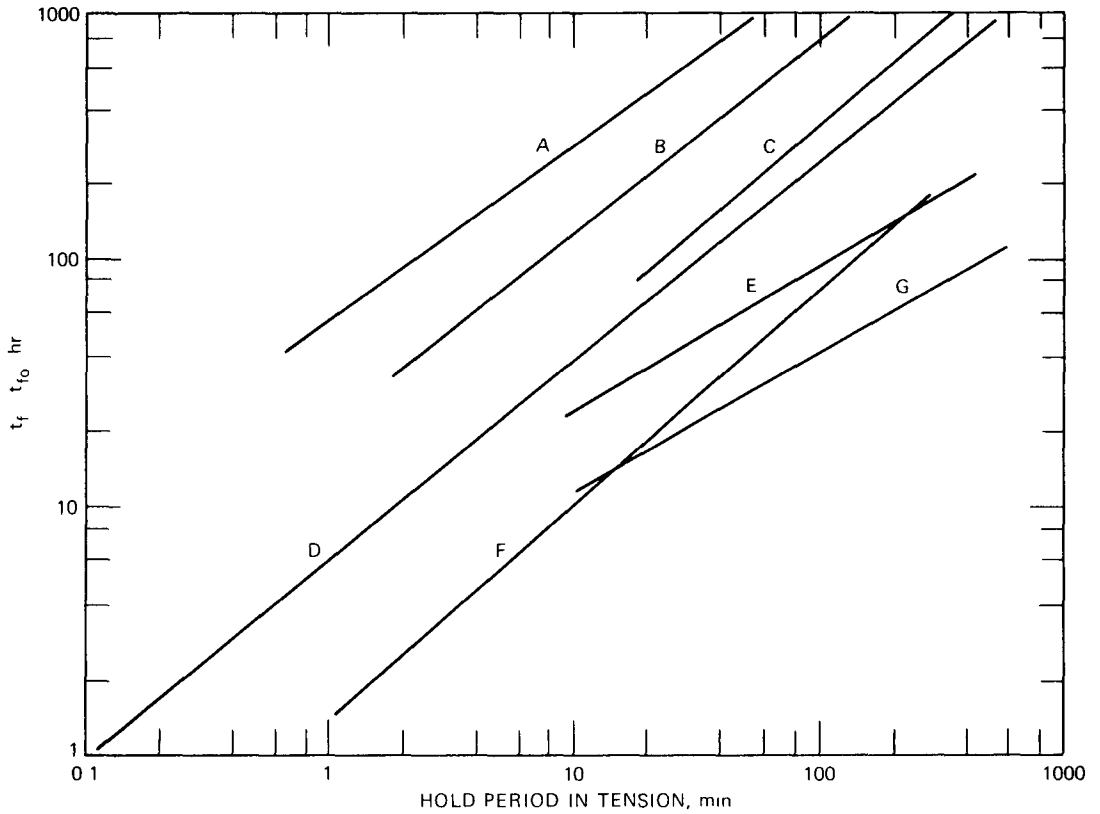

	Material	Temp., °C	t_{f_0}, hr	$\dot{\epsilon}_t$, sec^{-1}	f, cycles/min	$\Delta\epsilon_t$, %	Ref.
A	304 S.S.	650	10	4×10^{-3}		0.5	GE–NSP
B	Cr–Mo–V steel	565	2		10	1	14, 15
C	2¼%Cr–1%Mo steel	600	6.67		1	2	22
D	304 S.S.	650	1.6	4×10^{-3}		2	GE–NSP
E	316 S.S. (A7)	600	2		2	3	12
F	1% Mo steel	510	0.8		~3	2	13
G	316 S.S. (A8)	600	2		2	3	12

Fig. 3.72 Comparison graph of $t_f - t_{f_0}$ data obtained in tension-hold-only low-cycle fatigue tests.

20 J B Conway, Short-Term Tensile and Low-Cycle Fatigue Studies of Incoloy 800, USAEC Report GEMP-732, General Electric Company, 1969

21 R W. Swindeman, Fatigue of Austenitic Stainless Steels in the Low and Intermediate Cycle Range, USAEC Report ORNL TM-1363, Oak Ridge National Laboratory, 1966

22. H G Edmunds and D J White, Observations of the Effect of Creep Relaxation on High-Strain Fatigue, *J. Mech. Eng. Sci.*, 8(3) 310 (1966)

23 J B Conway, J T Berling, and R H Stentz, A Temperature Correlation of the Low-Cycle Fatigue Data for 304 Stainless Steel, *Met. Trans.*, 2(11) 3247 (1971)

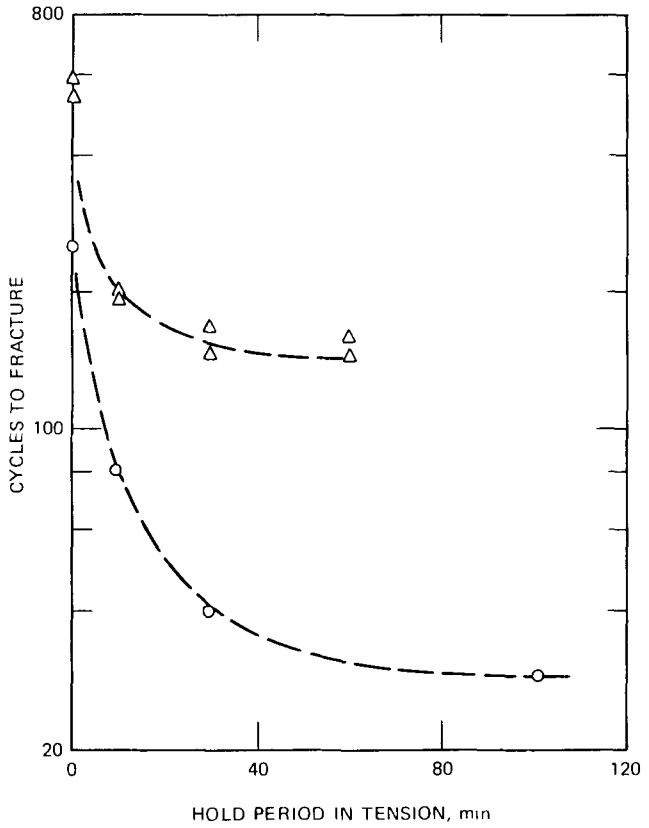

Fig. 3.73 Cycles to fracture vs. hold period in tension for AISI 304 and 316 stainless steels. Δ, AISI 304 stainless steel tested at 650°C with a strain rate of 4×10^{-3} sec^{-1} and a strain range of 2% (from Table 3.8). ○, AISI 316 stainless steel tested at 600°C with a strain rate of 2×10^{-3} sec^{-1} and a strain range of 3% (from Ref. 12).

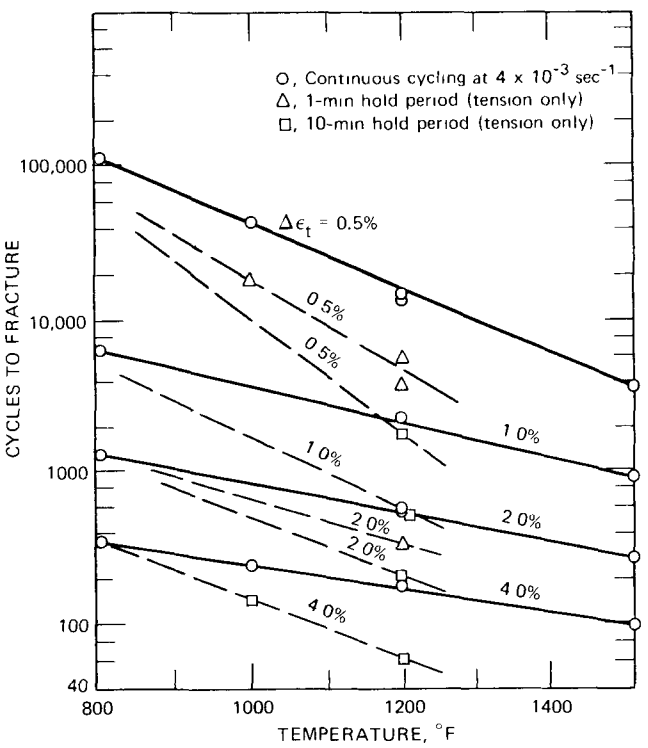

Fig. 3.74 A temperature correlation of the low-cycle-fatigue data for AISI 304 stainless steel.

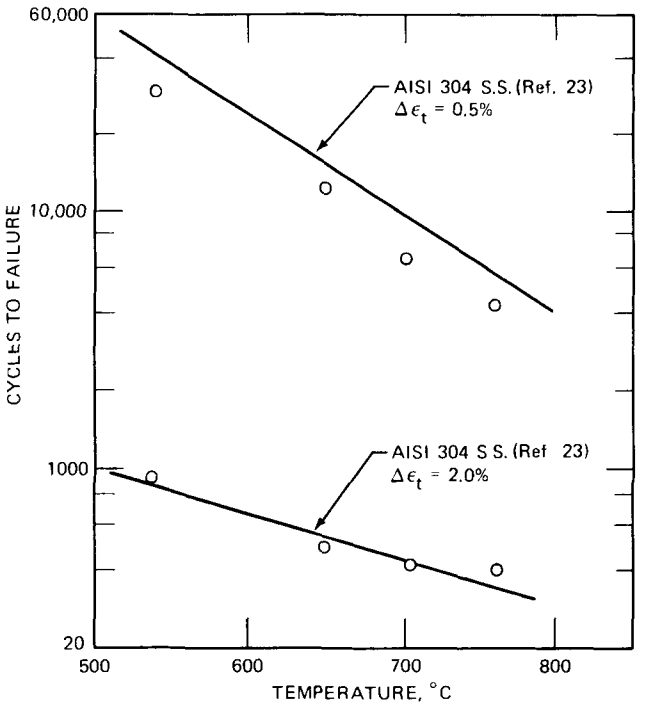

Fig. 3.75 Temperature correlation of low-cycle-fatigue data for AISI 304 stainless steel and Incoloy 800. ○, data points for Incoloy 800.

Chapter 4

ESTIMATING LOW-CYCLE-FATIGUE DATA

Many investigators have identified an interesting association between short-term tensile and low-cycle-fatigue behavior. This association, of course, is important since it suggests the possibility of using short-term tensile results to obtain reliable estimates of low-cycle-fatigue characteristics. This chapter gives a fairly detailed review of the available estimating procedures. These procedures are important in low-cycle-fatigue evaluations since experience has shown that estimates obtained from these expressions can also serve as experimental-program guides.

COFFIN–MANSON EQUATIONS

A simple mathematical formulation having a direct relation to short-term tensile behavior was reported by Coffin[1] in the form:

$$\Delta\epsilon_p = \frac{C}{2} N_f^{-1/2} \tag{4.1}$$

where $\Delta\epsilon_p$ is the plastic strain range, N_f is the number of cycles to failure, and C is a constant that is related to some characteristic of the material. Coffin reasoned that, in a short-term tensile test, the value of N_f could be considered as equal to $1/4$, in which case the value of C is interpreted as the tensile ductility (ϵ_f) measured in such a test. Therefore, if the Coffin equation is assumed to be applicable to a given material, it is a simple matter to predict the low-cycle-fatigue behavior. Once the tensile ductility is known, this point is located at $N_f = 1/4$ on a log–log plot of $\Delta\epsilon_p$ vs. N_f, and a line is drawn through this point with a slope of $-1/2$ to yield a prediction for the fatigue life. Although this equation is quite useful, it is not generally applicable because experiment has shown that the value of $-1/2$ does not reflect the relation between $\Delta\epsilon_p$ and N_f for all materials or even for a given material over all temperature ranges.

An equation similar to the Coffin equation was proposed almost simultaneously by Manson.[2] This expression had the form:

$$\Delta\epsilon_p = AN_f^{-m} \tag{4.2}$$

The value of m was originally reported to be $1/3$, but this was changed in later studies to a much greater value; in fact, the value of m was not considered to be a constant, but rather a function of both the material itself and the test conditions. In later developments (see Four-Point Method below), specific values could, in general, be assigned to A and m to yield fairly representative predictions for the $\Delta\epsilon_p$ vs. N_f behavior.

LANGER EQUATION

Equations 4.1 and 4.2 are limited to plastic-strain-range considerations and offer no information on either the elastic strain range ($\Delta\epsilon_e$) or the total strain range ($\Delta\epsilon_t$). Since the Coffin and Manson equations were first formulated, many studies have suggested approaches by which an elastic-strain-range component can be added to the plastic strain range in order to calculate the total strain range. Two such studies are those of Tavernelli and Coffin[3] and Langer,[4] where the elastic strain range was equated to twice the endurance limit (S_e) divided by the modulus of elasticity (E). This led to

$$\Delta\epsilon_t = \Delta\epsilon_p + \frac{2S_e}{E} \tag{4.3}$$

Substituting Eq. 4.1 yields

$$\Delta\epsilon_t = \frac{C}{2} N_f^{-1/2} + \frac{2S_e}{E} \tag{4.4}$$

Originally, some thought was given to using the yield strength in place of S_e, but this resulted in an overprediction of the fatigue life.

If $\Delta\epsilon_t$ is converted to a stress amplitude (σ_a) following the procedure used in an elastic analysis, then

$$\sigma_a = \frac{CE}{4} N_f^{-1/2} + S_e \tag{4.5}$$

Although this relation has the interesting characteristic that σ_a is equal to S_e as the N_f value becomes very large, it has

other limiting features that restrict its range of usefulness. Tavernelli and Coffin used data for 12 materials (including aluminum, copper, and AISI 347 stainless steel) to show what was termed fairly good agreement, but this comparison has not been completely accepted.

FOUR-POINT METHOD

Manson[5] performed a particularly extensive evaluation of the Tavernelli and Coffin study and found the following deficiencies in Eq 4.4 (1) the elastic strain range varies with N_f and is not constant, as indicated by the S_e term, (2) the exponent on N_f is not equal to -0.5 but varies slightly from this value, depending on the material and the test temperature, and (3) the value of the plastic strain range at $N_f = \frac{1}{4}$ is not equal to the value of C as given in Eq. 4.1. On the basis of these noted defects, Manson suggested a more general form for the total-strain-range equation A detailed study of various materials indicated that an effective expression might be

$$\Delta\epsilon_t = \Delta\epsilon_p + \Delta\epsilon_e \tag{4.6}$$

or

$$\Delta\epsilon_t = MN_f^Z + \frac{G}{E}N_f^\gamma \tag{4.7}$$

where M, Z, G, and γ are material constants that can be identified in fatigue tests. In the limit, only two fatigue tests would be needed since each test establishes a point on both the elastic- and plastic-strain-range lines (on logarithmic coordinates), and these two points can be used to define these lines. Slope and intercept calculations then lead to the desired material constants.

Manson noted that it might be possible to obtain these material constants through the use of the more readily available tensile properties. An extensive study of these relations led to the general observations given below.

For the definition of the elastic-strain-range line on logarithmic coordinates

1. Position a point at $N_f = 0.25$ cycle and an elastic strain range of $2.5\sigma_f/E$, where σ_f is the fracture stress in a tensile test (load at fracture divided by the area as measured after fracture).

2. Position a second point at $N_f = 10^5$ cycles and at an elastic strain range of $0.9\sigma_u/E$, where σ_u is the conventional ultimate tensile strength

For the definition of the plastic-strain-range line on logarithmic coordinates

1. Position a point at $N_f = 10$ cycles, where the plastic strain range is $0.25D^{3/4}$ and D is the conventional logarithmic ductility.

2 Position a second point at $N_f = 10^4$ cycles, where the plastic strain range is given by

$$(\Delta\epsilon_p)_{10^4} = 0.0069 - 0.525(\Delta\epsilon_e)_{10^4}$$

where $(\Delta\epsilon_e)_{10^4}$ is determined from the elastic-strain-range line at $N_f = 10^4$ cycles. This relation follows from the fact that, in general, all materials exhibit a cyclic-fatigue life of 10^4 cycles at a total strain range of 1.0%.

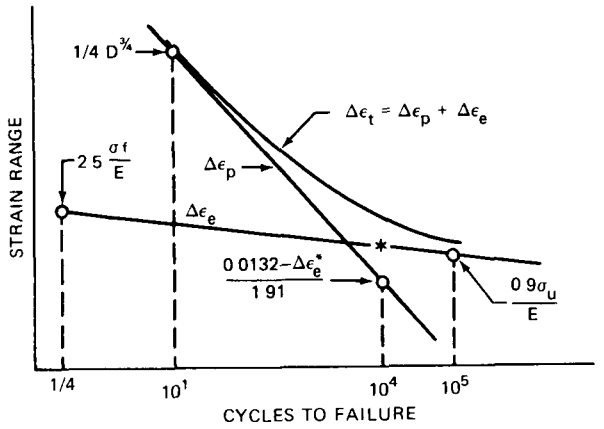

Fig 4.1 Graphical representation of elastic- and plastic-strain-range lines positioned by the four-point method.[6] ($\Delta\epsilon_e^*$ is read from the elastic-strain range line at $N_f = 10^4$).

Figure 4.1 shows[5,6] the positioning and summation of the elastic- and plastic-strain-range lines ($\Delta\epsilon_e$ and $\Delta\epsilon_p$) to yield the curve describing the fatigue behavior in terms of total strain range.

Assigning numerical values to the constants in Eq. 4.7, Manson reported

$$G = \frac{9}{4}\sigma_u\left(\frac{\sigma_f}{\sigma_u}\right)^{0.9}$$

$$\gamma = -0.083 - 0.166\log\frac{\sigma_f}{\sigma_u}$$

$$M = 0.827D\left[1 - 82\frac{\sigma_u}{E}\left(\frac{\sigma_f}{\sigma_u}\right)^{0.179}\right]^{1/3}$$

$$Z = -0.52 - \frac{1}{4}\log D + \frac{1}{3}\left[1 - 82\frac{\sigma_u}{E}\left(\frac{\sigma_f}{\sigma_u}\right)^{0.179}\right] \tag{4.8}$$

These constants give mathematical form to the calculation of cyclic-fatigue life for various total strain ranges by using short-term tensile properties. Manson noted that the Z term contains the value of -0.52, which corresponds to the value of $-\frac{1}{2}$ in Eq 4.1 but which is modified by correction terms involving ductility, fracture stress, and ultimate tensile strength.

The effectiveness of this relation was studied, and the results were compared to those obtained using Eq. 4.4. One such study is presented in Fig. 4.2 to indicate that the elastic- and plastic-strain-range data are in excellent agreement with the concepts of Eq. 4.7. Also, the total-strain-

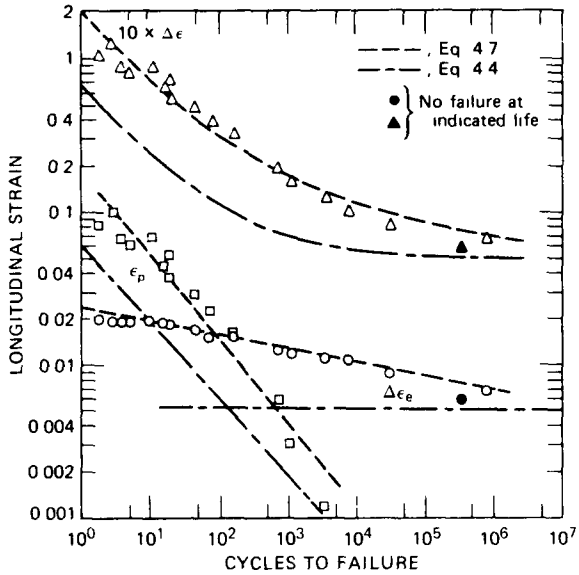

Fig. 4.2 Comparison of the effectiveness of Eqs. 4.4 and 4.7 for predicting the fatigue life of 52100 steel. (From Ref. 5.)

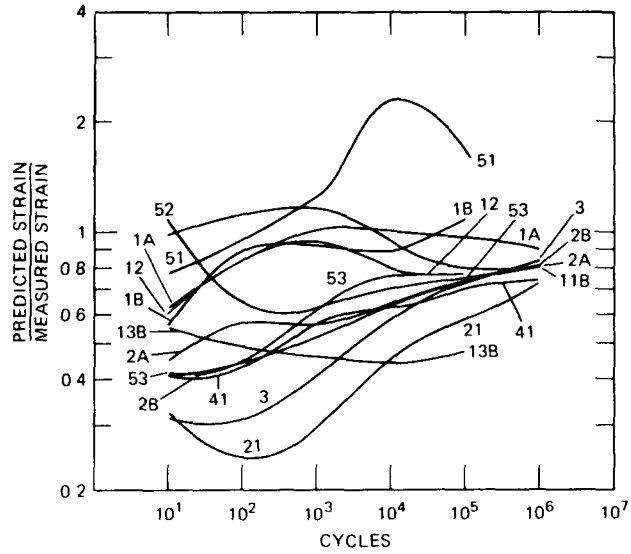

Fig. 4.4 The ratio of predicted total strain to measured total strain based on Eq. 4.4.

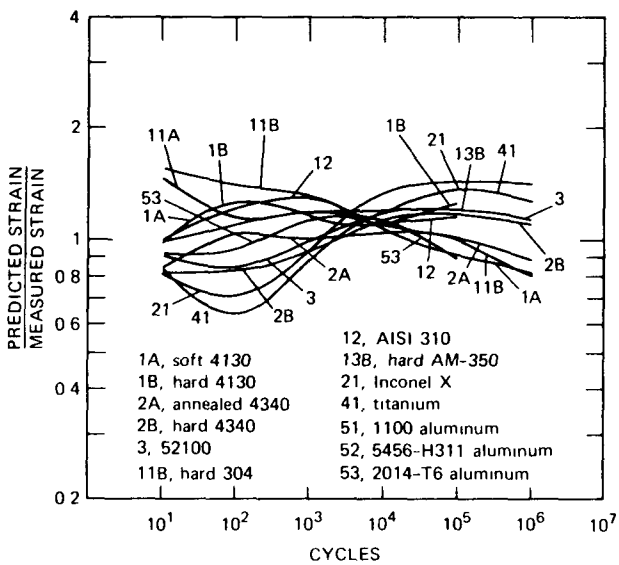

Fig. 4.3 The ratio of predicted total strain to measured strain based on Eq. 4.7.

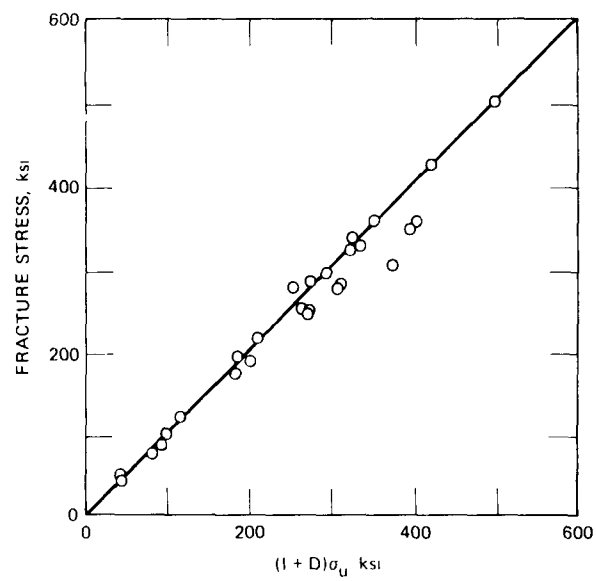

Fig. 4.5 Fracture stress related to tensile ductility.[6]

range prediction is extremely consistent with the experimental results. This comparison was used to conclude that Eq. 4.7 is much more effective than Eq. 4.4. A more comprehensive study of the comparable effectiveness of the two equations is presented in Figs. 4.3 and 4.4. Clearly, better results are obtained through the use of Eq. 4.7.

Manson[6] recognized the fact that the use of Eq. 4.7 required the knowledge of the fracture stress. Since this value is not always readily available in the literature, it can be estimated[7] by means of the approximate relation between fracture stress, ultimate tensile stress, and fracture ductility; thus

$$\sigma_f = \sigma_u(1 + D) \tag{4.9}$$

This relation follows from Fig. 4.5, where each point is fixed by the data for one material. (This calculation and that relating to the four-point method for defining the elastic- and plastic-strain-range lines were based on data for the materials listed in Table 4.1.)

On the basis of the approximate equality in Eq. 4.9, Manson noted that only two tensile properties, σ_u, and the reduction in area (to give D) are needed to position the lines in Fig. 4.1 and thus obtain a prediction of fatigue behavior. Figure 4.6 shows a convenient graphical solution by Manson for locating the four points in Fig. 4.1. For

TABLE 4.1

MATERIALS USED IN LOW-CYCLE-FATIGUE STUDY[6]

4130 soft	Titanium 6Al–4V
4130 hard	Titanium 5Al–2.5Sn
4130 X-hard	Magnesium AZ31B-F
4340 annealed	1100 aluminum
4340 hard	5456-H311 aluminum
304 annealed	2014-T6 aluminum
304 hard	2024-T4 aluminum
52100 hard	7075-T6 aluminum
52100 X-hard	Silver 0.99995 pure
AM-350 annealed	Beryllium
AM-350 hard	Inconel X
310 stainless	A-286 aged
Vascomax 300 CVM	A-286 34% cold reduced and aged
Vascojet MA	D-979
Vascojet 1000	

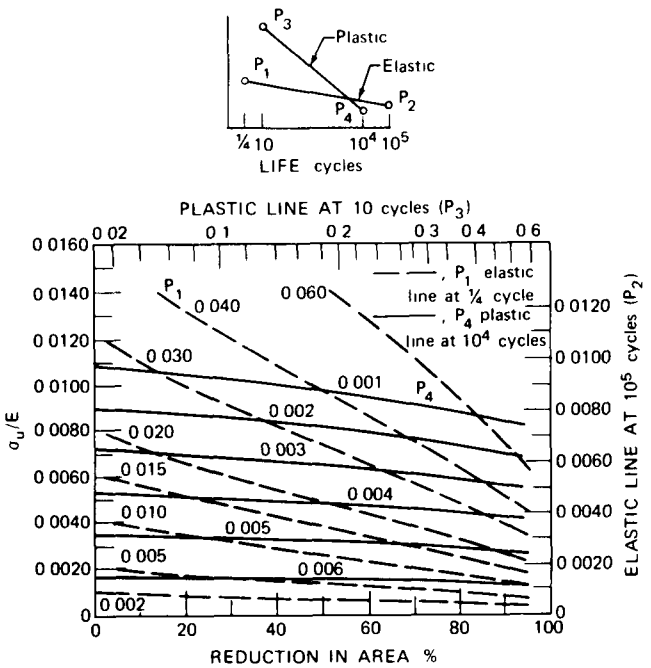

Fig. 4.6 Graphical solution to obtain the four points to position the elastic- and plastic-strain-range lines.[6]

example, if σ_u/E is 0.01 and the reduction in area is 50% (D = 0.694), the value of P_2 from the left-hand scale is 0.009 and that of P_3 from the bottom scale is 0.18. Then locating the point with the coordinates $\sigma_u/E = 0.01$ and reduction in area equal to 50% gives values for P_1 and P_4 of 0.042 and 0.0009, respectively. These points will locate the two strain-range lines, and the total-strain-range curve can then be positioned to relate $\Delta\epsilon_t$ and N_f for the material in question.

METHOD OF UNIVERSAL SLOPES

In another very extensive study of the relation between the elastic and plastic strain ranges and short-term tensile properties, Manson[6] presented the graphs shown in Figs. 4.7 and 4.8. These graphs were used to show that, within reasonable accuracy, the plastic strain range is related to D and N_f through the relation

$$\Delta\epsilon_p = \left(\frac{N_f}{D}\right)^{-0.6} \tag{4.10}$$

and that the elastic strain range was related to the ultimate tensile strength, the modulus of elasticity, and N_f through the relation

$$\Delta\epsilon_e = \frac{3.5\sigma_u}{E} N_f^{-0.12} \tag{4.11}$$

Combining these terms led to

$$\Delta\epsilon_t = \frac{3.5\sigma_u}{E} N_f^{-0.12} + D^{0.6} N_f^{-0.6} \tag{4.12}$$

which has been termed the *Method of Universal Slopes* since the slopes in Figs. 4.7 and 4.8 apply, in general, to all the materials tested.

The lines in Figs. 4.7 and 4.8 identify the existence of two lines paralleling the construction shown in Fig. 4.1. For example, if N_f is set equal to unity in Eqs. 4.10 and 4.11, the $\Delta\epsilon_p$ and $\Delta\epsilon_e$ values will be $D^{0.6}$ and $3.5\sigma_u/E$, respectively. These points can then be located, and elastic- and plastic-strain-range lines can be drawn using slopes of −0.12 and −0.6, respectively. This construction is shown in Fig. 4.9 to reveal how the fatigue curve relating $\Delta\epsilon_t$ and N_f can be positioned from one short-term tensile test that yields values for σ_u, E, and D. A graphical solution to allow the type of construction shown in Fig. 4.9 is presented in Fig. 4.10.

A detailed study of the effectiveness of the Method of Universal Slopes was reported by Manson in analyzing

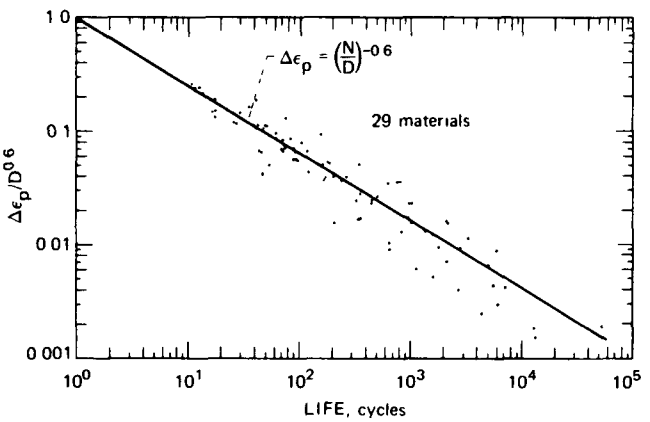

Fig. 4.7 Relation[6] between plastic strain range, tensile ductility, and N_f.

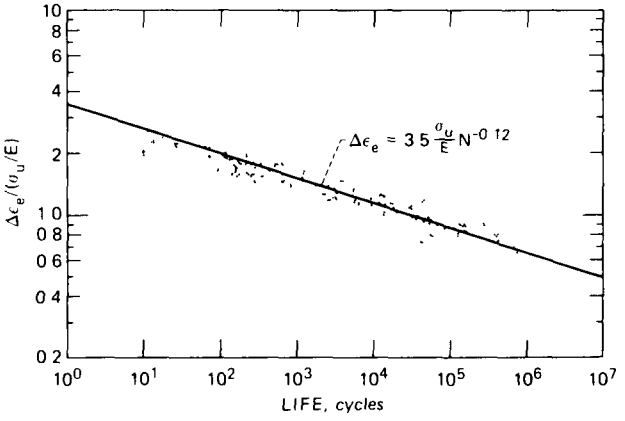

Fig. 4.8 Relation[6] between elastic strain range, ultimate tensile strength, modulus of elasticity, and N_f.

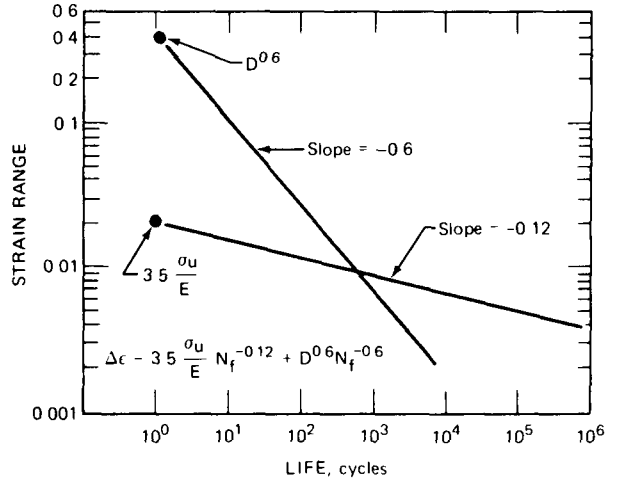

Fig. 4.9 Elastic- and plastic-strain-range lines based on Method of Universal Slopes.[6]

fatigue data for 29 materials. The results of this analysis are given in Figs. 4.11 to 4.13. Except for AM-350 (annealed) and beryllium, the agreement is excellent.

An overall evaluation of the four-point method is shown in Fig. 4.14, where the measured life for each of the test points is plotted against the life predicted from a knowledge of the fracture stress, ultimate tensile strength, and ductility. The relation between the data points and the correlation line is indicated by the table at the lower right in the figure. Thirty-five percent of the data points fall within a factor of 1.5 in life from the predicted value. Almost 90% fall within a life factor of 5. Since some scatter in life is expected in fatigue data, this correlation must be regarded as satisfactory. A few data points, notably those associated with poorly behaved materials like beryllium, are fairly remote from the correlation line, thus resulting in the conclusion indicated by the table that, with an allowable error of a factor of 20 in life, about 97% of the data points will be satisfactory. Similarly, Fig. 4.15 compares the data

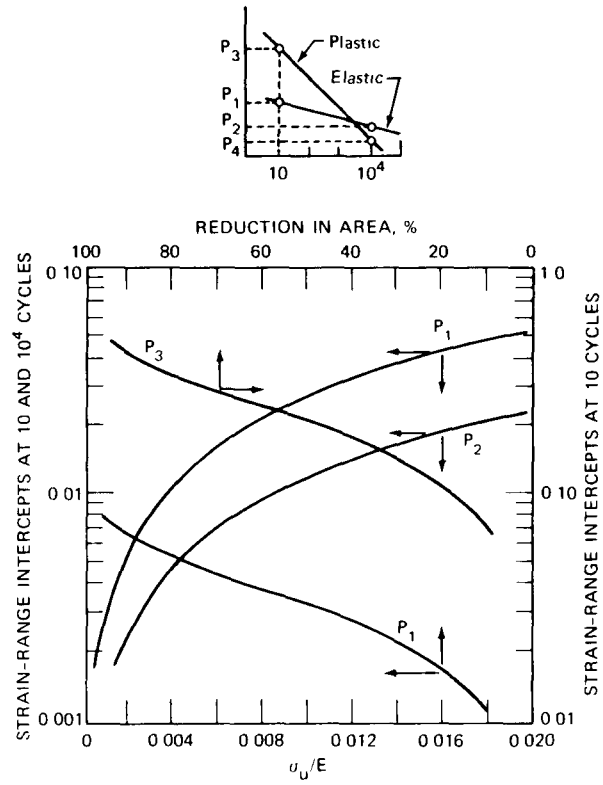

Fig. 4.10 Graphical solution to allow positioning of elastic- and plastic-strain-range lines based on Method of Universal Slopes.[6]

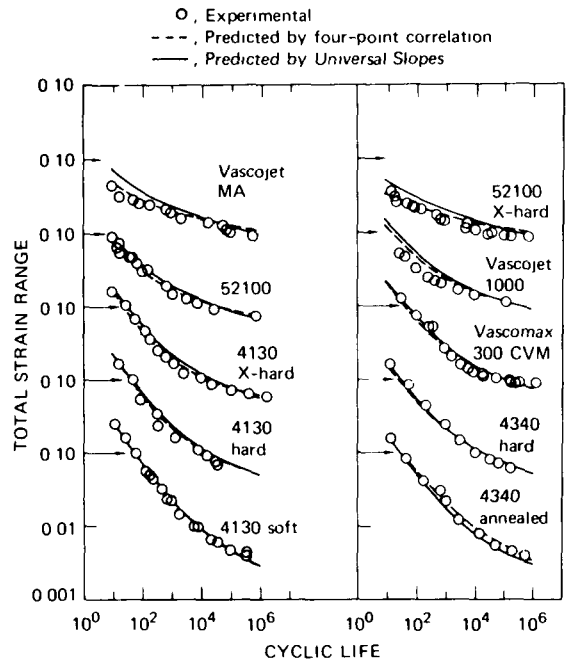

Fig. 4.11 Comparison of experimental and predicted axial-fatigue data for high-strength steels.[6]

on the basis of measured and predicted strain range rather than on the basis of life. The correlation is, as might be expected, considerably better.

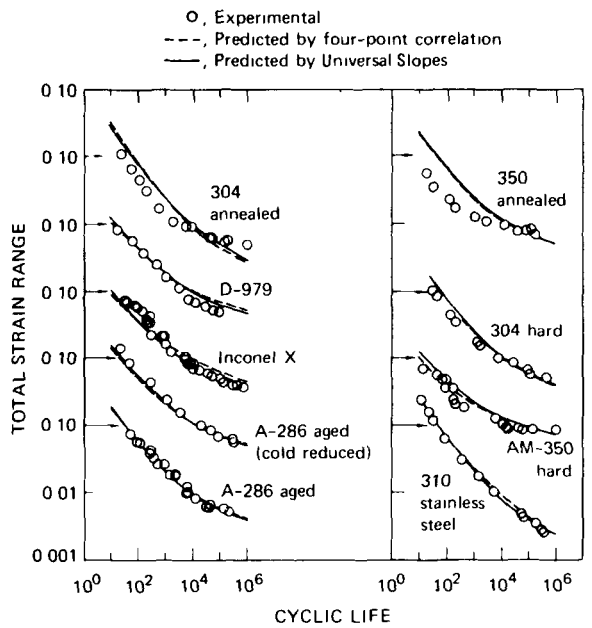

Fig. 4.12 Comparison of experimental and predicted axial-fatigue data for stainless steels and high-temperature alloys.[6]

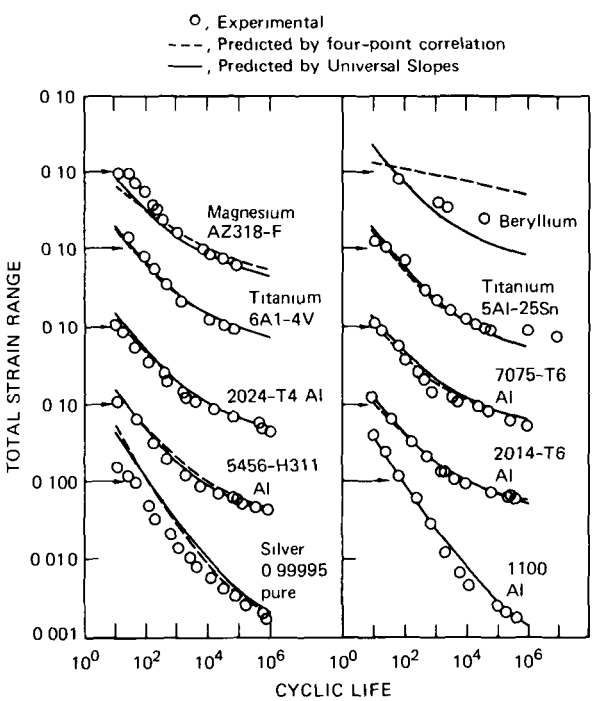

Fig. 4.13 Comparison of experimental and predicted axial-fatigue data for nonferrous metals.[6]

Figure 4.16 shows a corresponding overall comparison on a life basis for the Method of Universal Slopes. Similarly, Fig. 4.17 shows the comparison on the basis of predicted strain for the same 29 materials as obtained by the Method of Universal Slopes. In both cases the agreement with

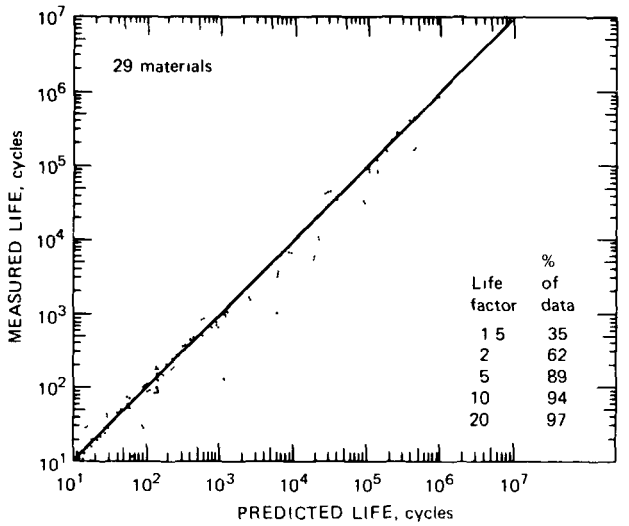

Fig. 4.14 Comparison of measured and predicted fatigue life based on four-point correlation.[6]

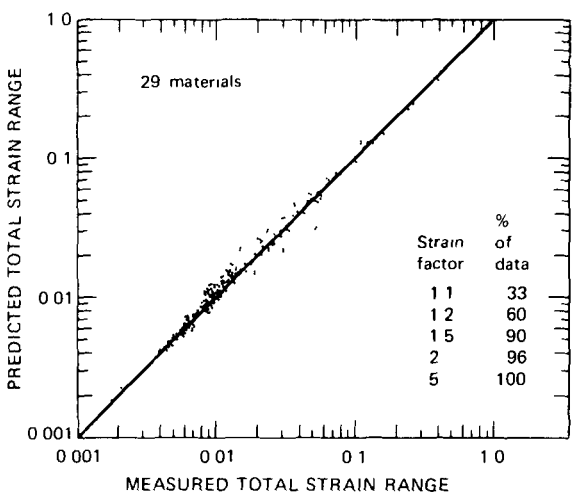

Fig. 4.15 Predicted vs. measured total strain range based on four-point correlation.[6]

experiment is approximately the same as that obtained by the four-point method.

Recently, more attention has been focused on the Method of Universal Slopes, which now is preferable to the four-point correlation procedure and is the most widely used expression for estimating fatigue behavior.

10% RULE

Although the Method of Universal Slopes originated in a study of the low-cycle-fatigue data for 29 materials tested at room temperature, some attention has been given to the use of this concept at elevated temperatures. A logical first approach, of course, was to use[8] tensile properties at the temperature in question, but this approach failed to yield

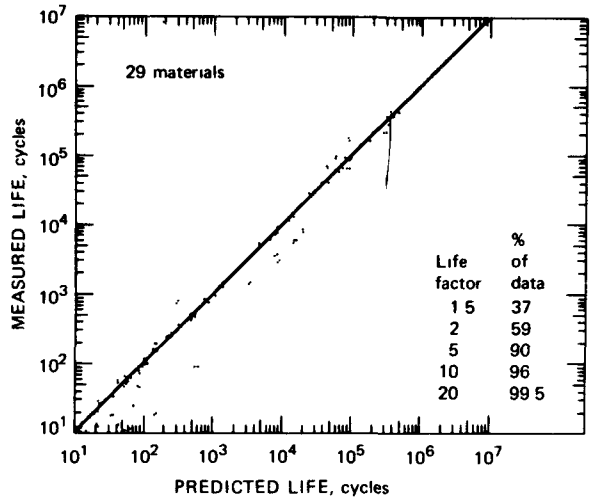

Fig. 4.16 Comparison of measured and predicted fatigue life based on Method of Universal Slopes.[6]

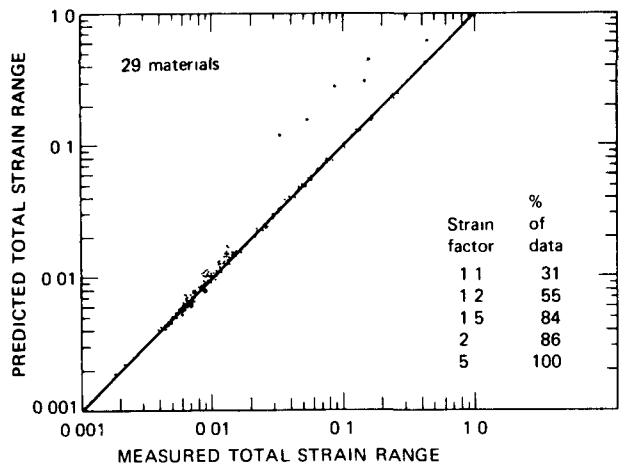

Fig. 4.17 Predicted vs. measured total strain range based on Method of Universal Slopes.[6]

satisfactory results since the predicted fatigue lives were higher than those actually observed. This difference was attributed to a creep effect in the elevated-temperature regime, and thus the number of cycles to failure is less than that resulting from pure fatigue. An initial attempt to modify the Method of Universal Slopes to accommodate this creep effect was described by Manson.[8] The crack-initiation and crack-propagation phases, discussed in Chap. 5 under the heading Double Linear-Damage Rule, were assumed to be affected to various degrees by the elevated-temperature exposure, and selected reduction factors were considered for each phase. Several cases are presented in Fig. 4.18 to show this effect. When the creep effect is assumed to completely eliminate the crack-initiation stage (that is, a crack is formed instantly), the behavior pattern shown by the uppermost curve is observed. The horizontal portion reflects the fact that, for N_f values below 730 cycles, the crack-propagation phase is given by $0.443(\Delta N_f)$ and hence $N_f = (\Delta N_f)$. Otherwise, $(\Delta N_f) = 14N_f^{0.6}$. Other curves with different fractions of the crack-initiation and crack-propagation phases show similar behavior patterns, but none was found to yield generally satisfactory results. It was felt that it would be just as accurate and a lot less complicated to assign a factor of 10% to each phase and let the fatigue life be estimated by taking 10% of that calculated by the Method of Universal Slopes. This approach has been termed the "10% rule."

Using the above concept, Manson[8] made a detailed analysis of lead[14] at room temperature (which is within its creep range because of its low melting point). Manson noted that, since Gohn and Ellis did not publish static tensile properties for the several types of lead studied, it was not possible to make the analytical predictions of hypothetical life according to the Method of Universal Slopes. Fortunately, however, tests were conducted at both the high frequency of 1650 cycles/min and the low frequency of ¼ cycle/min. Since the time available for creep effects is much less at the high frequency of straining than at the low frequency, an alternate approximation can be used. The data for the high-frequency tests (Fig. 4.19) were assumed to represent the results that would have been obtained by computation from the tensile properties, and these data were used to compute lives for the low-frequency tests by several of the rules previously cited. For pure lead, both chemical and antimony grades, reasonable agreement exists between the experimental data at ¼ cycle/min and the predictions of the two rules using the tests at 1650 cycles/min as the basis for the computations. There is a definite trend for the data to indicate a greater percentage of reduction at the higher lives than at the lower lives, implying that the crack-initiation phase is reduced more by intergranular cracking than is the crack-propaga-

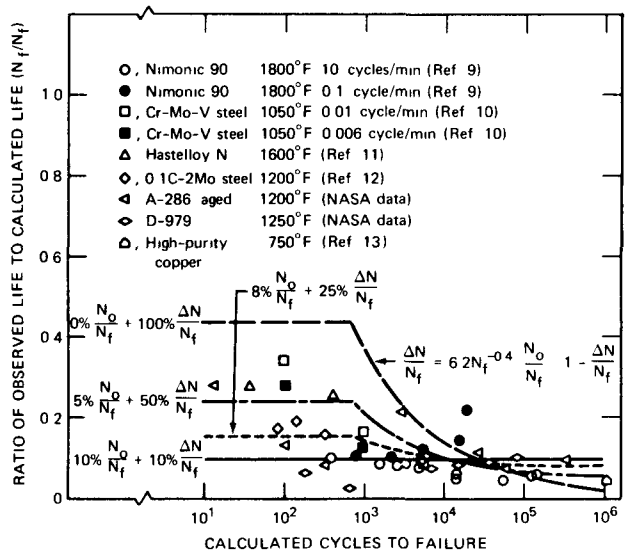

Fig. 4.18 Comparison of observed vs. calculated low-cycle-fatigue life. (From Ref. 8.)

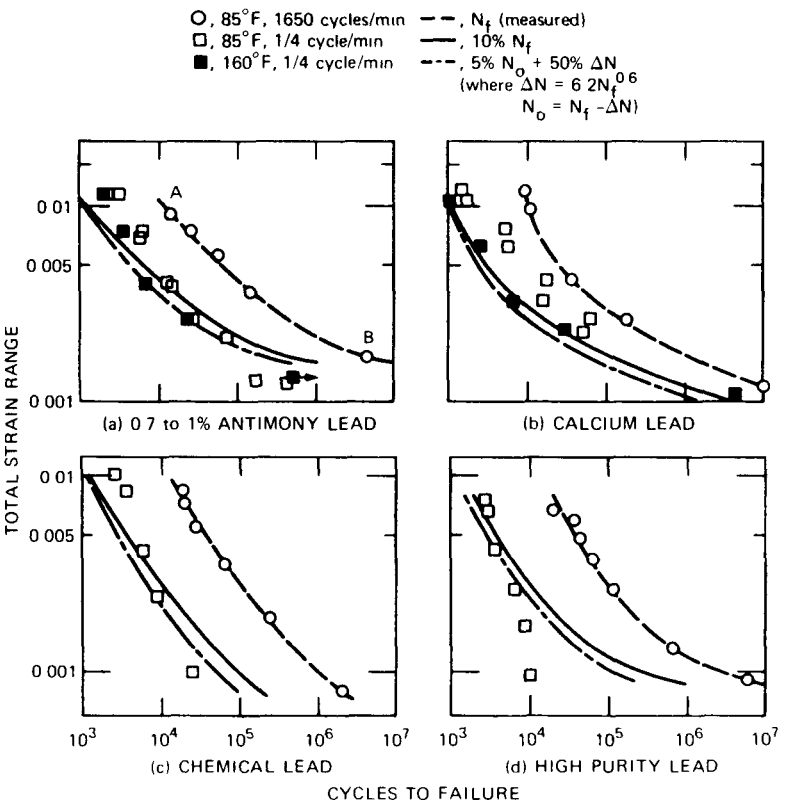

Fig. 4.19 Analysis of low-cycle-fatigue data for lead. O– – –O, high-frequency tests.—, computations based on the 10% rule. – —, computations obtained by the 5–50% rule. (From Ref. 8.)

tion phase. Gohn and Ellis observed that intercrystalline cracking was characteristic of these tests.

Of special interest are the tests on calcium lead. At room temperature, little intercrystalline cracking was observed, and the computations overcorrect to predict considerably lower lives than were actually obtained. When the test temperature was raised to 180°F, however, intercrystalline cracking appeared more notably, and the data are in better agreement with the analytical predictions. Thus the corrections appear to be most important when intercrystalline cracking is present.

In a subsequent study, Manson and Halford[15] described an extension of the 10% rule for use in estimating low-cycle-fatigue behavior at elevated temperatures. As before, the Universal Slopes equation was used with σ_u, E, and D being determined at the temperature in question and at the moderate strain rates normally employed in conventional tensile testing (this was set arbitrarily as within a factor of 10 of that specified by ASTM standards).

Estimates of the fatigue life can be obtained by taking certain percentages (see below) of the N_f values calculated using the Universal Slopes equation. In extreme cases involving low frequencies and high temperatures, failures may be time dependent, and an additional correction is needed. This correction was developed from stress-rupture considerations and gave an adjusted value for the cyclic-fatigue life in the form

$$N_f' = \frac{N_f}{1 + \frac{k}{Af}(N_f)^{(m+0.12)/m}} \tag{4.13}$$

where N_f' = corrected fatigue life
N_f = Universal Slopes fatigue life
k = effective fraction of each cycle for which the material may be considered to be subjected to maximum stress (k was suggested to be 0.3)
f = frequency of stress application
A = coefficient characterizing a time intercept of the creep-rupture curve of the material at test temperature. The curve of stress, σ_r, against rupture time, t_r, is linearized on logarithmic coordinates and is represented by the equation $\sigma_r = 1.75\sigma_u(t_r/A)^m$, so that A is the time intercept at an extrapolated value of $\sigma_r = 1.75\sigma_u$
m = slope of the stress-rupture line (negative slope)

Equation 4.13 is applicable[15] only if $N_f' < 10\%\ N_f$ and if $N_f' < 10^5$ cycles. Figure 4.20 provides a simple criterion for determining whether Eq. 4.13 is necessary. If the point representing the coordinates m and Af that apply to the test conditions of the material lies above the curve and above the lowest coordinates shown, N_f' is computed; if this point falls below the curve, the value of N_f need not be computed.

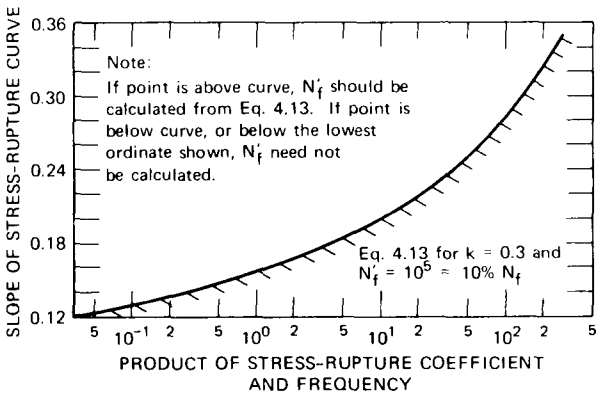

Fig. 4.20 Criterion[15] for determining whether Eq. 4.13 should be used.

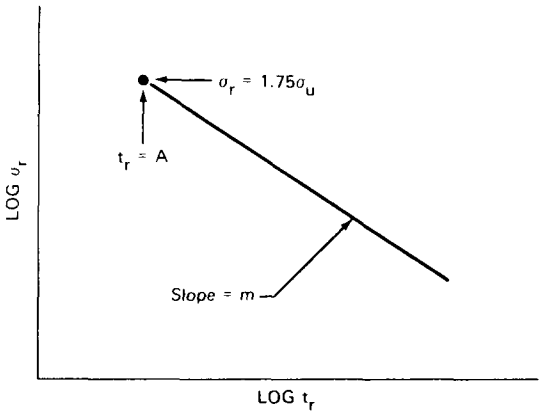

Fig. 4.21 Stress-rupture graph illustrating Eq. 4.14.

Estimates of the low-cycle-fatigue life[15] are made as follows:

1. For the lower-bound life, use either 10% N_f or N_f', whichever is smaller. Although 10% N_f accounts for some creep damage, it is not sufficient to account for those high-temperature and low-frequency cases in which the creep damage is so severe as to reduce the life below 10% N_f.
2. For the average life, use twice the lower-bound life.
3. For the upper-bound life, use 10 times the lower-bound life.

In Eq. 4.13, assume that N_f' represents the actual number of cycles to failure; then the time to fracture is given by N_f'/f. Then assume that the effective time within which the maximum stress in the cycle is applied is given by $t' = kN_f'/f$ (from experience, a representative value of k is given by 0.3). Thus the creep-rupture damage associated with a given exposure can be calculated by the ratio of the effective time at maximum stress to the creep-rupture time at this stress. In the calculations, the creep-rupture time is interpreted as that associated with a steadily applied stress (σ_r) equal to the fatigue stress amplitude (σ_a). The creep-rupture relation is written in the form

$$\sigma_r = 1.75\sigma_u(t_r/A)^m \tag{4.14}$$

to define a straight line on logarithmic coordinates having a slope of m and a time intercept equal to A, when $\sigma_r = 1.75\sigma_u$ (Fig. 4.21). Then the stress amplitude (σ_a) is written as

$$\sigma_a = \frac{\Delta\epsilon_e E}{2} \tag{4.15}$$

which, from Eq. 4.11, yields

$$\sigma_a = \frac{3.5}{2}\sigma_u N_f^{-0.12} \tag{4.16}$$

$$= 1.75\sigma_u N_f^{-0.12} \tag{4.17}$$

Comparing Eqs. 4.14 and 4.17 shows that the creep-rupture time (t_r) is given by

$$t_r = A(N_f)^{-0.12/m} \tag{4.18}$$

Then the creep-rupture damage (t'/t_r) is given by

$$\frac{t'}{t_r} = \frac{kN_f'}{Af(N_f)^{-0.12/m}} \tag{4.19}$$

As a next step, assume that the fatigue damage is given by the ratio of the actual number of cycles to failure to the cycles that would have been encountered in the absence of creep damage. This ratio is written as N_f'/N_f.

A cumulative-linear-damage law is then assumed wherein the creep damage is given by time ratios and fatigue damage is given by cycle ratios. These ratios are summed to yield unity at failure. Thus,

$$\frac{N_f'}{N_f} + \frac{t'}{t_r} = 1 \tag{4.20}$$

$$\frac{N_f'}{N_f} + \frac{kN_f'}{Af(N_f)^{-0.12/m}} = 1 \tag{4.21}$$

Solving for N_f' gives Eq. 4.13.

A very extensive evaluation of the N_f' and 10% N_f concepts was published by Halford and Manson.[16] Over 75 sets of high-temperature, strain-controlled, low-cycle-fatigue data were taken from the literature in making this study. More than 600 data points were involved, and the life range spanned the region from 10 to 10^5 cycles. Test temperatures ranged from 932 to 1650°F for the higher melting temperature alloys and from 300 to 900°F for the aluminum alloys. The materials, test conditions, and pertinent material properties are given in Table 4.2; included are nickel-base alloys, high- and low-alloy steels, stainless steels, and aluminum-base alloys. Ultimate tensile strengths ranged from about 2 to 160 ksi and reductions of area from 4.5 to 99%. Except for a few tests in argon or vacuum, all tests

TABLE 4.2

ALLOY, TEST CONDITION, AND PROPERTY DATA USED IN HALFORD–MANSON STUDY[16]

Alloy designation (as reported)	Test temp, °F	Approx. homologous temp	Test frequency, cycles/min	Reduction in area, %	Tensile strength, ksi	Elastic modulus, 10^3 ksi	Ref.
1197 aluminum	300	0 46	10	95	4 0	9 0*	17
	600	0 64	10	99	2 12	6 5	
1132 aluminum	300	0 46	10	80	8 5	9 0*	
	600	0 64	10	99	5 41	6 5	
M 257 aluminum (SAP)	600	0 64	10	27	17*	8 2*	
	900	0 82	10	23 0	9 1	6 1*	
Esshete 1250 (B1)	1110	0 50	0 5 9 0	54	54 5	22*	18
Esshete 1250 (B2)	1110	0 50	0 5	55	51 5	22*	
Esshete 1250 (B3)	1110	0 50	0 5,9 0	56	69 6	22*	
Esshete 1250 (B4)	1110	0 50	2 0	63	60 0	22*	
A 286, aged	1110	0 50	0 5,2 0,9 0	15	115	23 1*	
2¼ Cr–1Mo steel	1110	0 48	1 0	80	43*	23 5	19
3Cr–½ Mo steel	932	0 43	0 5	81 7	78 0	24*	20
2¼ Cr–1Mo steel	1020	0 45	0 5,9 0	60	65	24*	21
1Mo steel	950	0 43	3 0	77*	50*	24*	22
1Cr–1Mo steel	950	0 43	3 0	72*	55*	24*	
12Cr–½ Mo steel	950	0 47	3 0	75*	75*	26*	
1Cr–1Mo–¼ V steel (A1)	1050	0 46	0 1,0 5,1 0, 5 0,10 0 13 5	70	69 5	24*	21
1Cr–1Mo–¼ V steel (A2)	1020	0 45	1 0,10 0	60	72 5	24*	
1Cr–1Mo–¼ V steel (A5)	1020	0 45	0 5 10 0	50	71 7	24*	
1Cr–1Mo–¼ V steel (A8)	1020	0 45	1 0,10 0	72	67 5	24*	
1Cr 1Mo–¼ V steel (A9)	1020	0 45	0 5 10 0	70	56	24*	
1Cr 1Mo–¼ V steel (A11)	1020	0 45	0 1,1 0,10 0	68	54 5	24*	
½ Cr ½ Mo–¼ V steel (B1)	1020	0 45	0 5	70	60	24*	
½ Cr–½ Mo ¼ V steel (B2)	1020	0 45	5 0	72	60 3	24*	
½ Cr–½ Mo ¼ V steel (B3)	1020	0 45	1 0 10 0	70	60	24*	
1Cr–1Mo–¼ V steel (A10)	1020	0 45	1 0,9 0	73	49 5	24*	
C–½ Mo steel	1020	0 45	5 0	72 5	47	24*	23
¾ Cr–¾ Mo–¼ V steel	1020	0 45	5 0	78	57	24*	
1Cr 1Mo–¼ V steel (A)	1020	0 45	0 5,9 0	77	60 7	24*	24
1Cr–1Mo–¼ V steel (B)	1020	0 45	0 5,9 0	75	57 4	24*	
18/8 stainless steel	932	0 46	0 5	65 7	70 3	24*	20
304 stainless steel	1300 (argon)	0 58	0 5	52*	36*	20 5*	25
	1500 (argon)	0 65	0 5	42*	20*	19*	
	1600 (argon)	0 68	0 5	40*	16*	18*	
20Cr–25Ni–0 7Nb stainless (solution treated)	1200	0 55	0 5	40	70	22 5	26
20Cr–25Ni–0 7Nb stainless (solution treated and aged)	1200	0 55	0 5	50	65	22 5	
20Cr–25Ni–0 7Nb stainless (annealed)	1200	0 55	0 5	54 1	61 4	22 5	
20Cr–25Ni–0 7Nb stainless (annealed)	1380	0 61	0 5	74 8	37 1	21 6	
316 stainless steel (A1 and A2)	1110	0 52	0 5,9 0	58	51 3	22*	18
316 stainless steel (A3 and A4)	1110	0 52	0 1,1 0, 2 0,10	58	51 3	22*	
316 stainless steel (A4)	1200	0 55	1 0	53*	44*	21*	
316 stainless steel	1500	0 65	300	45*	29*	19*	27
316 stainless steel (A5)	1110	0 52	0 5,1 0,9 0	74	56	22*	18

(Table continues on the next page.)

TABLE 4.2 (Continued)

Alloy designation (as reported)	Test temp., °F	Approx. homologous temp.	Test frequency, cycles/min	Reduction in area, %	Tensile strength, ksi	Elastic modulus, 10^3 ksi	Ref.
316 stainless steel (A6)	1110	0.52	2 0	74	60	22*	
316 stainless steel (A7)	1110	0.52	2 0	73	54 6	22*	
316 stainless steel (A8)	1110	0 52	1 0,2 0	78	58 7	22*	
316 stainless steel (A9)	1110	0.52	0.5,9 0	70	51 5	22*	
Udimet 700 ("E")	1400	0 64	0 67–1 8	31	155	23 6	28
Nimonic 75	1200	0.57	0 1	29 5	81 5	25 7*	29
	1380	0 63	0.1	42	53 1	24 5*	
	1600	0.71	0 1	62 5	28	22 8*	
Nimonic 105 (standard heat)	1380	0 63	0.1	18	151	25 2*	
	1600	0 71	0 1	32 5	99 5	23 2*	
Nimonic 105 (brittle heat)	1380	0 63	10	15	141 5	25 2*	
	1600	0 71	10	4.5	112 5	23 2*	
Nimonic 105 (ductile heat)	1380	0.63	10	36 5	154	25 2*	
	1600	0 71	10	43	103 5	23 2*	
Nimonic 90	1500	0 67	10	13	96	24*	
	1600	0 71	0 0077	14	76	23 2*	
	1650	0 73	10	22	61	22 5*	

*Handbook or other reference-source data

were conducted in air environments at homologous temperatures (ratio of absolute test temperature to absolute melting-point temperature) ranging from 0.43 to 0.82. Test frequencies were as low as 0.0077 cycle/min and as high as 300 cycles/min, with some tests involving dwell times at maximum strain up to 24 hr. All the fatigue tests were conducted under strain control, either in plane bending or axial push–pull. The fatigue data for these materials are plotted in Figs. 4.22 to 4.39 as total strain range vs. cycles to failure on logarithmic coordinates. Unless noted in the figures, the tests were conducted in plane bending. Three curves are shown with each set of data. The lowest curve is the estimate of the lower bound, using the rule associated with 10% N_f or N_f', the middle curve is the estimate of average behavior, and the upper curve is the estimate of the upper bound. Continuous curves represent life estimates based on Eq. 4.12, and dashed curves denote that Eq. 4 13 was applied in making the estimates. Values of the stress-rupture slope (m) and the time intercept (A) used in the latter estimates are shown in the respective figures. In each instance the criterion in Fig. 4.20 was checked to determine whether it would be necessary to base the estimates on Eq. 4.13. Since only eight sets of data required the use of Eq. 4 13, the validity of this expression was not tested to any great extent. In fact, the dashed curves shown in Fig. 4.39(b) provide overly conservative estimates of the low-cycle-fatigue behavior. The results shown in Figs. 4.22 to 4.39 indicate that qualitative estimates of the experimental results can be achieved by the proposed method. When applied to the present data, the method provided a lower bound for about 85% and an upper bound for about 95% of the data points. A measure of the degree of dispersion of the data from the estimated average behavior is given in Table 4.3. Agreement between the estimates and the data is reasonable, when it is recognized that (1) the experimental results represent a wide variety of materials with divergent properties tested over a broad range of conditions, (2) several different types of testing equipment and techniques were used, and (3) only a limited number of easily determined tensile and stress-rupture properties were used in making the estimates. In conclusion, it is suggested that, at temperatures well into the "creep range" (homologous temperatures above approximately 0.5), stress-rupture damage may reduce cyclic lives beyond any reductions reflected by the effect of strain rate on the tensile properties. Even if the suggestion that the influence of strain rate on tensile properties is considered when estimating fatigue behavior, it is nevertheless recognized that creep effects on fatigue life are important and should also be accounted for

METHOD OF CHARACTERISTIC SLOPES

Some recent low-cycle-fatigue data[30,31] for 304 and 316 stainless steels at 800 and 1200°F and at strain rates ranging from 4×10^{-5} to 4×10^{-3} sec^{-1} were studied in evaluating a new approach[32] to the prediction of low-cycle-fatigue behavior A log–log plot of $\Delta\epsilon_p$ vs. time to fracture (given by N_f/f, where f is the frequency) yields a linear relation. Furthermore, this line has a slope of -1, and passes through the point corresponding to the tensile ductility. The time value corresponding to the tensile-ductility point is given by the measured tensile ductility divided by the total true strain rate (ϵ_t) used in the short-term tensile measurement. In other words, the ten-

sile-ductility point is plotted at a time value that corresponds to the actual time involved in the tensile test. Actual time periods in the short-term tensile tests performed in this study ranged from 0.03 to about 3.0 hr.

Figure 4.40 gives $\Delta\epsilon_p$ vs. time to fracture, i.e., N_f/f, for 304 stainless steel at 1200°F and a strain rate of 4×10^{-3} sec^{-1}. Definite linearity is indicated to identify a slope of minus unity. This line is also in definite accord with the tensile-ductility point corresponding to a short-term tensile test at the same strain rate. Similar graphs are presented in Fig. 4.41 for 316 stainless steel at room temperature and at

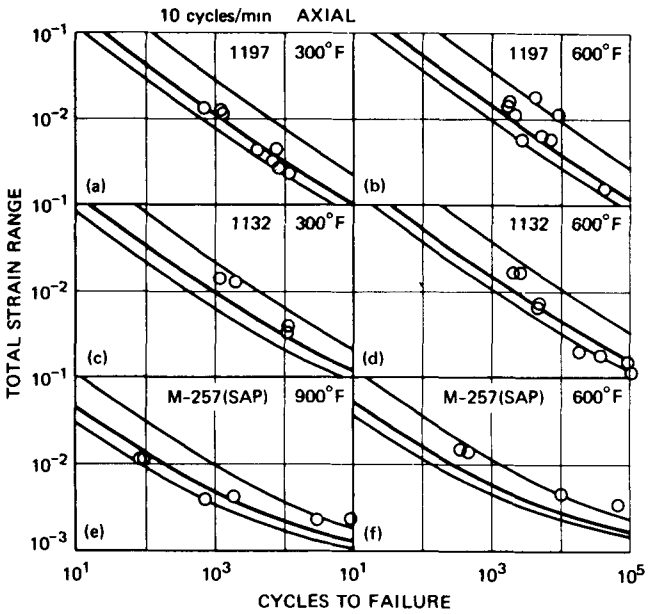

Fig. 4.22 Comparison of estimated and observed behavior of aluminum alloys.[17]

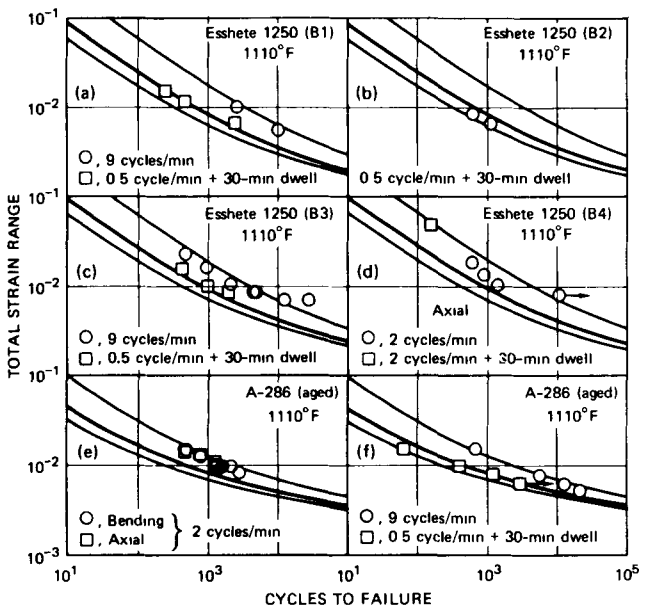

Fig. 4.23 Comparison of estimated and observed behavior of Fe–Ni–Cr–Mo alloys.[18]

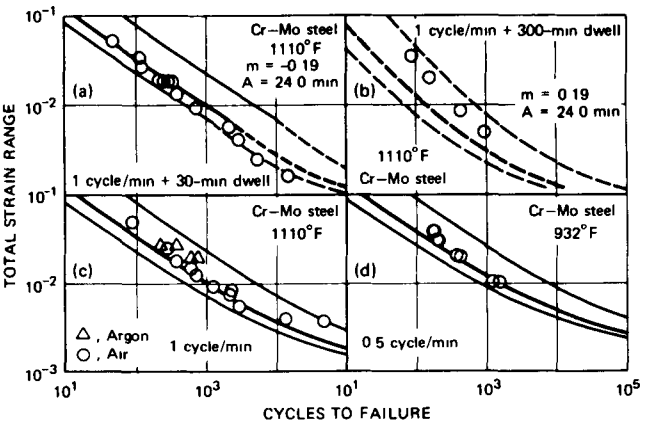

Fig. 4.24 Comparison of estimated and observed behavior of Cr–Mo steels. a to c, Ref. 19; d, Ref. 20.

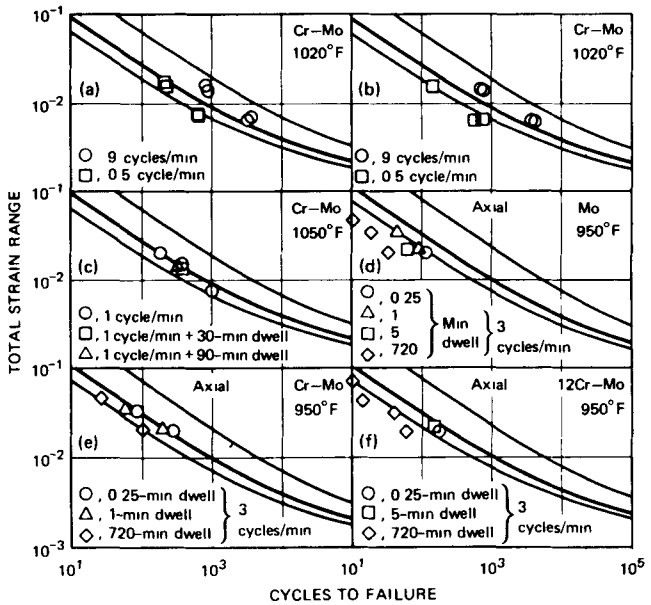

Fig. 4.25 Comparison of estimated and observed behavior of Cr–Mo steels. a to c, Ref. 21; d to f, Ref. 22.

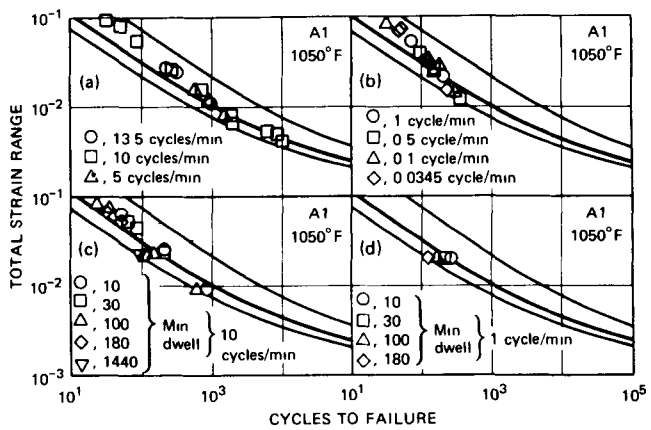

Fig. 4.26 Comparison of estimated and observed behavior of Cr–Mo–V steels.[21]

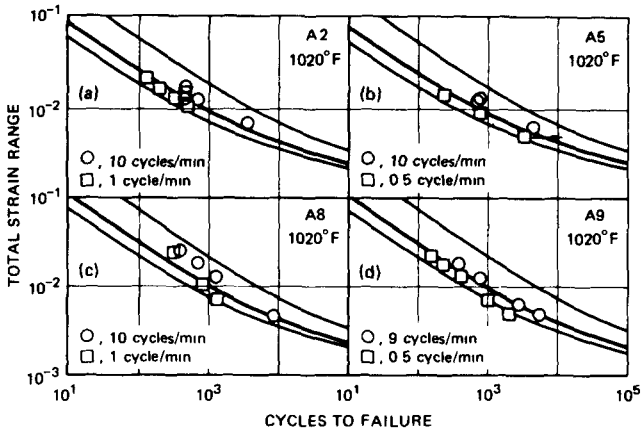

Fig. 4.27 Comparison of estimated and observed behavior of Cr–Mo–V steels.[21]

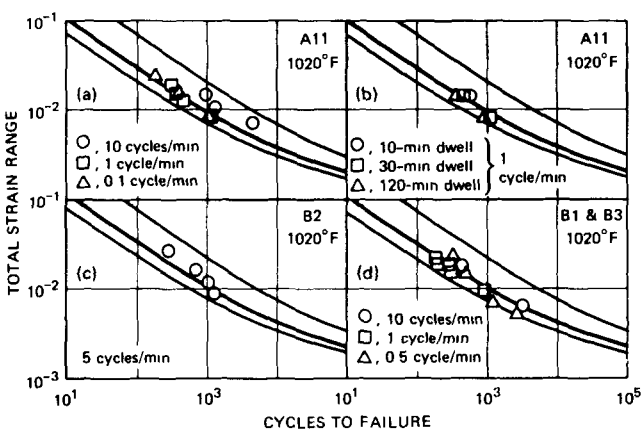

Fig. 4.28 Comparison of estimated and observed behavior of Cr–Mo–V steels.[21]

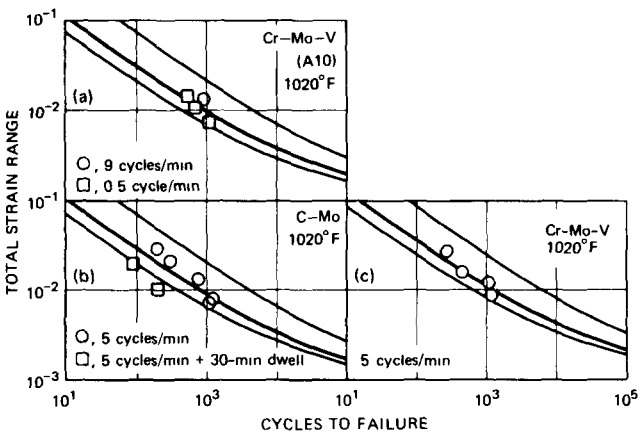

Fig. 4.29 Comparison of estimated and observed behavior of Cr–Mo–V steels. a, Ref. 21; b and c, Ref. 23.

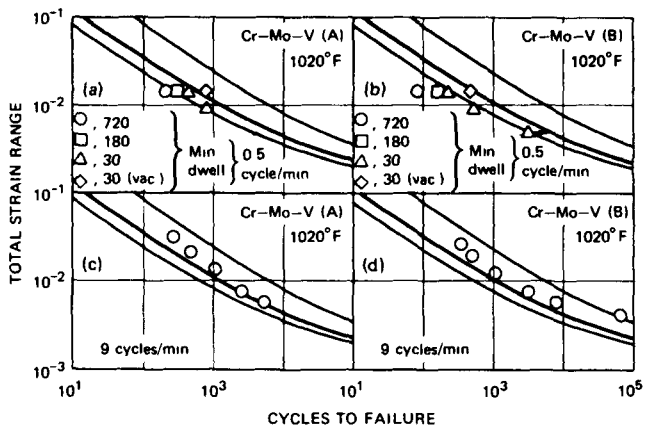

Fig. 4.30 Comparison of estimated and observed behavior of Cr–Mo–V steels.[24]

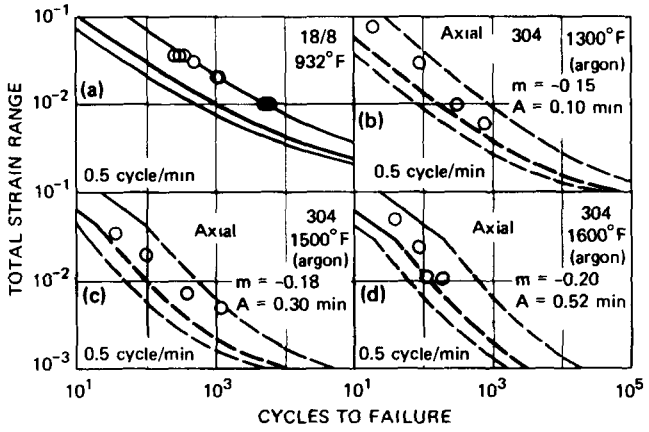

Fig. 4.31 Comparison of estimated and observed behavior of stainless steel. a, Ref. 20; b to d, Ref. 25.

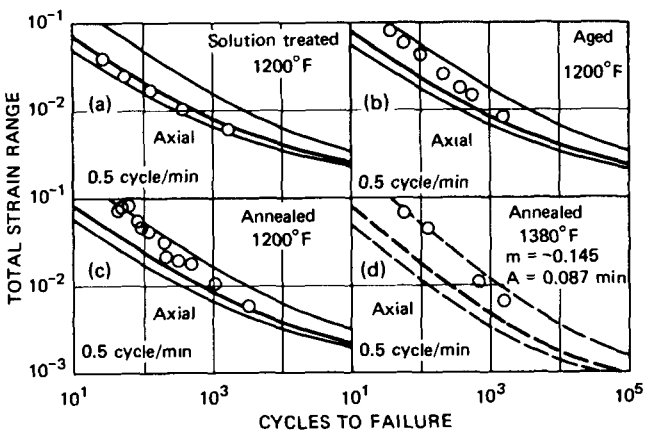

Fig. 4.32 Comparison of estimated and observed behavior of 20 Cr–25Ni–0.7Nb stainless steel.[26]

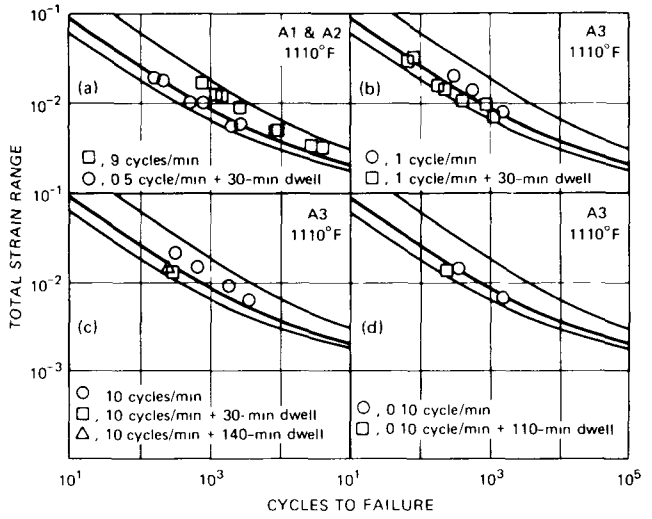

Fig. 4.33 Comparison of estimated and observed behavior of 316 stainless steel.[18]

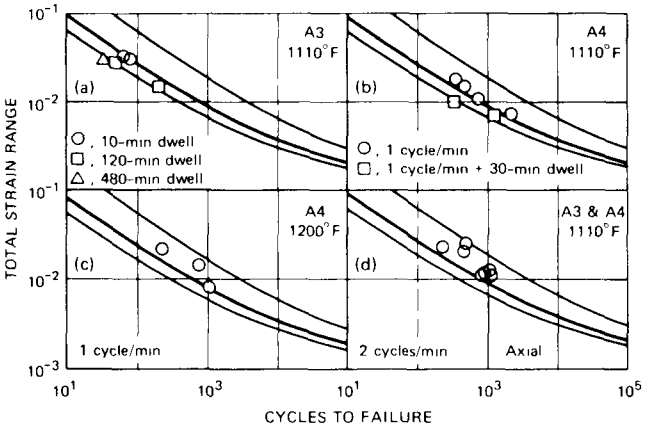

Fig. 4.34 Comparison of estimated and observed behavior of 316 stainless steel.[18]

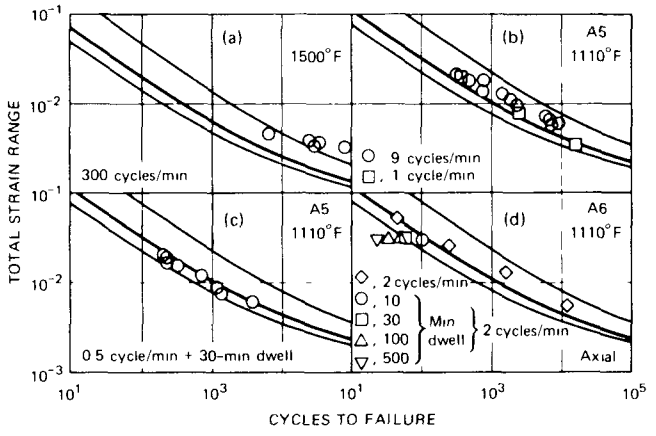

Fig. 4.35 Comparison of estimated and observed behavior of 316 stainless steel. a, Ref. 27; b to d, Ref. 18.

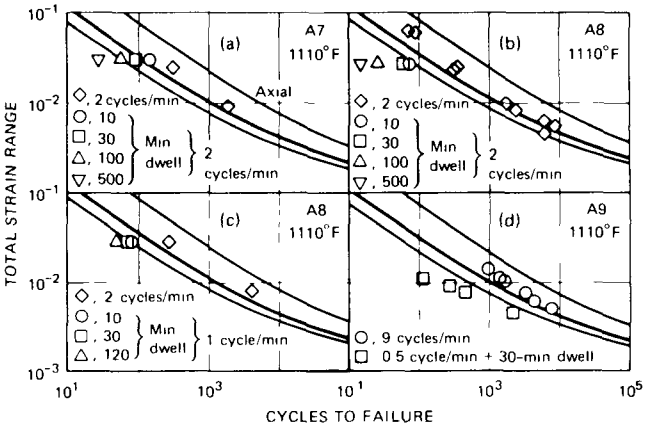

Fig. 4.36 Comparison of estimated and observed behavior of 316 stainless steel.[18]

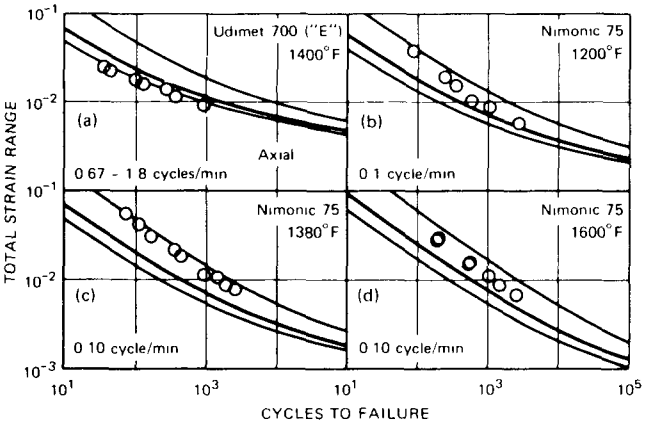

Fig. 4.37 Comparison of estimated and observed behavior of nickel-base alloys. a, Ref. 28; b to d, Ref. 29.

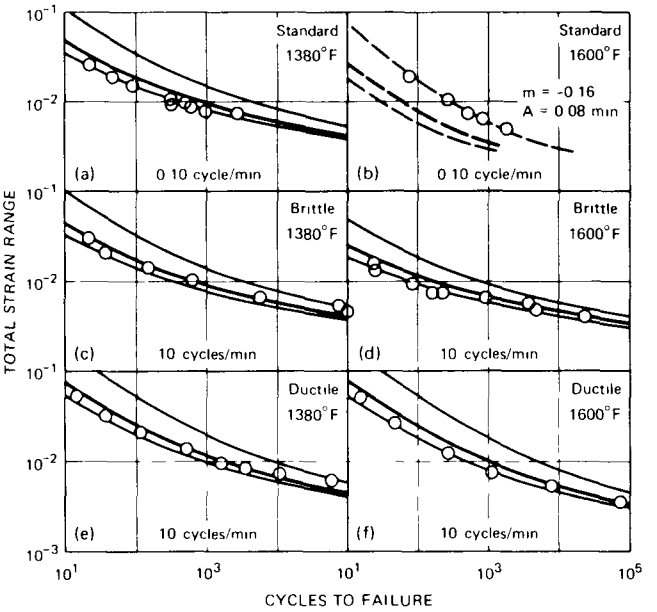

Fig. 4.38 Comparison of estimated and observed behavior[29] of Nimonic 105.

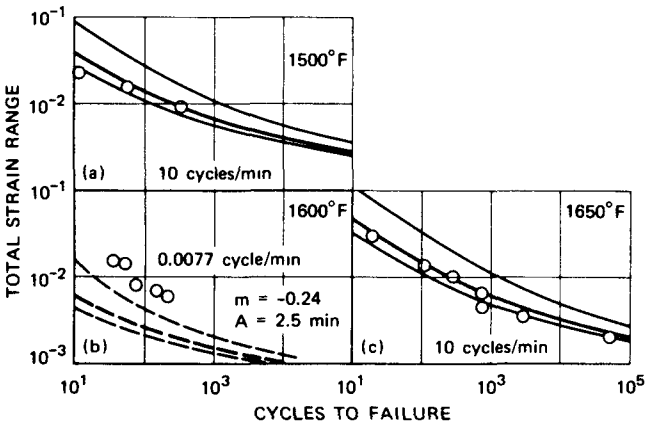

Fig. 4.39 Comparison of estimated and observed behavior[29] of Nimonic 90.

TABLE 4.3

DISPERSION OF EXPERIMENTAL FATIGUE LIFE FROM ESTIMATED VALUES[16]

Factor in life above and below estimated average life	Percent of data included
1.5	36
2	59
3	80
4	89
5	94
6	96
8	97
10	98

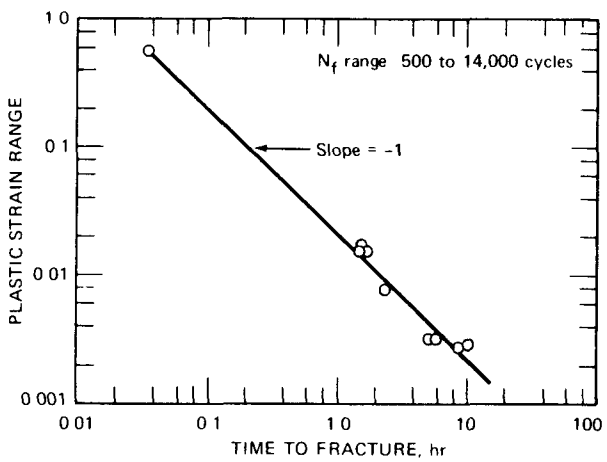

Fig. 4.40 Plastic strain range vs. N_f/f for 304 stainless steel tested at 1200°F and a strain rate of 4×10^{-3} sec^{-1}.

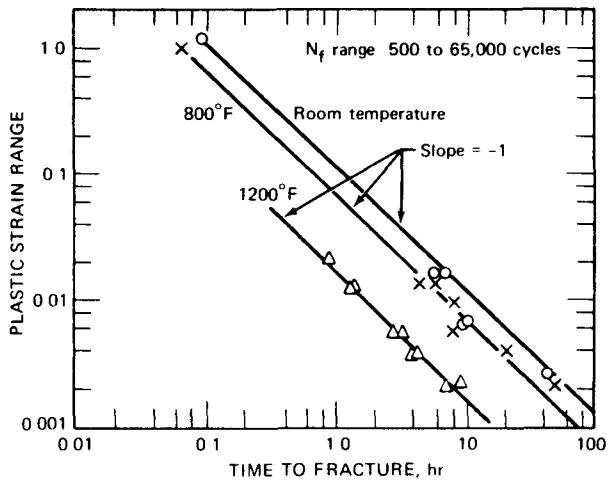

Fig. 4.41 Plastic strain range vs. N_f/f for 316 stainless steel tested at room temperature and at 800 and 1200°F and a strain rate of 4×10^{-3} sec^{-1}.

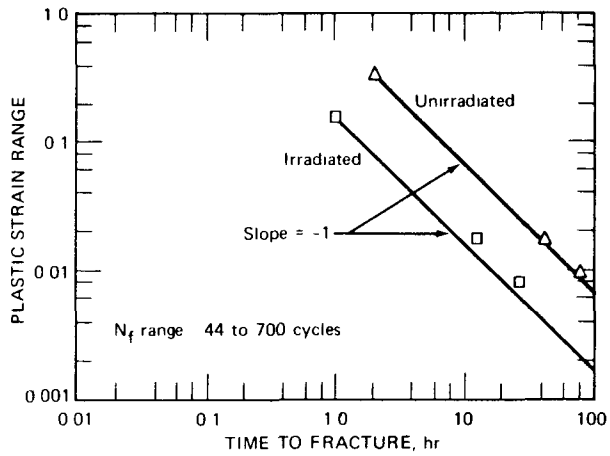

Fig. 4.42 Plastic strain range vs. N_f/f for irradiated and unirradiated 316 stainless steel tested at 1200°F and a strain rate of 4×10^{-5} sec^{-1}.

800 and 1200°F (no tensile ductility is available at 1200°F).

Data for 316 stainless steel at 1200°F and a strain rate of 4×10^{-5} sec^{-1} are presented in Fig. 4.42. For unirradiated material, agreement with the above concept is quite striking. Two tests of material irradiated in the Oak Ridge Research Reactor to a fast fluence ($E > 1$ MeV) of 3×10^{18} neutrons/cm^2 at reactor ambient temperature also agree with the above concept, even though the irradiated material exhibits different fatigue behavior from that noted in the unirradiated tests. It is important to note that this difference in fatigue behavior could have been predicted from a short-term tensile test. Had the tensile-ductility point for this irradiated material been plotted and a line drawn through this point with a slope of −1, the fatigue behavior would have been fairly accurately predicted.

Predictions of the low-cycle-fatigue behavior of irradiated (Fig. 4.42) 316 stainless steel[33] at 1200°F and a

strain rate of 4×10^{-5} sec^{-1} are shown in Fig. 4.43 based on the Coffin–Manson (Method of Universal Slopes) and Berling–Conway approaches. Better results follow from the new procedures proposed herein. A similar conclusion follows from the comparison shown in Fig. 4.44 for unirradiated 304 stainless-steel data at 1200°F and a strain rate of 4×10^{-3} sec^{-1}.

From the linearity described above, the following relation applies:

$$\Delta\epsilon_p = A\left(\frac{N_f}{f}\right)^{-1} \tag{4.22}$$

If $\Delta\epsilon_p = \epsilon_f$ at $N_f/f = \epsilon_f/\dot{\epsilon}_t$, then

$$\Delta\epsilon_p = \frac{\epsilon_f^2}{\dot{\epsilon}_t}\left(\frac{N_f}{f}\right)^{-1} \tag{4.23}$$

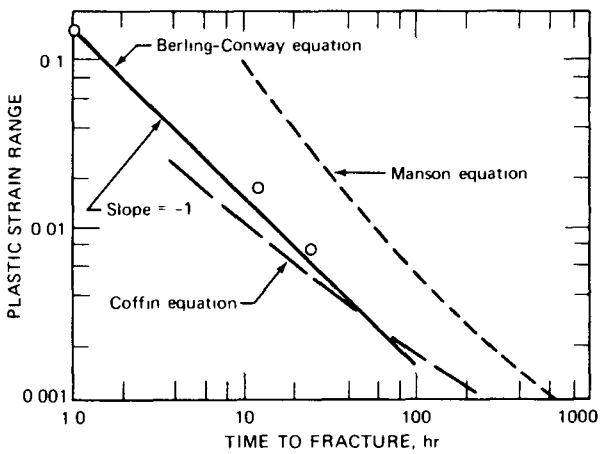

Fig. 4.43 Comparison of the effectiveness of the Coffin–Manson and Berling–Conway equations for predicting fatigue behavior of irradiated 316 stainless steel tested at 1200°F and a strain rate of 4×10^{-5} sec^{-1}.

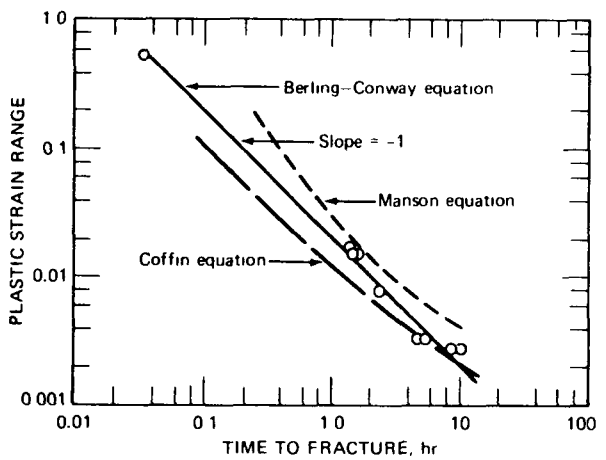

Fig. 4.44 Comparison of the effectiveness of the Coffin–Manson and Berling–Conway equations for predicting fatigue behavior of unirradiated 304 stainless steel tested at 1200°F and a strain rate of 4×10^{-3} sec^{-1}.

Once ϵ_f is measured in a short-term tensile test at a certain strain rate, an accurate prediction of the low-cycle-fatigue behavior at this same strain rate follows immediately. Note also from Eq. 4.23 that the time (or N_f at a given frequency) required for fatigue fracture at a given strain range, say 1%, will be given by equations of the type

$$t_1 = \left(\frac{N_f}{f}\right)_1 = \frac{\epsilon_f^2}{0.01\dot{\epsilon}_t} \tag{4.24}$$

for $\Delta\epsilon_p = 2\%$,

$$t_2 = \left(\frac{N_f}{f}\right)_2 = \frac{\epsilon_f^2}{0.02\dot{\epsilon}_t} \tag{4.25}$$

If it is assumed that the total strain rate is given by $2f\,\Delta\epsilon_p$ (rigorously, $\dot{\epsilon}_t = 2f\,\Delta\epsilon_t$, where $\Delta\epsilon_t$ is the total strain range), substitution in Eq. 4.23 leads to

$$\Delta\epsilon_p = \frac{\epsilon_f}{\sqrt{2}} N_f^{-1/2} \tag{4.26}$$

This is a modification of the Coffin equation, in which the tensile ductility is plotted at $N_f = 1/2$ rather than at $N_f = 1/4$. For fatigue life below 1000 cycles, the assumption made above is fairly accurate, and Eq. 4.26 would yield approximate results. At lower strain ranges, however, larger errors would result from the use of this expression, and hence the approach defined in Eq. 4.23 is definitely preferable.

Since $\dot{\epsilon}_t = 2f\ \Delta\epsilon_t$ for a triangular strain wave form, where $\Delta\epsilon_t$ is the total strain range, it follows from Eq. 4.23 that

$$\Delta\epsilon_p\ \Delta\epsilon_t\ N_f = \frac{\epsilon_f^2}{2} \tag{4.27}$$

This relation[34] specifies that the product of fatigue life, plastic strain range, and total strain range is constant for a given material at a given test condition. Once the tensile ductility is determined, the value for this product is identified. Applying this approach to data for 304 stainless steel at 650°C and a strain rate of 4×10^{-3} sec^{-1} yielded the results in Table 4.4. The product identified by Eq. 4.27 is fairly constant and, except for two points, is in good agreement with the value of $\epsilon_f^2/2$. For these conditions, ϵ_f is 0.548 (Table 4.5), and hence the product in Table 4.4 should be 0.150. It should be emphasized that Eqs. 4.23 and 4.27 are empirical in nature and are recommended for use on the basis of the excellent results obtained in analyzing the stainless-steel data cited above. These equations do not apply when stainless-steel data at 816°C (1500°F) are used. Apparently at such temperatures the creep effect is so significant that the damage mechanism differs from that involved when Eqs. 4.23 and 4.27 are applicable. Later modifications are obviously in order if an effective correlation for these higher temperature fatigue

TABLE 4.4

LOW-CYCLE-FATIGUE DATA FOR AISI 304 STAINLESS STEEL*

Plastic strain range ($\Delta\epsilon_p$)	Total strain range ($\Delta\epsilon_t$)	Cycles to failure (N_f)	$(\Delta\epsilon_p)(\Delta\epsilon_t)(N_f)$
0.0033	0.0059	7,944	0.155
0.0033	0.0059	7,320	0.142
0.0079	0.0111	1,740	0.152
0.0171	0.0210	566	0.203
0.0027	0.0050	13,400	0.181
0.0028	0.0052	14,620	0.213
0.0158	0.0198	592	0.185
0.0158	0.0198	546	0.171

*Tested at 650°C and a strain rate of 4×10^{-3} sec^{-1}. (Analyzed in terms of Eq. 4.27.)

results is to be obtained. However, even at these high temperatures, marginal value can be assigned to Eq. 4.23 since data trends can be identified, and, hence, it would seem possible to establish the true fatigue behavior by performing only a minimum number of tests.

Another limitation on Eqs. 4.23 and 4.27 relates to the strain-range regime within which these expressions are applicable. Like the Manson[8] equation, these expressions do not accommodate a fatigue limit and hence cannot be applied when very low strain values are encountered and the cycles to fracture approach the high-cycle-fatigue region. However, since the effectiveness of these expressions is such as to provide a valuable estimating procedure for fatigue behavior in the low-cycle regime, it seems justified to accept this new approach as another important tool in the area of fatigue behavior.

TABLE 4.5

TENSILE PROPERTIES OF ANNEALED AISI 304, 316, AND 348 STAINLESS STEELS TESTED IN AIR

Material	Temp. °C	Temp. °F	Strain rate, sec^{-1}	Elastic constants E 10^6, psi	Elastic constants E 10^3 kg/mm²	ν_e	Ultimate tensile strength Psi	Ultimate tensile strength Kg/mm²	Reduction in area, %	Tensile ductility, %
304	21	70	4×10^{-3}	28.7	20.2	0.264	89,000	62.6	80.6	164.0
304	21	70	4×10^{-4}	28.7	20.2	0.264				
304	21	70	4×10^{-5}	28.7	20.2	0.264				
304	430	806	4×10^{-3}	23.4	16.5	0.282	62,400	43.9	64.0	102.2
304	430	806	4×10^{-4}	23.4	16.5	0.282				
304	430	806	4×10^{-5}	23.4	16.5	0.282	64,600	45.4	64.5	103.6
304	650	1202	4×10^{-3}	21.6	15.2	0.315	45,600	32.1	42.2	54.8
304	650	1202	4×10^{-4}	21.6	15.2	0.315				
304	650	1202	4×10^{-5}	21.6	15.2	0.315	35,400	24.9	33.4	40.6
304	816	1500	4×10^{-3}	18.8	13.2	0.323	25,000	17.6	51.0	71.3
304	816	1500	4×10^{-4}	18.8	13.2	0.323				
304	816	1500	4×10^{-5}	18.8	13.2	0.323	13,400	9.5	32.1	38.7
348	21	70	4×10^{-3}	28.2	19.8	0.250				
348	21	70	4×10^{-4}	28.2	19.8	0.250				
348	21	70	4×10^{-5}	28.2	19.8	0.250				
348	430	806	4×10^{-3}	23.8	16.7	0.275	59,600	41.9	66.4	109.1
348	430	806	4×10^{-4}	23.8	16.7	0.275				
348	430	806	4×10^{-5}	23.8	16.7	0.275	62,600	44.0	57.5	85.6
348	650	1202	4×10^{-3}	21.8	15.3	0.295	47,700	33.6	68.6	115.8
348	650	1202	4×10^{-4}	21.8	15.3	0.295				
348	650	1202	4×10^{-5}	21.8	15.3	0.295	40,800	28.7	40.4	51.8
348	816	1500	4×10^{-3}	19.05	13.4	0.340	25,900	18.2	87.0	204.0
348	816	1500	4×10^{-4}	19.05	13.4	0.340				
348	816	1500	4×10^{-5}	19.05	13.4	0.340	17,000	12.0	84.0	183.3
316	21	70	4×10^{-3}	30.1	21.2	0.295	90,000	63.3	74.6	137.0
316	21	70	4×10^{-4}	30.1	21.2	0.295				
316	21	70	4×10^{-5}	30.1	21.2	0.295				
316	430	806	4×10^{-3}	24.0	16.9	0.315	67,700	47.6	62.1	97.0
316	430	806	4×10^{-4}	24.0	16.9	0.315				
316	430	806	4×10^{-5}	24.0	16.9	0.315	73,900	52.0	60.6	93.1
316	650	1202	4×10^{-3}	21.95	15.4	0.326	54,700	38.5	61.1	94.0
316	650	1202	4×10^{-4}	21.95	15.4	0.326				
316	650	1202	4×10^{-5}	21.95	15.4	0.326	42,800	30.1	32.1	38.7
316	816	1500	4×10^{-3}	18.4	12.9	0.321	29,700	20.9	61.6	95.7
316	816	1500	4×10^{-4}	18.4	12.9	0.321				
316	816	1500	4×10^{-5}	18.4	12.9	0.321	21,300	14.9	49.9	69.1

If Eq. 4.23 is used to represent the plastic-strain-range term in the Method of Universal Slopes proposed by Manson,[6] then

$$\Delta\epsilon_t = \frac{3.5\sigma_u}{E} N_f^{-0.12} + \frac{\epsilon_f^2}{\dot{\epsilon}_t}\left(\frac{N_f}{f}\right)^{-1} \tag{4.28}$$

where σ_u is the ultimate tensile strength, and E is the modulus of elasticity. Substituting $f = \dot{\epsilon}_t/2\Delta\epsilon_t$ yields

$$\Delta\epsilon_t = \frac{3.5\sigma_u}{E} N_f^{-0.12} + \frac{\epsilon_f^2}{2\Delta\epsilon_t N_f} \tag{4.29}$$

Multiplying throughout by $\Delta\epsilon_t$ yields

$$\Delta\epsilon_t^2 - \frac{3.5\sigma_u}{E}\Delta\epsilon_t N_f^{-0.12} - \frac{\epsilon_f^2}{2N_f} = 0 \tag{4.30}$$

which will be recognized as a quadratic in $\Delta\epsilon_t$. The quadratic solution leads to

$$\Delta\epsilon_t = \frac{\frac{3.5\sigma_u}{E} N_f^{-0.12} \pm \sqrt{\left(\frac{3.5\sigma_u}{E} N_f^{-0.12}\right)^2 + \frac{2\epsilon_f^2}{N_f}}}{2} \tag{4.31}$$

This expression provides a direct solution for corresponding $\Delta\epsilon_t$ and N_f values to allow the estimated fatigue curve to be defined.

A comprehensive evaluation of the elastic term in Eq. 4.29 revealed another interesting relation. Detailed studies of the low-cycle-fatigue tests[30,31] of 304, 316, and 348 stainless steels at temperatures to 1500°F and at strain rates of 4×10^{-5}, 4×10^{-4}, and 4×10^{-3} sec^{-1} showed that the exponent on N_f was not a constant for the various materials and test conditions considered. Although linearity on a log $\Delta\epsilon_e$ (elastic strain range) vs. log N_f graph was generally noted, the slope was found to be dependent on temperature and strain rate for a given material. This slope variation was closely related to and could be associated with that observed in logarithmic stress–strain graphs of data obtained in short-term tensile tests at the same conditions. Such typical behavior is shown in Figs. 4.45 and 4.46. A study of these graphs revealed that the slope (represented by $-m'$) of the logarithmic $\Delta\epsilon_e$ vs. N_f graph was essentially identical (except for sign) to one-half the strain-hardening exponent (represented by m) obtained in a short-term tensile test[35,36] at the same test conditions. Since the logarithmic graphs of true stress vs. true plastic strain were not linear over the entire strain range, the value of m' was taken as the slope of the linear segment representing the data in the high strain region. Associating m with m is an important observation because it defines one additional relation between low-cycle-fatigue and short-term tensile behavior.

Another extremely important observation defined one additional equality: the value of $\Delta\epsilon_e$ at $N_f = 10$ cycles was equal to twice the true elastic strain at fracture (represented by ϵ_{ef}) in a short-term tensile test at the same conditions of temperature and strain rate. Table 4.6, based on the stainless-steel data in this study, illustrates this equality along with that between m' and m.

From the equalities just described, it follows that

$$\Delta\epsilon_e = 2\epsilon_{ef}\left(\frac{N_f}{10}\right)^{-m'/2} \tag{4.32}$$

This can be substituted in Eq. 4.29 to yield a completely modified Universal Slopes equation in the following form:

$$\Delta\epsilon_t = 2\epsilon_{ef}\left(\frac{N_f}{10}\right)^{-m/2} + \frac{\epsilon_f^2}{\dot{\epsilon}_t}\left(\frac{N_f}{f}\right)^{-1} \tag{4.33}$$

Actually, the expression is somewhat more than just a modification. More appropriately, it is a complete revision or a redefinition of the Universal Slopes equation. In effect, Eq. 4.33 refutes the existence of slopes which are the same for all materials and test conditions and hence which are

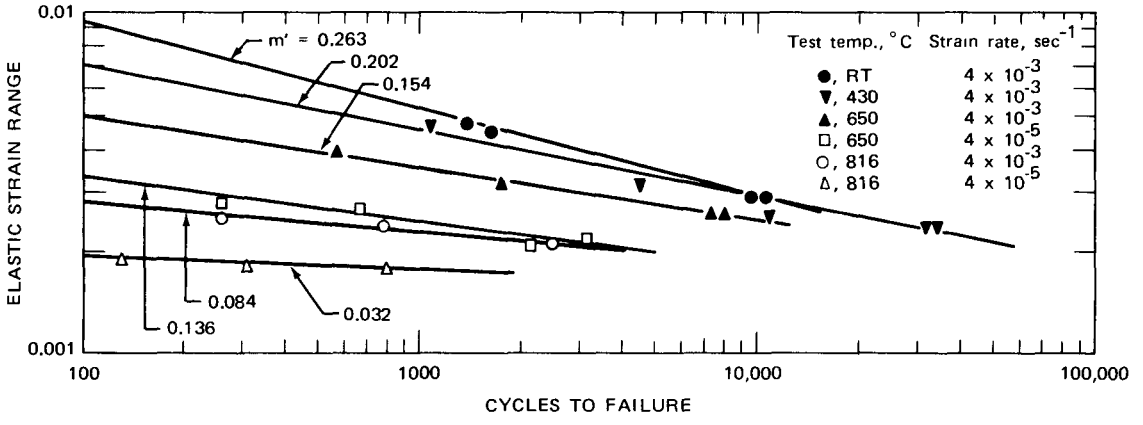

Fig. 4.45 Elastic strain range vs. N_f for annealed AISI 304 stainless steel tested in air.

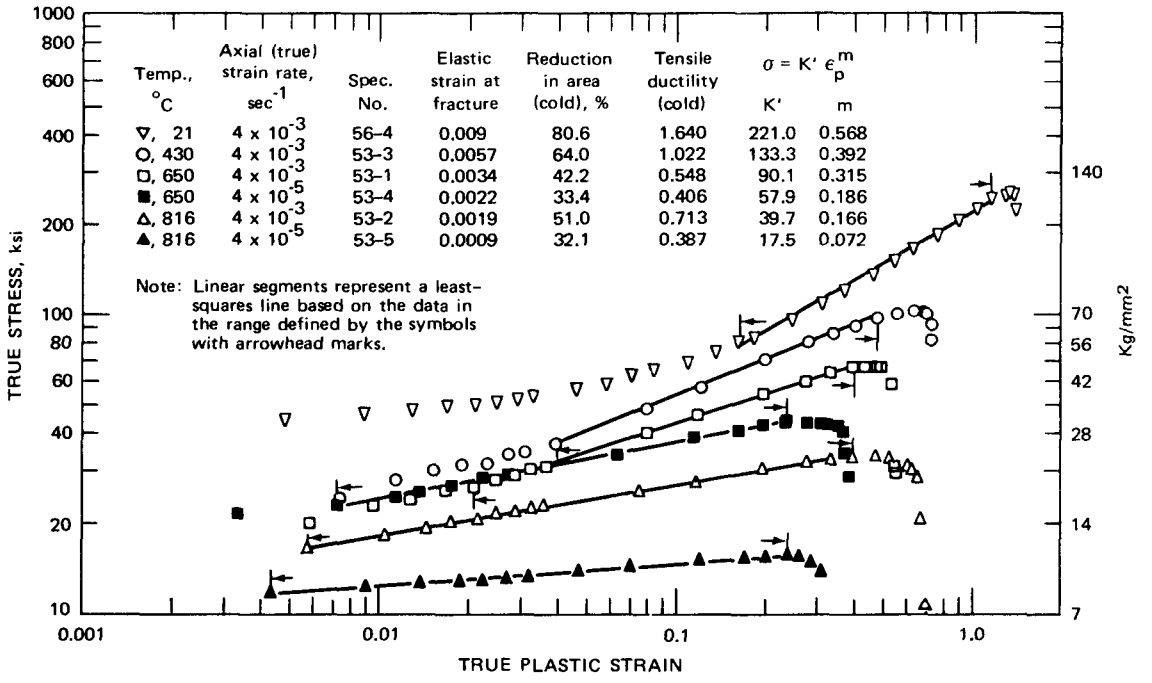

Fig. 4.46 True stress vs. true plastic strain for annealed AISI 304 stainless steel tested in air.

TABLE 4.6

LOW-CYCLE-FATIGUE AND SHORT-TERM TENSILE CHARACTERISTICS FOR ANNEALED AISI 304, 316, AND 348 STAINLESS STEELS

Test temp.,* °C	Axial strain rate, sec^{-1}	Strain-hardening exponent divided by 2 (m/2)	Slope of log $\Delta\epsilon_e$ vs. log N_f plot (m')	Elastic strain† at fracture multiplied by 2 ($2\epsilon_{ef}$)	Elastic strain range at $N_f = 10$
		AISI 304 Stainless Steel			
RT	4×10^{-3}	0.284	0.263	0.0181	0.0171
430	4×10^{-3}	0.196	0.202	0.0115	0.0112
650	4×10^{-3}	0.157	0.154	0.0068	0.0071
650	4×10^{-5}	0.093	0.136	0.0045	0.0045
816	4×10^{-3}	0.083	0.084	0.0039	0.0034
816	4×10^{-5}	0.036	0.032	0.0018	0.0021
		AISI 316 Stainless Steel			
RT	4×10^{-3}	0.242	0.24	0.0164	0.0150
430	4×10^{-3}	0.250	0.241	0.0146	0.0155
650	4×10^{-3}	0.143	0.152	0.0095	0.0090
650	4×10^{-5}	0.150	0.095	0.0058	0.0049
816	4×10^{-3}	0.100	0.106	0.0053	0.0048
816	4×10^{-5}	0.032	0.069	0.0029	0.0027
		AISI 348 Stainless Steel			
430	4×10^{-3}	0.151	0.153	0.010	0.0090
650	4×10^{-3}	0.110	0.093	0.0078	0.0060
650	4×10^{-5}	0.090	0.079	0.0054	0.0056
816	4×10^{-3}	0.073	0.097	0.0046	0.0039
816	4×10^{-5}	0.025	0.046	0.0023	0.0018

*RT = room temperature.

†The true stress at fracture was determined by extrapolating the true stress–strain diagram (logarithmic plot) to the true fracture strain. This value of true stress divided by the modulus of elasticity yielded ϵ_{ef}.

universally applicable Instead, terms are identified which define elastic and plastic components that are uniquely related to the short term tensile behavior of a given material at a given set of test conditions For the elastic contribution in particular the slope (exponent on N_f) is specifically related to the strain hardening exponent for the particular material and testing condition being considered Thus it appears more appropriate to refer to Eq 4 33 as the Method of Characteristic Slopes

Multiplying both sides of Eq 4 33 by $\Delta\epsilon_t$ leads to a form similar to that given in Eq 4 30 and another quadratic in $\Delta\epsilon_t$ Applying the quadratic solution yields

$$\Delta\epsilon_t \quad \epsilon_{ef}\left(\frac{N_f}{10}\right)^{m/2} \pm\sqrt{\epsilon_{ef}^2\left(\frac{10}{N_f}\right)^{m}+\frac{\epsilon_f^2}{2N_f}} \quad (4\ 34)$$

which is a convenient solution leading to corresponding $\Delta\epsilon_t$ and N_f values Once ϵ_{ef} m and ϵ_f are identified in a short term tensile test at a given temperature and strain rate, the use of Eq 4 34 will lead to estimated low cycle fatigue behavior at these same test conditions Strain rate effects are properly accounted for in the effect that strain rate has on the short term tensile quantities ϵ_{ef} m, and ϵ_f

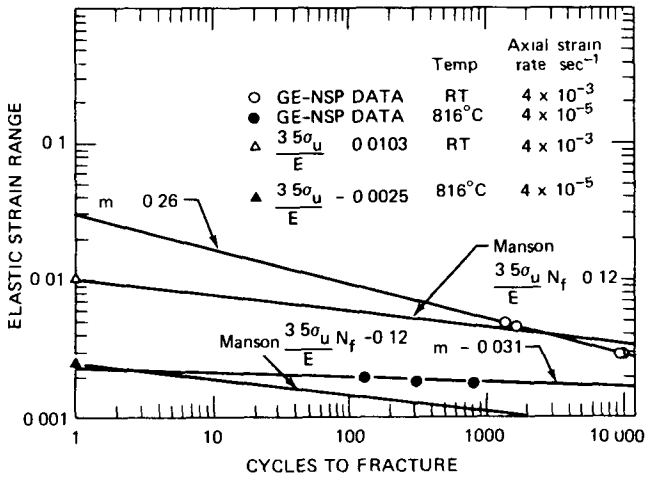

Fig 4 47 Elastic strain range data compared to Eq 4 32 and the term in the Universal Slopes equation

Values of σ_u and E (Eq 4 28) have been used (Table 4 5) along with values for ϵ_{ef} and m at the same test conditions to yield the comparisons in Fig 4 47 The elastic strain range values corresponding to Eq 4 32 are more representative of actual experimental values than those given by the elastic term in the Universal Slopes equation It is important to note that the experimental values for the elastic strain range define a slope that deviates significantly from the 0 12 value suggested by the Universal Slopes equation Also shown for comparison in Fig 4 47 are the values of $3\ 5\sigma_u/E$ corresponding to the elastic term in Eq 4 28

Equation 4 34 and the data in Table 4 6 have been used to estimate $\Delta\epsilon_t$ vs N_f behavior of 304 stainless steel at 1200°F and a strain rate of 4×10^{-5} sec^{-1} and of 316 and 348 stainless steels at 800°F and a strain rate of 4×10^{-3} sec^{-1} These results are presented in Fig 4 48, along with similar predictions made from the data in Table 4 5 in conjunction with the Universal Slopes[6] equation Better estimates follow from the approach suggested in Eq 4 33

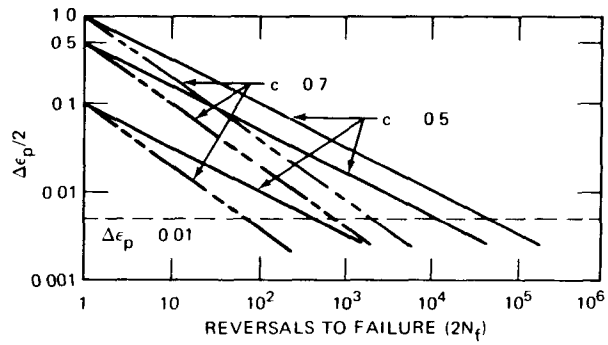

Fig 4 48 Schematic of plastic strain amplitude vs N_f behavior (From Ref 37)

For the stainless steel data considered,[35] Eq 4 34 provides estimates of fatigue life which are in excellent agreement with experimental results at temperatures to 650°C (1200°F) and at strain rates ranging from 4×10^{-5} to 4×10^{-3} sec^{-1} Such effectiveness identifies Eq 4 34 as an important relation in low cycle fatigue studies within the temperature range corresponding to the majority of applications for stainless steel (i e , up to about 650°C) At 816°C (1500°F), this expression predicts a fatigue life larger than that observed experimentally The overestimation of fatigue life is also evident in the Universal Slopes equation At about 816°C it appears that creep damage is particularly severe and is not accommodated by the equations proposed to date

MORROW–LANDGRAF–FELTNER APPROACH

Morrow,[38] in a very excellent study, defined the following fatigue properties in terms of the data obtained in a series of strain controlled evaluations fatigue ductility coefficient, fatigue ductility exponent, fatigue strength coefficient and fatigue-strength exponent Morrow also showed how these properties relate to stress range, strain range, and cycles to fracture

On the basis of a series of completely reversed tests at different strain ranges, a linearity between the stable plastic strain amplitude and fatigue life was found to exist on logarithmic coordinates This linearity is identical to the Coffin Manson relation except that Morrow expressed such behavior in terms of plastic strain amplitude and the reversals to failure Mathematically this relation becomes

$$\frac{\Delta\epsilon_p}{2} = \epsilon_f' (2N_f)^c \tag{4.35}$$

to identify the fatigue-ductility exponent (c) as the slope of the linear relation between $\Delta\epsilon_p/2$ and $2N_f$ on logarithmic coordinates. Similarly the plastic-strain intercept at 0.5 cycle (one reversal) gives the fatigue-ductility coefficient (ϵ_f'). The similarity between this expression and the Coffin–Manson equation is obvious.

Morrow further pointed out that cyclic stress–strain behavior, based on stable hysteresis loops and analyzed in terms of plastic-strain amplitude and stress amplitude (σ_a), led to a linear relation on logarithmic coordinates to give

$$\frac{\Delta\epsilon_p}{2} = \epsilon_f' \left(\frac{\sigma_a}{\sigma_f'}\right)^{1/n'} \tag{4.36}$$

where n′ is the cyclic strain-hardening exponent. Combining Eqs. 4.35 and 4.36 to eliminate the plastic-strain amplitude led to

$$\sigma_a = \sigma_f' (2N_f)^{n'c} = \sigma_f' (2N_f)^b \tag{4.37}$$

This was noted to be identical in form to the Basquin[39] exponential law of fatigue proposed in 1910.

Equation 4.37 was used to evaluate the fatigue-strength coefficient (σ_f') and the fatigue-strength exponent (b). Special mention was made of the linearity (on logarithmic coordinates) defined by Eq. 4.37, and Morrow commented that this has been found to remain linear even to fatigue-life values in excess of 10^9 cycles. Some qualification was made, however, to acknowledge that this graph, for some metals, becomes essentially horizontal at about 10^6 cycles to exhibit an endurance limit.

Expressing the total strain amplitude in terms of the plastic and elastic components, Morrow used Eq. 4.35 for the plastic contribution and divided Eq. 4.37 by the modulus of elasticity to obtain the elastic-strain amplitude. This led to

$$\frac{\Delta\epsilon_t}{2} = \frac{\sigma_f'}{E} (2N_f)^b + \epsilon_f' (2N_f)^c \tag{4.38}$$

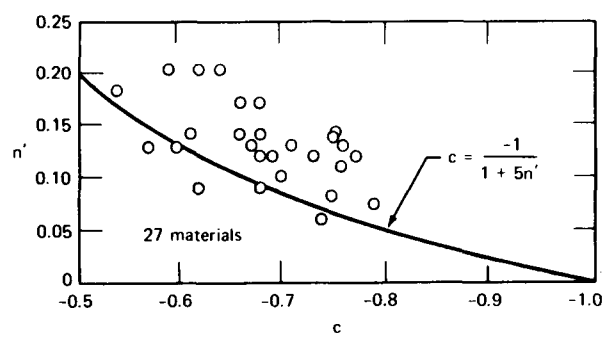

Fig. 4.49 Correlation of n′ and c values. (From Ref. 38.)

which defines the fatigue life in terms of the total strain amplitude and various fatigue properties.

When N_f is very large (the strain is predominantly elastic), the first term in Eq. 4.38 is controlling; conversely, when N_f is small (the strain is predominantly all plastic), the second term is controlling. These considerations have led[37] to the conclusions that the short-term strain resistance depends primarily on the fatigue-ductility coefficient (ϵ_f') and the fatigue-ductility exponent (c). An illustration[37] of this effect is shown in Fig. 4.48 to indicate that a material with a high intercept value (i.e., large ϵ_f') and a shallow slope (i.e., a small value of c) will have the best fatigue resistance. Selected values of c and ϵ_f' led to the following comparisons of fatigue life for $\Delta\epsilon_p = 0.01$:

	N_f	
ϵ_f'	c = −0.5	c = −0.7
0.1	210	36
0.5	5,000	360
1.0	20,000	1,000

For a 10-fold increase in ϵ_f', when c = −0.5, the fatigue life increases by a factor of 100; when c = −0.7, the increase is only a factor of 30 or so.

Morrow[38] has shown (Fig. 4.49) that

$$c = \frac{-1}{1 + 5n'} \tag{4.39}$$

and hence, with c and n′ known, the value of b in Eq. 4.38 is obtainable. However, before Eq. 4.38 can be used to calculate the $\Delta\epsilon_t$ vs. N_f behavior, values for ϵ_f' and σ_f' must be determined. Feltner and Landgraf[37] have suggested that σ_f' be equated to σ_f (the true fracture stress obtained in a monotonic tension test) and that ϵ_f' be calculated using

$$\epsilon_f' = 0.002 \left(\frac{\sigma_f}{\sigma_y'}\right)^{1/n'} \tag{4.40}$$

In this formulation the concept of a 0.2% offset cyclic-flow stress was introduced such that

$$\sigma_a = \sigma_y' = \sigma_{0.002} \tag{4.41}$$

when $\Delta\epsilon_p/2 = 0.002$. Using these new values in Eq. 4.36 yielded

$$\epsilon_f' = 0.002 \left(\frac{\sigma_f}{\sigma_y'}\right)^{1/n'} \tag{4.42}$$

which has been referred to as the Landgraf equation.

All terms in Eq. 4.38 were thus defined to allow calculations to be made of the $\Delta\epsilon_t$ vs. N_f relation. It is noteworthy at this point to recognize an important distinction between this relation, given in Eq. 4.38, and the other relations of this type described in previous sections.

The other relations required only short-term tensile measurements, whereas Eq. 4.38 requires the usual short-term tensile measurements in addition to cyclic stress–strain information. The procedure[37] for using Eq. 4.38 has been delineated as follows:

1. Obtain σ_f from a monotonic tension test.
2. Obtain n′ and $\sigma_{0.002}$ from the cyclic stress–strain information established in an incremental step test.
3. Compute c from Eq. 4.39 and ϵ_f' from Eq. 4.42.
4. Compute b from the n′c product.
5. Substitute these constants in Eq. 4.38 along with the modulus of elasticity, and then calculate $\Delta\epsilon_t$ corresponding to various assumed values of N_f.

Feltner and Landgraf[37] reported an interesting application of Eq. 4.38 when the plastic-strain component is dominating. Data for seven steels were used along with the appropriate values for c and ϵ_f'. Using only the plastic-strain term in Eq. 4.38, they calculated the values of $\Delta\epsilon_p$ for each material for an assumed value of N_f. These results are presented in Tables 4.7 and 4.8 to rank the materials in order of their ability to resist repeated straining. Good agreement between estimated and actual behavior is noted, and hence the value of this procedure is established.

TABLE 4.7*

RANKING OF STEELS IN TERMS OF 50-CYCLE FATIGUE LIFE BY PREDICTED AND ACTUAL STRAIN RESISTANCE

Steel†	$\Delta\epsilon_p/2$		Rank	
	Predicted	Actual	Predicted	Actual
18% nickel maraging, 460 BHN	0.032	0.021	1	1
SAE 1045 QT, 450 BHN	0.026	0.0175	2	2
SAE 4142 QT, 380 BHN	0.021	0.017	3	3
SAE 4142 QD, 400 BHN	0.017	0.0155	4	4
SAE 4142 QT, 450 BHN	0.014	0.012	5	5
SAE 1045 QT, 500 BHN	0.011	0.010	6	6
SAE 4142 QT, 475 BHN	0.0056	0.0055	7	7

*From Ref. 37.
†QT = quenched and tempered; QD = quenched and deformed.

TABLE 4.8*

RANKING OF STEELS IN TERMS OF 5000-CYCLE FATIGUE LIFE BY PREDICTED AND ACTUAL STRAIN RESISTANCE

Steel†	$\Delta\epsilon_p/2$		Rank	
	Predicted	Actual	Predicted	Actual
SAE 1045 QT, 450 BHN	0.00186	0.00065	1	1
SAE 4142 QT, 380 BHN	0.00172	0.00055	2	2
SAE 4142 QD, 400 BHN	0.00131	0.00051	3	4
18% nickel maraging, 460 BHN	0.00111	0.00054	4	3
SAE 4142 QT, 450 BHN	0.00103	0.00031	5	7
SAE 1045 QT, 500 BHN	0.00069	0.00045	6	5
SAE 4142 QT, 475 BHN	0.00034	0.00035	7	6

*From Ref. 37.
† QT = quenched and tempered; QD = quenched and deformed

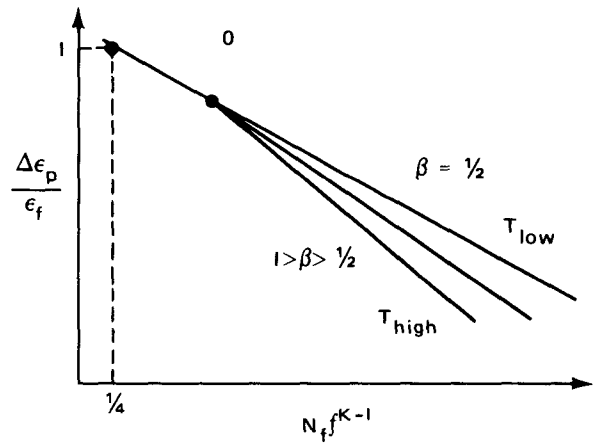

Fig. 4.50 Generalized representation of plastic strain range vs. frequency-modified fatigue life.[40]

One feature of the above concept is that Eq. 4.38 was the first fatigue-estimating equation involving the use of cyclic stress–strain characteristics. This distinguishing feature also identifies the equation as one which requires more material-property information than the others. Another feature worth noting is that the concept was based exclusively on room-temperature behavior, and very little is known regarding the applicability of this concept at elevated temperatures.

GENERALIZED EQUATION FOR ESTIMATING FATIGUE LIFE

In a very important development, Coffin[40] proposed a generalized equation to use in predicting low-cycle-fatigue behavior and also to account for hold-time effects. This development expanded on the concept of the frequency-modified fatigue life described by Coffin in an earlier publication.[41] In the previous publication, Coffin showed that, for a given temperature, a single-valued relation existed between plastic strain range and a combination of frequency (f) and the total time to failure (t). Stated mathematically, this relation had the form

$$\Delta\epsilon_p(f^k t)^\beta = C_2 \tag{4.43}$$

or

$$\Delta\epsilon_p(N_f f^{k-1})^\beta = C_2 \tag{4.44}$$

A generalized representation of this relation is shown in Fig. 4.50 for several test temperatures. In commenting on this graph, Coffin[40] made the following observations:

1. The abscissa $N_f f^{k-1}$ is a logarithmic scale and represents a combination of frequency and cycles to

failure such that, for a specific temperature, frequency effects are accounted for in the parameter. The quantity k is a function of temperature.

2. The ordinate $\Delta\epsilon_p/\epsilon_f$ is also a logarithmic scale and is the plastic strain range divided by the short time tensile ductility of the material. This normalized quantity permits consideration of several temperatures in a single diagram.

3. An upper-bound curve is envisaged which is obtained by cycling at high frequency such that the fatigue failure process occurs by a ductile, transgranular mode. The physical picture for this was described by Coffin in a separate discussion. It would be anticipated that, no matter what the circumstances, a point of fatigue failure could not fall outside of this line. The exponent which represents the slope of this line is assumed to be 0.5.

5. The quantity k is determined from tests at a given temperature and a constant plastic strain range but at different frequencies. Using logarithmic coordinates, k is the exponent of f and represents the slope of a straight line drawn on the plot of f versus t.

Some experimental support for the equality in Eq. 4.46 was provided by an analysis of some data[30] for AISI 304 stainless steel. The results of this analysis are presented in Fig. 4.51 to reveal that the value of β is 0.5 for the lowest temperature, in accord with the Fig. 4.50 construction. Clearly, these results provide convincing evidence for the Coffin approach.

Experiments were also performed using specimens of annealed AISI C-1010 steel at 600°C. Both large and small

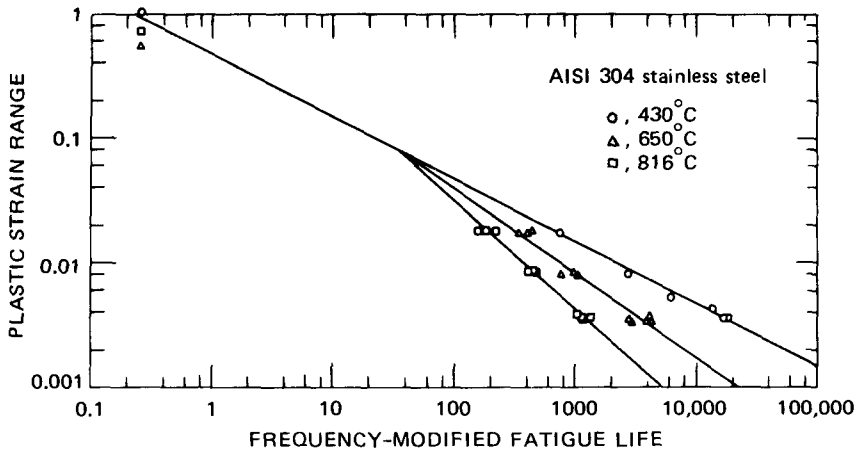

Fig. 4.51 Plastic strain range[40] vs. frequency-modified fatigue life for AISI 304 stainless steel[30] at 430, 650, and 816°C.

4. For specific test temperatures, straight lines are constructed whose slope is represented by β,* such that β increases with increasing temperature. At low temperatures where the fracture mode is ductile, the upper-bound curve applies. At higher temperatures, all curves converge at 0. Experimental evidence indicates that the frequency-modified fatigue life at 0 is of the order of 25 to 100 when f is in cycles per minute. For the upper-bound curve (low temperature) frequency effects are assumed to be small and k = 1. The equation for this line is:

$$\frac{\Delta\epsilon_p}{\epsilon_f}(N_f)^{0.5} = C \qquad [4.45]$$

By letting $N_f = 1/4$ and $\Delta\epsilon_p = \epsilon_f$, $C = 1/4$. The equation for any specific elevated temperature is given by:

$$\Delta\epsilon_p = C_2 N_f^{\beta} f^{(1-k)\beta} \qquad [4.46]$$

where C_2 depends on ϵ_f and the specific location of 0. [Equation 4.46 is a simple rearrangement of Eq. 4.44, and the value of β is obtained from the slope in Fig. 4.50.]

*Actually, β is the exponent of $N_f f^{k-1}$.

values of plastic strain range were applied to uniaxially loaded hourglass-shaped specimens subjected to controlled diametral strain. For small strains the specimen diameter was 0.25 in., and the hourglass radius was 1.5 in. For large strains the diameter was reduced to 0.125 in. and the hourglass radius to 0.5 in. to minimize the possibility of buckling. Three frequencies were used for strains less than 0.2 so that the frequency-modified life could be determined as shown in Fig. 4.52. For these smaller strains, β was 0.79. For the larger strains a single intermediate frequency was used, and β was 0.5. The short-term tensile ductility falls on this latter line. A well-defined break in the graph is shown at a life of $40f^k t$, in support of the plastic-strain model described by Coffin, to indicate a change in the fracture mode at the tip of the crack.

Coffin cited the work of Morrow[38] that introduced the relation

$$\Delta\sigma = A(\Delta\epsilon_p)^n \qquad (4.47)$$

where A is the stress range for a plastic strain range of unity, and n is the cyclic strain-hardening exponent.

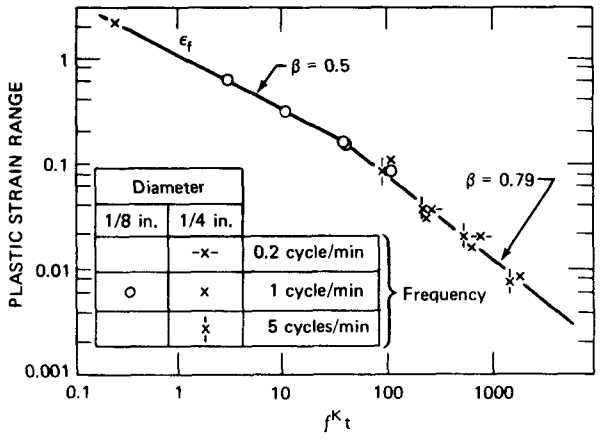

Fig. 4.52 Plastic strain range vs. frequency-modified fatigue life for C-1010 steel[40] at 600°C.

Equation 4.47 usually neglects any consideration of frequency. Since the frequency effect can become important at elevated temperatures and can influence the stress range for a given plastic strain range, Coffin proposed the expression

$$\Delta\sigma = A(\Delta\epsilon_p)^n f^{k_1} \tag{4.48}$$

In this form a frequency term is introduced which exerts an effect except when $k_1 = 0$. Equation 4.48 was also written as

$$\Delta\sigma' = \Delta\sigma f^{-k_1} \tag{4.49}$$

to identify $\Delta\sigma'$ as the frequency-modified stress range.

Verification of Eq. 4.48 was provided by experiments using AISI C-1010 steel at 600°C (1112°F). In these tests the plastic strain range was held constant at a value of 0.00312, and the frequency was varied from 0.0016 to 22 cycles/min. Since cyclic hardening was a function only of plastic strain range but not of cycles of strain at this temperature, a single specimen was used. Data obtained in these tests are shown in Fig. 4.53 to reveal a linear relation on logarithmic coordinates. The slope of this line led to the values of k_1 that are listed in Table 4.9 along with other constants associated with Eqs. 4.44 and 4.48.

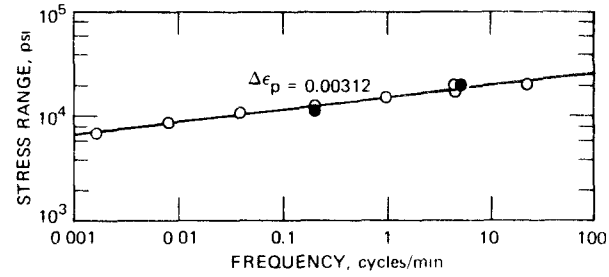

Fig. 4.53 Stress range vs. frequency for C-1010 steel[40] at 600°C.

In other tests the frequency was fixed, and the strain range was varied. Three frequencies were used to yield the results shown in Fig. 4.54. All the slopes appear identical to support the relation given by Eq. 4.48. Values of k_1, obtained from Fig. 4.54, were then used to calculate A and n.

Another interesting confirmation of the validity of Eq. 4.48 was obtained from the graph shown in Fig. 4.55. This graph of the frequency-modified stress range is based on data for C-1010 steel at 600°C and A-286 alloy at 1100°F.

Adding the plastic-strain-range term from Eq. 4.44 to the elastic strain range ($\Delta\sigma$ in Eq. 4.48 divided by E) yielded an expression for total strain range in the form:

$$\Delta\epsilon_t = C_2 N_f^{-\beta} f^{(1-k)\beta} + \frac{A}{E}(\Delta\epsilon_p)^n f^{k_1} \tag{4.50}$$

Eliminating $\Delta\epsilon_p$ through the use of Eq. 4.44 led to:

$$\Delta\epsilon_t = C_2 N_f^{-\beta} f^{(1-k)\beta} + \frac{AC_2^n}{E} N_f^{-\beta n} f^{k_1 + (1-k)\beta n} \tag{4.51}$$

which is the generalized fatigue equation. At high temperatures, specific values for A, C_2, n, β, k, and k_1 must be determined for each temperature. At low temperatures, Eq. 4.51 can be directly converted to the Universal Slopes equation or the Langer equation. Assuming no frequency effects at low temperature, $k = 1$ and $k_1 = 0$; then letting $\beta = 0.6$, $n = 0.2$, $C_2 = D^{0.6}$ (where D is the tensile ductility) and $A = 3.5\ \sigma_u/D^{0.12}$ yields

TABLE 4.9

CONSTANTS FOR USE IN EQS. 4.44 AND 4.48

Material	Temp., °C	k	C_2	β	A	E ($\times 10^{-6}$)	n	k_1
AISI C-1010	600	0.763	3.0	0.79	53,300	23.3	0.22	0.118
AISI 304 S.S.	650	0.81	1.10	0.70	150,000	23.0	0.257	0.20
René 41	760	0.80	0.398	0.65	552,000	24.8	0.185	0
1Cr–Mo–V	565	0.9	1.31	0.75	94,900	24	0.15	0

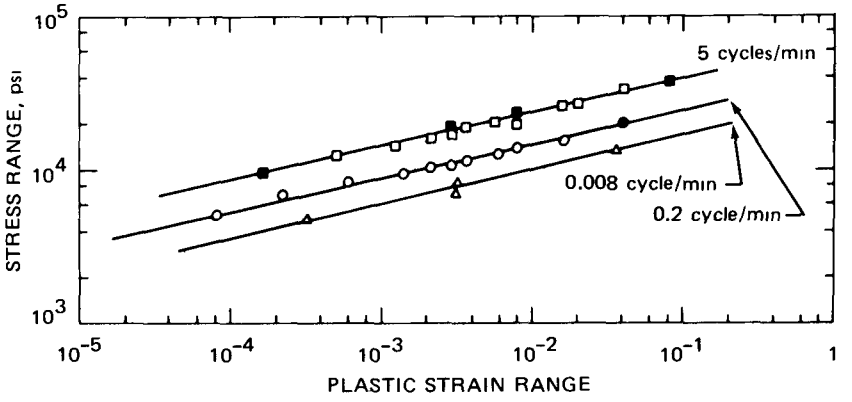

Fig. 4.54 Stress range vs. plastic strain range for C-1010 steel[40] at 600°C.

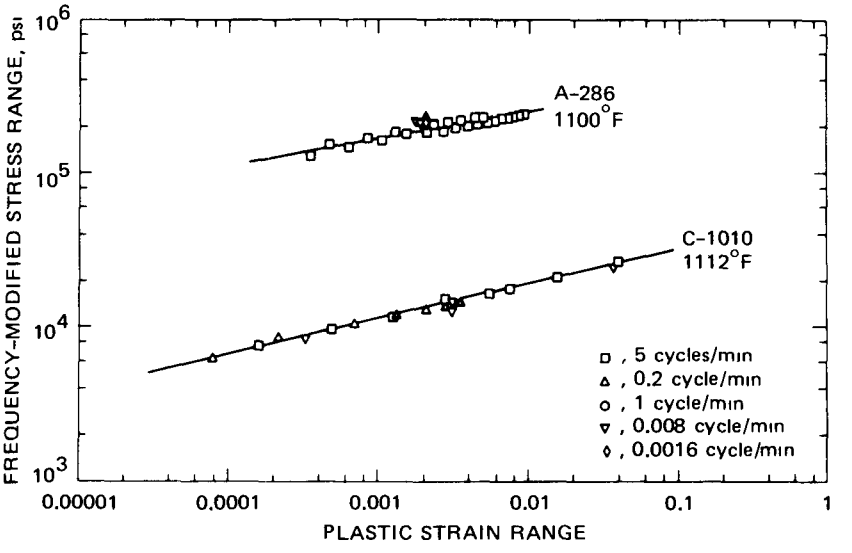

Fig. 4.55 Frequency-modified stress range vs. plastic strain range[40] for A-286 alloy at 1100°F and C-1010 steel at 1112°F.

$$\Delta\epsilon_t = \frac{3.5\sigma_u}{E} N_f^{0.12} + D^{0.6} N_f^{0.6} \qquad (4.52)$$

which is the Universal Slopes equation. If, however, $k = 1$, $k_1 = 0$, $\beta = 0.5$, $n = 0$, $C_2 = 0.5D$, and $A = 2\sigma_e$ (where σ_e is the endurance limit), the following result is obtained:

$$\Delta\epsilon_t = \frac{2\sigma_e}{E} + \frac{\epsilon_f}{2N_f^{0.5}} \qquad (4.53)$$

to yield the Langer equation.

Equation 4.51 is useful for evaluating the performance of materials subjected to high-temperature low-cycle fatigue. The constants have physical significance since each is either directly or indirectly related to other better known physical properties. As indicated earlier, β is a function of temperature, ranging from 0.5 at low temperatures to 1.0 at very high temperatures. The exponent n is the cyclic strain-hardening exponent and relates to the cyclic strain-hardening coefficient of the material.[38] The quantity C_2 is related to the tensile ductility of the material, as indicated in Eq. 4.46 and Fig. 4.50.

The strength of the material is reflected in the constant A and is the stress range when $f = 1$ cycle/min and $\Delta\epsilon_p = 1.0$ from Eq. 4.48. The time-dependent effects are introduced by the quantities k and k_1; the constant k modifies the plastic strain range at a given frequency, as seen in Eq. 4.46. Hence k reflects a time-dependent ductility loss attributable to such factors as creep or other diffusional processes, leading to grain-boundary fracture, or to such environmental influences as a stress–oxidation interaction at the crack tip.[42] In the absence of time-dependent ductility changes, $k = 1$. Finally, k_1 modifies the stress range, as seen in Eq. 4.48, and hence relates to the

time-dependent strength of the material. It closely approximates the strain-rate sensitivity exponent (m) used in monotonic time-dependent deformation analysis. It may be a positive or negative quantity, depending on the degree of strain and time aging occurring in the alloy. For metals unalloyed for creep strength, k_1 is a high positive number (about 0.2).

long lives shown in Fig. 4.57 indicates how a low or even negative value of k_1 can improve the long-life fatigue behavior at low frequencies.

Coffin emphasized that at least nine tests would be required to identify values for C_2, k, and β. Three frequencies and three plastic strain ranges would be selected, and the procedures outlined earlier[40] would be

TABLE 4.10

HYPOTHETICAL[40] MATERIAL CONSTANTS FOR EQ. 4.51

Material	Temp.	k	C_2	β	A/E ($\times 10^6$)	n	k_1
A	High	0.85	1.0	0.7	800	0.15	0.15
B	High	0.85	0.04	0.7	20,000	0.05	0.15
C	High	0.85	0.2	0.7	4,000	0.15	0.15
D	High	0.85	0.2	0.7	4,000	0.15	0
E	High	0.85	0.2	0.7	4,000	0.15	−0.075

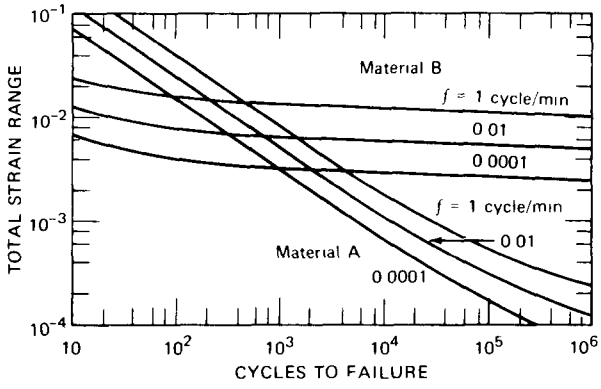

Fig. 4.56 Effect[40] of frequency on total strain range vs. cycles to failure for hypothetical materials A and B; ductility vs. strength.

Some hypothetical materials are assumed to show the effect of the various material constants on the shape of the $\Delta\epsilon_t$–N_f relation given in Eq. 4.51. The constants for these alloys are listed in Table 4.10. First, a comparison is made between a very ductile, low-strength (at high temperature) alloy (A) with a low-ductility, high-creep-strength, high-temperature alloy (B). Thus alloy A has a high C_2 and n and a low A, and alloy B has a low C_2 and n and a high A. Other constants (β, k, and k_1) are the same in each alloy. The results are given in Fig. 4.56. Of particular interest is the large difference in slope between the two alloys and the effect of frequency on life at particular total strain ranges. Alloy B is extremely frequency sensitive; alloy A, much less so.

Another analysis can be made for a material in which k_1 is varied. An intermediate-strength intermediate-ductility material is assumed, as identified in Table 4.10, in which three values of k_1 are used, namely, 0.15, 0, and −0.075. The large difference in the effect of frequency at

followed. Furthermore, a single specimen could be used in the determination of A, n, and k_1.

An extension of the value of Eq. 4.51 was identified by Coffin in its application to the prediction of the effects of hold times on fatigue life. It was assumed that the frequency in a hold-time test (hold periods in only the tension portion of the cycle were considered in the Coffin study) could be expressed by the reciprocal of the total cycle time. This frequency was then used in Eq. 4.51 to provide estimates of the fatigue life affected by hold periods.

To assess the effectiveness of this method of defining cyclic frequency in hold-time tests, Coffin made a detailed analysis of the hold-time data[43] for 304 stainless steel at 1200°F. Only the data on hold periods in tension were used, and these were used in conjunction with no-hold-time data. Equation 4.51 was used, along with the appropriate constants listed in Table 4.9. Predicted values of the fatigue life are compared in Fig. 4.58 with actual experimental values. With the exception of one point, the predicted values are concluded to be within 30% of the measured values.

A similar analysis was made using fatigue data[44] for René 41 at 1400°F. A comparison between predicted and actual experimental results (Fig. 4.59) reveals very close agreement; the results fall within an error band of ±80%.

In another comparison, Coffin analyzed the data[21] for a 1% Cr–Mo–V steel at 565°C, and the results are shown in Fig. 4.60.

Special importance must be attached to the generalized equation proposed by Coffin. Although a certain amount of low-cycle-fatigue data is required to evaluate all the constants, this can be considered a minor objection if hold-time effects can be predicted with any degree of accuracy. In other words, continuous-cycling fatigue tests usually involve durations of less than 100 hr, whereas

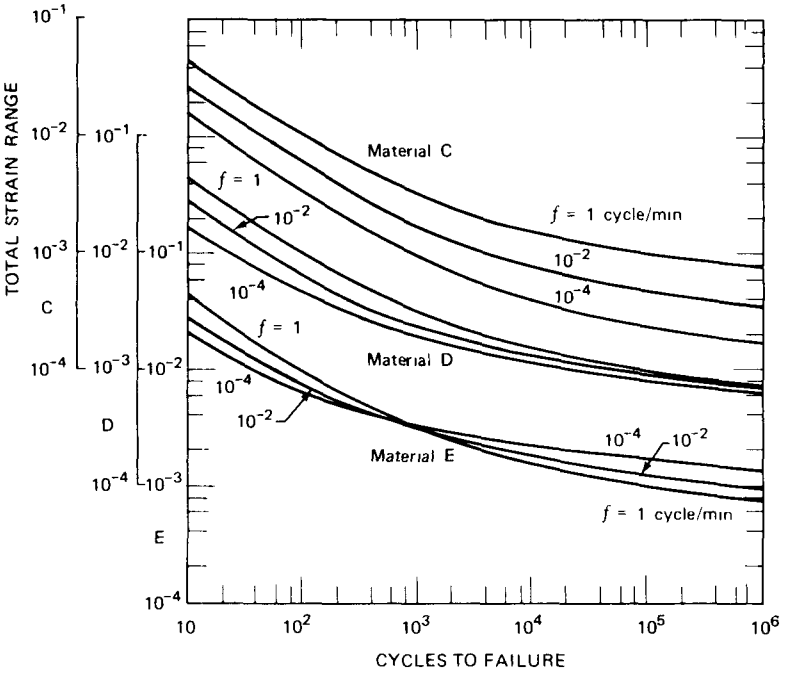

Fig. 4.57 Effect of frequency on total strain range vs. cycles to failure for hypothetical materials C, D, and E; various k_1 values.[40]

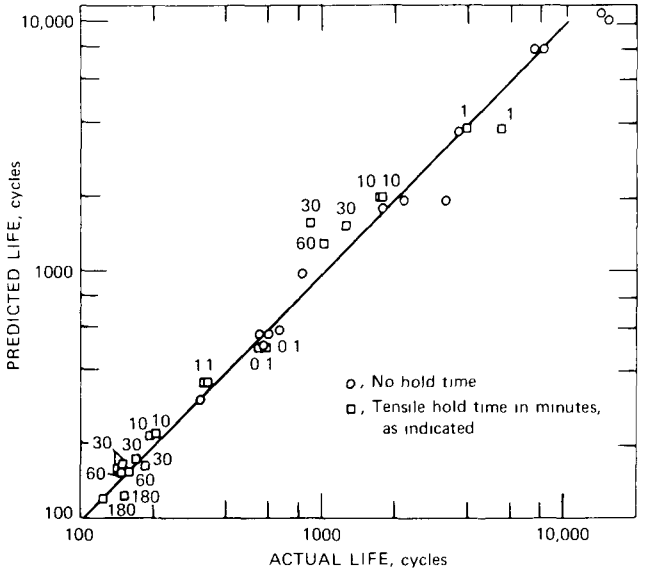

Fig. 4.58 Comparison[40] of actual and predicted fatigue life with hold times for AISI 304 stainless steel at 650°C.

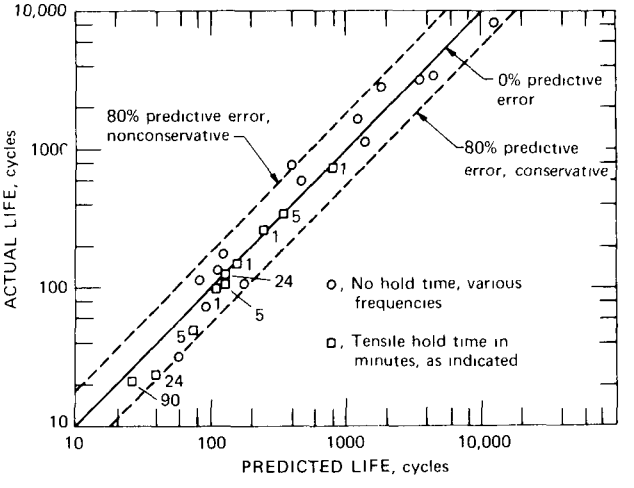

Fig. 4.59 Comparison[40] of actual and predicted fatigue life with hold times for René 41 at 1400°F.

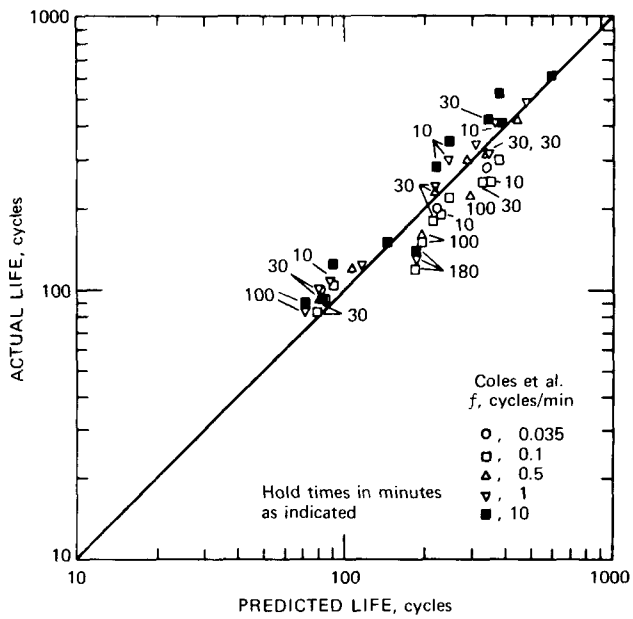

Fig. 4.60 Comparison[40] of actual and predicted fatigue life with hold times for 1Cr–Mo–V steel at 565°C.

hold-time tests may require durations greater than 1000 hr. Hence, if the former can be used to predict hold-time behavior, a considerable cost savings will be effected.

If the equation constants in Table 4.9 for 304 stainless steel at 650°C are used in conjunction with Eq. 4.51, then

$$\Delta\epsilon_t = 6.67 \times 10^{-3} N_f^{-0.18} f^{0.234} + 1.10 N_f^{-0.7} f^{0.133} \quad (4.54)$$

This equation has been applied[45] to an evaluation of hold-time effects using the frequency as the reciprocal of the cycle time. For a strain rate in the range of 4×10^{-3} sec^{-1} and for hold periods in excess of 10 min, the frequency is very close to the reciprocal of the hold time itself. When these substitutions are made in Eq. 4.60, the first term becomes negligible in comparison to the second term. Thus Eq. 4.54 becomes

$$\Delta\epsilon_t = 1.10 N_f^{-0.7} f^{0.133} \quad (4.55)$$

and, since this expression is limited to hold periods in excess of 10 min, it follows that

$$\Delta\epsilon_t = \frac{1.10 N_f^{-0.7}}{(HT)^{0.133}} \quad (4.56)$$

This is an interesting observation because it identifies a linear relation on logarithmic coordinates when N_f is plotted as a function of hold time at a total constant-strain range. Thus rearrangement of Eq. 4.56 gives

$$N_f = \left(\frac{1.10}{\Delta\epsilon_t}\right)^{1.43} (HT)^{-0.19} \quad (4.57)$$

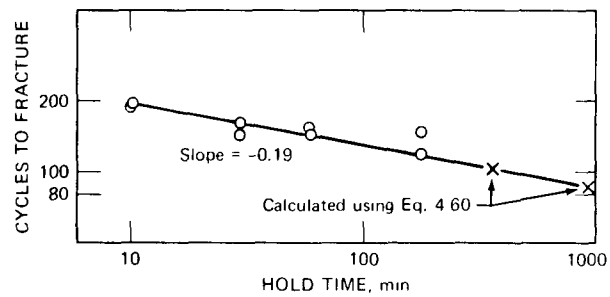

Fig. 4.61 Comparison of hold-time results[43] for AISI 304 stainless steel at 650°C with behavior given by Eq. 4.63.

which, of course, only applies to hold times for 304 stainless steel at 650°C.

Special significance is attached to this expression since a logarithmic graph of N_f vs. HT is linear with a slope equal to –0.19. And, if a 10-min hold-period test is performed, the N_f value obtained can be plotted, and a line can be drawn through this point using a slope of –0.19 to yield predictions of the fatigue life for longer hold periods. This type of construction is shown in Fig. 4.61 for the 304 stainless-steel data at 650°C. When a 10-min hold period was used at a strain range of 2.0%. the N_f value was 193 and 201 in duplicate tests. These data were located, and a line was drawn through the data points using a slope of –0.19. This construction does indeed provide an accurate prediction of the longer hold-period results,[43] which are plotted in Fig. 4.61 for comparison. In addition, the data points calculated with Eq. 4.54 also demonstrate the validity of this approach. This important concept should be given careful consideration in hold-time studies since it can save a great deal of test time. With Eq. 4.57 as a guide, only a minimal number of tests need be performed to confirm the trend behavior specified by this expression. It seems certain that this approach will have considerable value in reducing the scope of experimental programs on hold-time effects.

Interestingly, Eq. 4.57 is identical to the relation reported by Conway and Berling[46] in the analysis of the hold-time (HT) results for 304 stainless steel at 650°C. This is particularly noteworthy since N_f was reported to be linear in hold times on logarithmic coordinates, and the slope was stated to be 0.19.

Data corresponding to hold times in both tension and compression and hold times in compression only were not included in the Coffin analysis.[40] However, since these types of operations[43] are less damaging than hold periods in tension only, Coffin reasoned that the generalized equation would lead to conservative results for such situations.

A limitation should be placed on Eq. 4.57 since some recent data[47] involving a hold period of 600 min in tension only indicate a deviation from the linear behavior in Fig. 4.61 (and, of course, from the generalized equation itself) for very long hold times. This test indicated a fatigue

life of 149 cycles (test duration was about 1500 hr) and can be compared to a predicted life of 95 cycles from the Fig 4 61 correlation. Obviously the linearity described by Eq 4 57 does not persist into the regime for very long hold periods Instead, a decided saturation effect seems (at least for the data involved in this analysis) to indicate a leveling off near a hold period of 100 min This, of course, indicates very little additional reduction in fatigue life beyond a hold period of several hundred minutes

REFERENCES

1 L I Coffin Jr, A Study of the Effects of Cyclic Thermal Stresses on a Ductile Material, *Trans. ASME (Amer. Soc. Mech. Eng.)*, 76 931 950 (1954)

2 S S Manson, Behavior of Materials Under Conditions of Thermal Stress, National Advisory Committee for Aeronautics, Technical Note 2933, 1953

3 J I Tavernelli and L I Coffin, Jr, Experimental Support for Generalized Equation Predicting Low-Cycle Fatigue, ASME Paper 61 WA-199, also, Report ME-83, General Electric Company Research Laboratory, September 1959

4 B I Langer, Design of Pressure Vessels for Low Cycle Fatigue, *J. Basic Eng.*, 84(3) 389 (1962)

5 S S Manson, discussion of ASME Paper 61-WA 199 by Tavernelli and Coffin, *J. Basic Eng.*, 84(4) 537-541 (December 1962)

6 S S Manson, Fatigue A Complex Subject—Some Simple Approximations, Report NASA-TM-X-52084, National Aeronautics and Space Administration, 1965

7 J O'Brien, unpublished notes on NASA contract (see Ref 6)

8 S S Manson, Interfaces Between Fatigue, Creep and Fracture, *Int. J. Fracture Mechanics*, 2(1) 327 (1966)

9 P G Forrest and K B Armstrong, The Thermal Fatigue Resistance of Nickel–Chromium Alloys, in *Joint International Conference on Creep*, The Institution of Mechanical Engineers, London, pp 3-1 to 3 7, 1963

10 A Coles and D Skinner, Assessment of Thermal-Fatigue Resistance of High Temperature Alloys, *J. Roy Aeronaut. Soc.*, 69 53 55, 649 (1965)

11 A E Carden, Thermal Fatigue of a Nickel Base Alloy, *J. Basic Eng.*, 87(1) 237 244 (March 1965)

12 L F Coffin Jr, Cyclic Strain and Fatigue Study of a 0 1% C, 2% Mo Steel, *Trans Met. Soc. AIME*, 230(7) 1690 1699 (December 1964)

13 W A Wood and H D Nine Differences in Fatigue Behavior of Single Copper Crystals and Polycrystalline Copper at Elevated Temperatures, Department of Civil Engineering and Engineering Mechanics, Columbia University, February 1965 (Also available from DDC as Report AD 612 713)

14 G R Gohn and W C Ellis, The Fatigue Test as Applied to Lead Cable Sheath, *Amer. Soc. Test. Mater., Proc.*, 51 721 (1951)

15 S S Manson and G R Halford, A Method of Estimating High Temperature Low Cycle Fatigue Behavior of Materials, in *Proceedings of the International Conference on Thermal and High Strain Fatigue*, held in London, June 6–7, 1967, Monograph and Report Series No 32 The Metals and Metallurgy Trust, London, 1967

16 G R Halford and S S Manson, Application of a Method of Estimating High Temperature Low Cycle Fatigue Behavior of Materials, Report NASA TM-X-52357, National Aeronautics and Space Administration, 1967

17 W F Anderson and W Wahl, Results of High-Temperature Strain Fatigue Tests on Reactor-Grade Aluminum-Base Materials AEC Report NAA-SR-4528, Atomics International, 1961

18 R A T Dawson, W J Elder, G J Hill, and A T Price, High Strain Fatigue of Austenitic Steels, in *Proceedings of the International Conference on Thermal and High Strain Fatigue*, held in London, June 6–7, 1967, Monograph and Report Series No 32, The Metals and Metallurgy Trust, London, 1967

19 H G Edmunds and D J White, Observations of the Effect of Creep Relaxation on High-Strain Fatigue, *J. Mech. Eng. Sci.*, 8(3) 310 (1966)

20 A Johansson, Fatigue of Steels at Constant Strain Amplitude and Elevated Temperature, Colloquium on Fatigue of Metals, p 112 Springer Verlag, Berlin, 1956

21 A Coles, G J Hill, R A T Dawson, and S J Watson, The High Strain Fatigue Properties of Low-Alloy Creep-Resisting Steels, in *Proceedings of the International Conference on Thermal and High Strain Fatigue*, held in London, June 6–7, 1967, Monograph and Report Series No 32, The Metals and Metallurgy Trust, London, 1967

22 C D Walker, Strain Fatigue Properties of Some Steels at 950°F (510°C) with a Hold in the Tension Part of the Cycle, in *Joint International Conference on Creep*, Session 3, Paper 24, p 49, The Institution of Mechanical Engineers, London, 1963

23 A Coles and A Chitty Ductility and Reverse-Bend Fatigue Behavior of C–Mo and Cr–Mo–V Steel, in *Proceedings of the International Conference on Thermal and High Strain Fatigue*, held in London, June 6–7, 1967, Monograph and Report Series No 32, The Metals and Metallurgy Trust, London, 1967

24 G J Hill, The Failure of Wrought 1% Cr–Mo–V Steels in Reverse Bending, in *Proceedings of the International Conference on Thermal and High Strain Fatigue*, held in London, June 6–7, 1967, Monograph and Report Series No 32, The Metals and Metallurgy Trust, London, 1967

25 R W Swindeman, Fatigue of Austenitic Stainless Steels in the Low and Intermediate Cycle Range, Oak Ridge National Laboratory, USAEC Report ORNL TM-1363, Oak Ridge National Laboratory, 1966

26 G Sumner, The Low Endurance Fatigue Behavior of a 20% Cr–25% Ni–0 7% Nb Stainless Steel at 25, 650, and 750°C, in *Proceedings of the International Conference on Thermal and High Strain Fatigue*, held in London, June 6–7, 1967, Monograph and Report Series No 32, The Metals and Metallurgy Trust, London, 1967

27 G J Danek, Jr, H H Smith, and M R Achter, High-Temperature Fatigue and Bending Strain Measurements in Controlled Environments, *Amer Soc. Test. Mater. Proc.*, 61 775 (1961)

28 C H Wells and C P Sullivan, Low Cycle Fatigue Damage of Udimet 700 at 1400°F, *ASM (Amer. Soc. Metals), Trans. Quart.*, 58: 391 (1965)

29 P G Forrest and K B Armstrong, Investigation of the Thermal Fatigue Behavior of Nickel–Chromium Base Alloys by Strain Cycling Tests, *J. Inst. Metals*, 94(8) 204 (1966)

30 J I Berling and P Slot, Effect of Temperature and Strain Rate on Low Cycle Fatigue Resistance of AISI 304, 316, and 348 Stainless Steels, in *Fatigue at High Temperature*, pp 3-30, American Society for Testing and Materials, Special Technical Publication No 459, 1969, also, USAEC Report GEMP 642, General Electric Company, 1968

31 I Slot and R H Stentz, Experimental Procedures for Low Cycle Fatigue Research at High Temperatures, *Exp. Mech.*, 8(3) 107 114 (March 1968)

32 J T Berling and J B Conway, A Proposed Method for Predicting the Low Cycle Fatigue Behavior of 304 and 316 Stainless Steel, *Trans. Met. Soc. AIME*, 245 1137-1140 (1969)

33 J P Smith J I Berling and J Moteff General Electric Company Nuclear Systems Programs Cincinnati Ohio unpublished

34 J I Berling and J B Conway New Approach to the Prediction of Low Cycle Fatigue Data *Met Trans*, 1 805 809 (1970)

35 J B Conway J T Berling R H Stentz and D G Salyards Stress Strain Behavior of Several Stainless Steels to Elevated Temperatures USAEC Report GEMP 686 General Electric Company May 1969

36 R H Stentz J T Berling and J B Conway A New Approach to Measuring Short Term Tensile Behavior USAEC Report GEMP 705 General Electric Company July 1969

37 C E Feltner and R W Landgraf Selecting Material To Resist Low Cycle Fatigue *Trans ASME (Amer Soc Mech Eng), Ser D, J Basic Eng*, 93 444 (September 1971)

38 Jo Dean Morrow Cyclic Plastic Strain Energy and Fatigue of Metals in *Symposium on Internal Friction, Damping and Cyclic Plasticity, Chicago, 1964*, American Society for Testing and Materials Special Technical Publication No 378 p 45 1965

39 O H Basquin The Exponential Law of Endurance Tests *Amer Soc Test Mater Proc*, 10 625 (1910)

40 L F Coffin Jr A Generalized Equation for Predicting High Temperature Low Cycle Fatigue Including Hold Times Report 69 C 401 General Electric Company Research and Development Center December 1969

41 L F Coffin Jr Predictive Parameters and Their Application to High Temperature Low Cycle Fatigue in *Proceedings of the Second International Conference on Fracture, Brighton, 1969*, pp 643 654 Chapman & Hall Ltd London 1969

42 C J McMahon and L F Coffin Jr Mechanisms of Damage and Fracture in High Temperature Low Cycle Fatigue of a Cast Nickel Based Superalloy General Electric Company Research and Development Center internal report 1969

43 J T Berling and J B Conway Effect of Hold Time on the Low Cycle Fatigue Resistance of 304 Stainless Steel at 1200°F in *First International Conference on Pressure Vessel Technology*, held at Delft Holland 1969 Part 2 Materials and Fabrication p 1233 American Society of Mechanical Engineers New York

44 J I Gammett Elevated Temperature Low Cycle Fatigue Behavior of Rene 41 Report R69 AEG 332 General Electric Company July 7 1969

45 J B Conway Mar Test Inc Cincinnati Ohio unpublished

46 J B Conway and J T Berling A New Correlation of Low Cycle Fatigue Data Involving Hold Periods *Met Trans*, 1 324 (1970)

47 J B Conway Evaluation of Plastic Fatigue Properties of Heat Resistant Alloys USAEC Report GEMP 740 General Electric Company 1969

Chapter 5

CUMULATIVE-DAMAGE CONCEPTS

Short term tensile, creep rupture, and fatigue evaluations all involve loadings that eventually result in fracture. Another common characteristic of these assessments of material strength is the important information obtained prior to fracture. This includes the yield and flow stress behavior in the tensile test, the strain time behavior in the creep-rupture evaluation, and the cyclic hardening or softening and crack initiation behavior in the fatigue tests. Still another common characteristic of these tests is that the material is being 'damaged' as the test endures. Damage is not always obvious, but it is not unreasonable to envision the period between load application and fracture as one in which the amount of damage is continually increasing with time. A direct conclusion from this interpretation is that damage gradually accumulates or builds up as the exposure time increases and the material quality or the remaining performance capability diminishes. Also, the cumulative effect tends toward a certain limit, and fracture or failure occurs once the total damage attains a certain critical value.

Just how much damage is sustained in a certain exposure time and how this relates to the ability of a material to withstand further exposure are difficult questions to answer quantitatively. So is the question of whether or not the damage accumulation rate is constant once the exposure begins. Of course, much work has been done to understand these important aspects of material behavior, but the results obtained, although valuable, have not led to a complete rationalization of the observed behavior patterns. Thus much work remains to be done before a general understanding can be obtained. For example, data are available which indicate that the exposure of certain materials to certain conditions for a certain time does nothing to impair the subsequent performance capabilities, and hence the material can be treated as if it had never been previously exposed. Other exposures have revealed different effects, which vary from increased performance to suggest an enhancing effect of the initial exposure, to proportionate performance commensurate with the damage done in the initial exposure, and even to decreased performance to suggest an exaggerated degradation of the material due to the initial exposure. Further complications are associated with the fact that the effect of an initial exposure or type of exposure is not completely confirmed in all instances. Some data identify a certain effect for a given material and test condition, whereas data obtained in another study have been known to refute this observation. In fact, this failure to agree on a specific effect has been noted within a given study when the type of exposure has been varied. Although much is known in this area of material behavior, these comments identify a need for more information if this phase of material response is to be understood.

Exposure to a fatigue influence has led to reductions in the original endurance limit,[1,2] a lowering in the ultimate tensile strength,[3,4] a reduction in the fracture ductility,[5] and changes in the apparent dynamic modulus of elasticity and the damping characteristics.[6] These factors, of course, represent definite indications of damage and have been employed in attempts to express fatigue damage in a quantitative manner. One well-known attempt to be quantitative about damage involves the determination of how much fatigue life remains at another condition once the material has been exposed to a fatigue influence at an initial condition. A detailed explanation of this problem area constitutes the primary objective of this chapter. Associated with this is a study of combined creep and fatigue interactions, for it is well established that creep effects play a vital part in certain fatigue exposures.

LINEAR-DAMAGE LAW

Special recognition has been accorded the Palmgren–Langer–Miner[7-9] relation, which is termed the "Linear Damage Rule" or the "Linear Cumulative-Damage Rule." Although experimental data have shown this rule to be only approximate under many conditions, it is still widely used and serves to provide useful approximations.

In discussing this very simple concept, Miner[9] assumed that the damage associated with an exposure to N cycles of a given cyclic loading could be expressed as the value of N divided by the number of cycles required to produce failure at the given loading level. Such an expression, of course, corresponds to a life or cycle fraction and can be viewed as that proportional or fractional part of the useful life which disappears or is lost owing to the given exposure. Miner further postulated that failure would occur when the summation of all the damage fractions was equal to unity.

Miner gave mathematical form to the linear-damage rule in a development that involved the net work absorbed by the material under a given set of exposure conditions The net work absorbed by the material at failure was represented by W, w_1 was the work absorbed by the material in a given exposure to n_1 cycles For failure in N_1 cycles, it was stated that

$$\frac{w_1}{W} = \frac{n_1}{N_1} \tag{5.1}$$

with similar expressions possible for w_2, n_2, N_2, etc Since the failure conditions corresponded to

$$w_1 + w_2 + w_3 + \ldots + w_n = W \tag{5.2}$$

it follows that

$$\frac{w_1}{W} + \frac{w_2}{W} + \frac{w_3}{W} + \ldots + \frac{w_n}{W} = 1 \tag{5.3}$$

and, of course, from Eq 5.1 that

$$\frac{n_1}{N_1} + \frac{n_2}{N_2} + \frac{n_3}{N_3} + \ldots + \frac{n_n}{N_n} = 1 \tag{5.4}$$

or more simply

$$\sum_{1}^{1} \frac{n_1}{N_1} \quad 1 \tag{5.5}$$

This is the mathematical relation for the Palmgren–Langer–Miner linear-damage law.

A widely used graphical representation of the relation given by Eq. 5.5 is as follows

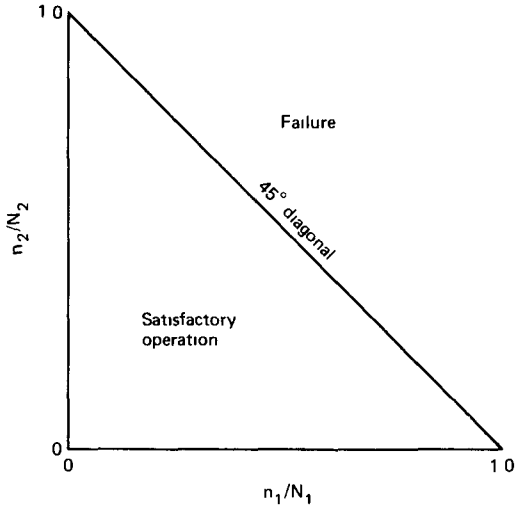

For a two-step loading condition,

$$\frac{n_1}{N_1} + \frac{n_2}{N_2} = 1 \tag{5.6}$$

where n_1 and n_2 represent the number of exposure cycles and N_1 and N_2 represent the cycles to failure at the exposure conditions if these conditions were imposed in separate single-condition tests. The mathematical form of Eq. 5.6 is represented by the 45° diagonal. This linearity is based on damage accumulating in the same manner at each condition so that the life that remains after exposure to a given condition is easily obtainable using this graphical solution. For example, if the initial condition is applied for 40% of the fatigue life, the linear damage rule requires that the specimen endure for 60% of the fatigue life corresponding to the second exposure condition. Also identified in this plot are areas of safe and unsafe operations. Any point above the 45° diagonal is a failure point if the linear-damage concept is applicable

Experimental verification of the linear-damage law was provided by Miner in tests of short specimens of Alclad 24S-T at room temperature Basic S–N curves were first established at R ratios (minimum to maximum stress) of 0.50, 0.20, and −0.20. Specimens were exposed to several different maximum stress values at R = 0 2 and −0 2 and in other tests to various stress and R-ratio combinations These exposures were used in conjunction with the S–N curves to calculate the damage fractions associated with each exposure condition, and then the damage summations were calculated. Damage summations ranged from 0.61 to 1 49, and it was reported that the average of all the damage summations was very close to unity. These axial-load-controlled tests were interpreted by Miner as being confirmatory, and it was concluded that the linear-damage law provided "a simple and conservative analysis."

Not always appreciated, and perhaps even overlooked, are the large errors involved in certain damage-fraction summations that deviate from unity. Deviations associated with summations greater than unity are not usually of great concern, since in these instances the actual performance is greater than predicted However, summations less than unity should be a cause for some concern For example, in one test reported by Miner the damage summation was 0.61, which in itself does not appear to be a large enough deviation from unity to be concerned about However, this summation obscures the fact that in this test the first two of three exposure conditions consumed 57% of the life according to the linear-damage law. And at the final exposure condition the material should have survived some 100,000 cycles, but the material failed after an exposure of only 9100 cycles. This is an order-of-magnitude error and one that is not readily appreciated by merely noting the relatively small deviation of the damage summation from unity.

A study by Rey[10] was oriented to provide a fairly extensive evaluation of the linear-damage law. Tests were performed at room temperature and at 400 and 800°F using SAE 4130 alloy steel Rotating-beam fatigue tests were performed using $\frac{5}{16}$-in -diameter specimens, and S–N curves were established for use with two-, three-, and

five-step loadings Damage-fraction summations ranged from 0.652 to 1 481 in the two-step loadings at room temperature, from 0 461 to 1 05 in the two-step loadings at 400°F, and from 0 379 to 0.884 in the five step loadings at 800°F. On the basis of these results, Rey concluded that the linear-damage law is not completely reliable, since it can overpredict the exposure life This study also concluded that, regardless of whether a high or low stress is applied first, the number of different stress amplitudes applied and the magnitude of each stress level relative to the endurance limit are among the variables affecting fatigue damage

In an excellent interpretive report on cumulative fatigue damage, Manson[11] cited two important limitations relating to the Palmgren–Langer–Miner law The first limitation concerns the fact that Eq 5 5 suggests no order of-loading effect, whereas experiments have shown that high-loads first exposures are more damaging than the reversed sequence A second shortcoming of the Palmgren–Langer–Miner law is associated with the effects of exposures to stress levels below the endurance limit Since N_1 would be infinite, the damage fraction for limited exposures should be zero, and these stress levels should have no effect on the subsequent performance of the material It is found, however, that prior exposure to a high stress level can reduce the endurance level by introducing imperfections or cracks in the material Subsequent operations at a stress level lower than the initial endurance limit may be able to propagate the imperfection because of the stress concentration associated with it, even though this stress level could cause no damage if used first Manson also referred to the review[12] of various damage studies all of which account in one way or another for the reduction in the endurance limit which is associated with fatigue damage As a final conclusion Manson suggested that the linear damage law can be used as a first approximation without fear of gross error for most practical cases

Manson[11] also briefly described the more recent approaches devoted to cumulative damage, these included the work of Manson,[13] Manson, Nachtigall, and Freche,[14] Fuller,[15] and Valluri[16] All approaches were designed to offer methods by which the deficiencies associated with the Palmgren–Langer–Miner law could be circumvented Admittedly, however, each approach is more involved than the simpler damage rule and, in addition, requires more information in terms of material properties For example, Manson,[13] in describing his proposed method, emphasized that a rotation of the S–N lines is involved and that the determination of the extent of this rotation requires additional data Mention was made that the Palmgren–Langer–Miner rule requires that the S–N line (a plot of stress vs log N was assumed to be linear for this illustration) for damaged material moves uniformly to the left as damage accumulates but is always parallel to the line for the original material [Fig 5 1(a)] In comparison, the Manson approach suggests that the S–N line for the damaged material is not parallel to the line for the original material but instead diverges from this line All lines for various damage fractions were assumed to intersect at a common point located on the original S–N line A given cycle fraction applied at a high stress leads to a steeper slope than the same cycle fraction applied at a low stress level [Fig 5 1(b)] This feature is consistent with the familiar experimental observation that high-to-low exposures were more damaging than low to-high exposures Before this approach can be used, the intersection point R must be determined, and some information must be obtained to determine the shift in the endurance limit for different damage levels

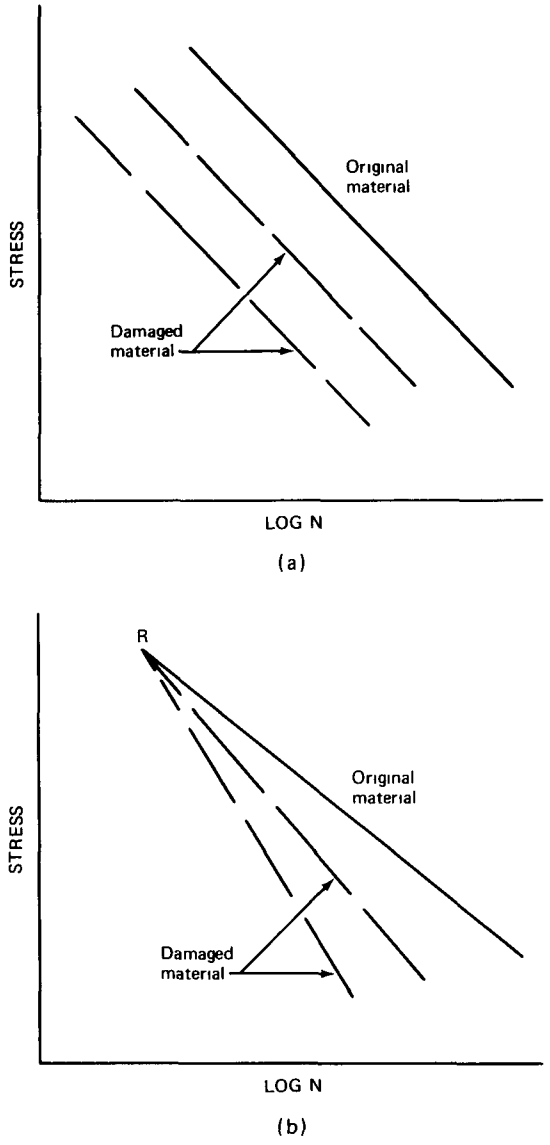

Fig 5.1 Graphical representation of different damage levels in (a) Palmgren–Langer–Miner and (b) Manson methods.

In a detailed study of cumulative damage and the effect of mean stress, Ohji, Miller, and Marin[17] referenced several studies of the linear-damage rule, this information is summarized in Table 5 1 Interestingly, the range of the

TABLE 5.1

SUMMARY OF RESULTS OBTAINED IN CUMULATIVE-DAMAGE STUDIES

Author	Ref.	Material	Type of test	Range of $\Sigma(n/N)$
Gross and Stout	20	A-302 steel	Bending	0.85–1.35
Low	21	Aluminum alloy	Bending	0.75–1.49
D'Amato	22	2024-T4 aluminum alloy	Axial	0.77–1.48
Gücer	23	A-201 and A-302 steels	Bending	0.83–1.31
Sachs and Weiss and Weiss et al.	18 19	A-302 and A-225 steels; 5454-O and 2024-T4 aluminum	Axial and bending	0.6–1.6
Kikukawa	24	Mild steel	Axial	0.73–1.12
Baldwin et al.	25	347 stainless steel	Axial	0.88–1.99

TABLE 5.2

SUMMARY OF CUMULATIVE-DAMAGE DATA FOR 2024-T351 ALUMINUM ALLOY TESTED AT ROOM TEMPERATURE (FROM REF. 17)

No.	ϵ_{TR_1}	ϵ_{TR_2}	n_1	N_1	n_2	N_2	n_1/N_1	n_2/N_2	$\Sigma n/N$	n_L/n_H^* ①	n_L/n_H^* ②
80	0.0500	0.0200	39	45	98	422	0.867	0.231	1.098	5	2.51
81	0.0500	0.0200	28	45	200	422	0.622	0.474	1.096	5	7.14
84	0.0500	0.0200	23	45	200	422	0.511	0.474	0.985	5	8.70
85	0.0250	0.0100	106	250	600	2200	0.424	0.273	0.697	5	5.66
86	0.0250	0.0100	111	250	601	2200	0.444	0 273	0.717	5	5.41
87	0.0250	0.0100	120	250	660	2200	0.480	0.300	0.780	5	5.50
88	0.0250	0.0100	40	250	1088	2200	0.160	0.494	0.654	20	27.2
89	0.0250	0.0100	60	250	1401	2200	0.240	0.636	0.876	20	23.4
95	0.0250	0.0100	52	250	1200	2200	0.208	0.545	0.753	20	23.1
102	0.0500	0.0200	10	45	248	422	0.222	0.588	0.810	20	24.8
103	0.0500	0.0200	10	45	250	422	0.222	0.592	0.814	20	25.1
105	0.0500	0.0200	10	45	251	422	0.222	0.594	0.816	20	25.1
111	0.1000	0.0200	3.25	8	400	422	0.406	0.947	1.353	100	123
112	0.1000	0.0200	3.25	8	400	422	0.406	0.947	1.353	100	123
113	0.1000	0.0200	2.5	8	300	422	0.312	0.711	1.023	100	120
115	0.0500	0.0200	14	45	282	422	0.311	0.668	0.979	20	20.1
126	0.0500	0.0200	14	45	194	422	0.311	0.460	0.771	20	13.9
118	0.0500	0.0200	14	45	214	422	0.311	0.505	0.818	20	15.3
128	0.0200	0.0500	288	422	2.5	45	0.681	0.056	0.737	20	115
125	0.0200	0.0500	288	422	2.5	45	0.681	0.056	0.737	20	115
119	0.0200	0.0500	288	422	4.5	45	0.681	0.100	0.781	20	64

*n_L are the cycles at the low strain range, n_H at the high strain range; ① and ② signify the programmed and actual ratios, respectively; total strain range is given by ϵ_{TR}.

summation values in Table 5.1 is essentially identical to that reported in the early studies of the linear-damage rule. Sachs and Weiss[18] and Weiss et al.[19] observed that a high precycling strain followed by a lower strain value gave a summation greater than unity, whereas a summation less than unity was observed when the lower strain value was imposed first. This is contrary to previously reported behavior and would appear to warrant further investigation.

Experimental studies by Ohji, Miller, and Marin focused on 2024-T351 aluminum alloy tested at room temperature in completely reversed constant-strain-range evaluations at a frequency of 10 cycles/min. These test results are summarized in Table 5.2. A test pattern was used in which selected n_L/n_H ratios (see Table 5.2 for definition) were repeated until failure; this was done to eliminate any effect of the order of imposing the strain levels. Most of these

data are seen to yield summations lower than unity. In the last six tests in Table 5.2, the repetitive straining pattern was abandoned and, instead, one strain level was applied for a selected number of cycles and then the specimen was tested at another strain level until fracture occurred. No definite effect of straining order was reported, but it would appear from these data that the low-to-high pattern is more damaging. This same conclusion was reached by Sachs and Weiss[18] and by Weiss et al.[19] and is contrary to that reported by previous investigators. Obviously this behavior pattern needs to be studied in more detail.

Cumulative-damage concepts were also studied extensively by Brook and Parry[6] in room-temperature high-frequency evaluations of a creep-resistant stainless steel (Rex 535) in the fatigue-life range from 10^4 to 10^8 cycles. Changes in apparent dynamic modulus of elasticity and in damping characteristics were used to assess fatigue damage, and this information was used in estimating the fatigue life in multiple stress exposures. Impressive correlations were described which related fatigue life to the rate of change of modulus and the rate of change of damping. These rates were found to develop early in the test at a given stress level and to remain constant until the fracture point was approached. Thus, in a given test, this rate was observed early in the test, and this information could be used to predict the fatigue life. Such information was used in cycling a specimen at a selected stress level until a certain life remained (10,000, 20,000, 30,000, or 40,000 cycles); then the stress level was changed, and the specimen was cycled until fracture occurred. In this way the remaining life at the second stress level was measured and used in conjunction with the remaining life at the first stress level to establish "points of equal damage" and "lines of equal damage." An example of the observed points of equal damage is as follows (from Ref. 6):

POINTS OF EQUAL DAMAGE[6]

Stress amplitude, ±tsi	Equivalent remaining fatigue life, cycles			
48	10,000	20,000	30,000	40,000
44	43,500	64,000	80,000	128,000
40	155,000	217,000	266,000	313,000
36	405,000	692,000	871,000	1,076,000
32	954,000	1,862,000		
28	$>55 \times 10^6$			

In other words, a specimen exposed to a stress amplitude of 48 tsi until the remaining life was 40,000 cycles would have a remaining life of 128,000 cycles if the exposure conditions were changed to ±44 tsi. The studies by Brook and Parry also provided an interesting comparison with the predictions based on the linear-damage rule, and three examples were cited:

1. If an average virgin specimen is cycled for 75% of the average life at 44 tsi (the remaining life now being 54,000 cycles) and is then cycled to failure at 48 tsi, the specimen will fail after almost exactly 25% of the average life at 48 tsi. Linear law is very good.

2. If an average virgin specimen is cycled for 75% of the average life of 40 tsi (remaining life is now 365,000 cycles) and is then cycled to failure at 44 tsi, the specimen will fail after about 70% of the average life at 44 tsi, and not after only 25% as forecast by the linear law. Linear law is rather pessimistic.

3. If an average specimen is cycled for 80% of the average life at 44 tsi (remaining life is now 43,000 cycles) and is then cycled to failure at 36 tsi, the specimen will fail after 405,000 cycles, and not after over 14.3 million cycles as forecast by the linear law. Linear law is dangerously optimistic.

Lines of equal damage were also developed for multiple stress exposures to demonstrate the effectiveness of this approach. Whether this equal-damage concept applies at elevated temperatures and when significant plastic straining occurs remains to be determined.

DOUBLE LINEAR-DAMAGE RULE

Grover,[26] Manson,[27] and Manson, Freche, and Ensign[28] suggested an improvement of the linear-damage rule. In this approach the fatigue life was considered in terms of a crack-initiating phase and a crack-propagation phase, and a linear-damage rule was applied in each phase. It was proposed[27] that the crack-propagation period $(\Delta N)_f$ and crack initiation N_0 can both be expressed in terms of the total fatigue life N_f. The following equations were written:

$$(\Delta N)_f = P N_f^{0.6} \tag{5.7}$$

and

$$N_0 = N_f - (\Delta N)_f = N_f - P N_f^{0.6} \tag{5.8}$$

where the value of P was identified to be 14.0. Then, for the crack-initiation phase,

$$\sum \frac{n}{N_0} = 1 \tag{5.9}$$

with the following stipulations:

When $N_f > 730$ cycles,

$$N_0 = N_f - 14 N_f^{0.6}$$

When $N_f < 730$ cycles,

$$N_0 \approx 0$$

In other words, if any portion of the exposure included a condition such that $N_f < 730$ cycles, an effective crack is presumed to initiate upon application of the first loading cycle.

For the crack-propagation phase, the relation of interest is written as

$$\sum \frac{n}{(\Delta N)_f} = 1 \tag{5.10}$$

with the following stipulations:

When $N_f > 730$ cycles,

$$(\Delta N)_f = 14N_f^{0.6}$$

When $N_f < 730$ cycles,

$$(\Delta N)_f = N_f$$

In the above definitions the following symbols apply:

N_0 = cyclic life to initiate an effective crack at a particular strain or stress level
$(\Delta N)_f$ = cyclic life to propagate a crack from initiation to failure at a particular strain or stress level
N_f = cyclic life to failure
n_i = number of cycles applied at a particular strain or stress level

An example of how these relations apply to a two-condition exposure begins by considering two stress levels for which the fatigue life is given by N_{f1} and N_{f2}. Assume also that the material was exposed to the first stress level for n_1 cycles, and then calculate the number of cycles remaining prior to failure at the second stress level. Values of ΔN_1 and ΔN_2 are first calculated using Eq. 5.7, and values of N_{01} and N_{02} are then obtained using Eq. 5.8. The ratio N_{01}/N_{f1} is then calculated. When $N_{f1} > 730$ cycles, if n_1/N_{f1} is equal to N_{01}/N_{f1}, the crack-initiation stage has just been completed, and the cyclic life remaining at the second stress level is exactly equal to that making up the crack-propagation period, or

$$n_2 = N_{f2} - N_{02} = \Delta N_2 \tag{5.11}$$

If the ratio $n_1/N_{f1} > N_{01}/N_{f1}$, the life remaining at the second stress level may be expressed as:

$$n_2 = \left(1 - \frac{n_1 - N_{01}}{\Delta N_1}\right) \Delta N_2 \tag{5.12}$$

If the ratio $n_1/N_{f1} < N_{01}/N_{f1}$, the life remaining at the second stress level may be expressed as:

$$n_2 = \left(1 - \frac{n_1}{N_{01}}\right) N_{02} + \Delta N_2 \tag{5.13}$$

When $N_{f1} < 730$ cycles, it is assumed that there is no lengthy crack-initiation period and that the total life consists only of crack propagation. Then the life remaining at the second stress level can be determined from the following expression:

$$n_2 = \left(1 - \frac{n_1}{N_{f1}}\right) \Delta N_2 \tag{5.14}$$

In this instance the remaining life at the second stress level is calculated from the linear-damage rule for crack propagation only.

The double linear-damage rule is shown[28] in Fig. 5.2, where the ordinate defines the remaining life-cycle ratio

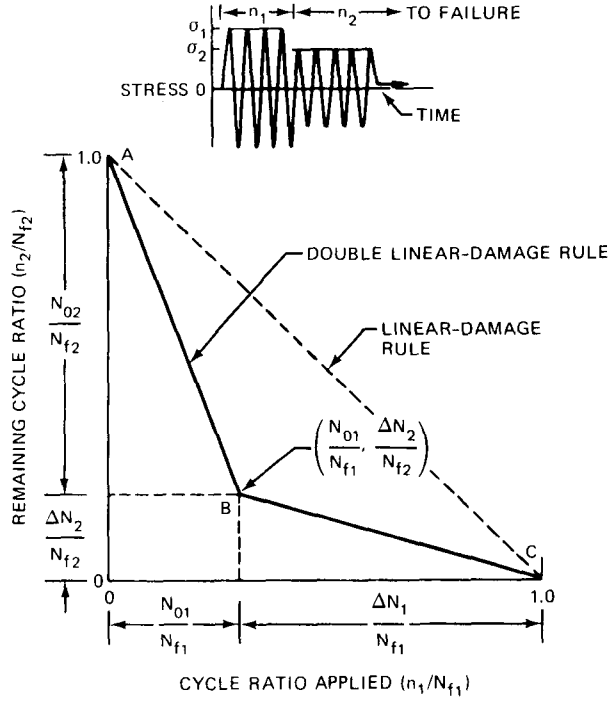

Fig. 5.2 Illustration of the double linear-damage concept. (From Ref. 28.)

n_2/N_{f2} at the second stress level when the cycle ratio for the first stress level is known. The dashed 45° line in Fig. 5.2 represents the linear-damage law discussed earlier. This figure corresponds to the case in which the prestress condition is the high stress, and this is followed by operation to failure at a lower stress. The position of lines AB and BC would be located to the left of the 45° line for the condition of low prestress followed by operation to failure at a high stress. According to the double linear-damage rule, if the cycle ratios applied (n_1/N_{f1}) are less than the number required to initiate an effective crack at a particular stress level, then the remaining predicted cyclic life ratio (n_2/N_{f2}) would lie along line AB. The linearity of line AB is implicit in the assumption of a linear-damage rule for crack initiation. Point B represents the cycle ratio applied at the first stress level which is sufficient to initiate an effective crack; thus, upon changing to the second stress

level, the remaining cycle ratio at that stress level is exactly equal to the total propagation stage. The coordinates of this point are designated as N_{01}/N_{f1} and $\Delta N_2/N_{f2}$. Beyond this initial cycle ratio, N_{01}/N_{f1}, the first applied cycle ratio is more than that required to initiate an effective crack, and the crack-propagation phase is entered. This is represented by line BC, which is also straight, reflecting the second assumed linear relation. The remaining cyclic life ratio then lies along line BC. Thus, in two-step tests in which a single stress level was applied for a given cycle ratio and the remainder of the life taken up at a second stress level, two straight lines positioned as shown would be expected Point B is significant because it permits determination of both the effective crack-initiation and -propagation periods for both stress levels used in the test.

A final point should be made on the graphical application of the double linear-damage rule. Since lines AB and BC are straight and since points A and C are fixed, ideally only two tests are required to establish the positions of these lines and consequently point B. The only requirement for selecting these tests is that in one test the cycle ratio applied at the initial stress level should be relatively large and in the other test it should be relatively small to ensure that the remaining cycle ratios n_2/N_{f2} do not both fall on the same straight line, either AB or BC.

In the study by Manson, Freche, and Ensign,[28] the specimens were subjected to rotating bending in modified Moore and Krouse rotating-beam fatigue machines and to reversed-axial strain cycling in hydraulically actuated axial-fatigue machines. An example of these test results is presented in Fig 5.3. The stress levels were so chosen that life at the initial stress was approximately 1000 cycles and, at the second stress, 500,000 cycles Experimental data are shown by the circles. The solid lines represent predicted behavior by the double linear-damage rule using different values of the coefficient in Eq. 5.7. For a value of the coefficient equal to 14, the predicted behavior was represented by the line ABG, for a coefficient of 12, it was ACG, etc If a linear-damage rule applied for the total life values, the behavior would be that shown by the dashed line AG. A reasonable agreement with the experimental data was obtained for a coefficient of 14. Since these data represent only one material and one combination of high and low stress, Eq. 5.7 was only tentatively proposed as being representative of cumulative-fatigue-damage behavior.

This approach was extended by conducting many additional tests with the same and with other materials in rotating bending and reversed-axial strain cycling. Predictions of fatigue behavior by the double linear-damage rule (using the expression $14N_f^{0.6}$ to represent the crack-propagation stage) and the conventional linear-damage rule are compared with experimental data in Figs. 5 4 and 5 5. Different loading combinations corresponding to different life levels were chosen. Figure 5.4(a) presents the results from rotating bending tests for maraged 300 CVM steel designed to give relatively low fatigue lives of 1280, 1870,

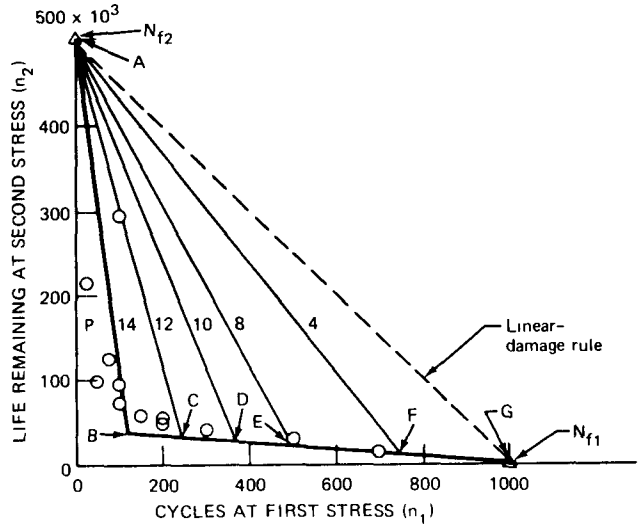

Fig. 5.3 Two stress-level fatigue test of 300 CVM steel. —, predicted using $(\Delta N)_f = PN_f^{0.6}$. ○, individual data for two stress-level tests. △, average of three data points for original S–N tests. P is the constant in Eq. 5.7. (From Ref. 28.)

2050, and 2350 cycles at the initial stress level. The loads at the second stress level were chosen to give lives up to 940,000 cycles. Generally the greater the difference between the initial and final life level (that is, initial and final stress applied), the greater the deviation between the experimental data and the predicted behavior by the conventional linear-damage rule shown by the 45° dashed line, also, the steeper is the first (corresponding to line AB, Fig 5.2) of the two solid lines, which predict fatigue behavior by the double linear-damage rule. Agreement between predicted fatigue behavior by the double linear-damage rule and experimental data is good for these test conditions. This might be expected since the higher stress level as well as some of the lower stress levels are generally of the same order as those selected originally for determining Eq 5.7 for this same material [27]

Figure 5.4(b) deals with the same material but considers other combinations of test conditions in which the initial life level is relatively high. It is apparent that the greatest discrepancies between experimental data and predicted fatigue behavior by the double linear-damage rule as originally proposed occur when both the initial and final life levels are high. This double linear-damage rule would be expected to predict almost the same fatigue behavior as the conventional linear-damage rule in these cases since the crack-propagation period as determined from Eq. 5.7 would be relatively small This is readily seen by using Eq 5.7 for N_{f1} values of 15,925 cycles, 47,625 cycles, 44,000 cycles, and so forth, the specific conditions considered in Fig. 5.4 The experimental data show appreciably lower values of remaining cycle ratios, n_2/N_{f2}, than would be expected by either rule.

Figure 5 4(c) shows the results obtained under conditions of axial strain cycling with maraged 300 CVM steel.

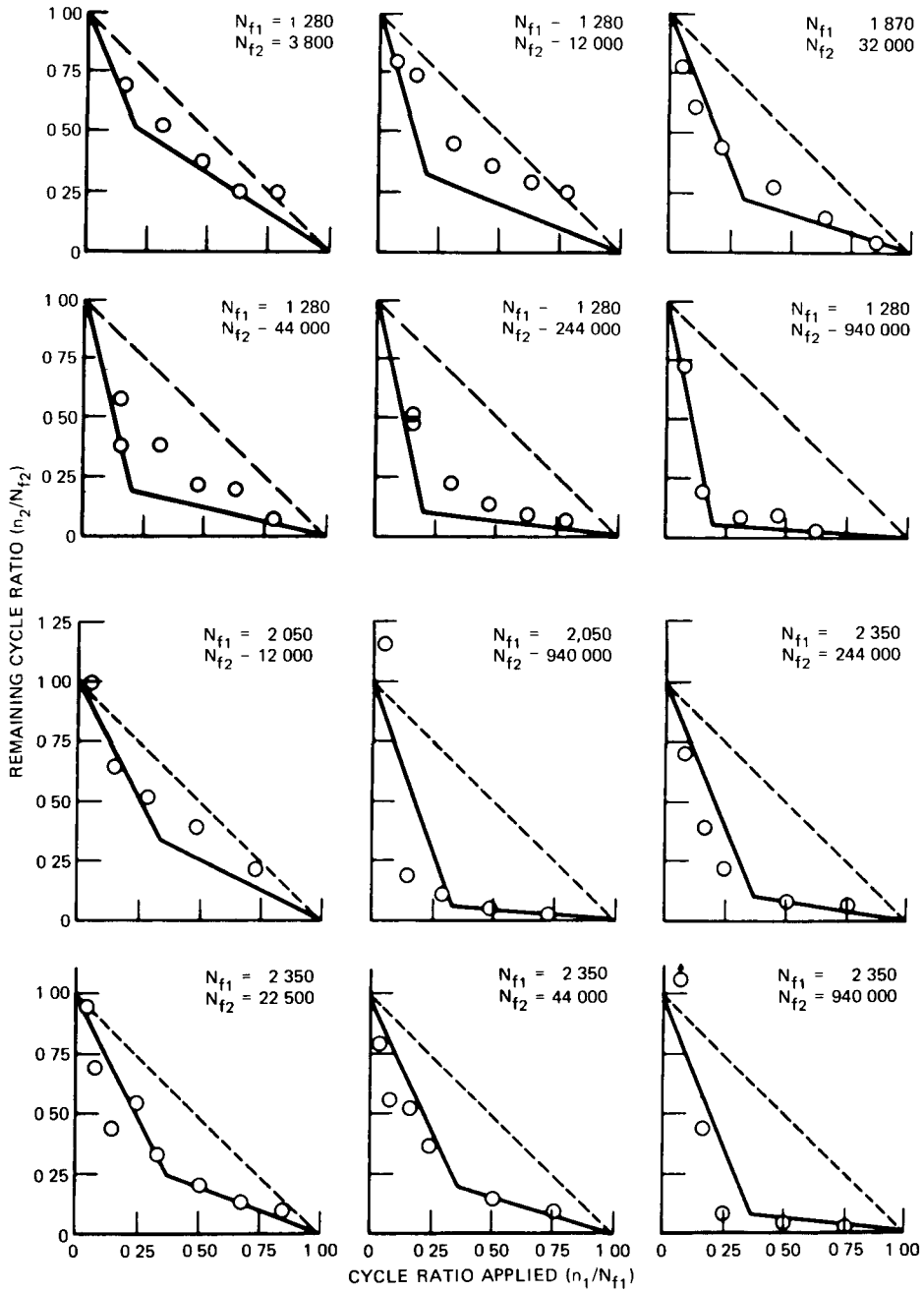

(a) G N Krouse rotating bending high to-low stress with low initial life

Fig. 5.4 Comparison of experimental data with predicted fatigue behavior based on linear- and double linear-damage rules for maraged 300 CVM steel. – – –, conventional linear-damage rule. —, double linear-damage rule. (Figure continued on pp. 120 and 121.) (From Ref. 28)

The initial life level was chosen in all cases to be less than 730 cycles. For this case the major part of the fatigue life would be taken up by the crack-propagation period according to the expressions thus far assumed for crack propagation and initiation in applying the double linear-damage rule. Since there is essentially no crack-initiation stage, the predictions by the double linear-damage rule should coincide with those by the conventional linear-damage rule. This was the case for the two conditions in which the final stress level was chosen so as to give a low value of life, N_{f2}, and the experimental data agreed well with the predictions. However, when the second stress level was chosen so as to give a long life, N_{f2} = 15,950 cycles, the predicted fatigue life by the double linear-damage rule was less than that obtained experimentally. From Figs. 5.4(b) and (c), it is apparent that there are deviations

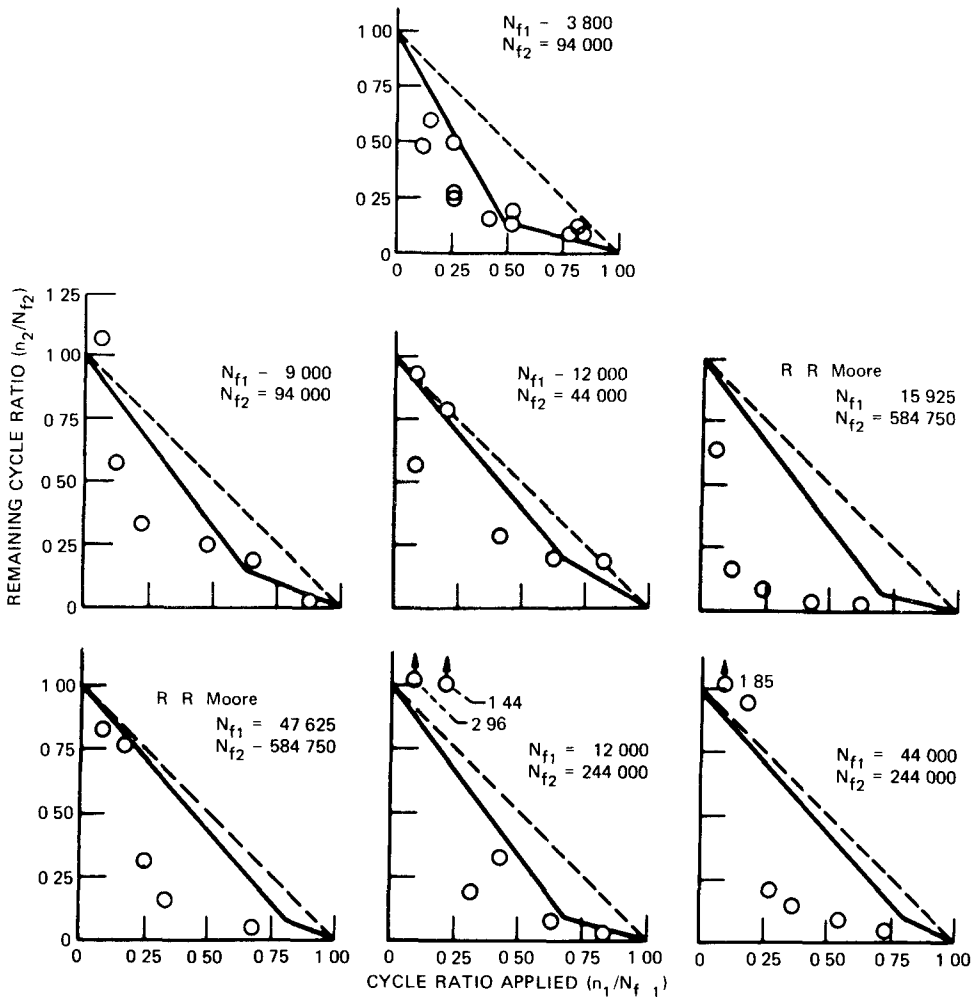

(b) G N Krouse rotating bending high to-low stress with high initial life

Fig. 5.4 (Continued)

of the experimental data on both sides of the predictions made by the double linear damage rule when the expression $14N_f^{0\ 6}$ was used to represent the crack-propagation stage

Figure 5 4(d) illustrates the case when the lower stress is applied first Except for the single axial-strain-cycling test, the predictions by the double linear damage rule show general agreement with the experimental data Regardless of deviations of individual data points from the predictions, it is evident from the figure that the order effect of loading is accounted for by the double linear-damage rule

The results for SAE 4130 steel are shown in Fig 5 5. Figure 5 5(a) deals with tests in which the initial life level was low, and loads at the second stress level were chosen to give various life values up to 203,000 cycles Figure 5.5(b) considers cases where the initial life level was relatively high In both cases, however, the order of load application was that of high stress followed by low stress In general, the results obtained with 4130 steel are the same as those obtained with the maraged 300 CVM steel for similar test conditions In general, agreement between predictions by the double linear rule using $(\Delta N)_f - 14N_f^{0\ 6}$ and experimental data was good, although deviations between predictions and data are clearly present in some cases. As was the case for the maraged 300 CVM steel, a more conservative prediction was always provided by the double linear-damage rule, assuming the expression $14N_f^{0\ 6}$ to be representative of the crack-propagation stage, than by the conventional linear-damage rule when the high stress was applied first

UNIFIED THEORY OF CUMULATIVE DAMAGE

In a very extensive review, Dubuc et al [29] outlined the various mathematical forms reported in cumulative-damage studies Citing the origin of such studies in the work of Palmgren, Langer, and Miner, the article by Dubuc et al. made special mention of the theories of Kommers,[1] Bennett,[30] Richart and Newmark,[31] Marco and Starkey,[32]

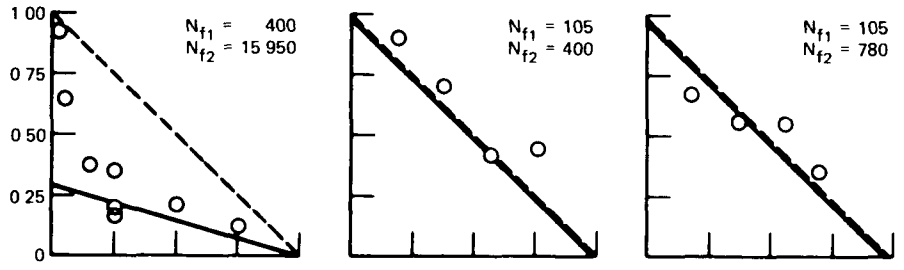

(c) Axial strain cycling high-to-low strain with low initial life

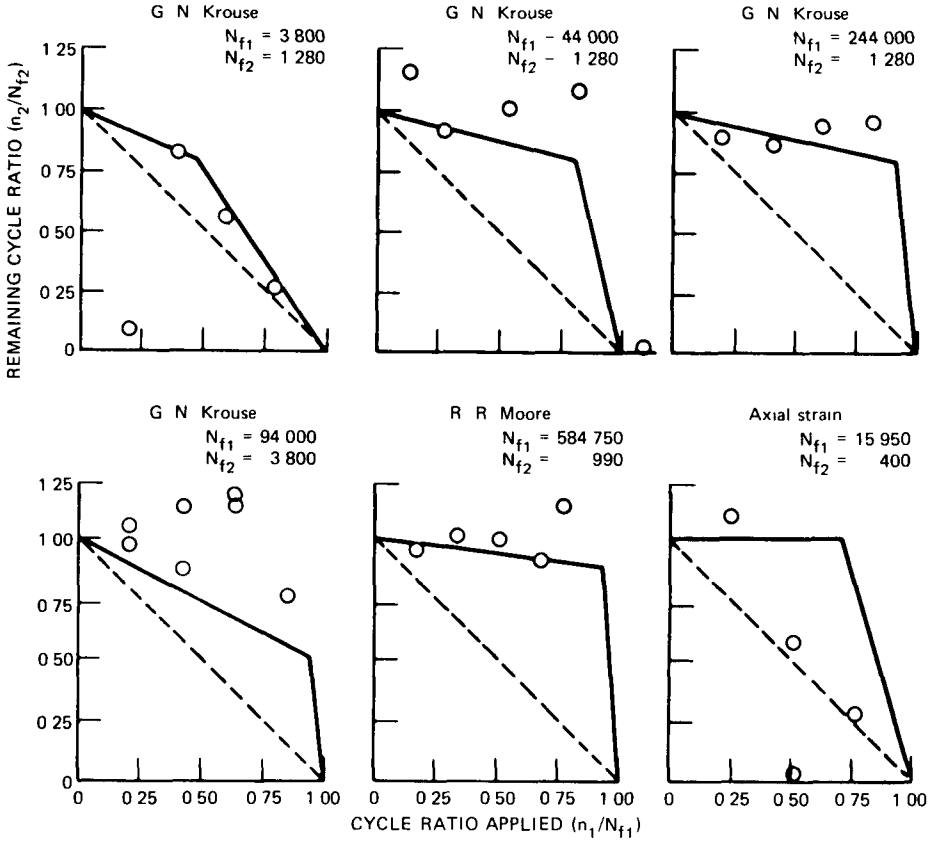

(d) Rotating bending and axial strain cycling low-to-high stress (strain)

Fig. 5.4 (Continued)

Grover,[26] Manson et al ,[28] Miller,[34] Henry,[35] Shanley,[36] Gatts,[37] Manson et al ,[2] Valluri,[3,16] Corten and Dolan,[38] Harris and Lipson,[39] and Freudenthal and Heller[40] Dubuc et al emphasized that most of the published information relating to cumulative fatigue damage was based on stress-controlled exposures in the high-cycle regime For strain-controlled fatigue behavior, Dubuc et al cited the cumulative-damage studies of Shanley,[41] Yao and Munse,[42] Ohji et al ,[17] Sachs et al ,[43] and Martin[44] which led to different equations for predicting the form of the plot of strain vs cycles to failure Dubuc et al also stated that, in such studies, cumulative-damage concepts are generally based on the linear-damage rule Another comment was that "it has been assumed that the damage is additive and monotonically accumulated with repeated strain cycles" and "at failure the sum of the cycle ratios should be equal to unity." These statements reflect the status at the moment, which is that cumulative damage in strain controlled low cycle fatigue tests has not been studied in any great detail, and, since no fully confirmed damage law has appeared, the linear damage law is being used in such investigations

Dubuc et al. also reported the development of a unified theory of cumulative damage The work of Manson et al [2] indicated that the effect of fatigue damage is more pronounced in the low stress region, and the reduction in the endurance limit seems to be a suitable expression of fatigue damage The work of Gatts[37] was referenced to

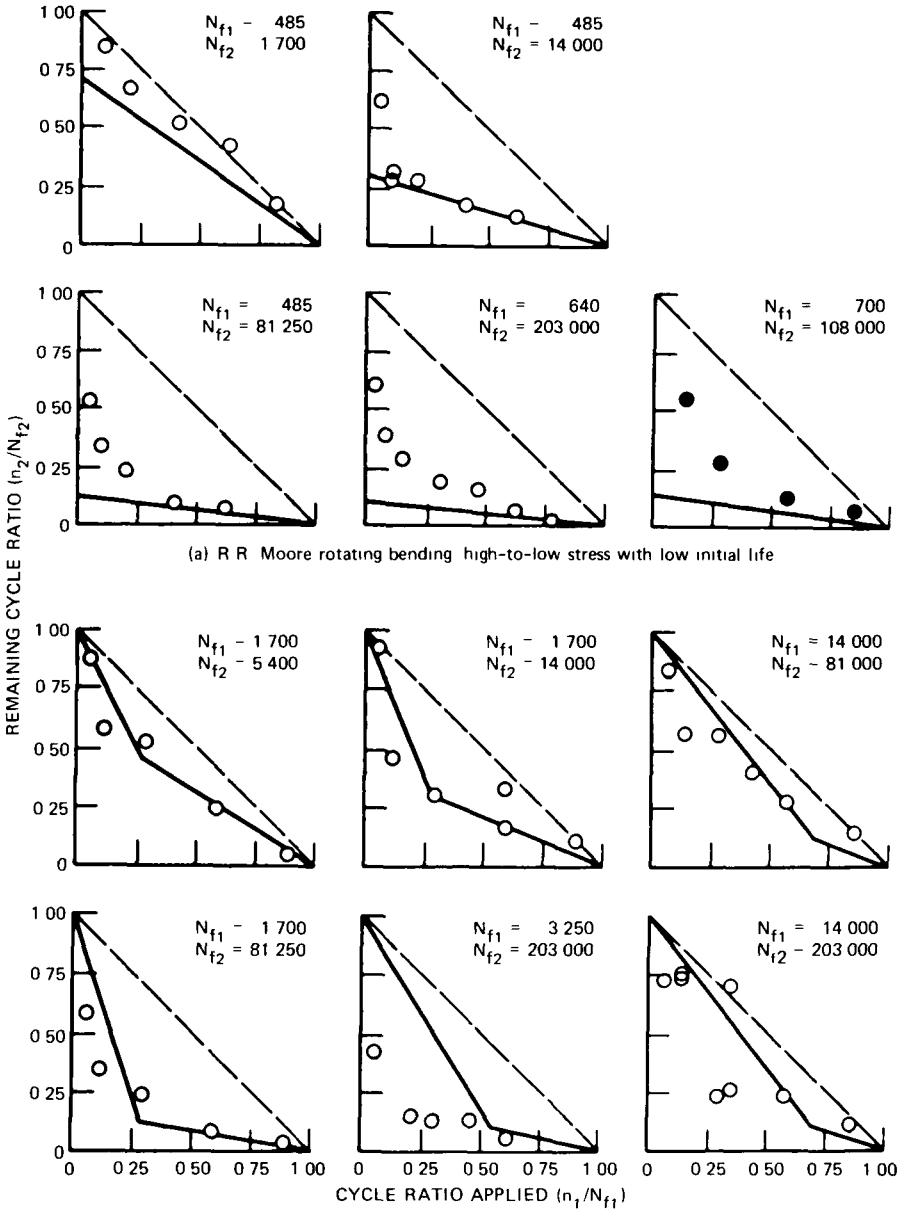

(a) R R Moore rotating bending high-to-low stress with low initial life

(b) R R Moore rotating bending high to-low stress with relatively high initial life

Fig. 5.5 Comparison of experimental data with predicted fatigue behavior based on linear- and double linear-damage rules for SAE 4130 steel. ○, soft (R_C = 26). ●, hard (R_C = 40). – – –, conventional linear-damage rule. —, double linear-damage rule for $(\Delta N)_f = 14N_f^{0.6}$. (From Ref. 28.)

suggest a relation between the instantaneous value of the endurance limit and the tensile strength in the form

$$\gamma_e = \left(\frac{\gamma_s}{\gamma_u}\right)^m \tag{5 15}$$

where γ_e = instantaneous nondimensional endurance limit
γ_s = instantaneous nondimensional strength
γ_u = nondimensional original ultimate tensile strength
m = a constant greater than unity

Also used in this development by Dubuc et al is the following expression[35] that relates the damage function D and the endurance limit γ_e

$$\Delta D = \mu \Delta \gamma_e \tag{5 16}$$

where μ is the weighting coefficient that yields the value of unity for the damage function at failure, μ depends uniquely on the magnitude of the applied stress Furthermore, γ_e varies from unity for the virgin material to a critical value γ_{ec} at failure

This unified theory proposed by Dubuc et al embodied the predominant characteristics of the theories of Shanley [36] Valluri [3] and Gatts [37] to define the rate of reduction of material strength The form of the expression adopted was

$$\frac{d\gamma_e}{dn} \quad K_1 \gamma^x \frac{\gamma \quad \gamma'}{\gamma_e^{(m \quad 1)/m}} (\gamma \quad \gamma_e)^2 \qquad (5\ 17)$$

where $\gamma > \gamma_e$

γ nondimensional maximum cyclic stress σ/σ_{e0} where σ_{e0} is the endurance limit

γ' nondimensional minimum cyclic stress σ'/σ_{e0}

K_1 x - material constants

When Eqs 5 15 and 5 17 are combined the rate of reduction of the endurance limit is

$$\frac{d\gamma_e}{dn} - \frac{-1}{K}\left(\frac{\gamma \quad \gamma'}{\gamma}\right)\gamma^b (\gamma \quad \gamma_e)^2 \qquad (5\ 18)$$

where $\gamma > \gamma_e$ and K and b are material constants

The solution of Eq 5 18 requires the knowledge of the variation of γ in terms of the number of applied cycles n Further, the boundary conditions that must be satisfied are

$$\gamma_e = \gamma_{e0} \quad 1 \qquad \text{when } n = 0$$

and

$$\gamma_e \quad \gamma_{ec} \qquad \text{when } n \quad N$$

where N is the number of cycles to failure and γ_{ec} is the nondimensional endurance limit corresponding to the onset of failure

Then, from Eq 5 15, it follows that

$$\gamma_{ec} \quad \left(\frac{\gamma}{\gamma_u}\right)^m \qquad (5\ 19)$$

Fatigue Under Stress-Controlled Conditions

When the stress ratio $R = \sigma'/\sigma$ and the maximum cyclic stress σ are maintained constant during the life of the specimen, Eq 5 18 integrates to give

$$n \quad \left(\frac{K_\sigma}{1 - R_\sigma}\right)\left(\frac{1}{\gamma^b}\right)\left(\frac{1}{\gamma \quad 1} \quad \frac{1}{\gamma \quad \gamma_e}\right) \qquad (5\ 20)$$

where K_σ is the value of K under stress controlled conditions This expression enables the reduction in the endurance limit to be calculated for a given number of applied cycles

At failure the specimen will have been subjected to N cycles, and, from Eqs 5 19 and 5 20, it follows that

$$N \quad \left(\frac{K_\sigma}{1 \quad R_\sigma}\right)\left(\frac{1}{\gamma^b}\right)\left[\frac{1}{\gamma \quad 1} \quad \frac{1}{\gamma \quad (\gamma/\gamma_u)^m}\right] \qquad (5\ 21)$$

This expression describes the fatigue curve for the most general case in which a specimen is subjected to a constant maximum cyclic stress γ at the stress ratio R_σ The values γ and γ_u are expressed in terms of the endurance limit associated with the stress ratio R_σ

A particular form of Eq 5 21 is applied when the stress ratio R_σ is equal to 1 (completely reversed stress cycling) In this case

$$N \quad \left(\frac{K_\sigma}{2}\right)\left(\frac{1}{\gamma^{b^*}}\right)\left[\frac{1}{\gamma - 1} - \frac{1}{\gamma \quad (\gamma/\gamma_u^x)^m}\right] \qquad (5\ 22)$$

where b' is the value of b which is associated with R_σ equal to 1

The fatigue curve described by this expression is of particular interest because experimental results are usually more available for the completely reversed condition (this has been called the "basic fatigue curve") Values for K_σ and b are determined from experimental results The constant K_σ gives the relative position of the curve in the fatigue diagram whereas b' governs the slope of the plot The constant m was reported to have no significant influence on the fatigue curve

Dubuc et al showed that the value of K_σ is independent of R_σ to enable the same value of K_σ to apply to both Eqs 5 21 and 5 22 The constant b however was found to be related to b* as follows

$$\frac{b}{b'} \quad \frac{\gamma_u^x \quad 1}{\gamma_u \quad 1}\left(\frac{\gamma_u}{\gamma_u'}\right)^{1/2} \qquad (5\ 23)$$

and

$$\gamma_u^x \quad \frac{\sigma_u}{\sigma_{e0}^*}$$

Stress controlled tests [29] of A 201 and A 517 steels yielded the data shown in Fig 5 6 The compositions and properties of these materials are given in Tables 5 3 and 5 4 The curves shown in Fig 5 6 are derived from Eq 5 22 in the following manner

1 The basic fatigue curve (R_σ 1) was first evaluated using m = 8 (this value of m was found to be optimum for mild steel and aluminum alloys) Values for b* and K_σ were then determined by selecting two arbitrary reference points (two solid symbols in Fig 5 6) The value of σ_u was available from static tensile tests, and, since no special tests were performed to determine σ_{e0}^* this value was obtained by means of extrapolating the available test data The value of σ_{e0}^* obtained was noted to be related to the ultimate tensile strength in the accepted fashion It was also pointed out that the effect of σ_{e0}^* on the shape of the theoretical fatigue curve in the low and intermediate cycle range is

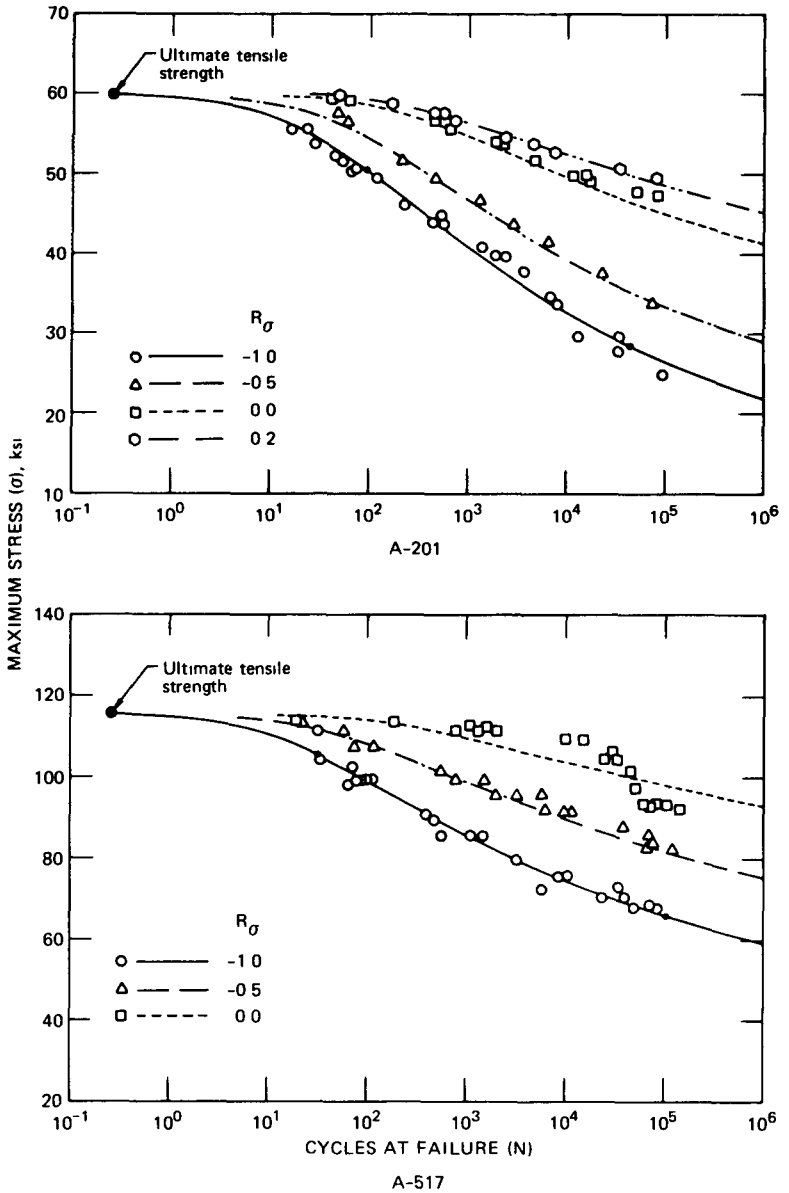

Fig. 5.6 Fatigue curves for A-201 and A-517 steels.[29] (Published by permission of the Welding Research Council.)

TABLE 5.3

CHEMICAL COMPOSITION OF A-201 AND A-517 STEELS (IN PERCENT)*

Material	C	Mn	P	S	Si	Cr	Mo	Ni	V	Cu	B
A-201, grade A†	0.15	0.75	0.012	0.034	0.22						
A-517, grade F‡	0.15	0.92	0.014	0.020	0.26	0.50	0.46	0.88	0.060	0.32	0.0031

*Published by permission of the Welding Research Council.
†Normalized at 1675° F and stress relieved at 1150° F.
‡Quenched and tempered.

TABLE 5.4

AVERAGE MECHANICAL PROPERTIES OF A-201 AND A-517 STEELS*

Material	Yield strength, psi	Ultimate strength, psi	Reduction of area, %	Elongation on 2 in., %	True strain at fracture, in./in.
A-201, grade A	36,600	59,300	66.9	42.4	1.114
A-517, grade F	105,200	116,000	60.9	21.5	0.940

*Published by permission of the Welding Research Council.

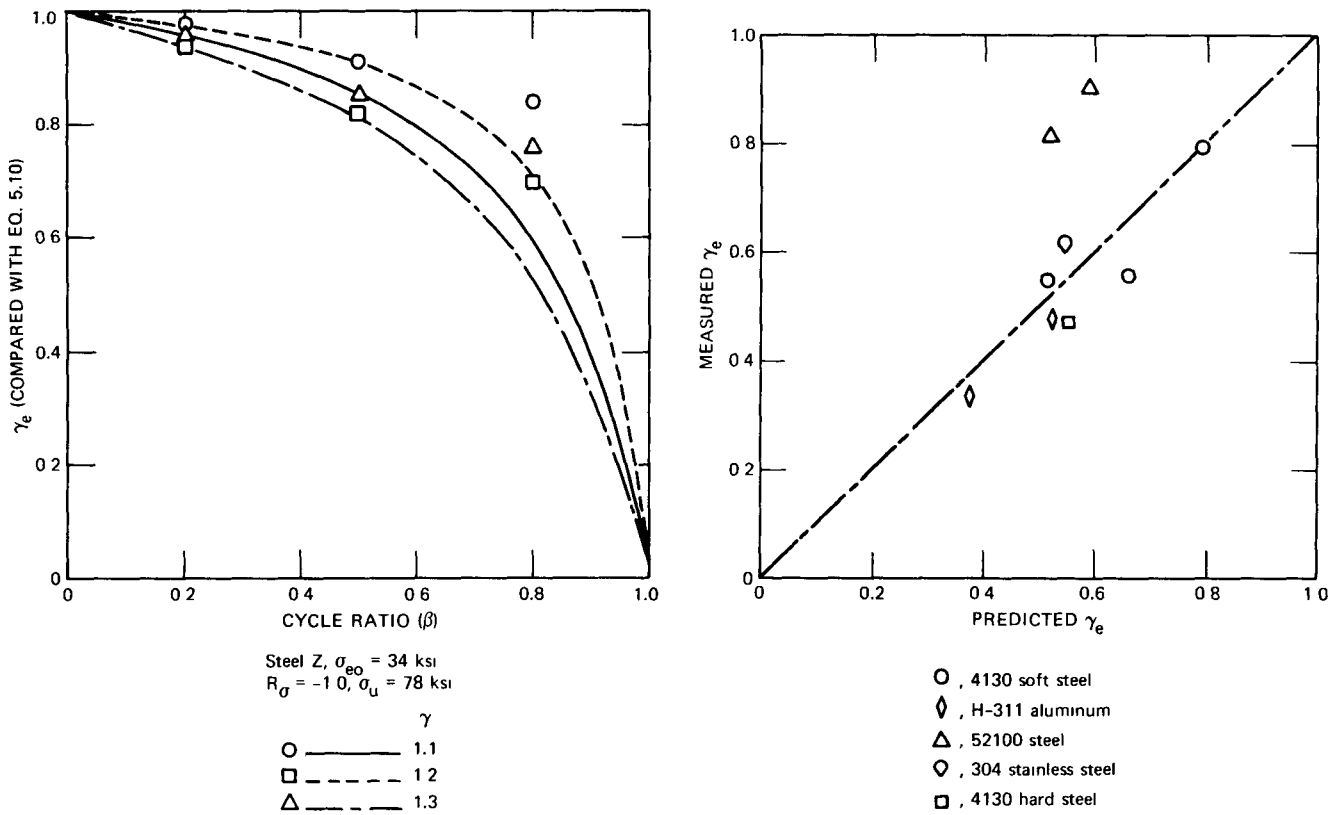

Fig. 5.7 Effect of cycle ratio on damage expressed as reduction in endurance limit.[29] (Published by permission of the Welding Research Council.)

small and well within the usual range of scatter of experimental results.

2. The fatigue curves for the other values of R_σ were evaluated using Eq. 5.21 with the same value of K_σ and with the value of b obtained from Eq. 5.23. The endurance limit σ_{e0} for a given value of R_σ was determined in conformity with experimental results[45] relating to the effect of mean stress.

Dividing Eq. 5.20 by 5.21 to yield the cycle ratio β and then rearranging lead to

$$\gamma_e = \gamma - \frac{1}{(1-\beta)/(\gamma-1) + \beta/[\gamma - (\gamma/\gamma_u)^m]} \quad (5.24)$$

This expression provides a direct method for calculating the effect on the endurance limit γ_e of fatigue damage corresponding to the cycle ratio β at the stress level γ.

A comparison of this expression with published data[2,46] led to the results shown in Fig. 5.7. Reasonable agreement was claimed. This plot was also used to point out that, when $\beta = 1$ (i.e., failure), the endurance limit is not reduced to zero but to a value of γ_{ec} which is small but finite in this particular instance. Figure 5.7 was used to compare the results for five steels tested in rotating bending.[2] Except for the 52100 steel, good agreement was noted.

Cumulative Damage. According to Eq. 5.16, a relation for the damage function D due to fatigue was written[29] in

the form

$$D = \frac{1 - \gamma_e}{1 - \gamma_{ec}} \tag{5.25}$$

and introducing Eqs. 5.19 and 5.24 yields

$$D = \frac{\beta}{\beta + (1 - \beta)[\gamma - (\gamma/\gamma_u)^m]/(\gamma - 1)} \tag{5.26}$$

This expression defines D as a function of the cycle ratio β with γ as a parameter. Typical variations of D with β and γ for $\gamma_u = 2.0$ are shown in Fig. 5.8 and compared to the theories of Henry[35] and Miner.[47] The nature of these plots reveals a curvature upward as β increases to indicate an acceleration of damage with increasing applied cycles. Also, as the value of γ increases, the damage function tends to be equal to β, and Eq. 5.26 becomes identical to the Miner concept in which $D = \beta$.

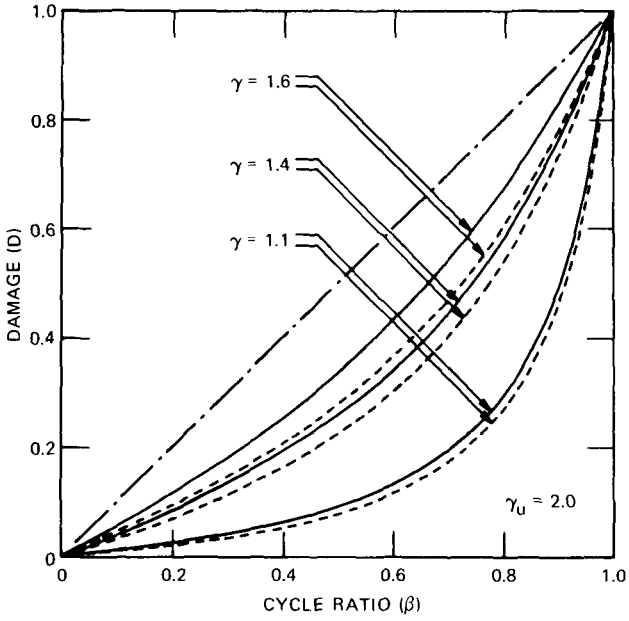

Fig. 5.8 Damage function plotted in terms of β and γ.[29] (Published by permission of the Welding Research Council.) —, present theory.[29] – – –, Henry theory. — – —, Miner theory.

The approach leading to Eq. 5.26 was based on the consideration that damage is caused only by stress levels greater than the endurance limit of the original material. Therefore, for the direct application of D to multistep tests, all stress levels should be greater than σ_{e0}. If one or more stress levels are below this value, Dubuc et al. recommended a different approach where the endurance limit γ_e is computed after each applied stress level, and then failure is assumed to occur when $\gamma_e = \gamma_{ec}$.

For a two-step loading, the damage accumulated at stress level γ_1 is given by Eq. 5.26 in the form

$$D_1 = \frac{\beta_1}{\beta_1 + (1 - \beta_1)[\gamma_1 - (\gamma_1/\gamma_{u1})^m]/(\gamma_1 - 1)} \tag{5.27}$$

where $\beta_1 = n_1/N_1$

N_1 = number of cycles to failure for the stress level γ_1

$\gamma_{u1} = \sigma_u/\sigma_{e0}$ for the stress ratio $R_{\sigma 1}$ at the first stress level

If the stress level is then changed to γ_2 and the specimen is subjected to this stress level until failure occurs, the predicted cycle ratio β_2 may be determined by first finding the equivalent cycle ratio β_{e2} that would have caused damage D_1 at stress level γ_2. Rearranging Eq. 5.26 to solve for β_{e2} and writing this expression for β_{e2} give

$$\beta_{e2} = \frac{D_1[\gamma_2 - (\gamma_2/\gamma_{u2})^m]/(\gamma_2 - 1)}{1 + D_1[1 - (\gamma_2/\gamma_{u2})^m]/(\gamma_2 - 1)} \tag{5.28}$$

where $\gamma_{u2} = \sigma_u/\sigma_{e0}$ for the stress ratio $R_{\sigma 2}$ of the second stress level (if $R_{\sigma 1} = R_{\sigma 2}$, then $\gamma_{u1} = \gamma_{u2}$). The predicted cycle ratio β_2 can then be found from

$$\beta_2 = 1 - \beta_{e2} \tag{5.29}$$

It has been shown[29] that the sum of the cycle ratio, $S = \beta_1 + \beta_2$, can be approximated by

$$S \approx \frac{(\gamma_2 - 1)[\gamma_1 - (\gamma_1/\gamma_{u1})^m] + \beta_1^2(\gamma_1 - \gamma_2)}{(\gamma_2 - 1)[\gamma_1 - (\gamma_1/\gamma_{u1})^m] + \beta_1(\gamma_1 - \gamma_2)} \tag{5.30}$$

This has been used to show that, when $\gamma_1 < \gamma_2$, that is, for increasing stress levels, the sum S is larger than unity; the opposite is true for decreasing stress levels. This theoretical result was noted to be consistent with experimental observations.

Some published data[10] were used in the study by Dubuc et al. to provide a measure of the effectiveness of Eq. 5.30. The results of this comparison are presented in Fig. 5.9. A decided data scatter was noted, but the qualitative agreement between the data and the theory confirms the fact that the order of application of stress levels has an influence on the fatigue life.

In a multistep exposure, Dubuc et al. outlined the calculation procedure. The equivalent damage D_e before applying the last stress level γ_k is the sum of the damage inflicted at each prior stress level. The equivalent cycle ratio β_{ek} corresponding to the last stress level γ_k, which would cause the same amount of damage D_e, is evaluated as follows using Eq. 5.27:

$$\beta_{ek} = \frac{D_e[\gamma_k - (\gamma_k/\gamma_{uk})^m]/(\gamma_k - 1)}{1 + D_e[1 - (\gamma_k/\gamma_{uk})^m]/(\gamma_k - 1)} \tag{5.31}$$

Then the number of cycles that the specimen should sustain at the last stress level would be

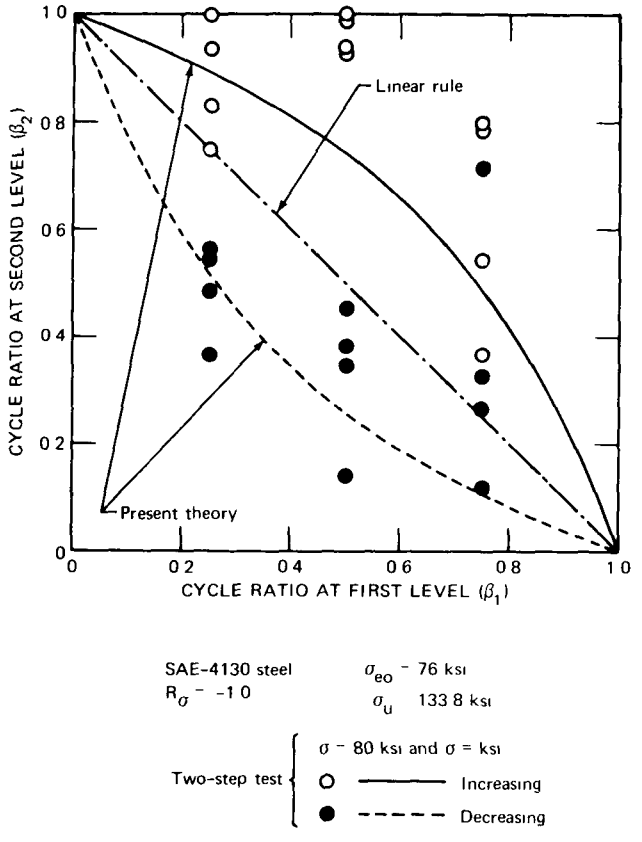

Fig. 5.9 Comparison[29] of experimental data with theory of Eq. 5.30. (Published by permission of the Welding Research Council.)

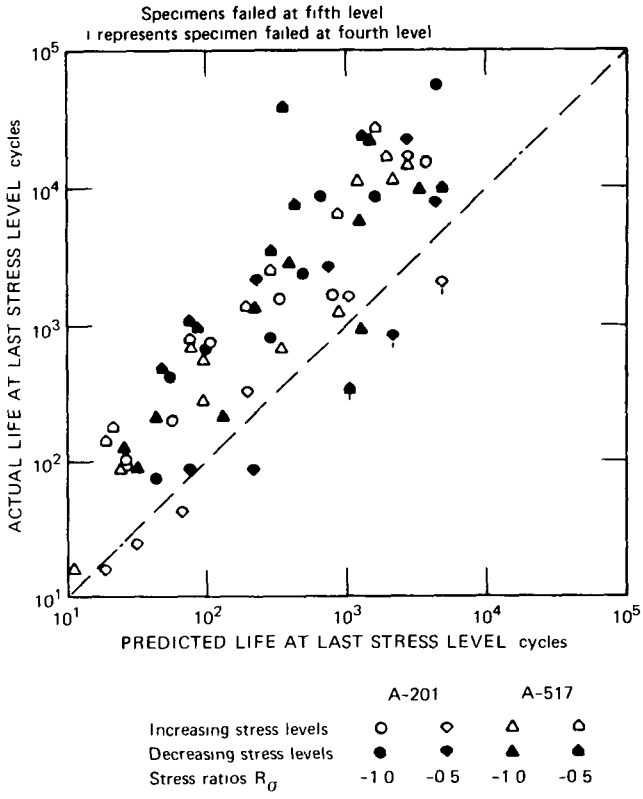

Fig. 5.10 Predicted[29] vs. actual fatigue life for A-201 and A-517 steels. (Published by permission of the Welding Research Council.)

$$n_k \quad N_k\,(1-\beta_{ek}) \tag{5.32}$$

where N_k is the fatigue life at stress level γ_k

A summary[29] of results obtained in cumulative-damage tests of A-201 and A-517 steels under several (usually five) increasing or decreasing stress levels is presented in Fig 5 10. The actual remaining life of the specimen at the last stress level is compared to the predicted remaining life given by the theoretical approach. It was noted that there is little difference between the value predicted by Dubuc et al. and the linear-damage rule. This was explained by the fact that the tests were performed in the low-cycle region, and the stress levels were closely spaced.

Fatigue Under Strain-Controlled Conditions

Paralleling the approach developed for stress controlled fatigue tests, Dubuc et al used a strain parameter defined as

$$\lambda = 1 + \ln\frac{\epsilon}{\epsilon_0} \tag{5.33}$$

where ϵ is the total cyclic strain and ϵ_0 is the endurance limit strain, σ_{e0}/E This parameter was used to transform a conventional log–log plot of ϵ vs N obtained in strain control into a semilog plot of λ vs. N similar to the γ–N diagram described in the previous section. This concept is illustrated in Fig. 5.11 to show the similarity between the γ–N plot obtained from stress-controlled tests and the λ–N plot obtained from strain-controlled evaluations. Corresponding to the ultimate tensile strength γ_u in the first diagram is λ_f

$$\lambda_f = 1 + \ln\frac{\epsilon_f}{\epsilon_0} \tag{5.34}$$

where ϵ_f is the true strain at fracture

This formulation led to an equation for the fatigue diagram, for the constant strain ratio $R_\epsilon = \epsilon'/\epsilon$, of the form

$$N = \left(\frac{K_\epsilon}{1-R_\epsilon}\right)\left(\frac{1}{\lambda^c}\right)\left[\frac{1}{\lambda-1} - \frac{1}{\lambda-(\lambda/\lambda_f)^m}\right] \tag{5.35}$$

where K_ϵ and c are material constants not necessarily equal to K_σ and b of Eq 5 21 and m is a constant assumed to be equal to 8.0.

A typical theoretical curve[29] for A-201 steel compared with experimental data obtained under completely reversed ($R_\epsilon = -1$) conditions is shown in Fig. 5 12. Values for K_ϵ and c for this curve were obtained by considering two data

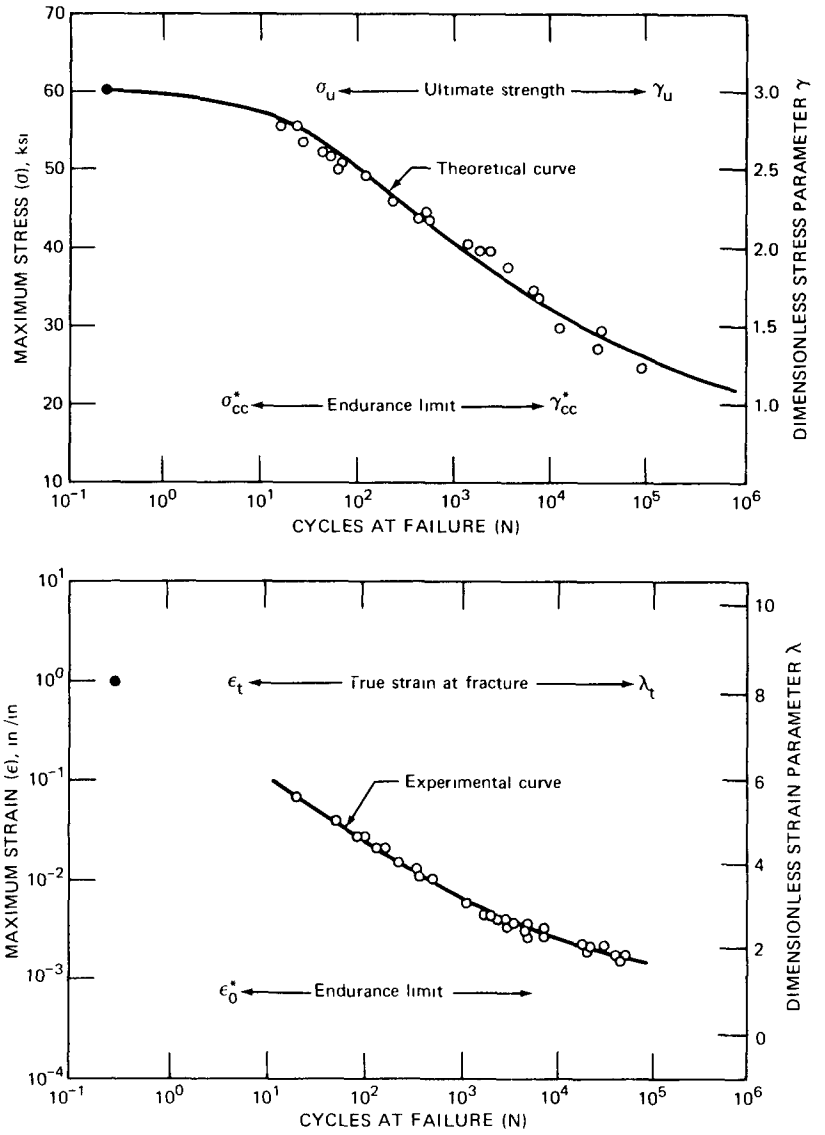

Fig. 5.11 Comparison[29] of stress-controlled and strain-controlled fatigue plots of A-201 steel. $R_\epsilon = -1.0$. (Published by permission of the Welding Research Council.)

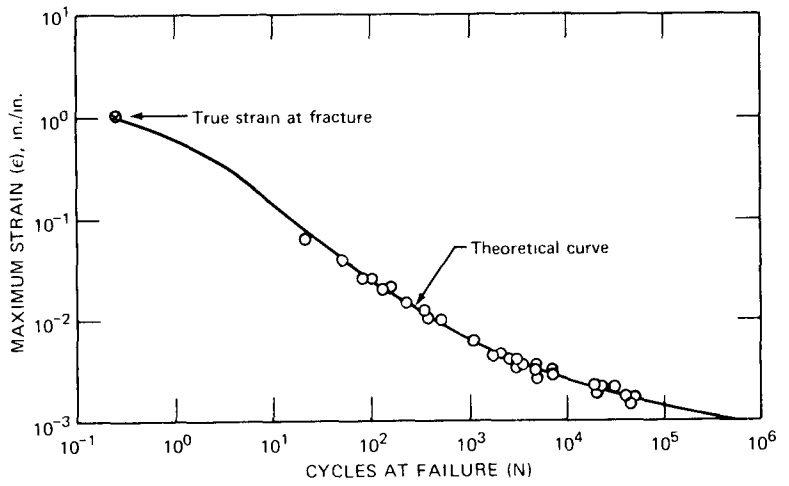

Fig. 5.12 Typical theoretical strain-controlled fatigue plot[29] of A-201 steel. $R_\epsilon = -1.0$. (Published by permission of the Welding Research Council.)

points in the intermediate range of the diagram Other curves[48] for more than 30 different materials show similar agreement.

In an attempt to predict strain-controlled fatigue behavior from a knowledge of static properties, Dubuc et al described studies that led to several important observations. Under completely reversed strain cycling, the endurance limit can be determined directly from $\sigma^*_{\epsilon 0}/E$ In the absence of any information on $\sigma^*_{\epsilon 0}$, ϵ^*_0 can be evaluated by using the reference value

$$\epsilon_s = 0.6\,\frac{\sigma_u}{E} \tag{5.36}$$

which is assumed to be the total strain at a life of $N = 10^5$ cycles A correlation between ϵ^*_0, ϵ_s, and ϵ_f was shown to have the form presented in Fig. 5.13, this led to

$$\frac{\epsilon^*_0}{\epsilon_s} = 0.6 \tag{5.37}$$

to allow ϵ^*_0 to be obtained from ϵ_s

It was stated that the constant c^* (c for $R_\epsilon = -1$) determines the overall slope of the fatigue curve and depends on the properties of the material. In general, the value of c^* is relatively small for a ductile material for which λ_f is very large. A good linear correlation was noted between c^* and known static properties of the material. A study of 30 different materials showed that

$$c^* = 3.08 + \frac{4.16}{\epsilon_f^{0.6} \ln (\epsilon_f E/0.36\sigma_u)} \tag{5.38}$$

When $R_\epsilon = -1$, Eq. 5.35 becomes

$$N = \left(\frac{K_\epsilon}{2}\right)^{\frac{1}{c^*}} \left[\frac{1}{\lambda - 1} - \frac{1}{\lambda - (\lambda/\lambda^*_f)^m}\right] \tag{5.39}$$

where λ equals $1 + \ln (\epsilon/\epsilon^*_0)$ and λ^*_f equals $1 + \ln (\epsilon_f/\epsilon^*_0)$ This expression defines the basic fatigue curve for strain control and is evaluated in the following manner

1. ϵ^*_0 is established using Eqs 5.36 and 5.37.
2. c^* is obtained using Eq. 5.38.
3. K_ϵ is then determined by using a known value of λ for a particular life N in Eq. 5.39, for $N = 10^5$, λ equals $1 + \ln (\epsilon_s/\epsilon^*_0) = 1.51$

In the high-cycle region, the correct value of ϵ^*_0 is required for the proper fit of the theoretical curve with experimental results. However, for a large number of materials, Eq. 5.37 was found to yield an adequate approximation for ϵ^*_0 Furthermore, because of the logarithmic coordinates of the fatigue diagram, small variations of the value of ϵ^*_0 do not greatly affect the fatigue curve. The position of the theoretical curve on the fatigue diagram depends on the value of K_ϵ, which can be determined from experimental results, either of two observations can be used ϵ_s (or λ_s) at 10^5 cycles at failure, based on the reported results of Manson et al.,[49] or $\epsilon = 0.01$ in./in. at 500 cycles at failure.[50]

Cumulative Damage. For strain-controlled fatigue testing, Dubuc et al. proposed an expression similar to Eq. 5.26. This is written in terms of λ to yield

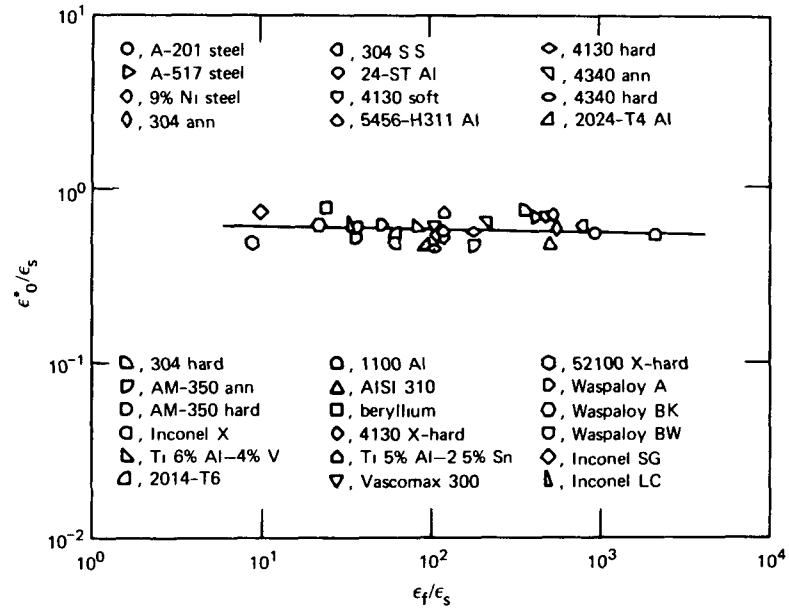

Fig. 5.13 Correlation[29] between ϵ^*_0, ϵ_s, and ϵ_f. (Published by permission of the Welding Research Council.)

$$D = \frac{\beta}{\beta + (1-\beta)[\lambda - (\lambda/\lambda_f)^m]/(\lambda - 1)} \qquad (5\,40)$$

This, of course, has the same characteristics as Eq 5 26, particularly to the extent that D approaches β with increasing values of λ Furthermore, the use of Eq 5 40 in estimating damage and remaining life follows the procedures used in conjunction with Eq 5 26

Figure 5 14 shows the results of two step exposures for A 517 steel The cycle ratio at the second level, β_2, is plotted against β_1 and compared to experimental results Again, the wide scatter of the data precludes confirmation of the effect of order of loading inherent in Eq 5 31 In this regard, Dubuc et al stated that this trend is confirmed in other studies [20 51]

Figure 5 15 shows the results of cumulative damage tests on several (usually five) increasing and decreasing strain levels for A 201 and A 517 steels Remaining life is compared with predicted life remaining at the last strain level In view of the large scatter included, no detailed conclusions could be offered except to state that, for the closely spaced strain levels involved, the predictions based on Eq 5 40 are not significantly different from those based on the linear damage rule

Dubuc et al also presented data obtained in a series of tests on two widely spaced strain levels using A-517 steel specimens, these results are shown in Fig 5 16 It is stated that the use of Eq 5 40 leads to predicted behavior that is closer to the actual test data than the predictions based on the linear damage rule Results of tests on maraging steel

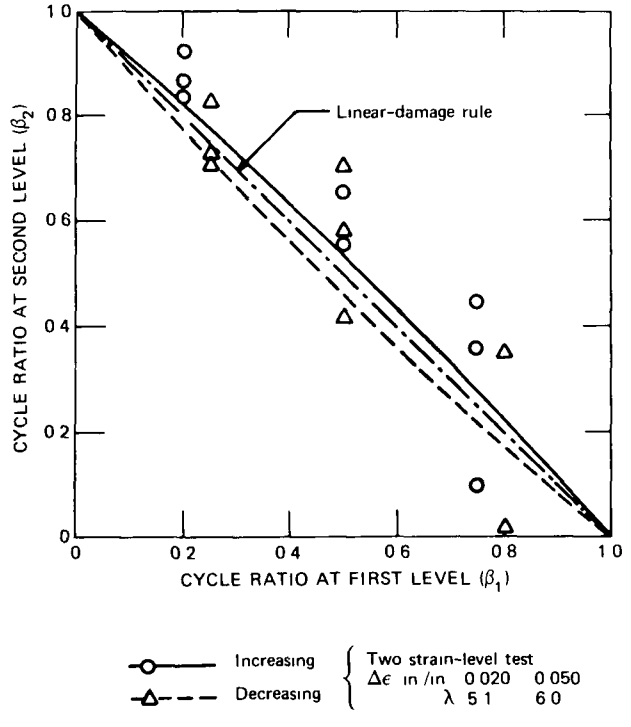

Fig 5.14 Two-step strain-controlled fatigue evaluation of A 517 steel.[29] $R_\epsilon = -1.0$. (Published by permission of the Welding Research Council.)

are presented in Fig 5 16, and again the predictions based on Eq 5 40 are closer to the data points than is the linear damage rule The upper and lower lines in Fig 5 17 were included to show the predicted behavior based on the double linear damage rule [28]

RECENT CUMULATIVE-DAMAGE TESTS

In a recent study[47] of the effect of combined loadings, AISI 304 stainless steel was evaluated in strain controlled low cycle fatigue tests at 1200°1 at a strain rate of 4×10^{-3} sec^{-1} These data, which are summarized in Table 5 5, represent the first reported information relating to cumulative damage evaluations in axial strain controlled fatigue tests at elevated temperature In the initial test the specimen was first subjected to the high (2%) strain range, and the time of exposure at this strain range was taken as 50% of that corresponding to failure at this strain range (the footnote in Table 5 5 contains the failure data for single strain range tests at a strain rate of 4×10^{-3} sec^{-1}) When this specimen (67 8) had been tested for 47 5 min at a strain range of 2% the strain range was changed to 1%, and the test continued to failure Specimen fracture occurred after 106 5 min at the lower strain range It was found that this time was more than 50% (actually 73 9%) of the fracture time observed in the 1% strain range tests The summation of these time ratios is seen in Table 5 5 to yield a value greater than unity In other words, if one half of the fracture life is devoted to a certain strain range, these results reveal that the test can be continued at a lower (1% in this case) strain range, and the fatigue life at this condition will be more than 50% of that observed in a test in which the strain range is maintained constant at 1% A similar behavior pattern is observed in terms of the number of fatigue cycles

In a second test the specimen was first exposed to the lower strain range and, after testing for a time corresponding to 50% of the fatigue life at 1% strain range, the strain range was increased to 2% As seen in Table 5 5, this test yielded the same behavior pattern as that observed in the first test The sum of the time ratios was greater than unity and essentially identical to the high–low sequence

A third test involved the use of the high strain range for a longer time, but this did not seem to affect the summation of the time ratios It was still found that the cyclic life remaining was greater than that which would correspond to a time ratio summation of unity

In the fourth and fifth tests, the specimens were subjected to continued transfers between the 1 and 2% strain ranges Specimen 67 7 was arbitrarily subjected to 11 cycles at the 2% strain range, followed by 34 cycles at the 1% strain range This ratio of 34 to 11 corresponds to the N_f ratio for these two strain ranges (see footnote in Table 5 5) This sequence was continued until specimen failure A similar test sequence was used with specimen 67 5, except each strain range was applied for 2 5 min In

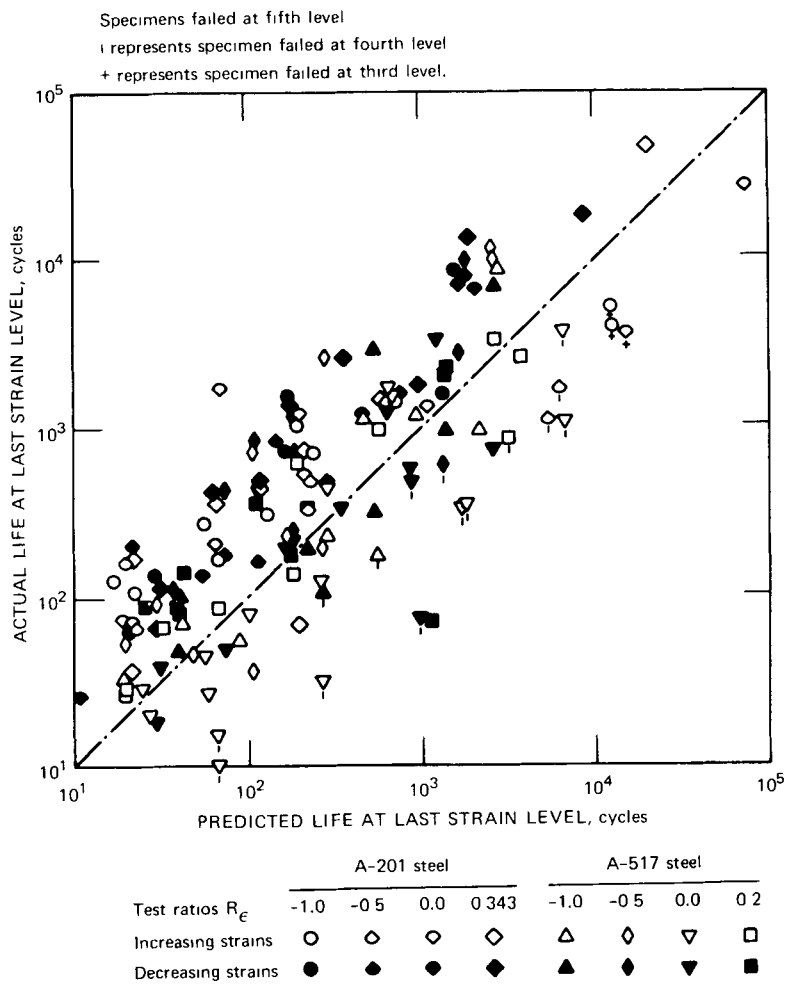

Fig. 5.15 Comparison of predicted and actual fatigue life for A-201 and A-517 steels.[29] (Published by permission of the Welding Research Council.)

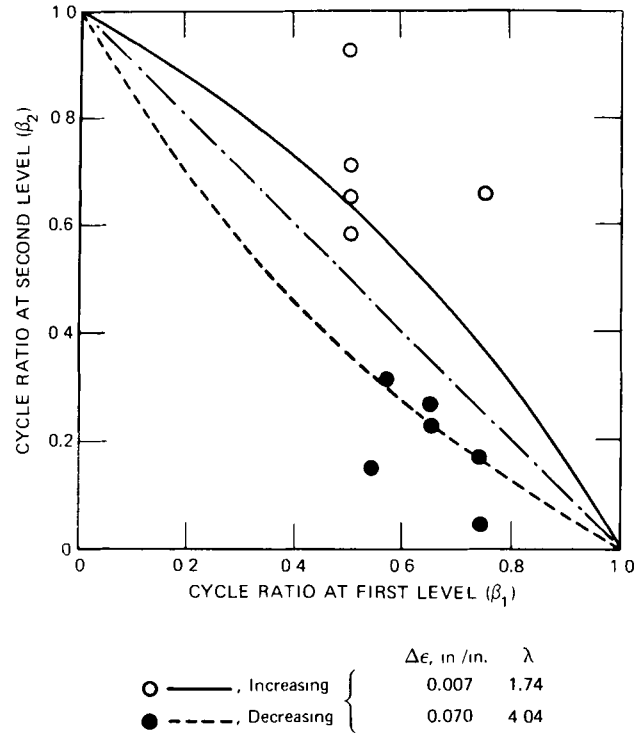

Fig. 5.16 Two-step fatigue tests of A-517 steel performed in strain control.[29] $R_\epsilon = -1.0$. (Published by permission of the Welding Research Council.)

TABLE 5.5

LOW-CYCLE-FATIGUE DATA OBTAINED IN TESTS OF AISI 304 STAINLESS STEEL IN AIR AT 650°C USING A STRAIN RATE OF 4×10^{-3} sec^{-1} AND COMBINED STRAIN RANGES OF 1 AND 2%

Spec. No.	Loading sequence	Time, min: At $\Delta\epsilon_t^2$	Time, min: At $\Delta\epsilon_t^1$	Cycles: At $\Delta\epsilon_t^2$	Cycles: At $\Delta\epsilon_t^1$	Frequency, cycles/min: At $\Delta\epsilon_t^2$	Frequency, cycles/min: At $\Delta\epsilon_t^1$	Time ratio: t_2/t_f^2	Time ratio: t_1/t_f^1	Cycle ratio: N_2/N_f^2	Cycle ratio: N_1/N_f^1	Summation of cycle ratios	Summation* of time ratios
67-8	High–low	47.5	106.5	277	1241	5.833	11.5	0.500	0.739	0.486	0.718	1.204	1.24
67-9	Low–high	72.6	72.0	441	876	6.08	12.0	0.764	0.500	0.773	0.507	1.280	1.26
67-10	High–low	72.6	68.6	441	834	6.08	12.0	0.764	0 476	0.774	0.482	1.256	1.24
67-7	High–low–high–low	53.9	80.1	315	934	5.833	11.5	0.567	0.555	0.552	0.54	1.092	1.12
67-5	High–low–high–low	62.5	62.5	364	728	5.833	11.5	0.657	0.434	0.638	0.421	1.059	1.09

Control data

$\Delta\epsilon_t$, %	N_f, cycles	Time to fracture, min
2	570	95
1	1728	144

Spec. No.	Loading sequence	$\Delta\epsilon_t$, %: No. 2	$\Delta\epsilon_t$, %: No. 1	$\Delta\epsilon_p$, %: No. 2	$\Delta\epsilon_p$, %: No. 1	$\Delta\epsilon_e$, %: No. 2	$\Delta\epsilon_e$, %: No. 1	$\Delta\sigma$ ksi, at $N_f/2$: $\Delta\epsilon_t^2$	$\Delta\sigma$ ksi, at $N_f/2$: $\Delta\epsilon_t^1$	N_f, cycles: $\Delta\epsilon_t^2$	N_f, cycles: $\Delta\epsilon_t^1$	Time to fracture, min
67-8	High–low	1.98	0.99	1.62	0.70	0.35	0 29	71.2	62.5	(277)†	1241	154.2
67-9	Low–high	1.98	0.99	1.63	0 70	0.35	0.29	75.6	61.7	441	(876)†	147
67-10	High–low	1.98	0.99	1.63	0.70	0.35	0.29	74.8	61.7	(441)†	834	141
67-7	High–low–high–low	1.98	0.99	1.62	0.68	0.35	0.31	76.4	67.0	315	934	134
67-5	High–low–high–low	1.98	0.99	1.62	0.68	0.35	0.31	76.2	67.6	364	728	125

*Summations of time and cycle ratios should be identical in a given test. They are not because the control data correspond to a frequency that was slightly different from that used in the combined strain-range tests.

†Number of cycles imposed first, strain range was changed, and specimen was tested to failure.

Note $\Delta\epsilon_t^1 = 1\%$, $\Delta\epsilon_t^2 = 2\%$ } Nominal values.

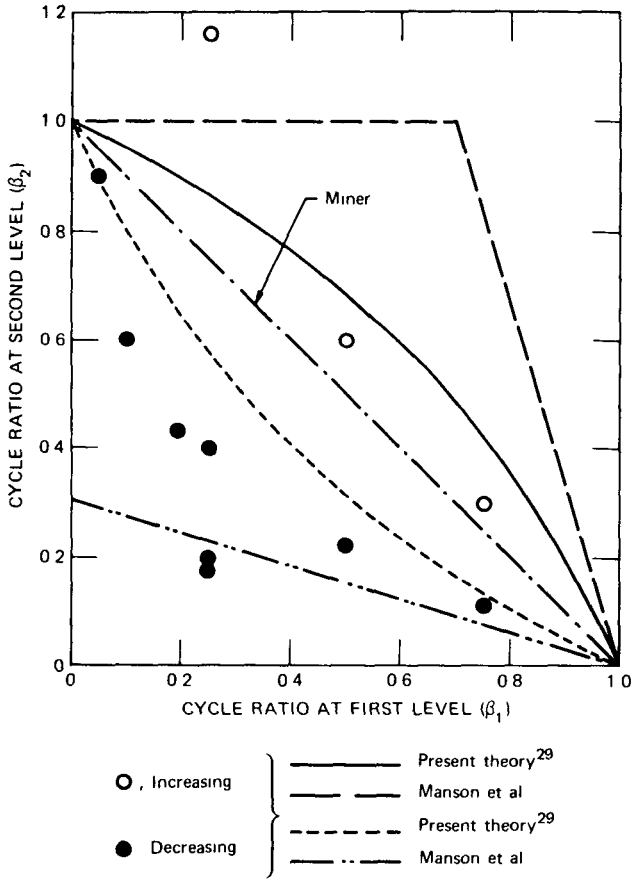

Fig. 5.17 Two-step fatigue tests performed in strain control to show the effect of order of loading.[29] (Published by permission of the Welding Research Council.)

tests of both specimens 67-7 and 67-5, the summation of the time (and cycle) ratio is greater than unity In the high–low–high–low sequencing, it is interesting to note that the summation of the time and cycle ratios is closer to unity than in the high–low or low–high testing Obviously this behavior pattern should be studied in more detail. However, it is encouraging that the application of the linear-damage rule leads to conservative results, since the data in Table 5.5 indicate that the cyclic fatigue life actually remaining in a material is greater than that calculated.

Typical load vs time and strain vs. time plots obtained in the test of specimen 67-7 are presented in Fig 5 18. Particularly noteworthy in the load–time plot is the strain hardening indicated at 2% strain range and the strain softening noted at the 1% strain range

Another interesting plot obtained in the test of specimen 67-7 is shown in Fig. 5.19 A definite hysteresis loop is indicated for each strain range, and the transfer from one loop to another is also highlighted. Arrows identify the hysteresis loops for the first and last cycles in the sequence, and these clearly indicate the cyclic hardening and softening mentioned in the discussion of Fig 5 18. In this evaluation, it is important to emphasize that the specimen was tested in axial strain control with zero mean strain.

In a limited extension of the above study, Berling, Conway, and Stentz[52] used a few interesting combinations of test variables in a further assessment of the linear-damage rule A summary of these four tests, which were all performed at a strain range of 2%, is presented in Table 5.6 to show the use of two strain rates at a constant temperature in one test, two temperatures at a constant strain rate in a second test, two different hold times at a given temperature and strain rate in a third test, and a combination of a 10-min hold period with a no-hold-period exposure in a final test. In the two tests involving no hold period, it is interesting that the cycle summation was always greater than unity. In the two tests that included hold periods, the cycle summation was always less than unity. This represents the first observation of this type and indicates a more damaging effect when hold periods are involved since the cycle summation is definitely less than unity. Hence, although these data and those in Table 5 5 indicate a cycle summation equal to or greater than unity for completely reversed strain cycling, the cycle summation is less than unity when tension-only hold periods are involved. Because of the limited nature of these results, no broad generalization can be offered, but certainly a more detailed evaluation is definitely suggested.

There is very striking similarity between the linear-damage law of Eq. 5.5 and the life-fraction rule proposed by Robinson[53] for use with stress-rupture data. This latter relation has the form

$$\sum_1^1 \frac{t_1}{t_{R1}} = 1 \tag{5.41}$$

where t_1 is the time of exposure to stress level 1 in a stress-rupture test and t_{R1} is the total rupture time at this particular stress This relation was based on the assumption that "the expenditure of each particular fraction of the life span at elevated temperature is independent of and without influence upon the expenditure of all other fractions of the life to rupture " A simple conversion of the N values in Eq 5 5 to time values is made by dividing numerator and denominator by the frequency Thus, for a two-condition exposure, it follows that

$$\frac{N_1/f_1}{N_{f1}/f_1} + \frac{N_2/f_2}{N_{f2}/f_2} = \frac{t_1}{t_{f1}} + \frac{t_2}{t_{f2}} = 1 \tag{5 42}$$

where t_1 and t_2 are the exposure times for two stress-cycling conditions and t_{f1} and t_{f2} are the failure times for these same conditions Equations 5.41 and 5.42 are not really identical, since in Eq. 5.41 the denominator involves the rupture time at constant load and the denominators in Eq 5.42 represent times to fracture as measured in a stress-cycling or strain-cycling evaluation.

Several interesting facts emerge from the studies described in this section. One relates to the observation that

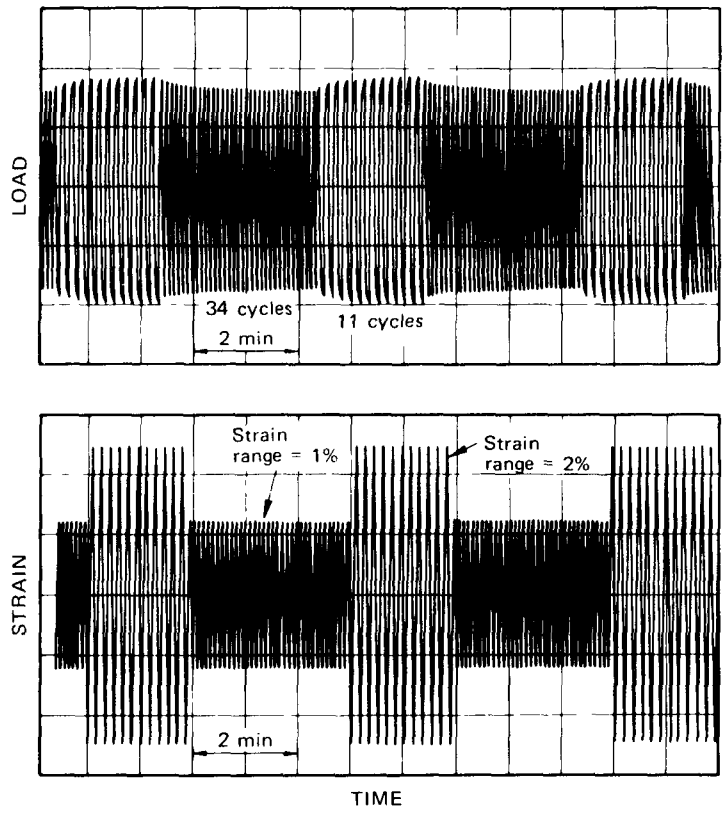

Fig. 5.18 Load vs. time and strain vs. time obtained for AISI 304 stainless steel tested in air at 650°C, a strain rate of 4×10^{-3} sec^{-1}, and using two strain ranges.

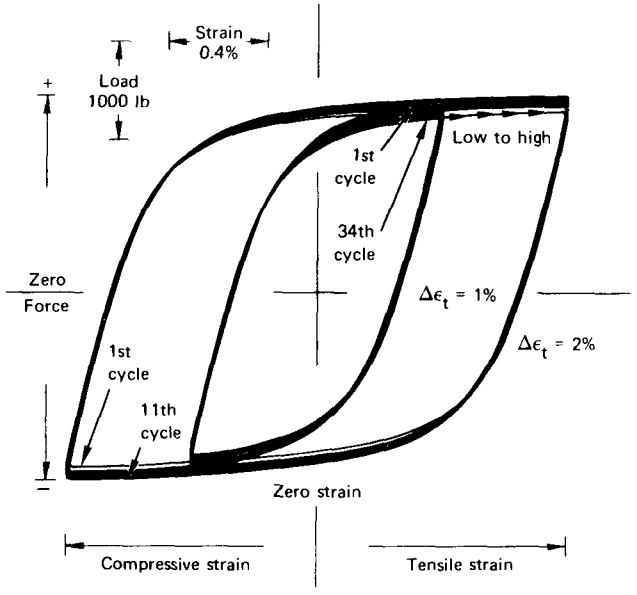

Fig. 5.19 Hysteresis loops obtained for AISI 304 stainless steel tested in air at 650°C, a strain rate of 4×10^{-3} sec^{-1}, and using two strain ranges.

TABLE 5.6

A SUMMARY OF CUMULATIVE-FATIGUE DAMAGE TESTS OF AISI 304 STAINLESS STEEL PERFORMED IN AIR IN AXIAL STRAIN CONTROL USING A STRAIN RANGE OF 2 0%

Tested variable	First condition	No of cycles	$\frac{n_1}{N_1}$	Second condition	No of cycles	$\frac{n_2}{N_2}$	$\sum \frac{n_i}{N_i}$	Remarks
Strain rate*	4×10^{-3}	284	0 5	4×10^{-4}	282	0 90	1 4	At 1200°F
Temp †	1200°F	284	0 5	1500°F	159	0 61	1 11	Strain rate of 4×10^{-3} sec^{-1}
Hold period	10 min	105	0 53	30 min	43	0 28	0 81	Strain rate of 4×10^{-3} sec^{-1} at 1200°F
Hold period	10 min	105	0 53	Zero min	154	0 27	0 80	Strain rate of 4×10^{-3} sec^{-1} at 1200°F

*Material cyclic hardened at 4×10^{-3} sec^{-1} and then cyclic softened when strain rate was changed to 4×10^{-4} sec^{-1}

†Material exhibited cyclic softening when temperature was changed to 1500°F

the same cycle summation was observed independent of order or loading This is the first mention of this type of effect in elevated temperature tests Some explanation of this effect might be obtained from the fact that the two strain ranges used were not drastically different, and hence the fatigue life corresponding to the lower strain range was within a factor of 3 of that associated with the higher strain range Some of the data of Manson et al[28] have already been interpreted in this manner, in that a closer approach to the linear damage rule was noted when the single condition fatigue lives were within a factor of 5 or so

Another interesting observation involves the comment made in connection with Table 5 5 that the cycle summation more closely approaches unity when high–low or low–high cycling is changed to a high–low–high–low pattern This latter pattern was used in the study by Ohji et al ,[17] but in this instance the cycle summation was higher in the repeated pattern than in the high–low or low high combination This is another area that needs further study, and much remains to be done before the interpretation of damage summations can be considered complete Furthermore, some statistical evaluation would seem to be in order so that the real significance of damage summations different from unity can be assessed Of special importance here would be a study of just how extensive the deviations from unity must be before the validity of the linear damage law becomes questionable

CREEP–FATIGUE INTERACTIONS

In the previous sections the discussion focused on the accumulation of fatigue damage And, of course, in many types of exposures this is the only type of damage encountered However, as the test temperature is increased and the cyclic frequency is decreased, the cyclic stresses lead to creep damage, which is known to be an important factor in determining operating life A recent review[54] of creep fatigue interactions emphasized frequency and hold time effects as influential factors in fatigue life determinations

The importance of the combined effects of creep and fatigue was recognized by Taira[55] in dynamic stressing when large stress ratios (stress amplitude to mean stress) are involved It was suggested that the total damage that occurs is composed of a creep damage component, ϕ_c, and a fatigue damage component, ϕ_f Total damage, ϕ_s, was expressed as

$$\phi_s = \phi_c + \phi_f \tag{5 43}$$

and it was reasoned that failure occurs when the sum of the creep- and fatigue damage terms reaches a critical value, ϕ_s'

Equation 5 43 is a little difficult to apply since the value for ϕ_s' is not readily identifiable For this reason the use of the critical damage concept has not been extensive, even though the mathematical formulation in Eq 5 43 appears very simple However, the simplicity is misleading since, in addition to identifying ϕ_s', some attention must be given to proving that both ϕ_c and ϕ_s can assume different values as the test conditions are varied and yet still yield the same value for ϕ_s' at fracture This equality has not been established, and hence the validity of Eq 5 43 is not completely confirmed

Expressions similar to Eq 5 43 have been proposed in an effort to develop analytical procedures for describing creep and fatigue interactions One of the simplest of these was described in Chap 4 and relates to creep damage occurring in a fatigue test when the temperature is high or when the frequency is low It was assumed that the damage associated with each mechanism could be summed linearly

to yield the total damage. It was further assumed that the fractional damage due to creep plus the fractional damage due to fatigue could be added together, and the sum would be unity at fracture. Of course, if Eq. 5.43 is valid, this summation to unity follows from a simple rearrangement, thus

$$\frac{\phi_c}{\phi_s'} + \frac{\phi_f}{\phi_s'} \quad 1 \tag{5 44}$$

Notice, however, that the qualifications mentioned above still apply to any assessment of this expression

In the Manson and Halford[56] study, the creep damage was assumed to be given by t'/t_R and the fatigue damage by N_f'/N_f to yield

$$\frac{t'}{t_R} + \frac{N_f'}{N_f} = 1 \tag{5 45}$$

where t' = effective time of exposure
t_R = rupture time corresponding to the peak tensile stress
N_f' = actual number of cycles to fracture
N_f = number of cycles to fracture calculated using the Method of Universal Slopes

Since it is known that the value of N_f' decreases with decreasing frequency, this effect is consistent with the concept of an increase in creep damage as the cycle time increases Clearly, under such conditions, the allowable cycles in a given exposure will decrease as the frequency decreases In other words, at least qualitative support for Eq. 5.45 is provided by these observations.

One of the real difficulties associated with Eq. 5 45 is the problem of assigning appropriate values to t' and t_R. In a continuous-cycling test, the value of t' can be selected as the total exposure time, the tension exposure time, or some fraction of the total exposure time. Which of these should be used still remains unidentified. A similar complexity is associated with t_R since any cyclic hardening or softening that takes place could change the rupture strength from that of the original material.

From an evaluation of available data, Manson and Halford[56] used t' to represent the effective time of application of the maximum stress. The value of t' was chosen equal to 0.3 times the total exposure time t, which is given by N_f' divided by the frequency. This led to

$$\frac{0.3t}{t_R} + \frac{N_f'}{N_f} = 1 \tag{5 46}$$

or, of course,

$$\frac{0.3N_f'}{ft_R} + \frac{N_f'}{N_f} = 1 \tag{5 47}$$

where f is the frequency and t_R is the time to rupture corresponding to the maximum tensile stress encountered in the fatigue exposure. It was recognized that the value of t' should really be chosen to fit each individual set of data, but it appeared reasonable to select $t' = 0\ 3t$ for general use when more specific information was not available

Fairly extensive use has been made of Eq. 5 45 in the analysis of creep–fatigue interactions during hold-time tests Hold-time effects were described in some detail in Chap. 3, and it was noted that hold periods introduced at peak tensile strain in elevated-temperature tests can have a pronounced influence on the fatigue life This hold-time effect is due to a decided creep influence that is exerted during the hold period Thus much has been done to analyze such tests and to separate, or at least attempt to separate, the creep and fatigue effects through the use of Eq. 5 45. This task is not straighforward, since the stress is not constant during hold periods at constant strain, and hence the t' and t_R values in Eq 5.45 are not easily identifiable Of course, in stress cycling, this difficulty is not encountered, but as yet no extensive evaluation or analysis in terms of creep–fatigue interactions has been made of this type of loading.

The similarity between Eq. 5.6 and Eqs. 5.44 and 5.45 is easily recognized. All involve simple summations of fractional quantities, and in each instance the total sum is equal to unity. Because of this similarity, it is logical to apply the graphical representation used in conjunction with Eq. 5.6 to the creep–fatigue concept presented by Eqs. 5 44 and 5.45. Such plots are referred to as creep–fatigue interaction diagrams, and ideally they serve a very useful purpose. From a practical standpoint, however, the real validity of this approach has not been completely established, and it has not been directly confirmed that creep- and fatigue-damage fractions do indeed provide a summation to unity Much remains to be done in this area before the complete usefulness of this interaction approach can be appreciated Although the evaluation of the fatigue fraction appears to offer no serious difficulty, the exact method for calculating the creep fraction has still not been identified. Equation 5.45, of course, represents one attempt to give mathematical form to the creep-damage term in a continuous-cycling exposure, and, although this approach has not been completely verified, it does represent the first attempt to assign a creep damage term to low-frequency exposures In hold-time exposures involving periods of constant strain (Fig. 5.20), the stress during the hold period decreases with time, and the t_R value in the creep-damage term is not easy to define For such an exposure the creep damage during the hold period of duration HT would be given by

$$\int_0^{HT} \frac{dt}{t_R} \tag{5.48}$$

and Eq. 5.45, written for the case where both strain rate and hold-time effects are encountered, would be

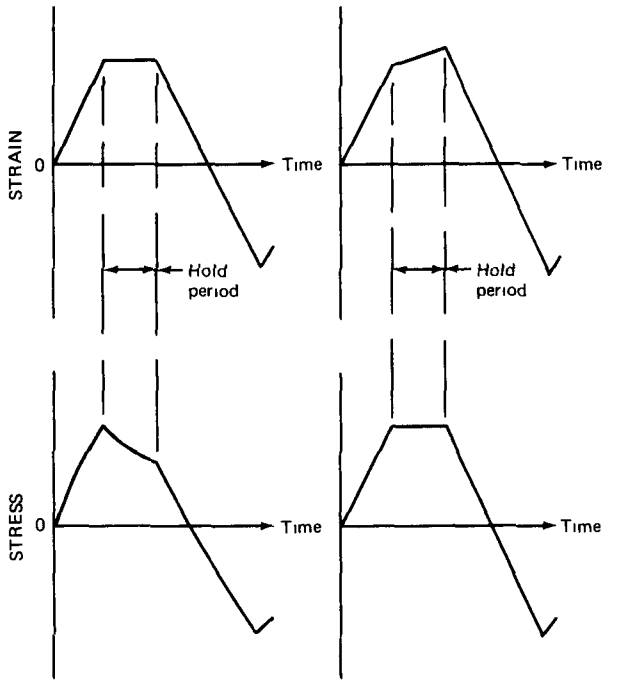

Fig. 5.20 Schematics of some fatigue cycles involving hold periods at constant strain and at constant stress.

$$\frac{t'}{t_R} + \int_0^{HT} \frac{N'_f\, dt}{t_R} + \frac{N'_f}{N_f} = 1 \qquad (5.49)$$

A similar expression for a hold period at constant stress (Fig. 5.20) would be

$$\frac{t'}{t_R} + \frac{N'_f(HT)}{t_R} + \frac{N'_f}{N_f} = 1 \qquad (5.50)$$

And finally the general expression for exposures involving i *different strain rates*, j *different hold periods at constant* strain, and k different hold periods at constant stress would be as follows

$$\sum^{i} \frac{t'_i}{t_R} + \sum^{J} \int_0^{HT_J} \frac{N_J\, dt}{t_{R_J}} + \sum^{k} \frac{N_k(HT_k)}{t_{Rk}} = 1 \qquad (5.51)$$

It is, of course, also possible to add an additional term to account for the occurrence of continuous-cycling exposures at different strain (or stress) ranges

A creep–fatigue interaction diagram is shown schematically in Fig. 5.21 In the plot on rectangular coordinates, the 45° diagonal line represents the type of relation given by Eq. 5.45. Also shown are lines corresponding to fatigue damage only and creep damage only. Two other curves are presented to acknowledge the possibility that the creep–fatigue damage summation could yield something other than unity. The other portion of Fig. 5.21 shows the interaction diagram plotted on logarithmic coordinates.

In one of the first applications of the creep–fatigue interaction diagram, Wood[57] performed axial strain tests on a low-carbon high-manganese steel at room temperature and at 350°C. A test frequency of 0.5 cycle/min was used in the continuous-cycling evaluations, and the specimens were cycled between strain limits using an A ratio of +1 0 (i e., tension–tension on strain) In other tests a creep influence was introduced by using a period of constant stress to yield a predetermined amount of creep strain in preselected time periods (10 min, 60 min, and 24 hr) These data revealed a decided decrease in the cycles to failure as the creep damage was introduced. An analysis of these data in terms of the creep–fatigue interaction diagram is shown in Fig 5.22, where the data points fail to define a summation to unity In this analysis the value for N_f used in the denominator of the fatigue-damage fraction was the value measured at room temperature. This usage of a room-temperature value of N_f to calculate fatigue damage at a test temperature of 350°C can be the cause for at least some of the low fatigue fractions Because Wood used room-temperature values of N_f, this study falls short of providing a definite assessment of the validity of the creep–fatigue interaction concept

Combined creep–fatigue effects have also been studied by Lagneborg and Attermo[58] in reverse-bending fatigue tests of 10-mil austenitic-stainless-steel sheet specimens at 700°C A constant tensile load was applied throughout the test, and within each bending cycle a hold period of 0.5 min to 10 hr was introduced at the position of zero strain amplitude. Bending strain amplitudes from 0.75 to 1 5% were used along with tensile stresses from 5.5 to 8.5 kg/mm^2 The cycling rate exclusive of the hold period was 75 cycles/min An analysis of these results in terms of the creep–fatigue interaction diagram is shown in Fig 5.23 A decided deviation from a summation to unity was noted, and it was concluded that such a summation overestimates the performance capability of the material. A modified creep–fatigue equation was proposed in the form

$$\frac{N_f}{N_{f0}} + B\left(\frac{N_f}{N_{f0}} \times \frac{N_f 2t_1}{t_{f0}}\right)^{1/2} + \frac{N_f 2t_1}{t_{f0}} = 1 \qquad (5.52)$$

where N_f = cycles to failure with a hold period
N_{f0} = cycles to failure without a hold period
t_1 = hold period duration (two per cycle)
t_{f0} = rupture life measured in a static test
B = a constant

This expression provides a good representation of the experimental results. However, it must be recognized that these results were obtained using a rather unique test procedure and they might not be relatable to the data obtained in the more conventional creep–fatigue tests.

Esztergar and Ellis[59] made a comprehensive study of creep–fatigue interactions associated with hold-time test-

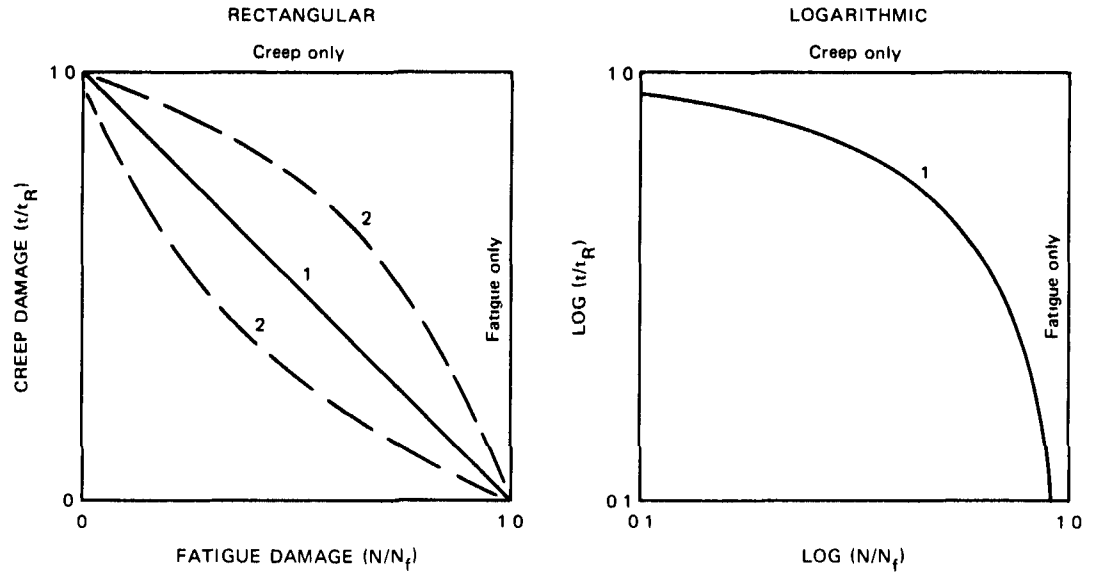

Fig. 5.21 Schematics of creep–fatigue interaction diagrams. (1) Linear creep–fatigue interaction. (2) Nonlinear creep–fatigue interaction.

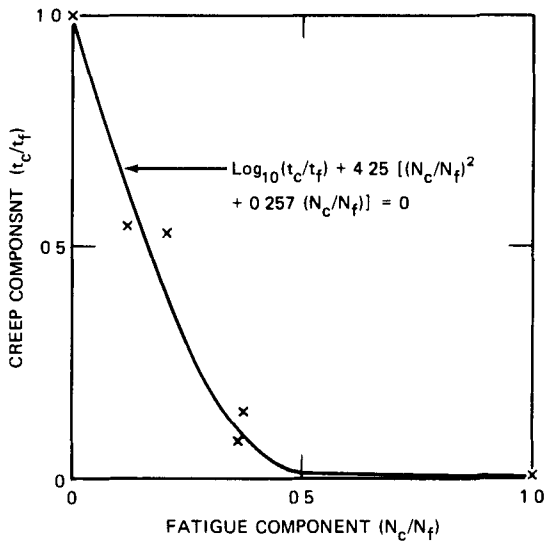

Fig. 5.22 Creep–fatigue interaction diagram for a low-carbon high-manganese steel at 350°C. The symbols t_c and N_c refer to the time and cycles associated with a creep failure. (From Ref. 57)

ing Data for 2¼% Cr–1% Mo steel[60] at 600°C, 1% Cr–1% Mo–0.25% V steel[61] at 1000°F, and for a low-carbon high-manganese steel[57] at 350°C were analyzed to identify creep and damage fractions Creep-damage fractions were calculated using both an equivalent hold-period concept and an equivalent rupture-time concept A creep–fatigue interaction diagram for all the data is shown in Fig 5 24 (t_c and N_c refer to the time and cycles associated with a creep influence) It was noted that the majority of the creep fractions were greater than unity to provide poor agreement with the linear creep–fatigue concept It was felt that the use of the equivalent concepts was responsible for the higher-than-expected creep-damage fractions Thus this study did not provide a proper assessment of the creep–fatigue interaction rule

In a recent[52] combined creep–fatigue evaluation of 304 stainless steel, an hourglass-shaped specimen was tested in axial strain control The specimen was heated to 1200°F, and a strain rate of 4×10^{-3} sec^{-1} was used to impose a total controlled strain range of 2% When the specimen had reached a tensile strain of 1%, the control circuit automatically shifted into stress control, and the stress was immediately reduced to a preselected level of 30,000 psi. This stress was held constant for 10 min to allow creep to occur and the strain to increase. At the end of this creep period, the control system automatically shifted back to strain control, and the load was reversed to apply the necessary compressive load to obtain a compressive strain of 1%. The stress and strain wave forms are shown schematically in Fig. 5.25a, and a schematic of an x–y hysteresis loop is shown in Fig. 5 25b.

Fracture occurred after 112 cycles (fracture time of 1136.1 min) to reveal a more detrimental effect than that observed using a 10-min hold period at peak strain [62] This reflects the greater creep damage resulting from the continued exposure to the higher stress level in the Fig 5.25 type of cycle.

Table 5.7 shows a comparison of the result of this test with that obtained in a continuous-cycling test and in the 10-min hold-period test. Continuous cycling (total strain range of 2%) yields a cyclic fatigue life of about 575 cycles, which is reduced to about 200 cycles when a 10-min hold period in tension only is introduced. Then, when a constant-stress hold period of 10 min at a tensile stress of

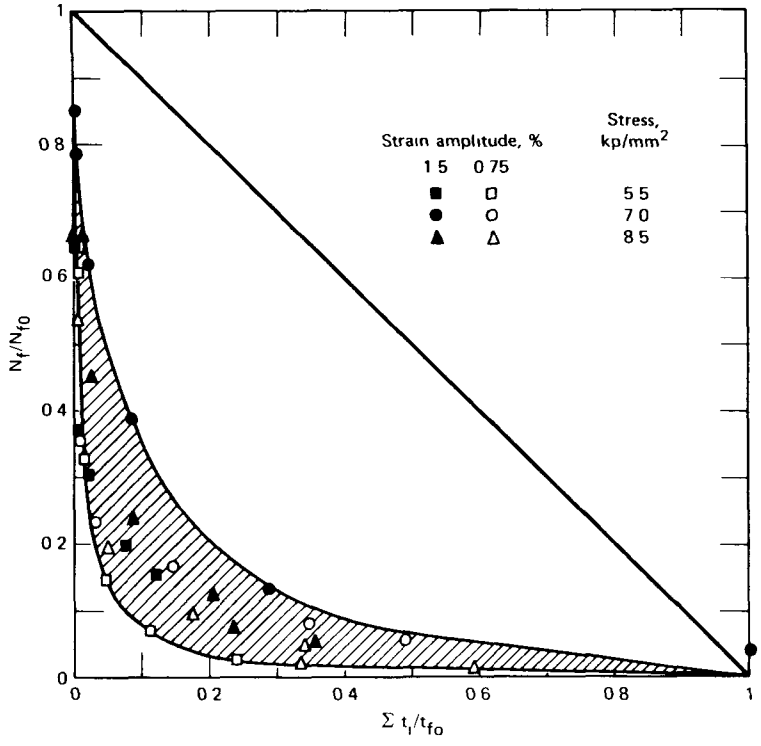

Fig. 5.23 Combined creep–fatigue data for austenitic-stainless-steel sheet tested in reversed bending at 700°C. (From Ref. 58.)

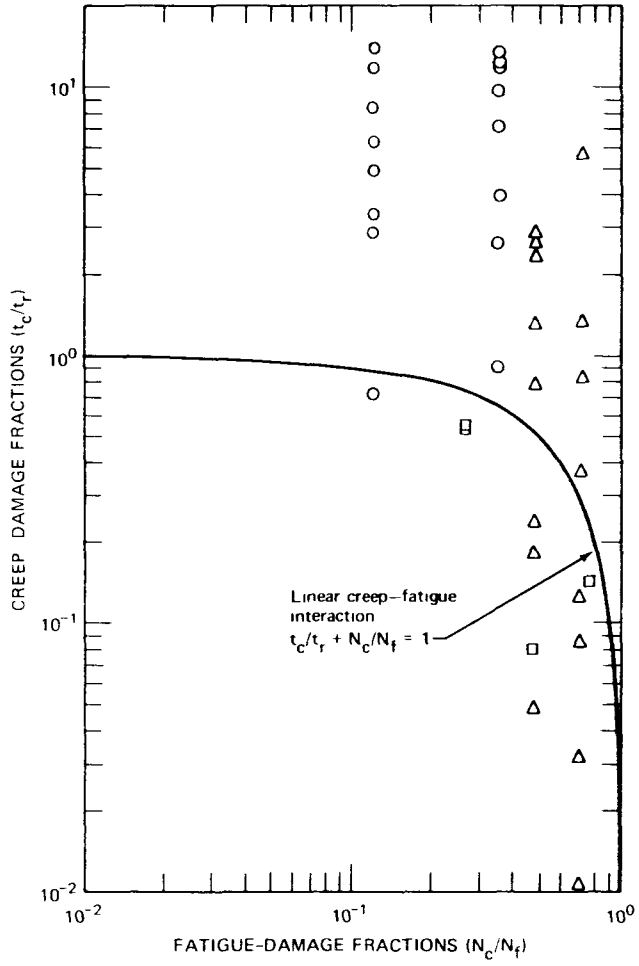

Fig. 5.24 Creep–fatigue interaction diagram for several materials based on use of equivalence concept. (The points that line up vertically are all associated with the same test; it is just that the creep-damage fraction was evaluated in eight different ways.) ○, 2¼% Cr–1% Mo steel. □, low-carbon–high-manganese steel. △, high-ductility 1% Cr–1% Mo–0.25% V steel. (From Ref. 59.)

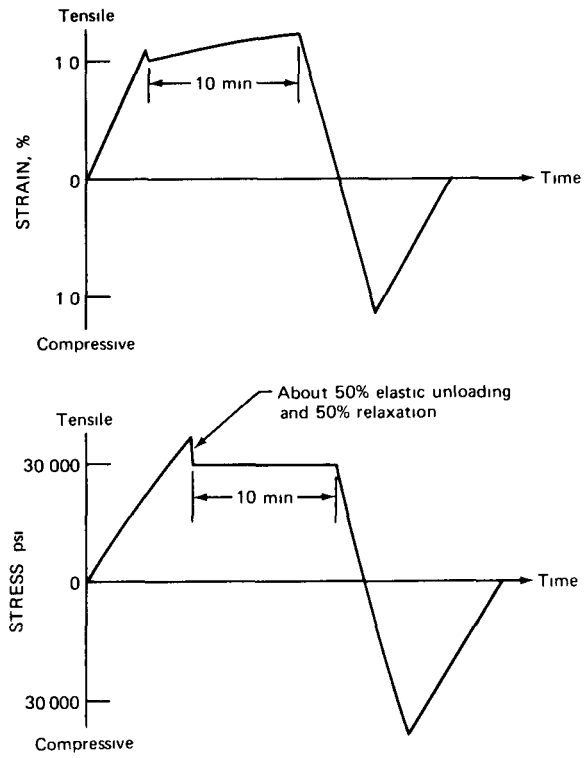

Fig. 5.25a Stress and strain wave forms for combined creep–fatigue test.

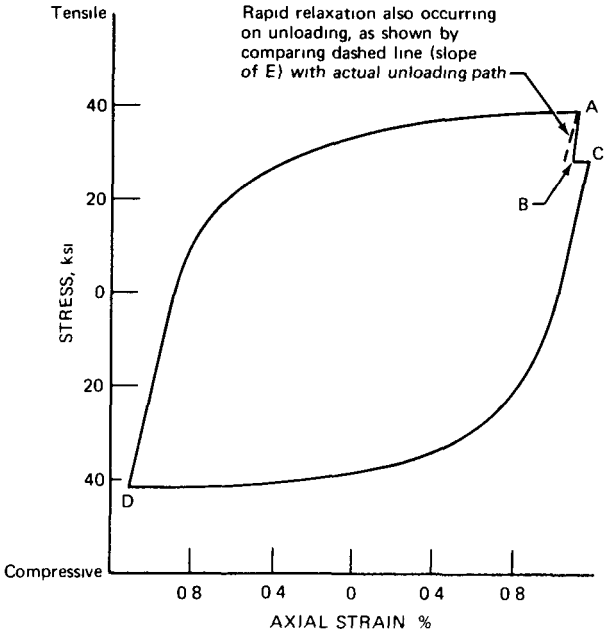

Fig. 5.25b Midtest hysteresis loop for 304 stainless steel tested at 1200°F in combined creep and fatigue. E = 21.6 x 10^6 psi. Points A to B to C are in load control, and points C to D to A are in strain control.

TABLE 5.7

LOW-CYCLE-FATIGUE DATA FOR 304 STAINLESS STEEL OBTAINED AT 1200°F AND A STRAIN RANGE OF 2% USING SEVERAL DIFFERENT STRAIN WAVE FORMS

	Cycles to failure	Time to failure, hr	Plastic strain range, %	Maximum tensile stress, psi	Relaxed tensile stress, psi	Maximum compressive stress, psi
Continuous cycling (two tests)	592/546	1 64/1 52	1 58	39,800/ 40,800		39,800/ 40,800
10-min hold period at peak strain (two tests)	193/201	32 7/33 0	1 71	36,800/ 36,800	22,880/ 22,880	36,800/ 36,800
10-min hold period at constant stress of 30,000 psi	112	18 9	1 68	41,800	36,480	44,250

30,000 psi is used, the cyclic fatigue life is further reduced to 112 cycles. Had this tensile stress been higher, it is expected that the fatigue life would have been reduced even further.

Several features of this test are worthy of special attention. Within each cycle the strain–time deformation exhibited a primary creep characteristic in that the creep rate decreased with time. It was also noted that the amount of strain was approximately constant at about 0.08% in each cycle, except for the last few cycles when the creep strain per cycle was seen to increase. Failure occurred during a constant-stress creep period, and the strain–time plot exhibited the shape of a tertiary creep curve. The average creep rate for the cycle was about 0.5%/hr, which is much higher than the generally reported (0.01 or so) secondary creep rate for 304 stainless steel at these conditions.

One of the objectives of this test was, of course, to use a creep and a fatigue influence in the same evaluation and to then determine if the observed behavior was consistent with the generally accepted creep–fatigue interaction rule. A value of 0.195 is calculated using the data of Table 5.7 to

obtain N/N_f. The rupture time for 304 stainless steel at 1200°F and a stress level of 30,000 psi was taken to be 23 hr. This yields a t/t_r value of 18.7/23, or 0.81, to provide a summation of almost exactly unity. This is a very impressive observation and is completely consistent with the creep–fatigue interaction rule. Thus it appears profitable to pursue this experimental approach in evaluating other hold times, other stress levels, and other strain ranges to obtain a more detailed assessment of the applicability of the above rule for handling creep–fatigue interactions. Admittedly, this one test yields promising results, but a more extensive evaluation is needed before it can be said with confidence that such observations fully confirm the linear creep–fatigue concept.

An analysis of creep–fatigue interactions was reported by Campbell[63] in a study of hold-time data[62] for 304 stainless steel at 1200°F. Relaxation results were used in conjunction with Eq. 5.48 to calculate the creep-damage fraction; and the cycle ratio of Eq. 5.49 was used to represent the fatigue-damage fraction, although the failure condition was described in terms of N_5, the cycles corresponding to a 5% reduction from the peak cyclic stress. The numerator was obtained in hold-time tests, and the denominator was obtained in separate continuous-cycling evaluations. A summary of the results of this evaluation is presented in Fig. 5.26. The data scatter is very pronounced, and a clear association with a linear creep–fatigue interaction relation is not discernible. There does seem to be a clustering of points in the lower left-hand corner of the diagram, which suggests a creep–fatigue summation less than unity. Obviously, however, a few points are positioned to define a summation greater than unity. Although not pointed out by Campbell, a definite trend seems to exist when the damage fractions at a given strain range are analyzed. The results of such an analysis are shown in Fig. 5.27 to define maxima in the plot of creep vs. fatigue fractions. This suggests a creep–fatigue summation close to, or perhaps even slightly greater than, unity when the fatigue fraction is close to unity and a gradual decrease to a summation less than unity as the fatigue fraction decreases. These trend curves establish different creep fractions for the same fatigue fractions and, of course, different creep–fatigue summations for the different strain ranges. Some additional study of this behavior pattern is obviously in order.

In studying dynamic creep-rupture behavior, Taira[55] assumed that fracture occurs when the total damage due to creep, ϕ_c, reaches a critical value, ϕ_{cc}. Also assumed was the fact that the rate of increase of creep damage can be represented by

$$\frac{d\phi_c}{dt} = a_c(|\sigma|)^{\alpha_c} \tag{5.53}$$

where a_c and α_c are constants independent of stress and $|\sigma|$ represents the absolute value of stress. When the applied stress is cyclic in nature and can be expressed as

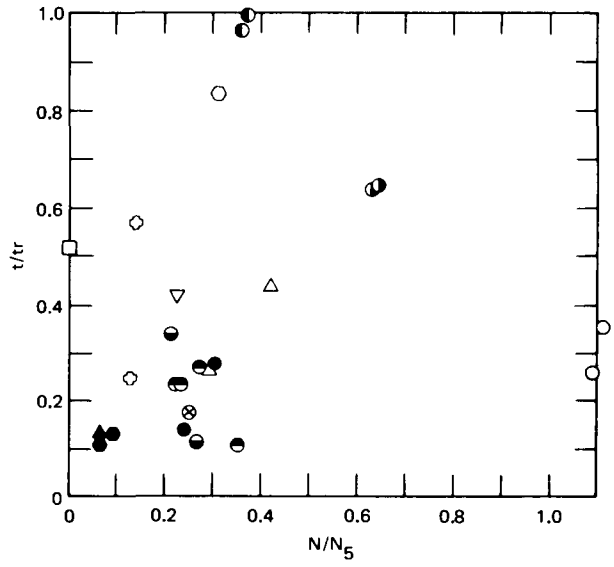

	Total strain range, %	Hold time, min		Total strain range, %	Hold time, min
□	0.25	10	◑	2.0	1
△	0.5	1	◐	2.0	10
⬡	0.5	10	◓	2.0	30
●	0.5	30	◒	2.0	60
▲	0.5	60	●	2.0	180
▽	1.0	10	⊗	2.0	600
○	2.0	0.1	○	4.0	10

Fig. 5.26 Creep–fatigue interaction plot for hold-time data obtained in tests of 304 stainless steel at 1200° F.

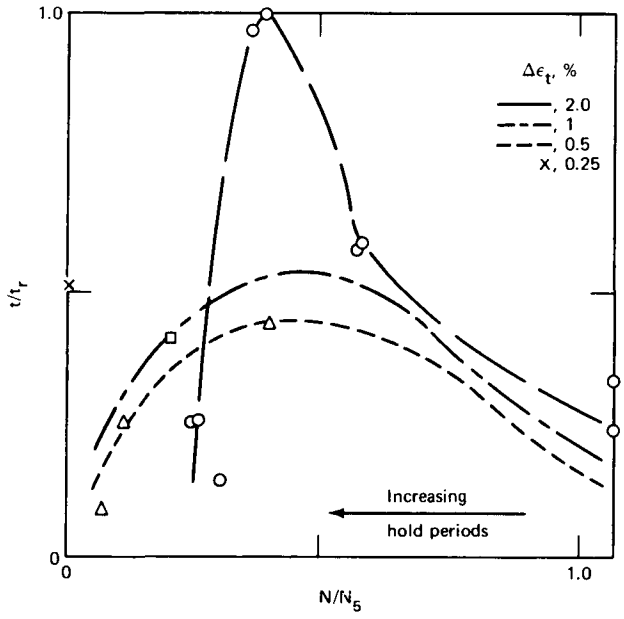

Fig. 5.27 Trends in creep–fatigue damage fractions from Fig. 5.26.

$$\sigma = \sigma_m + \sigma_a \sin \omega t \tag{5.54}$$

(where σ_m is the mean stress, σ_a is the alternating component and ω is the angular velocity of the alternating component) a substitution in Eq. 5.53 leads to

$$\frac{d\phi_c}{dt} = a_c(|\sigma_m + \sigma_a \sin \omega t|)^{\alpha_c} \tag{5.55}$$

$$= a_c \sigma_m^{\alpha_c}(|1 + A \sin \omega t|)^{\alpha_c} \tag{5.56}$$

where A is the stress ratio, σ_a/σ_m. Integration, after noting that the time to fracture, t_c, is related to the cycles to fracture, N, through the expression $\omega t_c = 2\pi N$ from time zero to the fracture time yields ϕ_{cc} as

$$\phi_{cc} = a_c \sigma_m^{\alpha_c} t_c I_c \tag{5.57}$$

where

$$I_c = \frac{1}{2\pi} \int_0^{2\pi} (|1 + A \sin \omega t|)^{\alpha_c} \, d(\omega t) \tag{5.58}$$

Defining an equivalent static stress for dynamic creep rupture σ'_{cd} as

$$\sigma'_{ed} = \sigma_m (I_c)^{1/\alpha_c} \tag{5.59}$$

it follows that

$$\phi_{cc} = a_c (\sigma'_{ed})^{\alpha_c} t_c \tag{5.60}$$

This indicates that fracture under dynamic stress occurs at the same time as static creep-rupture under the stress σ'_{ed}. This value for the equivalent stress can be determined for any combination of σ_m and σ_a once the value of α_c is known from static creep-rupture tests (α_c is the slope of a log σ vs. log t plot).

Taira used the above equations to establish the stress-range diagram shown in Fig. 5.28. Various values of α_c are used as parameters, and each curve represents a typical value.

A nondimensional stress-range diagram for 0.15% carbon steel at 450°C is shown in Fig. 5.29 to define 10- and 100-hr cyclic-rupture behavior. The analytical curve is in good agreement with the experimental results as long as the A ratio is less than about 1.5. Thus it was concluded that, for high stress ratios, the effect of fatigue damage had to be taken into account.

In calculating fatigue damage, Taira thought it reasonable to assume that damage is related to the difference between the instantaneous and mean stress values. If the absolute value of this difference is denoted as σ^*, it follows that

$$\sigma^* = |\sigma - \sigma_m| \tag{5.61}$$

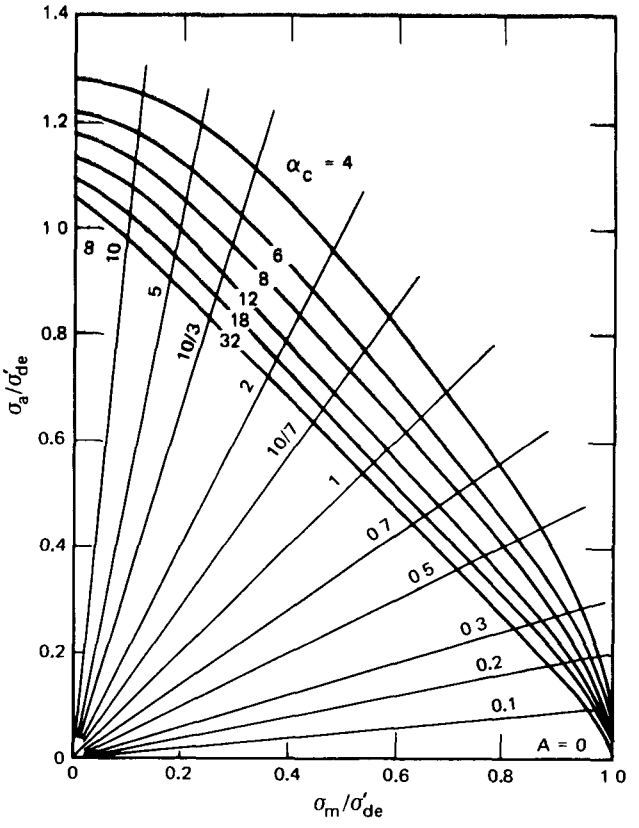

Fig. 5.28 Theoretical stress-range diagram. (From Ref. 55.)

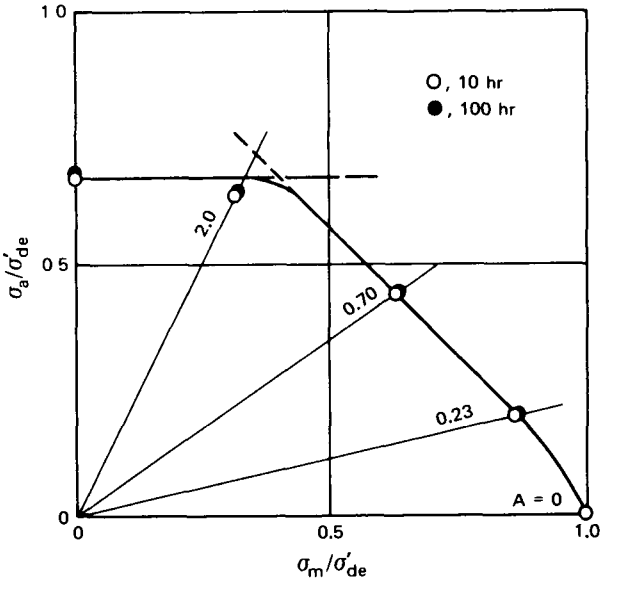

Fig. 5.29 Nondimensional stress-range diagram for dynamic creep rupture of 0.15% carbon steel at 450°C. (From Ref. 55.)

The rate of fatigue-damage accumulation was then written in the following form

$$\frac{d\phi_f}{dt} = a_f(\sigma^*)^{\alpha f} \tag{5.62}$$

where the constants a_f and α_f are assumed to be independent of stress.

If Eq. 5.54 is assumed to represent the stress variation, it follows that

$$\sigma^* = |\sigma_a \sin \omega t| \tag{5.63}$$

Substitution in Eq. 5.62 and integration lead to

$$\phi_f = a_f' \sigma_a^{\alpha f} t_c \tag{5.64}$$

where

$$a_f' = \frac{a_f}{2\pi} \int_0^{2\pi} (|\sin \omega t|)^{\alpha f} \, d(\omega t) \tag{5.65}$$

Then the total damage at any time is composed of creep and fatigue components and, in accordance with Eq. 5.43,

$$\phi_s = a_c \sigma_a^{\alpha c} I_c' t_c + a_f' \sigma_a^{\alpha f} t_c \tag{5.66}$$

where $I_c' = 1/A^{\alpha c}$. Taira then defined a stress level for static creep rupture which leads to fracture at the same time as the dynamic stress, σ_{ed}'; thus

$$\phi_s = a_c(\sigma_{ed}')^{\alpha c} t_c \tag{5.67}$$

and, in comparing Eqs. 5.66 and 5.67, it was stated that

$$\frac{\sigma_a}{\sigma_{ed}'} = \left(I_a + \frac{k_f}{k_c} \sigma_a^{\alpha f - \alpha c}\right)^{\frac{-1}{\alpha c}} \tag{5.68}$$

where

$$k_c = \frac{a_c}{\phi_s} \text{ and } k_f = \frac{a_f'}{\phi_s}$$

The right-hand side of Eq. 5.68 can be evaluated once values of α_c, α_f, and k_f/k_c are known for any combination of σ_a and σ_m. The value of α_c is obtained from static creep-rupture tests, and α_f is obtained from completely alternating stress exposures. The value of k_f/k_c is known when α_c and α_f are determined.

The solid curve in Fig. 5.28 represents the whole range of A ratios and gives a good representation of the experimental results from A = 0 (static loading) to A = ∞ (completely reversed stressing). The dotted and dot–dash lines apply to fracture based on the influences of creep and fatigue considered separately. For rupture under dynamic stress, the creep damage is important when the stress ratio is small, and the fatigue damage is important when the stress ratio is large.

Taira applied Eq. 5.66 to some reported[64] data for 24-ST-4 aluminum alloy at 500°C. As shown in Fig. 5.30, the agreement is very good.

Cyclic-Creep-Rupture Behavior

Manson, Halford, and Spera[65] and Halford[66] noted that the use of monotonic-creep-rupture data in evaluating creep-damage fractions yields only approximate results. It was felt that the use of such data was too severe and led to a computed life that was lower than the actual observed life. This, it was felt, was because of the nature of the monotonic results. During a constant-load rupture test, the cross-sectional area decreases as the specimen elongates, and the true stress increases as time progresses. Furthermore, as the strain becomes larger, cavities and small cracks are formed, and the load-carrying area is further reduced. All these factors, plus any local necking that takes place, tend to promote early failure, and the degree of severity would be expected to be greatest for high creep-ductility materials.

From the above observations, it was reasoned that more realistic rupture information was needed if a more accurate assessment was to be made of the rupture resistance of a material subjected to constrained cyclic loading. It was proposed that this information could be made available in special cyclic-creep-rupture tests. Alternate tensile and compressive loads would be applied, and the specimen would be allowed to creep between fixed limits. A schematic of such a test cycle is shown in Fig. 5.31. A tensile load, A, is applied and held constant until creep deformation leads to the preestablished strain limit at B. When point B is reached, the specimen is loaded in compression to an amount equal to the tensile stress. A few

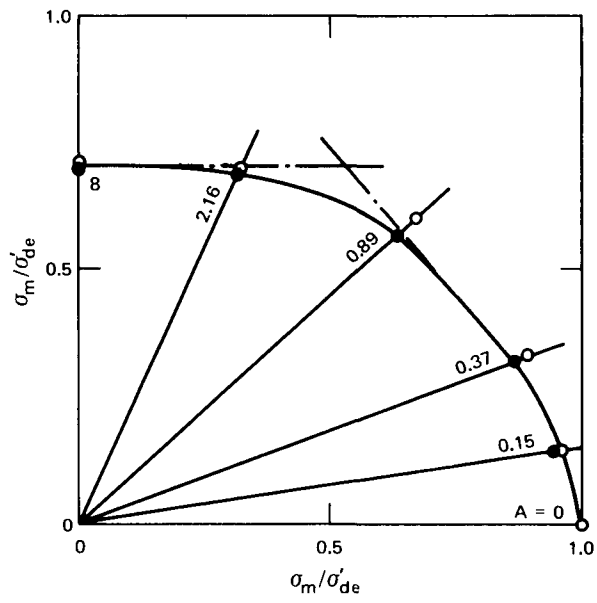

Fig. 5.30 Nondimensional stress-range diagram for 24-ST-4 aluminum alloy at 500°C. ○, 10^6 cycles. ●, 10^7 cycles. (From Ref. 55.)

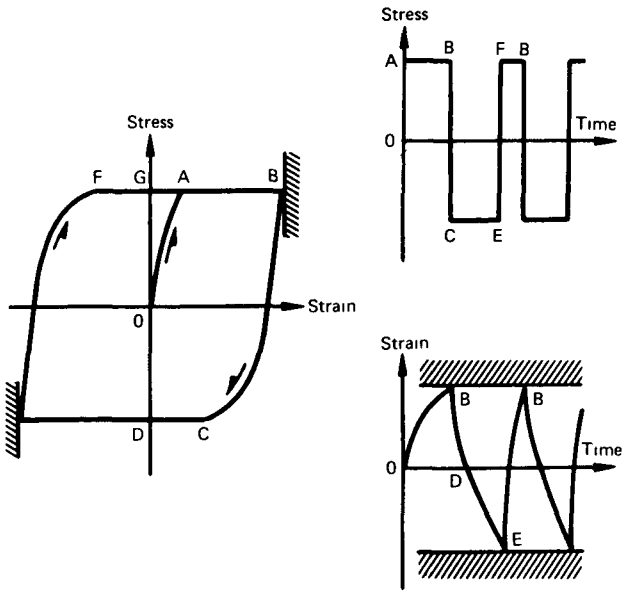

Fig. 5.31 Schematic of cyclic-creep rupture test. (From Ref. 66)

seconds are usually required in this transfer from the full tension to the full compression load at C After the full compression load is established, it is held constant as the strain is reversed past zero strain at D and to some strain limit at E. This is equal in magnitude to the tensile strain limit at B. When point E is reached, the load is reversed to F (the original tensile stress), and the cycle is repeated until fracture.

In the cyclic-creep-rupture tests described by Halford, the frequency was not controlled, but instead was dictated by the creep resistance of the material. As the creep rates increased, the test frequency also increased.

Schematics of the load and strain vs. time behavior patterns are shown in Fig 5.31. In addition to this information, the total elapsed test time was recorded along with the cycles to failure and the time corresponding to the total exposure to a tensile load

The tensile value of the cyclic-creep stress was plotted against the "pure" tensile time to rupture in generating cyclic-creep-rupture curves The pure tensile time to rupture, t_R, was calculated from the measured tensile time to rupture, t, and the creep–fatigue interaction law

$$\frac{t}{t_R} + \frac{N}{N_f} = 1 \qquad (5.69)$$

where the N/N_f ratio expresses the fatigue-damage fraction In this ratio the value of N_f was obtained using the Method of Universal Slopes (see Chap 4). Furthermore, when t_R was calculated, the magnitude of the compressive stress and its duration were ignored.

Halford noted that cyclic-creep-rupture curves can be significantly above and to the right of the corresponding conventional (constant-load) monotonic-creep-rupture curves, as indicated by the results presented in Fig. 5.32. The experimental data for all the materials tested are shown in Tables 5.8 to 5.11.

The cyclic-creep-rupture lives based on pure tensile time to rupture for a given tensile stress are about 10 times greater than the corresponding monotonic lives. Had the additional time spent under the compressive stress been retained when plotting the cyclic time to rupture, the difference between the monotonic and the cyclic rupture times would be a factor of 20. The additional factor of 2 arises since the tensile and compressive creep rates are approximately equal for this material, and hence the times spent in compression and in tension are approximately equal. The large differences between the cyclic and the monotonic rupture curves are attributed to the high monotonic-creep-rupture ductility (as indicated by the 60 to 90% reduction in area) of this material.

A 2% total strain range was used in these tests except at the 70-ksi (485 MN/m^2) stress level, where a 0.9% range was used instead. Note the extremely low fatigue damage associated with those tests (N/N_f = 0.003 to 0.025). The differences in life between the conventional monotonic curve and the curve based on total cyclic time (tension plus compression) is also a factor of 20 for this material. However, the elapsed time spent under the tensile stress was only one-tenth of the time spent under the equal compressive stress, because the compressive creep rates were only one-tenth of the tensile creep rates As a result the cyclic-(pure tensile time) and the monotonic-creep-rupture curves differ by only a factor of 2. This small difference should be expected considering the low creep ductility of this material The creep ductility is low because of the significant strain-age hardening that occurs in the creep-rupture tests. For example, in the cyclic-creep-rupture tests, it was necessary to harden the material to the high stress levels used by applying a few (two to five) strain cycles. Monotonic-creep-rupture tests were subsequently performed on specimens subjected to this hardening procedure. A 10 to 14% reduction in area was observed, which is significantly below the 47% reduction in area measured for this material in a conventional tensile test.

As would be expected from the high monotonic-creep-rupture ductility (approximately 75% reduction in area), there is a significantly large difference between the cyclic- and the conventional monotonic-creep-rupture curves. Each plotted point represents the average time to rupture of all data available at the indicated stress (Table 5.11) Geometric mean values (arithmetic average of the logarithms) were used. There is no significant difference between the results at the different strain ranges, and hence the averaging process is justifiable. In the cyclic tests the time spent in tension was found to be only about four-tenths of the amount of time spent under compression

Also shown in Fig. 5.32 are two test results obtained under constant true stress control. In these tests, diametral strain was monitored and used to compute the instanta-

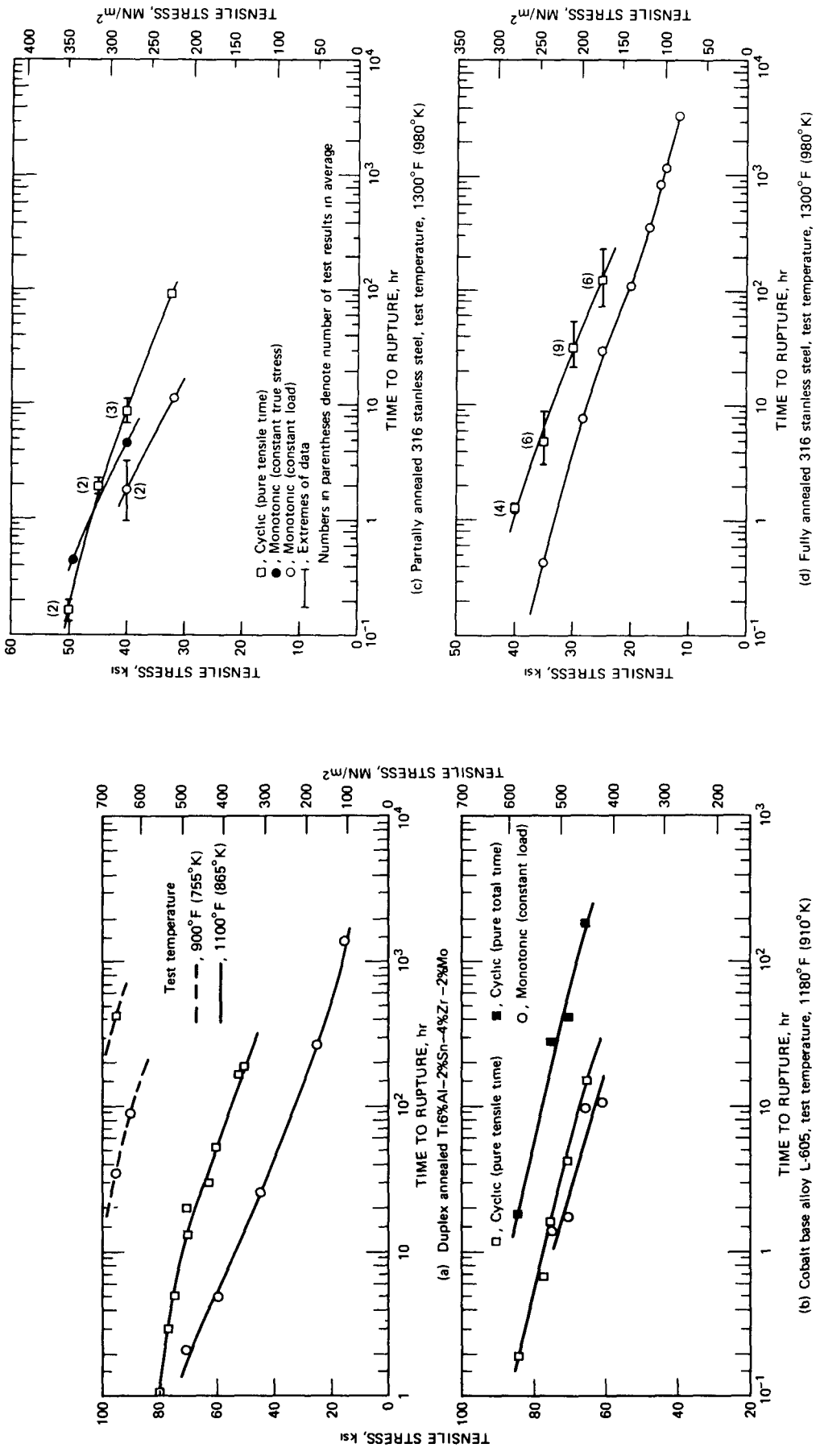

Fig. 5.32 Creep-rupture curves. (From Ref. 66.)

TABLE 5.8

MONOTONIC- AND CYCLIC-CREEP-RUPTURE RESULTS FOR TITANIUM ALLOY 6Al–2Sn–4Zr–2Mo (FROM REF. 66)

Specimen	Total strain range, %	Tensile stress		Compressive stress		Cycles to failure, N	Pure fatigue life,* N_f	Total time to rupture, hr	Tensile time to rupture, hr	Pure tensile time to rupture, hr
		Ksi	MN/m^2	Ksi	MN/m^2					
				Test Temperature, 900° F (775° K)						
ATT-69	4.05	95.0	655	95.0	655	73	380	855	347	430
AT-51	†	95.0	655					35.5	35.5	
AT-53	†	90.0	620					91.8	91.8	
				Test Temperature, 1100° F (865° K)						
ATT-5	3.90	80.0	550	80.0	550	101	400	1.89	0.82	1.09
ATT-22	3.96	77.2	530	60 8	420	87	385	11.16	2.34	3.02
ATT-6	3.90	75.0	515	75.0	515	80	400	8.90	4.10	5.12
ATT-3	3.96	71.4	490	55 0	380	93	385	48.80	15.40	20.10
ATT-72	3.92	70.0	485	70.0	485	151	390	16.96	8.15	12.90
ATT-21	3.90	62.5	430	62.5	430	72	400	53.94	25.24	30.80
ATT-8	3.90	60.0	415	60.0	415	155	400	52.90	33.00	54.00
ATT-29	3.90	52.0	360	52 0	360	108	400	234.5	124.0	170.0
ATT-14	3.90	50.0	345	50.0	345	147	400	233.8	120.5	190.5
AT-52	†	70.0	485					2.1	2.1	
AT-54	†	60.0	415					5.0	5.0	
AT-55	†	45.0	310					26.4	26.4	
AT-62	†	25.0	170					265.0	265.0	
AT-57	†	15.0	105					1373.0	1373.0	

*Based on Universal Slopes equation.
†Monotonic; constant load.

TABLE 5.9

MONOTONIC- AND CYCLIC-CREEP-RUPTURE RESULTS FOR COBALT-BASE ALLOY L-605 AT 1180° F (910° K) (FROM REF. 66)

Specimen	Total strain range, %	Tensile stress		Compressive stress		Cycles to failure, N	Pure fatigue life,* N_f	Total time to rupture, hr	Tensile time to rupture, hr	Pure tensile time to rupture, hr
		Ksi	MN/m^2	Ksi	MN/m^2					
ZZ-75	2.00	83.7	575	83.7	575	$20\frac{1}{2}$	810	1.87	0.194	0.199
ZZ-60	2.04	77.3	535	72.2	500	12	780	2.34	0.635	0.645
ZZ-92	2.00	75.0	515	75.0	515	$9\frac{1}{2}$	810	29.5	1.67	1.69
ZZ-73	0.90	70.0	485	70.0	485	17	5800	42.0	4.34	4.35
ZZ-74	2.00	65.0	450	65.0	450	$2\frac{1}{2}$	810	196.0	15.2	15.3
ZN-12	†	75.0	515					1.4	1.4	
ZN-11	†	70.0	485					1.7	1.7	
ZN-13	†	65.0	450					9.6	9.6	
ZN-15	†	60.0	415					10.8	10.8	

*Based on Universal Slopes equation.
†Monotonic; constant load.

neous cross-sectional area at the minimum test section. The creep load was then manually decreased with time to maintain an approximately constant true stress. Since these tests were conducted on tubular specimens, however, it was not possible to control the true stress beyond the point of tensile necking instability.

From these preliminary results, it appears that the monotonic- (constant true stress) creep-rupture curve may be approximately coincident with the cyclic- (pure tensile a given tensile stress and represents from four to nine individual tests. For the cyclic-creep-rupture tests with completely reversed stresses, the time spent under the tensile stress was only four-tenths of the amount of time spent under the compressive stress. This result is identical with that found for the partially annealed 316 stainless steel discussed in the preceding section.

Separate tests were performed by Halford to show that the cyclic-creep-rupture curve is essentially independent of

TABLE 5.10

MONOTONIC- AND CYCLIC-CREEP-RUPTURE RESULTS FOR PARTIALLY ANNEALED 316 STAINLESS STEEL AT 1300°F (980°K) (FROM REF. 66)

Specimen	Total strain range, %	Tensile stress		Compressive stress		Cycles to failure, N	Pure fatigue life,* N_f	Total time to rupture, hr	Tensile time to rupture, hr	Pure tensile time to rupture, hr
		Ksi	MN/m^2	Ksi	MN/m^2					
YY-111	4.09	50.0	345	50.0	345	33	270	0.230	0.115	0.132
YY-110	1.94	50.0	345	50.0	345	118	1150	0.366	0.183	0.205
YY-51	4.09	45.0	310	45.0	310	52	270	6.00	1.71	2.13
YY-135	1.95	45.0	310	45.0	310	120	1150	11.33	1.53	1.72
YY-138	4.05	40.0	275	30.0	205	85	275	134.4	5.79	8.37
YY-136	4.09	40.0	275	40.0	275	30	270	13.6	6.17	6.95
YY-133	1.95	40.0	275	40.0	275	113	1150	30.0	10.17	11.25
YY-141	4.05	32.5	225	32.5	225	90	275	215.8	60.6	90.2
YY-27	†	40.0	275					1.00	1.00	
YY-28	†	40.0	275					3.33	3.33	
YY-36	†	32.0	220					11.6	11.6	
YY-26	‡	49.3	340					0.453	0.453	
YY-32	‡	40.0	275					4.68	4.68	

*Based on Universal Slopes equation.
†Monotonic; constant load.
‡Monotonic; constant true stress.

time) creep-rupture curve and could possibly be used in its place.

If the cyclic- and the true-stress creep-rupture curves are identical, the implication is that the conventional monotonic-creep-rupture curve is below the cyclic curve solely because the true stresses in the monotonic test are higher and not because of the accumulation of internal voids or cavities as net strain increases.

The difference in rupture time for cyclic and monotonic behavior for a given stress is strikingly large (between a factor of 5 and 20). This would be expected for a material exhibiting high monotonic-creep-rupture ductility (58 to 77% reduction in area). Several different strain ranges (0.8 to 4%) and levels of compressive stress (25 to 45 ksi; 170 to 310 MN/m^2) were used in generating these cyclic rupture results. Each plotted point is based on the geometric mean of the pure tensile time to rupture of all tests conducted at the strain range used. It was also shown that these curves are independent of the magnitude of the compressive stress so that the testing time can be reduced by using high stresses in the compression portion of the cycle.

New Studies

As this text was being prepared for publication, two new developments appeared which promise to contribute significantly to the area of creep–fatigue interactions and, for this reason, are mentioned in this chapter. In one study,[67] a special creep-interspersion test was adopted to make an assessment of separate creep and fatigue contributions. In the other study,[33] a new interpretation was introduced in the form of "strain-range partitioning." Both of these efforts should have an important bearing on subsequent evaluations of creep–fatigue interactions.

TABLE 5.11

MONOTONIC AND CYCLIC CREEP RUPTURE RESULTS FOR FULLY ANNEALED 316 STAINLESS STEEL AT 1300°F (980°K) (FROM REF 66)

Specimen	Total strain range, %	Tensile stress		Compressive stress		Cycles to failure, N	Pure fatigue life,* N_f	Total time to rupture, hr	Tensile time to rupture, hr	Pure tensile time to rupture, hr
		Ksi	MN/m^2	Ksi	MN/m^2					
AYY 110	4 05	25 0	170	25 0	170	41	188	299 2	151 8	194 0
AYY-153	4 05	25 0	170	30 0	205	37	188	259 0	187 4	234 0
AYY-140	4 05	25 0	170	35 0	240	18	188	96 0	90 2	100 0
AYY-145	4.05	25 0	170	40 0	275	12	188	121 9	120 0	128 2
AYY 161	4 05	25 0	170	45 0	310	7	188	75 8	72 7	75 5
AYY 103	4 05	30 0	205	25 0	170	86	188	479 0	30 0	55 3
AYY 129	4 05	30 0	205	30 0	205	98	188	58 0	13 6	28 4
AYY-153	4 05	30 0	205	35 0	240	21	188	35 4	30 8	34 7
AYY-127	4 05	30 0	205	40 0	275	15	188	30 8	30 5	33 1
AYY 152	4 05	30 0	205	40 0	275	15	188	33 9	33 3	35 1
AYY-108	4 05	30 0	205	45 0	310	8	188	22 4	22 2	23 2
AYY-102	4 05	35 0	240	30 0	205	94	188	90 4	1 71	3 92
AYY 96	4 05	35 0	240	35 0	240	100	188	17 4	3 44	7 36
AYY 167	4 05	35 0	240	40 0	275	25	188	6 08	4 41	5 09
AYY-160	4 05	35 0	240	45 0	310	12	188	9 27	8 49	9 07
AYY 162	4.05	40 0	275	30 0	205	100	188	66 97	0 675	1 44
AYY 101	4 05	40 0	275	35 0	240	130	188	11 60	0 52	1 69
AYY 130	4 05	40 0	275	40 0	275	130	188	4 22	0 50	1 62
AYY-119	4.05	40 0	275	45 0	310	18	188	1 58	1 20	1 33
AYY 151	1 67	30 0	205	30 0	205	285	1040	93 7	36 1	50 3
AYY 155	1 67	30 0	205	40 0	275	38	1040	21 4	21 3	22 2
AYY 139	1 67	35 0	240	35 0	240	395	1040	16 7	1 95	3 15
AYY-159	0 785	25 0	170	35 0	240	275	5100	88 6	88 4	95 2
AYY 150	0 785	30 0	205	30 0	205	1330	5100	37 5	19 3	26 1
AYY 136	0 785	35 0	240	35 0	240	1150	5100	9 21	2 89	3 75
AYY 99	†	35 0	240					0 434	0 434	
AY 1	†	28 3	195					7 87	7 87	
AY-2	†	25 0	170					30 6	30 6	
AY 3	†	20 0	140					111 1	111 1	
AY-5	†	17 0	120					362 4	362 4	
AY 4	†	15 0	105					848 3	848 3	
AY-6	†	14 0	95					1184 0	1184 0	
AY-7	†	11 7	80					3408 0	3408 0	

*Based on Universal Slopes equation.
†Monotonic, constant load.

REFERENCES

1 J B Kommers, The Effect of Overstressing in Fatigue on the Endurance Life of Steel, *Amer. Soc. Test Mater, Proc*, 45 532 541 (1945)

2 S S Manson, A J Nachtigall, C R Ensign, and J C Freche, Further Investigation of a Relation for Cumulative Fatigue Damage in Bending, *Trans. ASME (Amer. Soc. Mech. Eng.), Ser. B, J. Eng. Ind.*, 87 25 35 (1965)

3 S R Valluri, A Unified Engineering Theory of High Stress Level Fatigue, *Aerosp Eng.*, 20 18 19, 68 89 (1961)

4 V Gallina, C P Galotto, and G Ruspa, Crack Propagation During Fatigue Experiments, *Int. J. Fracture Mech.*, 6 21 31 (1970)

5 J G Sessler and V Weiss, Low Cycle Fatigue Damage in Pressure Vessel Materials, *Trans ASME (Amer. Soc. Mech. Eng.), Ser D, J Basic Eng.*, 85 539 547 (1963)

6 R H W Brook and J S C Parry, Cumulative Damage in Fatigue A Step Towards Its Understanding, *J. Mech Eng. Sci.*, 11(3) 243 (1969)

7 A Palmgren, Die Lebendauer Von Lugellagern, *Z.V.D I. (Z. Deut. Ingr.)*, 68 339 341 (1924)

8 B F Langer, Fatigue Failure from Stress Cycles of Varying Amplitude *Trans ASME (Amer. Soc. Mech. Eng.), Ser. A, J. Eng. Power*, 59 A160 A162 (1937)

9 M A Miner, Cumulative Damage in Fatigue, *Trans ASME (Amer. Soc. Mech. Eng.), Ser. E, J Appl Mech.*, 67 A159-A164 (1945)

10 W K Rey, Cumulative Fatigue Damage at Elevated Tempera tures, Report NACA TN-4284, National Advisory Committee for Aeronautics, 1958
11 S S Manson, Interpretive Report on Cumulative Fatigue Damage in the Low Cycle Range, *Weld. J.*, 43(8) 344s (1964)
12 W J Crichlow, A J McCulloch, L Young, and M A Melcon, An Engineering Evaluation of Methods for the Prediction of Fatigue Life of Airframe Structures, Report ASD TR 61 434, Lockheed–California Company, Burbank, Calif, March 1962
13 S S Manson, Cumulative Fatigue Damage, *Mach Design*, 32(17) 160 166 (Aug 18, 1960)
14 S S Manson, A J Nachtigall, and J C Freche, A Proposed New Relation for Cumulative Damage in Rotating Bending Cyclic Stresses, *Amer Soc Test. Mater, Proc*, 61 679 (1961)
15 J R Fuller, Cumulative Fatigue Damage Due to Variable Cycle Loading, *Noise Control*, pp 11 24 (July/Aug 1961)
16 S R Valluri, A Theory of Cumulative Damage in Fatigue, Report ARL 182, Aeronautical Research Laboratory, Office of Aerospace Research, United States Air Force, December 1961
17 K Ohji, R W Miller, and J Marin, Cumulative Damage and Effect of Mean Strain in Low Cycle Fatigue of a 2024 T351 Aluminum Alloy, *Trans ASME (Amer Soc Mech Eng), Ser. D, J. Basic Eng.*, 88 801 810 (1966)
18 Georg Sachs and Volker Weiss, Beitrage zur Kurzzeitermudung, *Z Metallk*, Band 53, pp 37 47 (1962)
19 V Weiss, J Sessler, and P Packman, Effect of Several Parameters on Low Cycle Fatigue Behavior, *Acta Met*, 11(7) 809 816 (1963) see also Low Cycle Fatigue of Pressure Vessel Materials, SURI Report MET E 575-662-F, Syracuse University Research Institute, June 1962
20 J H Gross and R D Stout Plastic Fatigue Properties of High Strength Pressure Vessel Steel *Weld J*, 34 161s 166s (1955)
21 A C Low, The Bending Fatigue Strength of Aluminum Alloy MG5 Between 10 and 10 Million Cycles, *J. Roy Aeronaut. Soc.*, 59 502 506 (1955)
22 Richard D'Amato, A Study of the Strain Hardening and Cumulative Damage Behavior of 2032 T4 Aluminum Alloy in the Low Cycle Fatigue Range, Report WADD TR-60 175, Wright Air Development Division, Wright-Patterson Air Force Base, Ohio, April 1960
23 Dogan E Gucer, Cumulative Fatigue at High Plastic Strains, *Trans. Amer. Soc Metals*, 54 176 184 (1961)
24 M Kikukawa, K Ohji A Sumiyoshi, and M Asai, On the Plastic Fatigue Under Varying Strain Amplitudes Part I, orally presented at the 41st Annual Meeting of the Japan Society of Mechanical Engineers, April 1964, abstracts of papers, No 105, pp 167 170, in Japanese
25 E E Baldwin, G Sokol, and L F Coffin, Jr Cylic Strain Fatigue Studies on AISI Type 347 Stainless Steel, *Amer Soc Test. Mater., Proc.*, 57 567 586 (1958)
26 H J Grover, An Observation Concerning the Cycle Ratio in Cumulative Damage, in *Fatigue in Aircraft Structures*, American Society for Testing and Materials Special Technical Publication No 274, pp 120 124 1960
27 S S Manson, Interfaces Between Fatigue, Creep, and Fracture, in Proceedings of the International Conference on Fracture, Sendai, Japan, September 14, 1965 also *Int J Fracture Mech*, 2(1) 327 (March 1966)
28 S S Manson, J C Freche, and C R Ensign, Application of a Double Linear Damage Rule to Cumulative Fatigue American Society for Testing and Materials, Special Technical Publication No 415, p 384, 1967
29 J Dubuc, B Q Thang, A Bazergui, and A Biron, Unified Theory of Cumulative Damage in Metal Fatigue, *Weld Res Counc. Bull.*, No 162 (June 1971)
30 J A Bennett, A Study of the Damage Effect of Fatigue Stressing on X 4130 Steel, *Amer. Soc. Test. Mater., Proc.*, 46 693 711 (1946)
31 F E Richart and N M Newmark, An Hypothesis for Determination of Cumulative Damage in Metal Fatigue, *Amer. Soc. Test. Mater, Proc.*, 48 767 800 (1948)
32 S M Marco and W L Starkey, A Concept of Fatigue Damage, *Trans ASME (Amer Soc. Mech. Eng.)*, 76 627 632 (1954)
33 S S Manson, G R Halford, and M H Hirschberg, Creep–Fatigue Analysis by Strain Range Partitioning, in *Design for Elevated Temperature Environment*, American Society of Me chanical Engineers, New York, 1971
34 K J Miller An Experimental Linear Cumulative Damage Law, *J Strain Anal.*, 5 177 184 (1970)
35 D L Henry A Theory of Fatigue Damage Accumulation in Steel, *Trans. ASME (Amer Soc. Mech Eng.)*, 77 913 918 (1955)
36 F R Shanley A Theory of Fatigue Based on Unbonding During Reversed Slip The Rand Corp, Report P 350, 1953
37 R R Gatts Application of Cumulative Damage Concept to Fatigue, *Trans. ASME, Ser D, J Basic Eng*, 83 529 540 (1961)
38 H T Corten and T J Dolan, Cumulative Fatigue Damage, in Proceedings of the International Conference on the Fatigue of Metals, pp 235 246, American Society of Mechanical Engineers, New York 1956
39 J P Harris and C Lipson, Cumulative Fatigue Damage Due to Spectral Loading, in Proceedings of the Third Aerospace Reliability and Maintainability Conference, Washington, D C, 1964, pp 589 592, Society of Automotive Engineers, New York
40 A M Freudenthal and R A Heller, On Stress Interaction in Fatigue and a Cumulative Damage Rule, *J. Aerosp Sci.*, 26 431 442 (1959)
41 F R Shanley, Discussion of Methods of Fatigue Analysis, in Fatigue of Aircraft Structures, Wright Air Development Center Symposium, Report WADC TR 59-507, pp 182 206, 1959
42 T J P Yao, and W H Munse, Low Cycle Axial Fatigue Behavior of Mild Steel, American Society for Testing and Materials, Special Technical Publication No 338, pp 5 24, 1962
43 G Sachs, W W Gerberich V Weiss, and J V Latorre, Low Cycle Fatigue of Pressure Vessel Materials, *Amer. Soc. Test. Mater., Proc.*, 60 512 529 (1960)
44 D E Martin, An Energy Criterion for Low-Cycle Fatigue, *Trans ASME (Amer. Soc. Mech. Eng.), Ser D, J. Basic Eng.*, 83 565 571 (1961)
45 J Dubuc, J Vanasse, A Biron, and A Bazergui, Effect of Mean Stress and Mean Strain in Low Cycle Fatigue of A 517 and A 201 Steels, *Trans. ASME (Amer Soc. Mech Eng), Ser. B, J Eng Ind.*, 92(1) 35 52 (1970)
46 J B Kommers, Effect of Overstressing and Understressing in Fatigue *Amer Soc. Test. Mater., Proc.*, 38 (Pt II) 249 268 (1938)
47 J B Conway, J T Berling, and R H Stentz, A Brief Study of Cumulative Damage in Low Cycle Fatigue Testing of AISI 304 Stainless Steel at 650°C, *Met Trans.*, 1 2034 (1970)
48 J Dubuc, T Bui Quoc, A Bazergui, and A Biron, Unified Theory of Cumulative Damage in Metal Fatigue, report sub mitted to Pressure Vessel Research Committee, Ecole Polytech nique, April 1969
49 S S Manson, and M H Hirschberg, Fatigue Behavior in Strain Cycling in Low and Intermediate Cycle Range, in Proceedings of the Tenth Sagamore Army Materials Research Conference, pp 133 178, Syracuse University Press, 1964
50 D T Raske and J Morrow, Mechanics of Materials in Low Cycle Fatigue Testing, American Society for Testing and

Materials, Special Technical Publication No 465, pp 1-26, 1969

51 T H Topper, B I Sandor, and J Morrow, Cumulative Fatigue Damage Under Cyclic Strain Control, *J. Mater.*, 4 189 199 (1969)

52 J T Berling, J B Conway, and R H Stentz, unpublished

53 E I Robinson, Effect of Temperature Variation on the Long-Time Rupture Strength of Steels, *Trans. ASME (Amer. Soc. Mech. Eng.)*, 74 777 (July 1952)

54 E Krempl and B M Wundt, Hold Time Effects in High Temperature, Low-Cycle Fatigue A Literature Survey and Interpretive Report, American Society for Testing and Materials, Special Technical Publication No 489, 1971

55 S Taira, *Creep in Structures*, p 96, Academic Press Inc , New York, 1962

56 S S Manson and G R Halford, A Method of Estimating High Temperature Low Cycle Fatigue Behavior of Materials, in *Proceedings of the International Conference on Thermal and High Strain Fatigue*, held in London, June 6–7, 1967, Monograph and Report Series No 32, The Metals and Metallurgy Trust, London, 1967

57 D S Wood, The Effect of Creep on the High Strain Fatigue Behavior of a Pressure Vessel Steel, *Weld. J*, 45(2) 90s (1966)

58 R Lagneborg and R Attermo, The Effect of Combined Low Cycle Fatigue and Creep on the Life of Austenitic Stainless Steels, *Met. Trans.*, 2 1821 (1971)

59 E P Esztergar and J R Ellis, Cumulative Damage Concepts in Creep–Fatigue Life Prediction, in *Proceedings of the International Conference on Thermal Stresses and Thermal Fatigue*, held in Berkeley, England, 1969, D J Littler (Ed), Butterworth & Co (Publishers) Ltd , London, 1971

60 H G Edmunds and D J White, Observations of the Effect of Creep Relaxation on High Strain Fatigue, *J. Mech. Eng. Sci.*, 8(3) 310 (1966)

61 E Krempl and C D Walker, The Effect of Rupture Ductility and Hold Time on the 1000°F Strain Fatigue Behavior of a 1Cr–1Mo–0 25V Steel, American Society for Testing and Materials, Special Technical Publication No 459, p 75, 1969

62 J T Berling and J B Conway, Effect of Hold Time on the Low Cycle Fatigue Resistance of 304 Stainless Steel at 1200°F, in *First International Conference on Pressure Vessel Technology, Delft, Holland, 1969*, Part 2, *Materials and Fabrication*, p 1233 American Society of Mechanical Engineers, New York

63 R D Campbell, Creep/Fatigue Interation Correlation for 304 Stainless Steel Subjected to Strain Controlled Cycling with Hold Times at Peak Strain, *Trans. ASME (Amer Soc. Mech. Eng.), Ser. B, J. Eng. Ind.*, 93(4) 887 (1971)

64 F W DeMoney and B J Lazan, Dynamic Creep and Rupture Properties of an Aluminum Alloy Under Axial Static and Fatigue Stress, *Amer. Soc Test Mater., Proc*, 54 769 (1954)

65 S S Manson, G R Halford, and D A Spera, The Role of Creep in High Temperature Low Cycle Fatigue, A E Johnson Memorial Volume, A I Smith (Ed) American Elsevier Publishing Company Inc , New York, 1971

66 G R Halford, Cyclic Creep Rupture Behavior of Three High Temperature Alloys, *Met Trans*, 3(8) 2247 (August 1972)

67 R M Curran and B M Wundt, A Program To Study Low Cycle Fatigue and Creep Interaction in Steels at Elevated Temperatures, in Current Evaluation of 2¼ Chromel, 1 Molybdenum Steel in Pressure Vessels and Piping American Society of Mechanical Engineers, 1972

Chapter 6

SHORT-TERM TENSILE TESTING

One of the most widely used measures of material strength is that associated with short-term tensile behavior. In evaluations of this type, a well-defined specimen, having an accurately measured cross-sectional area and gage length, is subjected to a gradually increasing tensile load (usually applied at a constant loading rate or under conditions that yield a constant deformation rate) at a carefully controlled temperature. As soon as the load is applied, small specimen elongations (extensions) are observed and simultaneous measurements of load and gage-length elongations give rise to the familiar load-extension type of plots. A typical plot is shown in Fig. 6.1, where several important features are to be noted. One of these features involves the linearity between load and elongation in the region 0A. This is associated with elastic deformation, and upon removal of the load, at any point along 0A, the specimen returns to its original, preloading dimensions. In other words, no permanent deformation has taken place. Beyond point A (actually, the elastic limit and the proportional limit do not usually coincide) the specimen begins to deform plastically, and a departure from the linear load-elongation behavior is observed. In this region beyond point A, the elongation that is measured consists of an elastic and a plastic component. When the load at any point beyond A is removed, the specimen will not return to its original dimension. Unloading from point B, for example, will follow a path essentially parallel to 0A, and after complete unloading the specimen will still contain a certain finite amount of plastic deformation corresponding to the length 0C.

Limited use is made of the load-extension curve in the form just described. More frequently this information is presented in the form of stress–strain plots. In one type of presentation, the load values are divided by the original gage-section cross-sectional area to yield what is termed engineering stress (σ_E); thus

$$\sigma_E = \frac{\text{Load}}{A_0} \tag{6.1}$$

where A_0 indicates the original cross-sectional area of the gage section. Elongation values are also converted into engineering strain (ϵ_E) values by calculating the increase in gage-section length and dividing this by the original gage length; thus

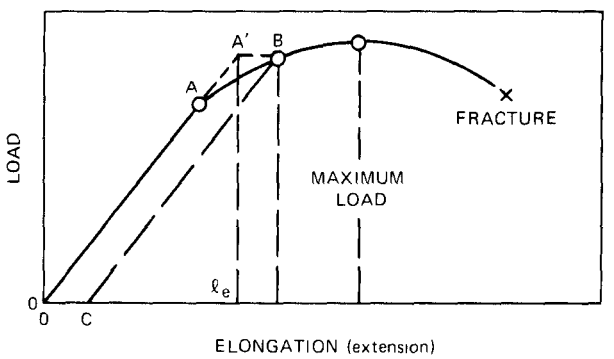

Fig. 6.1 Load-extension plot for tensile loading.

$$\epsilon_E = \frac{\ell - \ell_0}{\ell_0} \tag{6.2}$$

where $(\ell - \ell_0)$ is the instantaneous elongation (values from Fig. 6.1) and ℓ_0 is the original gage length. Stress values are usually presented in pounds per square inch (psi), thousands of pounds per square inch (ksi), tons per square inch (tsi), and kilograms per square millimeter (kg/mm^2). And the strain values are dimensionless since they represent, for instance, a length change in inches divided by a gage length in inches.

In the region beyond point A, the plastic deformation that occurs leads to strain hardening of the material. As a result, if the metal is to be subjected to additional deformation at the same rate of straining, the load must be increased. In other words, the strain hardening has made the metal stronger. Also, as the material deforms beyond point A, the cross-sectional area of the specimen begins to gradually decrease. This decrease causes the actual stress which exists in the specimen to assume larger values than those given by the calculated engineering-stress levels. As deformation continues, the strain-hardening effect, which predominates in the early stages of plastic flow, is gradually exceeded by the stress increase due to the reduction in area. When these two effects are exactly equal, the load-

extension curve exhibits a maximum; beyond this point the reduction-in-area effect is controlling and causes the load to decrease. This combination of work-hardening and reduction-in-area effects leads to the maximum point, which is fairly characteristic of load-extension diagrams. In general, the maximum load point also corresponds to the point at which localized necking of the specimens begins (i.e., uniform deformation over the entire gage length is no longer observed).

Material-property data obtained in short-term tensile tests include modulus of elasticity, ultimate tensile strength, yield strength, percentage elongation, reduction of area, tensile ductility, and fracture stress. Some of these values have shown (see Chap. 4) a relation to low-cycle-fatigue behavior, and therefore an important association exists between these two types of material information.

In this chapter, special emphasis is given to stress–strain behavior and to an interesting new technique development that allows short-term tensile tests to be performed under conditions that maintain the total axial true strain rate at a constant value from the instant of loading all the way to fracture. Some comparison is also made between the data obtained using this test procedure and the data obtained using the standard short-term tensile-testing approach.

TRUE STRESS AND TRUE STRAIN

Engineering strain, ϵ_E, is defined by Eq. 6.2 as the measured elongation divided by the original gage-section length. It is considered more reasonable to refer the instantaneous elongation, $d\ell$, to the instantaneous gage-section length rather than refer it to ℓ_0. When this is done, the following equation applies:

$$d\epsilon = \frac{d\ell}{\ell} \tag{6.3}$$

where ϵ is referred to as the true strain. Integration for a finite amount of deformation from ℓ_0 to ℓ leads to

$$\epsilon = \int_{\ell_0}^{\ell} \frac{d\ell}{\ell} = \ln \frac{\ell}{\ell_0} \tag{6.4}$$

This quantity, ϵ, in addition to being called "true strain" is also referred to as logarithmic or even natural strain. For small amounts of deformation, i.e., ℓ/ℓ_0 close to unity, it is readily shown that true strain and engineering strain are essentially identical.

If the equation for engineering strain is rearranged to

$$\epsilon_E = \frac{\ell}{\ell_0} - 1 \tag{6.5}$$

it then follows that

$$\epsilon = \ln \frac{\ell}{\ell_0} = \ln (1 + \epsilon_E) \tag{6.6}$$

This is the widely used relation between true and engineering strain which is applicable within the region of uniform deformation; when $\epsilon_E = 0.3$, then ϵ will be 0.262. In other words, for large engineering strains the difference between true and engineering strain can be fairly significant.

For the condition of constant-volume* deformation it follows that

$$A_0\ell_0 = A\ell \tag{6.7}$$

or

$$\frac{\ell}{\ell_0} = \frac{A_0}{A} \tag{6.8}$$

From Eq. 6.6,

$$\epsilon = \ln \frac{\ell}{\ell_0} = \ln \frac{A_0}{A} \tag{6.9}$$

Also, from Eq. 6.5,

$$\frac{\ell}{\ell_0} = \frac{A_0}{A} = 1 + \epsilon_E \tag{6.10}$$

and hence, if true stress, σ, is defined as the instantaneous load, P, divided by the instantaneous area,

$$\sigma = \frac{P}{A} = \frac{P}{A_0}(1 + \epsilon_E) \tag{6.11}$$

or

$$\sigma = \sigma_E (1 + \epsilon_E) \tag{6.12}$$

True stress therefore is always greater than the engineering stress and can be calculated from σ_E by multiplying the latter by $(1 + \epsilon_E)$.

If Eqs. 6.6 and 6.12 are used, it will be a simple matter to convert the standard engineering stress–strain curve into one that involves a plot of true stress vs. true strain. In this type of plot, the true stress continuously increases to fracture. An interesting relation between true strain and engineering strain is given in the appendix to this chapter.

One important consideration associated with any discussion of strain is that involving the addition and subtraction of strain values. True strains can be summed directly, whereas engineering strains cannot. However, engineering strains can be combined by observing certain

*Within the elastic region of deformation, the condition of constant volume does not exist. To be completely accurate in this regime, the equations based on the constant-volume condition should not be used. Of course, since elastic deformations are small, the errors in stress due to the assumption of constant-volume deformation are also very small.

procedures. For example, assume that a certain specimen is strained to such an extent that its length is twice that of the original length. If this specimen is strained further until its new length is three times the original length, the total amount of engineering strain will be

$$\epsilon_E = \frac{3\ell_0 - \ell_0}{\ell_0} = 2 \text{ or } 200\% \tag{6.13}$$

The corresponding true strain will be

$$\epsilon = \ln \frac{\ell}{\ell_0} = \ln \frac{3\ell_0}{\ell_0} = \ln 3 = 1.099 \tag{6.14}$$

For the first deformation:

$$\epsilon_{E_1} = \frac{2\ell_0 - \ell_0}{\ell_0} = 1 \text{ or } 100\% \tag{6.15}$$

and

$$\epsilon_1 = \ln 2 = 0.693 \tag{6.16}$$

For the second deformation:

$$\epsilon_{E_2} = \frac{3\ell_0 - 2\ell_0}{2\ell_0} = 0.5 \text{ or } 50\% \tag{6.17}$$

and

$$\epsilon_2 = \ln \frac{3\ell_0}{2\ell_0} = \ln 1.5 = 0.406 \tag{6.18}$$

Equations 6.16 and 6.18 can be added directly to yield the true strain given in Eq. 6.14. However, the engineering strains given by Eqs. 6.17 and 6.15 do not add to give the engineering strain in Eq. 6.13. Engineering strains can be combined properly, however, by using the following relation:

$$1 + \epsilon_{E_t} = (1 + \epsilon_{E_1})(1 + \epsilon_{E_2})(1 + \epsilon_{E_3}), \text{ etc.} \tag{6.19}$$

Applying this approach to the engineering strains given by Eqs. 6.17, 6.15, and 6.13 gives

$$1 + 2 = 3 = (1 + 1)(1 + 0.5) = 3 \tag{6.20}$$

Therefore engineering strains can be combined by adding unity to each strain in the sequence and multiplying these quantities to yield 1 plus the total engineering strain.

In view of the above-mentioned considerations, some comment should be made regarding the addition and subtraction of strain values when the separation of total strain into elastic and plastic components is being considered. If the type of behavior shown in Fig. 6.1 is involved, and, if it is assumed that elastic deformation proceeds along $0A'$ until the stress at point B is reached and then plastic deformation begins and continues until a length corresponding to point B is attained, it is possible to define the various engineering-strain components as

elastic
$$\epsilon_{Ee} = \frac{\ell_e - \ell_0}{\ell_0} \tag{6.21}$$

total
$$\epsilon_{Et} = \frac{\ell - \ell_0}{\ell_0} \tag{6.22}$$

plastic
$$\epsilon_{Ep} = \frac{\ell - \ell_e}{\ell_e} \tag{6.23}$$

The addition of the plastic and elastic strain components yields

$$\frac{\ell - \ell_e}{\ell_e} + \frac{\ell_e - \ell_0}{\ell_0} \tag{6.24}$$

which is not quite equal to the total engineering strain. This summation yields a value that is very close to the ϵ_{Et} value defined by Eq. 6.22, but, for a completely rigorous approach, the equality does not exist. However, a rigorous combination of strains follows from the application of Eq. 6.19. For example:

$$\left(1 + \frac{\ell - \ell_e}{\ell_e}\right)\left(1 + \frac{\ell_e - \ell_0}{\ell_0}\right) = 1 + \epsilon_{Et} \tag{6.25}$$

which reduces to

$$\frac{\ell}{\ell_0} = 1 + \epsilon_{Et} \tag{6.26}$$

which is identical to Eq. 6.22.

Applying the same reasoning used in Eq. 6.4 to develop the relation for true total strain, it is possible to define true elastic strain as

$$\epsilon_e = \ln \frac{\ell_e}{\ell_0} \tag{6.27}$$

and true plastic strain as

$$\epsilon_p = \ln \frac{\ell}{\ell_e} \tag{6.28}$$

Equations 6.21 and 6.23 may now be used to show that

$$\epsilon_e = \ln (1 + \epsilon_{Ee}) \tag{6.29}$$

and

$$\epsilon_p = \ln (1 + \epsilon_{Ep}) \tag{6.30}$$

Since true strains can be summed directly, it is possible to write

$$\epsilon_t = \epsilon_e + \epsilon_p \tag{6.31}$$

and

$$\ln (1 + \epsilon_{Et}) = \ln (1 + \epsilon_{Ee}) + \ln (1 + \epsilon_{Ep}) \tag{6.32}$$

This expression rearranges to yield

$$(1 + \epsilon_{Et}) = (1 + \epsilon_{Ee})(1 + \epsilon_{Ep}) \tag{6.33}$$

which will be seen to be the exact form defined by Eq. 6.19.

In the plastic region it is usually accepted that the elastic engineering strain will be given by

$$\epsilon_{Ee} = \frac{\sigma}{E} \tag{6.34}$$

where σ is the true stress. Therefore, since total elongation measurements are usually available to define true total strain, then true plastic strain can be calculated using

$$\epsilon_p = \ln \frac{\ell}{\ell_0} - \ln \left(1 + \frac{\sigma}{E}\right) \tag{6.35}$$

Since E is so much larger than σ, the value of $\ln (1 + \sigma/E)$ is very close to σ/E. It is usually accurate enough, therefore, to write

$$\epsilon_p = \ln \frac{\ell}{\ell_0} - \frac{\sigma}{E} \tag{6.36}$$

In this expression, σ/E is not really a true strain and hence cannot be added to or subtracted from other true strains. However, this value is so close to the actual value of the true strain that the approximation given in Eq. 6.36 is accurate enough for most purposes.

Equation 6.36 can also be written as

$$\epsilon_p = \ln (1 + \epsilon_{Et}) - \frac{\sigma}{E} \tag{6.37}$$

Little error is introduced by using

$$\epsilon_p = \ln \left(1 + \epsilon_{Et} - \frac{\sigma}{E}\right) \tag{6.38}$$

Although this form is not mathematically rigorous, it yields true-plastic-strain values that contain only very small errors.

Generalized Strain

In a very unique treatment of strain, Seth[1] proposed the concept of generalized strain, $\bar{\epsilon}$, defined as

$$\bar{\epsilon} = \frac{1}{n}\left[1 - \left(\frac{\ell_0}{\ell}\right)^n\right] \tag{6.39}$$

when ℓ is the instantaneous length, ℓ_0 is the reference length, and n is a constant called the coefficient of strain measure. Seth showed that the different definitions of strain used in various studies are all particular cases of the generalized strain; thus

n = + 2	Almansi
n = + 1	Swainger
n = 0	Hencky (natural strain)
n = – 1	Cauchy (engineering strain)
n = – 2	Green

A plot of ℓ/ℓ_0 vs. $\bar{\epsilon}$ is shown in Fig. 6.2 to indicate the effect of various n values. These data are generated using Eq. 6.39 and assuming different values for the coefficient of strain measure. In this figure, when the deformation is small (low values of ℓ/ℓ_0), the value of n has essentially no effect on $\bar{\epsilon}$. Hence, for metals in the elastic region, no matter which value of n is used, the stress–strain curve will have a slope very close to that given by the modulus of elasticity. As the deformation becomes larger, the choice of n will have a direct bearing on the shape of the stress–strain curve.

Differentiating Eq. 6.39, Hsu, Davies, and Royles[2] showed that

$$d\bar{\epsilon} = \frac{d\ell}{\ell_0(\ell/\ell_0)^{n+1}} \tag{6.40}$$

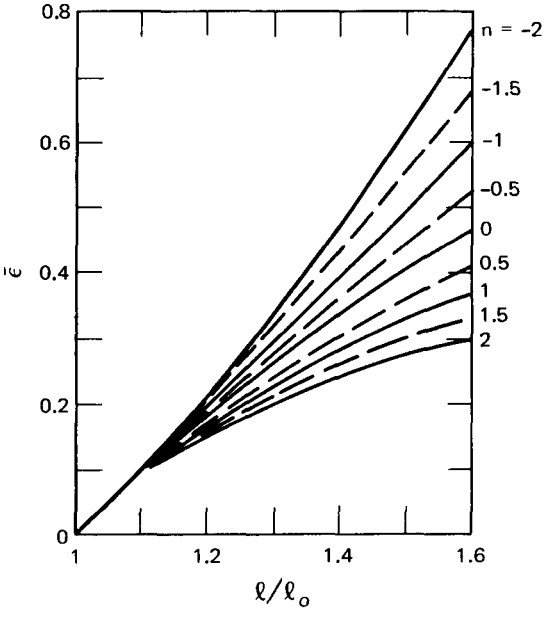

Fig. 6.2 Variation of generalized strain with n, the coefficient of strain measure. (From Ref. 2.)

and, when n = −1,

$$d\bar{\epsilon} = \frac{d\ell}{\ell_0} \tag{6.41}$$

to define the relation for engineering strain with the deformation, $d\ell$, referred to the reference length ℓ_0. Also, when n = 0, Eq. 6.40 yields

$$d\bar{\epsilon} = \frac{d\ell}{\ell} \tag{6.42}$$

which will be the definition of true or logarithmic strain where the deformation, $d\ell$, is referred to the instantaneous length. In general, the basis of the strain in Eq. 6.39 is a mixture of the reference length and the instantaneous length with the effect of each being determined by n. Although integers have previously been considered for n values, there seems to be no need to impose this restriction. Fractional values need not be excluded from consideration. In the discussion by Hsu et al.,[2] the value of $n = \frac{1}{2}$ was cited as defining the length basis as the geometric mean of the instantaneous and reference lengths. Further discussions and several applications of this concept will be considered in later sections of this chapter.

STRESS–STRAIN RELATIONS

Many studies have been devoted to the graphical and analytical representation of stress–strain behavior. In most of these studies, the use of true stress (load divided by instantaneous area) has been preferred, but no such agreement has been reached in expressing the deformation. Some authors have used engineering strain and others have used true strain or some quantity related to this deformation measure. Furthermore, the mathematical formulations used in relating stress and strain have been numerous, and no single expression has as yet attained widespread acceptance. For example, Voce[3] has commented that, since Hooke's law was introduced in 1678, a rather extensive list of equations for expressing stress–strain behavior has been in existence. A review of this listing was presented by Osgood[4] in a treatment of 22 of these empirical expressions. In general, these equations attempted to describe the stress–strain behavior from the instant of loading and because of this were faced with the complexity of accounting for elastic and plastic deformation behavior in a single equation. As a result, many of these expressions were found to be of limited utility. Some of the equations considered in the Osgood review are listed in Table 6.1 along with a brief comment regarding the effectiveness of the expression.

In recent years some effort has continued to be devoted to the analytical representation of stress–strain data. In these studies, however, attention has been limited to the region beyond the yield point, and equations were studied that had application from the initial point of plastic flow to the point corresponding to necking. One of these equations which has attained particular prominence is referred to as the power function (see below) for plastic deformation and has been used very extensively in the analysis of stress–strain results. Also, somewhat effective and noteworthy is the Voce[3] equation (see below). Although this has not attained the status enjoyed by the power function, it has some very impressive characteristics and warrants serious consideration. Another fairly recent stress–strain relation is that due to Mazzoleni[17] in the form

$$\sigma = \sigma_\infty \frac{a\,(L/L_0)^b}{1 + a\,(L/L_0)^b} \tag{6.43}$$

This expression has some similarity to the Voce equation but is not able to describe stress–strain behavior as effectively as the Voce relation. In other fairly recent developments, Stowell[18] discussed the applicability of

$$\epsilon = \frac{\sigma}{E} + \epsilon_0 \sinh \frac{\sigma}{\sigma_0} \tag{6.44}$$

where E, ϵ_0, and σ_0 are constants, and Hsu, Davies, and Royles[2] used the concept of generalized strain to linearize stress–strain results.

In the following sections special attention is given to the power function, Voce equations, and generalized strain concept. Particular emphasis is given to the use of these methods of analysis, and some discussion is presented to evaluate the effectiveness of these approaches.

Power Function

A brief study of the Bulffingeri[5] expression of Table 6.1 reveals a simple rearrangement to yield

$$\sigma = K'\epsilon^m \tag{6.45}$$

This form failed to attain special prominence probably because attempts were made to apply it in describing both elastic and plastic behavior. This same form,* generally attributed to Ludwik,[19] has, however, attained widespread usage in evaluations limited to the plastic-flow region. Many correlations based on the power function of Eq. 6.45 have

*Although this form is generally attributed to Ludwik, the expression actually proposed by Ludwik had the form

$$\sigma = \sigma_0 + K\epsilon^m$$

This expression has not been studied to any great extent but rather has been abbreviated to yield Eq. 6.45. This abbreviation followed, undoubtedly, from a certain amount of linearity observed in log–log graphs of stress–strain behavior. Actually, no such linearity follows from the original Ludwik equation, for the equation specifies a stress–strain curve that is concave upward on logarithmic coordinates.

TABLE 6.1

TYPICAL EQUATIONS FOR EXPRESSING STRESS–STRAIN BEHAVIOR*

Equation	Author	Year	Ref.	Remarks
$\epsilon = K\left(\frac{\sigma}{K}\right)^n$	Bulffinger	1729	5	Does not apply in elastic range, may be applicable in region of large strains
$\frac{\sigma}{E} - Ke^{-1/\epsilon}$	Riccati	1731	6	Slope at origin not consistent with modulus of elasticity
$\frac{\sigma}{E} - \epsilon + b\epsilon^2$ for $b < 0$	Gerstner	1831	7	Leads to negative σ values when $\epsilon > -1/b$
$\epsilon - \frac{\sigma}{E}[1 + \beta(e^{\alpha\sigma} - 1)]$	Poncelet	1841	8	Parameters difficult to determine
$\epsilon^2 = \frac{\alpha\sigma}{E} + \beta\left(\frac{\sigma}{E}\right)^2$	Wertheim	1847	9	Slope is zero at origin
$\epsilon = \frac{\sigma}{1 + \alpha\sigma}$	Cox	1851	10	Considered not generally applicable
$\epsilon = \frac{1}{\alpha}(e^{\alpha\sigma} - 1)$	Imbert	1880	11	Considered not generally applicable
$\frac{\sigma}{E} = \left(\frac{\epsilon}{1 - \epsilon}\right)e^{a\epsilon}$	Hartig	1893	12	Considered not generally applicable
$\frac{\sigma}{E} = L\epsilon^m + b\epsilon^2$	Schule	1898	13	Similar to Gerstner equation
$\frac{\sigma}{E} - a\epsilon + b\tanh\left[\frac{(1 - a)}{b}\epsilon\right]$	Prager	1939	14	Constants are difficult to evaluate
$\epsilon = \frac{\sigma}{E}$ for $\sigma < \sigma_p$	Holmquist–Nadai	1959	15	σ_p is proportional limit, ϵ_y is strain at yield strength, σ_y
$\epsilon = \frac{\sigma}{E} + \epsilon_y\left(\frac{\sigma - \sigma_p}{\sigma_y - \sigma_p}\right)^n$ for $\sigma > \sigma_p$	Holmquist–Nadai			
$\epsilon = \frac{\sigma}{E} + K\left(\frac{\sigma}{E}\right)^n$	Ramberg–Osgood	1943	16	Special case of Holmquist–Nadai equation
$\epsilon = \frac{\alpha\sigma}{E} + \beta[-1 + \exp(1 - \alpha)\sigma/\beta E]$	Holmquist–Nadai	1939	15	Constants are difficult to evaluate

*It is usually recommended that true stress and true strain be used when strain values become greater than about 1%.

been shown to be fairly effective, and as a result this relation is widely quoted and extensively used. Some aspects of this equation format are subject to some criticism, and these features will be discussed in the section dealing with the Voce equation.

Taking logarithms of what has been called the Ludwik power function leads to

$$\log \sigma = \log K' + m \log \epsilon \qquad (6.46)$$

in which σ is the true stress and ϵ is the true strain (more consistency seems to be observed when true plastic strain is used instead of total true strain). This expression will yield a linear relation between σ and ϵ when logarithmic coordinates are used. Also, the slope of this line will yield the value of m, which is known as the strain-hardening rate or strain-hardening exponent. Intercept calculations lead to the value for K', the strength coefficient that represents the true stress corresponding to a true strain of unity.

Many examples can be cited which illustrate the applicability of Eq. 6.46. One typical plot is presented in Fig. 6.3 based on data reported by Low and Garofalo.[20]

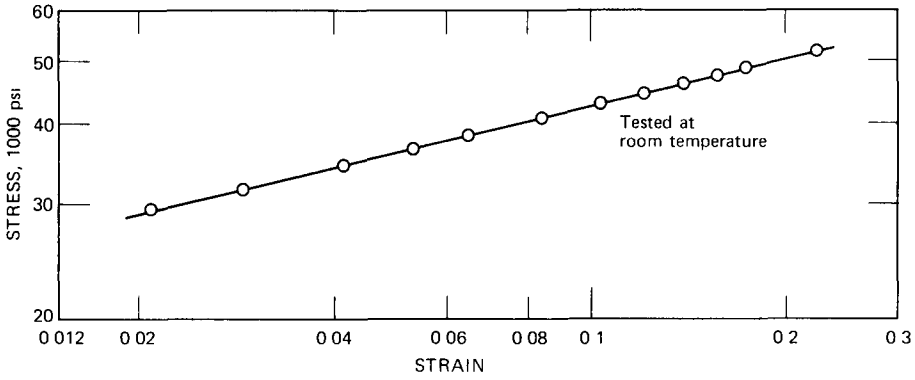

Fig. 6.3 Plot of true stress vs. true strain for temper-rolled killed deep-drawing steel sheet. (From Ref. 20.)

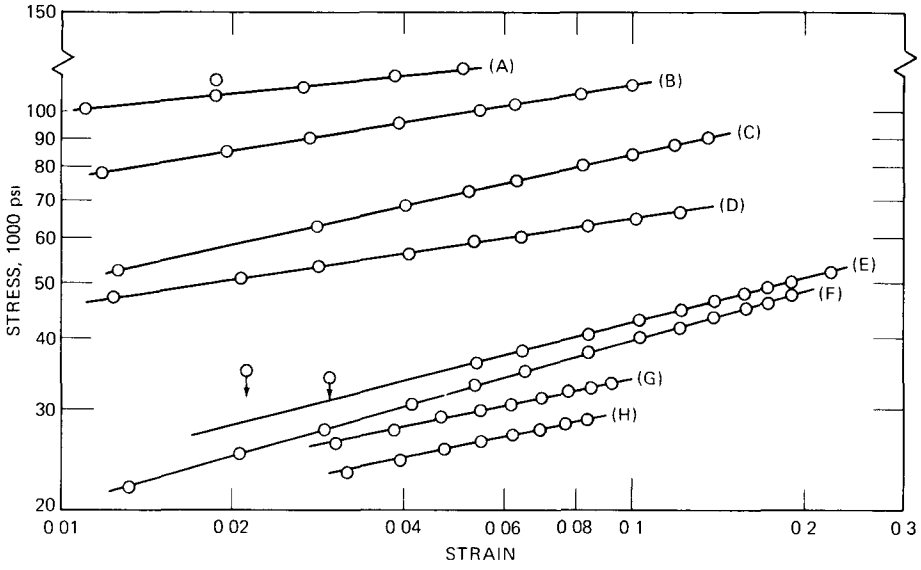

Fig. 6.4 True stress–strain plots for several materials at room temperature. (From Ref. 20.)

A, SAE 4130 annealed
B, SAE 4130 normalized temper rolled
C, stainless type 430 annealed
D, 0.05/0.07% phosphor, low-carbon steel
E, low carbon rimmed steel annealed
F, completely decarburized steel
G, 245–O aluminum alloy
H, R–301–O aluminum alloy

Actually, 48 tests were made using specimens from a specific sheet of steel, and m values ranged from 0.230 to 0.238 with K′ values ranging from 71,700 to 74,400 psi. Data for other materials were also reported by Low and Garofalo[20] and are shown in Fig. 6.4. Values for m and K′ are listed in Table 6.2.

Values for the strain-hardening exponent, m, of steel are a function[21] of strength level, composition, and structure. Illustrations of these effects are shown in Figs. 6.5 and 6.6. Temperature also exerts a pronounced effect on the strain-hardening exponent. Although very little work has been done to completely evaluate this behavior, it is established that increasing temperature decreases the value of m. Studies of this effect will be discussed in a later section dealing with experimental results. Strain rate also seems to have an effect on the value of the strain-hardening exponent. This effect is not completely confirmed, but, in general, it seems that reducing the strain rate leads to a reduction in the value of m.

As already mentioned, most metals exhibit an increase in strength as deformation proceeds. This strain-hardening phenomenon functions to increase the load-carrying capacity of the specimen as straining takes place. Opposing this effect is the gradual decrease in the cross-sectional area of the specimen as the elongation increases. Necking or localized deformation usually begins at maximum load when the increase in stress due to the decrease in the cross-sectional area of the specimen becomes greater than

TABLE 6.2

VALUES OF m AND K′ FOR SEVERAL MATERIALS TESTED AT ROOM TEMPERATURE (FROM REF. 20)

Material	Treatment	m	K′, psi	Thickness, in.
1. 0.05% carbon-rimmed steel	Annealed	0.261	77,100	0.037
2. 0.05% carbon-killed steel	Annealed and temper rolled	0.234	73,100	0.037
3. Same as No. 2 above but completely decarburized	Annealed in wet hydrogen	0.284	75,500	0.037
4. 0.05/0.07% phosphorus low-carbon steel	Annealed	0.156	93,330	0.037
5. SAE 4130	Annealed	0.118	169,400	0.037
6. SAE 4130	Normalized and temper rolled	0.156	154,500	0.037
7. Type 430 stainless steel (17% chromium)	Annealed	0.229	143,000	0.050
8. Alcoa 24-S	Annealed	0.211	55,900	0.040
9. Reynolds R-301	Annealed	0.211	48,450	0.040

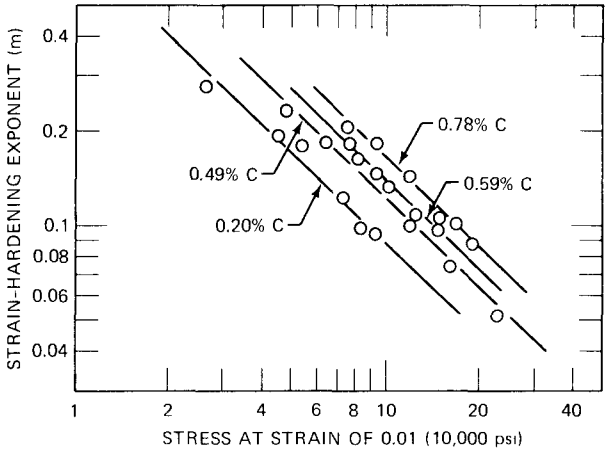

Fig. 6.5 Strain-hardening exponent as a function of strength and composition of steel. (From Ref. 21.)

the increase in the load-carrying ability of the metal due to strain hardening. This condition on a load vs. strain plot is described by $dP = 0$. Then, since $P = \sigma A$, it follows that

$$dP = \sigma\, dA + A d\sigma \tag{6.47}$$

where P is the load and σ is the true stress. When this equation is set equal to zero for the condition at the maximum load point, it follows that

$$\left(\frac{-dA}{A} = \frac{d\sigma}{\sigma}\right)_{max.} \tag{6.48}$$

Applying the concept of constant volume deformation gives

$$\left(\frac{d\sigma}{\sigma}\right)_{max.} = \frac{dL}{L} = d\epsilon = \frac{d\epsilon_E}{1 + \epsilon_E} \tag{6.49}$$

where ϵ and ϵ_E are the true and engineering strains, respectively. Therefore

$$\left(\frac{d\sigma}{d\epsilon}\right)_{max.} = \sigma_{max.} \tag{6.50}$$

or

$$\left(\frac{d\sigma}{d\epsilon_E}\right)_{max.} = \left(\frac{\sigma}{1 + \epsilon_E}\right)_{max.} \tag{6.51}$$

According to Eq. 6.50, maximum load occurs at a strain at which the slope of the true-stress–true-strain curve equals the true stress.

An interesting geometrical construction results from Eq. 6.51 and is shown in Fig. 6.7. In this plot of true stress vs. engineering strain, the point F corresponding to a strain of -1 is located. A line drawn from this point and tangent to the stress–strain curve locates point G, which is the maximum load point. This follows from Eq. 6.51, which defines the slope at the maximum load point as being equal to $\sigma/(1 + \epsilon_E)$. The stress at this point is σ_m, the true stress at the maximum load. Had Fig. 6.7 been plotted in terms of engineering stress, this value would be the ultimate tensile strength, σ_u. It can be seen that

$$\frac{\sigma_u}{\sigma_m} = \frac{A}{A_0} = \frac{\ell_0}{\ell} \tag{6.52}$$

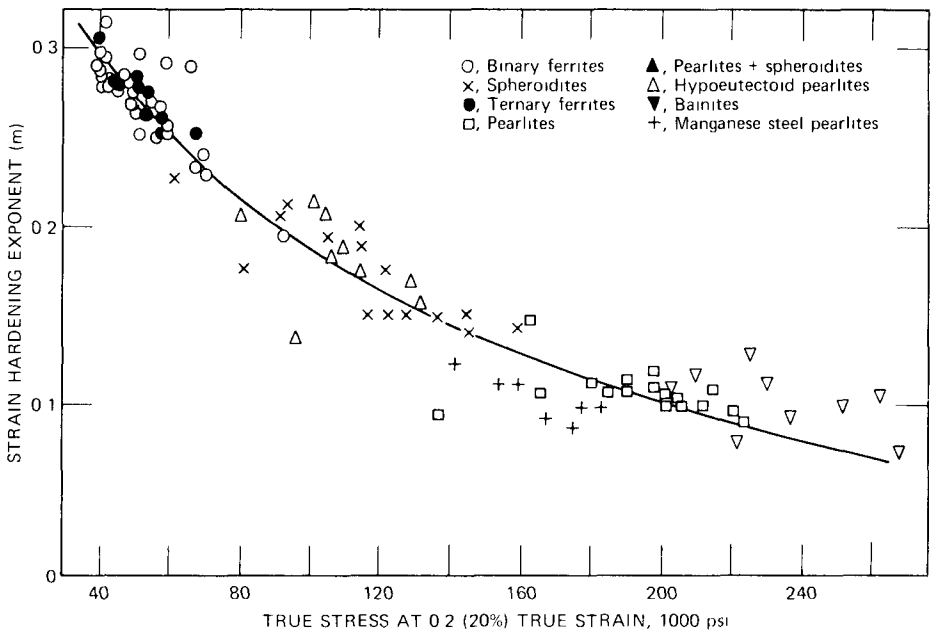

Fig. 6.6 Strain-hardening exponent as a function of strength level and structure. (From Ref. 21.)

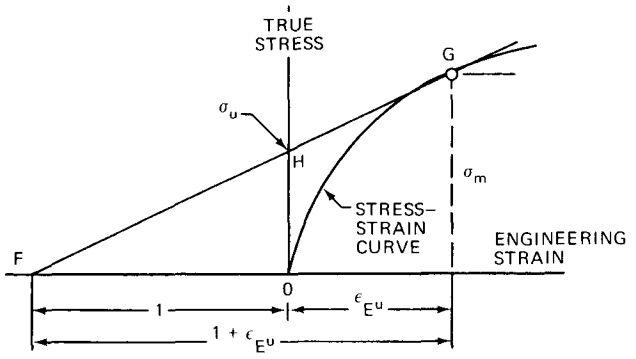

Fig. 6.7 Plot of true stress vs. engineering strain.

Then, from the definition of engineering strain,

$$\frac{\ell_0}{\ell} = \frac{1}{1 + \epsilon_E} \tag{6.53}$$

and hence

$$\sigma_u = \frac{\sigma_m}{1 + \epsilon_E} \tag{6.54}$$

Therefore in Fig. 6.7 the intercept at H locates σ_u.

If the plastic-flow curve is given by Eq. 6.45 written in terms of true strain, then

$$\frac{d\sigma}{d\epsilon} = mK'\epsilon^{m-1} \tag{6.55}$$

and, in view of Eq. 6.50,

$$\left(\frac{d\sigma}{d\epsilon}\right)_{max.} = \sigma_m = K'\epsilon_{max.}^{m} = mK'\epsilon_{max.}^{m-1} \tag{6.56}$$

It must follow, therefore, that

$$\epsilon_{max.} = m \tag{6.57}$$

This expression reveals that the strain-hardening exponent is numerically equal to the true strain at the maximum load or necking point. It also follows that

$$K' = \frac{\sigma_m}{(\epsilon_{max.})^{\epsilon_{max.}}} \tag{6.58}$$

and hence

$$\sigma = \frac{\sigma_m}{(\epsilon_{max.})^{\epsilon_{max.}}} (\epsilon)^{\epsilon_{max.}} \tag{6.59}$$

Thus it is possible to derive the constants in the power-function equation from the conditions at the maximum load point on the engineering-stress–strain curve. In a similar derivation involving Eq. 6.A, after Eq. 6.46, it is possible to show that

$$\frac{\sigma - \sigma_0}{\sigma_m - \sigma_0} = \left(\frac{\epsilon}{\epsilon_{max.}}\right)^{(\epsilon_{max.})(\sigma_m)/(\sigma_m - \sigma_0)} \tag{6.60}$$

Once again all the equation constants are obtainable from conditions at the maximum load point. Experience has shown, however, that the use of constants derived in this fashion do not yield an equation that provides the most effective representation of the stress–strain data. Actually a

more effective representation can be obtained by using values for the constants that evolve from a least-squares analysis of the stress–strain data. These values will be close to those derived from the maximum-load-point considerations but will yield a better analytical expression.

Voce Equation

Recognizing the fairly universal usage of the Ludwik power function

$$\sigma = K'\epsilon^m \tag{6.61}$$

in describing stress–strain behavior, Voce[3] noted certain features of this equation which were not consistent with material behavior. On the basis of a study of some compression curves, Voce identified a very effective relation between true stress and true strain that was also shown to be applicable to tension testing. On the basis of constant-volume deformation, Voce used the following definitions:

A_0 = cross-sectional area before deformation
A = cross-sectional area at any instant
ℓ_0 = length before deformation
ℓ = instantaneous length
W = applied load
S = true stress = W/A
N = nominal or engineering stress = W/A_0
R = strain ratio, i.e., the ratio between the final and the original cross-sectional area or length, so arranged that the greater area or length, whether before or after deformation, appears in the numerator. In this way the ratio is always greater than unity

Consideration of constant-volume deformation will show that, for tension,

$$R = \ell/\ell_0 = A_0/A = S/N \tag{6.62}$$

and, for compression,

$$R = \ell_0/\ell = A/A_0 = N/S \tag{6.63}$$

ϵ = true (logarithmic) strain = $\ln R$
P' = the instantaneous plastic modulus, comparable with Young's modulus, and defined as the instantaneous rate of change of true stress with respect to true strain, i.e., $P' = dS/d\epsilon$. The reciprocal of this differential, $d\epsilon/dS$, is a measure of the ease of deforming the material or simply the deformability
S_0 = the initial or threshold stress at which homogeneous plastic deformation begins to be appreciable. It is usually above the limit of proportionality and corresponds roughly with the 0.1% proof (yield) stress
S_∞ = the final constant stress, attainment of which at indefinitely large strains, appears to be a characteristic of homogeneous deformation
C_0 = the total or initial plastic stress capacity, i.e., the capcity of the material to accept stress capable of producing plastic deformation. At stresses below the threshold, stress deformation is insignificant, whereas stresses above the final constant stress cannot be applied under homogeneous conditions; therefore

$$C_0 = S_\infty - S_0 \tag{6.64}$$

C = the plastic stress capacity that remains available after the application of a given stress, S; thus

$$C = S_\infty - S \tag{6.65}$$

k = a constant
m = a subscript to denote the conditions at the maximum load or necking point in tension. For instance, the ordinary tensile strength is N_m, and the corresponding true stress is S_m. Similarly, R_m is the strain ratio, and ϵ_m is the true strain at the maximum load. P'_m is the plastic modulus or slope of the true stress–strain curve at the point where necking commences

In discussing stress–strain plotting, Voce[3] cited a well-established although not widely recognized fact that, when true tensile stress is plotted vs. the strain ratio, a line drawn from the origin and tangent to the curve defines a slope that is equal to the ordinary (nominal) tensile strength. Thus, under the conditions at maximum load, the slope of the stress–strain curve itself, plotted in this way, is equal to the ordinary tensile strength. For such a curve the conditions at the maximum load are therefore

$$\text{Ordinate} = S_m, \quad \text{abscissa} = R_m, \quad \text{slope} = N_m \tag{6.66}$$

Similarly, when using true strain, it can be shown that the slope of the curve at the maximum load is numerically equal to the true stress at this point, so that

$$\text{Ordinate} = S_m, \quad \text{abscissa} = \epsilon_m, \quad \text{slope} = S_m \tag{6.67}$$

These equations were based on no assumptions with regard to the shape of the stress–strain curve and hence are universally applicable.

Some stress–strain data obtained in homogeneous compression tests of eight copper-base alloys were reported by Cook and Larke.[22] Voce[3] used these data in the form shown in Fig. 6.8. Although these curves extend to only 60% reduction in specimen height (length), apparently each is already approaching a constant stress under which the load necessary to promote deformation is directly propor-

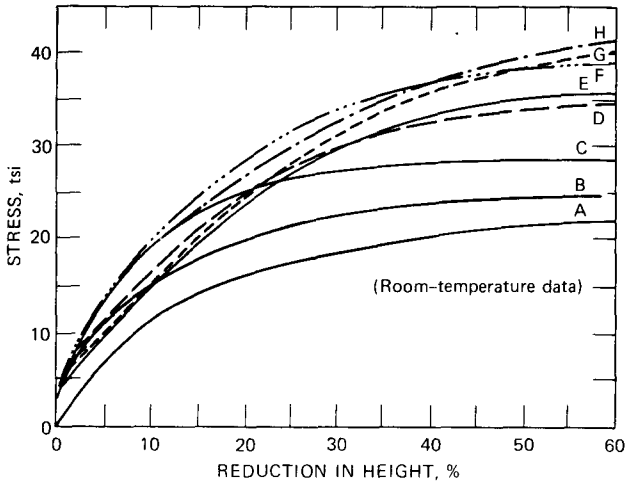

Fig. 6.8 True stress vs. percent reduction in specimen height for eight copper-base alloys. (From Ref. 3.)

A, copper	**E, 64–36 brass**
B, gilding metal	**F, nickel silver**
C, cupronickel	**G, aluminum bronze**
D, 70–30 brass	**H, phosphor bronze**

tional to the increasing cross-sectional area. This is particularly apparent in the case of curve C, but the freehand extrapolation of each curve gave a good indication of the final stress, S_∞, attained at 100% reduction in height (infinite strain). The threshold stresses, S_0, at which plastic deformation began to be appreciable, were read directly from an enlarged replot of Fig. 6.8. This plot was also used to obtain values of S corresponding to various values of the decrease in specimen height. These data were then used to calculate

$$\ln \frac{S_\infty - S_0}{S_\infty - S} = \ln \frac{C_0}{C} \tag{6.68}$$

These values were then plotted as a function of the true strain (ln R) to yield the linear relations shown in Fig. 6.9 for the different alloys. These relations yielded the form

$$\ln \frac{\ell_0}{\ell} = k \ln \frac{C_0}{C} \tag{6.69}$$

which leads to

$$\epsilon = k \ln \frac{S_\infty - S_0}{S_\infty - S} \tag{6.70}$$

or

$$R = \left(\frac{S_\infty - S_0}{S_\infty - S}\right)^k \tag{6.71}$$

or

$$\frac{S_\infty - S}{S_\infty - S_0} = e^{-\epsilon/k} \tag{6.72}$$

or

$$S = S_\infty - (S_\infty - S_0)\, e^{-\epsilon/k} \tag{6.73}$$

Equation 6.73 is referred to as the Voce equation and will be discussed in more detail in a later section.

Values of S_∞, S_0, and k for the eight copper-base alloys studied by Cook and Larke are presented in Table 6.3. The

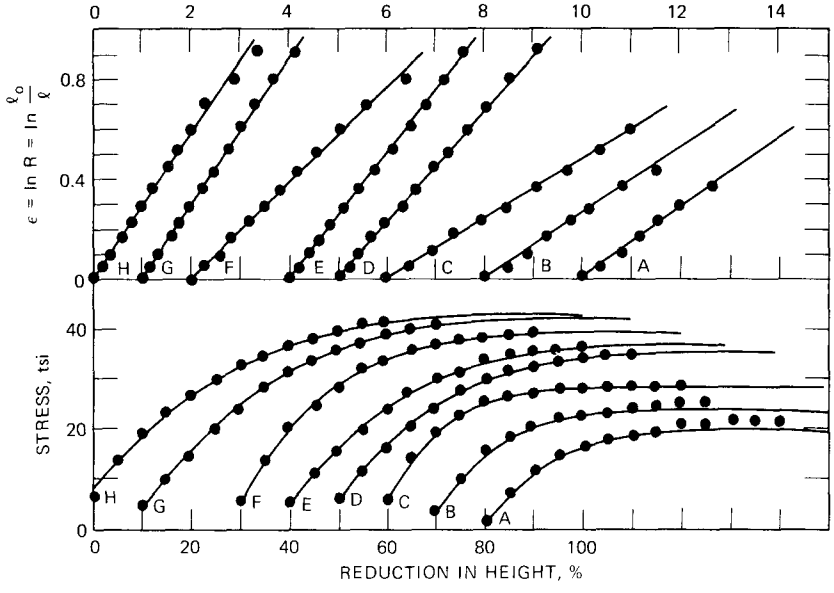

Fig. 6.9 Analysis[3] of the compression data of Cook and Larke.[22] The individual curves have been displaced along the horizontal axis for clarity; all should begin at the origin. (From Ref. 3.)

TABLE 6.3

VALUES OF S, S_0, AND k REPORTED BY VOCE FOR THE COMPRESSIVE DEFORMATION OF COPPER ALLOYS (FROM REF. 3)

Curve	Material	Threshold stress (S_0), tsi	Final stress (S_∞), tsi	k
A	Copper	1.0	19.7	0.14
B	Gilding metal	2.8	23.5	0.13
C	Cupronickel	5.5	28.3	0.12
D	70 : 30 brass	5.5	35.3	0.22
E	64 : 36 brass	5.0	37.0	0.25
F	Nickel silver	5.5	39.0	0.19
G	Aluminum bronze	4.0	42.0	0.29
H	Phosphor bronze	8.0	42.5	0.29

straight lines in Fig. 6.9, which were used to calculate k values, were used to plot true-stress vs. reduction-in-height data. These results are shown in the lower part of Fig. 6.9. Agreement between the curves and the experimental points is quite good except that the threshold stress demanded by the general trend of curve H for phosphor bronze is somewhat higher than the experimental value and that curves A for copper and B for gilding metal lie beneath the experimental points for large deformations. Even for these, however, the fit is satisfactory up to strains well beyond those at which necking would occur in tension.

Differentiation of Eq. 6.70 gives

$$\frac{d\epsilon}{dS} = \frac{k}{S_\infty - S} = \frac{k}{C} \tag{6.74}$$

Since the derivative, $d\epsilon/dS$, represents the amount of deformation caused by a small increment in stress, it can be considered as a measure of the deformability of the material at a given instant. Thus Eq. 6.74 signifies that for homogeneous compression the deformability at any instant is inversely proportional to the available stress capacity. Inverting Eq. 6.74 leads to

$$\frac{dS}{d\epsilon} = \frac{C}{k} = P' \tag{6.75}$$

which relates the instantaneous plastic modulus to the available stress capacity. Although empirical in its derivation, the relation seems to have somewhat of a rational significance.

Voce[3] was also quite successful in applying the previous considerations to deformation in tension. For conditions at the maximum load point, combination of Eqs. 6.74 and 6.67 yielded

$$P'_m = S_m = \frac{S_\infty - S_m}{k} \tag{6.76}$$

Hence

$$S_\infty = (1 + k)\, S_m \tag{6.77}$$

Substitution of this value of S_∞ in Eq. 6.71 and rearranging led to

$$R_m = \left[\frac{1}{k}\left(1 + k - \frac{S_0}{S_m}\right)\right]^k \tag{6.78}$$

The values of the threshold stress, S_0, and the true stress, S_m, along with the strain ratio, R_m, at the maximum load are readily obtained from direct stress–strain measurements. Equations 6.77 and 6.78 then enable values of S_∞ and k to be determined, and Eq. 6.71 can then be used to calculate the stress–strain curve and allow it to be compared with the experimental observations.

There is no direct solution of Eq. 6.78 for k. One approach that was suggested by Voce involved the family of curves shown in Fig. 6.10, where values of (S_0/S_m) were chosen and values of R_m calculated from Eq. 6.78 for various k values. With this network available, it is a simple matter to calculate a value of k from measured values of

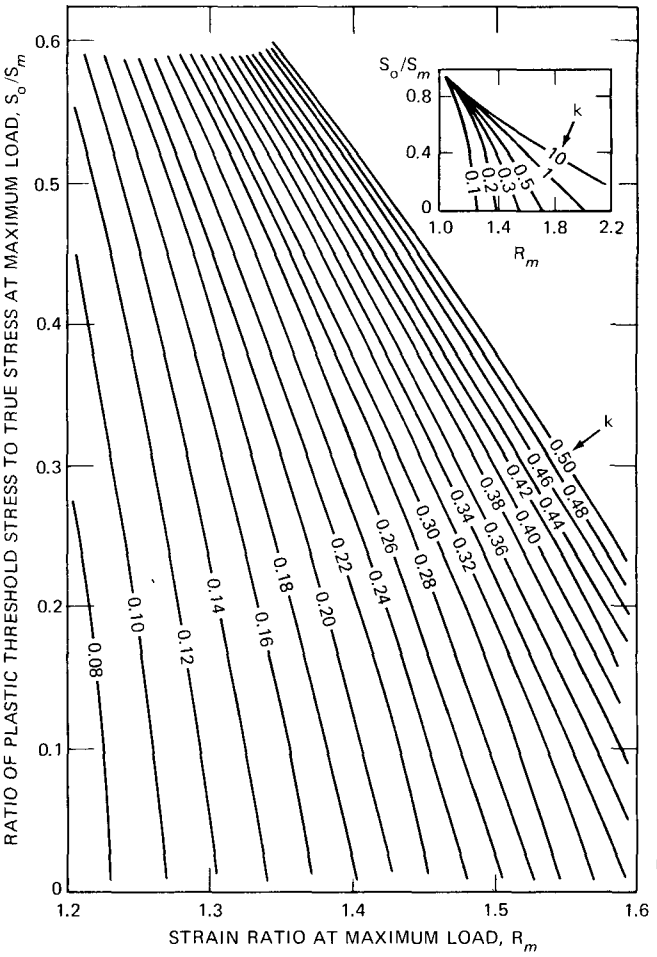

Fig. 6.10 Plot of S_0/S_m vs. R_m for use in calculating k. (From Ref. 3.)

R_m, S_0, and S_m The small insert in Fig 6 10 was included to indicate the general trend of this plot over a long range of R_m values.

Voce illustrated the use of Fig 6.10 in a consideration of some tensile data for annealed electrolytic copper tested in such a way as to yield instantaneous measurements of the diameter. These measurements enabled instantaneous or true stresses to be calculated, and the diametral measurements were also used to yield corresponding values of the strain ratio, R. A plot of these results was prepared as shown in Fig. 6.11. Extrapolation of the general trend of the curve led Voce to conclude that at unit strain ratio (zero plastic deformation) a stress of 3.0 tsi was indicated for the threshold stress, S_0. Also, the true stress at the maximum load point was accepted as 19.7 tsi, and the corresponding strain ratio was 1.40. Values of S_0/S_m = 3.0/19.7 = 0.152 and R_m = 1.40 were used in conjunction with Fig. 6.10 to obtain k = 0.21, Eq. 6.77 was then used to calculate S_∞ = 1.21 × 19.7 - 23.8 tsi. Then these constants were used in Eq. 6.71 to calculate the solid curve shown in Fig. 6.11. Except at low stresses, all the experimental observations were in good agreement with the calculated curve.

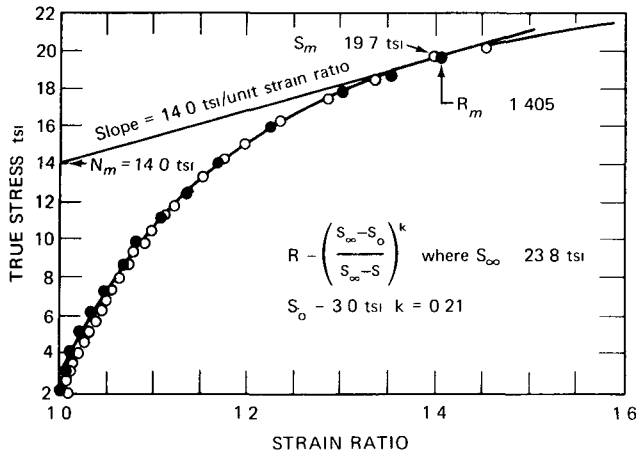

Fig. 6.11 Tensile data for copper. •, experimental results for electrolytic H.C. copper, ○, experimental results for electrolytic deoxidized copper. (From Ref. 3.)

In a brief reevaluation of the data presented in Fig 6.11, Conway[23] used a slightly different approach to the evaluation of k. This technique does not require the use of Fig. 6.10 and can be effected using either an analytical (least squares) or graphical approach. Viewing Eq. 6.71, note that a plot of R vs. (S_∞ − S) on logarithmic coordinates will yield a linear relation having a slope equal to (−k). This calculation procedure is illustrated using the data shown in Table 6.4 (data are read from Fig. 6.11 and may not be the actual data points used in the original study by Voce). A plot is made of R vs (S_∞ − S) on logarithmic coordinates as shown in Fig. 6.12. This construction re-

TABLE 6.4

ANALYSIS[23] OF DATA FROM FIG 6.11

(S_∞ = 23.8 tsi, S_0 = 3.0 tsi, R_m = 1 40)

True stress (S), tsi	R	True strain (ϵ = ln R)	$S_\infty - S$	Engineering strain (R-1)	Engineering stress (S/R)
4.0	1 01	0.01	19.8	0.01	3.960
5.1	1.022	0 0218	18.7	0.022	4.990
6.1	1.035	0.0345	17.7	0.035	5.894
7.2	1.048	0.047	16.6	0.048	6.870
8.6	1.066	0.064	15.2	0 066	8 068
9.7	1.084	0 081	14.1	0.084	8.948
11 1	1.109	0.1035	12.7	0.109	10.009
12.4	1.135	0.127	11.4	0.135	10.925
14 2	1.17	0.157	9.6	0.17	12 137
16.0	1.224	0.202	7.8	0.224	13.072
18.0	1.3	0.262	5.8	0.3	13.846
18 7	1.352	0.3	5.1	0.352	13.831
19.7	1.406	0.34	4.1	0.406	14.011

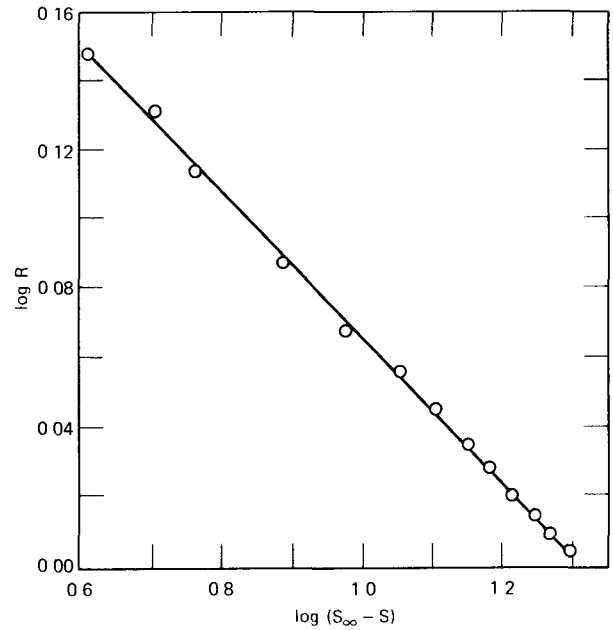

Fig. 6.12 Plot of log R vs. log (S_∞−S) for Fig. 6.11 data.[23]

quires the same data (S_0, S_m, and R_m) as used in conjunction with Fig. 6.10. Also, the value of S_∞ is first calculated through the use of Eq. 6.77. In Fig. 6.12, definite linearity is indicated, and a slope calculation reveals a value of −0.21 to identify the same k value as calculated using Fig. 6.10. These procedures identify an approach that can be used in the development of a very effective expression for describing stress–strain behavior in the plastic region.

Figure 6.13 shows the curve of engineering stress vs. engineering strain and Fig. 6.14 the curve of true stress vs. true strain on logarithmic coordinates. A typical curve

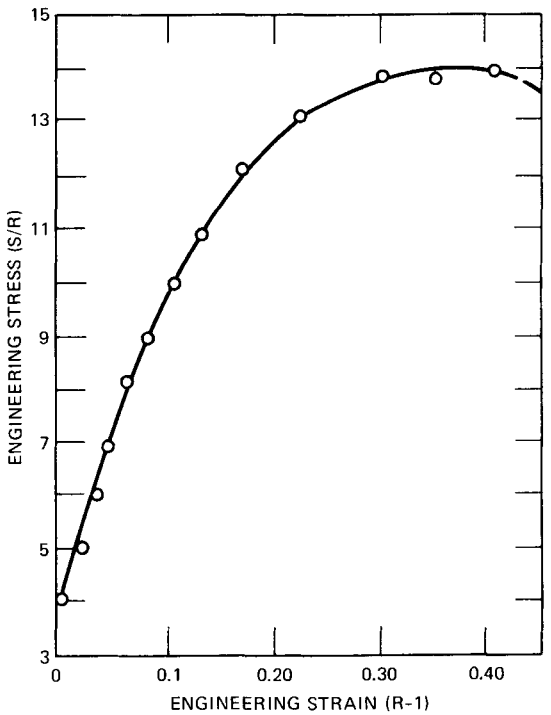

Fig. 6.13 Engineering stress vs. engineering strain plot of Fig. 6.11 data.[23]

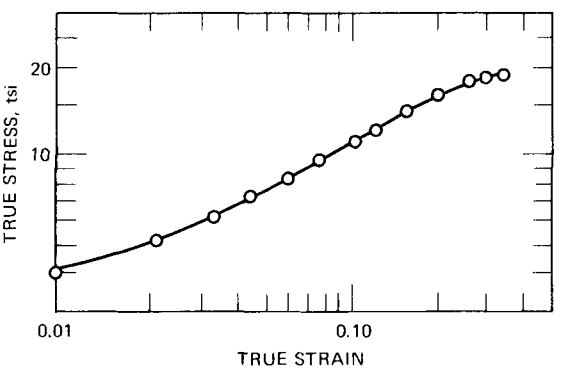

Fig. 6.14 Logarithmic true-stress–true-strain plot of Fig. 6.11 data.[23]

shape is indicated in Fig. 6.13, but that in Fig. 6.14 is fairly unusual and obviously precludes the use of the Ludwik power function, which, were it applicable, would make this curve linear. Such behavior in Fig. 6.14 necessitates the use of an equation form completely different from that corresponding to the Ludwik relation. For an accurate description of this type of behavior, the Voce expression shown in Eq. 6.73 is obviously very effective.

In a later article by Voce,[24] the use of Eq. 6.73 was further emphasized. According to Voce, this expression has been applied to several hundred sets of stress–strain data, and in every case an extremely effective representation was obtained. Voce also referenced the stress–strain data of Halstead, McCaughey, and Markus[25] in demonstrating that the validity of the power function is unequivocally denied. Data furnished by these authors describe the stress–strain behavior of several materials in compressive tests, and these results assume a form suggesting the applicability of the Voce equation. A logarithmic plot obtained in the study by Halstead et al.[25] described the type of behavior shown schematically in Fig. 6.15 and will be seen to approximate a flattened S-shape curve. Obviously this curvilinear form is not amenable to the Ludwik expression, and this departure led to a fairly definite refuting of this power function.

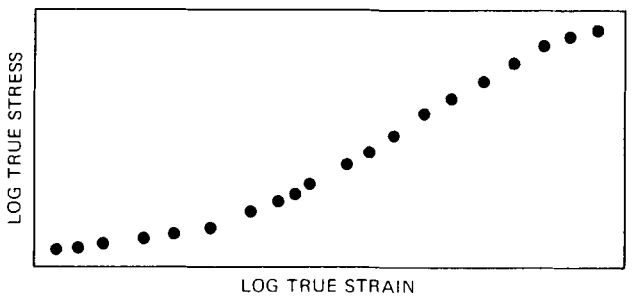

Fig. 6.15 Schematic stress–strain behavior indicating flattened S-shape curve on logarithmic coordinates.

Voce was also critical of the power function because of its empirical nature. It was argued that the Voce equation should be assigned higher status since it can be deduced after a few credible assumptions are made. In this development it was visualized that within unstrained metal there exists a large number of minute sites at which resistance to deformation can be created as deformation proceeds. Any infinitesimally small increment of strain may or may not lead to the blockage of one of the sites. If it does, the resistance to further deformation is slightly increased and the metal is correspondingly strain hardened. It was assumed that the total number of strain-hardening sites would be given by N, and n would represent the number of these which have become blocked after the application of a true strain, ϵ. On the basis of random distribution, the chance that a minute increment of strain, occurring anywhere within the metal, will give rise to a new blockage is proportional to the number of sites still remaining to be blocked, i.e., N – n. Hence

$$\frac{dn}{d\epsilon} = \frac{N - n}{A} \tag{6.79}$$

where A is a constant of proportionality. Integration between zero and a strain of ϵ leads to

$$\frac{dn}{N - n} = \frac{d\epsilon}{A} \tag{6.80}$$

$$-\ln (N - n)\Big|_0^n = \frac{\epsilon}{A}\Big|_0^{\epsilon} \tag{6.81}$$

$$\ln \frac{N}{N-n} = \frac{\epsilon}{A} \tag{6.82}$$

and

$$\frac{n}{N} = 1 - e^{-\epsilon/A} \tag{6.83}$$

On the average, each blockage will contribute the same small quota to the stress that is required to deform the metal. It follows that the ratio of blocked sites to total sites, n/N, is the same as the ratio of the current (plastic) stress to the final stress obtained after all the sites have been blocked. Therefore

$$\frac{n}{N} = \frac{S - S_0}{S_\infty - S_0} \tag{6.84}$$

where S is the current yield stress, S_∞ is the yield stress attained after all the available sites have been blocked, and S_0 is the original yield stress of the material or threshold stress below which strain hardening does not occur. Combining Eqs. 6.83 and 6.84 gives the Voce equation.

Another shortcoming of the power function was cited by Voce and is based on the fact that this equation suggests that materials become indefinitely strong after severe deformation. Such a condition is obviously contrary to all known material behavior. On the other hand, the Voce equation was viewed as being more consistent with experimental observations in that this expression sets an upper limit on the degree of strain hardening obtainable.

Writing Eq. 6.73 in the form

$$S = S_\infty - (S_\infty - S_0)\, e^{-\epsilon/A} \tag{6.85}$$

Voce identified ϵ as the true strain, S as the true stress, S_0 as the threshold stress, S_∞ as the asymptotic stress, and A as the characteristic strain that determines the shape of the stress–strain curve. Tensile stress–strain data for annealed high-conductivity copper (see Table 6.5) were used by Voce to yield the curve shown in Fig. 6.16. A very definite S-shaped curve is indicated and is similar to that in Fig. 6.15. An expression of the type in Eq. 6.85 was used to define the solid curve in Fig. 6.16. This curve provides a very accurate description of the experimentally determined stress–strain measurements.

A brief study of Eq. 6.85 shows that it does indeed possess those characteristics which make it applicable to the type of curve shown in Fig. 6.16. For example, when the strain is zero, it follows that $S = S_0$; also, when large strains are involved, Eq. 6.85 yields $S = S_\infty$. Furthermore, a differentiation of Eq. 6.85 leads to

TABLE 6.5

TENSILE STRESS–STRAIN DATA FOR ANNEALED HIGH-CONDUCTIVITY COPPER (FROM REF. 24)

(S_0 = 2.8 tsi; S_∞ = 23.3 tsi; A = 0.195)

Load, tons	Diameter, in.	Sectional area, in.^{2}	True stress, tsi	Deformation ratio* ($A_0/A = \exp \epsilon$)	Logarithmic strain [$\epsilon = \ln (A_0/A)$]
0.0	0.357	0.1001	0.00	1.000	0.000
0.2	0.357	0.1001	2.00	1.000	0.000
0.3	0.356$_5$	0.0998	3.01	1.002	0.002
0.4	0.355	0.0990	4.04	1.011	0.011
0.5	0.353	0.0979	5.11	1.022	0.022
0.6	0.350$_5$	0.0966	6.21	1.035	0.034
0.7	0.348	0.0951	7.35	1.050	0.049
0.8	0.346	0.0940	8.51	1.064	0.062
0.9	0.343	0.0924	9.74	1.082	0.079
1.0	0.339	0.0903	11.08	1.108	0.102
1.1	0.335	0.0881	12.48	1.135	0.127
1.2	0.330	0.0855	14.06	1.170	0.157
1.3	0.323	0.0819	15.88	1.222	0.201
1.37	0.314	0.0774	17.70	1.290	0.255
1.40†	0.307	0.0740	18.92	1.352	0.302
1.40†	0.301	0.0712	19.68	1.405	0.340
1.395	0.296	0.0688	20.28	1.454	0.374

*The deformation ratio diminished by unity is equal to the fractional increase in length.

†Ordinary tensile strength, 14.0 tsi.

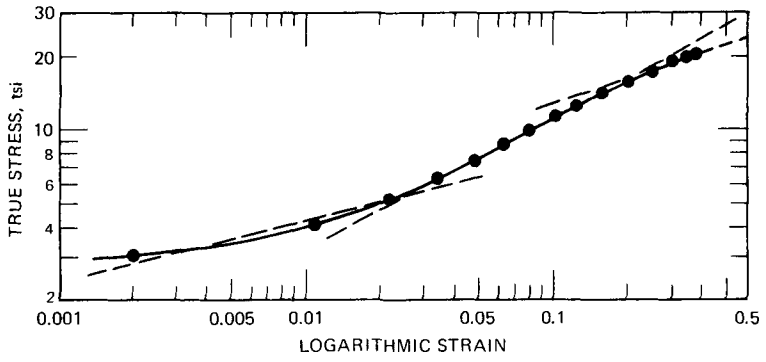

Fig. 6.16 True stress–strain plot of tensile data presented in Table 6.5. (From Ref. 24.)

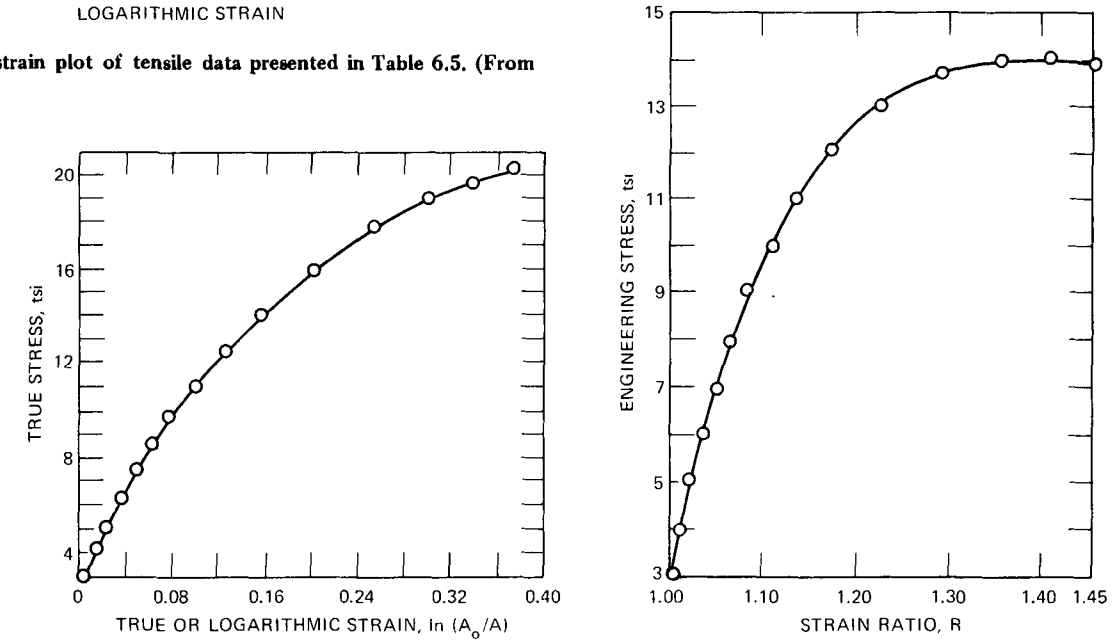

Fig. 6.17 True-stress–true-strain and engineering stress vs. strain ratio plots of Table 6.5 data.[2,3]

$$\frac{dS}{d\epsilon} = \left(\frac{S_\infty - S_0}{A}\right) e^{-\epsilon/A} \tag{6.86}$$

which describes a finite slope at $\epsilon \approx 0$ and also a slope that continually decreases as the true strain is increased. Such behavior is in complete accord with the shape of the true stress–strain curve on rectangular coordinates in Fig. 6.17 (the engineering stress vs. strain ratio curve is also presented). Also, the shape of the rectangular plot of true stress–strain behavior is essentially identical to that exhibited by stress–strain curves in general. In other words, curves described by Eq. 6.85 are similar in shape to those subjected to analysis by the Ludwik power function. Thus any data analyzed in terms of the Ludwik equation could be analyzed with equal and perhaps even more effectiveness using the Voce equation. Some additional studies will be required before full support can be given to this statement, but it certainly seems correct in view of existing evidence.

Multiplying both sides of Eq. 6.86 by the ratio ϵ/S gives

$$\frac{\epsilon\, dS}{S\, d\epsilon} = \frac{d \log S}{d \log \epsilon} = \left(\frac{S_\infty - S_0}{A}\right)\left(\frac{\epsilon}{S}\right) e^{-\epsilon/A} \tag{6.87}$$

which from Eq. 6.85 yields

$$\frac{d \log S}{d \log \epsilon} = \left(\frac{S_\infty - S_0}{A}\right) \frac{(\epsilon)\, e^{-\epsilon/A}}{[S_\infty - (S_\infty - S_0)\, e^{-\epsilon/A}]} \tag{6.88}$$

This expression reveals that as the true strain approaches zero the slope of a log S vs. log ϵ curve will approach zero; furthermore, as the true strain assumes large values, the slope in Eq. 6.88 also approaches zero. This behavior is obviously completely consistent with the shape of the curve in Fig. 6.16 and identifies Eq. 6.85 as having the proper form to describe the S-shaped curves in Figs. 6.15 and 6.16.

Although not mentioned by Voce, it is obvious that the constants in Eq. 6.85 can be identified even though S_∞ and S_0 might not be available from experimental observations. In such a case, a plot would be made of log $(S_\infty - S)$ vs. ϵ (semilogarithmic plot). Values of S_∞ would be assumed until this relation is found to be linear; when this value is found, a slope calculation will yield the value of A and an intercept calculation allows $(S_\infty - S_0)$ to be determined. This latter value leads to the constant S_0 since S_∞ is known from the linearity condition. Of course, this is a trial and

error approach, but usually the proper value of S_∞ can be identified after only a few attempts. An illustration of this approach is shown in Fig. 6.18 using the data in Table 6.5. In this calculation, S_∞ and S_0 were assumed to be unobtainable from the original experimental observations. Values of S_∞ were assumed as shown in Fig. 6.18, and linearity was obtained with a value of $S_\infty = 23.3$. An intercept calculation led to $S_0 = 3.0$, and a slope calculation yielded $A = 0.196$. These constants are in exact agreement with those listed in Table 6.5 for these data.

Further criticism of the power function was offered by Voce on the basis of the slope of the true stress–strain curve at the point of maximum load. This slope, as has already been stated, is well known as being numerically equal to the value of the true stress at the maximum load point independent of the form of the true stress–strain curve. If the power function of Eq. 6.45 were applicable, then the slope of the true stress–strain curve at the maximum load point would be given by Eq. 6.56 and the relation given in Eq. 6.57 would be identified. The constants, m and K′, were noted as having some semblance of physical meaning, but they require the entire course of the stress–strain curve to be fixed by the coordinates of a single point (point at maximum load). Such a situation would mean that, if several different materials happen to reach their respective maximum load points at the same stress and strain, then they must necessarily have identical strain-hardening properties if the power function is to be believed. This type of behavior is hard to reconcile with known experimental observations of the stress–strain relations for different materials. In contrast to the power function, the Voce equation allows different materials to reach the same maximum load point by different paths.

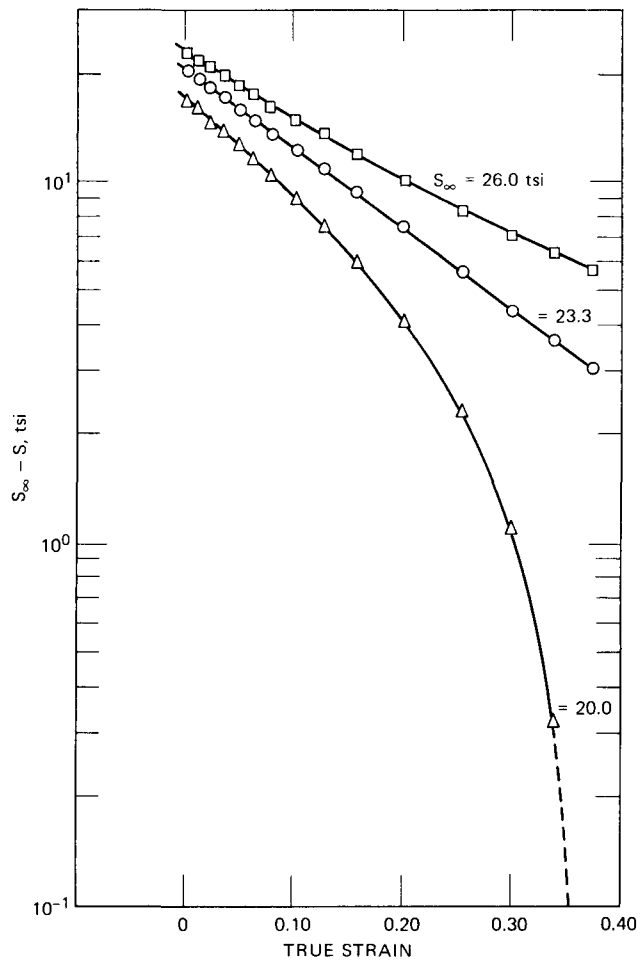

Fig. 6.18 Graphical solution for Voce-equation constants.[23]

Voce[24] discussed another shortcoming of the power function by considering a case in which this function applied to a material in the annealed condition. If, however, the only specimen available for test contained a small unknown strain, ϵ_1, owing perhaps to some pretest mechanical handling during production, some difficulty in data analysis by the power function would arise. In the analysis of the test data for this specimen, a graph would be made of stress vs. measured strain, ϵ, when actually the measured strain value would really be $\epsilon - \epsilon_1$. Of course, if a logarithmic coordinate graph yielded a linear relation for σ vs. ϵ for the annealed material, a linear relation could not result from plotting stress vs. $(\epsilon - \epsilon_1)$. Since this condition could not be recognized, an attempt to draw a straight line through these data points would yield erroneous values for the constants in the power function. In similar circumstances the Voce equation would merely reveal an appropriately increased value for the threshold stress, with no significant changes in the major constants and no alteration in the shape of the curve. This effect corresponds to moving the stress ordinate along the strain axis to a new position at ϵ_1 on rectangular coordinates. Therefore one of the real distinguishing features of the Voce equation is the presence of a term to define the stress at which plastic deformation begins. Although this adds some complication to the identification of the equation constants, the ability of the equation to provide effective representations of experimental results is noticeably enhanced.

Also discussed by Voce[24] was the existence, in certain cases at least, of two consecutive regimes of strain hardening in the same stress–strain curve. Assuming a power-function relation, this would involve two linear segments, one for each of the consecutive strain-hardening regions. At the transition point of these regions, special conditions must prevail. According to the power function, the slope at any point is given by

$$\frac{d\sigma}{d\epsilon} = mK' \epsilon^{m-1} = \frac{m\sigma}{\epsilon} \tag{6.89}$$

It follows, therefore, that two adjacent regimes characterized by different values of m cannot have the same slope at a point defined by any particular stress and strain. In other words, tangential junction of these two regimes is impossible, and any change of regime must be marked by an abrupt change of direction in the stress–strain curve.

Slope considerations for the Voce equation lead to

$$\frac{dS}{d\epsilon} = \frac{S_\infty - S_0}{A} e^{-\epsilon/A} = \frac{S_\infty - S}{A} \tag{6.90}$$

If the constants for the second strain-hardening regime are S'_0, S'_∞, and A', then perfect tangential transition can, and does, take place at the transition stress, S_t, where the slopes of the two branches become equal. This condition is defined by

$$\frac{S_\infty - S_t}{A} = \frac{S'_\infty - S_t}{A'} \tag{6.91}$$

from which

$$S_t = \frac{A' S_\infty - A S'_\infty}{A' - A} \tag{6.92}$$

Obviously, the transition strain, ϵ_{TS}, can be found by substituting in the Voce equation using the first-regime constants. The transition point is clearly the starting point of the second regime, and in accordance with Eq. 6.85 this regime could be described by

$$\epsilon = \epsilon_{TS} + A' \ln \frac{S'_\infty - S_t}{S'_\infty - S} \tag{6.93}$$

It is, however, convenient to extrapolate the second regime backward to zero strain by calculating the appropriate threshold stress S'_0 from a rearrangement of Eq. 6.85; thus

$$S'_0 = S'_\infty - (S'_\infty - S_t) e^{\epsilon_{TS}/A} \tag{6.94}$$

Although this leads to three constants for each regime, it is important to note that one of them is derived from the others. Six independent constants would not allow the two branches to touch even though they would be parallel at the transition point.

Plotting the data of Table 6.5, Voce[24] obtained Fig. 6.16. Applying the concept of the power function makes it clear that three linear segments would be required to provide approximate representation. Values for K′ and m for these three segments are presented in Table 6.6 along with other related quantities. In Fig. 6.16, the middle regime is more representative of the test as a whole than either of the others, and it could be this approximate linearity of the central regime which has caused the power function to be used in many instances. However, as shown in Table 6.6, the constants associated with the linear central portion lead to erroneous values for the tensile strength.

Voce[24] reasoned that, if Eq. 6.85 were considered to apply, then the instantaneous slope values on a rectangular S vs. ϵ plot would be given by Eq. 6.90. Therefore a plot of $dS/d\epsilon$ vs. stress would yield a linear relation on rectangular coordinates to allow identification of S_∞ and A. Such calculations of instantaneous slope could be based on the curve faired through the experimental points. An analysis of this type is shown in Fig. 6.19; values of S_∞ = 23 tsi and A = 0.20 follow from intercept and slope calculations. It was reported that some slight adjustments to these constants resulted in an excellent representation of the data. Final values for these constants are presented in Table 6.7 along with the associated tensile data. These constants were used in conjunction with Eq. 6.85 to yield the solid curves shown in Figs. 6.16 and 6.19. Thus a single equation can express the true stress–strain behavior that in Fig. 6.16 would require three linear segments of the type defined by the power function.

Because of the equality between stress and slope at the maximum load point, it follows from Eq. 6.90 that

$$S_{max.} = \frac{S_\infty}{1 + A} \tag{6.95}$$

The corresponding strain, $\epsilon_{max.}$, can be found by writing Eq. 6.85 as

$$\epsilon = A \ln \frac{S_\infty - S_0}{S_\infty - S} \tag{6.96}$$

TABLE 6.6

TENSILE STRESS–STRAIN DATA FOR ANNEALED HIGH-CONDUCTIVITY COPPER

(S_0 = 2.8 tsi; S_∞ = 23.3 tsi; A = 0.195)

	First regime	Second regime	Third regime
Primary constants			
Stress at unit strain, K′	13.6	38	27.5
Index, m	0.25	0.535	0.32
Conditions at maximum load			
True stress, S_m	9.6	27.1	19.1
Logarithmic strain, ϵ_m	0.25	0.535	0.32
Deformation ratio, exp ϵ_m	1.28	1.71	1.38
Tensile strength, T_m	7.5	15.8	13.8
Uniform extension, %	28	71	27.4

TABLE 6.7

POWER-FUNCTION CONSTANTS FOR LINEAR SEGMENTS IN FIG. 6.16 (FROM REF. 24)

	Calculated	By experiment
Primary constants		
Threshold stress, S_0	2.8	
Asymptotic stress, S_∞	23.3	
Characteristic strain, A	0.195	
Conditions at maximum load		
True stress, S_m	19.5	18.9–19.7
Logarithmic strain, ϵ_m	0.328	0.302–0.340
Tensile strength, T_m	14.0	14.0
Uniform extension, %	38.8	35.2–40.5

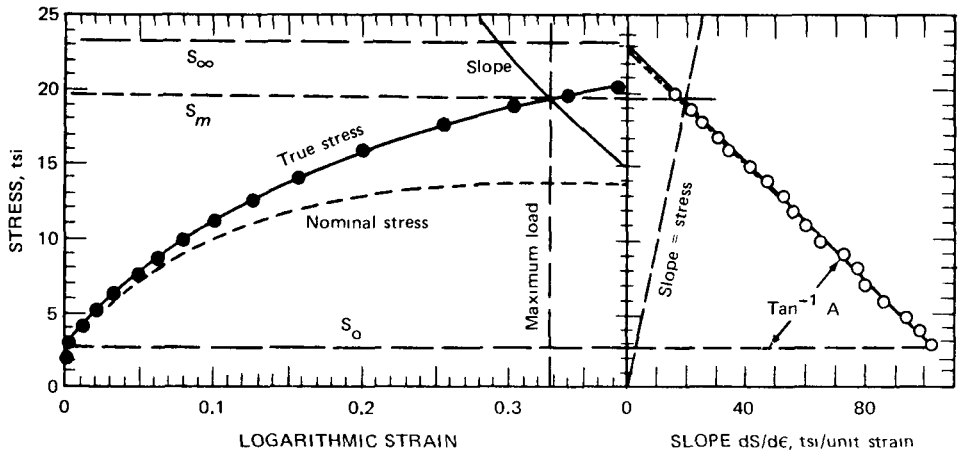

Fig. 6.19 Rectangular plot of S vs. ϵ and dS/dϵ vs. S for Table 6.5 data. (From Ref. 24.)

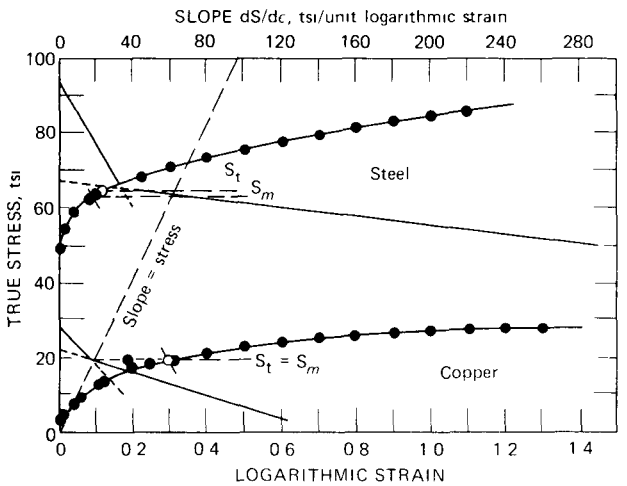

Fig. 6.20 Tensile true stress–strain curves for copper and steel corrected for radial stresses at the neck. (From Ref. 24.)

TABLE 6.8
VOCE-EQUATION CONSTANTS FOR DATA IN FIG. 6.20 (FROM REF. 24)

(All stresses are in tsi)

	Copper	Steel
First regime		
Threshold stress, S_0	2.9	42.1
Asymptotic stress, S_∞	22.1	67.0
Characteristic strain, A	0.158	0.062
Second regime		
Threshold stress, S'_0	11.5	59.8
Asymptotic stress, S'_∞	28.8	95.4
Characteristic strain, A'	0.51	0.85
Transition point		
Transition stress, S_t	19.05	64.8
Transition strain, ϵ_t	0.292	0.127
Maximum load point		
Critical stress, S_m	19.05	63.0
Critical strain, ϵ_m	0.292	0.095
Tensile strength, T_m	14.2	57.3
Uniform extension, %	33.8	9.9

and using S_m for S. Also, the ordinary tensile strength, $T_{max.}$, will be noted to be given by

$$T_{max.} = S_m \, e^{-\epsilon max.} \tag{6.97}$$

These expressions were used in the evaluation of the tensile properties listed in Table 6.7.

Voce noted that for the data in Fig. 6.16 a single strain-hardening regime existed up to the maximum load point. At this point, however, the radial stresses that accompany necking introduced a complication. Using the Bridgman corrections, Voce cited the work of Marshall and Shaw[26] in applying these corrections to the extension of the tensile stress–strain curves for copper and steel beyond the necking point. These data are presented in Fig. 6.20, where the solid curves are based on the Voce-equation constants shown in Table 6.8. The tentative plots used to suggest trial values for the constants are not shown, but the curves based on the finally accepted values are superimposed on this plot. Each derivative plot is made up of two straight lines representing the two successive regimes of strain hardening. The branches intersect at the transition point where the derivatives of the two regimes must be equal. For the copper specimen the transition point fortuitously coincides with the maximum load point, but, for the steel data, the maximum load is appreciably exceeded before the second regime begins.

In connection with the Voce equation, it is interesting to note that this same expression was developed independently by Palm[27] in a paper published just after the appearance of the Voce article. In this study by Palm, however, the equation was derived on the basis of theoretical considerations involving the strain-hardening mechanism. This coincidence is somewhat surprising, in view of the complexity of the relation involved and the fact that

the two independently proposed expressions were identical in form.

Linearization of the Stress–Strain Curve

Using the concept of generalized strain, $\bar{\epsilon}$, Hsu et al.[2] noted that the shape of the stress–strain curve depends on the choice of the way in which strain is described. It was stated that a certain strain measure could therefore be selected such that the stress–strain curve would be linear. In this instance, the equation would be

$$\sigma = m\bar{\epsilon} + k \tag{6.98}$$

where m and k are constants and $\bar{\epsilon}$ is a generalized strain value based on a certain yet unknown value of n (see previous section on stress–strain calculations for definition of n).

For application of this approach, a plot is made of true stress vs. engineering strain (see Fig. 6.21) and three points are selected at random but such that

$$\frac{\ell_1}{\ell_2} = \frac{\ell_2}{\ell_3} = \alpha \tag{6.99}$$

Then for linearity of the stress vs. generalized strain curve:

$$\sigma_1 = m\bar{\epsilon}_1 + k \tag{6.100}$$

$$\sigma_2 = m\bar{\epsilon}_2 + k \tag{6.101}$$

and

$$\sigma_3 = m\bar{\epsilon}_3 + k \tag{6.102}$$

Combining yields

$$\frac{\sigma_1 - \sigma_2}{\sigma_2 - \sigma_3} = \frac{\bar{\epsilon}_1 - \bar{\epsilon}_2}{\bar{\epsilon}_2 - \bar{\epsilon}_3} \tag{6.103}$$

From Eqs. 6.99–6.101 it can be shown that

$$\frac{\sigma_1 - \sigma_2}{\sigma_2 - \sigma_3} = \frac{1 - \frac{1}{\alpha^n}}{\alpha^n - 1} = \frac{1}{\alpha^n} \tag{6.104}$$

which leads to

$$n = \frac{\ln \frac{\sigma_1 - \sigma_2}{\sigma_2 - \sigma_3}}{\ln \frac{\ell_1}{\ell_2}} \tag{6.105}$$

The constants m and k are therefore

$$m = \frac{\sigma_1 - \sigma_2}{\bar{\epsilon}_1 - \bar{\epsilon}_2} \tag{6.106}$$

and

$$k = \frac{\sigma_2\bar{\epsilon}_1 - \sigma_1\bar{\epsilon}_2}{\bar{\epsilon}_1 - \bar{\epsilon}_2} \tag{6.107}$$

Thus, if the restriction shown in Eq. 6.99 is observed, the three selected points on the true stress vs. engineering strain plot will allow the determination of a certain n value that will lead to a linear stress–strain relation. It should follow that all other points shown in Fig. 6.21 will fall along the linear curve just identified using only three points.

For the analysis shown in Fig. 6.21, Hsu et al.[2] found n = 7.00 to establish the plot presented in Fig. 6.22. All points from Fig. 6.21 between P and N do indeed fall on the straight line drawn in Fig. 6.22. Beyond point N, Hsu et al. pointed to a triaxial stress condition within the necked portion of the specimen, and the strain could not be considered to be uniform. In this region then the condition of pure tension does not exist, and there are no tensile stress–strain data to be linearized.

In Fig. 6.22 the stress–strain curve consists of a straight elastic portion between the origin and point Y and an inelastic portion between Y and N within which the portion PN is linear. The PY segment is called a "transition range." For this reason, Hsu et al. recommended that this region be avoided when selecting the three points for use in conjunction with Eq. 6.99.

According to Hsu et al., the work-hardening characteristics are represented by two constants: m, the shape of the straight line in Fig. 6.22, and, n, the coefficient of strain measure, without which the value of m has no meaning. The constant k, the intercept S in Fig. 6.22, is the "yield stress by backward extrapolation." This quantity is equal to

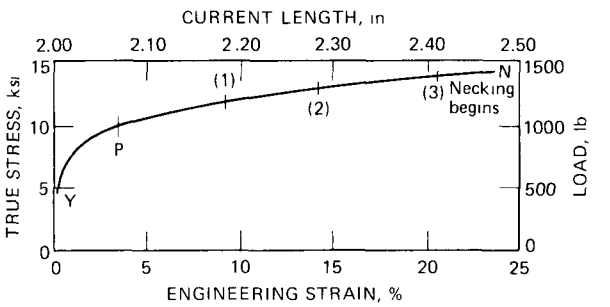

Fig. 6.21 True stress vs. engineering strain for aluminum. (From Ref. 2.)

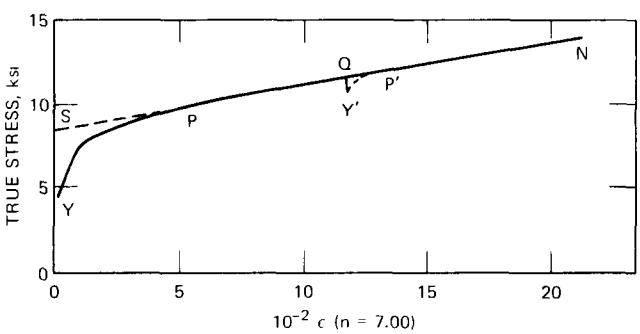

Fig. 6.22 Linearized stress–strain plot for aluminum. (From Ref. 2.)

the flow stress in prestrained materials. Thus, in Fig. 6.22, if the specimen at Q is unloaded to Y′ and reloaded, the stress–strain curve would be like Y′P′N. If the linear portion of this curve is extrapolated backward, it gives Q. Hsu et al. pointed out that in fully annealed materials the point S can only be called "flow stress of the annealed material" analogous to Q and is not measurable.

In the PN range of Fig. 6.22, the mechanical properties of the material can be represented completely by the three constants, n, m, and k, all of which may be considered to be material constants in a stress–strain expression similar to Eq. 6.98; thus

$$\sigma = \frac{m}{n}\left[1 \quad \left(\frac{\ell_0}{\ell}\right)^n\right] + k \qquad (6.108)$$

Values for these constants for several materials are shown in Table 6.9. Both types of copper show a transition range like that shown in Fig. 6.23, whereas the brasses show little or no transition region (see Fig. 6.24). In the linearized curve for mild steel (see Fig. 6.25), the part before work hardening begins is not replotted in full because, as is well known, that portion represents the characteristics of the testing machine rather than the property of the material. The quantity p in Table 6.9 is defined by

$$p = \frac{\text{inelastic (engineering) strain at P in Fig. 6.21}}{\text{elastic (engineering) strain at P}} \qquad (6.109)$$

Some reflection will show that this quantity is a measure of the length of the transition range, being zero if point P in Fig. 6.21 coincides with the yield point and infinity if the stress–strain curve cannot be linearized.

This use of the generalized strain concept of Hsu et al.[2] was noted to be applicable not only to fully annealed materials but also to materials of unknown tensile prestrains. And the appropriate coefficient of strain measure remains constant irrespective of the amount of prestrain. Also, the straight-line equation for the prestrained material cannot be the same as that for the same material in the annealed state because the mechanical properties for the material are changed by cold work.

To demonstrate that the appropriate coefficient of strain measure remains constant irrespective of the amount of prestrain, suppose that ℓ_0, the distance between two gage marks, is used as the datum length of the annealed material and that ℓ_0', the distance between the same gage marks in the prestrained material, is used as the new datum length (of course, due to the prestraining $\ell_0' > \ell_0$). In the annealed specimen, three points on the stress–strain curve are chosen in accordance with Eq. 6.99 to identify a value for n. If now the same three points on the stress–strain curve for the prestrained specimen are used, it will be seen from Eqs. 6.99 to 6.105 that in determining the n value no datum lengths are involved. Since the ratio ℓ_1/ℓ_2 in Eq. 6.105 remains constant irrespective of datum length, the value of n will be the same for the two material conditions.

To show that the stress–strain curves for annealed and prestrained material could both be linearized using generalized strain, Hsu et al.[2] suggested using $\bar{\epsilon}$ and $\bar{\epsilon}'$ as the strain quantities for these two material conditions. These two strain measures have the same coefficient n but are

TABLE 6.9
CONSTANTS n, m, k, AND p FOR VARIOUS MATERIALS
(FROM REF. 2)

Material	n	m, ksi	k, ksi	p
BA-24-W aluminum alloy (0.5% Mn, 0.5% Mg naturally aged)	15.4	350	17.1	0
251-W aluminum alloy (0.01% Cu, 0.67% Mg, 0.98% Si, 0.35% Fe, 0.23% Mn, 0.02% Zn naturally aged)	11.3	343	23.1	2.45
NORAL-2S-M aluminum alloy (99.25% pure, as extruded)	7.0	54	8.4	29.0
60-40 brass (as extruded)	5.3	428	27.8	0
70-30 brass (annealed)	2.0	204	15.9	2.40
Pure copper (99.92%) (annealed)	7.8	195	18.3	26.6
Pure copper (BSS 1433) (annealed)	4.8	204	11.3	34.6
Mild steel (0.20–0.25% C) (annealed)	8.4	376	43.3	26.3

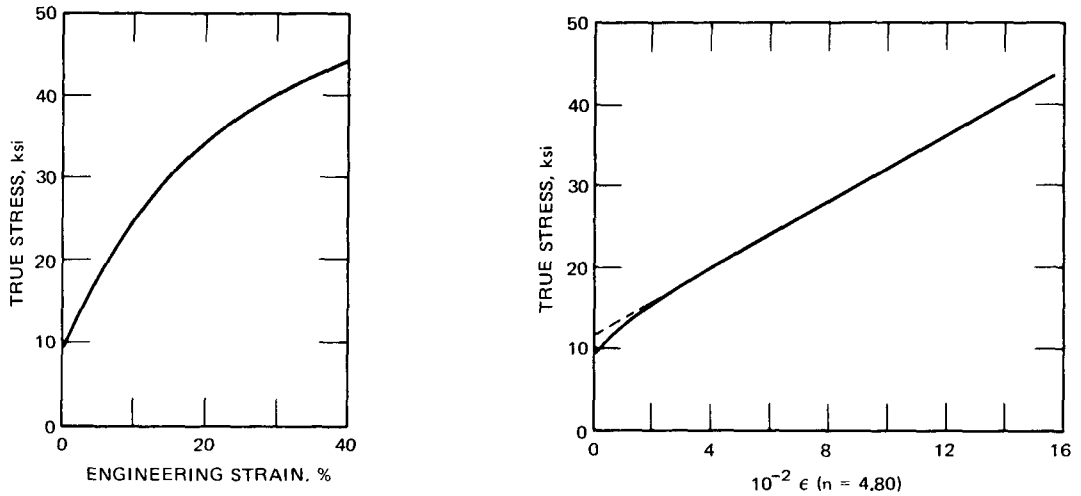

Fig. 6.23 Stress–strain plots for copper. (From Ref. 2.)

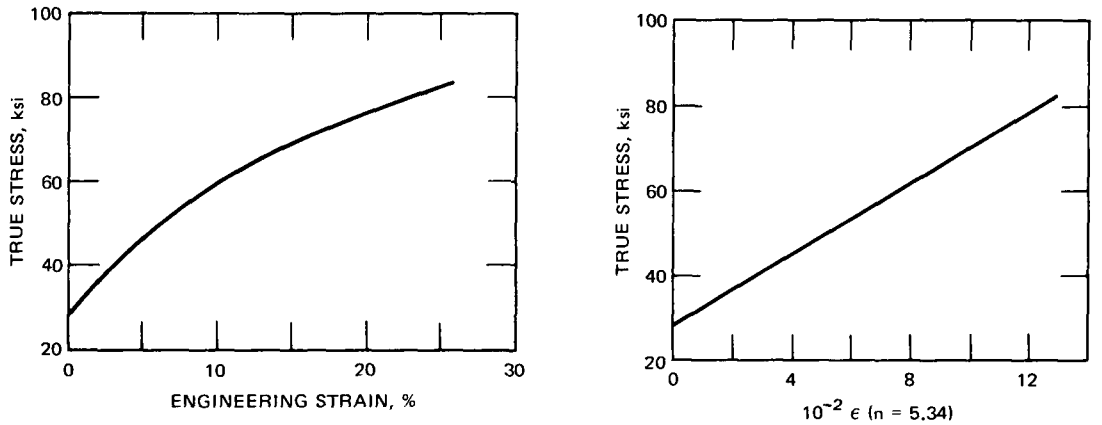

Fig. 6.24 Stress–strain plots for 60–40 brass. (From Ref. 2.)

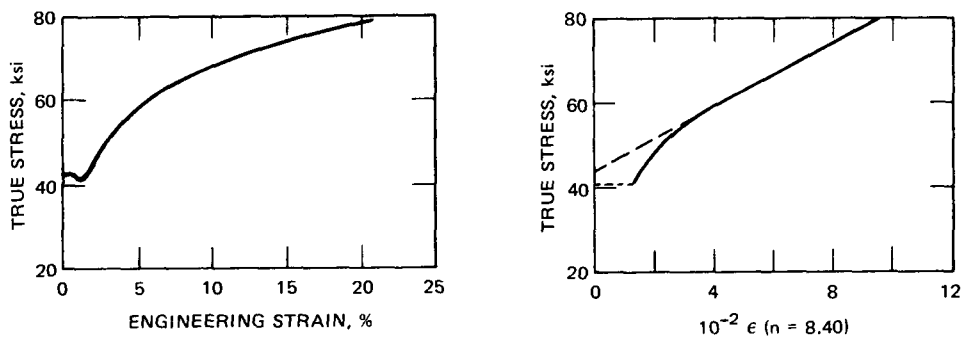

Fig. 6.25 Stress–strain plots for mild steel. (From Ref. 2.)

based on different datum lengths ℓ_0' and ℓ_0. Then it was shown that

$$\bar{\epsilon}' = \frac{1}{n}\left[1 - \left(\frac{\ell_0'}{\ell}\right)^n\right] \tag{6.110}$$

and using β, a measure of the prestrain, in the form

$$\beta = \frac{\ell_0'}{\ell_0} \tag{6.111}$$

it was indicated that

$$\bar{\epsilon}' = \frac{1}{n}\left[1 - \beta^n\left(\frac{\ell_0}{\ell}\right)^n\right] \tag{6.112}$$

Combining Eq. 6.112 with Eq. 6.39 gives

$$\bar{\epsilon}' = \frac{1}{n}\left[(1 - \beta^n) + n\,\beta^n\,\bar{\epsilon}\right] \tag{6.113}$$

In other words, $\bar{\epsilon}'$ is a linear function of $\bar{\epsilon}$; hence what appears as a straight line on $(\sigma, \bar{\epsilon})$ coordinates must appear also as a straight line on $(\sigma, \bar{\epsilon}')$ coordinates.

Hsu et al.[2] also added that the linearity between $\bar{\epsilon}'$ and $\bar{\epsilon}$ is a feature of Seth's[1] generalized strain measure. This point was illustrated by supposing that a strain measure different from Eq. 6.39 be adopted; e.g.,

$$\bar{\bar{\epsilon}} = \left(1 - \frac{\ell_0}{\ell}\right)^2 \tag{6.114}$$

This quantity increases with the current length, ℓ, is zero when ℓ is equal to ℓ_0, and hence can apparently serve as a definition of strain. For the prestrained specimen, however, the strain measure $\bar{\bar{\epsilon}}'$ is

$$\bar{\bar{\epsilon}}' = \left(1 - \frac{\ell_0'}{\ell}\right)^2 \tag{6.115}$$

and combining Eqs. 6.111, 6.114, and 6.115 gives

$$\bar{\bar{\epsilon}}' = (1 - \beta)^2 + 2\beta(1 - \beta)\sqrt{\bar{\bar{\epsilon}}} + \beta^2\,\bar{\bar{\epsilon}} \tag{6.116}$$

This indicates that $\bar{\bar{\epsilon}}'$ is not linear in $\bar{\bar{\epsilon}}$.

With the strain measure in Eq. 6.39, Hsu et al. mentioned that the slope of the straight line for the prestrained case compared to the annealed condition was given by

$$m' = \frac{m}{\beta^n} \tag{6.117}$$

and hence, from Eqs. 6.108 and 6.113, the value of k' would be given by

$$k' = \left[\frac{1 + (n - 1)\beta^n}{n\beta^n}\right] k \tag{6.118}$$

Thus, of the three constants in Eq. 6.108, n is more of a material constant than m and k because n is independent of the prestrain. Also, if the values of the three constants are known for the annealed material, say, from published data, the prestrain in a cold-worked specimen can be determined by carrying out a tensile test and using either Eq. 6.117 or 6.118 to calculate β.

Voce Equation Identical to Generalized Strain Equation

A recent study[28] shows that, although the Voce equation and the generalized strain equation appear to be quite different, they are really identical. This identity can be shown in a simple mathematical rearrangement. Referring to Eq. 6.93, the substitution of $\ln(1 + \epsilon_E)$ for ϵ (where ϵ_E is the engineering strain, S is replaced by σ, and ϵ_c replaces A) yields

$$\sigma = \sigma_\infty - (\sigma_\infty - \sigma_0)e^{-(1/\epsilon_c)\ln(1 + \epsilon_E)} \tag{6.119}$$

or

$$\sigma = \sigma_\infty - (\sigma_\infty - \sigma_0)(1 + \epsilon_E)^{-1/\epsilon_c} \tag{6.120}$$

Replacing $(1 + \epsilon_E)$ with its equivalent, (ℓ/ℓ_0), gives

$$\sigma = \sigma_\infty - (\sigma_\infty - \sigma_0)\left(\frac{\ell_0}{\ell}\right)^{1/\epsilon_c} \tag{6.121}$$

Adding and subtracting the quantity $(\sigma_\infty - \sigma_0)$ yields

$$\sigma = \sigma_\infty - (\sigma_\infty - \sigma_0) + (\sigma_\infty - \sigma_0)\left[1 - \left(\frac{\ell_0}{\ell}\right)^{1/\epsilon_c}\right] \tag{6.122}$$

$$= \sigma_0 + (\sigma_\infty - \sigma_0)\left[1 - \left(\frac{\ell_0}{\ell}\right)^{1/\epsilon_c}\right] \tag{6.123}$$

$$= \sigma_0 + \frac{(\sigma_\infty - \sigma_0)}{\epsilon_c}\,\frac{1 - (\ell_0/\ell)^{1/\epsilon_c}}{1/\epsilon_c} \tag{6.124}$$

Letting $n = 1/\epsilon_c$, it follows that

$$\sigma = \sigma_0 + \frac{(\sigma_\infty - \sigma_0)}{\epsilon_c}\,\frac{1}{n}\left[1 - \left(\frac{\ell_0}{\ell}\right)^n\right] \tag{6.125}$$

This equation is identical to the generalized strain expression in Eq. 6.108, the coefficients k and m being equal to σ_0 and $(\sigma_\infty - \sigma_0)/\epsilon_c$ or $n(\sigma_\infty - \sigma_0)$, respectively.

Confirmation of the above-noted relation was provided by fitting experimental stress–strain data for 304 stainless steel (total strain from 0.072 to 1.15) at room temperature

at a true total strain rate of 4×10^{-3} sec^{-1} to Eqs. 6.85 and 6.108.

In this study nonlinear regression analyses were used to evaluate the equation constants. The results of this evaluation are shown in Table 6.10. When these constants are used in Eqs. 6.85 and 6.108, the curves obtained are coincident. Note that the value of n is equal to $1/\epsilon_c$, the value of k is equal to σ_0, and the value of m is equal to $(\sigma_\infty - \sigma_0)/\epsilon_c$. These equalities are illustrated in Table 6.10, where the Voce constants in parentheses were calculated from k, m, and n values. Excellent agreement exists. Thus the Voce equation is indeed identical to the linear expression involving generalized strain.

TABLE 6.10

VALUES FOR THE CONSTANTS IN EQS. 6.85 AND 6.108; BASED ON TENSILE DATA FOR 304 STAINLESS STEEL AT ROOM TEMPERATURE AND AT A TRUE STRAIN RATE OF 4×10^{-3} sec^{-1}

Constant	Eq. 6.85	Eq. 6.108
σ_∞, psi	545,317 (545,328)*	
σ_0, psi	46,805 (46,805)	
ϵ_c or A	2.2780 (2.2781)	
k, psi		46,805
m, psi		218,833
n		0.438963

*Numbers in parentheses were calculated from k, m, and n values.

As noted in Ref. 2, when the generalized strain concept is applied to stress–strain data, the data within what was termed the transition region (first few points in the plastic-flow region) must be excluded from the analysis in order to obtain the linearity in Eq. 6.108. A similar exclusion applies in the use of the Voce equation since an expression that would describe the strain-hardening region would usually be found to be not too effective in the elastic–plastic fillet[24] that connects the elastic line to the strain-hardening region. These considerations further substantiate that Eqs. 6.85 and 6.108 do indeed describe identical behavior.

EXPERIMENTAL PROCEDURES

In recent studies[29,30] of the low-cycle-fatigue behavior of AISI 304, 316, and 348 stainless steels, a test facility was described which subjected round specimens having hourglass-shaped gage sections to programmed push–pull loading in a servo-controlled hydraulically actuated test machine. The specimen configuration is shown in Fig. 6.26. Test temperatures were attained by heating the specimen inductively using a specially shaped induction coil, and

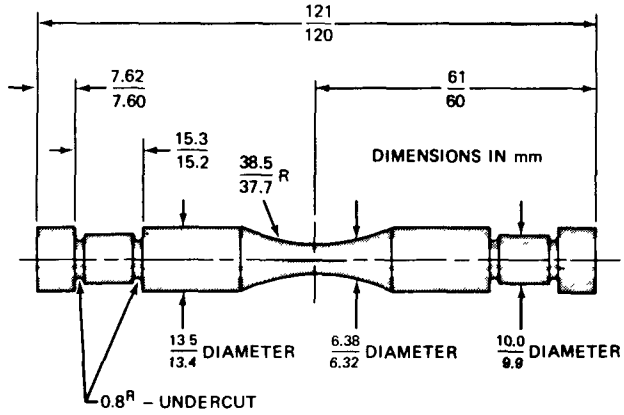

Fig. 6.26 Low-cycle-fatigue specimen.

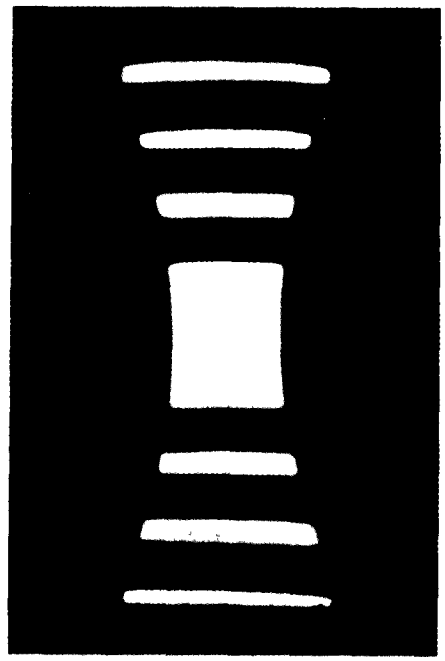

Fig. 6.27 Infrared photograph of 304 stainless-steel specimen heated inductively to 800°C.[30]

these temperatures were measured by using two chromel–alumel thermocouples spot welded to the surface of the sample near the minimum diameter. A special (infrared) photograph of a specimen at temperature is shown in Fig. 6.27 to indicate the spacing and position of the induction coil. Diametral-strain measurements were made using a specially developed[29,30] elastic-hinge extensometer that contacted the specimen at the point of minimum diameter (about 0.25 in.). The strain sensor furnished an electrical signal proportional to the change in diameter, and a load cell in series with the specimen supplied a signal proportional to the load on the specimen. A computer

network was developed that combined the two signals to provide an instantaneous signal proportional to the axial strain at the minimum diameter. The testing machine could therefore be operated with closed-loop control of either diametral strain, axial strain, or stress in the specimen. It was also possible to program plastic strain instead of total strain and to operate at constant strain rate. Furthermore, the cyclic mode could be varied with respect to wave form, loading frequency, and the duration of the hold time in each cycle.

Considering the reliability and outstanding control features of the fatigue machines used in the low-cycle-fatigue tests, it was recognized that these features offered fairly unique capabilities with respect to short-term tensile testing. However, considering the use of these test machines in making short-term tensile tests, it was recognized that several modifications were necessary. For example, a modification had to be made to allow the diametral extensometer to respond to larger deformations (maximum of 2% encountered in the fatigue studies). This new device is compared in Fig. 6.28 with the extensometer used in the low-cycle-fatigue studies.

Another modification involved the induction coil. In tensile tests large deformations were encountered which necessitated additional precautions to keep the coil positioned properly with respect to the deforming specimen so that temperature uniformity could be maintained in the region of the minimum diameter. Since the top of the specimen is rigidly fixed and symmetrical axial elongation is assumed, the center of the specimen moves downward at a rate which is just one-half that associated with the bottom portion of the specimen. The coil mounting fixture shown in Fig. 6.29 causes the coil to move downward at just this rate. A fairly constant temperature profile is thus maintained all the way to specimen fracture.

The requirement to maintain a constant strain rate during the short-term tensile tests generated the need for another system modification. In fatigue testing, the engineering diametral strain is measured, and, because strains of only a few percent are involved, these measurements are assumed to represent the true diametral strain. This assumption results in an error of less than 1% over the normal strain range encountered. In a tensile test, however, the deformations involved are so large that the differences between true strain and engineering strain become significant. For this reason, two different techniques were considered in order to produce a constant true strain rate. One technique operated upon the extensometer signal to convert it into a signal representative of true diametral strain according to the relation

$$\epsilon_d = \ln\left(1 - \frac{\Delta D}{D_0}\right) \tag{6.126}$$

where ϵ_d is the total diametral true strain, D_0 is the original diameter of the specimen, and ΔD is the measured reduction in the specimen diameter ($D_0 - D$). This signal can then be compared to a linear command signal representing a preselected diametral strain rate. In this way the short-term tensile test could be conducted at a constant value of the total diametral true strain rate.

The other technique involved the use of the signal from the extensometer directly, comparing it with a programmed demand signal that varies with time so as to produce the proper total diametral true strain rate. This approach was selected since it required no internal modification of the

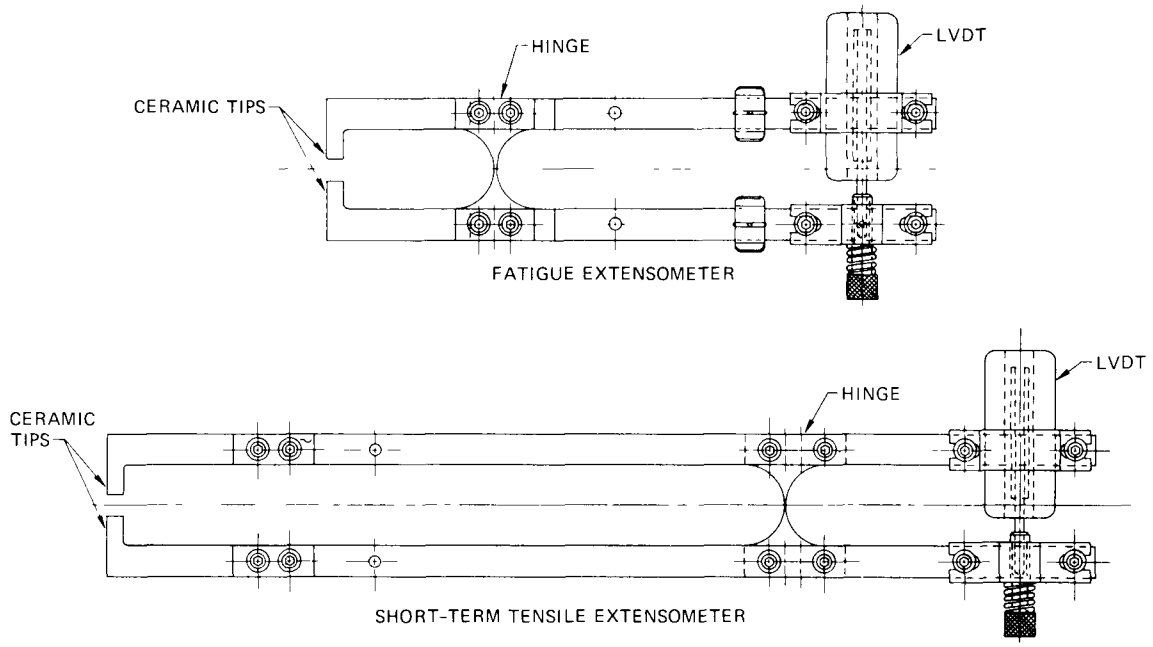

Fig. 6.28 Diametral extensometers used in fatigue and short-term tensile evaluations. Scale: approximately $\frac{1}{2}$.

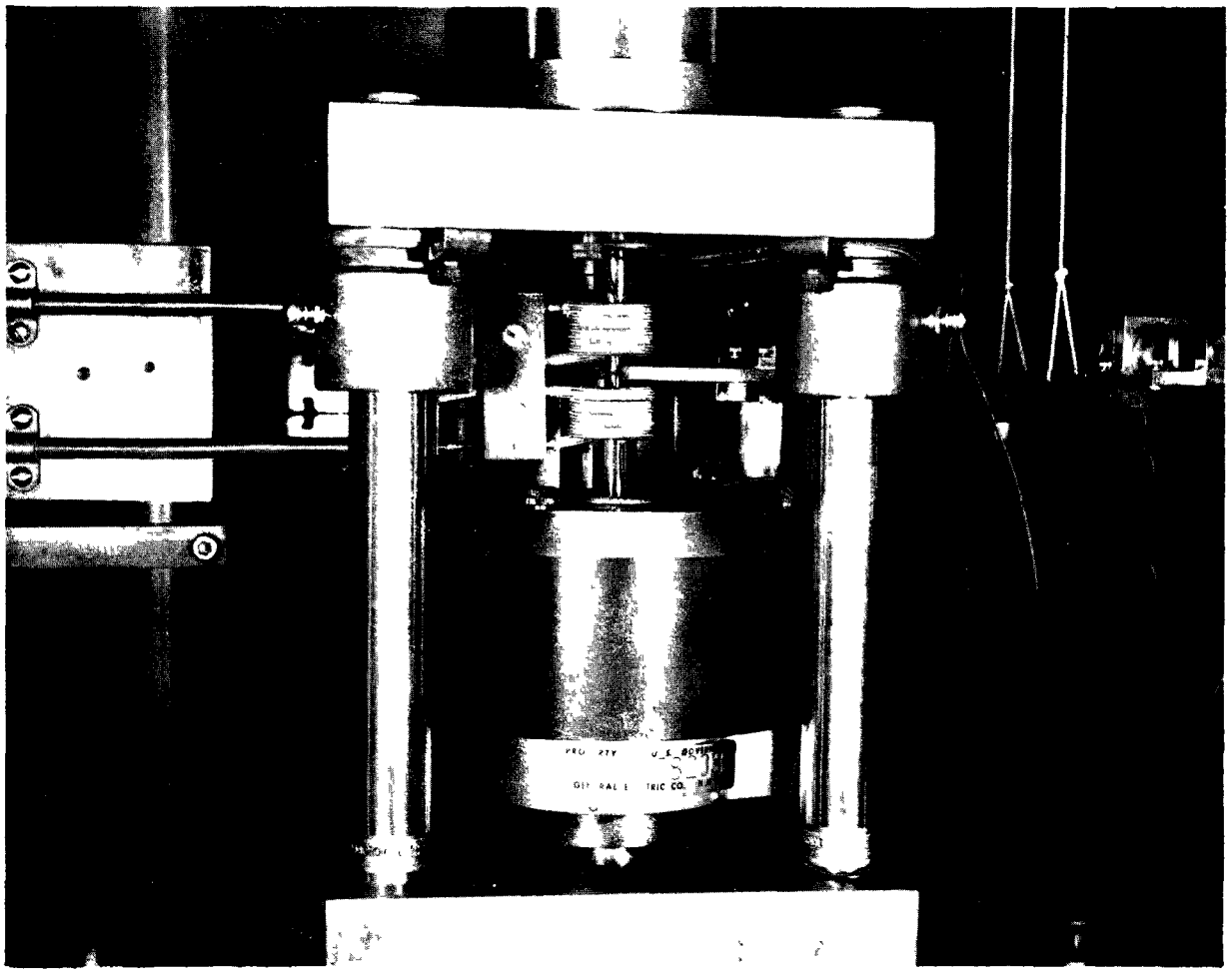

Fig. 6.29 Mounting fixture for induction coil to maintain proper position.

servo controller. It was also possible to design a very simple external programmer that produced a remarkably constant total diametral true strain rate in the specimen.

Solving Eq. 6.126 for ΔD and substituting $\dot{\epsilon}_d t$ (where $\dot{\epsilon}_d$ is the total diametral true strain rate) for ϵ_d results in an expression describing how ΔD must vary with time to produce a constant total diametral true strain rate, $\dot{\epsilon}_d$:

$$\Delta D = D_0 (1 - e^{\dot{\epsilon}_d t}) \tag{6.127}$$

Over the strain range (less than 100%) encountered in these tests, a very good approximation of this relation can be produced with the following circuit:

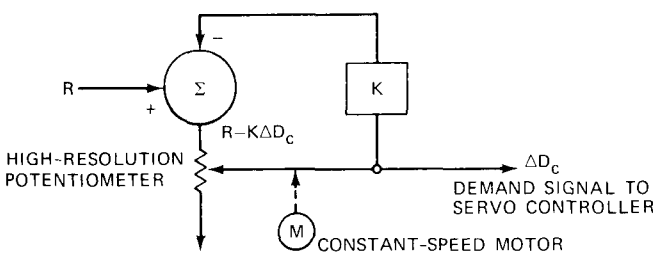

where ΔD_c is the programmed change in diameter and R and K are constants.

The following equations apply:

$$r = \frac{\Delta D_c}{R - K\Delta D_c} \tag{6.128}$$

$$r = vt \tag{6.129}$$

where r is the ratio of the potentiometer output to input; v is the slider velocity, a constant; and t is the time.

Equations 6.128 and 6.129 yield

$$\Delta D_c = \frac{Rvt}{1 + Kvt} \tag{6.130}$$

The servo controller causes $D_c = D$, and from Eqs. 6.126 and 6.130:

$$\epsilon_d = \ln \left[1 - \frac{Rvt}{D_0 (1 + Kvt)}\right] \tag{6.131}$$

The diametral strain rate can be found by differentiating Eq. 6.131 with respect to time:

$$\dot{\epsilon}_d = \frac{-Rv}{D_0 + 2D_0vKt - Rvt + D_0v^2K^2t^2 \quad Rv^2Kt^2} \tag{6.132}$$

At t = 0,

$$\dot{\epsilon}_d = \frac{Rv}{D_0} \tag{6.133}$$

which defines the initial strain rate. At full rotation of the potentiometer, r = 1 and t = T, where T is the time required to reach full rotation. Therefore, from Eq. 6.129,

$$vT = 1 \tag{6.134}$$

and

$$\dot{\epsilon}_d T = \frac{-RvT}{D_0} \tag{6.135}$$

or

$$\epsilon_{d\ max.} = \frac{-R}{D_0} \tag{6.136}$$

if the strain rate is constant.

Thus the strain rate and maximum strain amplitude can be determined by the proper choices of R and v. It remains to select a value of K that will produce the required constant strain rate. The approximate value of K can be found by solving:

$$\Delta D = D_0 (1 - e^{\epsilon d}) \tag{6.137}$$

$$\Delta D_c = \frac{Rvt}{1 + vtK} \tag{6.138}$$

$$\epsilon_{d\ max.} = \frac{-R}{D_0} \tag{6.139}$$

At the boundary condition of vt = r = 1 and $\epsilon_d = \epsilon_{d\ max.}$, again assuming that $\Delta D_c = \Delta D$,

$$K = -\left(\frac{\epsilon_{d\ max}}{1 - e^{\epsilon d\ max.}} + 1\right) \tag{6.140}$$

A value of K can be found which will produce a very accurate strain rate for any $\epsilon_{d\ max.}$ less than 100%. In this testing, $\epsilon_{d\ max.} = 80\%$ was sufficient to accommodate the actual strain values encountered. Figure 6.30 shows the programmed value of strain, as a function of r, using this technique; Fig. 6.31 contains a simplified schematic of the programmer circuit.

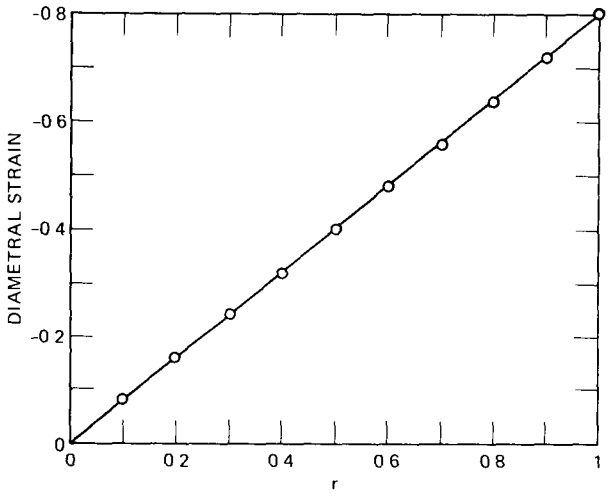

Fig. 6.30 Programmed value of diametral strain as a function of r.

The diametral true strain rate is really the controlled parameter, and it is this strain rate that is held constant throughout the test. There is, however, a definite relation between diametral and axial strain as given in the following equations:

$$\epsilon = -\left[\frac{\epsilon_d}{\nu_p} + \epsilon_{de}\left(\frac{\nu_p - \nu_e}{\nu_p\nu_e}\right)\right] \tag{6.141}$$

$$\epsilon_{de} = -\frac{\nu_e}{E}\sigma \tag{6.142}$$

where ϵ = true axial strain
ϵ_d = total diametral true strain
ϵ_{de} = elastic diametral true strain
σ = true stress
ν_e = Poisson's ratio in elastic region
ν_p = Poisson's ratio in plastic region
E = Young's modulus

Combining these two equations gives

$$\epsilon = -\left[\frac{\epsilon_d}{\nu_p} - \left(\frac{\nu_p - \nu_e}{E\nu_p}\right)\sigma\right] \tag{6.143}$$

or

$$\epsilon = -\left[2\epsilon_d - \left(\frac{1 - 2\nu_e}{E}\right)\sigma\right] \tag{6.144}$$

assuming $\nu_p = 0.5$. Equation 6.144 can be used in conjunction with a stress vs. diametral strain curve to determine the axial-strain behavior in a tensile test. Figure 6.32 shows a comparison between the axial and diametral true strain in a typical short-term tensile test in which the diametral true strain rate was held constant at 2×10^{-3} sec^{-1}. It can be seen that the axial true strain rate is exactly twice the diametral true strain rate during most of the test. A recent

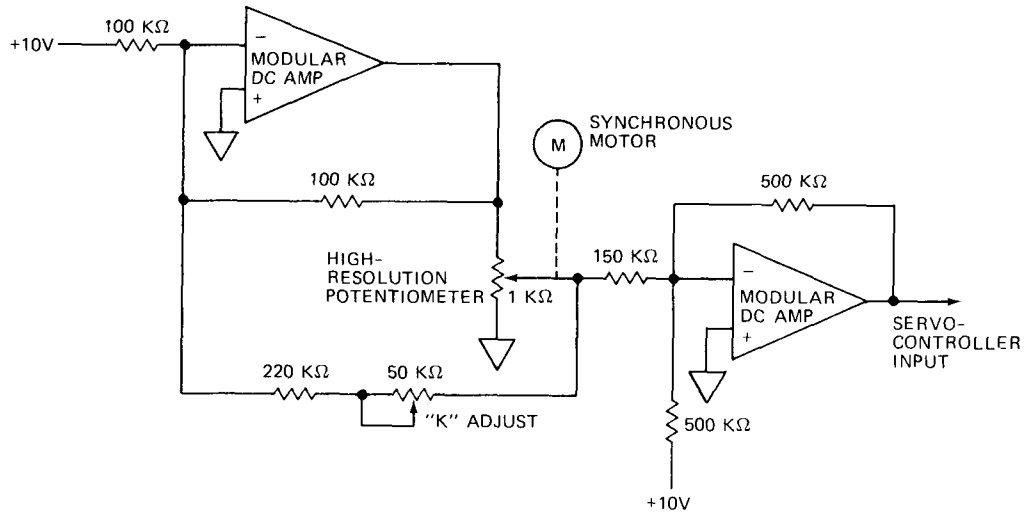

Fig. 6.31 Simplified schematic of programmer circuit.

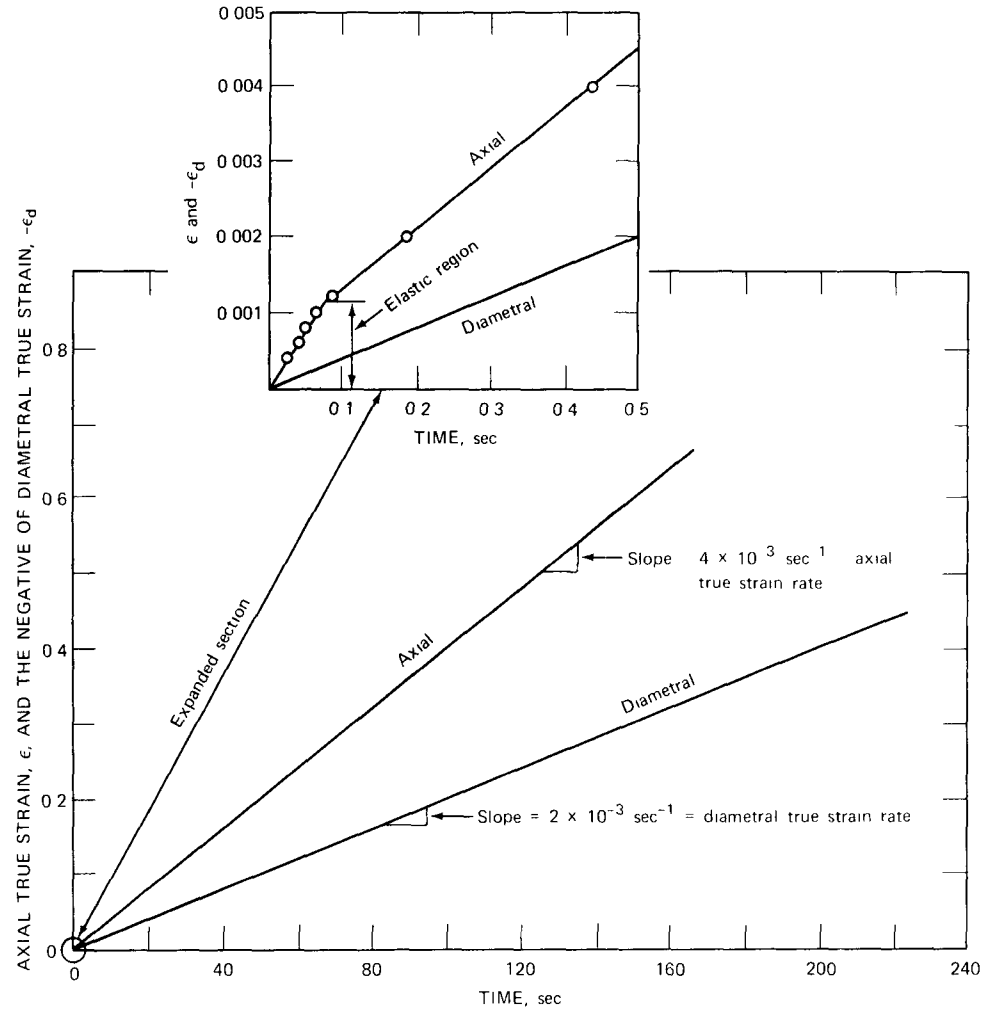

Fig. 6.32 Comparison of true axial and true diametral strain when the diametral true strain rate is constant.

technique development has permitted further refinements so that the axial true strain rate can now be maintained constant even through the initial elastic deformation. Under these conditions, of course, slight variations in the diametral true strain rate are noted.

A short-term tensile test was performed in a fairly standard fashion using the above-mentioned control features. An hourglass-shaped specimen was positioned within the induction coil and clamped in place between the two end fixtures of the fatigue machine (see Fig. 6.33). This specimen was then inductively heated to the desired test temperature. Three chromel-alumel thermocouples attached to the external surface of the specimen allowed for the measurement and control of test temperature, with feedback from one of the thermocouples being used to adjust power to the induction coil as needed. Once the desired test temperature was established, the control system was activated to load the specimen so as to maintain a constant value of the total axial true strain rate. A flat load cell* (see Fig. 6.33) in series with the specimen provided an automatically recorded trace of the applied load as a function of time. Readings from the extensometer were also recorded automatically as a function of time to provide a proper record of the instantaneous diameter measurements. These measurements were then used (see next section) to calculate and analyze the stress–strain behavior obtained at a constant value of the total axial true strain rate. Tests were made of AISI 304, 316, and 348 stainless steels at room temperature, 430, 650, and 816°C in air at total axial true strain rates of 4×10^{-3} and 4×10^{-5} sec^{-1}.

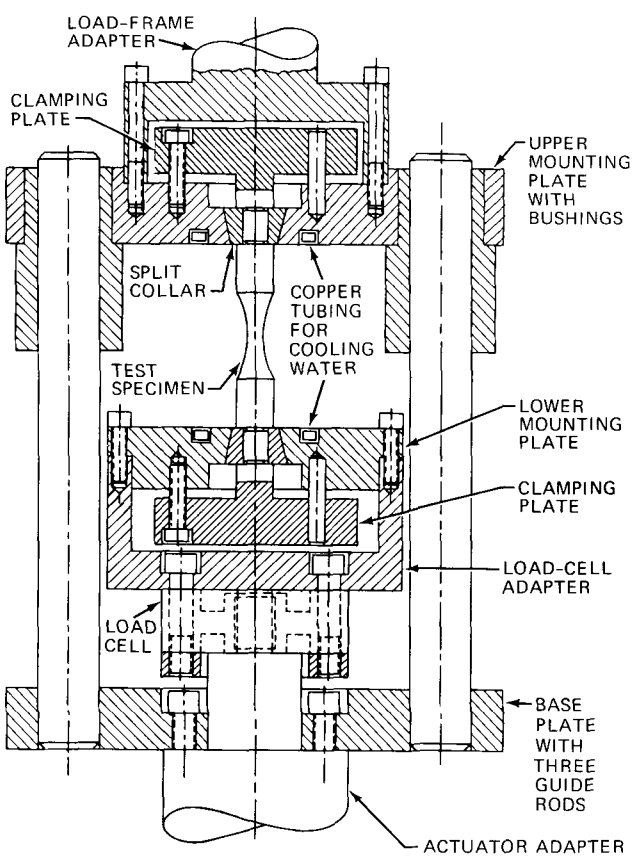

Fig. 6.33 Schematic of test specimen and loading fixture used in short-term tensile testing. Scale: approximately ½.

*Model FL 10U-2SP, 10,000-lb capacity, Strainsert Co., Bryn Mawr, Pa.

In separate tests the constant-strain-rate control features of the low-cycle-fatigue machines were used in making measurements of the modulus of elasticity. These evaluations made use of cylindrical gage length specimens having a gage-section length of 1 in. and a gage-section diameter of 0.25 in. Axial strain in the gage length was measured using a standard microformer-type extensometer equipped with Inconel extension arms to allow for reliable operation at the elevated temperatures involved. A commercial resistance-wound furnace was used to heat the test specimen to the desired temperature. Chromel–alumel thermocouples were spot-welded to the shoulders of the specimen, and sheathed, chromel–alumel thermocouples were wired to the test specimen at ½-in. intervals along the gage length. With this arrangement it was possible to assure that the entire gage length was being held at a uniform temperature. The signal from the axial-strain extensometer provided a feedback signal that was used for control purposes. The demand signal of the system was selected to produce a constant-strain-rate condition.

In these tests the loading of the specimen was limited to the elastic range to permit accurate measurement of the effect of temperature and strain rate on a given material while making use of a single specimen. Values of Young's modulus were determined from autographic records of load vs. axial strain. Strain vs. time traces were recorded to verify that a constant strain rate was actually being obtained. Also, the test temperature was recorded as a function of time.

Measurements were also made to identify values of Poisson's ratio. In these tests the same hourglass-shaped specimens were used as in the stress–strain determinations and were machined from the same rod of material as that used in the Young's-modulus determinations. Chromel–alumel thermocouples were spot-welded to each specimen $^3/_{16}$ in. from the minimum diameter. An induction coil heated the test specimen to the desired temperature. The output of the diametral-strain sensor, positioned at the minimum diameter of the test specimen, was used as a feedback signal for closed-loop control of the diametral strain. The specimen was loaded at various controlled strain rates, taking care not to exceed the elastic limit. This technique allowed Poisson's-ratio determinations at several temperatures and strain rates, using a single specimen. Autographic records of diametral strain vs. load permitted the calculation of E/ν_e [Young's modulus divided by Poisson's ratio (elastic)] by dividing the instantaneous value of stress by the corresponding value of diametral strain. Appropriate values for E, of course, were obtained from

tests using the same material as outlined above. These E values were then used to solve for the corresponding ν_e values.

In special short-term tensile tests of annealed AISI 304 stainless steel, cylindrical gage section specimens (made from the same heat of material used in fabricating hourglass-shaped specimens) were used in conjunction with the above-mentioned diametral extensometer technique. These tests were performed at 650°C and axial true strain rates of 4×10^{-5} and 4×10^{-3} sec^{-1} to compare the short-term behavior with that obtained using the hourglass-shaped samples at these same conditions. In these evaluations each specimen had a gage section 0.25 in. in diameter by 2.0 in. in length (see Fig. 6.34), and the diametral extensometer was positioned at the midpoint of the longitudinal gage section. Diameter readings were used just as they were in the tests of hourglass-shaped samples. In other words, these diametral measurements were monitored to yield a constant value for the diametral true strain rate and, as mentioned previously, an essentially constant value for the axial true strain rate. The position occupied by the diametral extensometer is shown in Fig. 6.35 along with the fracture points. Also shown in Fig. 6.35 is the thermocouple position along the gage length. These thermocouples were spaced 0.375 in. apart, and temperature uniformity was maintained within 3°C.

These tests of cylindrical gage section specimens in diametral-strain control yielded the results in Figs. 6.36 and

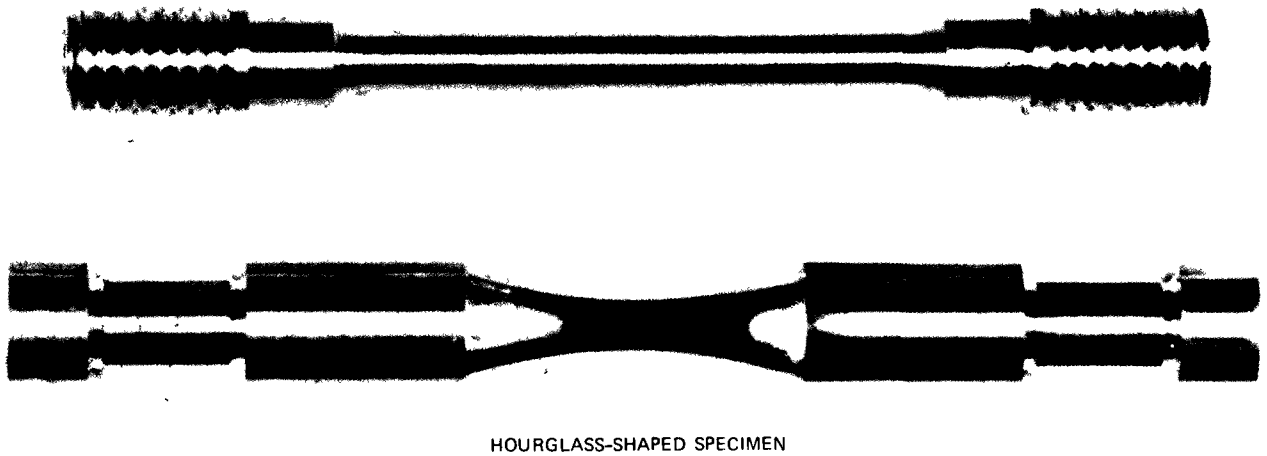

Fig. 6.34 Cylindrical and hourglass-shaped specimens used in tensile tests. (Scale: approximately 1.7.)

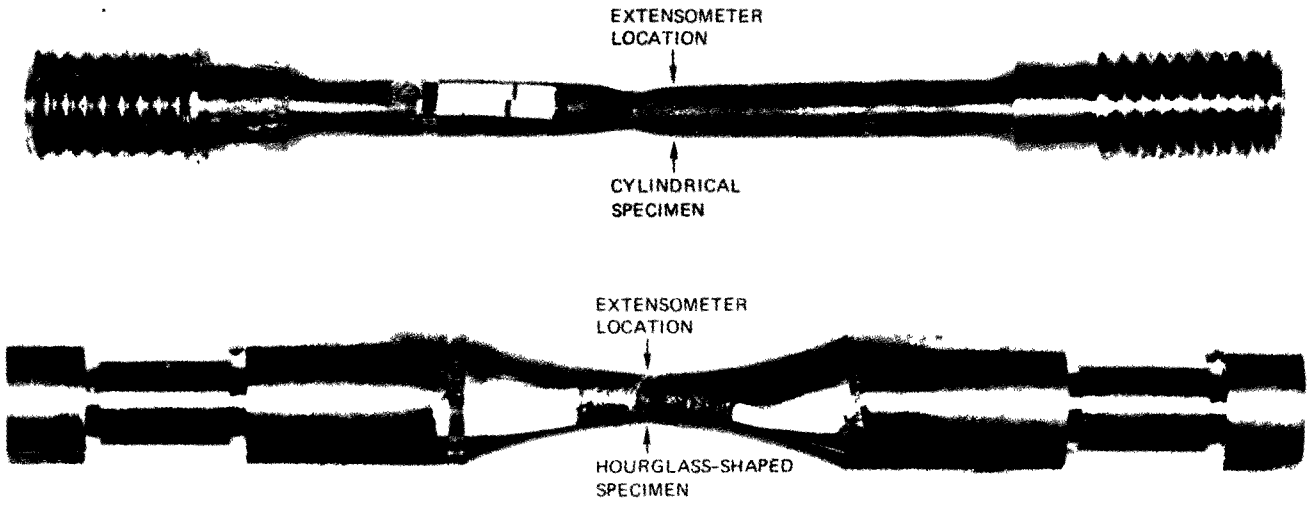

Fig. 6.35 Cylindrical and hourglass-shaped AISI 304 stainless-steel tensile specimens after testing at 650°C in air.

6.37. The flow stress curves are essentially identical for the two specimen geometries involved, at least within the range shown in these figures. In Figs. 6.36 and 6.37, essentially identical strain-hardening behavior is indicated for the two specimen configurations. These results provide convincing evidence that the use of hourglass-shaped specimens in diametral-strain control provides meaningful and characteristic short-term tensile results.

One difficulty involved with the testing of cylindrical gage section specimens is that severe necking and fracture might occur at a location other than that corresponding to the position occupied by the diametral extensometer. This situation was actually observed in the present tests, as indicated in Fig. 6.35. In other words, fracture occurs while the extensometer is measuring something other than the diametral strain at fracture. For this reason, the final points (near a strain of 0.2 in Fig. 6.36 and 0.3 in Fig. 6.37) do not represent the fracture condition but rather the last reading at the particular point of diametral-strain measurement. Therefore the final points on the cylindrical gage section curves in Figs. 6.36 and 6.37 have no meaning as far as fracture behavior is concerned. These final points cannot be viewed as fracture ductilities. However, had the diametral extensometer been reading the dimensional changes at the actual necking point, the stress–strain curve for the cylindrical gage section specimen would have been essentially identical to that obtained with the hourglass-shaped specimen. In such a situation the fracture ductilities would be expected to be identical.

Posttest measurements to identify values for the reduction in area (and tensile ductilities) in the above-mentioned tests provided an interesting comparison. In this study the "hot" reduction-in-area values were those measured (from

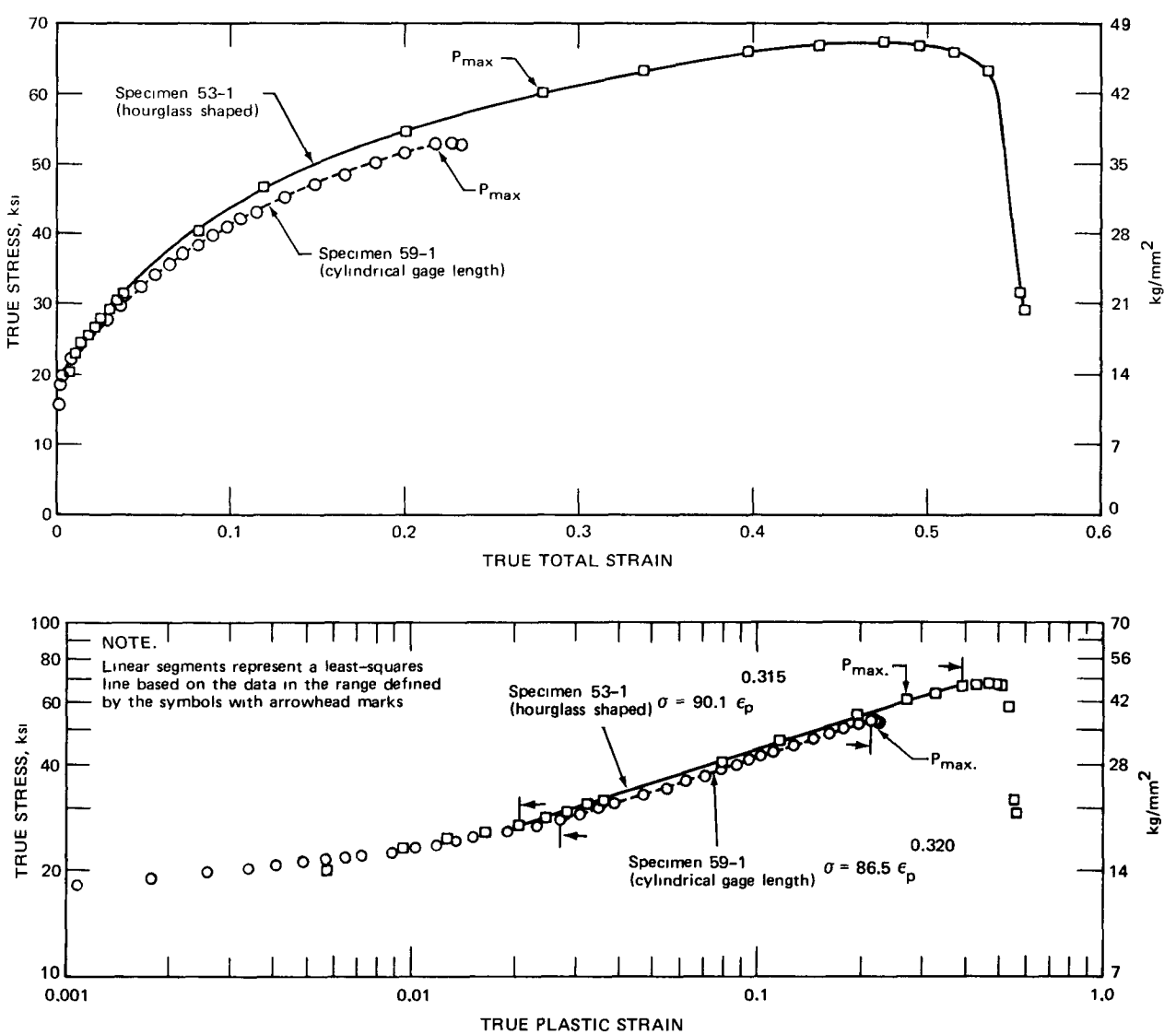

Fig. 6.36 True stress–strain data obtained at 650°C and a strain rate of 4×10^{-3} sec^{-1} in air for annealed AISI 304 stainless steel using hourglass-shaped and cylindrical gage section specimens.

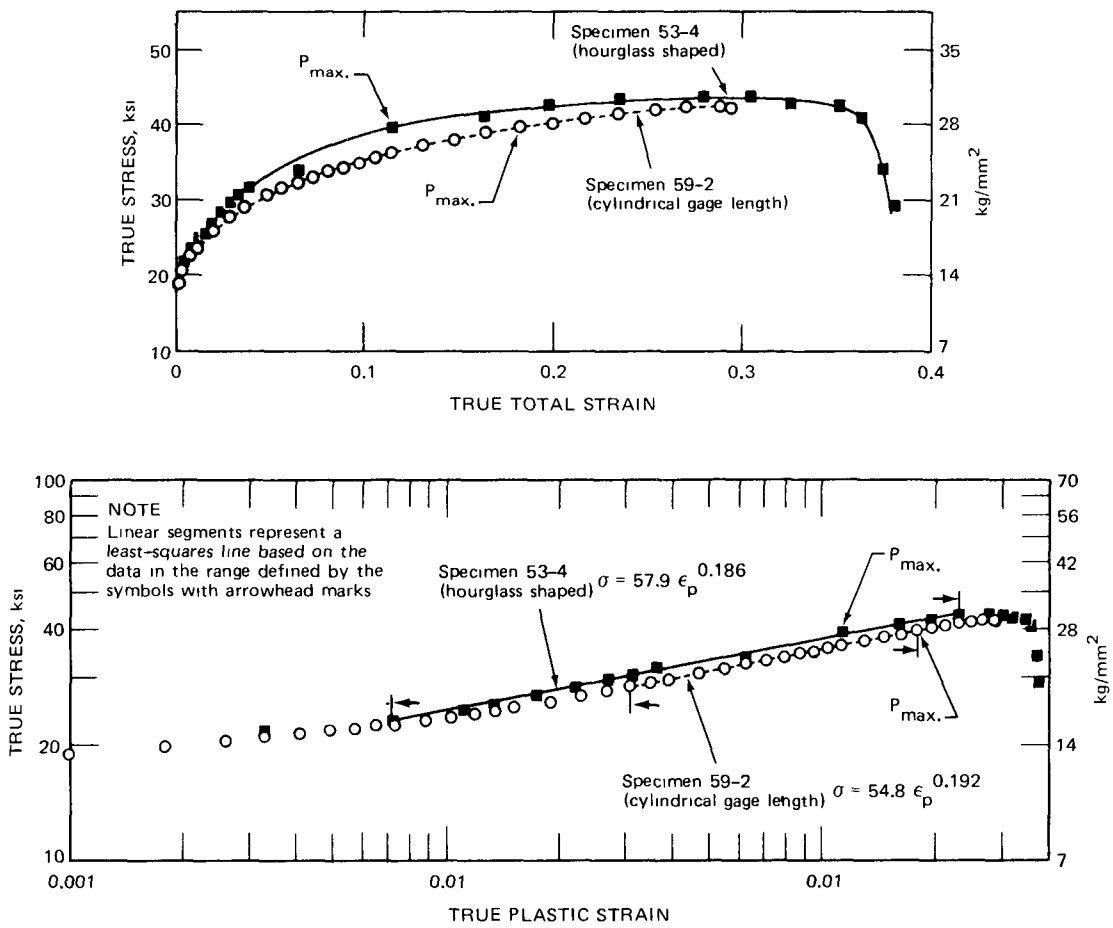

Fig. 6.37 True stress–strain data obtained at 650°C and a strain rate of 4×10^{-5} sec^{-1} in air for annealed AISI 304 stainless steel using hourglass-shaped and cylindrical gage section specimens.

diametral strain) at test temperature at the instant before fracture. These results are as follows:

Programmed strain rate, sec^{-1}	Specimen geometry	Measured* (hot) reduction in area, %	Measured (posttest, cold) reduction in area at fracture point, %
4×10^{-3}	Hourglass	42.6 (0.555)	42.2 (0.548)
4×10^{-3}	Cylindrical	20.7 (0.232)	64.0 (1.022)
4×10^{-4}	Hourglass	31.6 (0.38)	33.4 (0.407)
4×10^{-4}	Cylindrical	25.5 (0.295)	42.2 (0.548)

*Corresponding tensile ductilities are given in parentheses.

For the hourglass specimen, excellent agreement between the hot reduction-in-area values and the posttest measurements is indicated. This consistency was found to be typical of tests involving this geometry; it was also found that duplicate tests yielded essentially identical values for hot and posttest reduction-in-area values. A desirable feature of this specimen type and test procedure stems from the fact that the strain at the minimum-diameter point is tracked all the way to fracture.

Reduction-in-area data for the cylindrical gage section specimen indicate a decided lack of agreement between the hot and posttest reduction-in-area values. As mentioned above, this lack of agreement follows from the fact that necking occurred at a point other than the extensometer location. Testing of such specimens in diametral-strain control should therefore be viewed with some reservation. It might be reasoned that little criticism of the use of cylindrical gage section specimens is in order since the discrepancy between hot and posttest reduction-in-area values does not represent a serious consideration. In other words, one might merely disregard the hot measurement and accept only the posttest value as an indication of fracture ductility. This approach appears reasonable, but the data compilation presented above emphasizes that such an assumption would not even be a good approximation. For example, at a strain rate of 4×10^{-3} sec^{-1}, the reduction-in-area (posttest) value for the hourglass specimen was 42.2%, and that for the cylindrical gage section specimen was 64%. This higher ductility for the cylindrical

geometry is believed to be attributable to a strain-rate effect. Since necking occurred, the local strain rate was much higher than the controlled, constant value at the extensometer location. Since increased strain rate leads to larger fracture ductilities (see Chap. 7), at least for this material and the conditions involved, this effect is probably responsible for the differences noted. In other words, the posttest reduction-in-area value for a cylindrical gage section specimen is ill-defined since it is difficult to relate it to a specific strain rate. One would then conclude that the use of a cylindrical gage section specimen and diametral-strain control in short-term tensile evaluations will probably not lead to completely meaningful results. This same criticism applies as well, although perhaps not as pointedly, to cylindrical gage section specimens tested using total gage-length elongations to control strain rate. It also applies when crosshead speed is used as an indication of strain rate.

In another evaluation of the relative merits of the short-term tensile-testing technique based on hourglass-shaped specimens, some comparative short-term tensile data were generated using standard procedures. Two cylindrical gage section (0.25 in. in diameter and 2 in. in length) specimens were fabricated from the same heat of 304 stainless steel used in preparing the hourglass-shaped specimens. These specimens were tested in accordance with approved American Society for Testing and Materials procedures[31] using a high-temperature extensometer to measure axial deformation. Tests were performed in air at 430 and 650°C using an initial strain rate of 5×10^{-5} sec^{-1}. After a strain of about 2.0% was reached, the rate of straining was increased to 5×10^{-4} sec^{-1}, as indicated by a deflectometer measurement. This latter rate was maintained until fracture occurred.

Data obtained in these tests are presented in Table 6.11 and Fig. 6.38, along with data for hourglass-shaped specimens of 304 stainless steel tested at 430 and 650°C and strain rates of 4×10^{-5} and 4×10^{-3} sec^{-1}. Figure 6.38 indicates very good agreement for the flow curves up to the maximum load point. Also, the ultimate strength values are in good agreement at the two test temperatures. Some effect of strain rate on tensile strength is definitely in evidence at 650°C, and the values for the cylindrical specimens seem to be consistent with those for the hourglass-shaped specimens when it is considered that the cylindrical samples experienced a strain rate of 5×10^{-4} sec^{-1} in the region of maximum load.

In the region beyond the maximum load point, serious disagreement is noted in the stress–strain curves for the two specimen geometries. The curve for the hourglass-shaped specimen is considered correct since the local strain values were actually being followed to the fracture point and the local true strain rate was maintained constant throughout the test. Thus little significance can be assigned to the stress–strain curve obtained with the cylindrical specimen. Local necking occurred with this specimen geometry, and the actual specimen strain was not being measured. Furthermore, the local strain rate at the necking point was much higher than that given by the deflectometer measurement.

Posttest measurements of specimen diameters at the fracture point provided an interesting comparison (see Table 6.11). At 430°C the values for the "cold reduction in area" are in excellent agreement. No effect of strain rate is indicated in the 4×10^{-3} and 4×10^{-5} sec^{-1} tests, and hence, even though the cylindrical specimen was not tested at a constant strain rate (owing to necking), the reduction-in-area value obtained at this temperature should be expected to be in agreement with the hourglass data. Note also that values for "hot reduction in area" were not obtained in cylindrical-specimen tests but were obtained in the hourglass tests. Typically, hourglass tests yielded hot and cold reduction-in-area values that were essentially identical. This relation is generally noted in Table 6.11, although in the 4×10^{-3} test at 430°C this consistency was not observed. In a few tests the diametral extensometer was apparently not positioned exactly at the minimum-diameter point, and the usual good agreement between the hot and cold reduction-in-area values was not observed.

At 650°C some effect of strain rate on ductility is indicated. In the cylindrical test the high value for the reduction in area would seem to indicate that the local strain rate in this test was much higher than that indicated by the deflectometer reading. In fact, this comparison would indicate that the local strain rate in the cylindrical test was higher than 4×10^{-3} sec^{-1}.

Extensometer readings defining the engineering strain at fracture are shown in Fig. 6.38. For the hourglass-shaped specimens, these strain values are in good (except for the above-mentioned occasional test) agreement with the engineering-strain values calculated from posttest measurements of the reduction in area. The cylindrical specimens show serious discrepancies between the two strain values.

On the basis of the observations of Table 6.11 and Fig. 6.38, additional evidence is made available to confirm the accuracy of the short-term tensile data obtained in tests of hourglass-shaped specimens. It also seems valid to conclude that such testing leads to a more representative evaluation of stress–strain behavior and enables strain-rate effects to be accurately investigated.

Some additional stress–strain data for 304 stainless steel tested at room temperature and a strain rate of about 3×10^{-5} sec^{-1} were reported recently.[32] In this study a cylindrical gage section specimen was used, and the test was interrupted periodically to obtain measurements of the reduction in area in the necking region. These data led to true-strain values and to the results shown in Fig. 6.39. A comparison of these results with those of Fig. 6.39 for an hourglass-shaped specimen indicates fairly good agreement. True-strain data obtained with the cylindrical gage-length specimen indicate a fracture ductility (true strain at fracture) value of 1.5 that is in fairly good agreement with

TABLE 6.11

SHORT-TERM TENSILE DATA FOR ANNEALED AISI 304 STAINLESS STEEL TESTED IN AIR AT 430° AND 650°C USING HOURGLASS-SHAPED AND CYLINDRICAL SPECIMENS

Specimen type	Test temp., °C	Strain rate, sec^{-1}	Hot reduction in area (RA), %	Cold reduction in area (RA), %	Ultimate tensile strength, ksi	Engineering strain, ϵ_E		
						Based on axial extensometer and deflectometer measurements*	Based on diametral-strain measurement at time of fracture	Based on cold RA values at fracture point
Cylindrical	430	5×10^{-5} to ~2% strain 5×10^{-4} to fracture		63.3	64.5	0 47		1.72
Hourglass	430	4×10^{-3}	51.5	64.0	62.4		1.07†	1.81†
Hourglass	430	4×10^{-5}	60.7	64.5	64.6		1.54	1.77
Cylindrical	650	5×10^{-5} to ~2% strain 5×10^{-4} to fracture		46.0	42.6	0.47		0.85
Hourglass	650	4×10^{-3}	42 6	42.2	45.6		0.74	0.74
Hourglass	650	4×10^{-5}	31.6	33.4	35.0		0.47	0.50

*Assuming uniform strain over 2-in. gage section

†In tests of hourglass-shaped specimens, it was generally noted that the measured strain at fracture was in close agreement with posttest (cold) measurements. In a few cases, however, the diametral extensometer was not positioned properly and was not measuring at the minimum-diameter point. When this happened, noticeable differences were seen in these two strain values. Usually such tests would be repeated.

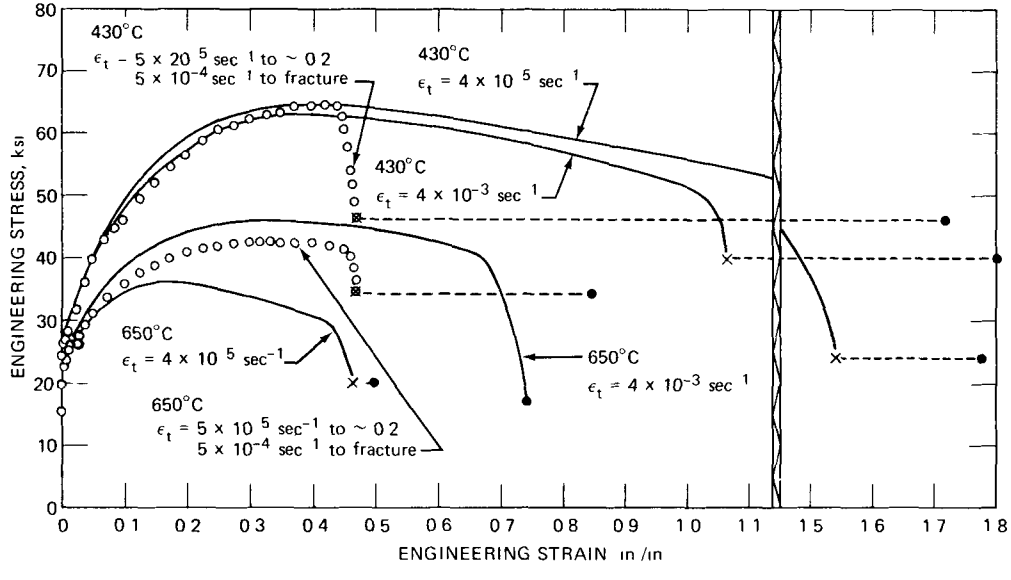

Fig. 6.38 Engineering stress–strain data for annealed AISI 304 stainless steel tested in air at 430° and 650°C using hourglass-shaped and cylindrical specimens. ○, data using standard tensile-test procedures (2-in. uniform gage length); ——, data represent tensile tests performed with hourglass-shaped specimen and diametral-strain measurement with programmed true strain rate; ×, fracture based on extensometer and deflectometer measurements; •, fracture based on cold RA values, $\epsilon_E = (A_0/A) - 1$.

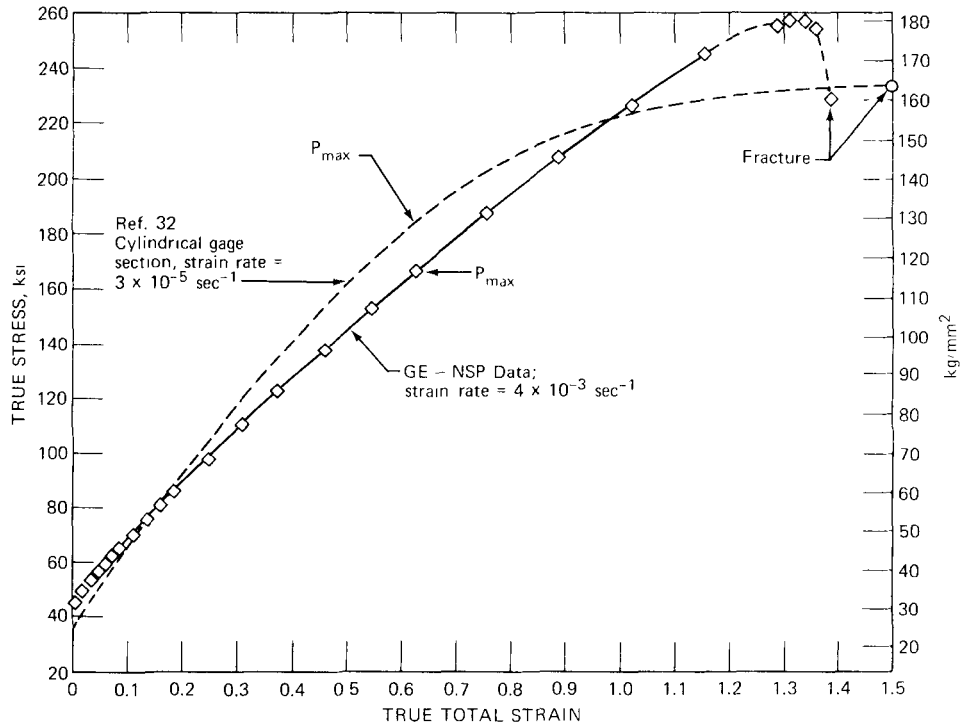

Fig. 6.39 Comparison of true-stress–true-strain data for annealed AISI 304 stainless steel tested at 21°C.

the value obtained using the hourglass-shaped specimen. At room temperature the effect of strain rate on tensile behavior is not large, and hence a direct comparison of the results at 3×10^{-5} sec^{-1} and 4×10^{-3} sec^{-1} is allowable. This same reasoning applies when considering that in the test of the cylindrical gage section specimen the strain rate in the necked region was much higher than that corresponding to the crosshead speed (about 3×10^{-5} in./sec) which was being held constant throughout the test. On the basis of the discussions relating to Figs. 6.36 and 6.37, the different strain rate in the region of necking would have led to inconsistent results in Fig. 6.39 if the test temperature had been high enough to allow strain-rate effects to become significant.

In conclusion, the hourglass-shaped specimens tested in diametral-strain control offer an improved procedure for evaluating short-term tensile behavior. Since the strain is forced to occur at a definite location (point of extensometer position), a more accurate control of the deformation process is obtained and the attainment of a test of constant true strain rate all the way to fracture is made possible.

APPENDIX: A COMPARISON OF TRUE AND ENGINEERING STRAINS

The difference between true and engineering strains is, of course, well established. It is also well established that this difference is quite small when the deformation is small and becomes larger as increased straining takes place. What might not be generally recognized is that, over a fairly broad range of strains, there exists an interesting relation between engineering strain and the difference between true and engineering strains. If it is assumed, for example, that a value of engineering strain is used instead of the true strain, then the error involved in so doing will be given by the difference between the two strain values. If this error is expressed as a percentage of the true-strain value and if this percentage error is calculated for various deformation levels, then a very simple relation exists between this percentage error and the value of the engineering strain. Some typical values that result from such a calculation are as follows:

Engineering strain, %	$\frac{\text{Engineering strain} - \text{true strain}}{\text{True strain}}$, %
1.0	0.499
2.0	0.996
3.0	1.494
4.0	1.994
5.0	2.48
10.0	4.93

A graph of these values will reveal a distinct linearity to confirm that the percentage error made by assuming that a given value of engineering strain is equal to the true strain is one-half of the engineering strain value expressed as a percent. This, of course, is only an approximation, but it is extremely accurate over a wide range of strain values.

A mathematical confirmation of this close approximation can be obtained by writing the percentage-error expression

$$\frac{\epsilon_E - \ln(1 + \epsilon_F)}{\ln(1 + \epsilon_E)} \times 100$$

and expressing the true strain in the form of a series expansion. Using only the first two terms of the series for $\ln(1 + \epsilon_E)$ leads to

$$\frac{\epsilon_E - [\epsilon_E - (\epsilon_E^2/2)]}{\epsilon_E - (\epsilon_E^2/2)} \times 100 = \% \text{ error}$$

$$\frac{\epsilon_E^2/2}{\epsilon_E - (\epsilon_E^2/2)} \times 100 = \% \text{ error}$$

$$\frac{\epsilon_E/2}{1 - (\epsilon_E/2)} \times 100 = \% \text{ error}$$

This shows that the percentage error is essentially equal to one half of the ϵ_E value expressed in percent. The ϵ_E term in the denominator is small compared to unity for ϵ_E values below 0.10, and the use of additional terms in the series expansion would prove the above mentioned approximation for engineering-strain values up to 0.50 (i.e., 50% engineering strain).

REFERENCES

1 B. R. Seth, Generalized Strain Measure with Applications to Physical Problems, in *International Symposium on Second Order Effects in Elasticity, Plasticity, and Fluid Mechanics*, Haifa, April 1962, p. 162, Pergamon Press Ltd., Oxford, 1962.

2 T. C. Hsu, S. R. Davies and R. Royles, A Study of the Stress–Strain Relationship in the Work Hardening Range, *J. Basic Eng.*, 89(3): 453 (September 1967).

3 E. Voce, The Relationship Between Stress and Strain for Homogeneous Deformation, *J. Inst. Metals*, 74: 537 (1947–1948).

4 W. R. Osgood, Stress–Strain Formulae, *J. Aeronaut. Sci.*, 13(1): 45 (1946).

5 G. B. Bulffingeri De Solidorum Resistentia Specimen, *Commentarii Academiae Scientiarum Imperialis Petropolitanae*, 4: 164 (1729).

6 J. Riccati, Verae et Germanae Virium Elasticarum Leges ex Phaenomenis Demonstratae, *De Bononiensi Scientiarum et Artium Instituto atque Academia Commentarii*, 1: 523 (1731).

7 F. J. R. von Gerstner, *Handbuch der Mechanik*, 1: 263 (1831).

8 J. V. Poncelet, Introduction à la Mecanique Industrielle, in *Physique ou Experimentale*, 2nd edition, p. 348, Metz, 1841.

9 G. Wertheim, Memoire sur l'Elasticité et la Cohesion des Principaux Tissus du Corps Humain, *Ann. Chim. Phys.*, 21: 385 (1847).

10 H. Cox, The Deflection of Imperfectly Elastic Beams and the Hyperbolic Law of Elasticity, *Trans. Cambridge Phil. Soc.*, 9(2): 177 (1851).

11 A. Imbert, *Recherches Theoriques et Experimentales sur l'Élasticite du Cautchouc*, p. 53, Lyon, 1880.

12 E. Hartig, Der Elastizitatsmodul des Geraden Stabes als Funktion der Spezifischen Beansprunchung, *Der Civilingenieur*, 39: 113 (1893).

13 W. Schule, Ueber das Gesetz der Elastischen Langenanderung Prismatischer Korper durch Zug und Druck, *Z. Ver. deut. Ing.*, 42: 855 (July 30, 1898).

14 W. Prager, On Isotropic Materials with Continuous Transition from Elastic to Plastic State, in *Proceedings of the Fifth International Congress for Applied Mechanics*, Cambridge, Mass., 1938, John Wiley & Sons, Inc., New York, 1939.

15 J. L. Holmquist and A. Nadai, A Theoretical and Experimental Approach to the Problem of Collapse of Deep Well Casing, *Drilling and Production Practice*, p. 392, 1939.

16 W. Ramberg and W. R. Osgood, Description of Stress–Strain Curves by Three Parameters, Report NACA TN 902, National Advisory Committee on Aeronautics, 1943.

17 F. Mazzolemi, Le Deformazioni Plastiche a Freddo e I Loro rudimenta dei Metalli, *Met. Ital.*, 33: 390 (1941).

18 E. Z. Stowell, A Study of the Energy Criterion for Fatigue, *Nucl. Eng. Des.*, 3: 32 (1966).

19 P. Ludwik, *Elemente der Technologischen Mechanik*, Julius Springer, Berlin, 1909.

20 J. R. Low, Jr., and F. Garofalo, Precision Determination of Stress–Strain Curves in the Plastic Range, *Proc. Soc. Exp. Stress Anal.*, 4(11): 16–24 (1947).

21 J. O. Brittain, Modern Applications of the Theories of Elasticity and Plasticity to Metals, edited from a talk given at symposium on Analytical Methods in the Study of Stress–Strain Behavior, Boston, Mass., Oct. 28, 1960, published by Instron Engineering Corp., Report No. M-5.

22 M. Cook and E. C. Larke, Resistance of Copper and Copper Alloys to Homogeneous Deformation in Compression, *J. Inst. Metals*, 71: 371 (1945).

23 J. B. Conway, Nuclear Systems Programs, General Electric Company, unpublished notes, 1968.

24 E. Voce, A Practical Strain Hardening Function, *Metallurgia*, 51: 219 (1955).

25 A. M. Halstead, J. M. McCaughey, and H. Markus, A New Look at Deformation in Copper and Alpha Brass, *Prod. Eng.*, 25: 181 (January 1954).

26 E. R. Marshall and M. C. Shaw, The Determination of Flow Stress from a Tensile Specimen, *Trans. Amer. Soc. Metals*, 44: 705 (1952).

27 J. H. Palm, Stress–Strain Relations for Uniaxial Loading, *Appl. Sci. Res. Sect. A*, 1: 198 (1948).

28 L. H. Sjodahl and J. B. Conway, Voce Equation Shown to be Identical to the Generalized Strain Concept, *Trans. Met. Soc. AIME*, 245: 1660 (1969).

29 J. T. Berling and T. Slot, Effect of Temperature and Strain Rate on Low Cycle Fatigue Resistance of AISI 304, 316, and 348 Stainless Steels, USAEC Report GEMP-642, General Electric Company, paper also presented at the ASTM Symposium on Fatigue at Elevated Temperatures, San Francisco, Calif., 1968, American Society for Testing and Materials, Special Technical Publication No. 459, 1970.

30 T. Slot and R. H. Stentz, Experimental Procedures for Low Cycle Fatigue Research at High Temperatures, *Exp. Mech.*, 8(3): 107 (1968).

31 *Physical and Mechanical Testing of Metals—Metallography, Nondestructive Testing, Fatigue, Effects of Temperature*, ASTM Standards, Part 31, 1968.

32 J. O. Stiegler and J. R. Weir, Jr., Effects of Irradiation on Ductility, USAEC Report ORNL-TM-2019, 1968, also in American Society for Metals Seminar on Ductility, Cleveland, Ohio, 1967.

Chapter 7

SHORT-TERM TENSILE DATA

A comprehensive summary of the results obtained in short-term tensile tests[1] of annealed AISI 304, 316, and 348 stainless steels tested in air at room temperature, 430, 650, and 816°C is presented in Tables 7.1 to 7.20. In this compilation, each tensile test is considered individually and measured, and calculated data are tabulated as a function of time. Extensometer measurements of the decrease in the minimum specimen diameter at selected time intervals are listed in column 2, followed by measured values of the applied load in column 3. Column 4 gives calculated values of the instantaneous diameter, and column 5 represents instantaneous values of the cross-sectional area of the specimen. Data listed in the remaining columns of Tables 7.1 to 7.20 are calculated results based on certain material characteristics and follow from the information contained in the first five columns. Procedures used in these compilations are illustrated below.

EXAMPLE CALCULATION

Reference point

Specimen 53-3, annealed 304 stainless steel at 430°C and a strain rate of 4×10^{-3} sec^{-1} after 10 sec of test (this case is underlined in Table 7.2).

Input data

Test temperature	$T = 430°C\ (806°F)$
Ambient temperature	$T_1 = 21°C\ (70°F)$
Modulus of elasticity	$E = 23.4 \times 10^6$ psi
Average coefficient of linear expansion	$\alpha = 18.0 \times 10^{-6}$ in. in.$^{-1}$ °C^{-1}
Poisson's ratio (elastic)	$\nu_e = 0.282$
Poisson's ratio (plastic)	$\nu_p = 0.5$
Initial specimen diameter	$D_i = 0.250$ in.
Measured diametral decrease	$\Delta D = 0.0050$ in.
Measured axial load	$P = 1788$ lb

Definition of additional symbols used

Initial cold cross-sectional area	A_i
Original hot diameter (diameter at temperature)	D_o
Original hot cross-sectional area	A_o
Instantaneous hot measured diameter	D
Instantaneous hot cross-sectional area	A
Instantaneous hot measured diameter at fracture	D_f
Instantaneous hot cross-sectional area at fracture	A_f
Measured cold diameter after fracture	D_f'
Cold cross-sectional area after fracture	A_f'
Engineering axial stress	σ_E
Axial true stress	σ
Engineering total axial strain	ϵ_E
Total axial true strain	ϵ
Elastic axial true strain	ϵ_e
Plastic axial true strain	ϵ_p
Total diametral true strain	ϵ_d
Elastic diametral true strain	ϵ_{de}
Plastic diametral true strain	ϵ_{dp}
Reduction in area (hot)	RA_h
Reduction in area (cold)	RA_c

Calculated data (rounded-off values)

Original hot diameter (D_o)

$$D_o = D_i + [D_i(T - T_1)\alpha]$$
$$= 0.250 + [0.250\,(430\text{-}21)\,18.0 \times 10^{-6}]$$
$$= 0.250 + 0.00184 = 0.25184 = 0.2518 \text{ in.}$$

Original hot cross-sectional area (A_o)

$$A_o = (\pi/4)(D_o)^2$$
$$= (\pi/4)(0.25184)^2 = 0.049813 = 0.04981 \text{ in.}^2$$

Instantaneous hot diameter (D)

$$D = D_o - \Delta D$$
$$= 0.25184 - 0.0050 = 0.24684 = 0.2468 \text{ in.}$$

Instantaneous hot cross-sectional area (A)

$$A = (\pi/4)(D)^2$$
$$= (\pi/4)(0.24684)^2 = 0.047854 = 0.04785 \text{ in.}^2$$

Engineering axial stress (σ_E)

$$\sigma_E = \frac{\text{measured axial load}}{\text{original hot cross-sectional area}} = \frac{P}{A_o}$$
$$= \frac{1788}{0.049813} = 35894.5 = 35{,}890 \text{ psi}$$

Axial true stress (σ)

$$\sigma = \frac{\text{measured axial load}}{\text{instantaneous hot cross-sectional area}} = \frac{P}{A}$$
$$= \frac{1788}{0.047854} = 37363.4 = 37{,}360 \text{ psi}$$

Elastic axial true strain (ϵ_e)

$$\epsilon_e = \frac{\text{axial true stress}}{\text{modulus of elasticity}} \quad \frac{\sigma}{E}$$
$$= \frac{37363.4}{23.4(10^6)} = 0.001596$$
$$= 0.0016 \text{ in./in.} \quad \text{(tensile strain)}$$

Plastic axial true strain (ϵ_p)

This axial strain component cannot be solved for directly from the input data available from the test measurements The plastic diametral true strain, ϵ_{dp}, must first be calculated and then converted into ϵ_p Various diametral-strain components must be calculated in order to do this

Total diametral true strain (ϵ_d)

$$\epsilon_d = \ln \frac{D}{D_o} - \ln \frac{0\ 24684}{0\ 25184}$$

$-0\ 020053$ in /in (minus sign indicates compressive strain)

Elastic diametral true strain (ϵ_{de})

ϵ_{de} = (elastic axial true strain x Poisson's ratio, elastic)

$= -\epsilon_e \nu_e$

$-0\ 001596\ (0\ 282)$

$-|-|0\ 000450$ in /in (minus sign indicates compressive strain)

Plastic diametral true strain (ϵ_{dp})

ϵ_{dp} = total diametral true strain–elastic diametral true strain

$= \epsilon_d - \epsilon_{de}$

$= -0\ 020053 - (-0\ 000450)$

$= -0\ 019603$ in /in (minus sign indicates compressive strain)

Plastic axial true strain (ϵ_p)

$$\epsilon_p = \frac{\text{plastic diametral true strain}}{\text{Poisson's ratio plastic}} = -\frac{\epsilon_{dp}}{\nu_p}$$

$$= -\frac{-0\ 019603}{0\ 5} = 0\ 039207$$

0 0392 in /in (tensile strain)

Total axial true strain (ϵ)

ϵ = elastic axial true strain + plastic axial true strain

$= \epsilon_e + \epsilon_p = 0\ 001596 + 0\ 039207 = 0\ 040803$

$= 0\ 0408$ in /in (tensile strain)

Engineering total axial strain (ϵ_L)

Since

$$\epsilon = \ln(1 + \epsilon_E)$$

$$1 + \epsilon_E = e^{\epsilon}$$

Then

$$\epsilon_E = e^{\epsilon} - 1 = e^{0\ 040803} - 1$$

$= 1\ 041647 - 1 = 0\ 041647$

$= 0\ 0416$ in /in (tensile strain)

Reduction in area hot (RA_h), %

$$RA_h = \frac{A_o - A_f}{A_o} \times 100 = \frac{\pi/4\,(D_o^2 - D_f^2)}{A_o} \times 100$$

$$\frac{\pi/4\,[D_o^2 - (D_o - \Delta D)^2\,]}{A_o} \times 100$$

$$\frac{\pi/4\,[(0\ 25184)^2 \quad (0\ 25184 - 0\ 0765)^2\,]}{0\ 049813}$$

$= 51\ 52$

$= 51\ 5\%$

Reduction in area cold (RA_c) %

$$RA_c \quad \frac{A_i \quad A_f'}{A_i} \times 100 = \frac{\pi/4\,[D_i^2 \quad (D_f')^2\,]}{\pi/4\,D_i^2} \times 100$$

$$= \frac{[D_i^2 - (D_i \quad \Delta D)^2\,]}{D_i^2} \times 100$$

$$\frac{[(0\ 250)^2 - (0\ 250 \quad 0\ 100)^2\,]}{(0\ 250)^2} \times 100$$

$= 64\ 00$

$= 64\ 0\%$

Values for the mean coefficients of linear thermal expansion used in the calculation of the results presented in Tables 7 2 to 7 7 and 7 9 to 7 20 were as follows [2]

Material	Temperature °C	Temperature °F	Mean coefficient of linear thermal expansion (α), 10^{-6} in in.$^{-1}$ °C^{-1}
304 S S	430	806	18 0
	650	1202	18 7
	816	1500	19 1
316 S S	430	806	18.0
	650	1202	19 1
	816	1500	19 1
348 S S.	430	806	17 55
	650	1202	18 63
	816	1500	18 9

Values for ultimate tensile strength, modulus of elasticity, tensile ductility, and Poisson's ratio obtained in the test program discussed previously are summarized in Table 7 21 The values for modulus of elasticity and Poisson's ratio were used in the calculations illustrated above Data for the yield strength, ultimate tensile strength, and reduction in area for 304, 316, and 348 stainless steels have been compared with data from the existing literature[3] to yield the results* shown in Table 7 22 In general, the latest data are within the range of previous data, exceptions to this are in some of the results at 650 and 816°C at the slow strain rate ($\dot{\epsilon}_t = 4 \times 10^{-5}$ sec^{-1}) In such cases the ultimate tensile strength values and the reduction in-area values are lower than the reported data range, however, these differences are probably due to strain rate effects Also included in Table 7 22 are data obtained in duplicate tests at some of the particular conditions, these data are annotated as supplemental tests In some cases these tests were performed to check the reproducibility of the data obtained in a given short term tensile test In a few cases, tests were rerun when it was felt that a certain experimental observation was questionable In such instances the test considered to be of lower quality is annotated as the supplemental test However, the stress–strain data tabulated in Tables 7 1 to 7 20 have not been presented for these supplemental tests

All General Electric Company, Nuclear Systems Program (GE–NSP)[1] data for yield strength, ultimate tensile strength, and reduction in area are shown in Figs 7 1 to 7 9 together with previously published[3] average data curves These graphs are presented to yield a visual comparison of the present data with published information In general, the agreement is quite good

(Text continues on page 212)

*See later section for a more detailed discussion

TABLE 7.1

STRESS–STRAIN DATA FOR FULLY ANNEALED AISI 304 STAINLESS STEEL TESTED IN AIR AT 21°C (70°F) AND AN AXIAL TRUE STRAIN RATE OF 4×10^{-3} sec^{-1}

(Specimen No. 56-4; Specimen diameter, 0.250 in.; Reduction in area measured at test temperature, 75.0%; Reduction in area calculated from posttest fracture diameter, 80.6%)

Time, sec	Measured diametral decrease, in.	Measured axial load, lb	Specimen diameter at test temp., in.	Specimen area at test temp., $in.^2$	Axial stress		Axial strain			
					Engineering, psi	True, psi	Engineering total strain	Elastic true strain	Plastic true strain	Total true strain
0	0	0	0.2500	0.04909						
2	0.0007	2200	0.2493	0.04881	44820	45070	0.0064	0.0016	0.0048	0.0063
3	0.0012	2270	0.2488	0.04862	46240	46690	0.0104	0.0016	0.0088	0.0104
4	0.0017	2330	0.2483	0.04842	47470	48120	0.0145	0.0017	0.0128	0.0144
5	0.0022	2380	0.2478	0.04823	48480	49350	0.0187	0.0017	0.0168	0.0185
6	0.0027	2410	0.2473	0.04803	49100	50170	0.0228	0.0017	0.0208	0.0225
7	0.0032	2450	0.2468	0.04784	49910	51210	0.0270	0.0018	0.0248	0.0266
8	0.0037	2500	0.2463	0.04765	50930	52470	0.0312	0.0018	0.0289	0.0307
9	0.0042	2540	0.2458	0.04745	51740	53530	0.0354	0.0019	0.0329	0.0348
12	0.0058	2660	0.2442	0.04684	54190	56790	0.0490	0.0020	0.0459	0.0479
15	0.0073	2750	0.2427	0.04626	56020	59440	0.0621	0.0021	0.0582	0.0602
18	0.0089	2850	0.2411	0.04565	58060	62430	0.0763	0.0022	0.0713	0.0735
21	0.0104	2940	0.2396	0.04509	59890	65210	0.0899	0.0023	0.0838	0.0861
27	0.0134	3080	0.2366	0.04397	62750	70050	0.1178	0.0024	0.1089	0.1113
33	0.0165	3250	0.2335	0.04282	66210	75900	0.1478	0.0026	0.1352	0.1378
39	0.0195	3380	0.2305	0.04173	68860	81000	0.1779	0.0028	0.1609	0.1638
45	0.0220	3500	0.2280	0.04083	71300	85730	0.2040	0.0030	0.1827	0.1856
60	0.0290	3750	0.2210	0.03836	76390	97760	0.2817	0.0034	0.2448	0.2482
75	0.0360	3970	0.2140	0.03597	80880	110400	0.3672	0.0038	0.3089	0.3128
90	0.0425	4140	0.2075	0.03382	84340	122400	0.4545	0.0043	0.3704	0.3747
110	0.0513	4270	0.1987	0.03101	86990	137700	0.5866	0.0048	0.4568	0.4616
130	0.0595	4350	0.1905	0.02850	88620	152600	0.7266	0.0053	0.5408	0.5461
150	0.0672	4370	0.1828	0.02624	89020	166500	0.8755	0.0058	0.6231	0.6289
180	0.0785	4330	0.1715	0.02310	88210	187400	1.132	0.0065	0.7503	0.7568
210	0.0895	4200	0.1605	0.02023	85560	207600	1.435	0.0072	0.8825	0.8897
240	0.1000	4000	0.1500	0.01767	81490	226400	1.788	0.0079	1.017	1.025
270	0.1095	3800	0.1405	0.01550	77410	245100	2.179	0.0085	1.148	1.157
300	0.1187	3450	0.1313	0.01354	70280	254800	2.641	0.0089	1.283	1.292
305	0.1202	3400	0.1298	0.01323	69260	256900	2.725	0.0090	1.306	1.315
310	0.1220	3300	0.1280	0.01287	67230	256500	2.831	0.0089	1.334	1.343
315	0.1233	3200	0.1267	0.01261	65190	253800	2.910	0.0088	1.355	1.363
321*	0.1250	2800	0.1250	0.01227	57040	228200	3.015	0.0079	1.382	1.390
				Based on Posttest Fracture-Diameter Dimension						
321	0.140	2800	0.1100	0.00950	57040	294600	4.190	0.0103	1.637	1.647

*Time at fracture.

TABLE 7.2

STRESS–STRAIN DATA FOR FULLY ANNEALED AISI 304 STAINLESS STEEL TESTED IN AIR AT 430°C (806°F) AND AN AXIAL TRUE STRAIN RATE OF 4×10^{-3} sec^{-1}

(Specimen No. 53-3; Specimen diameter, 0.250 in.; Reduction in area measured at test temperature, 51.5%; Reduction in area calculated from posttest fracture diameter, 64.0%)

Time, sec	Measured diametral decrease, in.	Measured axial load, lb	Specimen diameter at test temp., in.	Specimen area at test temp., $in.^2$	Axial stress		Axial strain			
					Engineering, psi	True, psi	Engineering total strain	Elastic true strain	Plastic true strain	Total true strain
0	0	0	0.2518	0.04981						
1	0.0005	400	0.2513	0.04962	8030	8060	0.0041	0.0003	0.0038	0.0041
2	0.0010	1200	0.2508	0.04942	24090	24280	0.0084	0.0010	0.0074	0.0084
3	0.0015	1388	0.2503	0.04922	27860	28200	0.0126	0.0012	0.0113	0.0125
4	0.0020	1480	0.2498	0.04902	29710	30190	0.0166	0.0013	0.0152	0.0165
5	0.0025	1536	0.2493	0.04883	30840	31460	0.0208	0.0013	0.0192	0.0205
6	0.0030	1560	0.2488	0.04863	31320	32080	0.0249	0.0014	0.0232	0.0246
7	0.0035	1648	0.2483	0.04844	33080	34020	0.0290	0.0015	0.0272	0.0286
8	0.0040	1688	0.2478	0.04824	33890	34990	0.0332	0.0015	0.0312	0.0327
10	0.0050	1788	0.2468	0.04785	35890	37360	0.0416	0.0016	0.0392	0.0408
20	0.0100	2232	0.2418	0.04594	44810	48590	0.0854	0.0021	0.0799	0.0819
30	0.0150	2532	0.2368	0.04406	50830	57470	0.1319	0.0025	0.1214	0.1239
50	0.0240	2920	0.2278	0.04077	58620	71620	0.2234	0.0031	0.1986	0.2016
70	0.0330	3080	0.2188	0.03761	61830	81890	0.3264	0.0035	0.2789	0.2824
85	0.0393	3108	0.2125	0.03548	62390	87600	0.4063	0.0037	0.3372	0.3410
100	0.0458	3088	0.2060	0.03334	61990	92620	0.4966	0.0040	0.3992	0.4032
120	0.0538	3012	0.1980	0.03080	60470	97780	0.6201	0.0042	0.4783	0.4825
140	0.0615	2908	0.1903	0.02845	58380	102200	0.7539	0.0044	0.5575	0.5619
160	0.0690	2728	0.1828	0.02626	54770	103900	0.9008	0.0044	0.6379	0.6423
165	0.0708	2668	0.1810	0.02574	53560	103600	0.9388	0.0044	0.6577	0.6621
170	0.0727	2600	0.1791	0.02520	52200	103200	0.9802	0.0044	0.6788	0.6832
175	0.0745	2500	0.1773	0.02470	50190	101200	1.020	0.0043	0.6990	0.7033
180	0.0765	2268	0.1753	0.02415	45530	93930	1.067	0.0040	0.7219	0.7259
181*	0.0765	2000	0.1753	0.02415	40150	82830	1.066	0.0035	0.7221	0.7257
				Based on Posttest Fracture-Diameter Dimensions						
181	0.100	2000	0.1518	0.01811	40150	110500	1.757	0.0047	1.009	1.014

*Time at fracture.

TABLE 7.3

STRESS–STRAIN DATA FOR FULLY ANNEALED AISI 304 STAINLESS STEEL TESTED IN AIR AT 430°C (806°F) AND AN AXIAL TRUE STRAIN RATE OF 4×10^{-5} sec^{-1}

(Specimen No. 53-6; Specimen diameter, 0.250 in.; Reduction in area measured at test temperature, 60.7%; Reduction in area calculated from posttest fracture diameter, 64.5%)

Time, min	Measured diametral decrease, in.	Measured axial load, lb	Specimen diameter at test temp., in.	Specimen area at test temp., $in.^2$	Axial stress		Axial strain			
					Engineering, psi	True, psi	Engineering total strain	Elastic true strain	Plastic true strain	Total true strain
0	0	0	0.2518	0.04981						
2	0.0002	1240	0.2516	0.04973	24890	24930	0.0021	0.0011	0.0010	0.0021
4	0.0006	1420	0.2512	0.04958	28510	28640	0.0053	0.0012	0.0041	0.0053
5	0.0008	1460	0.2510	0.04950	29310	29500	0.0069	0.0013	0.0057	0.0069
7	0.0014	1512	0.2504	0.04926	30350	30690	0.0118	0.0013	0.0104	0.0117
9	0.0020	1576	0.2498	0.04902	31640	32150	0.0167	0.0014	0.0152	0.0165
10	0.0023	1620	0.2495	0.04891	32520	33120	0.0191	0.0014	0.0176	0.0190
12	0.0029	1672	0.2489	0.04867	33570	34350	0.0241	0.0015	0.0223	0.0238
14	0.0035	1752	0.2483	0.04844	35170	36170	0.0291	0.0015	0.0271	0.0287
16	0.0042	1812	0.2476	0.04816	36380	37620	0.0349	0.0016	0.0327	0.0343
20	0.0052	1900	0.2466	0.04778	38140	39770	0.0434	0.0017	0.0408	0.0425
30	0.0083	2180	0.2435	0.04658	43760	46800	0.0703	0.0020	0.0659	0.0679
50	0.0142	2588	0.2376	0.04435	51950	58350	0.1243	0.0025	0.1147	0.1172
70	0.0200	2880	0.2318	0.04221	57820	68220	0.1815	0.0029	0.1638	0.1668
85	0.0240	3000	0.2278	0.04077	60230	73580	0.2234	0.0031	0.1985	0.2017
100	0.0280	3100	0.2238	0.03935	62230	78780	0.2677	0.0034	0.2338	0.2372
120	0.0333	3160	0.2185	0.03751	63440	84240	0.3301	0.0036	0.2816	0.2852
140	0.0386	3220	0.2132	0.03571	64640	90160	0.3971	0.0039	0.3306	0.3344
160	0.0434	3188	0.2084	0.03412	64000	93430	0.4623	0.0040	0.3760	0.3800
180	0.0484	3160	0.2034	0.03251	63440	97210	0.5352	0.0042	0.4245	0.4287
200	0.0532	3100	0.1986	0.03099	62230	100000	0.6104	0.0043	0.4722	0.4765
220	0.0580	3040	0.1938	0.02951	61030	103000	0.6912	0.0044	0.5210	0.5254
240	0.0625	2980	0.1893	0.02816	59820	105800	0.7726	0.0045	0.5679	0.5725
260	0.0670	2880	0.1848	0.02683	57820	107300	0.8601	0.0046	0.6160	0.6206
280	0.0715	2800	0.1803	0.02554	56210	109600	0.9541	0.0047	0.6653	0.6699
300	0.0760	2720	0.1758	0.02428	54600	112000	1.056	0.0048	0.7157	0.7205
320	0.0802	2640	0.1716	0.02314	53000	114100	1.157	0.0049	0.7640	0.7689
330	0.0824	2600	0.1694	0.02255	52200	115300	1.214	0.0049	0.7898	0.7947
340	0.0844	2548	0.1674	0.02202	51150	115700	1.267	0.0049	0.8135	0.8185
350	0.0864	2500	0.1654	0.02150	50190	116300	1.322	0.0050	0.8376	0.8425
360	0.0885	2360	0.1633	0.02095	47380	112600	1.382	0.0048	0.8632	0.8680
370	0.0905	2148	0.1613	0.02044	43120	105100	1.441	0.0045	0.8880	0.8925
380	0.0925	1880	0.1593	0.01994	37740	94280	1.502	0.0040	0.9132	0.9173
385	0.0935	1520	0.1583	0.01969	30510	77190	1.533	0.0033	0.9262	0.9295
388*	0.0940	1220	0.1578	0.01957	24490	62350	1.549	0.0027	0.9329	0.9356
				Based on Posttest Fracture-Diameter Dimension						
388	0.101	1220	0.1508	0.01787	24490	68270	1.791	0.0029	1.624	1.026

*Time at fracture.

TABLE 7.4

STRESS–STRAIN DATA FOR FULLY ANNEALED AISI 304 STAINLESS STEEL TESTED IN AIR AT 650°C (1200°F) AND AN AXIAL TRUE STRAIN RATE OF 4×10^{-3} sec^{-1}

(Specimen No. 53-1; Specimen diameter, 0.250 in.; Reduction in area measured at test temperature, 42.6%; Reduction in area calculated from posttest fracture diameter, 42.2%)

Time, sec	Measured diametral decrease, in.	Measured axial load, lb	Specimen diameter at test temp., in.^{2}	Specimen area at test temp., in.^{2}	Axial stress		Axial strain			
					Engineering, psi	True, psi	Engineering total strain	Elastic true strain	Plastic true strain	Total true strain
0	0	0	0.2529	0.05025						
2	0.0008	1000	0.2521	0.04993	19900	20030	0.0067	0.0009	0.0058	0.0067
3	0.0013	1132	0.2516	0.04973	22530	22760	0.0108	0.0011	0.0096	0.0107
4	0.0017	1208	0.2512	0.04958	24040	24370	0.0140	0.0011	0.0128	0.0139
5	0.0022	1260	0.2507	0.04938	25070	25520	0.0181	0.0012	0.0167	0.0179
6	0.0027	1300	0.2502	0.04918	25870	26430	0.0222	0.0012	0.0207	0.0219
7	0.0032	1368	0.2497	0.04899	27220	27930	0.0263	0.0013	0.0246	0.0259
8	0.0037	1420	0.2492	0.04879	28260	29100	0.0304	0.0013	0.0286	0.0300
9	0.0042	1480	0.2487	0.04860	29450	30460	0.0346	0.0014	0.0326	0.0340
10	0.0047	1520	0.2482	0.04840	30250	31410	0.0388	0.0015	0.0366	0.0381
20	0.0100	1860	0.2429	0.04636	37010	40120	0.0848	0.0019	0.0795	0.0814
30	0.0146	2080	0.2383	0.04462	41390	46620	0.1272	0.0022	0.1175	0.1197
50	0.0240	2248	0.2289	0.04117	44740	54610	0.2218	0.0025	0.1978	0.2003
70	0.0327	2292	0.2202	0.03810	45610	60160	0.3203	0.0028	0.2751	0.2779
85	0.0390	2280	0.2139	0.03595	45370	63420	0.3993	0.0029	0.3331	0.3360
100	0.0453	2240	0.2076	0.03386	44580	66150	0.4856	0.0031	0.3928	0.3958
110	0.0495	2180	0.2034	0.03251	43380	67060	0.5476	0.0031	0.4336	0.4367
120	0.0533	2120	0.1996	0.03130	42190	67720	0.6071	0.0031	0.4713	0.4744
125	0.0553	2068	0.1976	0.03068	41150	67410	0.6398	0.0031	0.4914	0.4946
130	0.0573	1992	0.1956	0.03006	39640	66260	0.6734	0.0031	0.5118	0.5149
135	0.0593	1720	0.1936	0.02945	34230	58400	0.7080	0.0027	0.5326	0.5353
140	0.0610	920	0.1919	0.02894	18310	31790	0.7375	0.0015	0.5510	0.5525
141*	0.0613	840	0.1916	0.02885	16720	29120	0.7429	0.0013	0.5542	0.5556
				Based on Posttest Fracture-Diameter Dimension						
141	0.060	840	0.1929	0.02924	16720	28730	0.7195	0.0013	0.5407	0.5420

*Time at fracture.

TABLE 7.5

STRESS–STRAIN DATA FOR FULLY ANNEALED AISI 304 STAINLESS STEEL TESTED IN AIR AT 650°C (1200°F) AND AN AXIAL TRUE STRAIN RATE OF 4×10^{-5} sec^{-1}

(Specimen No. 53-4; Specimen diameter, 0.250 in.; Reduction in area measured at test temperature, 31.6%; Reduction in area calculated from posttest fracture diameter, 33.4%)

Time, min	Measured diametral decrease, in.	Measured axial load, lb	Specimen diameter at test temp., in.	Specimen area at test temp., $in.^2$	Axial stress		Axial strain			
					Engineering, psi	True, psi	Engineering total strain	Elastic true strain	Plastic true strain	Total true strain
0	0	0	0.2529	0.05025						
5	0.0005	1080	0.2524	0.05005	21490	21580	0.0043	0.0010	0.0033	0.0043
7	0.0010	1160	0.2519	0.04985	23080	23270	0.0084	0.0011	0.0072	0.0083
9	0.0015	1228	0.2514	0.04966	24440	24730	0.0124	0.0011	0.0112	0.0123
10	0.0018	1260	0.2511	0.04954	25070	25440	0.0148	0.0012	0.0135	0.0147
12	0.0023	1320	0.2506	0.04934	26270	26750	0.0189	0.0012	0.0175	0.0187
14	0.0029	1388	0.2500	0.04910	27620	28270	0.0238	0.0013	0.0222	0.0235
16	0.0035	1440	0.2494	0.04887	28660	29470	0.0288	0.0014	0.0270	0.0284
18	0.0041	1492	0.2488	0.04863	29690	30680	0.0338	0.0014	0.0318	0.0332
20	0.0047	1528	0.2482	0.04840	30410	31570	0.0388	0.0015	0.0366	0.0381
30	0.0080	1600	0.2449	0.04712	31840	33950	0.0670	0.0016	0.0633	0.0649
50	0.0140	1780	0.2389	0.04484	35420	39700	0.1214	0.0018	0.1127	0.1146
70	0.0197	1760	0.2332	0.04273	35020	41190	0.1769	0.0019	0.1610	0.1629
85	0.0237	1760	0.2292	0.04127	35020	42640	0.2183	0.0020	0.1955	0.1975
100	0.0280	1728	0.2249	0.03974	34390	43480	0.2654	0.0020	0.2334	0.2354
120	0.0330	1660	0.2199	0.03799	33030	43690	0.3236	0.0020	0.2783	0.2803
130	0.0357	1620	0.2172	0.03707	32240	43710	0.3567	0.0020	0.3030	0.3050
140	0.0380	1560	0.2149	0.03629	31040	42990	0.3859	0.0020	0.3243	0.3263
150	0.0407	1500	0.2122	0.03538	29850	42400	0.4213	0.0020	0.3496	0.3516
155	0.0420	1432	0.2109	0.03495	28500	40980	0.4389	0.0019	0.3620	0.3639
160	0.0432	1180	0.2097	0.03455	23480	34150	0.4552	0.0016	0.3736	0.3751
161*	0.0438	1000	0.2091	0.03435	19900	29110	0.4634	0.0013	0.3794	0.3808
				Based on Posttest Fracture-Diameter Dimension						
161	0.046	1000	0.2069	0.03364	19900	29730	0.4947	0.0014	0.4006	0.4020

*Time at fracture.

TABLE 7.6

STRESS–STRAIN DATA FOR FULLY ANNEALED AISI 304 STAINLESS STEEL TESTED IN AIR AT 816°C (1500°F) AND AN AXIAL TRUE STRAIN RATE OF 4×10^{-3} sec^{-1}

(Specimen No. 53-2; Specimen diameter, 0.250 in.; Reduction in area measured at test temperature, 50.4%; Reduction in area calculated from posttest fracture diameter, 51.0%)

Time, sec	Measured diametral decrease, in.	Measured axial load, lb	Specimen diameter at test temp., in.	Specimen area at test temp., $in.^2$	Axial stress		Axial strain			
					Engineering, psi	True, psi	Engineering total strain	Elastic true strain	Plastic true strain	Total true strain
0	0	0	0.2538	0.05059						
2	0.0008	840	0.2530	0.05027	16610	16710	0.0067	0.0009	0.0057	0.0066
3	0.0014	920	0.2524	0.05003	18190	18390	0.0115	0.0010	0.0104	0.0114
4	0.0019	964	0.2519	0.04983	19060	19340	0.0155	0.0010	0.0144	0.0154
5	0.0023	1004	0.2515	0.04967	19850	20210	0.0188	0.0011	0.0175	0.0186
6	0.0028	1032	0.2510	0.04948	20400	20860	0.0228	0.0011	0.0215	0.0226
7	0.0032	1064	0.2506	0.04932	21030	21570	0.0261	0.0011	0.0246	0.0258
8	0.0037	1084	0.2501	0.04912	21430	22070	0.0302	0.0012	0.0286	0.0298
9	0.0042	1108	0.2496	0.04893	21900	22650	0.0344	0.0012	0.0326	0.0338
10	0.0046	1128	0.2492	0.04877	22300	23130	0.0377	0.0012	0.0358	0.0370
20	0.0095	1212	0.2443	0.04687	23960	25860	0.0798	0.0014	0.0754	0.0768
30	0.0145	1252	0.2393	0.04497	24750	27840	0.1255	0.0015	0.1167	0.1182
50	0.0240	1264	0.2298	0.04147	24990	30480	0.2205	0.0016	0.1976	0.1993
70	0.0330	1236	0.2208	0.03829	24430	32280	0.3221	0.0017	0.2775	0.2792
85	0.0390	1192	0.2148	0.03623	23560	32900	0.3970	0.0017	0.3326	0.3343
100	0.0452	1144	0.2086	0.03417	22610	33480	0.4813	0.0018	0.3911	0.3929
120	0.0535	1060	0.2003	0.03151	20950	33640	0.6066	0.0018	0.4723	0.4741
135	0.0590	992	0.1948	0.02980	19610	33290	0.6986	0.0018	0.5280	0.5298
155	0.0668	872	0.1870	0.02746	17240	31750	0.8432	0.0017	0.6098	0.6115
160	0.0688	820	0.1850	0.02688	16210	30510	0.8832	0.0016	0.6314	0.6330
165	0.0705	748	0.1833	0.02639	14790	28350	0.9182	0.0015	0.6499	0.6514
170	0.0725	540	0.1813	0.02581	10670	20920	0.9605	0.0011	0.6721	0.6732
175	0.0740	272	0.1798	0.02539	5380	10710	0.9930	0.0006	0.6891	0.6896
177*	0.0750	100	0.1788	0.02511	1980	3980	1.015	0.0002	0.7005	0.7007
				Based on Posttest Fracture-Diameter Dimension						
177	0.075	100	0.1788	0.02511	1980	3980	1.015	0.0002	0.7005	0.7007

*Time at fracture.

TABLE 7.7

STRESS–STRAIN DATA FOR FULLY ANNEALED AISI 304 STAINLESS STEEL TESTED IN AIR AT 816°C (1500°F) AND AN AXIAL TRUE STRAIN RATE OF 4×10^{-5} sec^{-1}

(Specimen No. 53-5; Specimen diameter, 0.250 in.; Reduction in area measured at test temperature, 26.8%; Reduction in area calculated from posttest fracture diameter, 32.1%)

Time, min	Measured diametral decrease, in.	Measured axial load, lb	Specimen diameter at test temp., in.	Specimen area at test temp., $in.^2$	Axial stress		Axial strain			
					Engineering, psi	True, psi	Engineering total strain	Elastic true strain	Plastic true strain	Total true strain
0	0	0	0.2538	0.05059						
2	0.0006	600	0.2532	0.05035	11860	11920	0.0050	0.0006	0.0043	0.0050
4	0.0012	632	0.2526	0.05011	12490	12610	0.0098	0.0007	0.0090	0.0097
6	0.0018	640	0.2520	0.04987	12650	12830	0.0146	0.0007	0.0138	0.0145
8	0.0024	644	0.2514	0.04963	12730	12970	0.0194	0.0007	0.0186	0.0192
10	0.0029	648	0.2509	0.04944	12810	13110	0.0235	0.0007	0.0225	0.0232
12	0.0035	652	0.2503	0.04920	12890	13250	0.0284	0.0007	0.0273	0.0280
14	0.0041	660	0.2497	0.04897	13050	13480	0.0334	0.0007	0.0321	0.0328
20	0.0060	680	0.2478	0.04822	13440	14100	0.0493	0.0008	0.0474	0.0481
30	0.0090	680	0.2448	0.04706	13440	14450	0.0752	0.0008	0.0717	0.0725
50	0.0150	680	0.2388	0.04478	13440	15180	0.1299	0.0008	0.1213	0.1221
70	0.0207	660	0.2331	0.04267	13050	15470	0.1858	0.0008	0.1696	0.1705
85	0.0247	640	0.2291	0.04122	12650	15530	0.2276	0.0008	0.2043	0.2051
100	0.0287	632	0.2251	0.03979	12490	15880	0.2716	0.0008	0.2395	0.2403
110	0.0313	608	0.2225	0.03888	12020	15640	0.3015	0.0008	0.2627	0.2635
120	0.0340	572	0.2198	0.03794	11310	15080	0.3337	0.0008	0.2872	0.2880
130*	0.0367	520	0.2171	0.03701	10280	14050	0.3671	0.0007	0.3119	0.3127
				Based on Posttest Fracture-Diameter Dimension						
130	0.044	480	0.2098	0.03457	9490	13890	0.4638	0.0007	0.3803	0.3811

*Time at fracture.

TABLE 7.8

STRESS–STRAIN DATA FOR FULLY ANNEALED AISI 316 STAINLESS STEEL TESTED IN AIR AT 21°C (70°F) AND AN AXIAL TRUE STRAIN RATE OF 4×10^{-3} sec^{-1}

(Specimen No. 9-4; Specimen diameter, 0.250 in.; Reduction in area measured at test temperature, 71.1%; Reduction in area calculated from posttest fracture diameter, 74.6%)

Time, sec	Measured diametral decrease, in.	Measured axial load, lb	Specimen diameter at test temp., in.	Specimen area at test temp., $in.^2$	Axial stress		Axial strain			
					Engineering, psi	True, psi	Engineering total strain	Elastic true strain	Plastic true strain	Total true strain
0	0	0	0.2500	0.04909						
2	0.0005	2030	0.2495	0.04889	41350	41520	0.0046	0.0014	0.0032	0.0046
3	0.0010	2100	0.2490	0.04870	42780	43130	0.0086	0.0014	0.0072	0.0086
4	0.0015	2150	0.2485	0.04850	43800	44330	0.0127	0.0015	0.0112	0.0126
5	0.0020	2200	0.2480	0.04831	44820	45540	0.0168	0.0015	0.0152	0.0167
6	0.0025	2250	0.2475	0.04811	45840	46770	0.0210	0.0016	0.0192	0.0207
7	0.0030	2300	0.2470	0.04792	46860	48000	0.0251	0.0016	0.0232	0.0248
8	0.0035	2350	0.2465	0.04772	47870	49240	0.0293	0.0016	0.0272	0.0289
9	0.0040	2400	0.2460	0.04753	48890	50500	0.0335	0.0017	0.0313	0.0329
12	0.0055	2550	0.2445	0.04695	51950	54310	0.0463	0.0018	0.0434	0.0452
15	0.0070	2700	0.2430	0.04638	55000	58220	0.0593	0.0019	0.0557	0.0576
18	0.0085	2830	0.2415	0.04581	57650	61780	0.0725	0.0021	0.0680	0.0700
21	0.0100	2970	0.2400	0.04524	60500	65650	0.0860	0.0022	0.0804	0.0825
27	0.0130	3170	0.2370	0.04412	64580	71860	0.1138	0.0024	0.1054	0.1078
33	0.0160	3400	0.2340	0.04301	69260	79060	0.1427	0.0026	0.1307	0.1334
39	0.0185	3600	0.2315	0.04209	73340	85530	0.1676	0.0028	0.1521	0.1549
45	0.0215	3750	0.2285	0.04101	76390	91450	0.1985	0.0030	0.1781	0.1811
60	0.0285	4000	0.2215	0.03853	81490	103800	0.2757	0.0034	0.2400	0.2435
75	0.0350	4200	0.2150	0.03631	85560	115700	0.3542	0.0038	0.2994	0.3032
90	0.0420	4300	0.2080	0.03398	87600	126500	0.4471	0.0042	0.3654	0.3696
110	0.0507	4370	0.1993	0.03120	89020	140100	0.5765	0.0047	0.4506	0.4552
130	0.0587	4420	0.1913	0.02874	90040	153800	0.7114	0.0051	0.5322	0.5373
150	0.0665	4420	0.1835	0.02645	90040	167100	0.8604	0.0056	0.6152	0.6208
180	0.0780	4300	0.1720	0.02324	87600	185100	1.118	0.0061	0.7443	0.7505
210	0.0890	4130	0.1610	0.02036	84140	202900	1.418	0.0067	0.8761	0.8829
230	0.0960	3900	0.1540	0.01863	79450	209400	1.643	0.0070	0.9649	0.9719
300	0.1125	3100	0.1375	0.01485	63150	208800	2.315	0.0069	1.192	1.199
305	0.1135	3050	0.1365	0.01463	62130	208400	2.364	0.0069	1.206	1.213
310	0.1145	3000	0.1355	0.01442	61120	208000	2.414	0.0069	1.221	1.228
316*	0.1155	2900	0.1345	0.01421	59080	204100	2.465	0.0068	1.236	1.243
				Based on Posttest Fracture-Diameter Dimension						
316	0.124	2900	0.1260	0.01247	59080	232600	2.949	0.0077	1.366	1.374

*Time at fracture.

TABLE 7.9

STRESS–STRAIN DATA FOR FULLY ANNEALED AISI 316 STAINLESS STEEL TESTED IN AIR AT 430°C (806°F) AND AN AXIAL TRUE STRAIN RATE OF 4×10^{-3} sec^{-1}

(Specimen No. 9-6; Specimen diameter, 0.250 in.; Reduction in area measured at test temperature, 47.8%; Reduction in area calculated from posttest fracture diameter, 62.1%)

Time, sec	Measured diametral decrease, in.	Measured axial load, lb	Specimen diameter at test temp., in.	Specimen area at test temp., $in.^2$	Axial stress		Axial strain			
					Engineering, psi	True, psi	Engineering total strain	Elastic true strain	Plastic true strain	Total true strain
0	0	0	0.2518	0.04979						
1	0.0005	1000	0.2513	0.04960	20080	20160	0.0043	0.0008	0.0034	0.0043
2	0.0010	1080	0.2508	0.04940	21690	21860	0.0083	0.0009	0.0074	0.0083
3	0.0015	1160	0.2503	0.04920	23300	23580	0.0124	0.0010	0.0113	0.0123
4	0.0020	1260	0.2498	0.04901	25300	25710	0.0165	0.0011	0.0153	0.0163
5	0.0026	1300	0.2492	0.04877	26110	26650	0.0214	0.0011	0.0201	0.0212
6	0.0031	1360	0.2487	0.04858	27310	28000	0.0255	0.0012	0.0240	0.0252
7	0.0036	1440	0.2482	0.04838	28920	29760	0.0297	0.0012	0.0280	0.0293
8	0.0041	1490	0.2477	0.04819	29920	30920	0.0339	0.0013	0.0320	0.0333
9	0.0046	1560	0.2472	0.04799	31330	32510	0.0381	0.0014	0.0360	0.0374
11	0.0057	1680	0.2461	0.04757	33740	35320	0.0474	0.0015	0.0449	0.0463
13	0.0065	1820	0.2453	0.04726	36550	38510	0.0543	0.0016	0.0513	0.0529
15	0.0075	1950	0.2443	0.04687	39160	41600	0.0630	0.0017	0.0594	0.0611
17	0.0087	2080	0.2431	0.04641	41770	44820	0.0736	0.0019	0.0691	0.0710
19	0.0097	2200	0.2421	0.04603	44180	47790	0.0825	0.0020	0.0773	0.0793
21	0.0107	2300	0.2411	0.04565	46190	50380	0.0916	0.0021	0.0855	0.0876
23	0.0118	2400	0.2400	0.04524	48200	53050	0.1017	0.0022	0.0946	0.0968
25	0.0127	2480	0.2391	0.04490	49800	55240	0.1100	0.0023	0.1021	0.1044
27	0.0135	2560	0.2383	0.04460	51410	57400	0.1175	0.0024	0.1087	0.1111
29	0.0145	2640	0.2373	0.04422	53020	59700	0.1270	0.0025	0.1171	0.1195
31	0.0154	2710	0.2364	0.04389	54420	61750	0.1356	0.0026	0.1246	0.1272
33	0.0163	2780	0.2355	0.04356	55830	63830	0.1443	0.0027	0.1322	0.1348
43	0.0210	3050	0.2308	0.04183	61250	72910	0.1916	0.0030	0.1723	0.1753
53	0.0257	3220	0.2261	0.04015	64670	80200	0.2418	0.0033	0.2132	0.2166
73	0.0345	3370	0.2173	0.03708	67680	90880	0.3446	0.0038	0.2923	0.2961
93	0.0428	3360	0.2090	0.03431	67480	97940	0.4537	0.0041	0.3700	0.3741
113	0.0512	3270	0.2006	0.03160	65670	103500	0.5781	0.0043	0.4519	0.4563
133	0.0590	3100	0.1928	0.02919	62260	106200	0.7085	0.0044	0.5312	0.5356
137	0.0605	3060	0.1913	0.02874	61450	106500	0.7354	0.0044	0.5468	0.5512
141	0.0621	3000	0.1897	0.02826	60250	106200	0.7648	0.0044	0.5636	0.5680
145	0.0637	2960	0.1881	0.02779	59440	106500	0.7950	0.0044	0.5805	0.5850
149	0.0650	2900	0.1868	0.02740	58240	105800	0.8200	0.0044	0.5944	0.5988
153	0.0666	2840	0.1852	0.02694	57030	105400	0.8516	0.0044	0.6116	0.6160
159	0.0688	2700	0.1830	0.02630	54220	102700	0.8963	0.0043	0.6356	0.6399
162*	0.0698	2600	0.1820	0.02601	52210	99950	0.9171	0.0042	0.6467	0.6508
				Based on Posttest Fracture-Diameter Dimension						
162	0.096	2600	0.1558	0.01906	52210	136400	1.618	0.0057	0.9566	0.9623

*Time at fracture.

TABLE 7.10

STRESS–STRAIN DATA FOR FULLY ANNEALED AISI 316 STAINLESS STEEL TESTED IN AIR AT 430°C (806°F) AND AN AXIAL TRUE STRAIN RATE OF 4×10^{-5} sec^{-1}

(Specimen No. 9-7; Specimen diameter, 0.250 in.; Reduction in area measured at test temperature, 57.8%; Reduction in area calculated from posttest fracture diameter, 60.6%)

Time, min	Measured diametral decrease, in.	Measured axial load, lb	Specimen diameter at test temp., in.	Specimen area at test temp., $in.^2$	Axial stress		Axial strain			
					Engineering, psi	True, psi	Engineering total strain	Elastic true strain	Plastic true strain	Total true strain
0	0	0	0.2518	0.04979						
4	0.0006	1100	0.2512	0.04956	22090	22200	0.0051	0.0009	0.0042	0.0051
6	0.0009	1180	0.2509	0.04944	23700	23870	0.0076	0.0010	0.0065	0.0075
8	0.0014	1260	0.2504	0.04924	25300	25590	0.0116	0.0011	0.0105	0.0115
10	0.0021	1300	0.2497	0.04897	26110	26550	0.0173	0.0011	0.0161	0.0172
12	0.0026	1360	0.2492	0.04877	27310	27890	0.0214	0.0012	0.0200	0.0212
14	0.0033	1420	0.2485	0.04850	28520	29280	0.0272	0.0012	0.0256	0.0268
16	0.0040	1500	0.2478	0.04822	30120	31100	0.0330	0.0013	0.0312	0.0325
20	0.0051	1630	0.2467	0.04780	32730	34100	0.0423	0.0014	0.0400	0.0415
24	0.0063	1750	0.2455	0.04733	35140	36970	0.0526	0.0015	0.0497	0.0512
30	0.0082	1920	0.2436	0.04660	38560	41200	0.0691	0.0017	0.0651	0.0669
40	0.0110	2260	0.2408	0.04554	45390	49630	0.0943	0.0021	0.0880	0.0901
50	0.0140	2510	0.2378	0.04441	50410	56520	0.1222	0.0024	0.1129	0.1153
60	0.0167	2760	0.2351	0.04341	55430	63580	0.1482	0.0026	0.1356	0.1382
70	0.0196	2930	0.2322	0.04234	58840	69200	0.1772	0.0029	0.1603	0.1631
90	0.0250	3240	0.2268	0.04040	65070	80200	0.2341	0.0033	0.2070	0.2104
110	0.0304	3480	0.2214	0.03850	69890	90400	0.2953	0.0038	0.2550	0.2587
130	0.0355	3600	0.2163	0.03674	72300	97980	0.3572	0.0041	0.3014	0.3055
150	0.0404	3660	0.2114	0.03510	73500	104300	0.4210	0.0043	0.3470	0.3514
180	0.0480	3680	0.2038	0.03262	73900	112800	0.5292	0.0047	0.4200	0.4247
210	0.0552	3600	0.1966	0.03036	72300	118600	0.6434	0.0049	0.4918	0.4968
240	0.0620	3520	0.1898	0.02829	70690	124400	0.7634	0.0052	0.5621	0.5673
270	0.0688	3350	0.1830	0.02630	67280	127400	0.8970	0.0053	0.6350	0.6403
300	0.0754	3160	0.1764	0.02444	63460	129300	1.042	0.0054	0.7084	0.7138
320	0.0796	3040	0.1722	0.02329	61050	130500	1.143	0.0054	0.7566	0.7620
340	0.0838	2960	0.1680	0.02217	59440	133500	1.251	0.0056	0.8059	0.8114
350	0.0858	2900	0.1660	0.02164	58240	134000	1.306	0.0056	0.8298	0.8354
360	0.0878	2480	0.1640	0.02112	49800	117400	1.362	0.0049	0.8545	0.8594
362*	0.0883	2280	0.1635	0.02099	45790	108600	1.376	0.0045	0.8608	0.8653
				Based on Posttest Fracture-Diameter Dimension						
362	0.093	2280	0.1588	0.01980	45790	115100	1.519	0.0048	0.9190	0.9238

*Time at fracture.

TABLE 7.11

STRESS–STRAIN DATA FOR FULLY ANNEALED AISI 316 STAINLESS STEEL TESTED IN AIR AT 650°C (1200°F) AND AN AXIAL TRUE STRAIN RATE OF 4×10^{-3} sec^{-1}

(Specimen No. 19-4; Specimen diameter, 0.250 in.; Reduction in area measured at test temperature, 60.0%; Reduction in area calculated from posttest fracture diameter, 61.1%)

Time, sec	Measured diametral decrease, in.	Measured axial load, lb	Specimen diameter at test temp., in.	Specimen area at test temp., $in.^2$	Axial stress		Axial strain			
					Engineering, psi	True, psi	Engineering total strain	Elastic true strain	Plastic true strain	Total true strain
0	0	0	0.2529	0.05024						
1	0.0005	800	0.2524	0.05005	15920	15990	0.0042	0.0007	0.0035	0.0042
2	0.0011	900	0.2518	0.04981	17910	18070	0.0090	0.0008	0.0082	0.0090
3	0.0017	970	0.2512	0.04957	19310	19570	0.0139	0.0009	0.0129	0.0138
4	0.0022	1050	0.2507	0.04937	20900	21270	0.0180	0.0010	0.0168	0.0178
5	0.0028	1100	0.2501	0.04914	21890	22390	0.0229	0.0010	0.0216	0.0226
6	0.0033	1170	0.2496	0.04894	23290	23910	0.0270	0.0011	0.0256	0.0266
7	0.0039	1230	0.2490	0.04871	24480	25250	0.0320	0.0012	0.0303	0.0315
8	0.0044	1300	0.2485	0.04851	25870	26800	0.0362	0.0012	0.0343	0.0355
9	0.0050	1370	0.2479	0.04828	27270	28380	0.0412	0.0013	0.0391	0.0404
12	0.0067	1550	0.2462	0.04762	30850	32550	0.0557	0l0015	0.0527	0.0542
15	0.0083	1700	0.2446	0.04700	33830	36170	0.0696	0.0016	0.0657	0.0673
18	0.0100	1870	0.2429	0.04635	37220	40350	0.0847	0.0018	0.0795	0.0813
21	0.0115	2000	0.2414	0.04578	39810	43690	0.0983	0.0020	0.0918	0.0938
27	0.0145	2250	0.2384	0.04465	44780	50390	0.1262	0.0023	0.1166	0.1189
33	0.0175	2400	0.2354	0.04353	47770	55130	0.1552	0.0025	0.1418	0.1443
39	0.0205	2500	0.2324	0.04243	49760	58920	0.1853	0.0027	0.1673	0.1700
45	0.0235	2600	0.2294	0.04134	51750	62890	0.2166	0.0029	0.1932	0.1960
60	0.0305	2720	0.2224	0.03886	54140	70000	0.2945	0.0032	0.2549	0.2581
75	0.0375	2750	0.2154	0.03645	54730	75450	0.3801	0.0034	0.3187	0.3222
90	0.0445	2720	0.2084	0.03412	54140	79720	0.4744	0.0036	0.3847	0.3883
105	0.0510	2670	0.2019	0.03202	53140	83370	0.5710	0.0038	0.4479	0.4517
120	0.0573	2600	0.1956	0.03006	51750	86500	0.6739	0.0039	0.5112	0.5151
135	0.0633	2530	0.1896	0.02824	50350	89580	0.7816	0.0041	0.5734	0.5775
150	0.0695	2430	0.1834	0.02643	48360	91960	0.9041	0.0042	0.6398	0.6440
165	0.0753	2330	0.1776	0.02478	46370	94020	1.031	0.0043	0.7040	0.7083
180	0.0810	2200	0.1719	0.02322	43790	94760	1.167	0.0043	0.7692	0.7736
192	0.0855	2080	0.1674	0.02202	41400	94470	1.286	0.0043	0.8223	0.8266
198	0.0877	2020	0.1652	0.02144	40200	94210	1.347	0.0043	0.8488	0.8530
204	0.0900	1700	0.1629	0.02085	33830	81540	1.413	0.0037	0.8772	0.8809
207	0.0908	1500	0.1621	0.02064	29850	72660	1.437	0.0033	0.8873	0.8906
210	0.0920	1300	0.1609	0.02034	25870	63910	1.473	0.0029	0.9024	0.9053
213*	0.0930	900	0.1599	0.02009	17910	44800	1.503	0.0020	0.9154	0.9175
				Based on Posttest Fracture-Diameter Dimension						
213	0.094	900	0.1589	0.01984	17910	45370	1.535	0.0021	0.9280	0.9300

*Time at fracture.

TABLE 7.12

STRESS–STRAIN DATA FOR FULLY ANNEALED AISI 316 STAINLESS STEEL TESTED IN AIR AT 650°C (1200°F) AND AN AXIAL TRUE STRAIN RATE OF 4×10^{-5} sec^{-1}

(Specimen No. 7-26; Specimen diameter, 0.250 in.; Reduction in area measured at test temperature, 32.2%; Reduction in area calculated from posttest fracture diameter, 32.1%)

Time, min	Measured diametral decrease, in.	Measured axial load, lb	Specimen diameter at test temp., in.	Specimen area at test temp., $in.^2$	Axial stress		Axial strain			
					Engineering, psi	True, psi	Engineering total strain	Elastic true strain	Plastic true strain	Total true strain
0	0	0	0.2529	0.05024						
2	0.0006	1000	0.2523	0.05001	19000	20000	0.0051	0.0009	0.0042	0.0051
4	0.0012	1115	0.2517	0.04977	22190	22400	0.0099	0.0010	0.0088	0.0099
6	0.0018	1200	0.2511	0.04953	23880	24230	0.0148	0.0011	0.0136	0.0147
8	0.0025	1285	0.2504	0.04926	25580	26090	0.0205	0.0012	0.0191	0.0203
10	0.0031	1375	0.2498	0.04902	27370	28050	0.0254	0.0013	0.0238	0.0251
12	0.0037	1450	0.2492	0.04879	28860	29720	0.0304	0.0014	0.0286	0.0299
15	0.0046	1550	0.2483	0.04843	30850	32000	0.0379	0.0015	0.0358	0.0372
18	0.0056	1615	0.2473	0.04804	32140	33610	0.0464	0.0015	0.0438	0.0453
21	0.0065	1715	0.2464	0.04770	34130	35960	0.0540	0.0016	0.0510	0.0526
24	0.0073	1775	0.2456	0.04739	35330	37460	0.0610	0.0017	0.0575	0.0592
30	0.0091	1875	0.2438	0.04669	37320	40160	0.0767	0.0018	0.0721	0.0739
36	0.0107	1950	0.2422	0.04608	38810	42310	0.0910	0.0019	0.0852	0.0871
42	0.0125	2015	0.2404	0.04540	40100	44380	0.1075	0.0020	0.1000	0.1021
48	0.0143	2050	0.2386	0.04472	40800	45840	0.1243	0.0021	0.1150	0.1171
54	0.0159	2075	0.2370	0.04413	41300	47020	0.1395	0.0021	0.1285	0.1306
63	0.0183	2100	0.2346	0.04324	41800	48570	0.1630	0.0022	0.1488	0.1510
72	0.0208	2125	0.2321	0.04232	42290	50210	0.1882	0.0023	0.1701	0.1724
81	0.0233	2150	0.2296	0.04141	42790	51920	0.2142	0.0024	0.1917	0.1941
90	0.0258	2150	0.2271	0.04052	42790	53060	0.2411	0.0024	0.2136	0.2160
99	0.0283	2150	0.2246	0.03963	42790	54250	0.2689	0.0025	0.2357	0.2382
108	0.0304	2125	0.2225	0.03889	42290	54640	0.2930	0.0025	0.2545	0.2570
117	0.0328	2075	0.2201	0.03806	41300	54520	0.3214	0.0025	0.2762	0.2787
126	0.0352	2015	0.2177	0.03723	40100	54120	0.3506	0.0025	0.2981	0.3006
135	0.0373	1935	0.2156	0.03652	38510	52990	0.3770	0.0024	0.3175	0.3199
144	0.0397	1700	0.2132	0.03571	33830	47610	0.4081	0.0022	0.3401	0.3422
150	0.0412	950	0.2117	0.03521	18910	26980	0.4277	0.0012	0.3548	0.3560
156	0.0427	500	0.2102	0.03471	9950	14400	0.4478	0.0007	0.3694	0.3701
159	0.0434	275	0.2095	0.03448	5470	7980	0.4573	0.0004	0.3763	0.3766
162	0.0442	150	0.2087	0.03422	2990	4380	0.4685	0.0002	0.3840	0.3842
165*	0.0447	35	0.2082	0.03405	700	1030	0.4754	0.0000	0.3889	0.3890
				Based on Posttest Fracture-Diameter Dimension						
165	0.044	35	0.2089	0.03428	700	1020	0.4656	0.0000	0.3822	0.3822

*Time at fracture.

TABLE 7.13

STRESS–STRAIN DATA FOR FULLY ANNEALED AISI 316 STAINLESS STEEL TESTED IN AIR AT 816°C (1500°F) AND AN AXIAL TRUE STRAIN RATE OF 4×10^{-3} sec^{-1}

(Specimen No. 9-5; Specimen diameter, 0.250 in.; Reduction in area measured at test temperature, 61.2%; Reduction in area calculated from posttest fracture diameter, 61.6%)

Time, sec	Measured diametral decrease, in.	Measured axial load, lb	Specimen diameter at test temp., in.	Specimen area at test temp., $in.^2$	Axial stress		Axial strain			
					Engineering, psi	True, psi	Engineering total strain	Elastic true strain	Plastic true strain	Total true strain
0	0	0	0.2538	0.05057						
2	0.0008	900	0.2530	0.05025	17800	17910	0.0067	0.0010	0.0057	0.0067
4	0.0016	1020	0.2522	0.04994	20170	20430	0.0131	0.0011	0.0119	0.0130
6	0.0026	1120	0.2512	0.04954	22150	22610	0.0213	0.0012	0.0198	0.0210
8	0.0036	1188	0.2502	0.04915	23490	24170	0.0295	0.0013	0.0277	0.0290
10	0.0047	1240	0.2491	0.04872	24520	25450	0.0386	0.0014	0.0365	0.0379
12	0.0057	1292	0.2481	0.04833	25550	26740	0.0470	0.0015	0.0445	0.0460
14	0.0067	1320	0.2471	0.04794	26100	27540	0.0555	0.0015	0.0526	0.0541
16	0.0078	1352	0.2460	0.04751	26730	28460	0.0650	0.0015	0.0614	0.0630
18	0.0088	1372	0.2450	0.04713	27130	29110	0.0737	0.0016	0.0696	0.0712
20	0.0098	1392	0.2440	0.04674	27520	29780	0.0826	0.0016	0.0777	0.0794
30	0.0147	1452	0.2391	0.04488	28710	32350	0.1275	0.0018	0.1182	0.1200
50	0.0240	1500	0.2298	0.04146	29660	36180	0.2207	0.0020	0.1975	0.1994
70	0.0330	1480	0.2208	0.03827	29260	38670	0.3223	0.0021	0.2773	0.2794
85	0.0393	1440	0.2145	0.03612	28470	39870	0.4012	0.0022	0.3351	0.3373
100	0.0457	1412	0.2081	0.03400	27920	41530	0.4888	0.0023	0.3957	0.3979
120	0.0540	1340	0.1998	0.03134	26500	42760	0.6151	0.0023	0.4771	0.4794
140	0.0620	1280	0.1918	0.02888	25310	44320	0.7527	0.0024	0.5588	0.5612
160	0.0693	1200	0.1845	0.02672	23730	44910	0.8942	0.0024	0.6364	0.6388
180	0.0767	1112	0.1771	0.02462	21990	45170	1.056	0.0025	0.7182	0.7207
190	0.0805	1056	0.1733	0.02358	20880	44790	1.147	0.0024	0.7617	0.7641
200	0.0840	1012	0.1698	0.02263	20010	44710	1.236	0.0024	0.8025	0.8049
210	0.0873	952	0.1665	0.02176	18820	43750	1.326	0.0024	0.8418	0.8441
215	0.0890	912	0.1648	0.02132	18030	42780	1.374	0.0023	0.8623	0.8647
220	0.0907	832	0.1631	0.02088	16450	39840	1.424	0.0022	0.8832	0.8853
225	0.0924	700	0.1614	0.02045	13840	34230	1.475	0.0019	0.9043	0.9062
230	0.0940	520	0.1598	0.02004	10280	25940	1.524	0.0014	0.9246	0.9260
235*	0.0947	228	0.1581	0.01962	4510	11620	1.578	0.0006	0.9465	0.9471
				Based on Posttest Fracture-Diameter Dimension						
235	0.095	228	0.1588	0.01979	4510	11520	1.555	0.0006	0.9376	0.9382

*Time at fracture.

TABLE 7.14

STRESS–STRAIN DATA FOR FULLY ANNEALED AISI 316 STAINLESS STEEL TESTED IN AIR AT 816°C (1500°F) AND AN AXIAL TRUE STRAIN RATE OF 4×10^{-5} sec^{-1}

(Specimen No. 7-23; Specimen diameter, 0.250 in.; Reduction in area measured at test temperature, 50.9%; Reduction in area calculated from posttest fracture diameter, 49.9%)

Time, min	Measured diametral decrease, in.	Measured axial load, lb	Specimen diameter at test temp., in.	Specimen area at test temp., in.^{2}	Axial stress		Axial strain			
					Engineering, psi	True, psi	Engineering total strain	Elastic true strain	Plastic true strain	Total true strain
0	0	0	0.2538	0.05057						
3	0.0008	1000	0.2530	0.05025	19770	19900	0.0067	0.0011	0.0056	0.0067
6	0.0017	1060	0.2521	0.04990	20960	21240	0.0140	0.0012	0.0127	0.0139
9	0.0026	1075	0.2512	0.04954	21260	21700	0.0212	0.0012	0.0198	0.0210
12	0.0035	1075	0.2503	0.04919	21260	21860	0.0286	0.0012	0.0270	0.0282
15	0.0043	1075	0.2495	0.04887	21260	22000	0.0352	0.0012	0.0334	0.0346
18	0.0052	1075	0.2486	0.04852	21260	22160	0.0427	0.0012	0.0406	0.0418
21	0.0061	1075	0.2477	0.04817	21260	22320	0.0503	0.0012	0.0479	0.0491
24	0.0071	1075	0.2467	0.04778	21260	22500	0.0589	0.0012	0.0560	0.0572
27	0.0078	1075	0.2460	0.04751	21260	22630	0.0649	0.0012	0.0617	0.0629
30	0.0087	1075	0.2451	0.04716	21260	22790	0.0727	0.0012	0.0690	0.0702
33	0.0096	1075	0.2442	0.04682	21260	22960	0.0807	0.0012	0.0763	0.0776
36	0.0102	1075	0.2436	0.04659	21260	23070	0.0860	0.0013	0.0812	0.0825
39	0.0111	1075	0.2427	0.04624	21260	23250	0.0941	0.0013	0.0886	0.0899
54	0.0157	1075	0.2381	0.04451	21260	24150	0.1368	0.0013	0.1269	0.1282
69	0.0198	1050	0.2340	0.04299	20760	24430	0.1770	0.0013	0.1616	0.1630
99	0.0280	1000	0.2258	0.04003	19770	24980	0.2641	0.0014	0.2330	0.2343
129	0.0362	975	0.2176	0.03717	19280	26230	0.3612	0.0014	0.3069	0.3083
159	0.0442	900	0.2096	0.03449	17800	26100	0.4671	0.0014	0.3819	0.3833
189	0.0515	850	0.2023	0.03213	16810	26460	0.5749	0.0014	0.4528	0.4542
219	0.0585	775	0.1953	0.02994	15320	25880	0.6898	0.0014	0.5232	0.5246
249	0.0650	700	0.1888	0.02798	13840	25020	0.8032	0.0014	0.5910	0.5923
258	0.0670	650	0.1868	0.02739	12850	23730	0.8471	0.0013	0.6123	0.6136
270	0.0695	580	0.1843	0.02666	11470	21750	0.8975	0.0012	0.6393	0.6405
276	0.0712	550	0.1826	0.02617	10880	21010	0.9330	0.0011	0.6579	0.6590
282	0.0725	500	0.1813	0.02580	9890	19380	0.9607	0.0011	0.6723	0.6733
288	0.0748	400	0.1790	0.02515	7910	15900	1.011	0.0009	0.6979	0.6988
297*	0.0760	150	0.1778	0.02482	2970	6040	1.038	0.0003	0.7117	0.7120
				Based on Posttest Fracture-Diameter Dimension						
297	0.073	150	0.1808	0.02566	2970	5850	0.971	0.0003	0.6783	0.6786

*Time at fracture.

TABLE 7.15

STRESS–STRAIN DATA FOR FULLY ANNEALED AISI 348 STAINLESS STEEL TESTED IN AIR AT 430°C (806°F) AND AN AXIAL TRUE STRAIN RATE OF 4×10^{-3} sec^{-1}

(Specimen No. 11-8; Specimen diameter, 0.250 in.; Reduction in area measured at test temperature, 65.5%; Reduction in area calculated from posttest fracture diameter, 66.4%)

Time, sec	Measured diametral decrease, in.	Measured axial load, lb	Specimen diameter at test temp., in.	Specimen area at test temp., $in.^2$	Axial stress		Axial strain			
					Engineering, psi	True, psi	Engineering total strain	Elastic true strain	Plastic true strain	Total true strain
0	0	0	0.2518	0.04981						
2	0.0006	1400	0.2512	0.04958	28110	28240	0.0053	0.0012	0.0041	0.0053
2	0.0008	1440	0.2510	0.04950	28910	29090	0.0069	0.0012	0.0057	0.0069
3	0.0012	1520	0.2506	0.04934	30510	30810	0.0102	0.0013	0.0088	0.0101
4	0.0016	1580	0.2502	0.04918	31720	32130	0.0134	0.0013	0.0120	0.0134
5	0.0020	1670	0.2498	0.04902	33530	34060	0.0167	0.0014	0.0152	0.0166
6	0.0025	1720	0.2493	0.04883	34530	35230	0.0208	0.0015	0.0191	0.0206
7	0.0030	1800	0.2488	0.04863	36140	37010	0.0250	0.0016	0.0231	0.0247
8	0.0035	1860	0.2483	0.04844	37340	38400	0.0291	0.0016	0.0271	0.0287
9	0.0040	1940	0.2478	0.04824	38950	40210	0.0333	0.0017	0.0311	0.0328
10	0.0045	2000	0.2473	0.04805	40150	41620	0.0375	0.0017	0.0351	0.0368
25	0.0125	2600	0.2393	0.04499	52200	57790	0.1084	0.0024	0.1005	0.1029
45	0.0230	2870	0.2288	0.04113	57620	69780	0.2127	0.0029	0.1899	0.1929
65	0.0320	2970	0.2198	0.03796	59620	78240	0.3143	0.0033	0.2700	0.2733
75	0.0370	2970	0.2148	0.03625	59620	81930	0.3762	0.0034	0.3159	0.3193
95	0.0460	2930	0.2058	0.03328	58820	88050	0.4994	0.0037	0.4014	0.4051
120	0.0570	2800	0.1948	0.02982	56210	93910	0.6736	0.0039	0.5111	0.5150
160	0.0730	2600	0.1788	0.02512	52200	103500	0.9869	0.0043	0.6822	0.6866
175	0.0786	2500	0.1732	0.02357	50190	106100	1.118	0.0045	0.7458	0.7502
190	0.0845	2400	0.1673	0.02199	48180	109100	1.270	0.0046	0.8150	0.8196
205	0.0900	2300	0.1618	0.02057	46170	111800	1.427	0.0047	0.8818	0.8865
220	0.0955	2200	0.1563	0.01920	44170	114600	1.600	0.0048	0.9509	0.9557
230	0.0990	2020	0.1528	0.01835	40550	110100	1.721	0.0046	0.9963	1.001
235	0.1007	1870	0.1511	0.01794	37540	104200	1.782	0.0044	1.019	1.023
240	0.1025	1600	0.1493	0.01752	32120	91340	1.849	0.0038	1.043	1.047
245*	0.1040	1200	0.1478	0.01717	24090	69900	1.906	0.0029	1.064	1.067
				Based on Posttest Fracture-Diameter Dimension						
245	0.105	700	0.1468	0.01693	14050	41340	1.944	0.0017	1.078	1.080

*Time at fracture.

TABLE 7.16

STRESS–STRAIN DATA FOR FULLY ANNEALED AISI 348 STAINLESS STEEL TESTED IN AIR AT 430°C (806°F) AND AN AXIAL TRUE STRAIN RATE OF 4×10^{-5} sec^{-1}

(Specimen No. 11-5; Specimen diameter, 0.250 in.; Reduction in area measured at test temperature, 55.6%; Reduction in area calculated from posttest fracture diameter, 57.5%)

Time, min	Measured diametral decrease, in.	Measured axial load, lb	Specimen diameter at test temp., in.	Specimen area at test temp., $in.^2$	Axial stress		Axial strain			
					Engineering, psi	True, psi	Engineering total strain	Elastic true strain	Plastic true strain	Total true strain
0	0	0	0.2518	0.04981						
2	0.0006	1400	0.2512	0.04958	28110	28240	0.0053	0.0012	0.0041	0.0053
3	0.0009	1440	0.2509	0.04946	28910	29120	0.0077	0.0012	0.0065	0.0077
5	0.0014	1540	0.2504	0.04926	30920	31260	0.0118	0.0013	0.0104	0.0117
7	0.0020	1640	0.2498	0.04902	32920	33450	0.0167	0.0014	0.0152	0.0166
9	0.0026	1720	0.2492	0.04879	34530	35250	0.0217	0.0015	0.0199	0.0214
10	0.0031	1800	0.2487	0.04859	36140	37040	0.0258	0.0016	0.0239	0.0255
12	0.0037	1880	0.2481	0.04836	37740	38880	0.0308	0.0016	0.0287	0.0303
14	0.0040	1932	0.2478	0.04824	38790	40050	0.0333	0.0017	0.0311	0.0328
20	0.0060	2160	0.2458	0.04747	43360	45500	0.0503	0.0019	0.0472	0.0491
30	0.0090	2480	0.2428	0.04632	49790	53550	0.0766	0.0022	0.0715	0.0738
50	0.0147	2800	0.2371	0.04417	56210	63400	0.1292	0.0027	0.1188	0.1215
70	0.0203	3000	0.2315	0.04211	60230	71250	0.1846	0.0030	0.1664	0.1694
90	0.0258	3120	0.2260	0.04013	62630	77750	0.2431	0.0033	0.2144	0.2176
110	0.0312	3120	0.2206	0.03823	62630	81600	0.3048	0.0034	0.2626	0.2661
130	0.0363	3120	0.2155	0.03649	62630	85510	0.3674	0.0036	0.3093	0.3129
150	0.0412	3120	0.2106	0.03485	62630	89530	0.4319	0.0038	0.3552	0.3590
170	0.0460	3040	0.2058	0.03328	61030	91350	0.4995	0.0038	0.4013	0.4051
190	0.0510	2980	0.2008	0.03168	59820	94060	0.5751	0.0040	0.4504	0.4543
210	0.0560	2880	0.1958	0.03012	57820	95610	0.6567	0.0040	0.5008	0.5048
230	0.0605	2840	0.1913	0.02875	57010	98770	0.7356	0.0041	0.5472	0.5514
250	0.0650	2740	0.1868	0.02742	55010	99940	0.8202	0.0042	0.5948	0.5990
270	0.0693	2720	0.1825	0.02617	54600	103900	0.9072	0.0044	0.6412	0.6456
290	0.0740	2580	0.1778	0.02484	51790	103900	1.009	0.0044	0.6934	0.6978
310	0.0782	2440	0.1736	0.02368	48980	103000	1.108	0.0043	0.7412	0.7456
314	0.0790	2420	0.1728	0.02346	48580	103100	1.127	0.0043	0.7505	0.7548
318	0.0798	2420	0.1720	0.02325	48580	104100	1.147	0.0044	0.7597	0.7641
322	0.0807	2320	0.1711	0.02300	46570	100900	1.170	0.0042	0.7703	0.7745
326	0.0815	2160	0.1703	0.02279	43360	94780	1.190	0.0040	0.7798	0.7838
330	0.0823	2000	0.1695	0.02258	40150	88590	1.210	0.0037	0.7894	0.7931
334	0.0833	1800	0.1685	0.02231	36140	80680	1.236	0.0034	0.8014	0.8048
338*	0.0840	1280	0.1678	0.02212	25700	57850	1.254	0.0024	0.8102	0.8127
				Based on Posttest Fracture-Diameter Dimension						
338	0.087	1280	0.1648	0.02134	25700	59980	1.337	0.0025	0.8463	0.8488

*Time at fracture.

TABLE 7.17

STRESS–STRAIN DATA FOR FULLY ANNEALED AISI 348 STAINLESS STEEL TESTED IN AIR AT 650°C (1200°F) AND AN AXIAL TRUE STRAIN RATE OF 4×10^{-3} sec^{-1}

(Specimen No. 11-23; Specimen diameter, 0.250 in.; Reduction in area measured at test temperature, 62.5%; Reduction in area calculated from posttest fracture diameter, 68.6%)

Time, sec	Measured diametral decrease, in.	Measured axial load, lb	Specimen diameter at test temp., in.	Specimen area at test temp., $in.^2$	Axial stress		Axial strain			
					Engineering, psi	True, psi	Engineering total strain	Elastic true strain	Plastic true strain	Total true strain
0	0	0	0.2530	0.05027						
2	0.0010	1160	0.2520	0.04988	23070	23260	0.0084	0.0011	0.0073	0.0084
3	0.0015	1240	0.2515	0.04968	24670	24960	0.0124	0.0011	0.0112	0.0124
4	0.0020	1360	0.2510	0.04948	27050	27490	0.0165	0.0013	0.0151	0.0164
5	0.0025	1460	0.2505	0.04928	29040	29620	0.0206	0.0014	0.0191	0.0204
6	0.0030	1520	0.2500	0.04909	30240	30970	0.0247	0.0014	0.0230	0.0244
7	0.0035	1600	0.2495	0.04889	31830	32730	0.0289	0.0015	0.0270	0.0285
8	0.0040	1640	0.2490	0.04870	32620	33680	0.0330	0.0015	0.0310	0.0325
9	0.0045	1700	0.2485	0.04850	33820	35050	0.0372	0.0016	0.0349	0.0366
10	0.0050	1760	0.2480	0.04831	35010	36440	0.0414	0.0017	0.0389	0.0406
16	0.0080	2000	0.2450	0.04714	39780	42420	0.0672	0.0019	0.0631	0.0651
20	0.0100	2120	0.2430	0.04638	42170	45710	0.0849	0.0021	0.0794	0.0815
24	0.0120	2200	0.2410	0.04562	43760	48230	0.1031	0.0022	0.0959	0.0981
28	0.0140	2260	0.2390	0.04486	44960	50380	0.1216	0.0023	0.1125	0.1148
32	0.0160	2300	0.2370	0.04411	45750	52140	0.1407	0.0024	0.1292	0.1316
53	0.0255	2400	0.2275	0.04065	47740	59040	0.2381	0.0027	0.2109	0.2136
73	0.0342	2380	0.2188	0.03760	47340	63300	0.3386	0.0029	0.2887	0.2917
93	0.0425	2320	0.2105	0.03480	46150	66660	0.4464	0.0031	0.3660	0.3691
113	0.0510	2260	0.2020	0.03205	44960	70520	0.5708	0.0032	0.4483	0.4516
133	0.0590	2160	0.1940	0.02956	42970	73070	0.7031	0.0034	0.5291	0.5324
153	0.0663	2060	0.1867	0.02738	40980	75250	0.8389	0.0035	0.6057	0.6092
173	0.0740	1940	0.1790	0.02516	38590	77090	1.001	0.0035	0.6899	0.6935
193	0.0810	1840	0.1720	0.02324	36600	79190	1.167	0.0036	0.7696	0.7733
213	0.0880	1720	0.1650	0.02138	34210	80440	1.355	0.0037	0.8527	0.8564
233	0.0943	1600	0.1587	0.01978	31830	80890	1.545	0.0037	0.9306	0.9343
239	0.0965	1420	0.1565	0.01924	28250	73820	1.617	0.0034	0.9587	0.9621
243	0.0979	1280	0.1551	0.01889	25460	67750	1.664	0.0031	0.9768	0.9799
245*	0.0981	1000	0.1549	0.01884	19890	53070	1.670	0.0024	0.9798	0.9822
				Based on Posttest Fracture-Diameter Dimension						
245	0.110	1000	0.1430	0.01606	19890	62260	2.134	0.0029	1.139	1.142

*Time at fracture.

TABLE 7.18

STRESS–STRAIN DATA FOR FULLY ANNEALED AISI 348 STAINLESS STEEL TESTED IN AIR AT 650°C (1200°F) AND AN AXIAL TRUE STRAIN RATE OF 4×10^{-5} sec^{-1}

(Specimen No. 11-3; Specimen diameter, 0.250 in.; Reduction in area measured at test temperature, 39.0%; Reduction in area calculated from posttest fracture diameter, 40.4%)

Time, min	Measured diametral decrease, in.	Measured axial load, lb	Specimen diameter at test temp., in.	Specimen area at test temp., $in.^2$	Axial stress		Axial strain			
					Engineering, psi	True, psi	Engineering total strain	Elastic true strain	Plastic true strain	Total true strain
0	0	0	0.2530	0.05027						
2	0.0006	1260	0.2524	0.05003	25060	25180	0.0052	0.0012	0.0041	0.0052
4	0.0011	1390	0.2519	0.04984	27650	27890	0.0093	0.0013	0.0080	0.0092
6	0.0017	1470	0.2513	0.04960	29240	29640	0.0141	0.0014	0.0127	0.0140
8	0.0023	1550	0.2507	0.04936	30830	31400	0.0190	0.0014	0.0174	0.0189
10	0.0029	1630	0.2501	0.04913	32420	33180	0.0240	0.0015	0.0222	0.0237
12	0.0035	1700	0.2495	0.04889	33820	34770	0.0289	0.0016	0.0269	0.0285
14	0.0041	1760	0.2489	0.04866	35010	36170	0.0339	0.0017	0.0317	0.0334
20	0.0058	1890	0.2472	0.04799	37600	39380	0.0483	0.0018	0.0453	0.0471
24	0.0071	1940	0.2459	0.04749	38590	40850	0.0594	0.0019	0.0558	0.0577
27	0.0080	1980	0.2450	0.04714	39390	42000	0.0672	0.0019	0.0631	0.0651
30	0.0089	1990	0.2441	0.04680	39580	42520	0.0751	0.0020	0.0705	0.0724
50	0.0146	2040	0.2384	0.04464	40580	45700	0.1272	0.0021	0.1176	0.1197
70	0.0202	2050	0.2328	0.04257	40780	48160	0.1821	0.0022	0.1651	0.1673
85	0.0242	2040	0.2288	0.04112	40580	49620	0.2239	0.0023	0.1997	0.2020
100	0.0283	1990	0.2247	0.03965	39580	50180	0.2690	0.0023	0.2359	0.2382
120	0.0334	1960	0.2196	0.03788	38990	51750	0.3286	0.0024	0.2818	0.2841
135	0.0372	1930	0.2158	0.03658	38390	52770	0.3758	0.0024	0.3166	0.3191
155	0.0423	1860	0.2107	0.03487	37000	53350	0.4433	0.0024	0.3645	0.3669
170	0.0460	1780	0.2070	0.03365	35410	52890	0.4953	0.0024	0.3999	0.4023
185	0.0495	1710	0.2035	0.03253	34010	52570	0.5472	0.0024	0.4340	0.4364
195	0.0519	1660	0.2011	0.03176	33020	52260	0.5843	0.0024	0.4578	0.4602
200	0.0531	1530	0.1999	0.03138	30430	48750	0.6033	0.0022	0.4698	0.4721
205	0.0543	1300	0.1987	0.03101	25860	41920	0.6225	0.0019	0.4821	0.4840
210*	0.0554	780	0.1976	0.03067	15520	25430	0.6401	0.0012	0.4936	0.4948
				Based on Posttest Fracture-Diameter Dimension						
210	0.057	580	0.1960	0.03017	11540	19220	0.6668	0.0009	0.5100	0.5109

*Time at fracture.

TABLE 7.19

STRESS–STRAIN DATA FOR FULLY ANNEALED AISI 348 STAINLESS STEEL TESTED IN AIR AT 816°C (1500°F) AND AN AXIAL TRUE STRAIN RATE OF 4×10^{-3} sec^{-1}

(Specimen No. 11-28; Specimen diameter, 0.250 in.; Reduction in area measured at test temperature, 57.8%; Reduction in area calculated from posttest fracture diameter, 87.0%)

Time, sec	Measured diametral decrease, in.	Measured axial load, lb	Specimen diameter at test temp., in.	Specimen area at test temp., $in.^2$	Axial stress		Axial strain			
					Engineering, psi	True, psi	Engineering total strain	Elastic true strain	Plastic true strain	Total true strain
0	0	0	0.2538	0.05059						
2	0.0008	870	0.2530	0.05027	17200	17310	0.0066	0.0009	0.0057	0.0066
3	0.0012	950	0.2526	0.05011	18780	18960	0.0098	0.0010	0.0088	0.0098
4	0.0016	1030	0.2522	0.04995	20360	20620	0.0131	0.0011	0.0119	0.0130
5	0.0020	1070	0.2518	0.04979	21150	21490	0.0163	0.0011	0.0151	0.0162
6	0.0026	1120	0.2512	0.04956	22140	22600	0.0212	0.0012	0.0198	0.0210
7	0.0032	1140	0.2506	0.04932	22540	23110	0.0261	0.0012	0.0246	0.0258
8	0.0038	1150	0.2500	0.04908	22730	23430	0.0310	0.0012	0.0293	0.0306
9	0.0044	1170	0.2494	0.04885	23130	23950	0.0360	0.0013	0.0341	0.0354
10	0.0050	1200	0.2488	0.04861	23720	24680	0.0410	0.0013	0.0389	0.0402
20	0.0100	1290	0.2438	0.04668	25500	27640	0.0842	0.0015	0.0794	0.0809
30	0.0153	1310	0.2385	0.04467	25900	29330	0.1330	0.0015	0.1233	0.1249
50	0.0253	1300	0.2285	0.04100	25700	31700	0.2344	0.0017	0.2089	0.2106
70	0.0347	1260	0.2191	0.03770	24910	33420	0.3426	0.0018	0.2929	0.2946
85	0.0413	1220	0.2125	0.03546	24120	34400	0.4273	0.0018	0.3540	0.3558
100	0.0480	1160	0.2058	0.03326	22930	34880	0.5218	0.0018	0.4181	0.4199
120	0.0565	1100	0.1973	0.03057	21740	35980	0.6558	0.0019	0.5024	0.5043
135	0.0628	1050	0.1910	0.02865	20760	36650	0.7668	0.0019	0.5673	0.5692
155	0.0707	970	0.1831	0.02633	19170	36840	0.9226	0.0019	0.6517	0.6537
170	0.0766	900	0.1772	0.02466	17790	36500	1.053	0.0019	0.7173	0.7192
185	0.0825	850	0.1713	0.02304	16800	36890	1.197	0.0019	0.7850	0.7869
200	0.0880	770	0.1658	0.02159	15220	35670	1.345	0.0019	0.8503	0.8522
203*	0.0890	670	0.1648	0.02133	13240	31410	1.373	0.0016	0.8626	0.8642
				Based on Posttest Fracture-Diameter Dimension						
203	0.160	670	0.0938	0.00691	13240	96980	6.334	0.0051	1.987	1.993

*Time at fracture.

TABLE 7.20

STRESS–STRAIN DATA FOR FULLY ANNEALED AISI 348 STAINLESS STEEL TESTED IN AIR AT 816°C (1500°F) AND AN AXIAL TRUE STRAIN RATE OF 4×10^{-5} sec^{-1}

(Specimen No. 11-25; Specimen diameter, 0.250 in.; Reduction in area measured at test temperature, 68.6%; Reduction in area calculated from posttest fracture diameter, 84.0%)

Time, min	Measured diametral decrease, in.	Measured axial load, lb	Specimen diameter at test temp., in.	Specimen area at test temp., $in.^2$	Axial stress		Axial strain			
					Engineering, psi	True, psi	Engineering total strain	Elastic true strain	Plastic true strain	Total true strain
0	0	0	0.2538	0.05059						
3	0.0006	760	0.2532	0.05035	15020	15090	0.0050	0.0008	0.0042	0.0050
6	0.0015	840	0.2523	0.04999	16610	16800	0.0122	0.0009	0.0113	0.0121
9	0.0023	860	0.2515	0.04967	17000	17310	0.0187	0.0009	0.0176	0.0185
12	0.0032	860	0.2506	0.04932	17000	17440	0.0260	0.0009	0.0248	0.0257
15	0.0041	860	0.2497	0.04897	17000	17560	0.0334	0.0009	0.0319	0.0329
18	0.0050	860	0.2488	0.04861	17000	17690	0.0409	0.0009	0.0392	0.0401
25	0.0071	860	0.2467	0.04780	17000	17990	0.0587	0.0009	0.0561	0.0571
28	0.0080	860	0.2458	0.04745	17000	18130	0.0665	0.0010	0.0634	0.0644
34	0.0100	860	0.2438	0.04668	17000	18420	0.0841	0.0010	0.0797	0.0807
41	0.0120	840	0.2418	0.04592	16610	18290	0.1021	0.0010	0.0962	0.0972
48	0.0140	840	0.2398	0.04516	16610	18600	0.1205	0.0010	0.1128	0.1138
55	0.0160	840	0.2378	0.04441	16610	18910	0.1395	0.0010	0.1296	0.1306
62	0.0180	840	0.2358	0.04367	16610	19240	0.1589	0.0010	0.1464	0.1475
69	0.0200	820	0.2338	0.04293	16210	19100	0.1788	0.0010	0.1635	0.1645
84	0.0240	800	0.2298	0.04147	15810	19290	0.2202	0.0010	0.1980	0.1990
98	0.0280	780	0.2258	0.04004	15420	19480	0.2638	0.0010	0.2331	0.2341
106	0.0300	780	0.2238	0.03933	15420	19830	0.2865	0.0010	0.2509	0.2519
116	0.0380	720	0.2158	0.03657	14230	19690	0.3837	0.0010	0.3237	0.3247
128	0.0415	700	0.2123	0.03540	13840	19780	0.4297	0.0010	0.3564	0.3574
158	0.0490	660	0.2048	0.03294	13050	20040	0.5363	0.0011	0.4283	0.4294
188	0.0565	640	0.1973	0.03057	12650	20940	0.6554	0.0011	0.5029	0.5040
218	0.0640	520	0.1898	0.02829	10280	18380	0.7887	0.0010	0.5805	0.5815
248	0.0703	480	0.1835	0.02644	9490	18150	0.9136	0.0010	0.6480	0.6490
278	0.0775	440	0.1763	0.02441	8700	18030	1.073	0.0009	0.7281	0.7291
308	0.0840	420	0.1698	0.02264	8300	18550	1.235	0.0010	0.8032	0.8042
312	0.0940	400	0.1598	0.02005	7910	19950	1.523	0.0010	0.9246	0.9256
338	0.0992	380	0.1546	0.01877	7510	20250	1.696	0.0011	0.9907	0.9918
368	0.1050	320	0.1488	0.01739	6330	18400	1.910	0.0010	1.067	1.068
388	0.1090	300	0.1448	0.01647	5930	18220	2.073	0.0010	1.122	1.123
398	0.1105	280	0.1433	0.01613	5540	17360	2.138	0.0009	1.143	1.144
400	0.1110	280	0.1428	0.01601	5540	17490	2.160	0.0009	1.150	1.151
402*	0.1115	240	0.1423	0.01590	4740	15090	2.182	0.0008	1.157	1.158
				Based on Posttest Fracture-Diameter Dimension						
402	0.150	240	0.1038	0.00846	4740	28370	4.982	0.0015	1.787	1.789

*Time at fracture.

TABLE 7.21

TENSILE PROPERTIES OF ANNEALED AISI 304, 316, AND 348 STAINLESS STEELS TESTED IN AIR

Mat'l	Temp. °C	Temp. °F	Strain rate, sec^{-1}	Elastic constants E 10^6 Psi	E 10^3 Kg/mm²	ν_e	Tensile strength Psi	Tensile strength Kg/mm²	Reduction in area, %	Tensile ductility, %
304	21	70	4×10^{-3}	28.7	20.2	0.264	89,000	62.6	80.6	164.0
304	21	70	4×10^{-4}	28.7	20.2	0.264				
304	21	70	4×10^{-5}	28.7	20.2	0.264				
304	430	806	4×10^{-3}	23.4	16.5	0.282	62,400	43.9	64.0	102.2
304	430	806	4×10^{-4}	23.4	16.5	0.282				
304	430	806	4×10^{-5}	23.4	16.5	0.282	64,600	45.4	64.5	103.6
304	650	1202	4×10^{-3}	21.6	15.2	0.315	45,600	32.1	42.2	54.8
304	650	1202	4×10^{-4}	21.6	15.2	0.315				
304	650	1202	4×10^{-5}	21.6	15.2	0.315	35,400	24.9	33.4	40.6
304	816	1500	4×10^{-3}	18.8	13.2	0.323	25,000	17.6	51.0	71.3
304	816	1500	4×10^{-4}	18.8	13.2	0.323				
304	816	1500	4×10^{-5}	18.8	13.2	0.323	13,400	9.5	32.1	38.7
348	21	70	4×10^{-3}	28.2	19.8	0.250				
348	21	70	4×10^{-4}	28.2	19.8	0.250				
348	21	70	4×10^{-5}	28.2	19.8	0.250				
348	430	806	4×10^{-3}	23.8	16.7	0.275	59,600	41.9	66.4	109.1
348	430	806	4×10^{-4}	23.8	16.7	0.275				
348	430	806	4×10^{-5}	23.8	16.7	0.275	62,600	44.0	57.5	85.6
348	650	1202	4×10^{-3}	21.8	15.3	0.295	47,700	33.6	68.6	115.8
348	650	1202	4×10^{-4}	21.8	15.3	0.295				
348	650	1202	4×10^{-5}	21.8	15.3	0.295	40,800	28.7	40.4	51.8
348	816	1500	4×10^{-3}	19.05	13.4	0.340	25,900	18.2	87.0	204.0
348	816	1500	4×10^{-4}	19.05	13.4	0.340				
348	816	1500	4×10^{-5}	19.05	13.4	0.340	17,000	12.0	84.0	183.3
316	21	70	4×10^{-3}	30.1	21.2	0.295	90,000	63.3	74.6	137.0
316	21	70	4×10^{-4}	30.1	21.2	0.295				
316	21	70	4×10^{-5}	30.1	21.2	0.295				
316	430	806	4×10^{-3}	24.0	16.9	0.315	67,700	47.6	62.1	97.0
316	430	806	4×10^{-4}	24.0	16.9	0.315				
316	430	806	4×10^{-5}	24.0	16.9	0.315	73,900	52.0	60.6	93.1
316	650	1202	4×10^{-3}	21.95	15.4	0.326	54,700	38.5	61.1	94.0
316	650	1202	4×10^{-4}	21.95	15.4	0.326				
316	650	1202	4×10^{-5}	21.95	15.4	0.326	42,800	30.1	32.1	38.7
316	816	1500	4×10^{-3}	18.4	12.9	0.321	29,700	20.9	61.6	95.7
316	816	1500	4×10^{-4}	18.4	12.9	0.321				
316	816	1500	4×10^{-5}	18.4	12.9	0.321	21,300	14.9	49.9	69.1

TABLE 7 22

COMPARISON OF GE NSP AND LITERATURE DATA* FOR YIELD STRENGTH TENSILE STRENGTH AND REDUCTION IN AREA FOR AISI 304 316 AND 348 STAINLESS STEELS IN THE ANNEALED CONDITION AT VARIOUS TEMPERATURES

Temp	Data source	304 stainless steel			316 stainless steel			348 stainless steel†		
		Yield strength, (0 2% offset) ‡ psi	Tensile strength, psi	Reduction in area, %	Yield strength (0 2% offset) ‡ psi	Tensile strength psi	Reduction in area %	Yield strength (0 2% offset),‡ psi	Tensile strength psi	Reduction in area, %
21°C	Curve*	37 000	83 000	79	37 000	82 000	73	35 000	85 000	70
(70°F)	Range*	27 000 56 000	77 000–94 000	68–83	32 000 45 000	76 000–88 000	65 79	22 000–50 000	77 000 97 000	45 75
	GE–NSP ($\dot{\epsilon}_t$ 4 x 10^{-3} sec^{-1})	45 000	89 000	80 6	41 500	90 000	74 6	No data	No data	No data
430°C	Curve	24 000	63 000	69	33 000	74 000	63	31 000	58 000	68
(806°F)	Range	17 000–38 000	58 000–68 000	65 74	20 000 38 000	67 000–76 000	57 63	20 000 38 000	56 000 66 000	59 72
	GE–NSP (ϵ_t 4 x 10^{-3} sec^{-1})	25 000	62 400	64 0	20 000	67 700	62 1	28 000	59 600	66 4
	GE NSP ($\dot{\epsilon}_t$ 4 x 10^{-3} sec^{-1})§				22 000	67 300	57 5			
	GE–NSP ($\dot{\epsilon}_t$ 4 x 10^{-5} sec^{-1})	28 000	64 600	64 5	22 500	73 900	60 6	28 000	62 600	57 5
	GE–NSP (ϵ_t 4 x 10^{-5} sec^{-1})§				20 000	73 300	64 0	28 000	65 600	58 5
650°C	Curve	20 000	48 500	47 5	26 000	50 000	61	25 000	45 000	61
(1202°F)	Range	11 000–28 000	43 500–52 000	23 57	15 000 35 000	48 000–60 500	55–71	12 000 37 000	41 000 57 000	28 68
	GE–NSP ($\dot{\epsilon}_t$ 4 x 10^{-3} sec^{-1})	21 000	45 600	42 2	17 000	54 700	61 1	22 000	47 700	68 6
	GE NSP ($\dot{\epsilon}_t$ 4 x 10^{-3} sec^{-1})§				18 500	55 900	54 3	19 000	46 700	67 7
	GE–NSP ($\dot{\epsilon}_t$ 4 x 10^{-5} sec^{-1})	22 000	35 400	33 4	20 000	42 800	32 1	25 000	40 900	40 4
	GE NSP ($\dot{\epsilon}_t$ 4 x 10^{-5} sec^{-1})§				18 500	42 200	27 4	25 500	42 200	36 0
816°C	Curve	15 000	20 000	54	17 000	21 000	69	18 000	21 000	65
(1500°F)	Range	10 000 18 000	18 000 22 000	42–65	12 000 18 000	20 000 31 000	69 76	16 000 20 000	19 000 27 000	50 78
	GE NSP ($\dot{\epsilon}_t$ 4 x 10^{-3} sec^{-1})	16 500	25 000	51 0	17 000	29 700	61 6	16 500	25 900	87 0
	GE NSP (ϵ_t 4 x 10^{-3} sec^{-1})§				17 000	33 600	56 4	17 500	26 100	82 7
	GE–NSP (ϵ_t 4 x 10^{-5} sec^{-1})	12 000	13 400	32 1	19 000	21 300	49 9	14 000	17 000	84 0
	GE NSP (ϵ_t 4 x 10^{-5} sec^{-1})§				17 000	18 800	50 4	15 000	15 800	68 6
	GE NSP (ϵ_t 4 x 10^{-5} sec^{-1})§							17 500	17 800	¶

*From Ref 3

†Cited literature data are for 347 stainless steel

‡The 0 2% offset yield strengths for these GE–NSP data were determined by extrapolation of the low strain range date (~0 5 to 3 0%) to the 0 2% offset

§ Data from supplemental test

¶ Not available

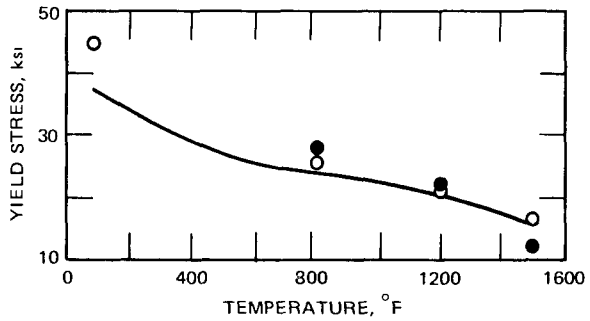

Fig. 7.1 GE–NSP 0.2% offset yield-strength data obtained from short-term tensile tests in air for annealed AISI 304 stainless steel. Average data curve from Ref. 3 for annealed bar, plate, and sheet. Axial strain rates: ○, 4×10^{-3} sec^{-1}; ●, 4×10^{-5} sec^{-1}.

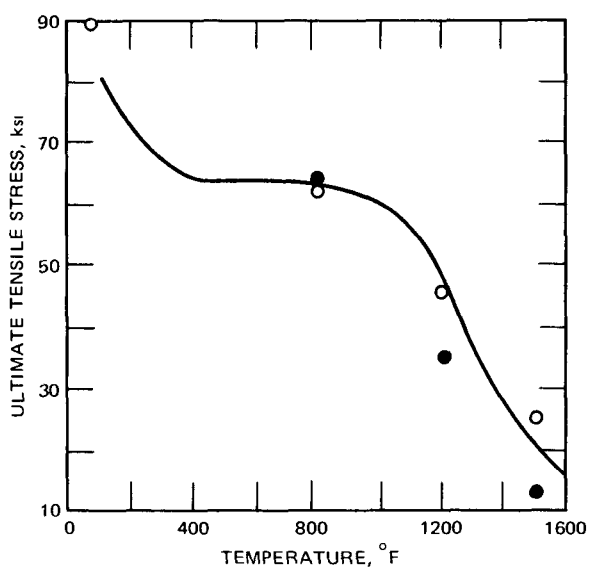

Fig. 7.2 GE–NSP ultimate-tensile-strength data obtained from short-term tensile tests in air for annealed AISI 304 stainless steel. Average data curve from Ref. 3 for annealed bar, plate, and sheet. Axial strain rates: ○, 4×10^{-3} sec^{-1}; ●, 4×10^{-5} sec^{-1}.

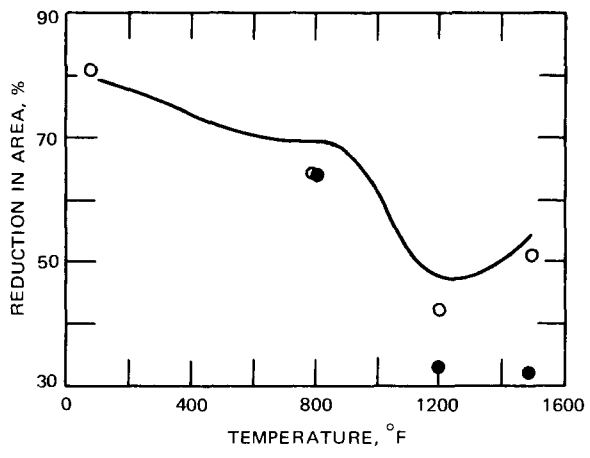

Fig. 7.3 GE–NSP reduction-in-area data obtained from short-term tensile tests in air for annealed AISI 304 stainless steel. Average data curve from Ref. 3 for annealed bar and plate. Axial strain rates: ○, 4×10^{-3} sec^{-1}; ●, 4×10^{-5} sec^{-1}.

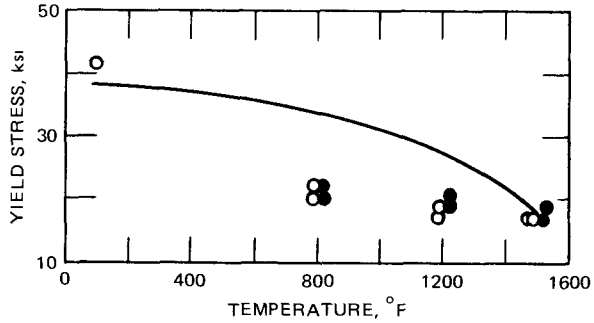

Fig. 7.4 GE–NSP 0.2% offset yield-strength data obtained from short-term tensile tests in air for annealed AISI 316 stainless steel. Average data curve from Ref. 3 for annealed bar. Axial strain rates: ○, 4×10^{-3} sec^{-1}; ●, 4×10^{-5} sec^{-1}.

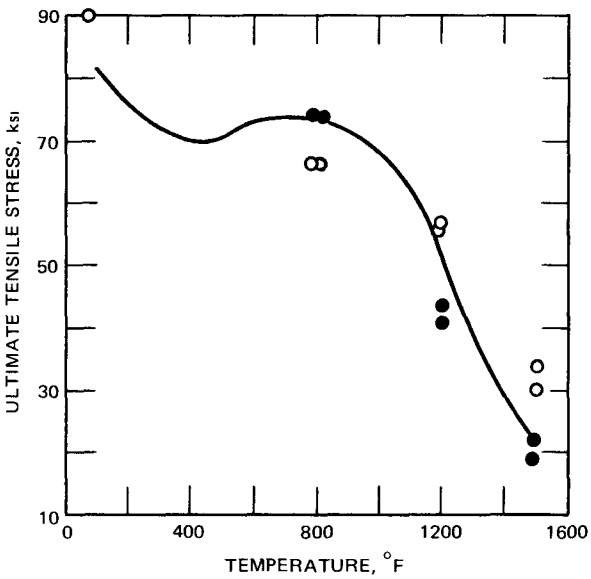

Fig. 7.5 GE–NSP ultimate-tensile-strength data obtained from short-term tensile tests in air for annealed AISI 316 stainless steel. Average data curve from Ref. 3 for annealed bar. Axial strain rates, ○, 4×10^{-3} sec^{-1}; 4×10^{-5} sec^{-1}.

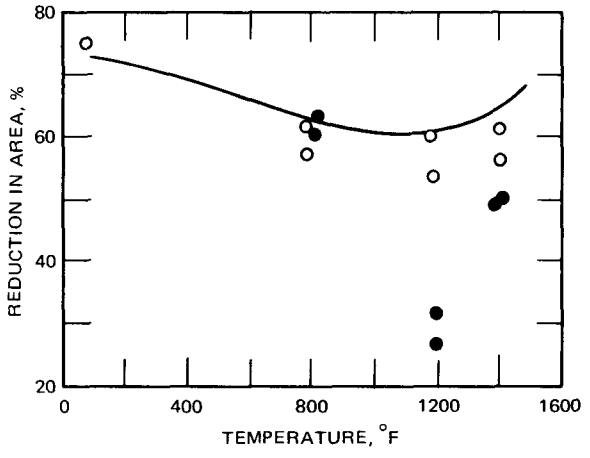

Fig. 7.6 GE–NSP reduction-in-area data obtained from short-term tensile tests in air for annealed AISI 316 stainless steel. Average data curve from Ref. 3 for annealed bar. Axial strain rates: ○, 4×10^{-3} sec^{-1}; ●, 4×10^{-5} sec^{-1}.

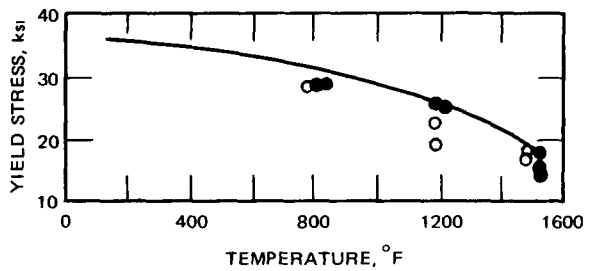

Fig. 7.7 GE–NSP 0.2% offset yield-strength data obtained from short-term tensile tests in air for annealed AISI 348 stainless steel. Average data curve from Ref. 3 for annealed 347 bar. Axial strain rates: ○, 4×10^{-3} sec^{-1}; ●, 4×10^{-5} sec^{-1}.

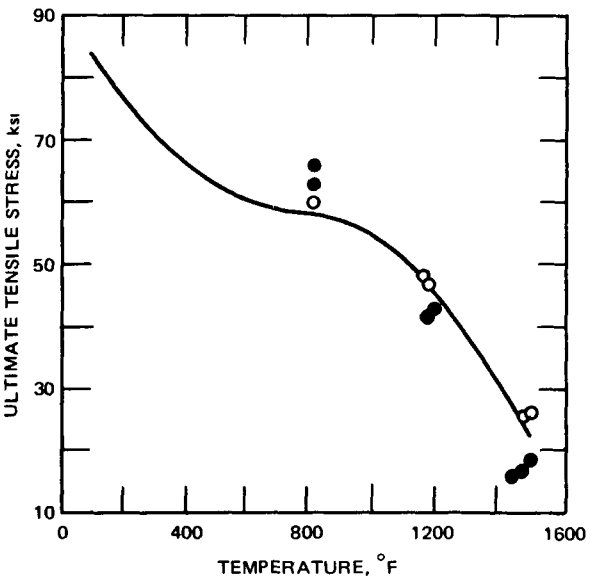

Fig. 7.8 GE–NSP ultimate-tensile-strength data obtained from short-term tensile tests in air for annealed AISI 348 stainless steel. Average data curve from Ref. 3 for annealed 347 bar. Axial strain rates: ○, 4×10^{-3} sec^{-1}; ●, 4×10^{-5} sec^{-1}.

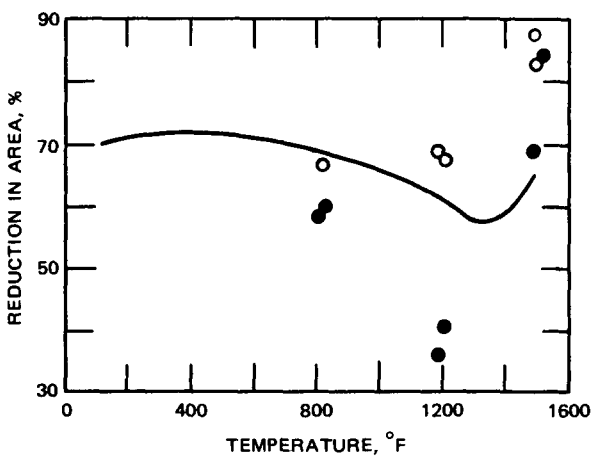

Fig. 7.9 GE–NSP reduction-in-area data obtained from short-term tensile tests in air for annealed AISI 348 stainless steel. Average data from Ref. 3 for annealed 347 bar. Axial strain rates: ○, 4×10^{-3} sec^{-1}; ●, 4×10^{-5} sec^{-1}.

True stress vs. true strain curves for the materials studied in this evaluation are shown in Figs. 7.10 to 7.12, based on the data given in Tables 7.1 to 7.20. These curves reveal a fairly interesting trend. For each material at 650 and 816°C, the true stress–strain curve for the higher strain rate (4×10^{-3} sec^{-1}) is positioned above the curve obtained at the lower strain rate. At 430°C, however, the reverse is true. Consistent with this behavior, the true strain at fracture at 650 and 816°C is greater at the higher strain rate; at 430°C the reverse is true.

All true stress–strain curves in Figs. 7.10 to 7.12 exhibit a maximum point that is contrary to what is expected in a true-stress plot. This phenomenon, which has not been frequently discussed before, is felt to be due, at least partially, to internal void formation. Near the fracture point the measured specimen diameter is not representative of the load-carrying area, and the apparent true stress is much smaller than the actual true stress that really exists. Of course, if the actual load-carrying area could be determined, the correct values of true stress could be calculated, and no maximum in the flow curve would be observed. For this reason the region near the fracture point has been shown dotted on these curves. The commonly observed[4–7] linearity between the maximum load point and the point of fracture is not present in these graphs. Behavior similar to the above has been observed in a recent study[8] of 316 stainless steel at various temperatures and strain rates. At 650°C and a constant strain rate of about 3×10^{-3} sec^{-1}, a true stress–strain curve was obtained that was quite similar to that noted in Fig. 7.11. This curve is shown dotted in this figure and indicates the same type of maximum stress behavior just mentioned. It is important to note, however, that the true strain at fracture (at 650°C) is about 0.3 in the Wray and Richmond[8] study and about 0.9 in the GE–NSP testing. At least some, and perhaps even a major part, of this difference in tensile ductility is due to the different techniques used in measuring the stress–strain behavior. In the Wray and Richmond tests, cylindrical gage-section specimens were used, and the longitudinal strain for the entire gage section (1.437 in.) was referred to the initial length in the calculation of true-strain values. This approach does not account for local necking, and hence local strains exist that are much larger than those based on total gage-section dimensions. This effect was indeed acknowledged by Wray and Richmond in specific analyses that corrected for localized necking. These calculations used local area measurements of the "necked" region of the specimen and caused the true stress–strain curve to be extended to much higher strain values. Such an approach could, of course, increase the tensile-ductility value above 0.3 and lead to better agreement with GE–NSP results. This special evaluation by Wray and Richmond caused the maximum in the true stress–strain curve to disappear, but this is thought to be due to the fact that the necking was causing the strain rate and hence the flow stress to increase significantly as deformation took place. Had the strain rate been kept constant within the necking

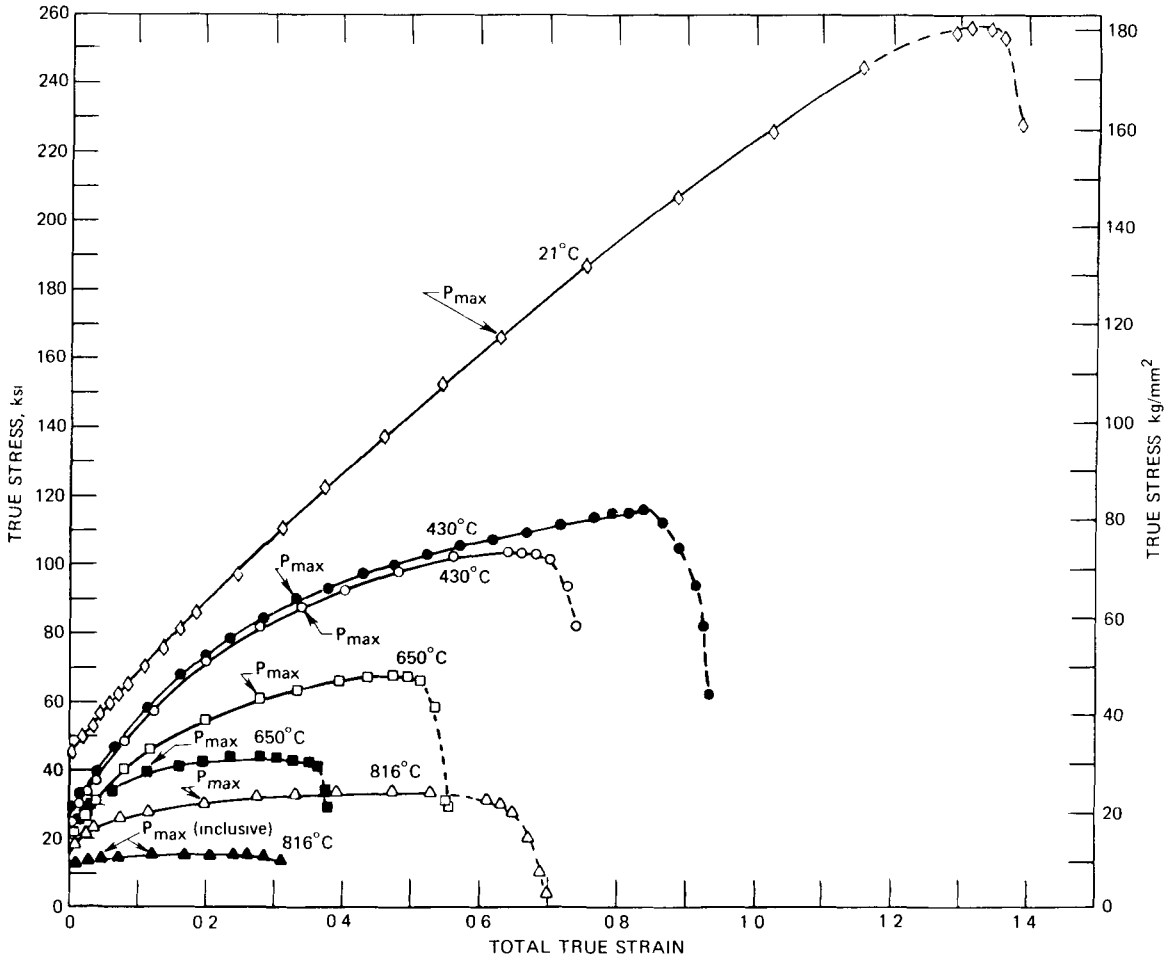

Temp., °C	Axial true strain rate, sec $^{-1}$	Spec. No.	Measured reduction in area (hot), %	Reduction in area (cold), %	Measured tensile ductility (hot)	Tensile ductility (cold)
◇ 21	4×10^{-3}	56-4	75.0	80.6	1.386	1.640
○ 430	4×10^{-3}	53-3	51.5	64.0	0.724	1.022
● 430	4×10^{-5}	53-6	60.7	64.5	0.934	1.036
□ 650	4×10^{-3}	53-1	42.6	42.2	0.555	0.548
■ 650	4×10^{-5}	53-4	31.6	33.4	0.380	0.406
△ 816	4×10^{-3}	53-2	50.4	51.0	0.701	0.713
▲ 816	4×10^{-5}	53-5	26.8	32.1	0.312	0.387

Fig. 7.10 True stress vs. true strain curves obtained from short-term tensile tests in air for annealed AISI 304 stainless steel at 21, 430, 650, and 816°C and constant axial true strain rates of $\sim 4 \times 10^{-3}$ sec $^{-1}$ and $\sim 4 \times 10^{-5}$ sec^{-1}.

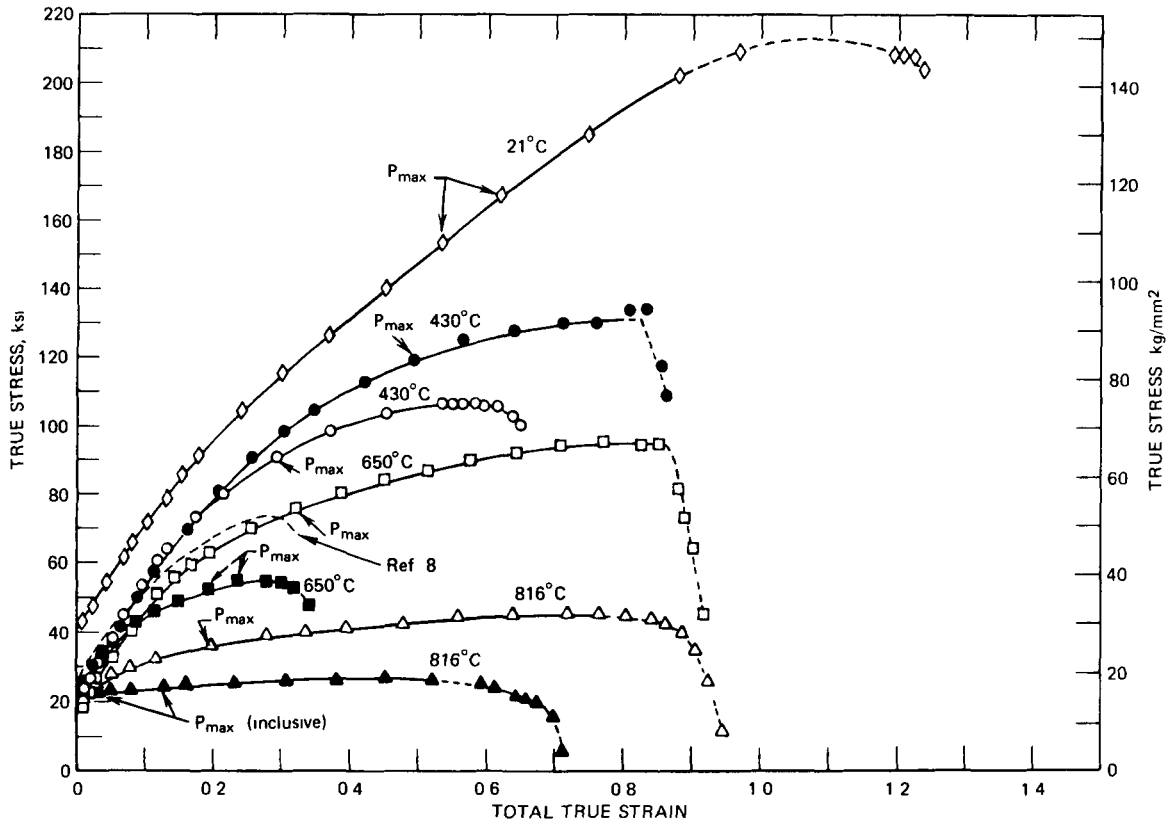

	Temp., °C	Axial true strain rate, sec $^{-1}$	Spec. No.	Measured reduction in area (hot), %	Reduction in area (cold), %	Measured tensile ductility (hot)	Tensile ductility (cold)
◇	21	4×10^{-3}	9 4	71 1	74.6	1.240	1.370
○	430	4×10^{-3}	9-6	47.8	62.1	0.649	0.970
●	430	4×10^{-5}	9-7	57 8	60.6	0.864	0.931
□	650	4×10^{-3}	19-4	60.0	61.1	0.917	0.944
■	650	4×10^{-5}	7-26	32.2	32.1	0.389	0.387
△	816	4×10^{-3}	9-5	61.2	61.6	0.947	0.957
▲	816	4×10^{-5}	7-23	50.9	49.9	0.712	0.691

Fig. 7.11 True stress vs. true strain curves obtained from short-term tensile tests for annealed AISI 316 stainless steel tested in air at 21, 430, 650, and 816°C and constant axial true strain rates of ~4×10^{-3} sec $^{-1}$ and ~4×10^{-5} sec^{-1}

region of the test, then, even in the special approach used by Wray and Richmond, the true stress–strain plot would still have exhibited a maximum point. This theorization follows from the GE–NSP data shown in Fig. 7.11 because the unique control features used allow the strain rate to be held constant up until fracture occurs, as discussed in Chap. 6, Experimental Procedures.

A summary tabulation of the measured ductility in terms of the reduction in area is included with each graph. Values for the "hot" reduction in area (calculated using the instantaneous on-test measurement of the decrease in the minimum specimen diameter just before fracture) and the "cold" reduction in area (calculated using posttest measurement of the final fracture diameter) are listed. In addition, the corresponding hot and cold tensile-ductility values given by the relation $\epsilon_f = \ln [1/(1 - RA)]$, which can also be stated as $\epsilon_f = \ln (A_o/A)$, are shown in the tabulations. In general, the hot and cold reductions in area are in good agreement. Exceptions are noted in the data for both 304 and 316 stainless steels at 430°C at the fast strain rate ($\dot{\epsilon}_t = 4 \times 10^{-3}$ sec^{-1}) and for the 348 stainless-steel data at 816°C at both strain rates. Apparently, in these cases, the diametral-strain sensor did not track the minimum-diameter region to the final fracture. A supplemental test was performed in each instance cited (except the 304 stainless steel), but the additional test did not improve the agreement. However, in these cases the values for the cold reductions in area indicate that the hot reduction-in-area

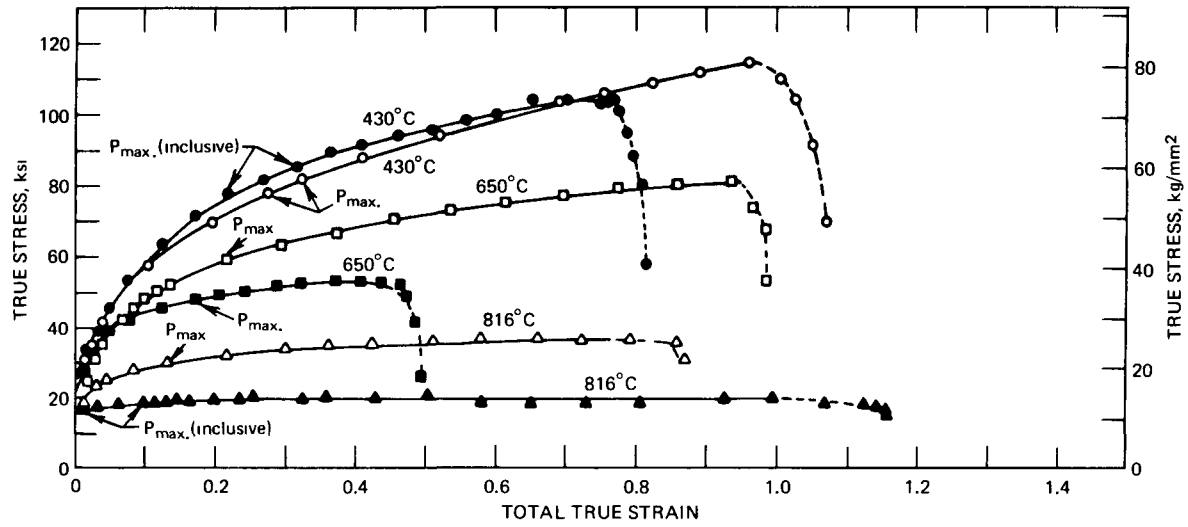

	Temp., °C	Axial true strain rate, sec^{-1}	Spec. No.	Measured reduction in area (hot), %	Reduction in area (cold), %	Measured tensile ductility (hot)	Tensile ductility (cold)
○	430	4×10^{-3}	11-8	65.5	66.4	1.065	1.091
●	430	4×10^{-5}	11-5	55.6	57.5	0.812	0.856
□	650	4×10^{-3}	11-23	62.5	68.6	0.981	1.158
■	650	4×10^{-5}	11-3	39.0	40.4	0.494	0.518
△	816	4×10^{-3}	11-28	57.8	87.0	0.864	2.040
▲	816	4×10^{-5}	11-25	68.6	84.0	1.157	1.833

Fig. 7.12 True stress vs. true strain curves obtained from short-term tensile tests in air for annealed AISI 348 stainless steel at 430, 650, and 816°C and constant axial true strain rates of ~4×10^{-3} sec^{-1} and ~4×10^{-5} sec^{-1}.

values of 51.5% (304 stainless steel), 47.8% (316 stainless steel), 57.8% (348 stainless steel), and 68.6% (348 stainless steel) are not truly representative of material behavior. Experience in this type of testing suggests that the true stress–strain curves in such instances should extend to strain values close to those corresponding to the cold reduction in area.

Values for the tensile ductility (essentially the total true strain at fracture) tabulated on these true stress vs. true strain graphs differ slightly from the corresponding calculated total axial true-strain values at fracture shown in Tables 7.1 to 7.20. These slight differences stem from the two different equations used to calculate what is generally termed the total true strain (see Sample Calculation for procedure used in these calculations).

Engineering stress vs. engineering strain curves based on the data given in Tables 7.1 to 7.20 are shown in Figs. 7.13 to 7.15; these curves have the standard shape for this type of graph. As in the true stress vs. true strain graphs, the region near the fracture point has been shown dotted. Noticeable strain-rate effects are indicated in the tests of the materials at 650 and 816°C. In all cases at 430°C, these effects are not too significant.

True stress vs. plastic true strain (similar results were obtained using total true strain) graphs on logarithmic coordinates are presented in Figs. 7.16 to 7.18. In some cases these logarithmic graphs yielded definite linearity so that entire sets of test data could be represented in the usual power-function form by the equation $\sigma = K'\epsilon_p^m$. In many other cases the data in the region of low strain values define curves that are concave upward. Examples of this behavior are given by the data for 304 and 316 stainless steels tested at room temperature, all three materials at 430°C at both the 4×10^{-3} and 4×10^{-5} sec^{-1} strain rates, 304 stainless steel at 650°C at the 4×10^{-3} sec^{-1} strain rate, and 316 stainless steel at 650°C at both strain rates. Although these plots exhibited a definite curvature, the data in the high strain region suggested a linear relation. These data were subjected to a least-squares analysis to identify values of m and K′ in the expression cited above. These values are listed in the columns of data shown on each figure. Also shown are data points obtained near the fracture region, but, as mentioned earlier, these points should not be considered the actual true stress that really exists in this regime.

On the basis of a fairly standard derivation,[9] the strain-hardening exponent m from the logarithmic true stress vs. true strain graph is numerically equal to the true strain at the point of maximum load. In Figs. 7.16 to 7.18, the points of maximum load, $P_{max.}$, as well as the points

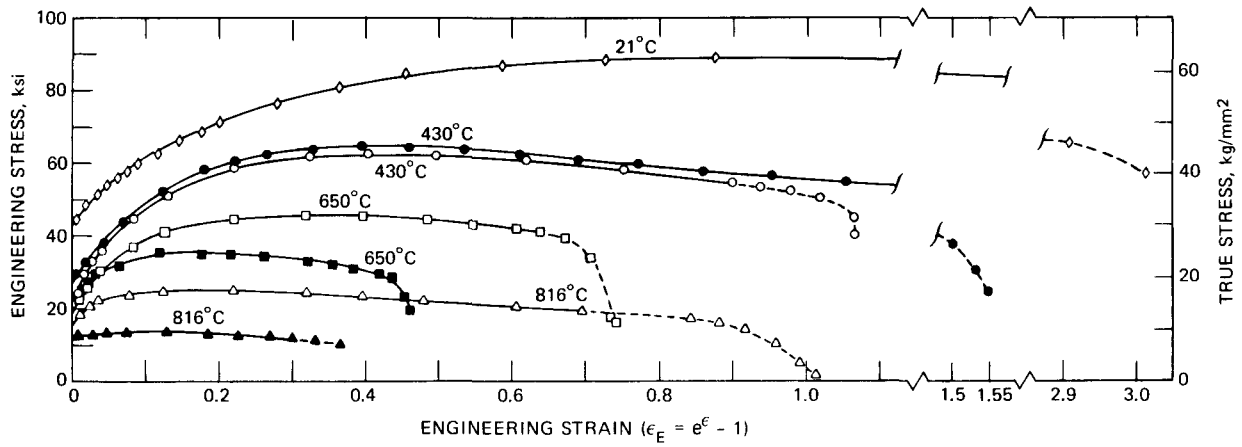

	Temp., °C	Axial true strain rate, sec^{-1}	Spec. No.	Measured reduction in area (hot), %	Reduction in area (cold), %	Measured tensile ductility (hot)	Tensile ductility (cold)
◇	21	4×10^{-3}	56-4	75.0	80.6	1.386	1.640
○	430	4×10^{-3}	53-3	51.5	64.0	0.724	1.022
●	430	4×10^{-5}	53-6	60.7	64.5	0.934	1.036
□	650	4×10^{-3}	53-1	42.6	42.2	0.555	0.548
■	650	4×10^{-5}	53-4	31.6	33.4	0.380	0.406
△	816	4×10^{-3}	53-2	50.4	51.0	0.701	0.713
▲	816	4×10^{-5}	53-5	26.8	32.1	0.312	0.387

Fig. 7.13 Engineering stress vs. engineering strain curves obtained from short-term tensile tests in air for annealed AISI 304 stainless steel at 21, 430, 650, and 816°C and constant axial true strain rates of ~4×10^{-3} sec^{-1} and ~4×10^{-5} sec^{-1}.

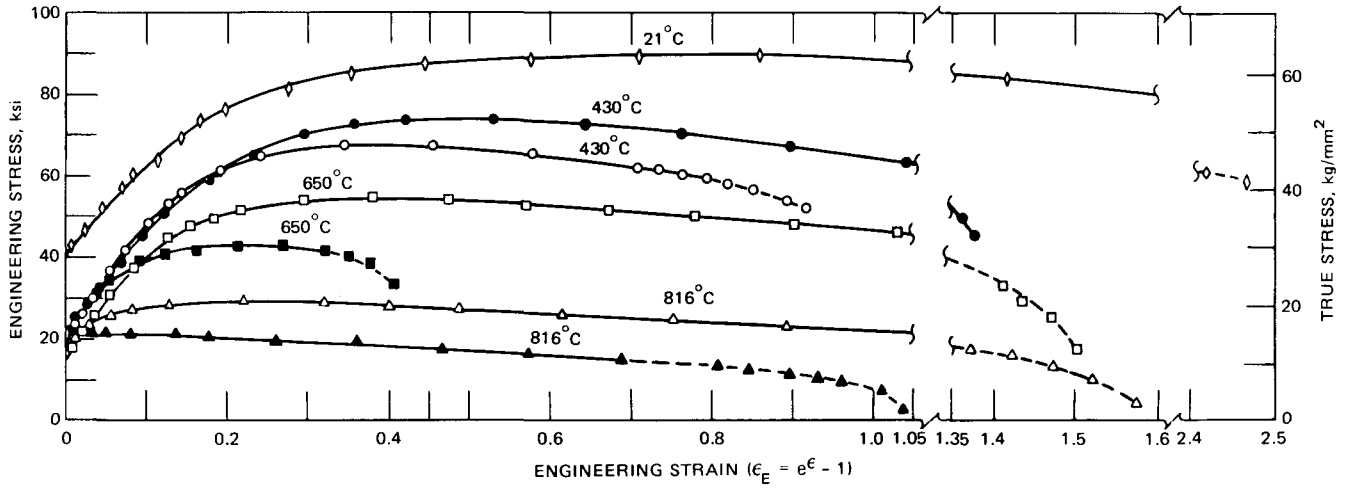

	Temp., °C	Axial true strain rate, sec^{-1}	Spec. No.	Measured reduction in area (hot), %	Reduction in area (cold), %	Measured tensile ductility (hot)	Tensile ductility (cold)
◇	21	4×10^{-3}	9-4	71.1	74.6	1.240	1.370
○	430	4×10^{-3}	9-6	47.8	62.1	0.649	0.970
●	430	4×10^{-5}	9-7	57.8	60.6	0.864	0.931
□	650	4×10^{-3}	19-4	60.0	61.1	0.917	0.944
■	650	4×10^{-5}	7-26	32.2	32.1	0.389	0.387
△	816	4×10^{-3}	9-5	61.2	61.6	0.947	0.957
▲	816	4×10^{-5}	7-23	50.9	49.9	0.712	0.691

Fig. 7.14 Engineering stress vs. engineering strain curves obtained from short-term tensile tests in air for annealed AISI 316 stainless steel at 21, 430, 650, and 816°C and constant axial true strain rates of ~4×10^{-3} sec^{-1} and ~4×10^{-5} sec^{-1}.

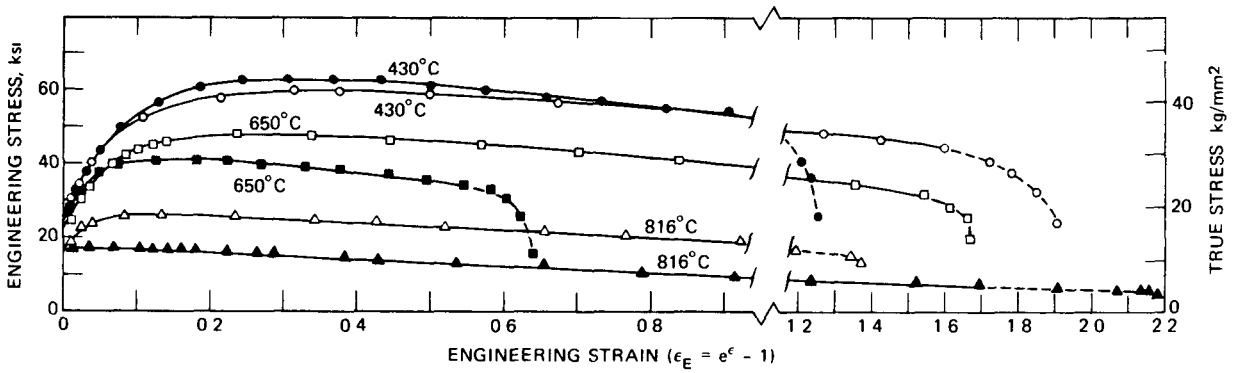

	Temp., °C	Axial true strain rate, sec $^{-1}$	Spec. No.	Measured reduction in area (hot), %	Reduction in area (cold), %	Measured tensile ductility (hot)	Tensile ductility (cold)
○	430	4×10^{-3}	11-8	65.5	66.4	1.065	1.091
●	430	4×10^{-5}	11-5	55.6	57.5	0.812	0 856
□	650	4×10^{-3}	11-23	62 5	68.6	0 981	1 158
■	650	4×10^{-5}	11-3	39 0	40 4	0 494	0.518
△	816	4×10^{-3}	11-28	57.8	87.0	0.864	2 040
▲	816	4×10^{-5}	11-25	68.6	84.0	1.157	1.833

Fig. 7.15 Engineering stress vs. engineering strain curves obtained from short term tensile tests in air for annealed AISI 348 stainless steel at 430, 650, and 816°C and constant axial true strain rates of ~4 x 10 $^{-3}$ sec $^{-1}$ and ~4 x 10 $^{-5}$ sec $^{-1}$

$>0\ 98P_{max}$, have been indicated, and the equivalency, ϵ_p (at maximum load) - m, is generally followed. The only three exceptions in the 20 short-term tensile tests are for the 316 stainless steel at 430°C at the 4×10^{-3} sec^{-1} strain rate and 650°C at both the 4×10^{-3} and 4×10^{-5} sec^{-1} strain rates. The particular test at 430°C was one of those instances in which a fairly wide discrepancy was observed between the hot and cold reductions in area. As mentioned earlier, this leads to a stress–strain plot that is not completely representative in the terminal region of the flow curve and could account for the deviation from the above-mentioned equivalency. No explanation is available for the data at 650°C and 4×10^{-3} sec^{-1} strain rate, however, the equivalency nearly holds since, when $\epsilon_p = m$, the load is $0\ 95P_{max}$ The case at 650°C at the 4×10^{-5} sec^{-1} strain rate is somewhat similar because the load is $0.94P_{max.}$, however, the material exhibited low ductility at this test condition and thus the total plastic strain at the fracture point was not appreciably greater than the numerical value of m for the data.

In accordance with the discussion presented in Chap. 6, the tensile data for 304 stainless steel obtained at 21°C and a strain rate of 4×10^{-3} sec^{-1} were used to yield the constructions presented in Fig 7.19. The tangent drawn from an engineering strain value of minus unity does indeed contact the true stress vs. engineering strain curve at the maximum load point. This tangent intersects the ordinate scale at zero strain to define an ultimate strength value of 89,000 psi. This latter value is identical to that reported in Table 7.21 for this material at these same conditions. In the true stress vs. true strain graph,[10] a tangent to the curve, drawn so that the length of the subtangent along the strain axis is unity, will define the maximum load point The experimental value of maximum load is in accord with this construction. This constructional relation of the true stress–strain curve means that the point of maximum load occurs at a value of strain where the slope of the curve equals the true stress.

Since in many instances the logarithmic plot of true stress vs total true strain behavior did not yield a linear relation, the use of the power function in describing such data was obviously not completely warranted A fairly detailed study was thus initiated to evaluate how effective the Voce equation would be in representing these results. A least-squares nonlinear regression analysis was used* to enable the Voce-equation constants to be calculated for each set of stress–strain data. For the data obtained in a test of 304 stainless steel in air at 430°C and a strain rate of 4×10^{-5} sec^{-1}, the Voce constants were

$$\sigma_\infty = 120{,}931 \text{ psi}$$
$$\sigma_0 = 27{,}623\ 4 \text{ psi}$$

and

$$\epsilon_c = 0.30508$$

*Computer program written by L H. Sjodahl, Technical Engineer, General Electric Company, Aircraft Engine Group, Evendale, Ohio.

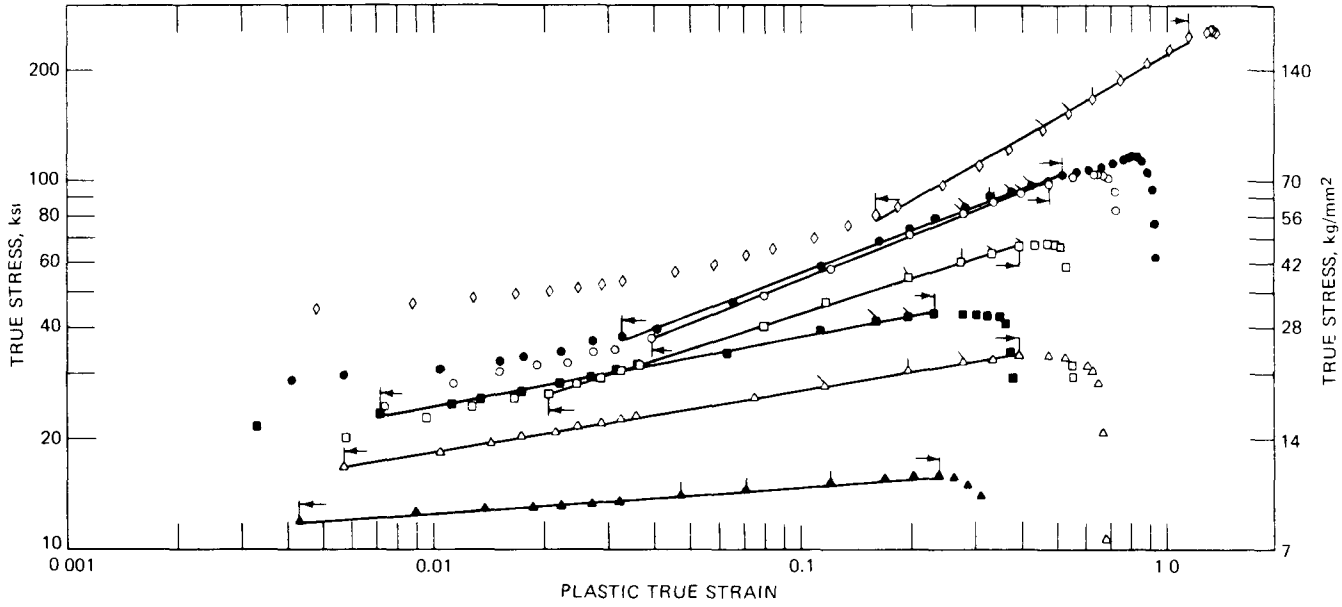

	Temp., °C	Axial true strain rate, sec^{-1}	Spec. No.	Measured reduction in area (hot), %	Reduction in area (cold), %	Measured tensile ductility (hot)	Tensile ductility (cold)	$\sigma = K'\epsilon_p^m$ K'	m
▽	21	4×10^{-3}	56-4	75.0	80.6	1.386	1.640	221.0	0.568
◦	430	4×10^{-3}	53-3	51.5	64.0	0.724	1.022	133.3	0.392
●	430	4×10^{-5}	53-6	60.7	64.5	0.934	1.036	134.5	0.376
□	650	4×10^{-3}	53-1	42.6	42.2	0.555	0.548	90.1	0.315
■	650	4×10^{-5}	53-4	31.6	33.4	0.380	0.406	57.9	0.186
△	816	4×10^{-3}	53-2	50.4	51.0	0.701	0.713	39.7	0.166
▲	816	4×10^{-5}	53-5	26.8	32.1	0.312	0.387	17.5	0.072

, , , etc., $P_{max.}$, , , etc , >0.98 $P_{max.}$

Fig. 7.16 True stress vs. plastic true strain curves for annealed AISI 304 stainless steel tested in air at 21, 430, 650, and 816°C and constant axial true strain rates of ~4×10^{-3} sec^{-1} and ~4×10^{-5} sec^{-1}. Linear segments represent a least-squares line based on the data in the range defined by the symbols with arrowhead marks.

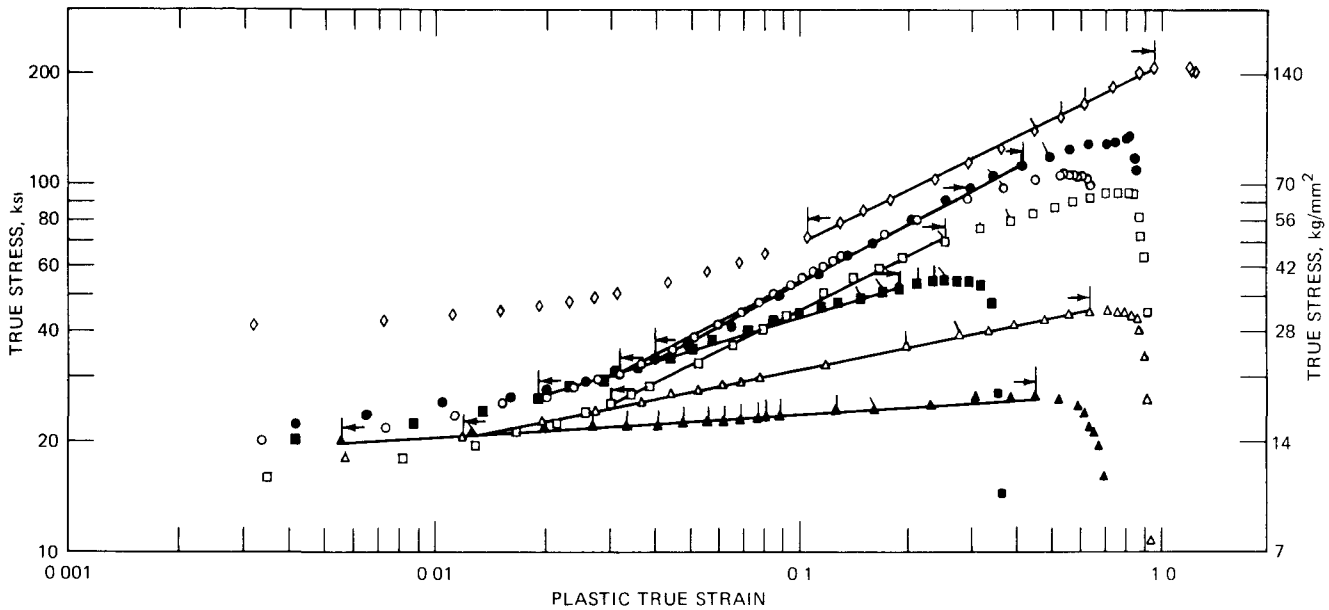

	Temp., °C	Axial true strain rate, sec^{-1}	Spec. No.	Measured reduction in area (hot), %	Reduction in area (cold), %	Measured tensile ductility (hot)	Tensile ductility (cold)	$\sigma = K'\epsilon_p^m$ K	m
◇	21	4×10^{-3}	9-4	71.1	74.6	1.240	1.370	211.4	0.485
○	430	4×10^{-3}	9-6	47.8	62.1	0.649	0.970	175.4	0.505
●	430	4×10^{-5}	9-7	57.8	60.6	0.864	0.931	183.3	0.531
□	650	4×10^{-3}	19-4	60.0	61.1	0.917	0.944	141.7	0.493
■	650	4×10^{-5}	7-26	32.2	32.1	0.389	0.387	87.0	0.299
△	816	4×10^{-3}	9-5	61.2	61.6	0.947	0.957	49.7	0.200
▲	816	4×10^{-5}	7-23	50.9	49.9	0.712	0.691	27.5	0.064

◇, ○, ●, △, etc., P_{max} ◇, ○, ●, △, etc., >0.98 P_{max}

Fig. 7.17 True stress vs. plastic true strain curves for annealed AISI 316 stainless steel tested in air at 21, 430, 650, and 816°C and constant axial true strain rates of $\sim 4 \times 10^{-3}$ sec^{-1} and $\sim 4 \times 10^{-5}$ sec^{-1}. Linear segments represent a least-squares line based on the data in the range defined by the symbols with arrowhead marks.

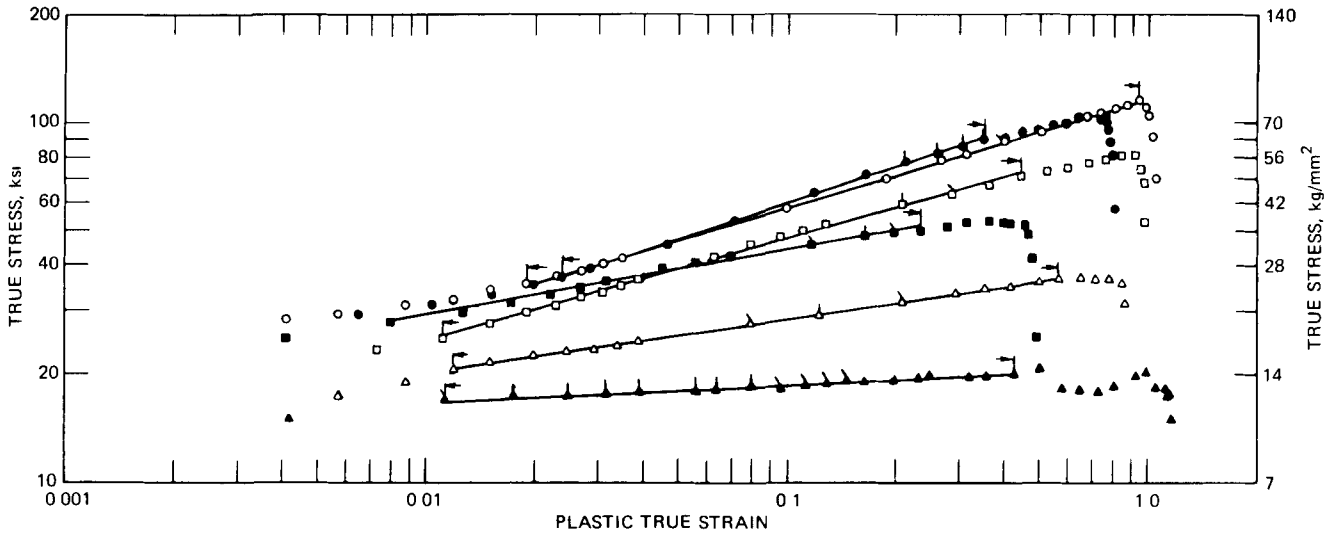

	Temp., °C	Axial true strain rate, sec^{-1}	Spec. No.	Measured reduction in area (hot), %	Reduction in area (cold), %	Measured tensile ductility (hot)	Tensile ductility (cold)	$\sigma = K'\epsilon_p^m$ K'	m
○	430	4×10^{-3}	11-8	65.5	66.4	1.065	1.091	116.0	0.302
●	430	4×10^{-5}	11-5	55.6	57.5	0.812	0.856	127.7	0.331
□	650	4×10^{-3}	11-23	62.5	68.6	0.981	1.158	91.0	0.281
■	650	4×10^{-5}	11-3	39.0	40.4	0.494	0.518	67.2	0.180
/	816	4×10^{-3}	11-28	57.8	87.0	0.864	2.040	39.9	0.147
▲	816	4×10^{-5}	11-25	68.6	84.0	1.157	1.833	20.9	0.049

◇, ○, ●, △, etc , P_{max} ◇, ○, ●, △, etc , >0 98 P_{max}

Fig. 7.18 True stress vs. plastic true strain curves for annealed AISI 348 stainless steel tested in air at 430, 650, and 816°C and constant axial true strain rates of ~4×10^{-3} sec^{-1} and ~4×10^{-5} sec^{-1} Linear segments represent a least-squares line based on the data in the range defined by the symbols with arrowhead marks.

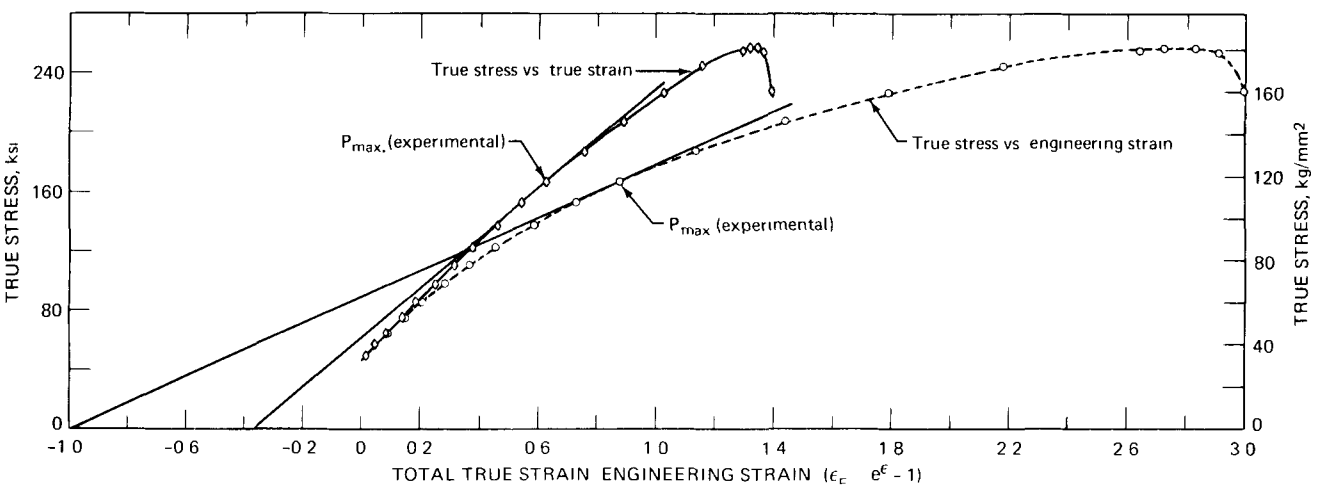

Fig. 7.19 Two graphical constructions illustrating analysis of the short-term tensile data for annealed AISI 304 stainless steel obtained at 21°C and a strain rate of 4×10^{-3} sec^{-1} in air.

These constants were used in conjunction with the Voce equation to yield the calculated curve shown in Fig. 7.20. Fairly good agreement with the experimental data points is indicated. A rectangular graph of these same data is also presented in Fig. 7.20. Although the agreement seems once again to be fairly good, the analysis indicated that the effectiveness of the Voce equation tended to decrease in the region of low strain values. This seems to be a recognized defect in the Voce equation and was acknowledged in the original discussions introducing this expression. Other plots of the Voce equation are shown in Fig. 7.21, and once again fairly good representations are indicated, except in the region involving small strains. Apparently an expression that will furnish an accurate description in the strain-hardening regime cannot yield an equally effective representation in the area of the elastic–plastic fillet.[11] A summary of all the Voce-equation constants obtained in the analyses performed in this program is presented in Table 7.23. In the column entitled "Regression Parameters," the effectiveness of the Voce equation in representing the true stress–strain behavior is indicated. Values of the "standard error of estimate" are defined as

$$\left[\sum_{i} (\sigma_i - \sigma_{c,i})^2/(N-3)\right]^{1/2}$$

where the quantity $(\sigma_i - \sigma_{c,i})$ is known as the residual, σ_i is

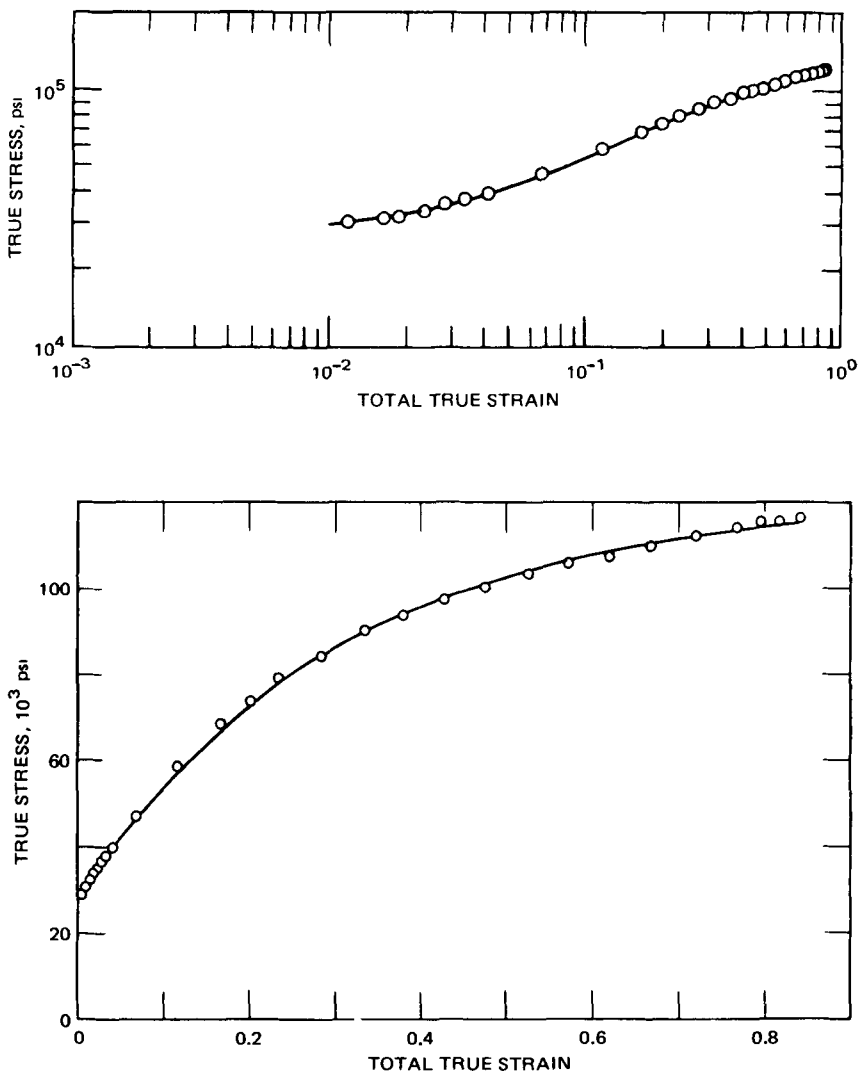

Fig. 7.20 Voce equation used to represent the true stress–strain data for annealed AISI 304 stainless steel tested in air at 430°C and a strain rate of 4×10^{-5} sec^{-1}. Voce equation: $\sigma = \sigma_\infty - (\sigma_\infty - \sigma_0) \exp(-\epsilon/\epsilon_c)$. σ_∞ = 120931 psi, σ_0 - 27623.4 psi, and ϵ_c = 0.30508. ○, experimental; —, calculated.

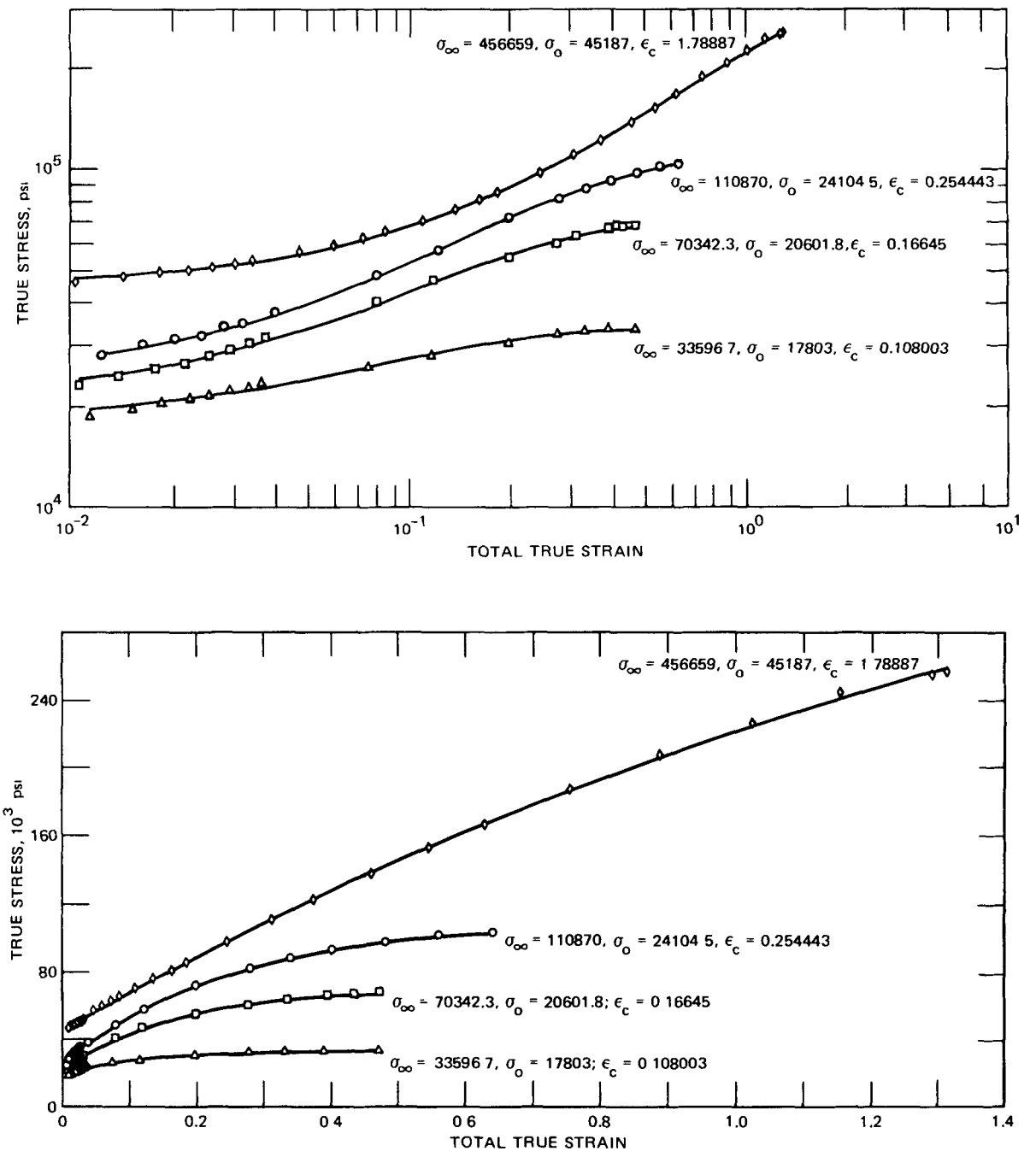

Fig. 7.21 Voce equation used to represent the true stress–strain data for annealed AISI 304 stainless steel tested in air at several temperatures and a strain rate of 4×10^{-3} sec^{-1}. Experimental data are fitted to the Voce equation: $\sigma = \sigma_\infty - (\sigma_\infty - \sigma_0)\exp(-\epsilon/\epsilon_c)$. ◇, 21°C; ○, 430°C; □, 650°C; △, 816°C.

the experimental stress, $\sigma_{c,i}$ is the calculated stress, and N is the number of experimental points.

This value is minimized by the least-squares procedure for the mathematical model used, and, when the value is compared with the average, it indicates the amount of scatter in the experimental data. The correlation coefficient is related to the fractional amount of variance in stress which is removed by fitting the equation. The closer this value is to 1, the more nearly perfect is the fit to the experimental data. Finally, the "student t value" indicates the deviation from randomness of the residuals. If only random error remained after the fit to the equation, the signs of the residuals would follow a pattern whose general nature is predictable. An expected value for the number of changes in sign and its standard deviation can be calculated on this assumption. The difference between this calculated

TABLE 7.23

SUMMARY OF VOCE-EQUATION CONSTANTS FOR ANNEALED AISI 304, 316, AND 348 STAINLESS STEELS TESTED IN AIR

Mat'l	Spec. No.	Temp., °C	Range of strain values		Total axial true strain rate, sec^{-1}	Voce constants			Regression parameters		
			Minimum value	Maximum value		Threshold stress, psi	Asymptotic stress, psi	Characteristic strain	Standard error of estimate, psi	Correlation coefficient	Student t value
304	56-4	21	0.01039	1.31511	4×10^{-3}	45187	456659	1.78887	1243.83	0.999862	3.6
	53-3	430	0.00841	0.64229	4×10^{-3}	24105	110870	0.25444	861.10	0.999636	0
	53-6	430	0.00530	0.84252	4×10^{-5}	27623	120931	0.30508	851.95	0.999701	3.6
	53-1	650	0.01069	0.47442	4×10^{-3}	20602	70342	0.16645	561.83	0.999558	2.5
	53.4	650	0.00832	0.30504	4×10^{-5}	21269	43878	0.06818	555.94	0.997774	1.3
	53-2	816	0.01141	0.47411	4×10^{-3}	17803	33597	0.10800	531.03	0.996144	2.0
	53-5	816	0.00972	0.24031	4×10^{-5}	12128	15880	0.07308	91.80	0.997558	0
316	9-4	21	0.00860	0.97187	4×10^{-3}	41910	289791	0.86733	1691.86	0.999553	3.6
	9-6	430	0.00830	0.55124	4×10^{-3}	17209	113753	0.20717	544.48	0.999813	4.0
	9-7	430	0.00753	0.83539	4×10^{-5}	19095	142265	0.30534	1123.77	0.999670	3.6
	19-4	650	0.00900	0.77356	4×10^{-3}	15086	95680	0.22156	1061.11	0.999316	4.5
	7-26	650	0.00987	0.25697	4×10^{-5}	18807	56258	0.08926	430.17	0.999266	2.5
	9-5	816	0.01305	0.72070	4×10^{-3}	20748	45077	0.18928	852.59	0.995408	3.0
	7-23	816	0.01386	0.30835	4×10^{-5}	21015	27750	0.22688	146.05	0.994753	1.5
348	11-8	430	0.00691	0.95569	4×10^{-3}	30610	116854	0.34416	2325.71	0.997657	3.5
	11-5	430	0.00771	0.64561	4×10^{-5}	28177	103351	0.20402	1540.22	0.998548	3.5
	11-23	650	0.01236	0.93427	4×10^{-3}	25666	78957	0.20693	2134.64	0.994545	3.2
	11-3	650	0.00924	0.36691	4×10^{-5}	25439	51991	0.07041	941.13	0.994602	2.5
	11-28	816	0.00980	0.65368	4×10^{-3}	19819	36295	0.14376	814.66	0.992588	2.5
	11-25	816	0.01214	0.50402	4×10^{-5}	16897	20564	0.17546	227.49	0.979933	1.5

number of sign changes and the observed number of sign changes, divided by the calculated standard deviation, can be interpreted as a student t value. If this value is greater than about 2, it indicates with 95% confidence that the observed number of changes of sign was not totally due to random error. In other words, a value greater than 2 indicates an imperfect mathematical model for the curve fit.

Examination of the student t values of the data sets summarized in Table 7.23 shows that more than 60% of the data sets analyzed have a student t value greater than 2. This indicates that the mathematical model used in the analysis does not exactly explain the functional relation underlying the experimental data. Thus selected data sets were chosen for their apparent poor fits to the Voce equation. These data sets were reanalyzed excluding the low strain points. The results of this second analysis, summarized in Table 7.24, show acceptable student t values in all cases. A comparison of the results summarized in these two tables shows that, in general, the Voce equation fits the experimental data much better if only those strains well above the transition region between the elastic and the plastic modes of strain are used in the analysis.

Some consideration was given to the use of the generalized strain concept to provide a representation of these same stress–strain data. However, as mentioned in the discussion on Table 6.10 in Chap. 6, this approach yields results identical to those obtained in the analyses based on the Voce equation. For this reason, no detailed analyses were made in which the effectiveness of the generalized strain concept was studied. For the few sets of data that were analyzed, the conclusions highlighted in Table 7.1 were further confirmed. In other words, the Voce equation and the generalized strain concept are, indeed, identical. Also, it was shown that linearity does result when the generalized strain concept is used, but only when the first few data points in the region of the elastic–plastic fillet are excluded from the analysis.

A fairly detailed analysis of the usefulness of the hyperbolic-sine equation (Chap. 6, Eq. 6.44) in describing stress–strain behavior indicated only average effectiveness. Average effectiveness was also noted in a study of the modified power function (Ludwik equation) given in Chap. 6, as Eq. 6.A in the footnote involving Eq. 6.46. Examples of how well these relations describe true stress–strain behavior were provided in the analysis of the data for 304 stainless steel. Table 7.25 summarizes the equation constants (identified in nonlinear regression analyses) associated with these expressions, which were used to provide the graphical comparison shown in Fig. 7.22. Also shown in Fig. 7.22 and in Table 7.26 is a comparison of the effectiveness of the Voce equation, hyperbolic-sine equation, and modified power function. On the basis of the standard deviations and correlation coefficients listed in Table 7.26 and the

TABLE 7.24

SUMMARY OF VOCE-EQUATION CONSTANTS BASED ON SELECTED DATA POINTS FROM STRESS–STRAIN MEASUREMENTS FOR 304, 316, AND 348 STAINLESS STEELS

Mat'l	Spec. No.	Temp., °C	Range of strain values		Total axial true strain rate, sec^{-1}	Voce constants			Regression parameters		
			Minimum value	Maximum value		Threshold stress, psi	Asymptotic stress, psi	Characteristic strain	Standard error of estimate, psi	Correlation coefficient	Student t value
304	56-4	21	0.07352	1.15650	4×10^{-3}	46633	546413	2.29089	268.03	0.999991	−1.0
	53-6	430	0.11716	0.52543	4×10^{-5}	28345	115955	0.27744	302.11	0.999837	−1.3
316	9-6	430	0.07102	0.55124	4×10^{-3}	15350	112527	0.19620	182.75	0.999971	1.0
	19-4	650	0.15493	0.88288	4×10^{-3}	53553	396191	1.54618	645.37	0.999898	0
348	11-8	430	0.19286	0.88649	4×10^{-3}	49238	133904	0.66832	591.98	0.999415	0.7
	11-23	650	0.11480	0.77328	4×10^{-3}	39180	85476	0.40003	392.67	0.999426	0

TABLE 7.25

CONSTANTS FOR USE WITH HYPERBOLIC-SINE AND MODIFIED POWER-FUNCTION EQUATIONS APPLIED TO ANALYSIS OF TRUE STRESS–STRAIN DATA FOR AISI 304 STAINLESS STEEL*

Temp., °C	$\epsilon = \epsilon_0 + b \sinh(\sigma/\sigma_c)$			$\sigma = \sigma_0 + K\epsilon^m$		
	ϵ_0	b	σ_c	σ_0	K	m
21	−0.1998	0.8276	190000	40300	179000	0.7882
430	−0.0273	0.0424	30500	3350	12400	0.3846
650	−0.0138	0.0151	16400	−2800	89000	0.2863
816	0.0103	0.0001	3800	−88600	126000	0.0375

*Tested in air at a strain rate of 4×10^{-3} sec^{-3} (stress is in pounds per square inch).

comparison graph in Fig. 7.22, the Voce equation, in general, yields the best representation. Both the hyperbolic-sine and modified-power-function equations seem to be equally effective but are definitely inferior to the Voce equation.

Neither the hyperbolic-sine equation nor the modified power function exhibits a logarithmic true stress–strain curve that asymptotically approaches a maximum stress at high strain values. However, the Voce equation does exhibit this phenomenon, as previously discussed. Thus it is concluded that, of all the available expressions, the most effective representation of true stress–strain behavior is afforded by the Voce equation. Although this relation has certain deficiencies in the region of the transition from elastic to plastic behavior (i.e., at low strain values), this same criticism also applies to the hyperbolic-sine equation and the modified power function.

Some status has been achieved by the Ramberg–Osgood equation (Chap. 6) in describing stress–strain behavior. A brief analysis of this relation using the tensile data for 304 stainless steel at room temperature, 430, 650, and 816°C indicated an effectiveness similar to that associated with the hyperbolic-sine equation and the modified power function. The Ramberg–Osgood equation is definitely less effective than the Voce equation.

STRAIN RATE AND TEMPERATURE EFFECTS

Although short-term tensile behavior has been studied extensively, many problem areas still exist in this important phase of material technology. Yield strength and tensile strength are known to be functions of temperature, strain rate, and the extent and type of prior heat-treatment, and yet a detailed understanding of these effects has not been acquired. Other factors[12] that add to the complexity of the issue include strain aging, recovery, and recrystallization, although these may or may not be important, depending on the material and the test conditions. Clearly, many factors can influence short-term tensile behavior, and a careful assessment of such behavior should be based on a proper evaluation of these important influences.

In a recent review and summarization[13] of available short-term tensile data for several stainless steels, the effects of temperature and material form were highlighted. In general, the graphs showing the effect of temperature on

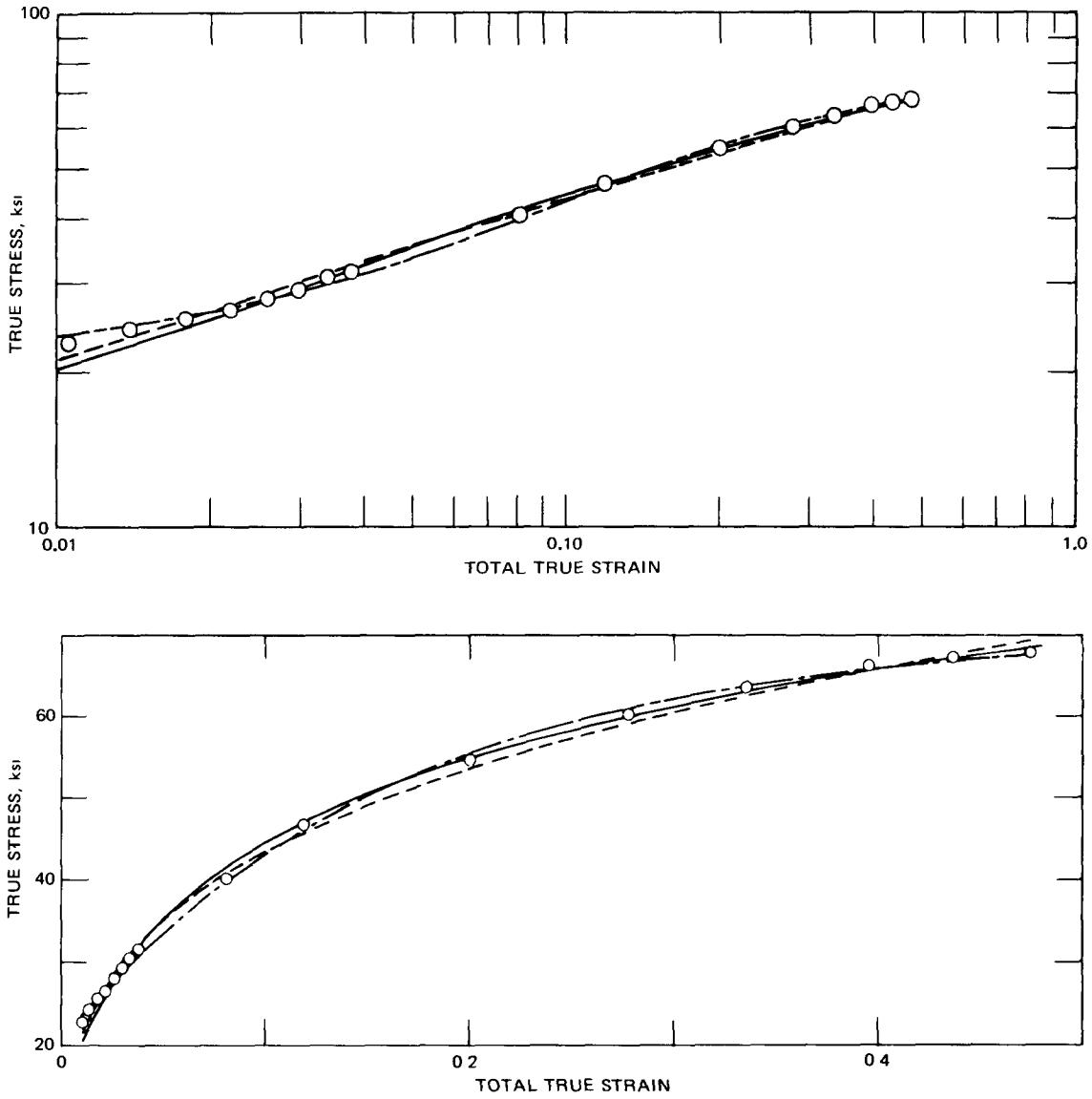

Fig. 7.22 Short-term tensile-test results for AISI 304 stainless steel tested at 650°C in air at a strain rate of 4×10^{-3} sec^{-1}. —, hyperbolic sine. - - - -, modified power function. — — —, Voce equation.

TABLE 7.26

COMPARISON OF THE EFFECTIVENESS OF THE VOCE EQUATION, HYPERBOLIC-SINE EQUATION, AND MODIFIED POWER-FUNCTION EQUATION IN REPRESENTING THE TRUE STRESS–STRAIN DATA FOR AISI 304 STAINLESS STEEL*

	Standard deviation			Correlation coefficient			Stress at zero strain		
Temp., °C	Voce	Mod. power function	Sinh†	Voce	Mod. power function	Sinh	Voce	Mod. power function	Sinh
21	1244	2481	1262	0 9999	0 9995	0 9998	41587	40275	45396
430	861	1986	1704	0 9996	0 9981	0 9987	24105	3349	18492
650	562	966	1020	0 9996	0 9987	0 9989	20602	−2854	13473
816	531	264	2301	0 9961	0 9998	0 9944	17803	−88631	−19639

*Tested in air at a strain rate of 4×10^{-3} sec^{-1} (stress is in pounds per square inch)

†Calculated from analysis that minimized the sum of the squares of the residuals of ϵ, best value would be somewhat smaller

tensile strength and yield strength were quite similar for the different stainless steels involved, and the shape of these curves was essentially the same as that shown in Figs. 7.7 and 7.8. Data were also presented to show the differences encountered using specimens from plate, bar, and pipe material. Special emphasis was given to individual data points to show the amount of scatter involved in tests of a given type of steel. Much more scatter was found to exist in the yield-strength measurements, and in some cases the high-to-low ratio of yield-strength values at a given temperature was close to a value of 2. And it is important to note that this wide variation was even noted in the room-temperature data. For tensile-strength data the range of measured values was not as great, but the high-to-low ratio was still fairly large and approached 1.5 in many instances. This pronounced variability in the test data is, no doubt, caused by some of the effects mentioned above and serves to emphasize the magnitude of the problem associated with the generation of reproducible tensile properties.

In a very excellent review of the effect of temperature and strain rate on the short-term tensile properties of various steels, titanium alloys, and aluminum alloys, Voorhees[12] offered the generalization that "for a reasonably broad sampling of steels, many tested at temperatures other than ambient, the lower yield stress (or the 0.2% offset yield strength) dropped roughly 2000 psi for each 10-fold decrease in testing rate (strain rate)." However, "the tensile strength of steels displayed such diverse response to differing strain rates (from 5770 psi drop to 12,770 psi rise for a 10-fold increase in testing rate) to preclude satisfactory engineering prediction of expected behavior in a particular case starting only with a general body of data." Despite these generalizations, Voorhees clearly pointed out that opposite behavior patterns have been reported. For example, the work of Manjoine[14] on a mild steel was cited to show material response as affected by strain aging, recovery, and recrystallization. At room temperature and a strain rate of 9.5×10^{-7} sec^{-1}, the ultimate strength was higher than that observed using a strain rate of 8.5×10^{-4} sec^{-1}. This was attributed to strain-aging effects. At 200°C a similar pattern was observed and again was attributed to strain aging. At 400 and 600°C the strain-aging effects were offset by recovery and/or recrystallization, and the tensile strength was found to increase as the strain rate increased.

An analysis of the data in Table 7.22 has led to some rather interesting observations. The effect of strain rate on tensile strength is shown in Fig. 7.23 to identify a trend that is quite similar to that noted in the Manjoine[14] study. At the two highest temperatures (650 and 816°C), a definite increase in tensile strength is noted as the strain rate is increased. And this effect seems almost identical for the three different stainless steels. At 430°C a small decrease with increasing strain rate is noted, and again this is almost identical for the three materials. Such behavior would suggest a temperature just slightly above 430°C, where there is no effect of strain rate on the tensile strength

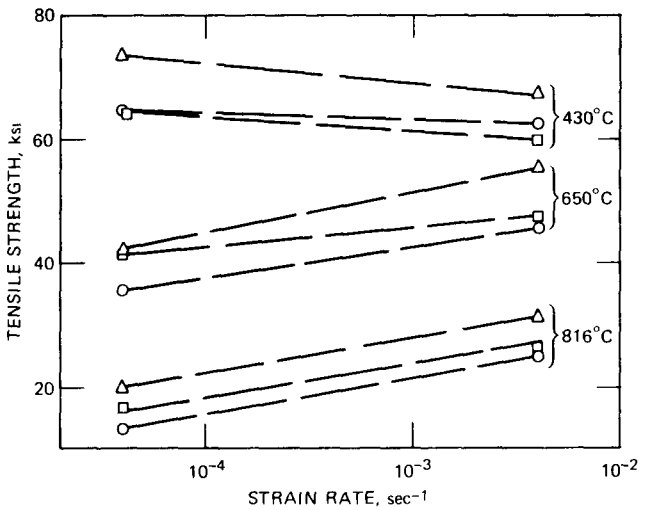

Fig. 7.23 Effect of strain rate on tensile strength.[1] ○, 304 stainless steel. △, 316 stainless steel. □, 348 stainless steel.

for the range of test conditions involved in this study. At 816°C the tensile strength increases about 5500 psi for a 10-fold increase in strain rate; this increase is about 4500 psi at 650°C, and at 430°C a decrease of about 2500 psi is noted. A point is being made of these magnitudes since the Voorhees summary reported very similar behavior for a stainless steel (see data for Steel A in Myers[15] as cited in the Voorhees summary) in the 650 to 800°C temperature range.

REFERENCES

1. J. B. Conway, J. T. Berling, R. H. Stentz, and D. G. Salyards, Stress–Strain Behavior of Several Stainless Steels to Elevated Temperatures, USAEC Report GEMP-686, General Electric Company, May 1969.
2. Aerospace Structural Metals Handbook, Ferrous Alloys, Vol. 1, Report ASD-TDR-63-741, Air Force Materials Laboratory, March 1963.
3. W. F. Simmons and J. A. VanEcho, *The Elevated-Temperature Properties of Stainless Steels,* American Society for Testing and Materials, Data Series No. 5-S1, 1965.
4. C. W. MacGregor, Relation Between Stress and Reduction in Area for Tensile Tests of Metals, *Trans. Met. Soc. AIME,* 124: 208 (1937).
5. M. Gensamer, E. B Pearsall, W. S. Pellini, and J R. Low, Jr., The Tensile Properties of Pearlite, Bainite, and Spheroidite, *Trans. Amer. Soc. Metals,* 30: 983-1020 (1942).
6. M. Gensamer, E. B. Pearsall, and G. V. Smith, The Mechanical Properties of the Isothermal Decomposition Products of Austenite, *Trans. Amer. Soc. Metals,* 28: 390-398 (1940).
7. J. H. Hollomon, Effect of Heat-Treatment and Carbon Content on the Work-Hardening Characteristics of Several Steels, *Trans. Amer. Soc. Metals,* 32: 123-133 (1944).
8. P. J. Wray and O. Richmond, Experimental Approach to a Theory of Plasticity at Elevated Temperatures, *J. Appl. Phys.,* 39(12). 5754 (1968).
9. G. E. Dieter, Jr., *Mechanical Metallurgy,* McGraw-Hill Book Company, Inc., New York, 1961.
10. W. Johnson and P. B. Mellor, *Plasticity for Mechanical Engineers,* D. Van Nostrand Company, Inc., Princeton, N. J., 1962.

11. E Voce, A Practical Strain-Hardening Function, *Metallurgia*, 51: 219 (1955).
12 H. R. Voorhees, A Survey of Effects of Lower-Than-Usual Rates of Strain on the Yield and Tensile Strengths of Metals, American Society for Testing and Materials, Data Series No. 44, 1969.
13. G. V. Smith, An Evaluation of the Yield, Tensile, Creep, and Rupture Strengths of Wrought 304, 316, 321, and 347 Stainless Steels at Elevated Temperatures, American Society for Testing and Materials, Data Series No. 5-S2, 1969.
14. M Manjoine, Influence of Rate of Strain and Temperature on Yield Stresses in Mild Steel, *Trans. ASME (Amer. Soc. Mech. Eng.) Ser. A, J. Eng. Power*, 66 211 (December 1944).
15. J. Myers, Hot Ductility of Three Austenitic Steels, *Brit. Weld. J.*, 9: 106 (March 1962).

Chapter 8

RELAXATION BEHAVIOR

In Chap. 3 the effects of a hold period at peak strain on the cyclic-fatigue life were described in some detail. It was pointed out that throughout the hold period the total strain was maintained constant and that this resulted in a continuously decreasing stress. This type of stress–time behavior involves a stress-relaxation effect and is characteristic of strain-controlled fatigue tests using hold periods. Such testing has not been extensive, and hence this type of relaxation has not been investigated in great detail. It was felt advisable, therefore, to devote this section to the relaxation behavior observed in fatigue testing and to relate this to the more familiar relaxation effects noted in simple tensile loadings. This has been done by reviewing the basic principles of relaxation with special emphasis on the mathematical formulations that describe the stress–time behavior. It was also felt desirable to include a detailed discussion of the interrelation between creep and relaxation since this is an extremely important aspect of the subject of relaxation. And, finally, the relaxation behavior observed in some actual low-cycle-fatigue testing is described and analyzed to focus on the similarity with monotonic tensile relaxation behavior. A new stress-rate correlation is described which has shown some merit in analyzing the relaxation occurring in both fatigue and tensile loadings.

REVIEW OF RELAXATION IN SIMPLE TENSILE LOADINGS

Relaxation has been defined as the reduction in stress level in an elastically strained member as some of the initial elastic strain is converted to inelastic strain while the length of the member remains unchanged. Thus relaxation involves a gradual transformation of elastic to inelastic strain, with the stress decreasing to maintain the proper correspondence with the remaining elastic strain. This transformation of elastic to inelastic strain is a time-dependent process and one that is obviously related to creep. Also, relaxation and strength are related since relaxation does, indeed, provide a direct measure of the ability to resist deformation.

Relaxation behavior is shown schematically in Fig. 8.1. In this figure a specimen has been strained elastically to obtain the condition at point A; at this point the elastic strain is given by the initial stress divided by the modulus of elasticity. Now, if the specimen length and total strain

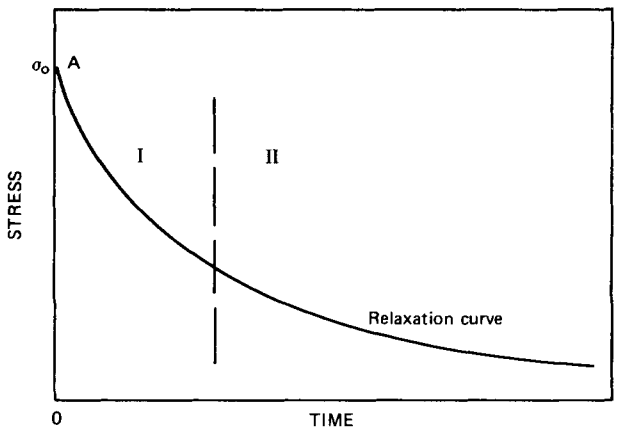

Fig. 8.1 Schematic for typical relaxation curve.

(considered to be all elastic in the initial loading) are maintained constant, the stress will decrease with time to provide the characteristic relaxation isotherm shown in Fig. 8.1.

A qualitative subdivision of the relaxation curve was offered by Oding[1] to accommodate two different sections. This separation is indicated in Fig. 8.1 by the dashed vertical line. In the first portion the behavior is characterized by an extremely rapid decrease in stress, whereas the stress reduction is rather slow in the second section of the relaxation process. Oding also emphasized that in the second section the relaxation curve asymptotically approached either zero stress or some limiting stress. There is no great amount of evidence to confirm the existence of two distinct stages within the relaxation process, even though it is difficult to dispute the large difference in stress rates which is known to be exhibited in every relaxation. Of course, this observation can be considered as being in complete accord with the large reduction in stress and need not of itself mean that the initial and final portions of the relaxation belong in two different stages of the relaxation process.

Oding gave special attention to the fact that available relaxation data seemed to indicate that beyond a certain time the quantity $(\sigma_0 - \sigma)$ was linear in σ_0. Such a behavior pattern is presented in Fig. 8.2 to indicate a slight curvature in the data corresponding to 1.5 hr and a definite

linearity for the 105- and 250-hr results. Oding also pointed out that the linear relations have different slopes and seem to have a focal point at a value of $(\sigma_0 - \sigma)$ equal to zero to define the relaxation limit σ_r. This limit was interpreted to be the maximum stress at which relaxation will not occur (more work must be done before this method of evaluating the relaxation limit can be accepted).

Oding claimed that the relaxation results for Cr–Mo–W steel published by Trumpler[2] confirmed the above approach. However, a separate analysis by Conway[3] failed to reach this same conclusion. A definite curvature was noted when the Trumpler[2] data were employed, and this only disappeared in the isochronous results for 100 hr. Apparently, therefore, little support for the Fig. 8.2-type correlation is offered by the Trumpler study. In the analysis by Conway,[3] a decided consistency with the Fig. 8.2 concept was provided by the data for a Cr–Mo–W steel at 850°F in tests by Boyd.[4] The results obtained in this analysis are shown in Fig. 8.3 to reveal well-defined linearities from 1 to 400 hr. Note also the fact that these lines have a common focal point to yield a relaxation limit of 5000 psi.

Oding provided mathematical form for the linear relation in Fig. 8.2 by first noting that the slope is given by

$$m = \frac{\Delta\sigma}{\sigma_0 - \sigma_r} = \frac{\sigma_0 - \sigma}{\sigma_0 - \sigma_r} \tag{8.1}$$

For a given value of σ_0 and a given time interval, the experimentally measured stress decrement was symbolized by $\Delta\sigma'$. Then the general equation for this specific time interval becomes

$$\Delta\sigma = \frac{\Delta\sigma'}{\sigma_0' - \sigma_r}(\sigma_0 - \sigma_r) \tag{8.2}$$

Since $\Delta\sigma = \sigma_0 - \sigma$, where σ is any relaxed stress value for the selected time period, it follows that

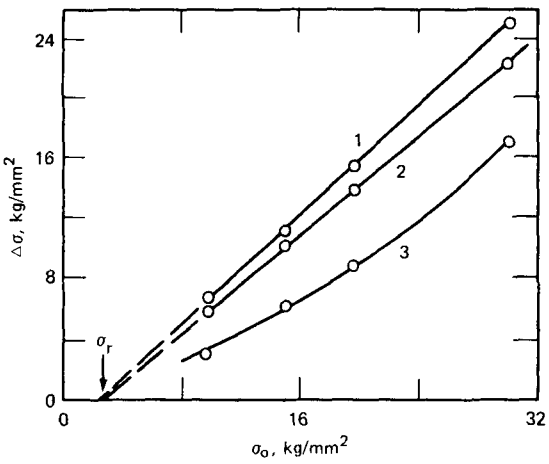

Fig. 8.2 Special correlation plot for relaxation data. 1, 250 hr; 2, 105 hr; 3, 1.5 hr. (From Ref. 1.)

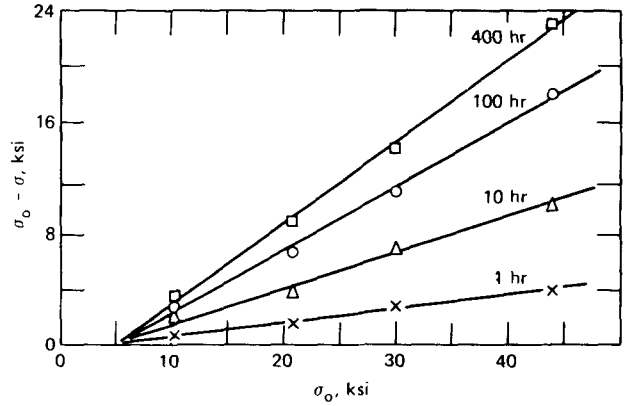

Fig. 8.3 Special correlation of some relaxation data for Cr–Mo–W steel obtained at 850° F. (From Ref. 4.)

$$\frac{\Delta\sigma}{\Delta\sigma'} = \frac{\sigma_0 - \sigma}{\sigma_0' - \sigma'} = \frac{\sigma_0 - \sigma_r}{\sigma_0' - \sigma_r} \tag{8.3}$$

This was viewed by Oding as the First Law of Relaxation.

Special importance was attached to this law, in that a single relaxation curve can be used to provide estimates of the relaxation behavior at the same temperature for any other initial stress value. This procedure is shown schematically in Fig. 8.4 for initial stress values of σ_0 and σ_0'. At time t, the values of $\Delta\sigma$ and $\Delta\sigma'$ are related through Eq. 8.3 as follows:

$$\frac{\Delta\sigma}{\Delta\sigma'} = \frac{\sigma_0 - \sigma_r}{\sigma_0' - \sigma_r} \tag{8.4}$$

Once σ_r is known, it is thus possible to estimate the curve for σ_0 from the available relaxation data based on σ_0'.

Oding further reasoned that, if the proportionality in Eq. 8.4 is to be maintained for all values of time, the relaxation rate v_r' on the σ_0' curve and the rate v_r on the σ_0 curve must remain proportional to $\Delta\sigma'$ and $\Delta\sigma$; thus

$$\frac{v_r}{v_r'} = \frac{\Delta\sigma}{\Delta\sigma'} \tag{8.5}$$

and from Eq. 8.3

$$\frac{v_r}{v_r'} = \frac{\Delta\sigma}{\Delta\sigma'} = \frac{\sigma_0 - \sigma}{\sigma_0' - \sigma'} = \frac{\sigma_0 - \sigma_r}{\sigma_0' - \sigma_r} \tag{8.6}$$

Equation 8.6 was termed the Second Law of Relaxation.

In view of Eq. 8.6, the functional dependence of the relaxation curve on stress is a simple one; at any time, t, the relaxation rate is directly proportional to both the difference between the initial and final stresses and the difference between the initial and limiting stresses. For the case where $\sigma_r = 0$, the relaxation rate at any time will be proportional to the initial stress.

A generalized correlation for relaxation results was proposed by Oding in terms of the concept of relative

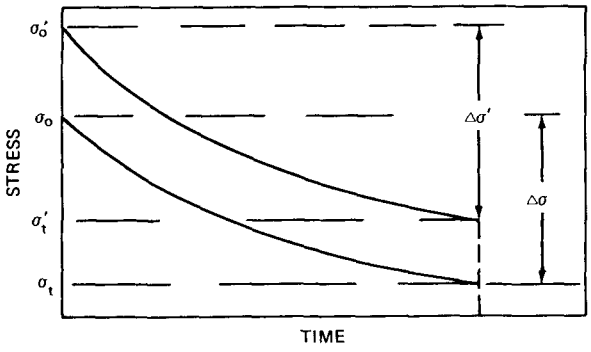

Fig. 8.4 Stress vs. time plot.

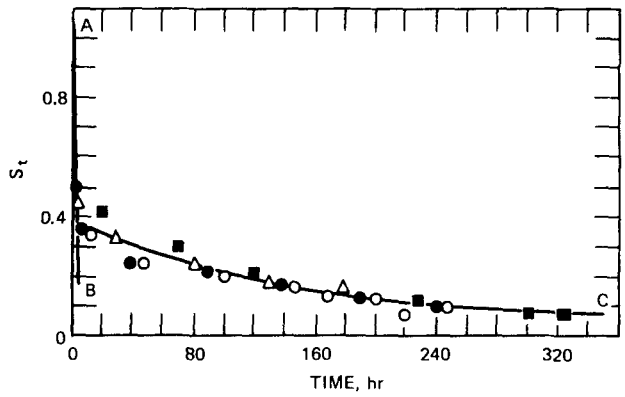

Fig. 8.5 Relative relaxation correlation for E169 steel. ■,σ_0 = 30 kg/mm²; ●,σ_0 = 19.6 kg/mm²; △,σ_0 = 14.6 kg/mm²; ○,σ_0 = 9.8 kg/mm². (From Ref. 1.)

relaxation. Noting that the total possible amount of relaxation is given by $(\sigma_0 - \sigma_r)$ or σ_0 when σ_r is zero, Oding defined the relative relaxation parameter, S_t, as

$$S_t = \frac{\sigma - \sigma_r}{\sigma_0 - \sigma_r} \tag{8.7}$$

Values of S_t lie between zero and unity.

A typical generalized relaxation curve was provided by Oding on the basis of some data for E-169 steel and is shown in Fig. 8.5. Special attention was focused on the very rapid decrease in S_t during the first few hours of relaxation and the gradual decrease in S_t which extends for several hundred hours. It was observed that different stages of relaxation must be involved in accordance with the subdivision noted in Fig. 8.1; these stages are identified by segments AB and BC.

Basic Mathematical Concepts

At point A in Fig. 8.1, the total strain, ϵ_t, will be all elastic, and the following equation applies:

$$\epsilon_t = \epsilon_e \tag{8.8}$$

where ϵ_e is the elastic strain. For any given time, t, along the relaxation curve, the value of ϵ_t is kept constant and the stress will be lower than that at point A. This reduction in stress is due to the conversion of some of the elastic strain to inelastic strain, and this is a time-dependent conversion. At any time the value of ϵ_t is given as

$$\epsilon_t = \epsilon_e + \epsilon_i \tag{8.9}$$

where ϵ_i is the inelastic strain. It is obvious that Eq. 8.9 can also be written as

$$\epsilon_t = \frac{\sigma}{E} + \epsilon_i \tag{8.10}$$

where σ is the instantaneous stress and E is the modulus of elasticity. Rearrangement of Eq. 8.10 yields

$$\epsilon_i = \epsilon_t - \frac{\sigma}{E} \tag{8.11}$$

to indicate that a plot of ϵ_i vs. σ on rectangular coordinates would be linear with a slope of $-(1/E)$. It also follows, of course, that for elastic straining the value of ϵ_t can be replaced by σ_0/E to yield

$$\epsilon_i = \frac{\sigma_0}{E} - \frac{\sigma}{E} = \frac{1}{E}(\sigma_0 - \sigma) \tag{8.12}$$

where σ_0 is the initial stress.

Relaxation is not necessarily limited to those instances in which the straining is all elastic. If a material is strained beyond the yield point to obtain a given value of ϵ_t, then Eq. 8.8 would be

$$\epsilon_t = \epsilon_{ei} + \epsilon_{ii} \tag{8.13}$$

where ϵ_{ei} and ϵ_{ii} are the initial elastic and inelastic strains, respectively. If ϵ_t is held constant, the stress will now relax through the conversion of elastic to inelastic strain just as in initial elastic straining. Furthermore, the type of relaxation curve in Fig. 8.1 would still be observed, although point A would correspond to an initial stress value above the yield point. Equation 8.11 would still be applicable, and the linearity between ϵ_i and σ would still persist. However, Eq. 8.12 would not be applicable because the value for ϵ_t would not be given by σ_0/E.

In what has been reported[1] to be the first description of relaxation, Maxwell[5] introduced an analytical expression based on an assumed linearity between the instantaneous stress and the corresponding stress rate. This equation was

$$-\frac{d\sigma}{dt} = k\sigma \tag{8.14}$$

which integrates to

$$\frac{\sigma_0}{\sigma} = e^{kt} \tag{8.15}$$

This expression is not generally applicable and has not been widely accepted in the representation of relaxation behavior.

Oding–Tseitlin Relation

Considering relaxation to be influenced by two effects occurring simultaneously, Oding and Tseitlin[6] proposed a special mathematical formulation. For the effect that was considered to be associated with the grain boundaries, the stress decay was expressed by an equation of the form

$$\sigma_I = \sigma_0 e^{-kt(1+pt)} \tag{8.16}$$

where σ_I is the stress at time t in the first stage of relaxation, σ_0 is the initial stress, and k and p are constants. This behavior is given by trace ab in Fig. 8.6.

The second effect is associated with processes taking place within the grains and was represented (see trace cd in Fig. 8.6) by

$$\sigma_{II} = \sigma_r + (\sigma_0 \quad \sigma_r)S_0 e^{t/t_0} \tag{8.17}$$

where σ_{II} is the stress at time t in the second stage of relaxation; σ_r is the relaxation limit; S_0 is given by σ_0'/σ_0, where σ_0' is the value of the initial stress in the second stage of relaxation. When σ_r is zero (in high-temperature relaxation), Eq. 8.17 simplifies to

$$\begin{aligned}\sigma_{II} &= \sigma_0 S_0 e^{t/t_0} \\ &= \sigma_0' e^{-t/t_0}\end{aligned} \tag{8.18}$$

The resultant relaxation curve is

$$\sigma = \sigma_I \quad (\sigma_0' \quad \sigma_{II}) \tag{8.19}$$

and is represented by the trace ad in Fig. 8.6.

Oding and Tseitlin[6] recommended that relaxation data should be plotted in the form of log stress vs. time (see Fig. 8.7) since the form of Eq. 8.18 suggests a linear relation between log σ and time for the second stage of relaxation (Eq. 8.18 is identical with Eq. 8.15, discussed previously). Therefore the type of plot shown in Fig. 8.7

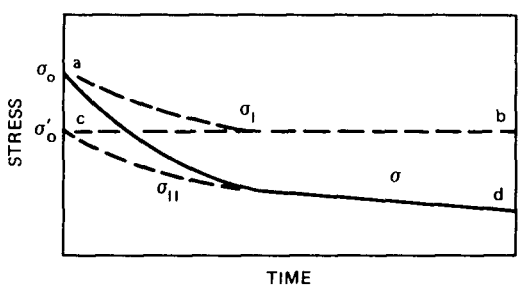

Fig. 8.6 Stress vs. time behavior.

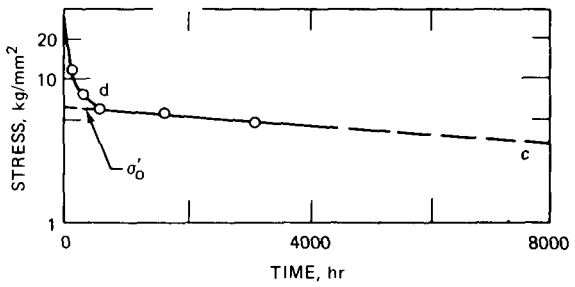

Fig. 8.7 Semilogarithmic relaxation plot. (From Ref. 1.)

not only allows t_0 to be evaluated from the slope of the segment dc but also yields the value of σ_0' as the intercept at zero time. This also allows S_0 to be calculated to characterize the relaxation strength of the grain boundaries in stage I. The value of t_0 also provides a measure of relaxation strength, but for stage II, since it measures the time for a stress relaxation from σ_0' to σ_0'/e.

Another interesting point made by Oding and Tseitlin involved the opinion that it was more reasonable to express relaxation behavior in terms of S_0 and t_0 than by merely quoting the stress decrement in a given time, t. The two relaxation coefficients, S_0 and t_0, were reported to be independent of the initial stress (at least below the yield point), and this is of special importance in relaxation comparison. For example, the data presented in Table 8.1 reveal the variations in these coefficients which result from differing heat treatments. Annealing and tempering were seen to lead to grain-boundary strengthening; normalization in the steels studied caused intragranular strengthening, as indicated by the increased values of t_0 and decreased values of S_0.

Robinson–Kanter Equation

Another early study of relaxation was reported by Robinson[7,8] for the case of an initial elastic straining. Considering Eq. 8.12 in the differential form

$$d\epsilon_p = -\frac{d\sigma}{E} \tag{8.20}$$

and

$$\frac{d\epsilon_p}{dt} = -\frac{d\sigma}{Edt} \tag{8.21}$$

it followed that

$$\dot{\epsilon}_p = -\frac{\dot{\sigma}}{E} \tag{8.22}$$

where $\dot{\epsilon}_p$ is the creep rate based on plastic strain, and $\dot{\sigma}$ is the stress rate. Robinson[7] and Kanter[9] assumed that a logarithmic plot of stress vs. creep rate was linear to define

TABLE 8.1

RELAXATION COEFFICIENTS FOR E-110 AND 30-KhMA STEELS[6]

E-110	S_0	t_0	30-KhMA	S_0	t_0
Anneal, 900°C	0.74	7,140	Anneal, 860°C	0.69	12,390
Normalize, 920°C	0.34	16,000	Normalize, 800°C	0.21	20,000
Normalize, 920°C; temper, 650°C, 2 hr	0.67	29,410	Normalize, 800°C temper, 650°C, 2 hr	0.58	20,000
Quench, 920°C; temper, 650°C, 2 hr	0.53	10,600	Quench, 880°C; temper, 650°C, 2 hr	0.44	16,130

$$\dot{\epsilon}_p = A\sigma^n \tag{8.23}$$

which can be written as

$$\dot{\epsilon}_p = \left(\frac{\dot{\epsilon}_{p0}}{\sigma_0^n}\right)\sigma^n \tag{8.24}$$

where the σ_0 and $\dot{\epsilon}_{p0}$ correspond to some reference condition. Sub ∞.ution of Eq. 8.24 into Eq. 8.21 yielded

$$-\frac{d\sigma}{Edt} = \left(\frac{\dot{\epsilon}_{p0}}{\sigma_0^n}\right)\sigma^n \tag{8.25}$$

which, when integrated from time zero to time t, gave

$$t = \frac{\sigma_0^n}{(n-1)\,\dot{\epsilon}_{p0}E^n}\left[\left(\frac{E}{\sigma}\right)^{n-1} - \left(\frac{E}{\sigma_0}\right)^{n-1}\right] \tag{8.26}$$

This expression contains the difference between two time quantities. When the initial stress is relatively high, the second term will be relatively small and can be neglected in those situations where relaxation times amount to a few thousand hours. In these instances, Eq. 8.26 yields

$$t = \frac{\sigma_0^n}{(n-1)\dot{\epsilon}_{p0}E\sigma^{n-1}} \tag{8.27}$$

and

$$\sigma = \left[\frac{\sigma_0^n}{(n-1)\dot{\epsilon}_{p0}Et}\right]^{n-1} \tag{8.28}$$

Equation 8.27 defines the time to achieve a certain relaxed stress, and Eq. 8.28 identifies the relaxed stress after a given time when the initial condition is negligible.

An examination of Eq. 8.26 indicates that a logarithmic plot of stress vs. time will be nonlinear except under the conditions (t very large) corresponding to Eq. 8.27. When linearity occurs, the slope is seen to be equal to $-1/(n-1)$.

An extensive evaluation of this type of behavior was reported by Robinson[8] for various materials. Some definitely linear relations were observed (see Fig. 8.8), but some definite curvatures were noted in other instances (see Fig. 8.9). It was cautioned that these differences question

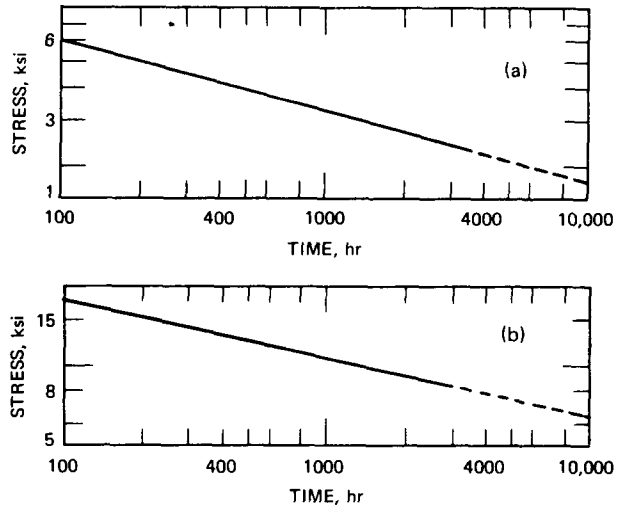

Fig. 8.8 Typical logarithmic relaxation plots. (a) Annealed 0.35% carbon steel at 850°F, n = 4.7; initial extension = 0.15%. (b) Annealed 0.58% carbon steel at 750°F; n = 5.6; initial extension = 0.2%. (From Ref. 8.)

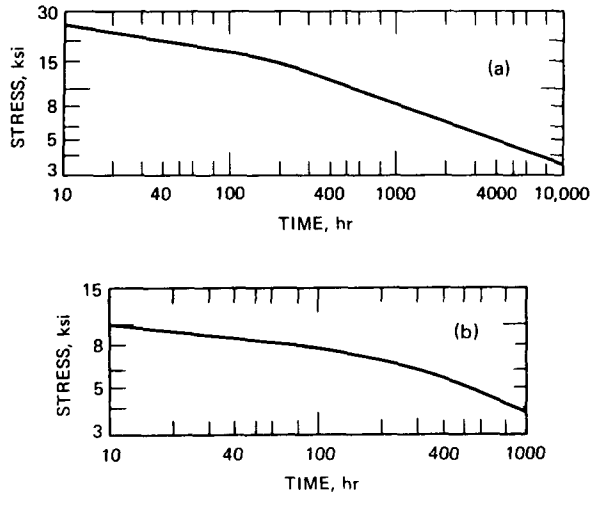

Fig. 8.9 Typical logarithmic relaxation plots. (a) SAE 4140 steel at 930°F; initial extension = 0.215%. (b) Carbon–molybdenum tubing material at 1050°F; initial extension = 0.2%. (From Ref. 8.)

the complete applicability of Eq 8.28 and suggest that a logarithmic plot of stress vs relaxation time should not be extrapolated indefinitely in either direction

In another paper[10] by Robinson dealing with the relaxation characteristics of high-temperature bolting materials, a further application of Eq 8 27 was cited. In this study of steel, low-alloy and high-alloy materials, relaxation data were reported for the temperature range to 1500°F in providing a detailed assessment of the relaxation characteristics of over one hundred materials Values of n in Eq 8 27 were reported along with residual stress values corresponding to 1000 and 10,000 hr

Special mention should be made of the comprehensive review[11] of available relaxation data for carbon steels, low-alloy Mo , Cr-, and V bearing steels, 12% Cr-type steels, stainless steels, superstrength steels, iron-base superstrength alloys with cobalt, cobalt-base superstrength alloys, nickel-base superstrength alloys, and cast iron. In this extensive summarization of available data (which included the Robinson[10] data), special attention was given to the presentation of residual (relaxed) stress values corresponding to 100, 500, 1000, and 10,000 hr Temperatures ranged from room temperature to 1500°F and detailed comparisons were provided in plots of the residual stress obtained in a selected relaxation period vs temperature A typical example is provided in Fig 8 10, based on 1000 hr relaxation behavior

Boyd Analysis

In an excellent discussion of the Robinson[8] article, Boyd[4] presented some relaxation data for Cr–Mo W steel tested at 850°F These data are presented in Fig 8 11 and are nonlinear on semilogarithmic coordinates A logarithmic plot of these same data is also found to be nonlinear although, in the time regime involved, this can be considered to be consistent with the form of Eq 8 26

Some additional relaxation data were reported by Boyd[4] in an evaluation of K-20 steel at 850°F These data are presented in Fig 8 12 to reveal relaxation curves similar to those shown in Fig 8 11 Also presented in Fig 8 12 is a special relaxation plot of initial vs remanent (i e , relaxed stress) stress for selected time intervals In addition a stress–strain plot was included to identify the initial stress values used in the relaxation curves labeled A to E

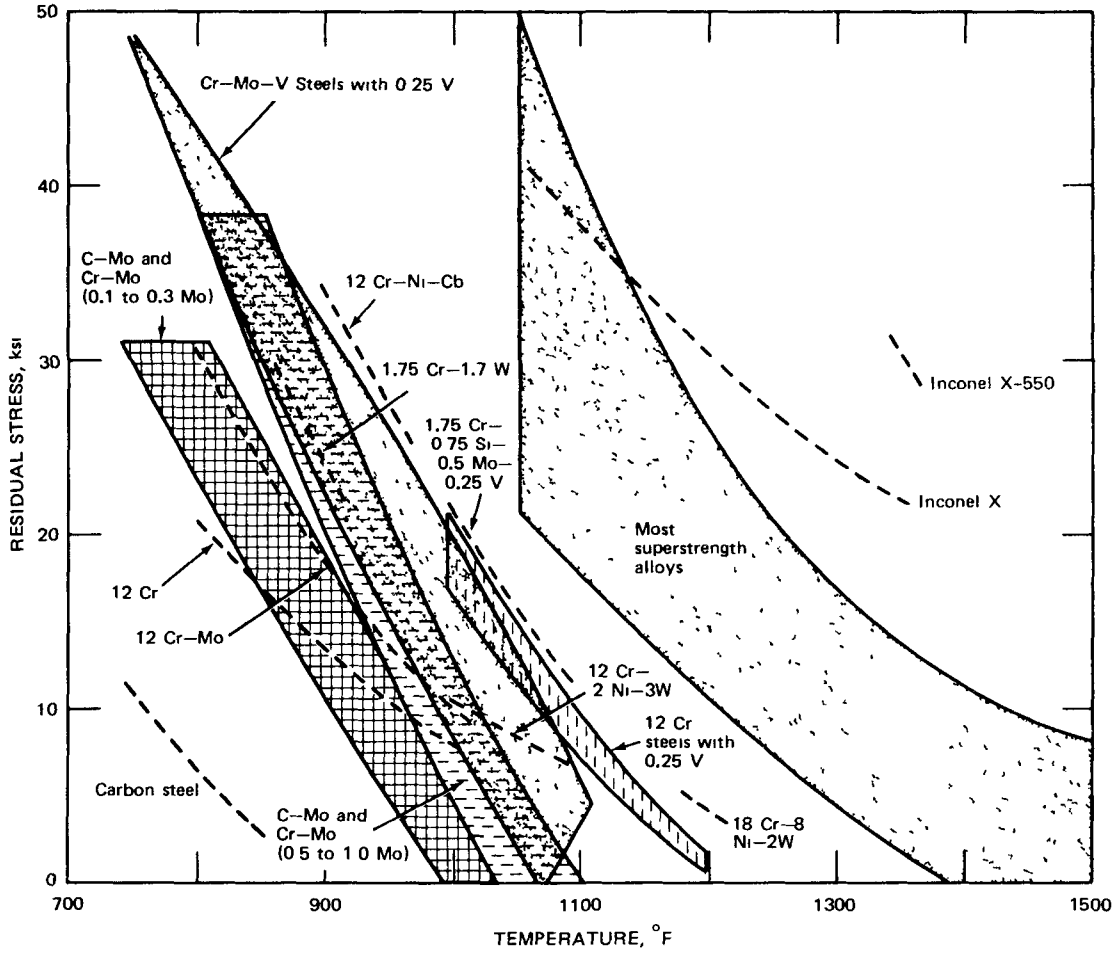

Fig. 8.10 Comparative 1000-hr relaxation strengths for several classes of alloys. (From Ref 11)

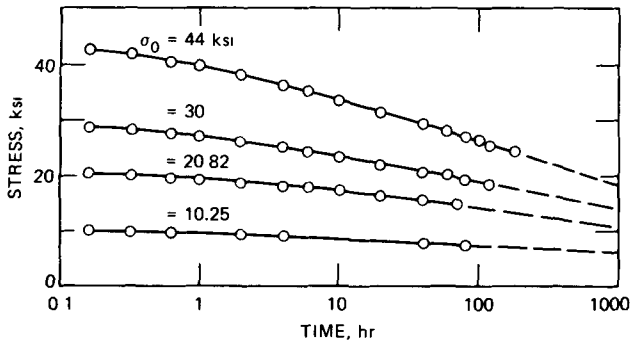

Fig. 8.11 Relaxation data for Cr–Mo–W steel at 455°C (850°F). (From Ref. 4.)

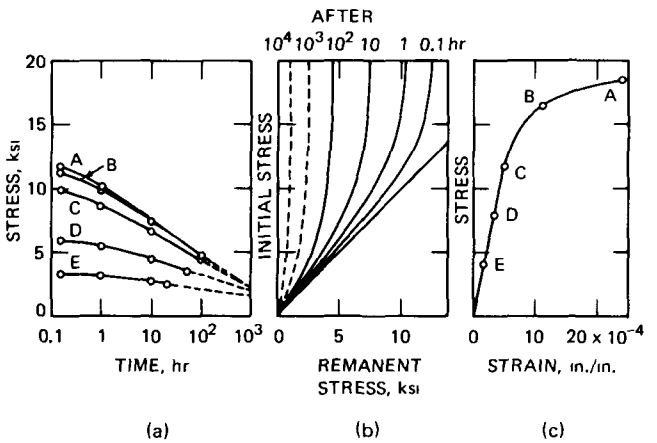

Fig. 8.12 Relaxation data for K-20 steel at 850°F. (a) Relaxation tests. (b) Initial stress vs. remanent stress. (c) Stress vs. strain during loading period. (From Ref. 4.)

Another interesting study reported by Boyd[4] emphasized the effect of reloading on relaxation behavior. These results are presented in Fig. 8.13 to indicate several reloadings to the same initial stress value following definite relaxation periods. These data were used to conclude that the relaxation becomes less pronounced in subsequent reloadings to the same initial stress value.

Trumpler Analysis

An extension of the relaxation studies of Boyd[4] was reported by Trumpler[2] in an evaluation of Cr–Mo–W steel at 500°C. These data are reported in Fig. 8.14 and are quite similar to the data reported by Boyd. A plot of initial vs. remanent stress is also shown in Fig. 8.14 and is similar to that reported in the Boyd study. In evaluating the constant-time lines in Fig. 8.14, Trumpler noted that the relation between initial (σ_i) and remanent (σ_r) stress could be expressed as

$$\sigma_i - \sigma_r = A(\sigma_r)^2 \qquad (8.29)$$

The curves drawn in the lower portion of Fig. 8.14 represent this mathematical form.

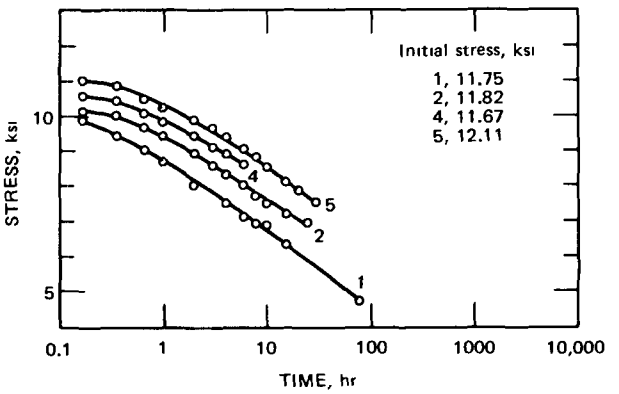

Fig. 8.13 Effect of reloading on the relaxation of K-20 steel at 850°F. (From Ref. 4.)

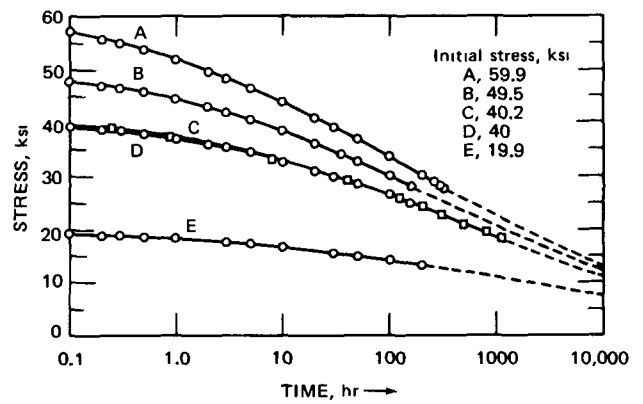

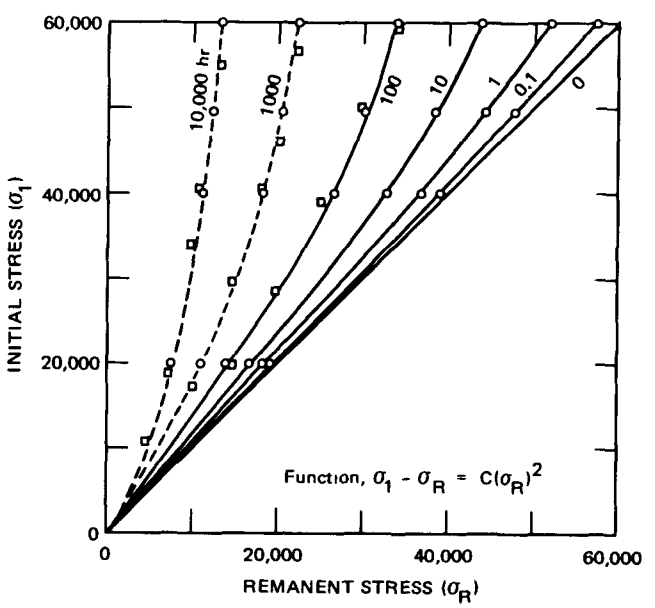

Fig. 8.14 Relaxation data for Cr–Mo–W steel at 500°C. (From Ref. 2.)

Trumpler[2] also presented an interesting comparison of relaxation behavior to reveal different creep resistances. This comparison is shown in Fig. 8.15 to indicate that the K-428 alloy has the greatest resistance to relaxation.

Newhouse–Seguin–Lape Analysis

A very thorough evaluation of 12% Cr alloys was reported by Newhouse, Seguin, and Lape.[12] Relaxation measurements were reported for several martensitic, 12% Cr alloys including Type 403, and six different alloy modifications: 12% Cr–Co–W–V, 12% Cr–W–V, 12% Cr–Mo–V, 12% Cr–Mo–W–V, 12% Cr–Cb, and 12% Cr–Ni–W. Relaxation data were reported for the temperature range from 800 to 1200°F for an initial total strain of 0.2%. Some typical data obtained in this study are reported in Table 8.2. An interesting analysis of all the relaxation results was made in terms of a Larson–Miller parameter plot, assuming a value of 25 for the Larson–Miller constant. This type of analysis is shown in Fig. 8.16, which includes stress-rupture data for comparison. Similar behavior patterns are evident. However, the curvature in Fig. 8.16 corresponds to curvature in a logarithmic plot of stress vs. relaxation time. This behavior is definitely not consistent with the relaxation equation of Robinson, except perhaps in the very-long-term regime.

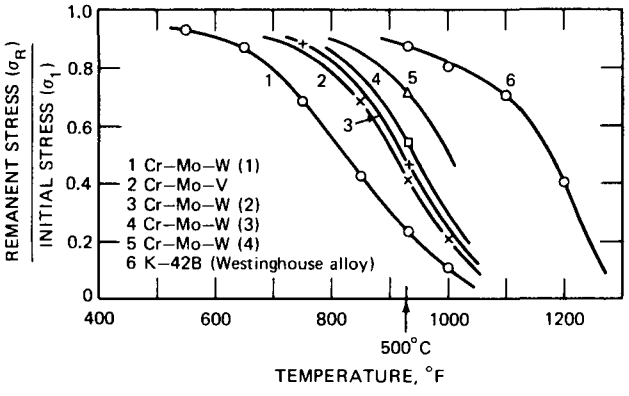

Fig. 8.15 Comparison of relaxation behavior in 1000 hr at an initial stress of 40,000 psi. (Numbers in parentheses identify different forms of Cr–Mo–W steel.) (From Ref. 2.)

Johnson Analysis

A comprehensive evaluation of the high-temperature relaxation characteristics of bolt and flange materials was reported by Johnson.[13] Logarithmic plots of stress vs. relaxation time were all shown to be concave downward with a definite tendency to be linear in the time region beyond a few hours. Some typical relaxation profiles are presented in Figs. 8.17 to 8.20 to reveal the effects of different initial stress levels, different initial total strain values, and different temperatures at 0.1% initial strain. An analysis of all relaxation results was made using an expression similar to Eq. 8.26, and it was noted that this type of relation can provide an accurate description of the

TABLE 8.2

RELAXATION DATA FOR SEVERAL 12% CHROMIUM ALLOYS; INITIAL TOTAL STRAIN IS 0.2% (FROM REF. 12)

Material	Temp., °F	Test duration, hr	Residual stress, ksi*						Estimated stress level at 10,000 hr, ksi
			1	10	100	300	1000	3000	
12Cr(403)	900	4055		26.5	22.5	20.8	19.2	17.5	(16)
12Cr(403)	1000	3550		17.0	13.5	12.2	10.4	8.0	
12Cr(403)	1060	2882		15.8	11.8	9.7	7.7	6.1	(4.5)
12Cr(403)	800	2545			35	33	31	29	(27)
12Cr(403)	1000	3530		21	16	14.3	12.3	10.1	(7)
12Cr(403)	1000	3531	18	13.8	10.7	9.4	8.0	6.8	(5.6)
12Cr(403)	800	2546			27	24	21	16.8	(16)
12Cr(403)	1000	3531	18	12.5	9.0	7.7	6.4	5.2	(5.6)
12Cr(403)	900	3016	32	26	20	17.8	15.6	(14.0)	(12.2)
12Cr(403)	1000	3311		16.7	12.0	10.3	8.7	(7.2)	(6)
12Cr(403)	1000	2540		17.8	13.9	12.2	10.7	9.3	(6.0)
12Cr(403)	1000	2540		18.2	14.4	12.7	11.1	(9.8)	(8.6)
12Cr–W–V	1000	3354		35.0	30.0	27.5	22.5	17.5	(13.3)
12Cr–W–V	1000	3480		27.0	32.0	21.0	18.0	15.0	(12.0)
12Cr–W–V	1000	2700		28	23	21.2	18	14.6	(11.7)
12Cr–W–V	1050	2160		23	16.2	15.4	12.5	10	(7.8)
12Cr–W–V	1050	3280		26	21.2	18.8	15.3	12.3	(9.5)
12Cr–W–V	1050	2478		21	16.8	14.4	12.0	10.0	(7.9)
12Cr–W–V	1050	2478		20.5	16.1	15.5	11.3	9.7	(8.0)

*Extrapolated data given in parentheses.

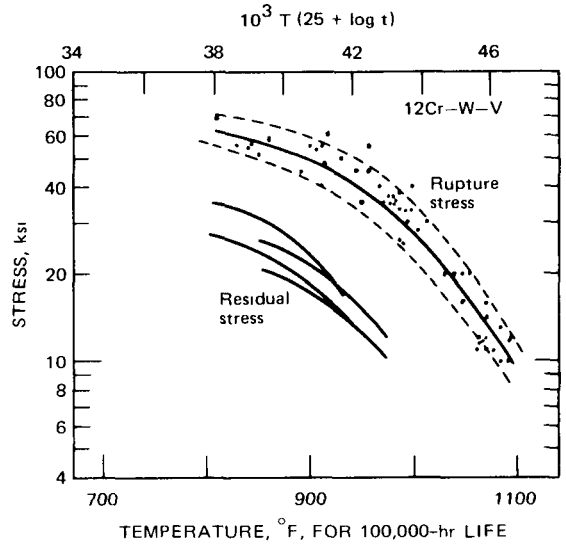

Fig. 8.16 Relaxation data for 12Cr–W–V analyzed in terms of Larson–Miller parameter. (From Ref. 12.)

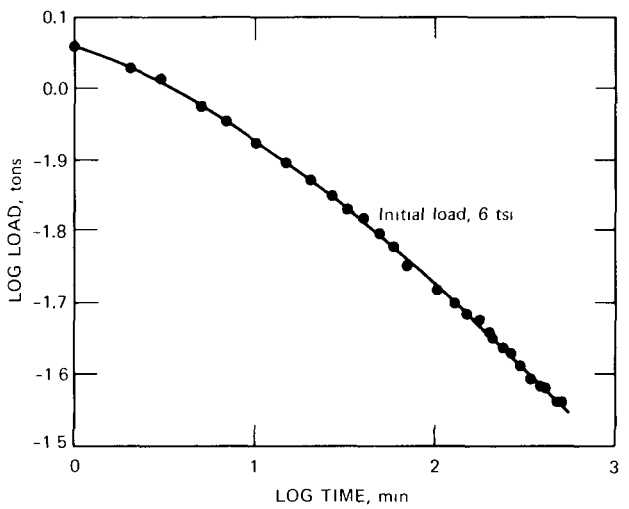

Fig. 8.17 Relaxation data for carbon flange steel at 575°C. (From Ref. 13.)

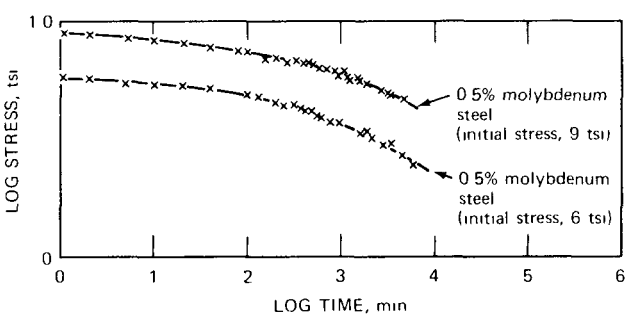

Fig. 8.18 Relaxation data for 0.5% molybdenum flange steel at 575°C. (From Ref. 13.)

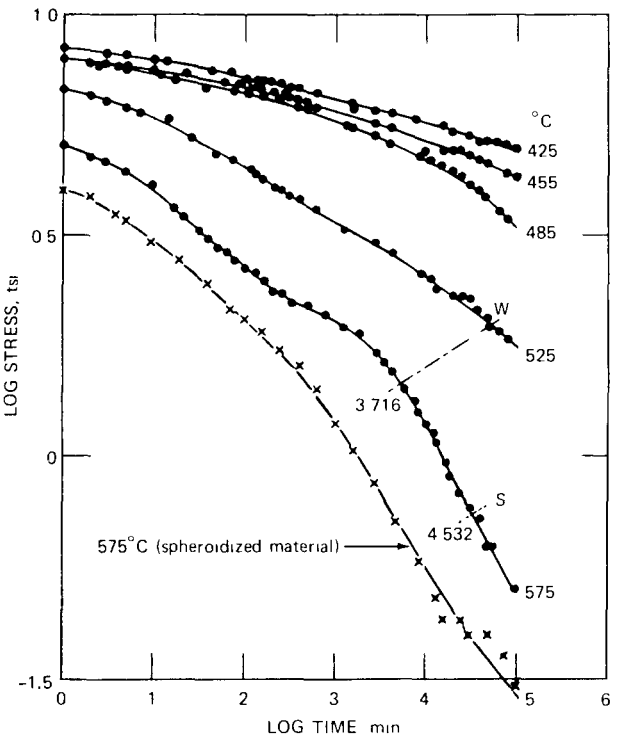

Fig. 8.19 Relaxation data for 0.17% carbon steel; initial strain of 0.1%. (From Ref. 13.)

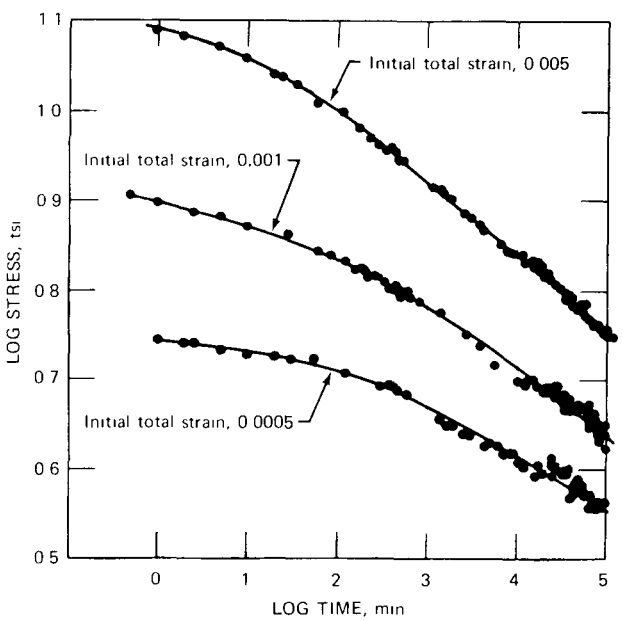

Fig. 8.20 Relaxation data for 0.17% carbon steel at 455°C. (From Ref. 13.)

relaxation curve (or a considerable portion of it) for all materials.

Smith–Jenkinson–Armstrong–Day Analysis

Another very comprehensive evaluation of high-temperature relaxation behavior in bolt steels was reported by Smith et al.[16] in tests involving an initial total strain of 0.15%. An interesting method of plotting was described, as shown in Fig. 8.21. The ordinate is temperature, and the abscissa is the logarithm of the time required for the stress to relax to a specific residual stress. A family of approximately straight and slightly converging lines was obtained to give an extensive definition of the relaxation characteristics of a given material. In Fig. 8.21(d) the relaxation behavior of various steels is compared, based on the relaxed stress observed in 10,000 and 30,000 hr. It was emphasized that this presentation clearly identifies the marked superiority of steels containing vanadium.

Draper[15] reported some relaxation data for a Cr–Mo bolt steel, using a 4-in.-diameter bar subjected to an initial strain of 0.15%. An analysis was made of the data using the temperature–log time plot described by Smith et al.,[16] with the results shown in Fig. 8.22a. A family of curves is defined, but the linearity noted by Smith et al. apparently is not observed. Draper also made an interesting study of the effect of re-straining. These results are shown in Fig. 8.22b to indicate a previously observed effect that the amount of relaxation observed in a given time decreased on subsequent re-straining.

A further study of relaxation behavior as affected by re-straining was reported by Smith et al.[14] With the use of an initial strain of 0.15% in tests of 1% Cr–Mo–V steel at

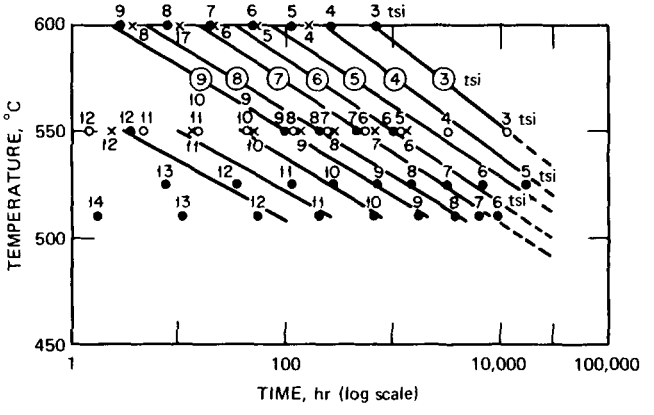

(a) On 0.66% Mo, 0.28% V bolt steel showing times to reach residual stresses at various temperatures, steel No. 152 (TYC, TYD).

●, 2-in.-diameter bar.
○, Repeat test at 550°C (TYC).
x, 4-in.-diameter bar (TYD).

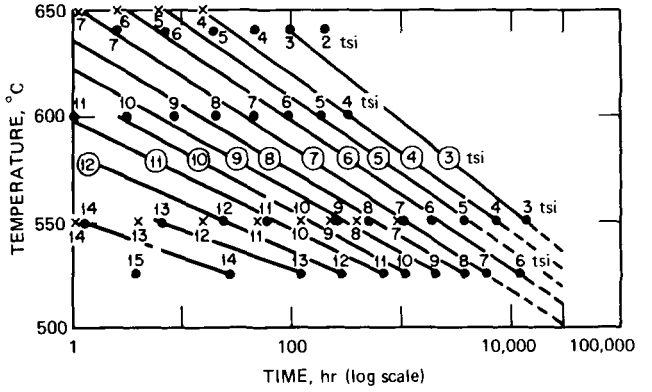

(b) On 0.21 C, 0.90Cr, 0.74 Mo, 0.24% V oil-quenched bolt steel, showing times to reach specific residual stresses at various temperatures, steel No. 150. All tests on 2-in.-diameter bar.

●, 2-in.-diameter bar (TXP). x, 4-in.-diameter bar (TXD).

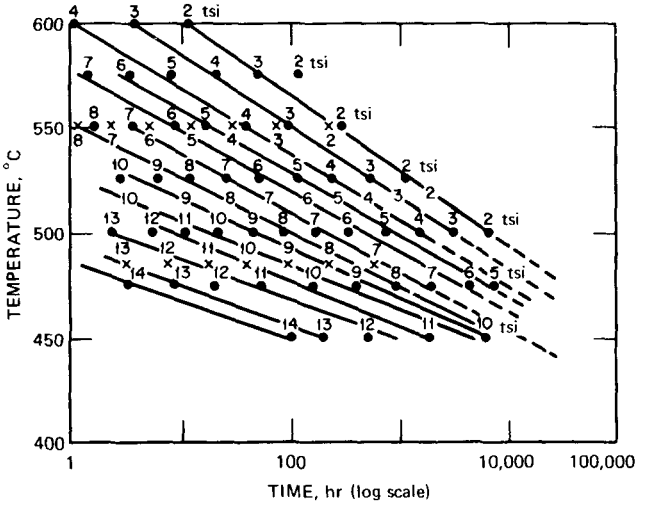

(c) On 0.45 C, 1.36 Cr, 0.63% Mo bolt steel, showing times to reach specific residual stresses at various temperatures, steel No. 149 (TXN).

x, N.P.L. results. ●, A.M.L. results.

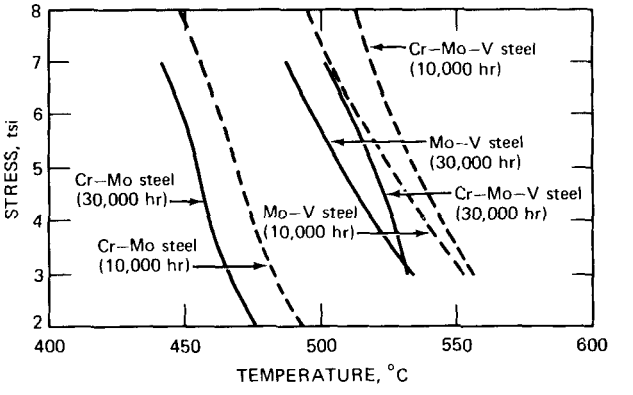

(d) Temperature to relax to specific stresses in 10,000 and 30,000 hr at 0.15% constant strain.

Fig. 8.21 Temperature correlations of relaxation data. (From Ref. 16.)

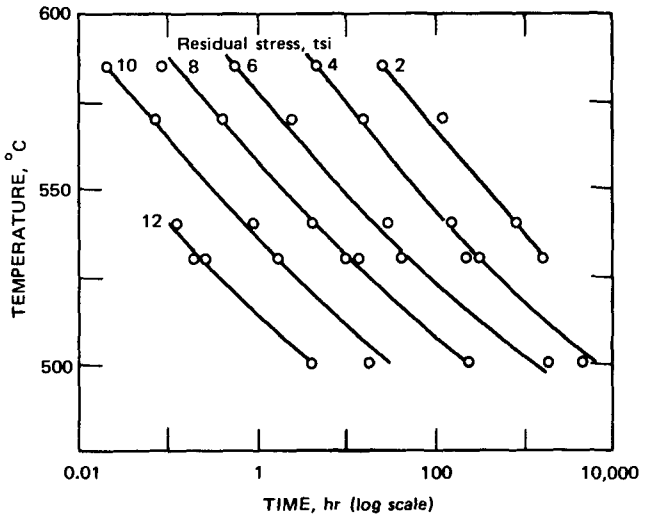

Fig. 8.22a Relaxation data for Cr–Mo bolt steel. Four-inch-diameter bar; strain of 0.15%. (From Ref. 15.)

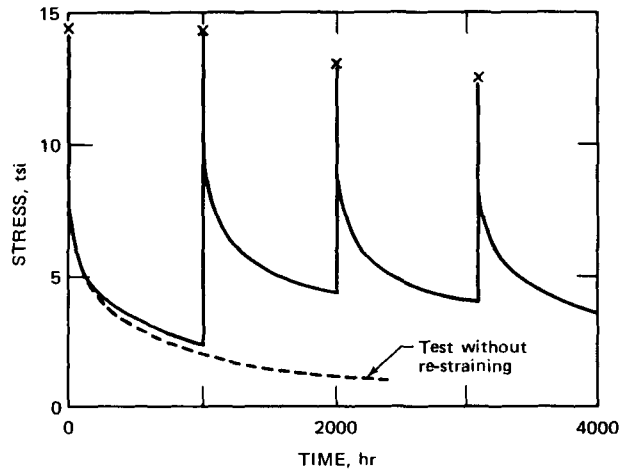

Fig. 8.22b Effect of re-straining on relaxation of an Mo–V steel. Temperature, 600°C; strain of 0.15%. Restressed to 0.15% strain at ~1000-hr intervals. (From Ref. 15.)

various temperatures, the specimens were re-strained 0.1% after the residual stress had reached 5 tsi. At each temperature, 550, 575, 600, 625, and 650°C, the time to reach the preselected residual stress level increased, leveled off, and then decreased in subsequent re-strainings. After 5 to 10 re-strainings at all temperatures except 550°C, the time to obtain a residual stress of 5 tsi was less than that observed in the first straining. A plot of temperature vs. the logarithm of the cumulative relaxation time in the re-straining tests was shown to be linear (see Fig. 8.23) and offered a possible method for extrapolating this type of relaxation behavior to longer times. It is interesting to note in this study that total relaxation times were well in excess of 20,000 hr in a few cases.

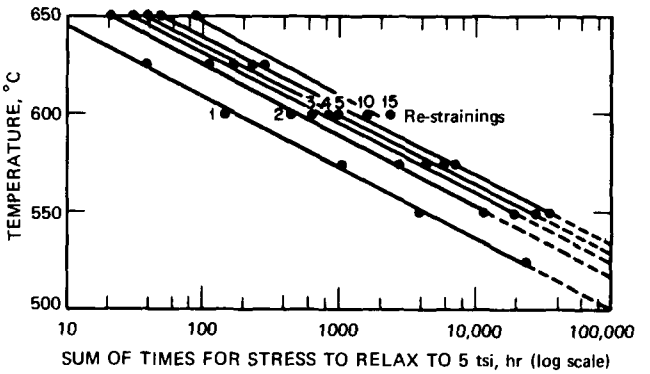

Fig. 8.23 Relaxation in repeated straining of 1% Cr–Mo–V steel. (From Ref. 14.)

Kennedy–Douglas Analysis

Relaxation studies dealing with Inconel were reported by Kennedy and Douglas[17] for temperatures of 1300, 1500, and 1650°F. Typical relaxation plots are presented in Figs. 8.24 and 8.25 to reveal different behavior patterns in the region of short relaxation times but a gradual merging of the relaxation profiles in the region close to 1 hr. All the data were analyzed in terms of Eq. 8.26, and this expression appeared to be applicable. Logarithmic plots of the type employed in Fig. 8.26 were shown to reveal a definite linearity except in the regime of very short relaxation times. Evaluation of the creep constants based on the relaxation results led to the comparison presented in Table 8.3. In general, the agreement with the same constants generated from creep data is fairly good. An impressive comparison between the stress vs. creep-rate behavior obtained from creep and relaxation tests is shown in Fig. 8.27. The agreement is excellent except at 1650°F, where the creep rates exhibited in the relaxation tests are much higher than corresponding values obtained in creep tests.

Manjoine Evaluation

A compliance method for measuring relaxation characteristics was reported by Manjoine,[18] and data were presented for a Cr–Mo–V rotor steel tested at 950°F (510°C). These results are shown in Fig. 8.28 and define a linear relation on semilogarithmic coordinates. It can be shown that these data also yield a linear relation when $(\sigma_0 - \sigma)$ is plotted against the logarithm of the relaxation time. But it can easily be deduced that the linearity in Fig. 8.28 must also yield such a linear relation. Another interesting plot that evolves from the data in Fig. 8.28 is shown in Fig. 8.29. The solid line is assumed to represent average behavior and can be used to estimate relaxation response for any value of the initial stress. The dashed line in Fig. 8.28 was obtained from the solid line in Fig. 8.29 and corresponds to an initial stress of 20,000 psi. Another analysis of the Fig. 8.28 data used the results obtained at the two highest initial stress values, and the Fig. 8.29 type

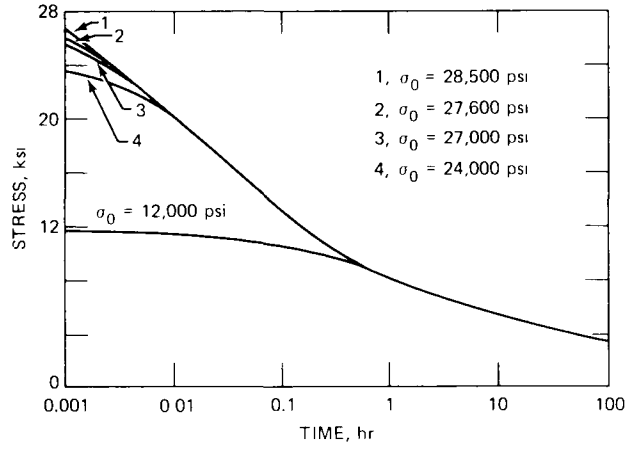

Fig. 8.24 Relaxation characteristics of as-received Inconel at 1300°F.[17]

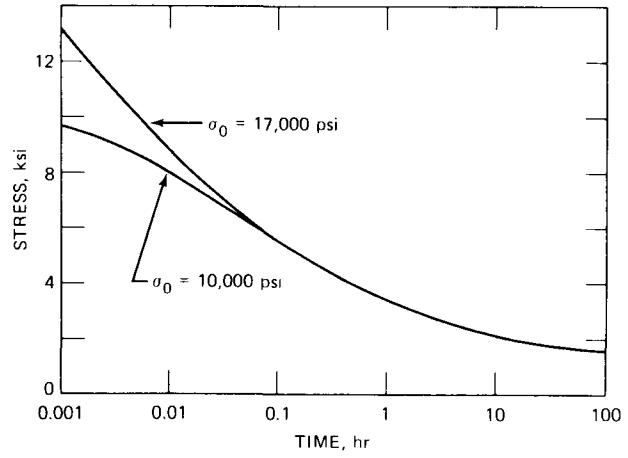

Fig. 8.25 Relaxation characteristics of as-received Inconel at 1500°F.[17]

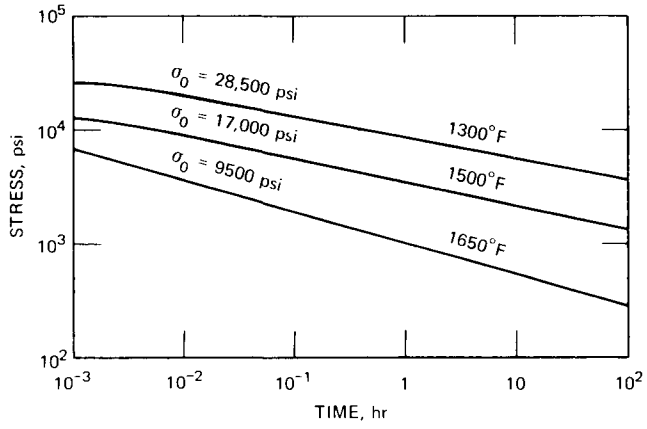

Fig. 8.26 Stress-relaxation characteristics of as-received Inconel.[17]

TABLE 8.3

VALUES OF CREEP CONSTANTS DETERMINED BY CONSTANT-STRESS CREEP TESTING AND BY RELAXATION TESTING[17]

Test type	Heat treatment of Inconel	Test temperature, °F	Creep constants*	
			A	n
Creep	†	1300	43,000	6.18
Relaxation	†	1300	38,700	6.31
Creep	†	1500	20,500	5.95
Relaxation	†	1500	20,100	5.81
Creep	†	1650	16,800	4.70
Relaxation	†	1650	10,800	4.61
Creep	‡	1300	31,600	6.85
Relaxation	‡	1300	30,700	7.37
Creep	‡	1500	17,900	5.50
Relaxation	‡	1500	19,600	5.42
Creep	‡	1650	10,500	5.20
Relaxation	‡	1650	13,100	4.79

*Creep strain, ϵ, given by $\epsilon = (\sigma/A)^n t$, where t is time and A and n are constants.

† As received.

‡ Annealed at 2050°F for 2 hr.

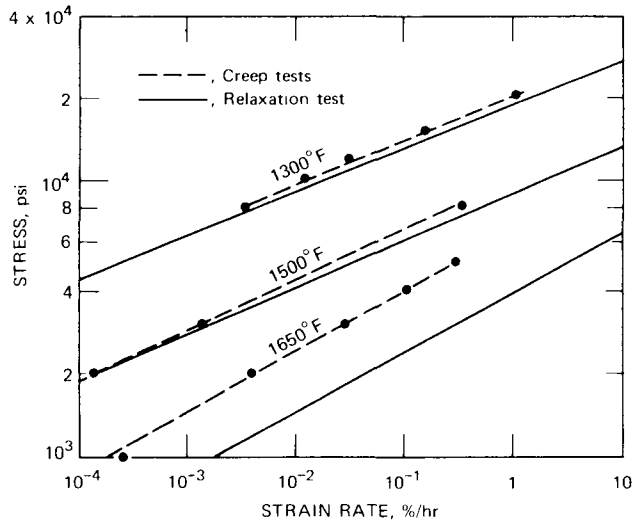

Fig. 8.27 Stress vs. strain rate for as-received Inconel.[17]

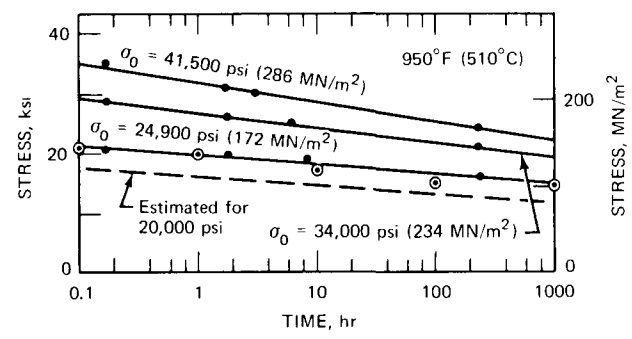

Fig. 8.28 Relaxation curves for Cr–Mo–V rotor steel. (From Ref. 18.)

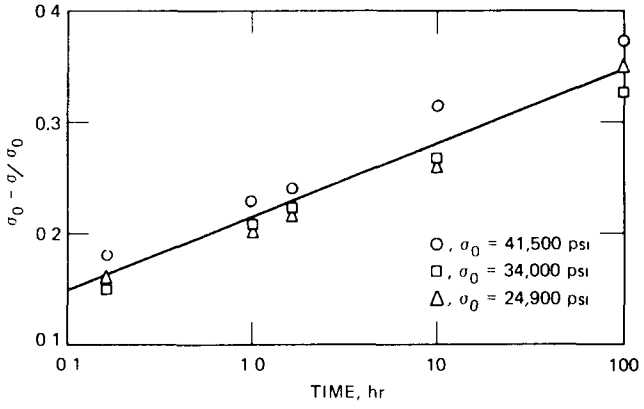

Fig. 8.29 Initial stress correlation of relaxation data from Fig. 8.28.

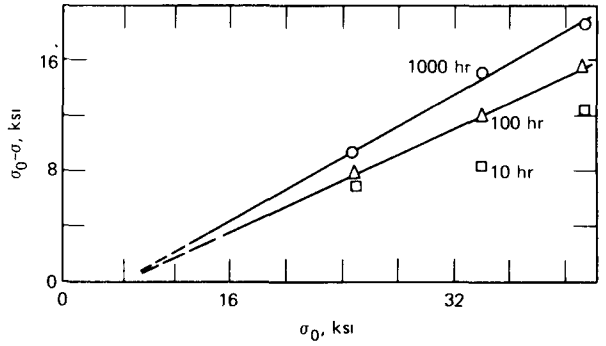

Fig. 8.30 Oding type of analysis of relaxation data from Fig. 8.28 (From Ref. 1.)

of plot was used to estimate the behavior for an initial stress value of 24,900 psi. The estimated behavior is shown as the circles in Fig. 8.28, and the results are in close accord with the experimentally positioned relaxation isotherm. Hence some consideration can be given to the Fig. 8.29 type of correlation for relaxation results since some reliable estimates can be made based on this approach.

Another interesting analysis of the Fig. 8.28 data involves the $(\sigma_0 - \sigma)$ vs. σ_0 rectangular plot suggested by Oding.[1] This is shown in Fig. 8.30, and the consistency is striking. For the longer relaxation times, linear relations seem to develop; and, for the limited data available, a relaxation limit of 8000 psi seems to be indicated. For the 10-hr data, the nonlinearity mentioned by Oding is exhibited.

Gittus Analysis

In an analysis of relaxation results, Gittus[19] used the Nutting equation,

$$\dot{\epsilon}_p = K\sigma^n t^m \tag{8.30}$$

where m (m is less than zero) and n are constants, and substituted this into Eq. 8.21 to yield

$$-\frac{d\sigma}{Edt} = K\sigma^n t^m \tag{8.31}$$

Integration, assuming n = 1, led to

$$\frac{\sigma_0}{\sigma} = e^{KEt^{m+1}} \tag{8.32}$$

Furthermore, for $n \neq 1$, it was shown that

$$\frac{\sigma_0}{\sigma} = \left[1 - E(1-n)K't^{m+1}\sigma_0^{n-1}\right]^{1/(n-1)} \tag{8.33}$$

where K′ is a constant containing K and m.

Equation 8.32 will be seen to yield

$$\ln \frac{\sigma_0}{\sigma} = KEt^{m+1} \tag{8.34}$$

which leads to

$$\log\left[\ln\left(\frac{\sigma_0}{\sigma}\right)\right] = \log KE + (m+1)\log t \tag{8.35}$$

For data that are in accord with Eq. 8.30 and for the case when n = 1, it follows that a logarithmic plot of $\ln(\sigma_0/\sigma)$ vs. time will be linear. Slope and intercept calculations identify values for m and the KE product for use in Eq. 8.32.

Relaxation data for Nimonic 80A at temperatures from 400 to 595°C were used by Gittus[19] to produce the results presented in Fig. 8.31. Sufficient linearity was obtained to substantiate the validity of Eq. 8.32, and m was found to be −0.78. A plot of log KE vs. 1/T yielded definite linearity to establish the temperature dependence for the K value in Eq. 8.32. Similar analyses for Inconel and EN50 steel led to

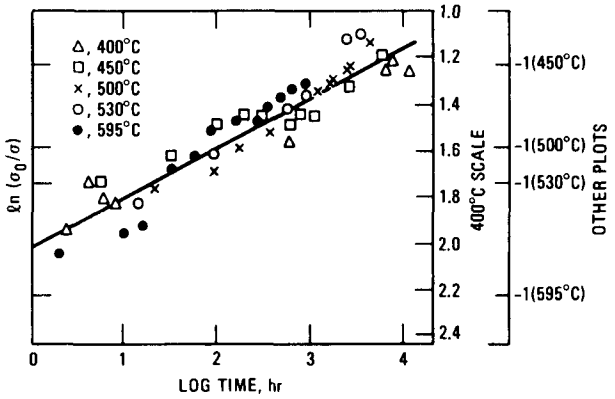

Fig. 8.31 Relaxation data for Nimonic 80A analyzed by Gittus. (The −1.0 locations of the scale for various temperatures are indicated on the right-hand ordinate.) (From Ref. 19.)

the same conclusion, in that the m values were −0.79 and −0.77. Furthermore, the log KE vs. 1/T plot was linear to yield the same type of correlation obtained with the Nimonic 80A data.

It is important to note that Eq. 8.32 shows that the quantity σ_0/σ is independent of the magnitude of the initial stress. In other words, a given value of the σ_0/σ ratio will be obtained at the same value of time in relaxation tests based on different initial stress values. This reasoning will, of course, not apply to Eq. 8.33, for it is clear, in this case, that σ_0/σ is a definite function of σ_0.

Additional support for the relaxation analysis proposed by Gittus[19] was provided in a study of Nimonic 80A by Taylor and Jeffs.[20] Relaxation tests at 325, 425, and 525°C were analyzed in terms of Eq. 8.32 to yield a value of m equal to −0.81, which is in good agreement with the value of −0.78 found by Gittus in tests of Nimonic 80A.

Conway Analysis

In a recent analysis of relaxation results, Conway[21] proposed an approach based on stress rate, and some effective correlations appeared to result. A logarithmic plot of $-\dot{\sigma}/\sigma$ (the instantaneous stress rate divided by the instantaneous stress) vs. time was found to yield a well-defined linearity. Expressed mathematically, this relation leads to

$$-\frac{\dot{\sigma}}{\sigma} = -\frac{d\sigma}{\sigma dt} = At^m \tag{8.36}$$

Integration from time zero to t and from the initial stress, σ_0, to σ yields

$$\ln\frac{\bar{\sigma}_0}{\sigma} = \frac{A}{1+m}t^{1+m} \tag{8.37}$$

which is identical to the Gittus[19] relation in Eq. 8.34. It is important to note, however, that the approach outlined in Eq. 8.36 does not depend on a knowledge of the initial stress value, σ_0, and, as a result, appears to be more effective. The initial stress value, if not measured accurately, can lead to erroneous conclusions when Eq. 8.34 is applied. The calculated value of $\bar{\sigma}_0$ is usually not equal to the experimental value for the initial stress. It is usually greater than σ_0 and hence is viewed as a "pseudo initial stress." The true significance of this pseudo value has not been established yet.

Equation 8.34 was applied to the relaxation data[4] for Cr–Mo–W steel at 455°C (850°F), using the σ_0 values reported (see Fig. 8.11). These data (see Fig. 8.32 for analysis at σ_0 = 44,000 psi) fail to conform to the linear relation specified by Eq. 8.34, and it might be concluded that these data are therefore not in accord with the type of behavior described by Gittus. However, if Eq. 8.36 is used, these same data exhibit a well-defined linearity on logarithmic coordinates. This is shown in Fig. 8.32 where

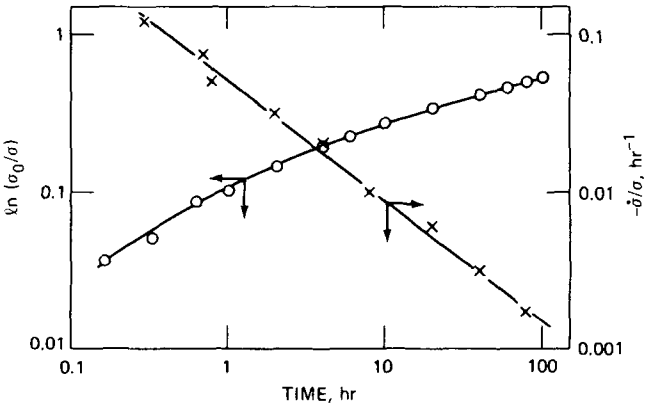

Fig. 8.32 Relaxation analyses of Fig. 8.11 data at σ_0 = 44,000 psi using σ_0/σ and $-\dot{\sigma}/\sigma$.

$\log(-\dot{\sigma}/\sigma)$ is plotted as a function of log time. This behavior will then lead to Eq. 8.37, with a value of m equal to −0.76. It is interesting to note that this is very close to the value of m reported by Gittus for Nimonic 80A.

Since Eqs. 8.34 and 8.35 are really identical, it might seem contradictory that the two logarithmic plots of Fig. 8.32 are not both linear. Actually, if σ_0 is an accurate measurement, these two plots will be linear and the same constants for use in Eq. 8.34 will follow. If, however, σ_0 is not representative of the real value of the initial stress, then the Gittus analysis will lead to the nonlinear σ_0/σ plot shown in Fig. 8.32. It seems that this is the case in connection with the Fig. 8.11 data, and, whereas the analysis represented by Eq. 8.36 identified the proper equation form, the approach based on σ_0/σ did not.

An interesting application of the approach defined by Eq. 8.36 involved the use of just the relaxation data below 10 hr in Fig. 8.11. The type of $(-\dot{\sigma}/\sigma)$ plot shown in Fig. 8.32 was used to evaluate the A and m values, and these were used in conjunction with Eq. 8.37 to estimate the relaxed stress at 100 hr. This result gave a stress of 25,400 psi compared to the measured value of about 26,000 psi given in Fig. 8.11. Such extrapolation could not be effected in this case, using the Gittus approach, since the nonlinearity in Fig. 8.32 would not have allowed the identification of the constants in the Gittus equation. Estimating relaxed stresses at 100 hr based on data to 10 hr is obviously an important consideration, and, from the analysis just mentioned, this appears to be possible using the stress-rate analysis of Eq. 8.36.

It is also worthy of mention that the nonlinearity in the σ_0/σ plot of Fig. 8.32 suggests a correction to σ_0 to change the Eq. 8.34 approach to

$$\frac{\sigma_0 + \sigma'}{\sigma} = e^{KEt^{m+1}} \tag{8.38}$$

In other words, it might not be possible to measure an "unrelaxed" value for σ_0 in certain instances when some

form of relaxation occurs during the loading to initial stress. This modification would linearize the Gittus type of plot in Fig. 8.32, but the σ' value would first have to be identified. Clearly, the approach defined by Eq. 8.36 is more straightforward.

Feltham–Kubát Logarithmic Relation

In an excellent study of the low-temperature (77 to 291°K) relaxation of copper and alpha brasses, Feltham[22] cited the logarithmic stress relaxation reported by Kubát[23] while proposing the expression

$$\sigma_0 - \sigma = s \log (1 + at) \tag{8.39}$$

for use in describing the stress–time behavior during relaxation. In this formulation σ_0 is the initial stress, and it is seen that at time zero the value of σ is equal to σ_0. Feltham plotted the quantity $(\sigma_0 - \sigma)$ as a function of log t to yield a linear relation for short relaxation times. This linearity persisted only to a relaxation time of about 20 min, after which the relaxed stresses were lower than those predicted by Eq. 8.39.

Actually Eq. 8.39 is not consistent with a linearity between $(\sigma_0 - \sigma)$ and log t except in the region where "at" values are much larger than unity. For small "at" values, the above semilogarithmic plot exhibits a definite nonlinearity and becomes concave upward (see Fig. 8.33). In this region the log (1 + at) value becomes essentially equal to the "at" value itself to define a linearity between $(\sigma_0 - \sigma)$ and relaxation time on rectangular coordinates. The time regime involved in such a linear relation is very small and persists for such a short period that, for practical purposes, it is not of great importance.

Feltham[22] reported that the value of "a" ranged between 10 and 30 min^{-1} and that the value of s was dependent upon whether the yield point had been exceeded in the initial load application. It was further noted that the value of "a" decreased as the test temperature was increased.

Behavior patterns similar to those observed by Feltham were also noted by Sargent and Shaw[24] and Sargent and Conrad[25] in low-temperature evaluations of molybdenum and titanium. Relaxation plots were found to be linear in $(\sigma_0 - \sigma)$ vs. log time in the range to about 10 min. The slope of this plot increased as the temperature increased in the molybdenum studies; the titanium studies were confined to 300°K and indicated an increase in the above slope as the initial stress increased. All loads were in the pre-yield region.

Noble–Hull Relations

An important study by Noble and Hull[26] involved stress-relaxation measurements of Si–Fe single crystals at 293°K. Equation 8.21 was used in conjunction with the dislocation theory that relates plastic strain rate to dislocation velocity, V, and dislocation density, ρ, in the form

$$\dot{\epsilon}_p = 0.5 b \rho V \tag{8.40}$$

where b is the Burgers vector of the dislocations. Direct substitution yielded

$$-\frac{d\sigma}{Edt} = 0.5 b \rho V \tag{8.41}$$

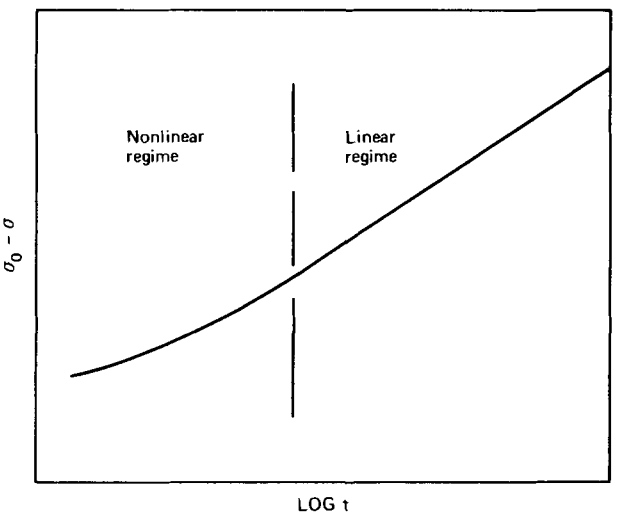

Fig. 8.33 Schematic of the equation $\sigma_0 - \sigma = s \log (1 - at)$ plotted on semilogarithmic coordinates.

Reference was made to the observation by Stein and Low[27] that

$$V = \left(\frac{\sigma}{\sigma_0}\right)^m \tag{8.42}$$

(where σ_0 is related to the resolved shear stress required to produce a dislocation velocity of 1 cm/sec and m is a constant) to obtain

$$-\frac{d\sigma}{E\,dt} = \left(\frac{0.5 b \rho}{\sigma_0^m}\right) \sigma^m \tag{8.43}$$

and

$$-\frac{d\sigma}{dt} = A\sigma^m \tag{8.44}$$

where $A = 0.5 b \rho E / \sigma_0^m$. Equation 8.44 defines the linearity between log $\dot{\sigma}$ and log σ which was described by Solomon and Nix.[28]

If it is assumed that ρ remains constant during relaxation, it was shown that

$$-\frac{1}{1-m}\sigma^{1-m} = At + K \tag{8.45}$$

This yields

$$(1-m)\ln\sigma = \ln(Bt + C) \tag{8.46}$$

and

$$\ln\sigma = \frac{1}{1-m}\ln(Bt + C) \tag{8.47}$$

Rearranging gives

$$\ln\sigma = \frac{1}{1-m}\ln\left(1 + \frac{B}{C}t\right) + \frac{1}{1-m}\ln C \tag{8.48}$$

When $t = 0$, $\sigma = \sigma_f$ and hence

$$(1-m)\ln\sigma_f = \ln C \tag{8.49}$$

This leads to

$$\ln\sigma = \frac{1}{1-m}\ln\left(1 + \frac{B}{C}t\right) + \ln\sigma_f \tag{8.50}$$

This defines a straight line when $\ln\sigma$ is plotted vs. $\ln t$ and when (Bt/C) is much greater than unity. The slope of such a line is equal to $1/(1-m)$. A plot of this type is presented in Fig. 8.34 to indicate a slight increase in the value of m as the initial strain is increased. Also noteworthy is the fact that the extent of the relaxation is small, amounting to only 3% or so of the initial stress.

Noble and Hull[26] noted that the Feltham equation

$$\sigma_f - \sigma = \frac{s}{2.3}\ln(1 + at) \tag{8.51}$$

was quite accurate in describing the relaxation measurements of Si–Fe at 293°K. However, it was shown that this should be expected since the Feltham equation is definitely related to Eq. 8.50. For example, the quantity $(\sigma_f - \sigma)$ in Eq. 8.51 can be written as

$$\sigma = \sigma_f - \Delta\sigma = \sigma_f\left(1 - \frac{\Delta\sigma}{\sigma_f}\right) \tag{8.52}$$

and, assuming that

$$\ln\left(1 - \frac{\Delta\sigma}{\sigma_f}\right) \approx -\frac{\Delta\sigma}{\sigma_f} \tag{8.53}$$

for small values of $(\Delta\sigma/\sigma_f)$, it follows that Eq. 8.50 becomes

$$\Delta\sigma = \frac{-\sigma_f}{1-m}\ln\left(1 + \frac{B}{C}t\right) \tag{8.54}$$

which is equivalent to Eq. 8.51 with

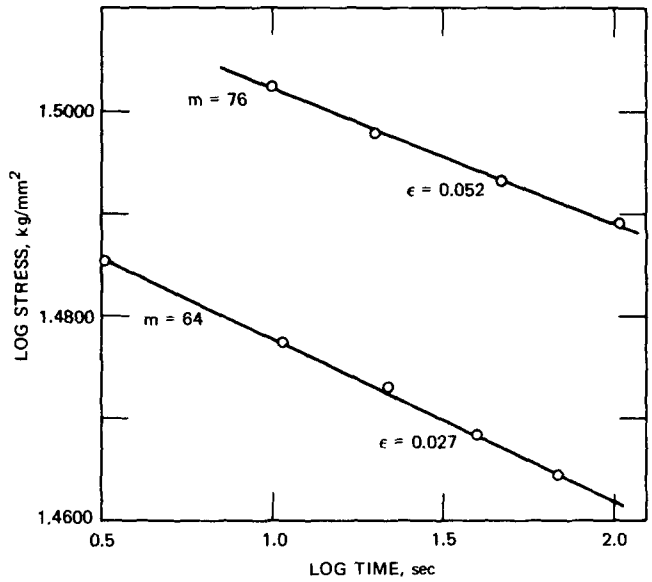

Fig. 8.34 Stress relaxation plot for Si–Fe single crystals at 293°K. (From Ref. 26.)

$$m - 1 = \frac{2.3\,\sigma_f}{s} \tag{8.55}$$

Li Equation

In a study of dislocation dynamics applied to relaxation, Li[29] proposed that the stress–time relation during relaxation can be expressed by

$$\sigma - \sigma_i = K(t + a)^{-n} \tag{8.56}$$

where σ_i is the long-range internal stress, and K, a, and n are constants. This expression describes the standard form of the relaxation curve shown in Fig. 8.1. In addition, it indicates that the relaxed stress, σ, approaches σ_i at long relaxation times. Equation 8.56 also indicates that a plot of $\log\sigma$ vs. $\log t$ would not be linear except at very long times and then only when σ_i is negligible. A nonlinearity between $\log\sigma$ and time is also to be expected.

Differentiating Eq. 8.56 with respect to time leads to

$$-\frac{d\sigma}{dt} = nK(t + a)^{-(n+1)} \tag{8.57}$$

which suggests that a plot of log stress rate vs. log time will be nonlinear in the short-term regime but will approach linearity as the relaxation time increases. In this linear regime the slope will identify the value of n, and then the intercept will yield the value of K. These values can then be combined with a stress-rate value in the short-term regime to calculate the value of "a." Then Eq. 8.56 can be solved to obtain σ_i.

Multiplying both sides of Eq. 8.57 by t and substituting Eq. 8.56 yield

$$-\frac{t d\sigma}{dt} = -\frac{d\sigma}{d \log t} = \frac{2.3nt(\sigma - \sigma_i)}{(t + a)} \quad (8.58)$$

$$= \frac{2.3n\sigma}{1 + (a/t)} - \frac{2.3n\sigma_i}{1 + (a/t)} \quad (8.59)$$

A plot then of $-d\sigma/d \log t$ vs stress should approach a straight line as the relaxation time increases The slope of this line will be $2.3n$ and the line will intersect the abscissa (i e , $d\sigma/d \log t$ equal to zero) at the value of $\sigma = \sigma_i$ Plots representing these relations are shown in Fig 8.35

Summary Remarks

A logical comment at the end of a review section of this type relates to the relative effectiveness of the various correlation schemes that have been presented Unfortunately no detailed assessment of this type has been made, and it is not possible to identify the one approach that is preferable to all others or even to say that there is in fact one such approach Until this kind of detailed evaluation is made, it will be necessary to be guided by the type of review presented above and to use this information as needed in any analysis of relaxation behavior Usually a simple graphical representation of the data will be sufficient to obtain at least some indication of the applicability of a given approach within the range of the experimental results Whether or not reliable extrapolations to long term be

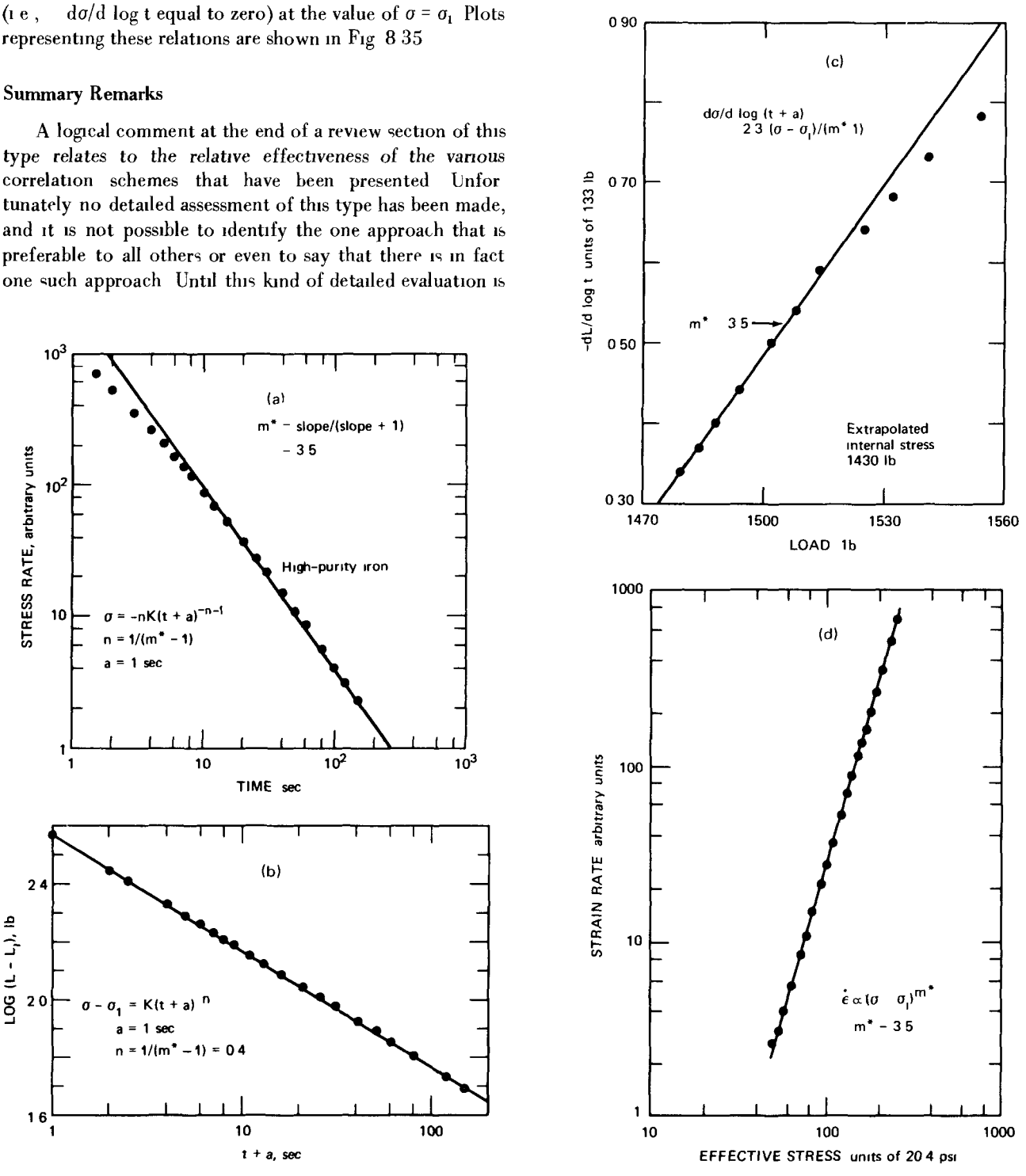

Fig. 8.35 Stress relaxation in high-purity iron (From Ref 29)

havior can be made is another question, however, and one that requires further study. Some success in extrapolations has been claimed through the approaches developed by Smith et al. (see the subsection entitled "Smith–Jenkinson–Armstrong–Day Analysis"), Gittus (see the subsection entitled "Gittus Analysis"), and Conway (see the subsection entitled "Conway Analysis"), and these are worthy of additional study. Parametric studies of relaxation data are needed and should serve an important purpose in this area of material behavior.

RELAXATION IN FATIGUE TESTING

Hold periods at constant strain within a fatigue cycle yield the same type of conditions encountered in the usual monotonic relaxation test. One difference is associated with the relative amounts of plastic strain which are involved. In the monotonic evaluations the initial loadings are generally confined to the elastic regime or at least to the regime wherein the plastic strains are small. In fatigue loadings the amount of the plastic-strain component can be several times that of the elastic component.

Another difference between monotonic and fatigue-hold-period relaxation relates to the possible presence of cyclic strain-hardening or strain-softening effects. These factors affect the stress level associated with a given strain amplitude, and some consideration must be given, therefore, to how these factors alter the relaxation behavior.

Still another difference concerns the cyclic nature of the fatigue exposures. For example, when completely reversed strain cycling is being studied and a hold period is used in tension only, some question must be raised concerning the possible effect of the cyclic exposure to a compressive strain on the relaxation observed in the following tensile exposure. Also related to this type of test is the case involving hold periods in both the tension and compression portions of the cycle. Of interest in this instance is the comparison between the relaxation that takes place in tension and compression and any effect that one has on the other. Furthermore, an interesting question arises relating to how these relaxation-behavior patterns compare to simple tension or compression relaxations measured in the monotonic case or in the cyclic case when only one type of hold period is involved.

Relaxation behavior in hold-time exposures has not been studied in great detail for the simple reason that hold-time tests in fatigue are not very numerous at the present time and this phase of fatigue evaluation is really just beginning. Some interesting results have been reported, however, and they are extensive enough to warrant special consideration in this chapter.

One other aspect of the relaxation behavior associated with hold periods in fatigue tests is the relatively short durations that have been studied to date. The longest hold period used to date for which relaxation data have been reported is about 10 hr. This is extremely short in terms of the usual relaxation studies reported in a previous section, but it should be possible to relate this behavior to that observed in the initial stages of the real long-term monotonic tests (with proper acknowledgment, of course, of the differences mentioned above). Special mention should also be made of the short-term relaxation studies that have application in dislocation-velocity measurements (Refs. 22, 26, 28-30). These investigations have focused on the relaxation during the early moments (for times less than 1 hr) following initial loading and hence involve time periods of the same magnitude as the fatigue hold periods. These relaxation analyses have been discussed in a previous section.

Krempl and Walker[31] reported some relaxation data obtained for 1Cr–1Mo 0.25V steel at 1000°F, using hold periods (in tension only) to 60 min. Although no attempt was made in this study to develop a stress–time relation for the relaxation results, certain qualitative observations were reported which are of interest. The first of these involves the higher relaxation resistance exhibited by the low-ductility material compared to the high-ductility material. This is shown in Fig. 8.36 for the case where the total strain range was 0.5%, and the hold-period durations were 1, 10, and 60 min. Also pointed out in connection with Fig. 8.36 was the relaxation behavior observed at various fractions of the fatigue life. Furthermore, using the plots of instantaneous stress divided by the initial stress (i.e., stress at the beginning of the hold period), it was shown that the data for the various hold-period durations were essentially coincident to indicate that the shape of the relaxation curve is not altered by increasing the length of the hold period. It is interesting to note, however, that (see Fig. 8.36) more relaxation seems to occur in the first cycle than in the cyclic regime near half-life. Also noteworthy is the fact that in the early portions of the test of the high-ductility material the amount of stress relaxation observed was something like 22,000 psi, whereas this decreased to about 11,000 psi near half-life. A similar decrease, although not as large, was noted in the low-ductility material.

A fairly extensive evaluation of the relaxation behavior of AISI 304 and 316 stainless steels was reported by Conway[21] based on a detailed study of hold-time effects at temperatures to 1200°F. These tests used hold periods to 600 min and led to the following general observations:

1. For a given hold period, the value of $\sigma_{t\ max.} - \sigma_{t\ min.}$ was independent of cycles, although the absolute values of both stresses changed during cycling.
2. The value of $\sigma_{t\ max.}$ depended upon hold period for a given strain range and decreased as the hold period increased.
3. The relaxation curve in tension was identical to the relaxation curve obtained in compression.
4. For all practical purposes $\sigma_{t\ max.}$ was equal to the maximum compressive stress amplitude $\sigma_{c\ max.}$
5. For a constant strain range, the configuration of the relaxation curve is independent of hold time.

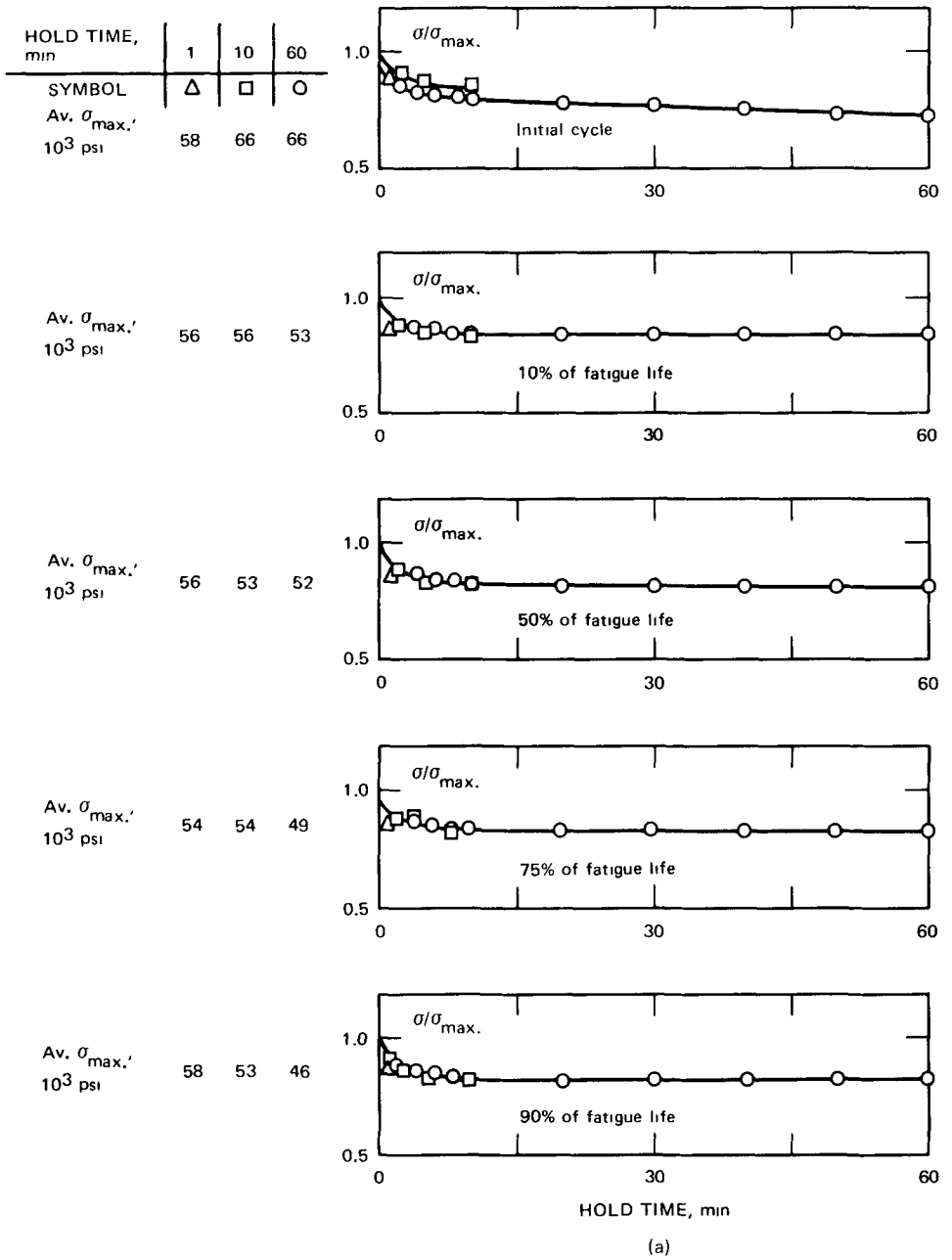

Fig. 8.36 Relaxation data obtained in hold-time tests of 1Cr–1Mo–0.25V steel at 1000°F. (a) Low-ductility material. (b) High-ductility material. (From Ref. 31.)

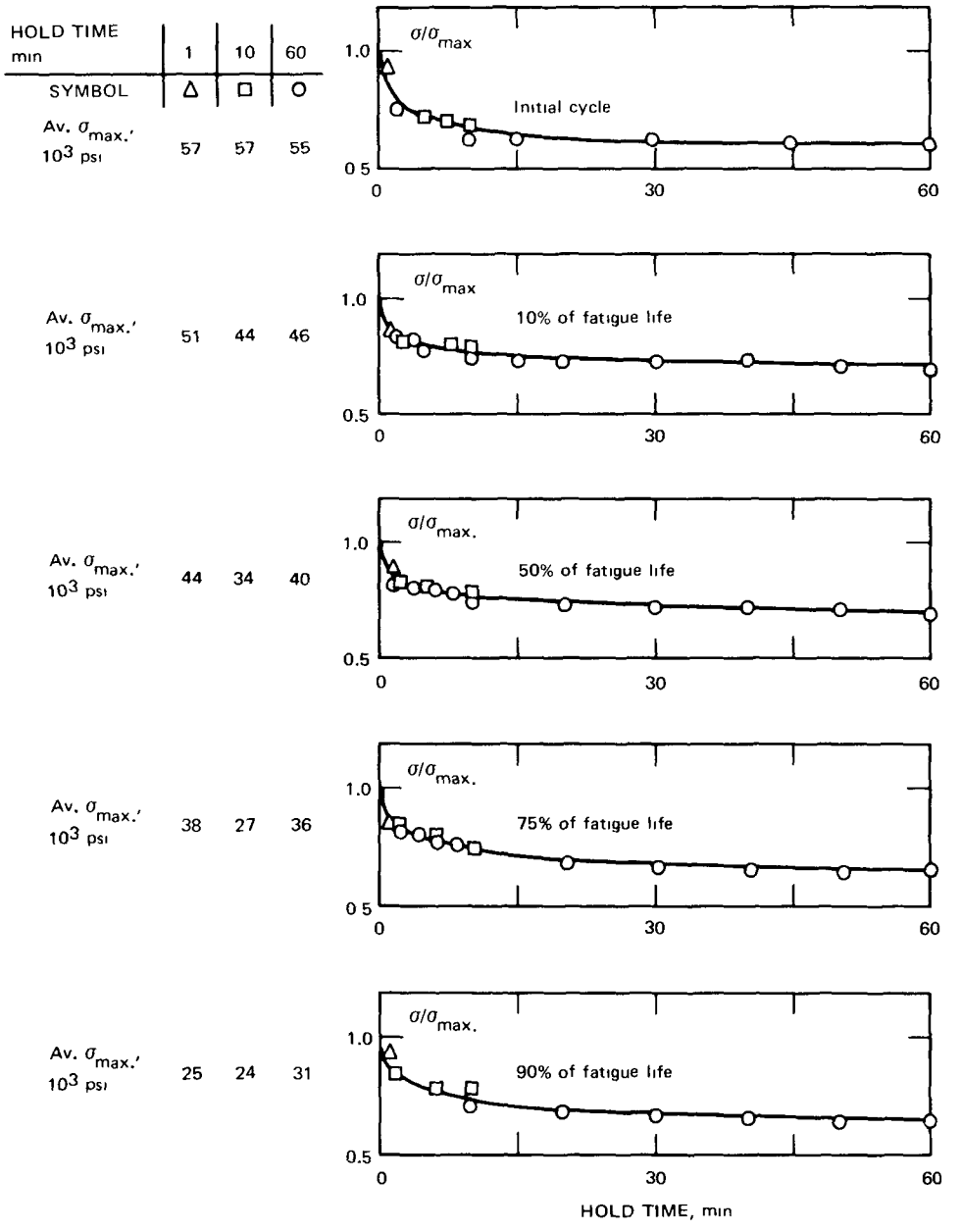

(b)

Fig. 8.36 (Continued)

6. The shape of the relaxation curve is strongly dependent on strain range.

7. Knowledge of the monotonic relaxation characteristics will yield one piece of information, i.e., $\sigma_{t\ max.} - \sigma_{t\ min.}$, which is identical to that obtained under cyclic conditions (see Fig. 3.47 in Chap. 3). Similar data at other strain ranges should be studied before this can be accepted as a general behavior pattern.

Some typical plots obtained in the analysis of the above-mentioned data are presented in Figs. 8.37 to 8.42 to indicate stress range, $\Delta\sigma$; maximum tensile stress, $\sigma_{t\ max.}$; maximum compressive stress, $\sigma_{c\ max.}$; and the corresponding minimum stress values $\sigma_{t\ min.}$ and $\sigma_{c\ min.}$ to define the extent of relaxation encountered throughout the test.

Typical stress vs. time plots (in general, these represent material behavior at $N_f/2$) for the materials and test conditions involved are presented in Figs. 8.43 to 8.54. These exhibit the standard shape characteristic of relaxation curves and show rapid decreases in stress in the early moments of the hold period. These results represent some of the first, if not the first, relaxation data for 304 and 316 stainless steels obtained in hold-period tests at elevated temperatures.

Included in the relaxation plots of Figs. 8.43 to 8.54 are:

1. Data to compare the relaxation curves obtained at various initial strain ranges (Figs. 8.43 and 8.44).

2. Relaxation curves obtained at the same strain range but using two different strain rates in the cycling portion of the test (Fig. 8.45).

3. Relaxation curves obtained at a strain range of 2% using hold periods ranging from 0.1 to 600 min (Figs. 8.46 and 8.47).

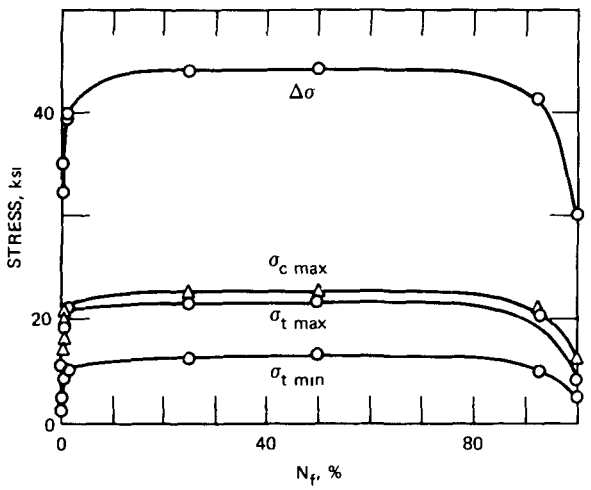

Fig. 8.37 σ vs. N plot.

Specimen 65-1	Strain rate, 4×10^{-3} sec^{-1}
Temp., 650° C	$N_f = 1{,}713$
Strain range, 0.50%	10-min hold period in tension only

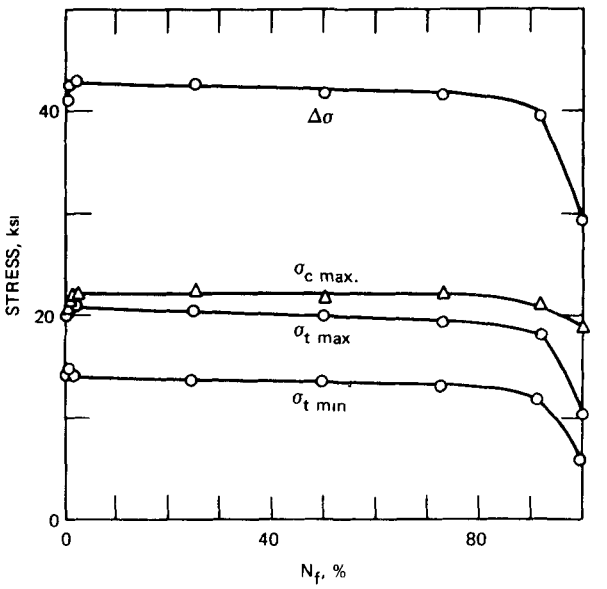

Fig. 8.38 σ vs. N plot.

Specimen 56-2	Strain rate, 4×10^{-3} sec^{-1}
Temp., 650° C	$N_f = 862$
Strain range, 0.50%	30-min hold period in tension only

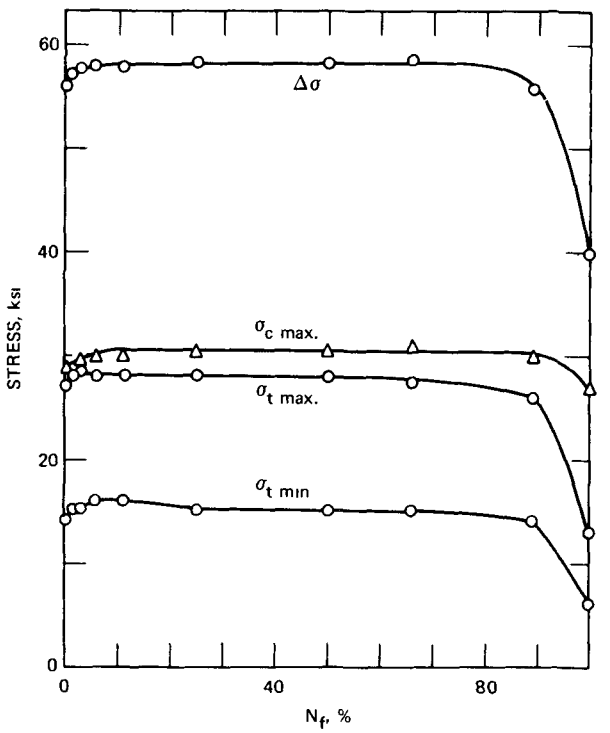

Fig. 8.39 σ vs. N plot.

Specimen 57-4	Strain rate, 4×10^{-5} sec^{-1}
Temp., 650° C	$N_f = 182$
Strain range, 2.00%	30-min hold period in tension only

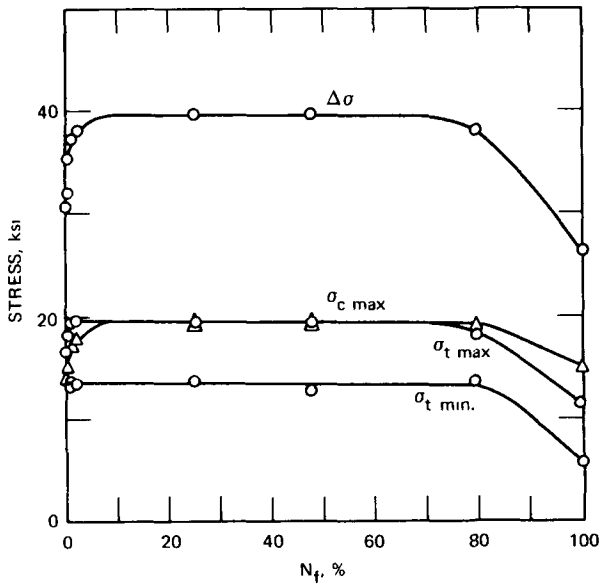

Fig. 8.40 σ vs. N plot.

Specimen 65-4	Strain rate, 4×10^{-3} sec^{-1}
Temp., 650°C	$N_f = 995$
Strain range, 0.50%	60-min hold period in tension only

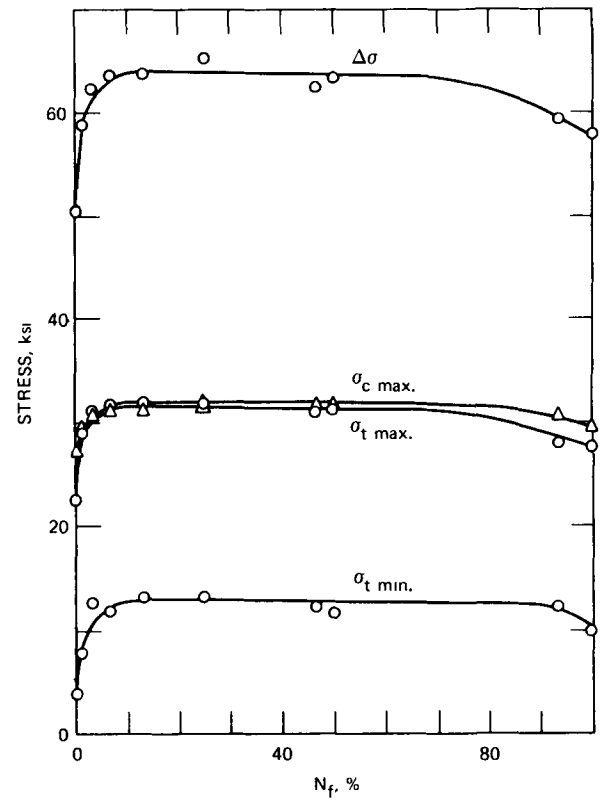

Fig. 8.41 σ vs. N plot.

Specimen 57.6	Strain rate, 4×10^{-3} sec^{-1}
Temp., 650°C	$N_f = 150$
Strain range, 2.00%	180-min hold period in tension only

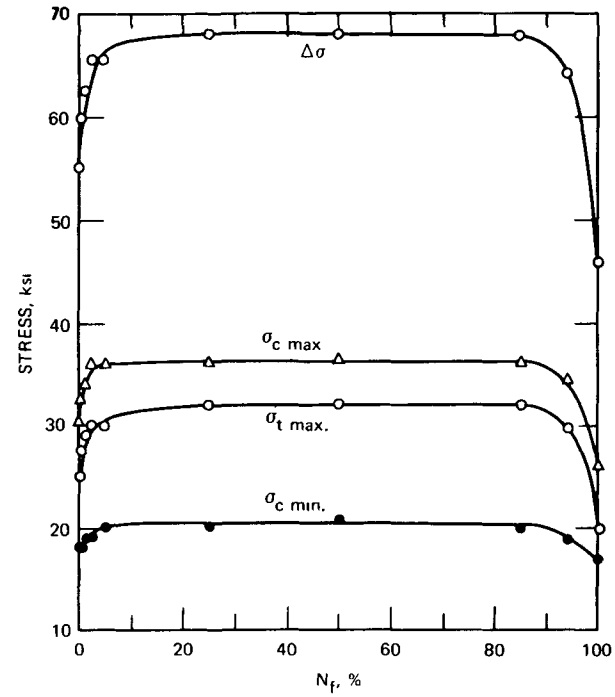

Fig. 8.42 σ vs. N plot.

Specimen 52-11	Strain rate, 4×10^{-3} sec^{-1}
Temp., 650°C	$N_f = 409$
Strain range, 2.00%	30-min hold period in compression only

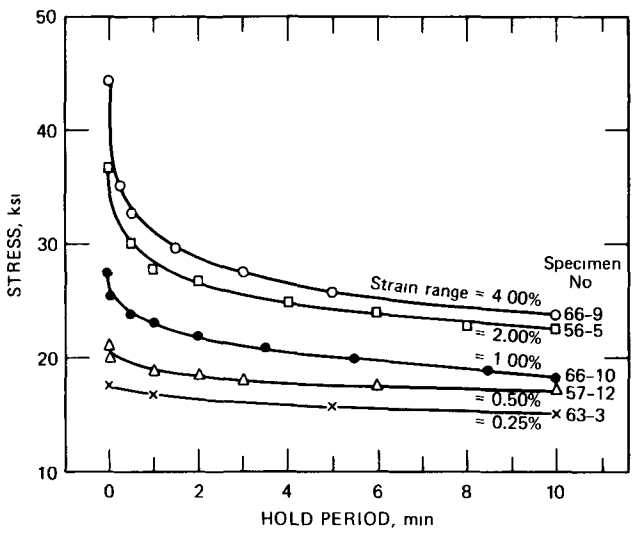

Fig. 8.43 Relaxation data obtained in hold-time tests of annealed AISI 304 stainless steel at 650°C in air (strain rate during cycling was 4×10^{-3} sec^{-1}, and the hold period was 10 min in tension only).

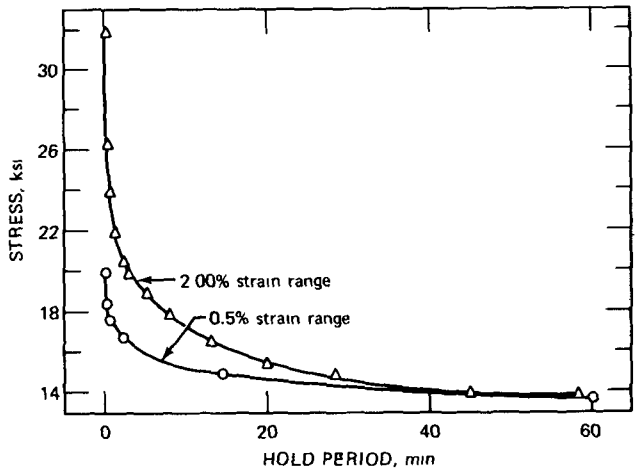

Fig. 8.44 Relaxation data obtained in hold-time tests of annealed AISI 304 stainless steel at 650°C in air (strain rate during cycling was 4×10^{-3} sec^{-1}, and the hold period was 60 min in tension only).

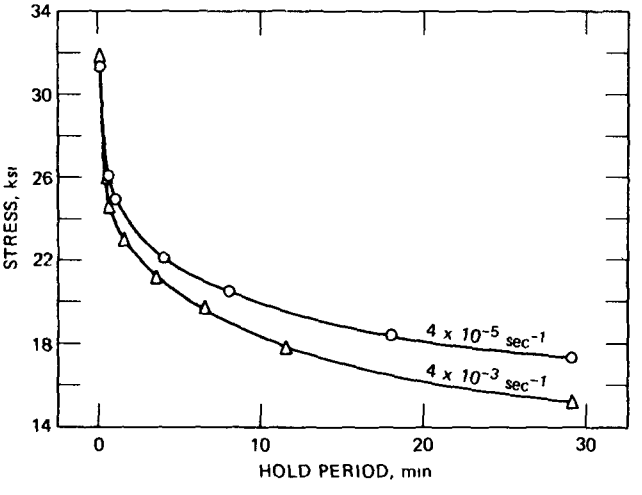

Fig. 8.45 Relaxation data obtained in hold-time tests of annealed AISI 304 stainless steel at 650°C in air (strain rate during cycling was 4×10^{-3} and 4×10^{-5} sec^{-1}, and the hold period was 30 min in tension only at a strain range of 2%).

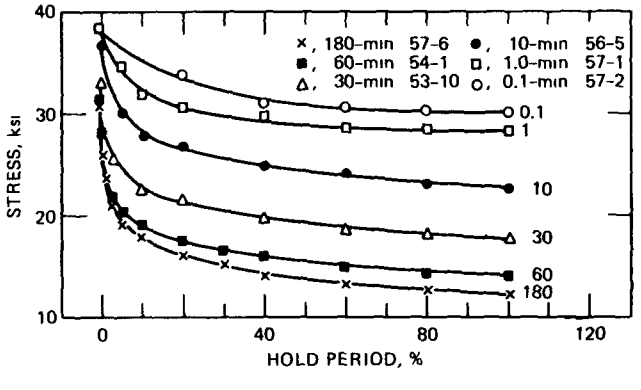

Fig. 8.46 Relaxation data obtained in hold-time tests of annealed AISI 304 stainless steel at 650°C in air (strain rate during cycling was 4×10^{-3} sec^{-1}, and the hold period in tension only varied from 0.1 to 600 min at a strain range of 2%).

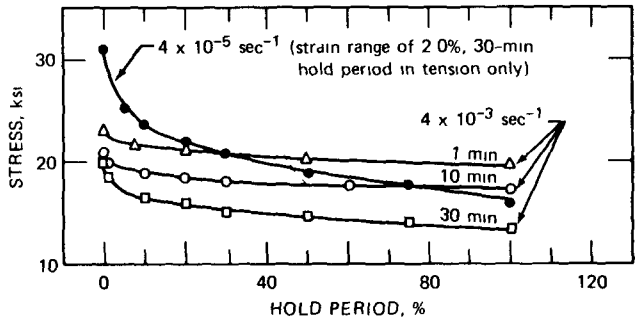

Fig. 8.47 Relaxation data obtained in hold-time tests of annealed AISI 304 stainless steel at 650°C in air (strain rate during cycling was 4×10^{-3} and 4×10^{-5} sec^{-1} with hold periods of 1 to 30 min in tension only at a strain range of 0.5%).

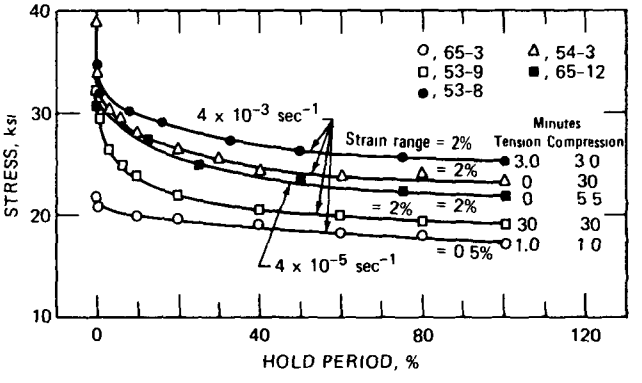

Fig. 8.48 Relaxation data obtained in hold-time tests of annealed AISI 304 stainless steel at 650°C in air (strain rate during cycling was 4×10^{-3} and 4×10^{-5} sec^{-1} at various hold times in tension and compression).

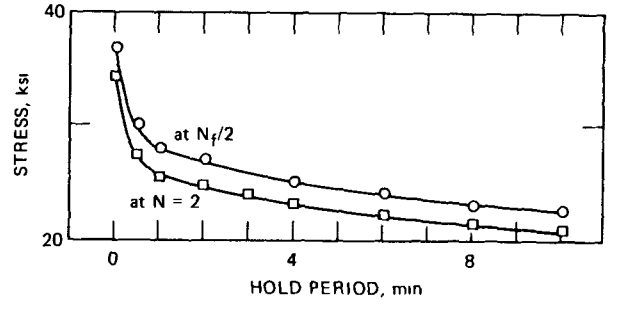

Fig. 8.49 Relaxation data obtained in hold-time tests of annealed AISI 304 stainless steel at 650°C in air (strain rate during cycling was 4×10^{-3} sec^{-1} and the hold period was 10 min in tension only at a strain range of 2%).

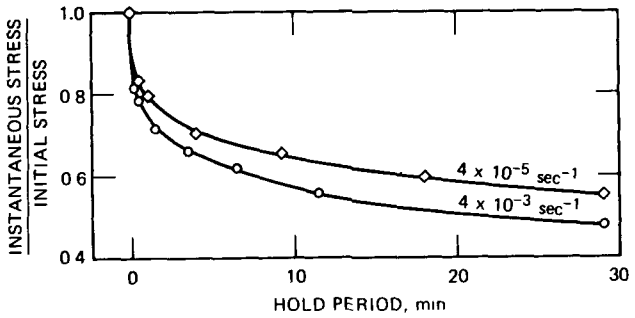

Fig. 8.50 Relaxation data obtained in hold-time tests of annealed AISI 304 stainless steel at 650°C in air (strain rate during cycling was 4×10^{-3} and 4×10^{-5} sec^{-1}, and the hold period was 30 min in tension only at a strain range of 2%).

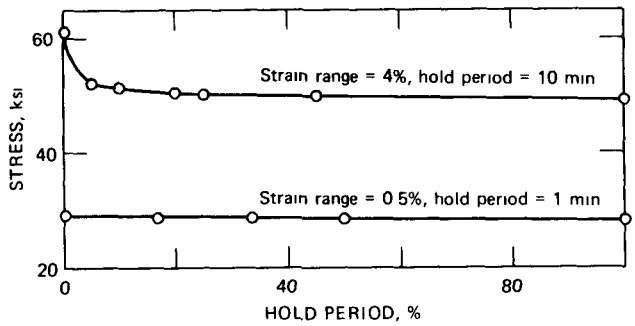

Fig. 8.53 Relaxation data for AISI 304 stainless steel obtained in tests in air at 538°C (1000°F), involving hold periods in tension only at a cycling strain rate of 4×10^{-3} sec^{-1}.

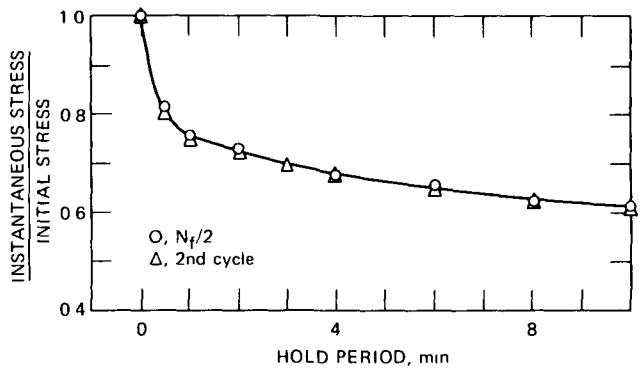

Fig. 8.51 Comparison of relaxation data for Fig. 8.12 in terms of stress ratio.

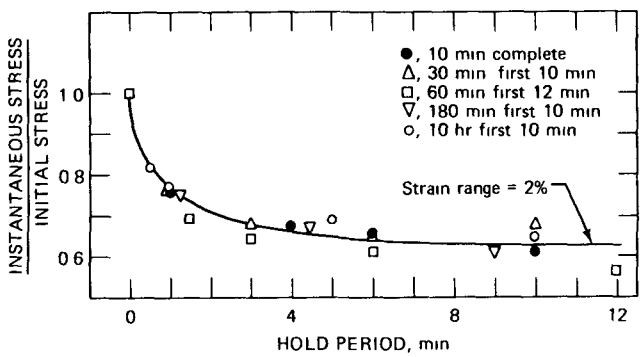

Fig. 8.52 Relaxation data for annealed AISI 304 stainless steel tested in air at 650°C using various hold times in tension only, compared in terms of the stress ratio.

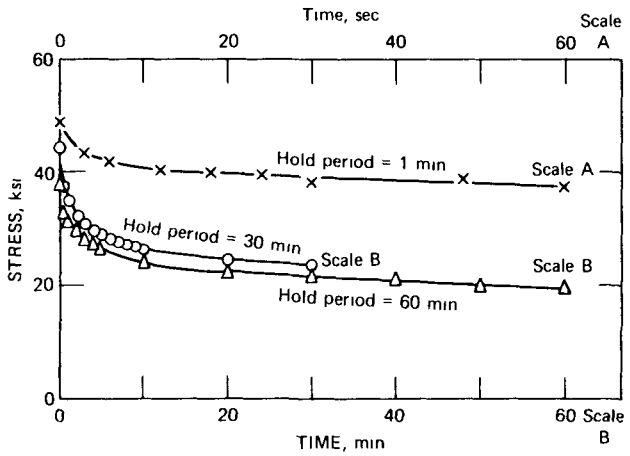

Fig. 8.54 Relaxation data for AISI 316 stainless steel tested in air at 650°C, using hold periods in tension only at a strain range of 2% and a cycling strain rate of 4×10^{-3} sec^{-1}.

4. Relaxation curves for various combinations of tension and compression hold periods (Fig. 8.48).

5. Relaxation curves at 2% strain range obtained during the second cycle and at $N_f/2$ (Fig. 8.49).

6. The σ/σ_0 plot of relaxation data obtained using various hold periods at a strain range of 2%; data in Fig. 8.52 indicate essentially identical behavior for the first 10 to 12 min of the hold period independent of the total length of the hold period.

7. Relaxation data for AISI 304 stainless steel at 538°C (1000°F) for comparison with the data at 650°C; comparing Fig. 8.53 with Fig. 8.43, it is noted that smaller stress relaxation occurs as the temperature is reduced from 650°C to 538°C.

8. Relaxation data for AISI 316 stainless steel at 650°C (see Fig. 8.54); on the basis of a limited analysis of these data, a definite similarity with the 304 stainless-steel data is indicated; for example, at a strain range of 2% and using a hold period of 60 min, the curve in Fig. 8.54 appears to be displaced about 6 ksi above the corresponding curve in Fig. 8.44.

An interesting analysis of the data in Fig. 8.43 is presented in Fig. 8.55 to reveal a fairly definite linearity between the instantaneous stress and the logarithm of time. This behavior pattern leads to an equation of the form

$$\sigma = A - B \log t \tag{8.60}$$

which provides an excellent representation of the relaxation profile for essentially the entire hold period. It does not accommodate the boundary condition at zero time, but a simple rearrangement to yield

$$\sigma = A - B \log (1 + t) \tag{8.61}$$

provides an effective mathematical form that applies at zero time to define A as the initial stress. This expression is identical to that described by Feltham. Slope calculations based on the data in Fig. 8.55 led to the calculation of A values for all the strain ranges involved. These calculations led to the following:

Strain range, %	Value of A calculated from Fig. 8.55, psi	Value of A from Fig. 8.43, psi
4.0	43,100	44,400
2.0	39,100	36,800
1.0	30,100	27,500
0.5	21,000	21,000
0.25	17,900	17,400

The initial stress values calculated from the linearities defined in Fig. 8.55 provide fairly accurate (within a few percent) estimates of the experimentally measured values for σ_0. Note also that the equations derived from Fig. 8.55 provide a very accurate representation of the relaxation behavior for all the strain ranges involved.

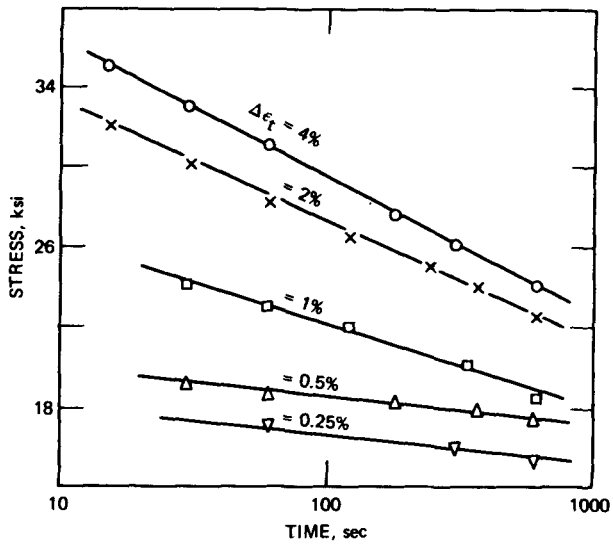

Fig. 8.55 Replot of relaxation data from Fig. 8.43.

An interesting analysis of these same data in terms of $(\sigma_0 - \sigma)$ is shown in the rectangular coordinate plot of Fig. 8.56. For each strain range the curves define the general shape of a primary creep curve. This plot also reveals that the decrease in stress in a given time period is a definite function of the strain range. This implies that the rate of conversion of elastic to plastic strain increases as the strain range increases. This is an interesting behavior pattern and one that warrants additional study. One obvious attempt to bring all these data into correlation is related to the use of σ_0/σ or $(\sigma_0 - \sigma)/\sigma_0$ in order to account for the different initial stress values that evolve as the strain range is changed. It can be shown, however, that this approach fails to provide an acceptable correlation inasmuch as the $(\sigma_0 - \sigma)/\sigma_0$ values for the higher strain ranges are much greater than those corresponding to the lower strain ranges.

Equation 8.61 also specifies linearity between $(\sigma_0 - \sigma)$ and log (1 + t) or merely log t for those cases where t is large compared to unity. Such a relation can be shown to result from the data in Fig. 8.43, and the slope of these lines gradually decreases as the strain range decreases. An analysis of this type has been performed for the data given in Fig. 8.43, with the results shown in Fig. 8.57. It should be recognized in connection with this plot that there exists a definite suggestion that a nonlinearity develops as the strain range decreases. This may be seen in the data for strain ranges of 1% and below. Apparently, in these lower strain ranges the $(\sigma_0 - \sigma)$ plot tends to flatten out in the region of short relaxation times to approximate the shape of the curve shown in Fig. 8.33. Of course, these data are somewhat limited, and more confirmation of this behavior pattern must be obtained before a definite conclusion can be drawn.

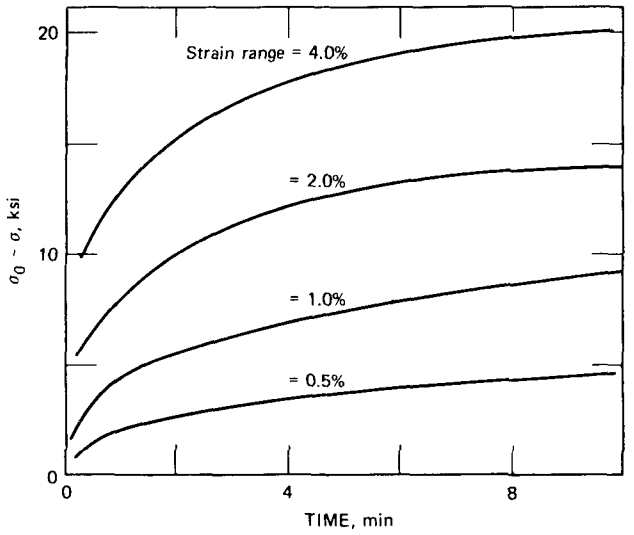

Fig. 8.56 Relaxation data from Fig. 8.43 expressed in terms of $\sigma_0 - \sigma$.

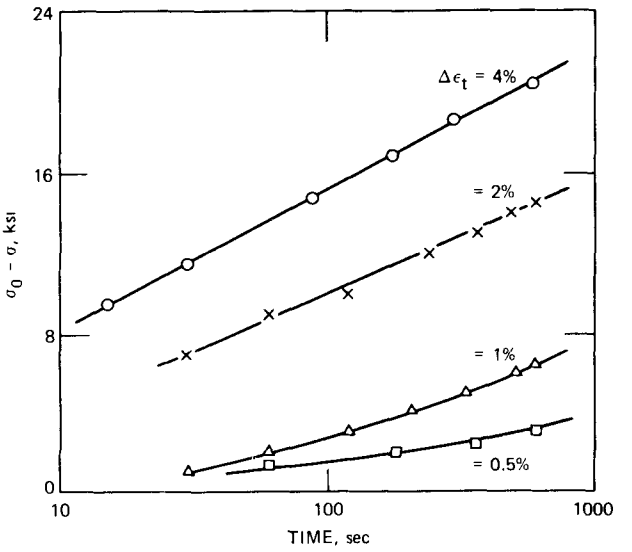

Fig. 8.57 Correlation of the relaxation data from Fig. 8.43.

A plot similar to the one shown in Fig. 8.57 has been prepared using the data from Fig. 8.46 and is presented in Fig. 8.58. This is an important result, for it highlights the following features:

1. The same linearity noted in Fig. 8.57 is seen to persist to relaxation times of 180 min; this is well beyond the limit of 20 min noted by Feltham.[22] A great deal of significance cannot be attached to this difference because of the different materials and different test temperatures involved in the two studies.

2. Although the slopes for the different hold-period durations appear to be close to the same value, there is a slight variability that suggests additional study of this point.

3. The position of the lines for the different hold-period durations is slightly different to reflect the slight differences in the initial stress values.

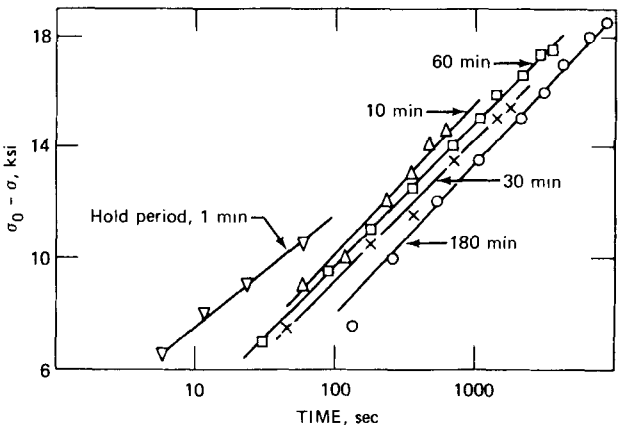

Fig. 8.58 Relaxation analysis of data from Fig. 8.46.

Another correlation of the Fig. 8.46 data is presented in Fig. 8.59 to reveal an impressive similarity in the data when normalized in terms of the σ/σ_0 values. When the initial stress values are taken into account, the relaxation curves for the different hold-period durations all appear to be similar.

In a recent development[21] an analysis of relaxation data in terms of stress rate was proposed (see the section entitled "Review of Relaxation in Simple Tension Loading"). Applying this concept to the data in Fig. 8.43 for several strain ranges led to the results shown in Fig. 8.60. No explanation is available as yet to account for the identical line for the 2 and 4% strain ranges and for the separate line at 0.5% strain range. It is impressive, however, that the two lines shown appear to be parallel (slope is about −0.92). More remains to be done in this area of relaxation analysis, and, as more data become available, a clearer understanding of this very interesting behavior pattern will develop.

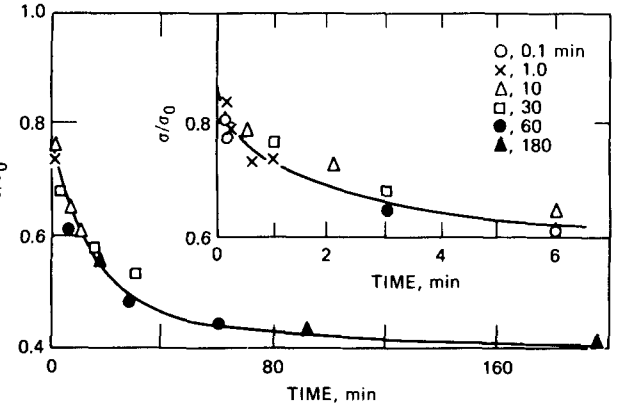

Fig. 8.59 Relaxation data from Fig. 8.46 analyzed in terms of σ/σ_0.

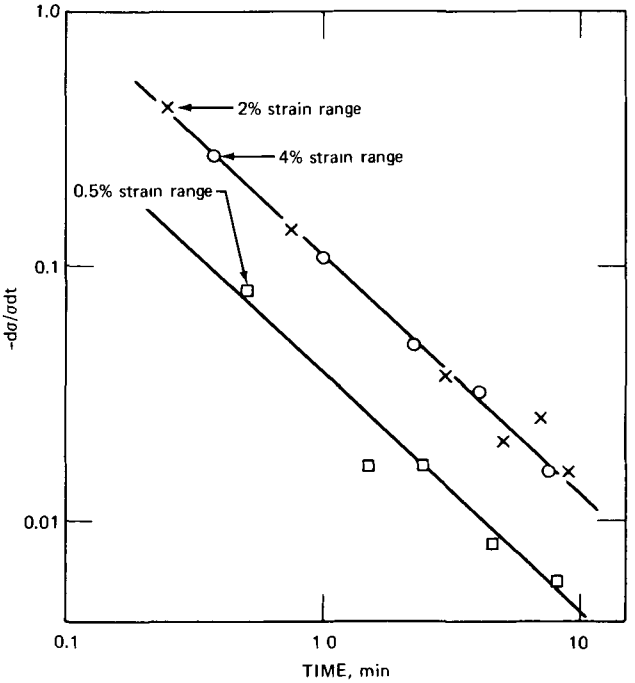

Fig. 8.60 Stress-rate correlation of the data from Fig. 8.43.

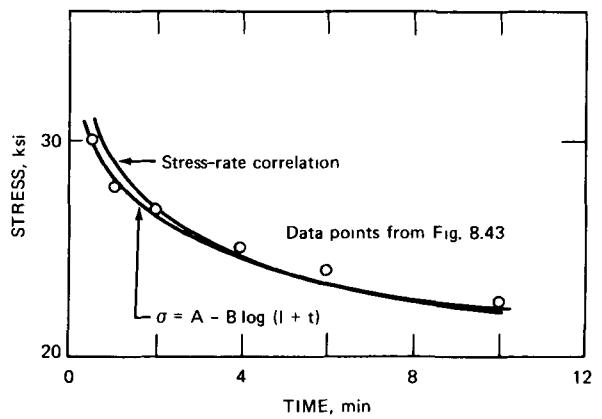

Fig. 8.61 Comparison of the effectiveness of several relaxation expressions.

A calculation of slope and intercept values for the 2% strain-range data in Fig. 8.60 led to a relaxation equation based on the stress-rate correlation. This expression led to the calculated relaxation curve shown in Fig. 8.61 and is seen to compare well with the selected points taken from Fig. 8.43. Also shown in this plot is the relaxation curve calculated using the equation derived from Fig. 8.55. Both expressions are fairly effective in providing an accurate (within a few percent) representation of the relaxation profile. Both expressions warrant additional study for use in relaxation calculations.

One real test of the effectiveness of a relaxation equation is the extent to which it provides an accurate representation of the experimental results. Another equally important test involves its effectiveness in extrapolating beyond the range of the data. Both approaches mentioned in Fig. 8.61 have been evaluated to assess their extrapolative capability. The data involving the 180-min hold period (see Fig. 8.46) were selected, and the analysis was limited to the data below 50 min. Equation constants were evaluated, and the relaxed stress at a time of 180 min was calculated. This led to a relaxed stress value of 11.8 ksi using the stress-rate correlation and 12.2 ksi using the semilogarithmic expression derived from Fig. 8.55. These extrapolations are in excellent agreement with the measured value of 12.0 ksi. Although the extrapolation involved here is very limited, the point is that the two approaches being considered seem to have merit in estimating relaxation behavior beyond the experimental regime. This is another area which should receive additional attention in subsequent relaxation studies.

RELATION BETWEEN CREEP AND RELAXATION

Although it is easy to recognize a definite association between creep and relaxation, it has proven rather difficult to define an accurate formulation to allow one effect to be used in calculating the other. It is not possible, for example, to calculate or derive a creep curve from a single relaxation curve. Neither is it possible to develop a relaxation curve from a single creep curve. But it is possible to obtain at least some qualitative information about one type of behavior from the measurement of the other. Oding[1] showed this quite conclusively in tests of an austenitic Cr–Ni steel having different initial heat treatments. Creep tests were performed at a stress of 12 kg/mm^2, and the relaxation tests were performed with an initial stress level of 12 kg/mm^2. Heat treatments that made the material more creep resistant also rendered the material more resistant to relaxation.

In commenting on relaxation, Oding[1] said that relaxation should really not be regarded as the conversion of elastic to plastic strain but rather as the increase of plastic strain accompanied by a simultaneous decrease in the elastic strain. Oding also stated that "the process which occurs during relaxation constitutes creep at a stress decreasing with time" and that "relaxation is creep occurring under variable stress."

Oding mentioned the possibility of constructing a creep curve from a series of relaxation curves obtained in a special sequence of reloadings of the same specimen. This is shown schematically in Fig. 8.62 for one preselected initial stress level. After relaxing for time t, the stress decrement corresponds to a certain amount of plastic strain, and this leads to one point on the strain–time plot. At time, t_1, the specimen load is increased to the initial value, and relaxation for a selected time period is allowed to occur. This yields another stress decrement and some additional plastic strain, and this plastic-strain component represents an increment that can be added on to the plastic strain

observed in the first relaxation period. In this way a second point on the strain–time plot is identified, and subsequent loadings will serve to completely define the creep curve. Oding also treated the case of a special creep evaluation that could be used to develop a relaxation curve. In each case, the smaller the time intervals the more accurate is the conversion of one type of data to the other.

Although it is not possible to generate a creep curve from a single relaxation curve, it is possible to derive some very valuable creep-rate information from a relaxation isotherm. Instantaneous-slope calculations yield stress-rate values that can be converted to creep-rate data that can then be plotted against the corresponding instantaneous values of stress. This type of stress vs. creep-rate information has been interpreted by Lee and Hart[32] as the proper method to be used in any presentation of relaxation results. The measured stress vs. creep-rate relation was cited by these investigators as a well-defined property of a material and one that is a directly measurable quantity in a relaxation test. Data of this type, based on the Lee and Hart[32] study of zirconium, are presented in Fig. 8.63.

An analysis of the relaxation data[21] obtained in the 60-min hold-time test of 316 stainless steel at 650°C and a strain range of 2% (see Fig. 8.54) led to the stress vs. creep-rate plot shown in Fig. 8.64. A fairly well-defined linearity is exhibited over the range of available data (highest stress corresponds to a relaxation time of about 0.5 min) to indicate an exponent on stress (value of n in Eq. 8.23) equal to 11.0. Also shown in Fig. 8.64 are some steady-state creep-rate data for 316 stainless steel at 650°C. These results reveal that the steady-state creep rate at 30,000 psi is about two orders of magnitude lower (although this difference is real, the magnitude of the difference might be influenced by the fact that the exact same heat of material was not employed in the two types of test) than the creep rate measured at this stress level in the relaxation test. Also of special interest is the fact that the value of n for the steady-state creep results in about 5.0. These observations indicate two important conclusions: (1) the creep rate obtained in the relaxation test is very much higher than the corresponding steady-state creep rate, and this suggests that the creep rate observed in the relaxation test is more closely related to a primary creep rate than to a steady-state value; (2) different stress dependencies exist in relaxation and steady-state creep studies.

The conclusions reached in the analysis of the Fig. 8.64 correlation are much different from those noted in the Kennedy–Douglas study (see Table 8.3). Here the creep constants appearing in Eq. 8.23 were the same, independent

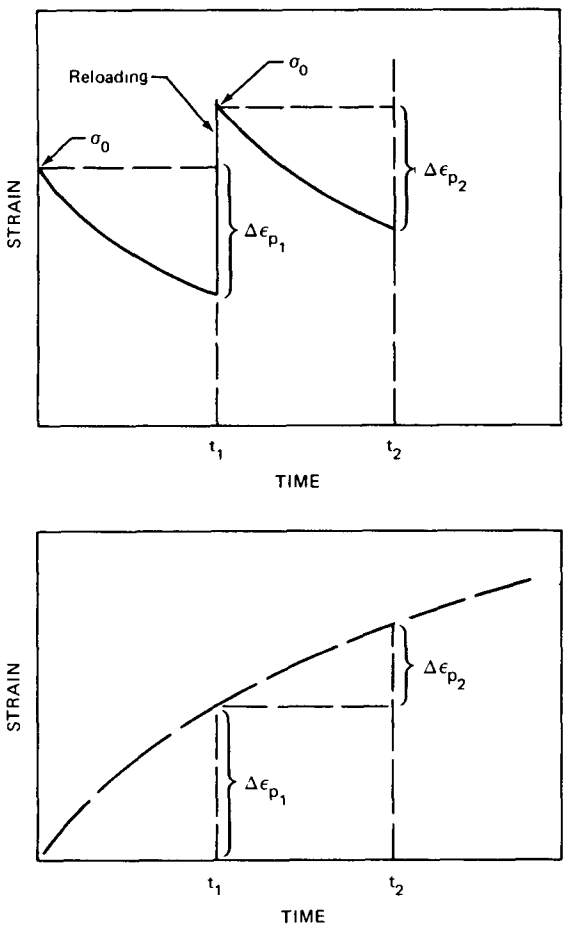

Fig. 8.62 Generation of creep curve from a relaxation study. (From Ref. 1.)

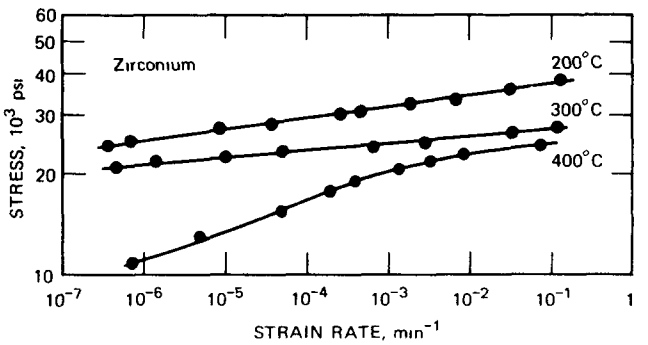

Fig. 8.63 Stress vs. creep-rate information obtained in relaxation test of zirconium. (From Ref. 32.)

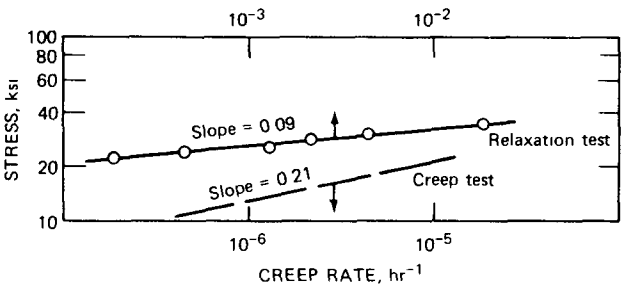

Fig. 8.64 Creep-rate information obtained in relaxation and creep tests of 316 stainless steel at 650°C; relaxation results obtained in a low-cycle-fatigue test at 2% strain range and using a 60-min hold period in tension only.

of whether they were determined in creep or relaxation measurements. It is not possible to reconcile these apparent discrepancies, although they might be explainable if the regime of primary creep is negligible in the Inconel material at the temperatures in question. A qualitative description of this interpretation is shown in Fig. 8.65. If one specimen is loaded to some initial stress in a creep test, the strain on loading is indicated to be ϵ_0 and the creep rate for the conventional test decreases with time and approaches a constant value as the steady-state creep regime is approached. In another specimen the same initial stress is applied, but the specimen is allowed to relax as the total strain is held constant at ϵ_0. In this instance it can be assumed that the creep rate at time zero is the same in both tests for the first few moments. In both tests the creep rates decrease from this initial value but certainly not to the same extent. It is clear, however, that, for a given stress level, a creep curve has many different creep rates associated with it, and, hence, which of these is to be used in interpreting relaxation behavior remains a problem. A part of this problem relates to how the decreasing stress in the relaxation test affects the instantaneous creep rate. If no primary creep is present and steady-state creep is observed from the instant of loading, the creep curve in Fig. 8.65 would be linear and a single creep rate could be associated with a given stress. Then a specific creep rate could be assigned at each stress level along the relaxation curve, and this might explain the agreement noted in Table 8.3.

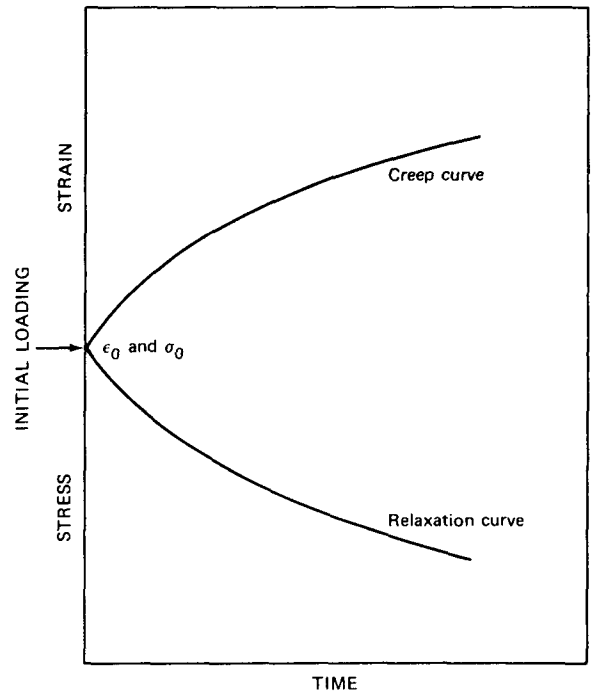

Fig. 8.65 Schematic comparison of creep and relaxation curves.

USING CREEP EQUATIONS TO DESCRIBE RELAXATION

Robinson–Kanter Equation

One of the first attempts to use a creep equation in the development of a mathematical expression to describe the stress–time behavior during relaxation was reported by Robinson[7] and Kanter.[9] The resulting expression has already been discussed and is given by Eq. 8.26. Once steady-state creep data are available, the creep constants in Eq. 8.26 can be calculated, and then the relaxation pattern can be calculated.

Soderberg Method

In another very early study of the interrelation between creep and relaxation, Soderberg[33] reasoned that the creep strain, ϵ_p, a stress function, S, and a time function, t*, were related in the form

$$\epsilon_p = St^* \tag{8.62}$$

He demonstrated further that, for 12% Cr steel at 850°F, the stress function led to

$$\epsilon_p = \frac{s_1}{E}(e^{\sigma/s_1} - 1)t^* \tag{8.63}$$

where E is the modulus, and s_1 is a constant to be evaluated from creep data.

A differential change in strain was then obtained from Eq. 8.62 as

$$d\epsilon_p = Sdt^* + t^*\left(\frac{\partial S}{\partial \sigma}\right)d\sigma \tag{8.64}$$

Using $d\epsilon_p = -d\sigma/E$, S from Eq. 8.63, and $\partial S/\partial\sigma$, it follows that

$$d\sigma = -s_1\frac{e^{\sigma/s_1} - 1}{1 + t^*e^{\sigma/s_1}}dt^* \tag{8.65}$$

An integration of Eq. 8.65 using the boundary conditions of $t = 0$ and $\sigma = \sigma_0$ would yield the relaxed stress as a function of t*. Then if the time function is known, each value of stress can be associated with a given time. Soderberg noted that Eq. 8.65 could not be directly integrated but rather had to be solved by a step-by-step approach.

A direct integration of Eq. 8.65 was described by Davenport.[34] Substituting $Y = e^{\sigma/s_1}$ lets Eq. 8.65 yield

$$\frac{dt^*}{dY} + \frac{1}{Y - 1}t^* = \frac{-1}{Y(Y - 1)} \tag{8.66}$$

which is a linear differential equation and integrable to

$$t^* = -\frac{(\sigma/s_1) + c}{e^{\sigma/s_1} - 1} \tag{8.67}$$

With the condition that, at $t = 0$ ($t^* = 0$), the stress is σ_0, the constant c is given by $-\sigma_0/s_1$, and hence

$$t^* = \frac{\sigma_0/s_1 - \sigma/s_1}{e^{\sigma/s_1} - 1} \tag{8.68}$$

In another study of the Soderberg equation, Roberts[35] showed that Eq. 8.68 could be derived without integration. Beginning with Eq. 8.9 and substituting σ_0/E for ϵ_t, σ/E for ϵ_e, and Eq. 8.63 for ϵ_p, Roberts showed that Eq. 8.68 follows by a simple rearrangement.

Davenport Method

Two theories were proposed by Davenport[36] in a study of the interrelation between creep and relaxation results. One theory was termed "the strain-hardening theory" and assumed that the creep rate at a given temperature was a function only of the stress and the instantaneous value of the plastic (creep) strain; the second theory was termed "the time-hardening theory" and assumed that the creep rate at a given temperature was a function only of the stress and the time. These theories are shown graphically in Fig. 8.66. If a material is strained to point A at stress level σ_1, and the stress level is changed to σ_2, the strain-hardening theory states that the creep rate at the instant of the change will correspond to that at point B on the curve for σ_2. This point is located by merely proceeding horizontally (i.e., at the same strain value) from the one creep curve to the next. At this second stress level, additional straining takes place along BC. Proceeding similarly in subsequent stress changes locates points C, D, E, and F.

In the time-hardening approach, the behavior obtained in transferring from one stress level to another is obtained by proceeding vertically from one creep curve to another. Points A through F are established in a process similar to that described for the strain-hardening concept.

Davenport proposed a graphical solution that allowed the positioning of relaxation curves based on a knowledge of creep data. This approach is illustrated by a series of creep curves that was assumed as shown in Fig. 8.67(a). A given stress level was considered, and calculations of the instantaneous slope at various strain values led to the strain vs. creep-rate plot of Fig. 8.67(b). Similar calculations at other stress levels served to develop other constant-stress isotherms. It was then reasoned that, since $d\epsilon_p/dt$ is given by $\dot{\epsilon}_p$,

$$dt = \frac{d\epsilon_p}{\dot{\epsilon}_p} \tag{8.69}$$

and the relaxation time, t, will be given by

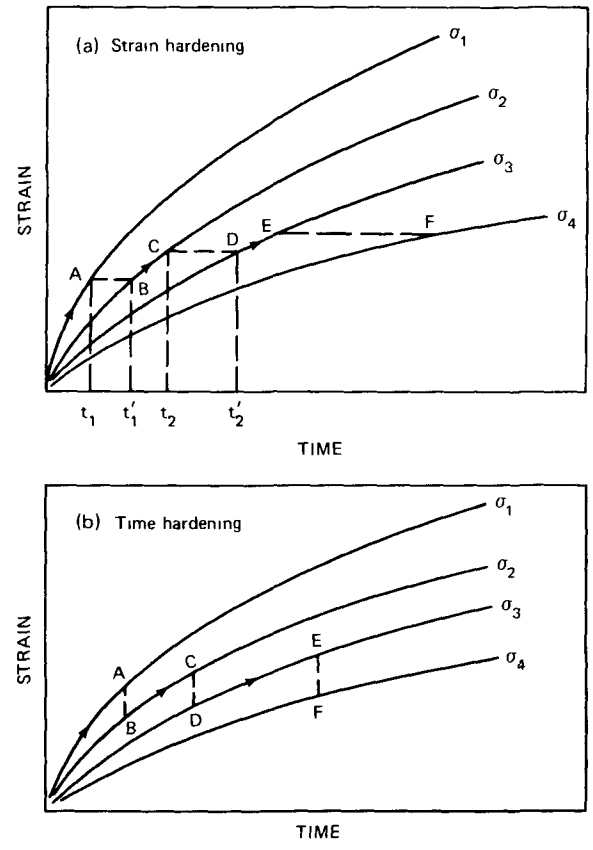

Fig. 8.66 Creep curves for various stress levels used to illustrate strain-hardening theories.

$$t = \int_0^t dt = \int \frac{d\epsilon_p}{\dot{\epsilon}_p} \tag{8.70}$$

The graphical integration suggested by Eq. 8.70 is shown schematically in Fig. 8.67(c) to define the relaxation time, t, as the area under the curve between a creep strain of zero (strain at σ_0) and a creep strain at any relaxed stress σ. It can be observed that the stress is decreasing during relaxation, and each $\dot{\epsilon}_p$ value used in Fig. 8.67(c) corresponds to a different stress level. Each strain value in Fig. 8.67(c)corresponds to a certain relaxed stress level, and it is this stress level that is used to establish $\dot{\epsilon}_p$. A similar approach, interchanging strain and time, applies to the case of time hardening.

Davis Equation

In a study of the creep and relaxation behavior of copper, Davis[37] expressed the creep rate using a hyperbolic sine equation of the form

$$\dot{\epsilon}_p = A \sinh \frac{\sigma}{B} \tag{8.71}$$

where A and B are constants that evolve from an evaluation of steady-state creep-rate data at different stress levels. Substituting Eq. 8.71 into Eq. 8.21 led to

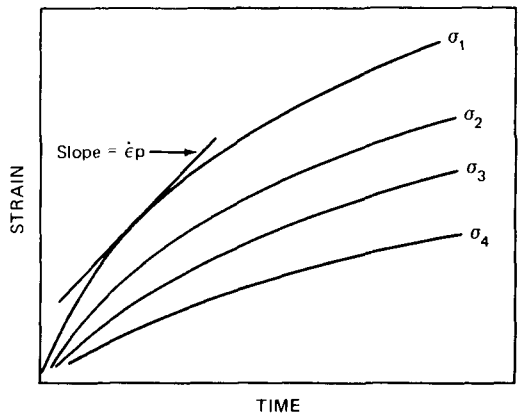

(a)

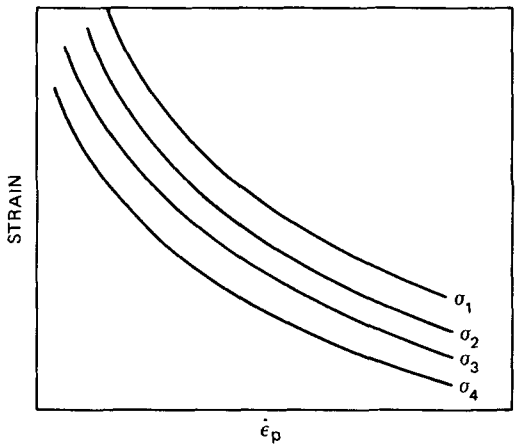

(b)

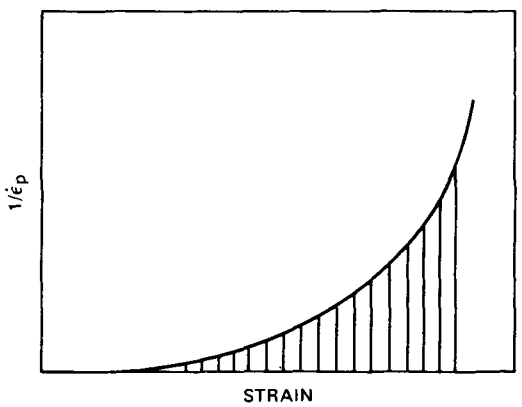

(c)

Fig. 8.67 Schematic illustration of graphical approach suggested by Davenport, based on strain-hardening theory. (From Ref. 36.)

$$t = \frac{B}{EA} \ln \frac{\tanh \frac{\sigma_i}{2B}}{\tanh \frac{\sigma}{2B}} \tag{8.72}$$

where σ_i is the initial stress level in the relaxation test. Davis assumed various values for σ_i and calculated corresponding relaxation curves but could not show good agreement with the experimental relaxation curve for copper at 165°C. For an initial stress level of 13,500 psi, Eq. 8.72 yielded much higher relaxed stress levels than the experimental measurements revealed, although the agreement improved considerably in the relaxation regime beyond 1000 hr.

An interesting analysis of the effectiveness of various relaxation equations derived from creep relations was reported by Finnie and Heller.[38] A portion of this comparison is presented in Fig. 8.68 to indicate the ineffectiveness of both Eqs. 8.26 and 8.72. In extending the comparison of Finnie and Heller, Conway[3] reported an analysis in which the relaxation data in Fig. 8.68 were used. Experimental values in the range to 100 hr were employed in conjunction with Eq. 8.37 to yield the excellent linearity shown in Fig. 8.69. This plot led to n = –0.79, A = 0.043, and $\bar{\sigma}_0$ = 14.3. Several calculated stress–time combinations are shown as open circles in Fig. 8.68 to attest to the excellent representation of the copper data provided by this stress-rate correlation. In making this analysis of the copper data, Conway noted that the logarithmic type of plot suggested in Eq. 8.30 and illustrated in Fig. 8.55 did not prove to be linear in this analysis, and hence the effectiveness of the stress-rate correlation was again shown to be worthy of special attention.

Davis[37] cited an important conclusion in connection with Eq. 8.71. He felt that a simple relation between stress and creep rate was not enough to give an adequate description of relaxation behavior and concluded that the use of only minimum creep-rate information could not be satisfactory in such analyses. Using some creep data for copper at room temperature, Davis noted that a strain–time plot was linear on logarithmic coordinates to define a primary creep regime extending over a period close to 1 year. An analysis of these results led to strain, time, strain-rate equations of the form

$$\sigma = K\epsilon_p^m (\dot{\epsilon}_p)^n \tag{8.73}$$

and

$$\epsilon_p = Bt^{\frac{n}{m+n}} \tag{8.74}$$

where ϵ_p is the plastic strain, $\dot{\epsilon}_p$ is the strain rate, and m and n are constants. The use of these expressions led to a relaxation equation having the form

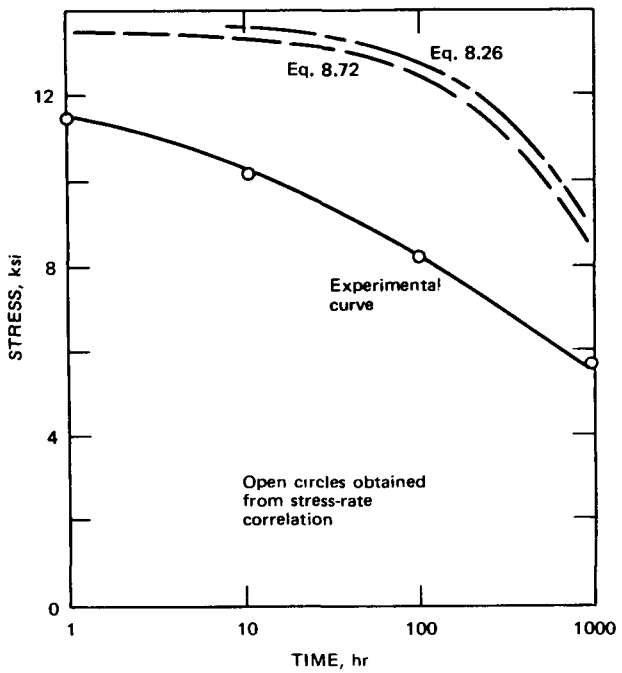

Fig. 8.68 Comparison of the effectiveness of several relaxation equations derived from creep expressions. (Relaxation data for copper at 165°C.) (From Ref. 38.)

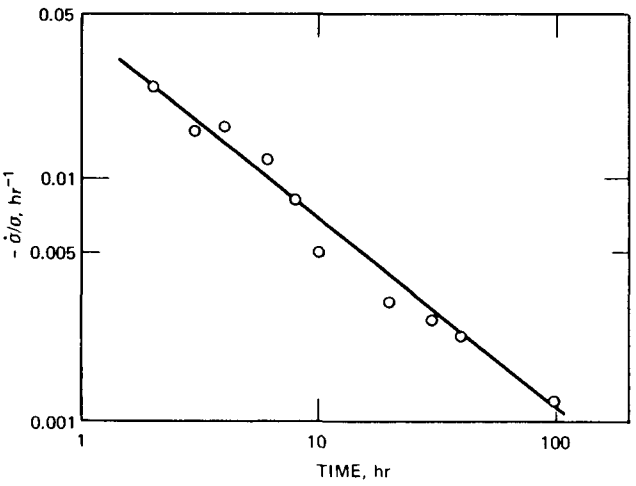

Fig. 8.69 Stress-rate correlation of the data for the first 100 hr in Fig. 8.68.

$$t = -c \int_{\sigma_0}^{\sigma} \frac{(\sigma_i - \sigma)^{m/n}}{\sigma^{1/n}} d\sigma \qquad (8.75)$$

This gave an excellent description of the room-temperature relaxation behavior. However, because the strain levels and the strain rates were small, it was not felt that this approach would be effective in high-temperature applications where a minimum creep rate is observed.

Davis used the McVetty[39] equation

$$\epsilon_p = \epsilon_0(1 - e^{-kt}) + \dot{\epsilon}_s t \qquad (8.76)$$

to account for both primary and secondary creep characteristics, but this approach was not evaluated in sufficient detail to warrant any specific conclusions.

Popov Method

A detailed review of the proposed methods used in calculating relaxation behavior from creep information was reported by Popov.[40] Special emphasis was given to a numerical solution for the relaxation curve based on the strain-hardening theory. This calculation procedure was described using a general creep expression containing terms to define both primary and secondary creep behavior. The form of this expression was as follows:

$$\epsilon_p = C_1 f(t) \sinh \frac{\sigma_a}{C_2} + u_0 t \sinh \frac{\sigma_a}{C_3}, \qquad (8.77)$$

where C_1, C_2, u_0, and C_3 are constants, t is time, and f(t) is the time function associated with the primary creep regime. During the relaxation from the initial stress, σ_0, to any stress, σ, the creep strain involved is given by

$$\epsilon_p = \frac{\sigma_0 - \sigma}{E} \qquad (8.78)$$

which, when equated to Eq. 8.77, gave

$$\frac{\sigma_0 - \sigma}{E} = C_1 f(t) \sinh \frac{\sigma_a}{C_2} + u_0 t \sinh \frac{\sigma_a}{C_3} \qquad (8.79)$$

Calculations begin at zero time with $\sigma = \sigma_0$; (for an explanation in terms of Fig. 8.66, assume $\sigma_0 = \sigma_1$); a relaxed stress level, σ_2, is assumed just slightly lower than σ_1; then σ_a is calculated as the average of the two stress levels, and Eq. 8.79 is solved for t_1 to give the relaxation time corresponding to the assumed stress level. This point may be visualized as being represented by point A in Fig. 8.66(a). The creep strain at this point is given by $(\sigma_1 - \sigma_2)/E$, and this value of strain can be used in conjunction with Eq. 8.77 to calculate the time, t_1', which is the time value on the creep curve for the stress level, σ_2. This, of course, is the strain-hardening type of transfer from one creep curve to another and locates point B in Fig. 8.66(a). Another stress level, σ_3, is then assumed to calculate the time required to achieve the creep-strain increment associated with the stress change from σ_2 to σ_3. This locates t_2 in Fig. 8.66(a), and a t_2' value is calculated using the above procedure. In this way the entire relaxation curve can be constructed, but the relaxation time for a given stress level must be calculated as the sum of the time

intervals $(t_n - t'_{n-1})$. In other words, the time to reach stress level, σ_3, is

$$(t_2 - t'_1) + t_1$$

Roberts Analysis

In an excellent analysis of creep and relaxation behavior, Roberts[41] used the primary creep type of expression

$$\epsilon_p = Ct^m \tag{8.80}$$

where m is a constant between zero and unity. Introducing the stress dependence for C led to

$$\epsilon_p = K(e^{\sigma/s} - 1)t^m \tag{8.81}$$

which is the stress–strain–time relation first proposed by Soderberg.[33]

Equation 8.81 traces the gradual accumulation of creep strain as time increases after the application of a given strain. It is not a single-valued function of stress and time, however, and for this reason must be used with caution. A special point was made of this by Roberts in noting that many different values of ϵ_p can be obtained from Eq. 8.81, depending on the stress history. For example, in the illustration shown in Fig. 8.70, all three tests are exposed to σ_2 at time t_1, but the creep strain in each case is different.

Differentiation of Eq. 8.81 led to

$$\dot{\epsilon}_p = \frac{d\epsilon_p}{dt} = mK(e^{\sigma/s} - 1)t^{m-1} \tag{8.82}$$

Another expression for $\dot{\epsilon}_p$ was obtained by taking the m*th* root of both sides of Eq. 8.81 and then differentiating. This yielded

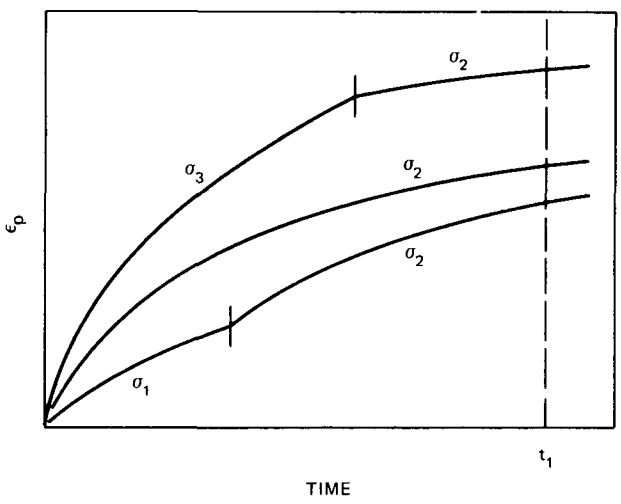

Fig. 8.70 Schematic figure to show how creep strain depends on stress history. (From Ref. 41.)

$$\dot{\epsilon}_p = \frac{m[K(e^{\sigma/s} - 1)]^{1/m}}{\epsilon_p^{(1/m)-1}} \tag{8.83}$$

Still another expression was obtained by squaring both sides of Eq. 8.81 and then differentiating. This led to

$$\dot{\epsilon}_p = \frac{m[K(e^{\sigma/s} - 1)]^2 \, t^{2m-1}}{\epsilon_p} \tag{8.84}$$

Roberts acknowledged that these equations appear identical since a substitution of ϵ_p or t from Eq. 8.81 will yield identical values for $\dot{\epsilon}_p$. However, these equations are not really identical since integration between t_1 and t_2 and ϵ_{p1} and ϵ_{p2} leads to

$$\epsilon_{p2} - \epsilon_{p1} = K(e^{\sigma/s} - 1)(t_2^m - t_1^m) \tag{8.85}$$

$$\epsilon_{p2} - \epsilon_{p1} = [K(e^{\sigma/s} - 1)]^{1/m}(t_2 - t_1) \tag{8.86}$$

and

$$\epsilon_{p2}^2 - \epsilon_{p1}^2 = [K(e^{\sigma/s} - 1)]^2 (t_2^{2m} - t_1^{2m}) \tag{8.87}$$

It was also noted by Roberts that Eqs. 8.82 to 8.84 when combined with Eq. 8.10 and integrated to define the relaxation behavior in terms of the $\sigma - t$ relation, yield completely different results. This observation further confirmed the fact that Eqs. 8.82 to 8.84 are not really identical, even though each expression when integrated at constant stress from zero time to t and from zero strain to ϵ_p will yield Eq. 8.81.

Equation 8.82 corresponds to the time-hardening theory since the creep rate at a given temperature is a function only of stress and time. Similarly, Eq. 8.83 is in accord with the strain-hardening theory since the creep rate is a function only of stress and strain. Furthermore, Eq. 8.84 was viewed as an expression that is applicable when the creep rate is a function of stress, strain, and time.

Applying Eq. 8.82 to relaxation, using Eq. 8.21, led to

$$\int_0^\sigma \frac{d\sigma}{e^{\sigma/s} - 1} = -mEK \int_0^t t^{m-1} \, dt \tag{8.88}$$

and

$$t = \left(\frac{s}{EK} \ln \frac{1 - 1/e^{\sigma_0/s}}{1 - 1/e^{\sigma/s}}\right)^{1/m} \tag{8.89}$$

where the constants s, m, and K are obtainable from creep data. This is the time-hardening approach to relaxation analysis and when applied, using the creep data for copper,[37] led to the estimated relaxation behavior shown in Fig. 8.71.

An illustration of the strain-hardening approach was provided by Roberts by using Eq. 8.83 in conjunction with

Eq. 8.21 and the fact that the initial strain is given by σ_0/E. Substituting and rearranging led to

$$t = -\int_{\sigma_0}^{\sigma} \frac{1}{m(EK)^{1/m}} \frac{(\sigma_0 - \sigma)^{(1/m)-1}}{(e^{\sigma/s} - 1)^{1/m}} \, d\sigma \qquad (8.90)$$

No direct integration was found possible, and so a graphical technique was used to yield the results shown in Fig. 8.71.

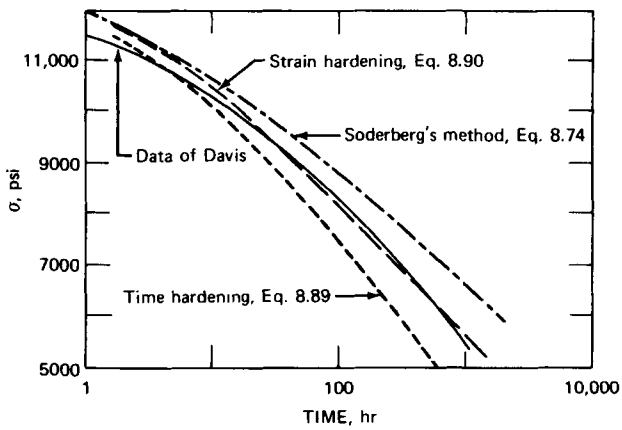

Fig. 8.71 Experimental vs. estimated relaxation behavior of copper at 165°C. (From Ref. 41.)

After the first few hours, the agreement with the experimental results is excellent.

Equation 8.68 for $T = t^m$ was also used by Roberts to provide the comparison shown in Fig. 8.21. This is seen to overestimate the relaxation results and along with Eq. 8.89 is much less effective than the strain-hardening approach of Eq. 8.90.

In general, it appears that the strain-hardening theory is better than the time-hardening theory in estimating relaxation behavior from creep data.

REFERENCES

1. I. A. Oding, V. S. Ivanova, V. V. Burdukskii, and V. N. Geminox, *Creep and Stress Relaxation in Metals*, I. A. Oding (Ed.), Oliver & Boyd, Edinburgh, 1965.
2. W. E. Trumpler, Jr., Relaxation of Metals at High Temperatures, *J. Appl. Phys.*, 12: 248 (1941).
3. J. B. Conway, Relaxation Analysis, unpublished notes, 1972.
4. J. Boyd, Discussion on Robinson Paper, *Trans. ASME (Amer. Soc. Mech. Eng.)*, 61: 551 (1939).
5. J. C. Maxwell, *Phil. Mag.*, 35(4): 129 (1868).
6. I. A. Oding and V. Z. Tseitlin, *Dokl. Akad. Nauk SSSR*, 5: 71 (1950).
7. E. L. Robinson, A Relaxation Test on 0.35C Steel K-20, *Trans. ASME (Amer. Soc. Mech. Eng.)*, 59: 451 (1937).
8. E. L. Robinson, The Resistance to Relaxation of Materials at High Temperature, *Trans. ASME (Amer. Soc. Mech. Eng.)*, 61: 543 (1939).
9. J. J. Kanter, Interpretation and Use of Creep Results, *Trans. Amer. Soc. Metals*, 24: 900 (1936).
10. E. L. Robinson, High-Temperature Bolting Materials, *Amer. Soc. Test. Mater., Proc.*, 48: 214 (1948).
11. J. W. Freeman and H. R. Voorhees, *Relaxation Properties of Steels and Super-Strength Alloys at Elevated Temperatures*, American Society for Testing and Materials, Special Technical Publication No. 187, 1956.
12. D. L. Newhouse, B. R. Seguin, and E. M. Lape, Some 12 Percent Chromium Alloys for 1000°F to 1200°F Operation, *Trans. ASME (Amer. Soc. Mech. Eng.)*, 76: 1107 (1954).
13. A. E. Johnson, Pipe Flanges Research Committee, Third Report, *Proc. Inst. Mech. Eng. (London)*, 168: 423 (1954).
14. A. I. Smith, D. J. Armstrong, M. F. Day, and L. M. T. Hopkin, Stress-Relaxation Properties of Bolt Steels Subjected to Repeated Straining, in *Joint International Conference on Creep*, 1963, New York and London, Paper 5, p. 6-1, The Institution of Mechanical Engineers, London, 1963.
15. J. H. M. Draper, Creep-Relaxation Testing, *Engineering*, 179: 564 (1955).
16. A. I. Smith, E. A. Jenkinson, D. J. Armstrong, and M. F. Day, Creep, Stress-Relaxation, and Metallurgical Properties of Steels for Steam Power Plant Operating with Steam Temperatures Above 950°F (510°C), *Proc. Inst. Mech. Eng. (London)*, 171: 918 (1957).
17. C. R. Kennedy and and D. A. Douglas, Relaxation Characteristics of Inconel at Elevated Temperatures, USAEC Report ORNL-2407, Oak Ridge National Laboratory, 1960.
18. M. J. Manjoine, Measuring Stress Relaxation Using a Compliance Method, *J. Mater.*, 6(2): 253 (June 1971).
19. J. H. Gittus, Implications of Some Data on Relaxation Creep in Nimonic 80A, *Phil. Mag.*, 9: 749 (1964).
20. R. Taylor and A. T. Jeffs, The Effect of Irradiation on Stress Relaxation in Nimonic 80A, *J. Nucl. Mater.*, 19: 142 (1966).
21. J. B. Conway, An Analysis of the Relaxation Behavior of AISI 304 and 316 Stainless Steel at Elevated Temperature, USAEC Report GEMP-730, General Electric Company, Nuclear Systems Programs, 1969.
22. P. Feltham, Stress Relaxation in Copper and Alpha Brasses at Low Temperatures, *J. Inst. Metals*, 89: 210 (1960–1961).
23. J. Kubát, *Proceedings of the Second International Congress on Rheology*, p. 178, Butterworths Scientific Publications, London, 1954.
24. G. A. Sargent and B. J. Shaw, Stress Relaxation and the Ductile–Brittle Transition Temperature of Molybdenum, *Acta Met.*, 14: 909 (1966).
25. G. A. Sargent and H. Conrad, Stress Relaxation and Thermally Activated Deformation in Titanium, *Scr. Met.*, 3: 43 (1969).
26. F. W. Noble and D. Hull, Stress Dependence of Dislocation Velocity from Stress-Relaxation Measurements, *Acta Met.*, 12: 1089 (1964).
27. D. F. Stein and J. R. Low, Jr., Mobility of Edge Dislocations in Silicon–Iron Crystals, *J. Appl. Phys.*, 31: 362 (1960).
28. A. A. Solomon and W. D. Nix, Interpretation of High-Temperature Plastic Deformation in Terms of Measured Effective Stresses, *Acta Met.*, 18: 863 (1970).
29. J. C. M. Li, Dislocation Dynamics in Deformation and Recovery, *Can. J. Phys.*, 45: 493 (1967).
30. H. D. Guberman, Stress Dependence of Dislocation Velocity in Single Crystal Niobium, *Acta Met.*, 16: 713 (1968).
31. E. Krempl and C. D. Walker, Effect of Creep-Rupture Ductility and Hold Time on the 1000°F Strain–Fatigue Behavior of a 1Cr–1Mo–0.25V Steel, American Society for Testing and Materials, Special Technical Publication No. 459, 1959.
32. D. Lee and E. W. Hart, Stress Relaxation and Mechanical Behavior of Metals, *Met. Trans.*, 2: 1245 (1971).
33. C. R. Soderberg, The Interpretation of Creep Tests for Machine Design, *Trans. ASME, (Amer. Soc. Mech. Eng.)*, 58: 733 (1936).
34. C. C. Davenport, Discussion of Soderberg Paper, *Trans. ASME, (Amer. Soc. Mech. Eng.)*, 59: 511 (1937).
35. I. Roberts, Correlation of Tension Creep Tests with Relaxation Tests, *J. Appl. Mech.*, 71: 208 (1949).

36. C. C. Davenport, Correlation of Creep and Relaxation Properties of Copper, *J. Appl. Mech.*, 60: A-55 (1938).
37. E. A. Davis, Creep and Relaxation of Oxygen-Free Copper, *J. Appl. Mech.*, 65: A-101 (1943).
38. I. Finnie and W. R. Heller, *Creep of Engineering Materials*, McGraw-Hill Book Company, Inc., New York, 1959.
39. P. G. McVetty, Working Stresses for High-Temperature Service, *Mech. Eng.*, 56: 149 (1934).
40. E. P. Popov, Correlation of Tension Creep Tests with Relaxation Tests, *J. Appl. Mech.*, 69: A-135 (1947).
41. I. Roberts, Prediction of Relaxation of Metals from Creep Data, *Amer. Soc. Testing Mater., Proc.*, 51: 811 (1951).

Appendix

CONVERSION TABLE

To convert from	To	Multiply by
Atmospheres (atm)	Pounds per square inch (psi)	14.7
Centimeters (cm)	Feet (ft)	0.03281
	Inches (in.)	0 3937
Centimeters per second (cm/sec)	Feet per second (ft/sec)	0.03281
Cubic centimeters (cm^3)	Cubic feet (ft^3)	3.531×10^{5}
	Cubic inches (in^3)	0.06103
Grams (g)	Pounds (lb)	0.002205
Grams per square centimeter (g/cm^2)	Pounds per square inch (psi)	0.01422
Kilograms (kg)	Pounds (lb)	2.205
Kilograms per square centimeter (kg/cm^2)	Atmospheres (atm)	0.9678
	Pounds per square foot (lb/ft^2)	2048
	Pounds per square inch ($lb/in.^2$)	14.22
	Newtons per square meter (N/m^2)	98,066
Kilograms per square millimeter (kg/mm^2)	Pounds per square inch (psi)	1422 32
Kilograms per square meter (kg/m^2)	Newtons per square meter (N/m^2)	9 806
Pounds per square foot (lb/ft^2)	Newtons per square meter (N/m^2)	47.88
Pounds per square inch (psi)	Newtons per square meter (N/m^2)	6,895
	Meganewtons per square meter (MN/m^2)	0.006895
Meters (m)	Inches (in.)	39.37
Meters per second (m/sec)	Feet per second (ft/sec)	3.281
Millimeters of mercury (mm Hg)	Atmospheres (atm)	0.001316
	Newtons per square meter (N/m^2)	133.3
Square centimeters (cm^2)	Square feet (ft^2)	0.001076
	Square inches ($in.^2$)	0.155
Tons, long (long tons)	Kilograms (kg)	1016
Tons, metric (metric tons)	Kilograms (kg)	1000
Tons, short, 2000 lb (tons)	Kilograms (kg)	907
Tons, short, per square foot ($tons/ft^2$)	Pounds per square inch (psi)	13.89
	Pounds per square foot (lb/ft^2)	2000
	Kilograms per square centimeter (kg/cm^2)	0 9765
	Millimeters of mercury (mm Hg)	718.26
Torrs	Millimeters of mercury (mm Hg)	1.0
	Atmospheres (atm)	0.001316
	Newtons per square meter (N/m^2)	133.3

Index

Prepared by James R Dulaney, Science and Technology Branch, Technical Information Center, U S. Atomic Energy Commission.

NUCLEAR SCIENCE ABSTRACTS

Nuclear Science Abstracts, a semimonthly publication of the U. S Atomic Energy Commission, provides the only comprehensive abstract ing and indexing coverage of the international nuclear science literature It covers scientific and technical reports of the AEC and its contractors, other U S Government agencies, other governments, universities, and industrial and research organizations In addition, books, conference proceedings, individual conference papers, patents, and journal litera ture on a worldwide basis are abstracted and indexed

SUBSCRIPTIONS AND PRICES

Nuclear Science Abstracts is available to the public on a subscription basis from the Superintendent of Documents, U S Government Printing Office, Washington, D C 20402. It is published in two volumes each calendar year, each volume containing 12 regular issues The annual subscription rate for the two volumes is $121 05 for domestic subscribers and $151.35 for foreign subscribers A single issue costs $5 05 domestic rates or $6.35 foreign rates Domestic rates apply to the United States, Canada, Mexico, and Cen tral and South American countries except Argentina, Brazil, Guyana, French Guiana, Surinam, and British Honduras

INDEXES

Indexes covering subject, author, corporate author, and report number are included in each issue These indexes are cumulated for each volume, i e , for 12 issues on a 6-month volume basis They are sold on an annual subscription basis (24 issues in 2 volumes) at $44 40 for domestic subscribers and $55 50 for foreign subscribers They are also sold separately by volume on the basis of pagination at the time of publication. The indexes provide a detailed and convenient key to the world's nuclear literature

EXCHANGES

Nuclear Science Abstracts is available on an exchange basis to universities, research institutions, industrial firms, and publishers of scientific information, in quiries regarding the exchange provision should be directed to the USAEC Tech nical Information Center, P O Box 62, Oak Ridge, Tennessee 37830.

Technical Information Center, Office of Information Services
UNITED STATES ATOMIC ENERGY COMMISSION